

Finite Element Modeling of Pretensioned Concrete Girders: A Methodological Approach with Applications in Large Strands and End Zone Cracking

By Amir A. Arab

B.S. in Civil Engineering, August 1995, Southern Illinois University-Edwardsville
M.S. in Structural Engineering, May 2000, Southern Illinois University-Edwardsville

A Dissertation submitted to

The Faculty of
The School of Engineering and Applied Science
of The George Washington University
in partial satisfaction of the requirements
for the degree of Doctor of Philosophy

May 20, 2012

Dissertation directed by

Sameh S. Badie
Associate Professor of Civil Engineering

Majid T. Manzari
Professor of Civil Engineering

UMI Number: 3503026

All rights reserved

INFORMATION TO ALL USERS

The quality of this reproduction is dependent on the quality of the copy submitted.

In the unlikely event that the author did not send a complete manuscript and there are missing pages, these will be noted. Also, if material had to be removed, a note will indicate the deletion.



UMI 3503026

Copyright 2012 by ProQuest LLC.

All rights reserved. This edition of the work is protected against unauthorized copying under Title 17, United States Code.



ProQuest LLC.
789 East Eisenhower Parkway
P.O. Box 1346
Ann Arbor, MI 48106 - 1346

The School of Engineering and Applied Science of The George Washington University certifies that Amir A. Arab has passed the Final Examination for the degree of Doctor of Philosophy as of March 9, 2012. This is the final and approved form of the dissertation.

Finite Element Modeling of Pretensioned Concrete Girders: A Methodological Approach with Applications in Large Strands and End Zone Cracking

Amir A. Arab

Dissertation Research Committee:

Sameh S. Badie, Associate Professor of Civil Engineering, Dissertation Co-Director

Majid T. Manzari, Professor of Civil Engineering, Dissertation Co-Director

Kim Roddis, Professor of Civil Engineering, Committee Chair

Pedro F. Silva, Associate Professor of Civil Engineering, Committee Member

Waseem Dekelbab, Senior Program Officer of the National Cooperative Highway Research Program, Committee Member

Dedications

I dedicate this dissertation to:

My lovely wife, Behnoush, who is the light of my life. So bright and so warm. This dream has come true because of her love and encouragements.

My son, Aryan, so dear and so close. With the hope that he also aims high in his life and follows his dreams, no matter how impossible.

To my parents, Elaheh and Hossein, who gave me the vision. I will always be grateful for their unconditional love and support.

Acknowledgements

I would like to thank my advisors and mentors, Dr. Sameh S. Badie and Dr. Majid T. Manzari, for their patience, guidance and continuous support. What I have learned from them goes beyond the limits of this research, which has profoundly affected my academic and professional career.

I would like to thank all my committee members for their guidance and support.

I would like to thank the George Washington University - Department of Civil and Environmental Engineering for providing me the opportunity to follow my academic and professional goals.

I would like to thank Dr. Amin Akhnoukh for his support by generously sharing the results of his research pertaining to the application of 0.7-in. diameter.

And finally, I would like to express my deepest gratitude to Dr. Bijan Khaleghi at the Washington Department of Transportation, Stephen J. Seguirant and Dave Chapman at Concrete Technology Corporation for their support and collaboration regarding the investigation of end zone cracking in Washington super-girders.

Abstract

Finite Element Modeling of Pretensioned Concrete Girders: A Methodological Approach with Applications in Large Strands and End Zone Cracking

Two issues pertaining to the current state of pretensioning industry are investigated in this research: spacing of 0.7-in. diameter strands and effectiveness of end zone reinforcing details.

Given the current economic constraints and the limitation of testing facilities, there is a great need for reliable and unified methodological approaches for simulation of the behavior of pretensioned concrete members to complement experimental investigations. Therefore, two finite element techniques are evaluated: extrusion and embedment techniques. Once the techniques are verified and validated against closed form solutions and experimental data, respectively, they are utilized for analytical purposes of this research.

Extrusion technique is utilized to show that 0.7-in. diameter strands can be potentially spaced at reduced spacing of 2-in. on center under certain conditions including minimum concrete compressive strength of 10,000 psi at the time of release.

Embedment technique is utilized for comparative investigation of four end zone reinforcing details: AASHTO LRFD , NCHRP Report 654, Illinois and combined AASHTO-Illinois details. The research indicates that NCHRP Report 654 offers an optimum end zone remedial scheme for typical AASHTO/PCI bulb-tee girders. Without requiring any additional reinforcement in comparison to AASHTO LRFD, it results in fabrication-friendly rebar spacing.

Finally, eight Washington WF100 Super-girders are instrumented and investigated for potential end zone cracking as part of the Alaskan Viaduct Project in the state of Washington. Each girder is 100 in. deep and over 200 ft long among the largest precast girders in North America at the time of this research. The instrumentation set-up is intended for on-site collection of strain data at the end zone reinforcing bars and the 0.6-in. diameter strands. The experimental observations indicate that the response of the super-girders at release is similar to other I-girders commonly used in practice. In addition, all eight girders experienced different levels of end zone cracking most severely along the web-bottom flange interface.

A new closed-form solution is proposed and validated against the experimental results, based on the shear-friction theory to estimate the tensile cracking at the web-bottom flange interface of precast I-girders immediately after the release of pretensioning.

Table of Contents

DEDICATIONS.....	iii
ACKNOWLEDGEMENTS.....	iv
ABSTRACT.....	v
LIST OF FIGURES	xiii
LIST OF TABLES	xlvi
CHAPTER 1 -INTRODUCTION.....	1
1.1. RESEARCH OBJECTIVES.....	1
1.2. RESEARCH SIGNIFICANCE.....	5
1.3. DISSERTATION OUTLINE.....	7
CHAPTER 2 -NOTATION & DEFINITIONS.....	12
CHAPTER 3 -A METHODOLOGICAL APPROACH FOR FINITE ELEMENT MODELING OF PRETENSIONED CONCRETE GIRDERS.....	38
3.1. OBJECTIVES.....	38
3.2. LITERATURE REVIEW	39
3.2.1. Concrete: Fundamental Properties.....	39
3.2.1. Poisson's Ratio	40
3.2.2. Concrete in Uniaxial Compression	41
3.2.3. Concrete in Uniaxial Tension.....	43
3.2.4. Fracture Mechanics.....	48
3.2.4.1. Maximum-Tensile-Stress Criterion (Rankine)	49
3.2.4.2. Shearing-Stress Criterion (Tresca & Von Mises).....	50
3.2.5. Finite Element Modeling of Pretensioned Concrete Members.....	52
3.3. OVERVIEW OF PRETENSIONING MECHANISM	62
3.3.1. Adhesion.....	62
3.3.2. Hoyer's (Wedging) Effect.....	65
3.3.3. Mechanical Interlocking.....	69

3.4.	MODELING APPROACHES	71
3.4.1.	<i>Material Simulation: Concrete Damage Plasticity Constitutive Model</i>	78
3.4.1.1.	<i>Degradation Damage</i>	82
3.4.1.2.	<i>Stiffness Degradation and Recovery Under Cyclic Loading</i>	83
3.4.2.	<i>Finite Element Techniques</i>	88
3.4.2.1.	<i>Extrusion Technique</i>	88
3.4.2.1.1.	<i>Contact Formulation: Tangential Behavior</i>	90
3.4.2.1.2.	<i>Contact Formulation: Normal Behavior</i>	91
3.4.2.2.	<i>Embedment Technique</i>	92
3.4.3.	<i>Simulation of Pretensioning</i>	94
3.4.4.	<i>Simulation of Casting Bed</i>	95
3.5.	METHOD VERIFICATION BASED ON SIMULATION OF MONO-STRAND RECTANGULAR BEAMS	95
3.5.1.	<i>Introduction</i>	95
3.5.2.	<i>Calibration of Constitutive Models</i>	96
3.5.2.1.	<i>Calibration of Concrete Constitutive Model</i>	96
3.5.2.2.	<i>Constitutive Parameters for Prestressing Strands and Other Structural Steel</i>	101
3.5.3.	<i>Finite Element Models</i>	101
3.6.	DISCUSSION OF RESULTS	104
3.6.1.	<i>Rectangular Beam with One Concentric Strand</i>	104
3.6.2.	<i>Rectangular Beam with One Eccentric Strand</i>	110
 CHAPTER 4 - RESPONSE OF PRETENSIONED CONCRETE BEAMS TO 0.7-IN. DIAMETER PRESTRESSING STRANDS WITH EXPERIMENTAL VERIFICATION		117
4.1.	OBJECTIVES & RESEARCH BACKGROUND	117
4.2.	LITERATURE REVIEW	120
4.2.1.	<i>0.7-in. Diameter Prestressing Strands: Transfer Length and Confinement</i>	120
4.2.2.	<i>0.7-in. Diameter Prestressing Strands: Spacing of prestressing strands</i>	122
4.3.	RECTANGULAR BEAMS WITH ONE CONCENTRIC PRETENSIONED 0.7-INCH DIAMETER STRAND	123
4.3.1.	<i>Finite Element Models</i>	123

4.3.2. <i>Material Calibration & Sectional Properties</i>	133
4.3.3. <i>Comparative Analysis of Results Based on Closed Form Solutions</i>	134
4.3.4. <i>Comparative Analysis of Results Based on Experimental Data</i>	137
4.4. RECTANGULAR BEAMS WITH NINE PRETENSIONED 0.7-INCH DIAMETER STRANDS	141
4.4.1. <i>Finite Element Models</i>	141
4.4.2. <i>Material Calibration & Sectional Properties</i>	155
4.4.3. <i>Comparative Analysis of Results Based on Closed Form Solutions</i>	156
4.4.4. <i>Discussion of Results</i>	160
4.4.4.1. <i>Transfer Length</i>	161
4.4.4.2. <i>Stress Analysis</i>	168
CHAPTER 5 -END ZONE CRACKING	198
5.1. INTRODUCTION.....	198
5.2. LITERATURE REVIEW	200
5.2.1. <i>Classification of End-Zone Tensile Cracks</i>	206
5.2.2. <i>End Zone Design of Pretensioned Concrete Members</i>	212
5.2.2.1. <i>Gergley-Sozen Model</i>	217
5.2.2.2. <i>Strut-and-Tie Model</i>	219
5.3. PROBLEM STATEMENT	221
5.3.1. <i>AASHTO/PCI Bulb-Tee</i>	222
5.3.1.1. <i>Jacking Stresses</i>	226
5.3.1.2. <i>Prestress Losses at Transfer</i>	228
5.3.1.3. <i>Top and Bottom Fiber Stresses Immediately After Release of Pretensioning</i>	228
5.3.2. <i>End Zone Reinforcement</i>	229
5.3.2.1. <i>AASHTO LRFD Details</i>	230
5.3.2.2. <i>Nebraska Details</i>	234
5.3.2.3. <i>IDOT Details</i>	237
5.3.2.4. <i>Modified IDOT-AASHTO Details</i>	239
5.4. NUMERICAL MODELING	239

5.4.1. Constitutive Models.....	240
5.4.2. Simulation of the Composite Interaction between Concrete and Prestressing Strands and Other Reinforcement.....	240
5.4.3. Simulation of Pretensioning.....	241
5.4.4. Transfer Length.....	242
5.4.5. Simulation of Casting Bed.....	243
5.5. NUMERICAL SIMULATIONS.....	246
5.5.1. Calibration of Material Constitutive Models.....	246
5.5.2. BT-72 FE Model without End Zone, Shear and Confinement Reinforcement.....	247
5.5.3. BT-72 FE Model with AASHTO LRFD End Zone Reinforcing Details in Addition to Shear and Confinement Reinforcement.....	260
5.5.4. BT-72 FE Model with Nebraska End Zone Reinforcing Details in Addition to Shear and Confinement Reinforcement.....	278
5.5.5. BT-72 Model with IDOT End Zone Reinforcing Details in Addition to Shear and Confinement Reinforcement.....	296
5.5.6. BT-72 Model with Modified IDOT-AASHTO End Zone Reinforcing Details in Addition to Shear and Confinement Reinforcement.....	314
5.6. COMPARISON OF RESULTS.....	332
CHAPTER 6 -ANALYTICAL STUDY OF EIGHT WSDOT BWF100 SUPER-GIRDERS WITH EXPERIMENTAL VERIFICATION.....	344
6.1. INTRODUCTION.....	344
6.2. WSDOT BWF100 SUPER-GIRDERS.....	350
6.3. EXPERIMENTAL INVESTIGATIONS.....	356
6.3.1. Test Specimens.....	356
6.3.2. Guidelines for Installation of Strain Gages.....	361
6.3.2.1. Strain Gages.....	361
6.3.2.2. Grinder.....	362
6.3.2.3. Chemical Solutions for Surface Preparation.....	363

6.3.2.4. Strain Gage Adhesive	363
6.3.2.5. Coating Agents.....	364
6.3.3. Installation Steps	366
6.3.4. Data Acquisition.....	370
6.3.5. Experimental Observations	400
6.3.5.1. End Zone Cracking.....	400
6.3.5.2. Transfer Length	402
6.3.5.3. Web Tie Bars	404
6.4. ANALYTICAL SOLUTIONS	405
6.4.1. Closed-Form Solutions.....	405
6.4.1.1. Gregly-Sozen Method	405
6.4.1.2. Strut-and-Tie Approach.....	409
6.4.1.3. Shear-Friction Analogy for Bursting Effects	413
6.4.2. Numerical Modeling.....	416
6.4.2.1. Constitutive Models	416
6.4.2.2. Simulation of the Composite Interaction Between Concrete and Prestressing Strands and Other Reinforcement.....	418
6.4.2.3. Simulation of Pretensioning.....	418
6.4.2.4. Transfer Length	420
6.4.3. Calibration of Material Constitutive Models.....	420
6.4.4. Numerical Simulations	422
6.5. COMPARISON OF RESULTS.....	436
CHAPTER 7 - CONCLUSIONS AND RECOMMENDATIONS FOR FUTURE RESEARCH.....	439
7.1. CONCLUDING REMARKS.....	439
7.2. RECOMMENDATIONS FOR FUTURE RESEARCH.....	447
REFERENCES	449
APPENDIX A: Sample Finite Element Code (Abaqus) for 6"x6" Rectangular Beams Pretensioned with One Concentric or Eccentric 0.6-in. Diameter Strand Based on Extrusion Technique	455

APPENDIX B: Sample Finite Element Code (Abaqus) for 6"X6" Rectangular Beams Pretensioned with One Concentric or Eccentric 0.6-in. Diameter Strand Based on Embedment Technique	473
APPENDIX C: Closed-Form Solution for 6"X6" Rectangular Beams Pretensioned with One Concentric or Eccentric 0.6-in. Diameter Strand	485
APPENDIX D: Closed-Form Solution for a 7"X7" Rectangular Beam Concentrically Pretensioned with One 0.7-in. Diameter Strand	498
APPENDIX E: Closed-Form Solution for a 7"X7" Rectangular Beam Concentrically Pretensioned with Nine 0.7-in. Diameter Strand	505
APPENDIX F: Experimental Data Related to Transfer Length.....	512
APPENDIX G: Gregly-Sozen Model @ $L_t = 36$ in.	517
APPENDIX H: Strut-&-Tie Model @ $h = 100$ in.	525
APPENDIX I: Shear-Friction Model @ $h = 100$ in.	527
APPENDIX J: Theoretical Stress Profile Based on Linear-Elastic Beam Theory	533

List of Figures

Chapter 1

Figure 1- 1: Research outline 8

Chapter 3

Figure 3-1: Relationship between stress-strength and Poisson's ration (Chen, Plasticity in Reinforced Concrete, 2007). 41

Figure 3-2: Typical compressive stress-strain curves for concretes with various compressive strengths (Collins & Mitchell, 1997). 43

Figure 3-3: Stress-strain relationships for high-strength concrete in uniaxial tension (Li & Ansari, 1999). 44

Figure 3-4: Common methods of estimating tensile strength of concrete (Collins & Mitchell, 1997). 46

Figure 3-5: Tensile stress-strain relationship for concrete with curvilinear tension softening (Piyasena, 2002). 47

Figure 3-6: Theoretical triaxial failure space of concrete. Adapted from (Chen, Plasticity in Reinforced Concrete, 2007). 49

Figure 3-7: Definition of angle of similarity, θ (Chen, Plasticity in Reinforced Concrete, 2007). 50

Figure 3-8: Tresca and Van Mises shearing stress criteria with inner and outer bounds (Chen, Plasticity in Reinforced Concrete, 2007). 52

Figure 3-9: Finite element solutions for load-deflection responses of pretensioned concrete railway sleepers by Kaewunruen and Remennikov (2006). 55

Figure 3-10: Load mid displacement curve by Rabczuk and Eibl (2004): (a) Beam I with bending failure and (b) Beam II with shear failure.....	57
Figure 3-11: Test specimens used for the analytical purposes by Ayoub and Filippou (2010).....	59
Figure 3-12: Analytical distribution of tensile force in the strands during the prestressing by Ayoub and Filippou (2010).....	59
Figure 3-13: Comparison of straining of strands by Ayoub and Filippou (2010): (a) the experimental results and (b) the corresponding finite element simulations.	61
Figure 3-14: Schematic stages of bond strength provided by adhesion between prestressing strands and concrete before and after slippage. Adapted from (Russell & Burns, 1996).....	62
Figure 3- 15: Schematic stages of bond strength provided by adhesion between prestressing strands and concrete before and after slippage. Adapted from (Russell & Burns, 1996).....	65
Figure 3-16: Pretensioning mechanism - Hoyer's (wedging) effect. Adapted from (Russell & Burns, 1996).....	66
Figure 3-17: Idealized transfer and development lengths in accordance with AASHTO LRFD. Adapted from (AASHTO LRFD, 2010).....	68
Figure 3- 18: Transfer and development lengths for pretensioned concrete members (Nilson, 1987).	69
Figure 3- 19: Typical 7-wire strands with helical formation.	70
Figure 3-20: Mechanical interlocking between concrete host and pretensioned strand upon being released: (a) Typical seven-wire strand undergoing twisting	

immediately after being released, and (b) Concrete matrix in the vicinity of the released strand under radial stresses imposed by the twisted strand.	71
Figure 3-21: Barcelona yield function in plane stress state.	81
Figure 3-22: Stiffness degradation of concrete under uniaxial: (a) tension and (b) compression (ABAQUS, 2010).	86
Figure 3-23: Response of concrete to triaxial compressive loading (Palaniswamy & Shah, 1974).	87
Figure 3-24: Volumetric strain of concrete under biaxial compression (Kupfer, Hilsdorf, & Rusch, 1969).	88
Figure 3-25: Typical three-dimensional 8-node linear brick element used for simulation of concrete continua.	89
Figure 3- 26: Typical schemes of finite element modeling of pretensioned concrete members using extrusion technique.	90
Figure 3-27: Schematic presentation of the techniques used for simulation of slippage surface upon releasing the strands: (a) Concrete-over-concrete slippage and (b) Steel-over-concrete slippage.	93
Figure 3- 28: Schematic presentation of finite element modeling of pretensioned concrete members using embedment technique.	93
Figure 3-29: Comparison of the stress-strain relationships obtained by the constitutive model with the theoretical stress-strain curves assumed for a concrete with initial compressive strength of $f'_{ci} = 5,800$ psi: a) subject due to uniaxial compression, and (b) subject to uniaxial tension.	100

Figure 3-30: Typical finite element models for simulation of rectangular beams with one prestressing strand supported on casting bed: (a) Extruded model, and (b) Embedded model.....	104
Figure 3-31: Schematic presentation of the analytical model with strand eccentricity parameter (e_p) relative to the center of gravity of the member.	104
Figure 3-32: Response of extruded models to concentric pretensioning based on various coefficients of friction at the slippage surface: (a) Coefficient of friction of $\mu=0.70$, and (b) Coefficient of friction of $\mu=1.40$	106
Figure 3-33: Axial pretensioning stress in the concentric strands immediately after the release (including elastic shortening losses).	107
Figure 3-34: Sample results for concentrically pretensioned specimens with friction-based contact formulation: (a) axial strain the strand after the release, (b) contact pressure at the interface between concrete host and strand, and (c) surface shear stresses at the interface between concrete and strand.	109
Figure 3-35: Concrete mesh sensitivity at interface with the pretensioned strand (extruded model with one concentric strand).	110
Figure 3-36: Longitudinal stress S33 measured at the extreme top fiber along the extruded member, corresponding to two levels of contact friction at the interface between the strand and concrete host: $\mu_f = 0.70$ and 1.40 . Response of an equivalent embedded model is also shown based on AASHTO LRFD linearized pretensioning.	112
Figure 3-37: Vertical stress contours for embedded model with one eccentric strand with coefficient of friction $\mu = 0.7$ at the following distances from the end face of the	

rectangular beam: (a) 0 in, (b) 3 in., (c) 6 in., (d) 12 in., (e) 36 in (Theoretical Transfer Length) and (f) 48 in. (Mid-span)	114
Figure 3-38: Vertical stress contours for embedded model with one eccentric strand with coefficient of friction $\mu = 1.4$ at the following distances from the end face of the rectangular beam: (a) 0 in, (b) 3 in., (c) 6 in., (d) 12 in., (e) 36 in (Theoretical Transfer Length) and (f) 48 in. (Mid-span)	115
Figure 3-39: Vertical stress distribution for embedded model with one eccentric strand along the span and at the following distances from the end face of the rectangular beam:.....	116
Chapter 4	
Figure 4-1: Typical experimental specimen with DEMEC discs on the outside faces to facilitate measurement of straining after the release of pretensioning (Akhnoukh, 2008).	119
Figure 4-2: Details of Class I [1-8L-3] finite element models.....	125
Figure 4-3: Details of Class I [1-8L-6] finite element models.....	126
Figure 4-4: Details of Class I [1-8L-9] finite element models.....	127
Figure 4-5: Details of Class I [1-8L-12] finite element models.....	128
Figure 4-6: Typical finite element model with embedded pretensioned strands and ties: (a) Concrete beam modeled as continuum elements, and (b) strands and ties modeled as truss and beam elements, respectively.....	129
Figure 4-7: Typical finite element model with extruded pretensioned strands and embedded ties: (a) Concrete beam modeled as continuum elements, and (b) strands and ties modeled as solid and beam elements, respectively.	130

Figure 4-8: Transfer length simulation for the finite element models with embedded strands: (a) 1-L8-3, (b) 1-8L-6, (c) 1-8L-9, and (d) 1-8L-12.....	132
Figure 4-9: Comparison of experimental measurements for strains versus the corresponding finite element results for 7-in. prisms confined with No.3 close stirrups spaced at 3 in. on center (Model 1-8L-3).....	138
Figure 4-10: Comparison of experimental measurements for strains versus the corresponding finite element results for 7-in. prisms confined with No.3 close stirrups spaced at 6 in. on center (Model 1-8L-6).....	139
Figure 4-11: Comparison of experimental measurements for strains versus the corresponding finite element results for 7-in. prisms confined with No.3 close stirrups spaced at 9 in. on center (Model 1-8L-9).....	139
Figure 4-12: Effect of confinement on transfer length (results of finite element models with embedded strands versus test data).....	140
Figure 4-13: Details of Class I [S280-U070-C3; S280-U140-C3] finite element models: (a) Typical cross section, (b) Finite element simulation, and (c) Layout of confinement reinforcement (No.3 closed stirrups spaced at 3 in. on center).....	145
Figure 4-14: Details of Class I [S280-U070-C6; S280-U140-C6] finite element models: (a) Typical cross section, (b) Finite element simulation, and (c) Layout of confinement reinforcement (No.3 closed stirrups spaced at 6 in. on center).....	146
Figure 4-15: Details of Class I [S280-U070-C9; S280-U140-C9] finite element models: (a) Typical cross section, (b) Finite element simulation, and (c) Layout of confinement reinforcement (No.3 closed stirrups spaced at 9 in. on center).....	147

Figure 4-16: Details of Class I [S280-U070-C12; S280-U140-C12] finite element models: (a) Typical cross section, (b) Finite element simulation, and (c) Layout of confinement reinforcement (No.3 closed stirrups spaced at 12 in. on center).....	148
Figure 4-17: Details of Class II [S200-U070-C3; S200-U140-C3] finite element models: (a) Typical cross section, (b) Finite element simulation, and (c) Layout of confinement reinforcement (No.3 closed stirrups spaced at 3 in. on center).....	151
Figure 4-18: Details of Class II [S200-U070-C6; S200-U140-C6] finite element models: (a) Typical cross section, (b) Finite element simulation, and (c) Layout of confinement reinforcement (No.3 closed stirrups spaced at 6 in. on center).....	152
Figure 4-19: Details of Class II [S200-U070-C9; S200-U140-C9] finite element models: (a) Typical cross section, (b) Finite element simulation, and (c) Layout of confinement reinforcement (No.3 closed stirrups spaced at 9 in. on center).....	153
Figure 4-20: Details of Class II [S200-U070-C12; S200-U140-C12] finite element models: (a) Typical cross section, (b) Finite element simulation, and (c) Layout of confinement reinforcement (No.3 closed stirrups spaced at 12 in. on center).....	154
Figure 4-21: Comparison of axial strains (transfer length) of Class I (nine 0.7-in. diameter strands spaced at 2.80 in. on center) and Class II finite element simulation of concrete beams (nine 0.7-in. diameter strands spaced at 2.00 in. on center) with no confinement reinforcement.	162
Figure 4-22: Comparison of axial strains (transfer length) of Class I (nine 0.7-in. diameter strands spaced at 2.80 in. on center) and Class II finite element simulation of concrete beams (nine 0.7-in. diameter strands spaced at 2.00 in. on center) confined with No.3 closed stirrups spaced at 3.00 in. on center. Note that the experimental	

data corresponds to 7 in. x 7 in. x 8 ft prisms with one concentric 0.7-in. diameter strand (Akhnoukh, 2008).	163
Figure 4-23: Comparison of axial strains (transfer length) of Class I (nine 0.7-in. diameter strands spaced at 2.80 in. on center) and Class II finite element simulation of concrete beams (nine 0.7-in. diameter strands spaced at 2.00 in. on center) confined with No.3 closed stirrups spaced at 6.00 in. on center. Note that the experimental data corresponds to 7 in. x 7 in. x 8 ft prisms with one concentric 0.7-in. diameter strand (Akhnoukh, 2008).	164
Figure 4-24: Comparison of axial strains (transfer length) of Class I (nine 0.7-in. diameter strands spaced at 2.80 in. on center) and Class II finite element simulation of concrete beams (nine 0.7-in. diameter strands spaced at 2.00 in. on center) confined with No.3 closed stirrups spaced at 9.00 in. on center. Note that the experimental data corresponds to 7 in. x 7 in. x 8 ft prisms with one concentric 0.7-in. diameter strand (Akhnoukh, 2008).	165
Figure 4-25: Comparison of axial strains (transfer length) of Class I (nine 0.7-in. diameter strands spaced at 2.80 in. on center) and Class II finite element simulation of concrete beams (nine 0.7-in. diameter strands spaced at 2.00 in. on center) confined with No.3 closed stirrups spaced at 12.00 in. on center. Note that the experimental data corresponds to 7 in. x 7 in. x 8 ft prisms with one concentric 0.7-in. diameter strand (Akhnoukh, 2008).	166
Figure 4-26: Comparison of axial strains (transfer length) of Class I (nine 0.7-in. diameter strands spaced at 2.80 in. on center) with various configurations of confinement reinforcement.	167

Figure 4-27: Comparison of axial strains (transfer length) of Class II (nine 0.7-in. diameter strands spaced at 2.00 in. on center) with various configurations of confinement reinforcement.	168
Figure 4-28: Typical local axis convention for the three-dimensional finite element models.....	169
Figure 4-29: Comparison of stresses obtained by Class I (nine 0.7-in. diameter strands spaced at 2.80 in. on center) and Class II (nine 0.7-in. diameter strands spaced at 2.00 in. on center) with no confinement: (a) Lateral Stresses (S11), and Vertical Stresses (S22).....	172
Figure 4-30: Comparison of stresses obtained by Class I (nine 0.7-in. diameter strands spaced at 2.80 in. on center) and Class II (nine 0.7-in. diameter strands spaced at 2.00 in. on center) confined with No.3 closed stirrups spaced at 3 in. on center: (a) Lateral Stresses (S11), and Vertical Stresses (S22).	174
Figure 4-31: Comparison of stresses obtained by Class I (nine 0.7-in. diameter strands spaced at 2.80 in. on center) and Class II (nine 0.7-in. diameter strands spaced at 2.00 in. on center) confined with No.3 closed stirrups spaced at 6 in. on center: (a) Lateral Stresses (S11), and Vertical Stresses (S22).	176
Figure 4-32: Comparison of stresses obtained by Class I (nine 0.7-in. diameter strands spaced at 2.80 in. on center) and Class II (nine 0.7-in. diameter strands spaced at 2.00 in. on center) confined with No.3 closed stirrups spaced at 9 in. on center: (a) Lateral Stresses (S11), and Vertical Stresses (S22).	178
Figure 4-33: Comparison of stresses obtained by Class I (nine 0.7-in. diameter strands spaced at 2.80 in. on center) and Class II (nine 0.7-in. diameter strands spaced at 2.00	

in. on center) confined with No.3 closed stirrups spaced at 12 in. on center: (a) Lateral Stresses (S11), and Vertical Stresses (S22).	180
Figure 4-34: The effect of confinement on the lateral stresses obtained by Class II (nine 0.7-in. diameter strands spaced at 2.00 in. on center) with contact friction coefficient $\mu_f = 1.40$	182
Figure 4-35: Comparison of maximum principal stresses obtained by Class I (nine 0.7-in. diameter strands spaced at 2.80 in. on center) and Class II (nine 0.7-in. diameter strands spaced at 2.00 in. on center) confined with No.3 closed stirrups spaced at 3 in. on center.	183
Figure 4-36: Comparison of pressure obtained by Class I (nine 0.7-in. diameter strands spaced at 2.80 in. on center) with various configuration of confinement reinforcement and upper slippage boundary ($\mu_f = 0.70$).	185
Figure 4-37: Comparison of pressure obtained by Class II (nine 0.7-in. diameter strands spaced at 2.00 in. on center) with various configuration of confinement reinforcement and upper slippage boundary ($\mu_f = 0.70$).	185
Figure 4-38: lateral stress (S11) contour at the end face of the specimens: (a) Class I Model (nine 0.7-in. diameter strands spaced at 2.80 in. on center) with contact friction coefficient of $\mu_f = 0.70$, (b) Class I Model (nine 0.7-in. diameter strands spaced at 2.80 in. on center) with contact friction coefficient of $\mu_f = 1.40$, (c) Class II Model (nine 0.7-in. diameter strands spaced at 2.00 in. on center) with contact friction coefficient of $\mu_f = 0.70$, and (d) Class II Model (nine 0.7-in. diameter strands spaced at 2.00 in. on center) with contact friction coefficient of $\mu_f = 1.40$	190

Figure 4-39: Lateral stress (S11.) contour at 6 in. from the end face of the specimens: (a) Class I Model (nine 0.7-in. diameter strands spaced at 2.80 in. on center) with contact friction coefficient of $\mu_f = 0.70$, (b) Class I Model (nine 0.7-in. diameter strands spaced at 2.80 in. on center) with contact friction coefficient of $\mu_f = 1.40$, (c) Class II Model (nine 0.7-in. diameter strands spaced at 2.00 in. on center) with contact friction coefficient of $\mu_f = 0.70$, and (d) Class II Model (nine 0.7-in. diameter strands spaced at 2.00 in. on center) with contact friction coefficient of $\mu_f = 1.40$ 191

Figure 4-40: Vertical stress (S22) contour at the end face of the specimens: (a) Class I Model (nine 0.7-in. diameter strands spaced at 2.80 in. on center) with contact friction coefficient of $\mu_f = 0.70$, (b) Class I Model (nine 0.7-in. diameter strands spaced at 2.80 in. on center) with contact friction coefficient of $\mu_f = 1.40$, (c) Class II Model (nine 0.7-in. diameter strands spaced at 2.00 in. on center) with contact friction coefficient of $\mu_f = 0.70$, and (d) Class II Model (nine 0.7-in. diameter strands spaced at 2.00 in. on center) with contact friction coefficient of $\mu_f = 1.40$ 192

Figure 4-41: Vertical stress (S22) contour at 6 in. from the end face of the specimens: (a) Class I Model (nine 0.7-in. diameter strands spaced at 2.80 in. on center) with contact friction coefficient of $\mu_f = 0.70$, (b) Class I Model (nine 0.7-in. diameter strands spaced at 2.80 in. on center) with contact friction coefficient of $\mu_f = 1.40$, (c) Class II Model (nine 0.7-in. diameter strands spaced at 2.00 in. on center) with contact friction coefficient of $\mu_f = 0.70$, and (d) Class II Model (nine 0.7-in. diameter strands spaced at 2.00 in. on center) with contact friction coefficient of $\mu_f = 1.40$ 193

Figure 4-42: Longitudinal stress (S33) contour at the end face of the specimens: (a) Class I Model (nine 0.7-in. diameter strands spaced at 2.80 in. on center) with contact

friction coefficient of $\mu_f = 0.70$, (b) Class I Model (nine 0.7-in. diameter strands spaced at 2.80 in. on center) with contact friction coefficient of $\mu_f = 1.40$, (c) Class II Model (nine 0.7-in. diameter strands spaced at 2.00 in. on center) with contact friction coefficient of $\mu_f = 0.70$, and (d) Class II Model (nine 0.7-in. diameter strands spaced at 2.00 in. on center) with contact friction coefficient of $\mu_f = 1.40$ 194

Figure 4-43: Longitudinal stress (S33) contour at 6 in. from the end face of the specimens: (a) Class I Model (nine 0.7-in. diameter strands spaced at 2.80 in. on center) with contact friction coefficient of $\mu_f = 0.70$, (b) Class I Model (nine 0.7-in. diameter strands spaced at 2.80 in. on center) with contact friction coefficient of $\mu_f = 1.40$, (c) Class II Model (nine 0.7-in. diameter strands spaced at 2.00 in. on center) with contact friction coefficient of $\mu_f = 0.70$, and (d) Class II Model (nine 0.7-in. diameter strands spaced at 2.00 in. on center) with contact friction coefficient of $\mu_f = 1.40$ 195

Chapter 5

Figure 5-1: Typical end zone cracking in the modern precast pretensioned concrete I-girders: (a) Common patterns of end zone cracks observed in the precast prestressed girders in state of Virginia (Crispino, Cousins, & Roberts-Wollmann, Anchorage Zone Design for Pretensioned Precast Bulb-T Bridge Girders in Virginia, 2009), and (b) Typical bursting and spalling cracks in a production AASHTO Type VI girder included in the Galveston Causeway Expansion Project, Texas (O'Callaghan & Bayrak, 2008). 202

Figure 5-2: Classification of stresses contributed to end zone cracking by Ujil. Adapted from (O'Callaghan & Bayrak, 2008). 206

Figure 5-3: Spalling stresses: (a) Position of maximum spalling stresses along the face of the member as a function of pretensioning eccentricity, and (b) Distribution of spalling stresses along the member span, affected by eccentricity of pretensioning force. Adapted from (Ujil, 1983).	207
Figure 5-4: Distribution of bursting stresses along the axis of pretensioning. Adapted from (Ujil, 1983).	209
Figure 5-5: Distribution of circumferential splitting stresses based on linear-elastic material response by Ujil. Adapted from (Ujil, 1983).	210
Figure 5-6: Splitting stresses: (a) Schematic distribution along a row of strands, and (b) Typical pattern of cracks due to excessive spalling stresses. Adapted from (Ujil, 1983).	211
Figure 5-7: Superposition of bursting and splitting stresses near the member end face. Adapted from (Ujil, 1983).	211
Figure 5-8: Test Group A - specimens A1 thru A14, investigated by Marshall and Mattock. Adapted from (Marshall & Mattock, 1962).	213
Figure 5-9: Test Group B, specimens B1 thru B14, investigated by Marshall and Mattock. Adapted from (Marshall & Mattock, 1962).	215
Figure 5-10: Test Group B, specimens B15 thru B25, investigated by Marshall and Mattock. Adapted from (Marshall & Mattock, 1962).	216
Figure 5-11: Gergley-Sozen equilibrium model. Adapted from (Gergley & Sozen, 1967).	218
Figure 5-12: A sample double-tie, strut-and-tie model for end anchorage design of pretensioned concrete members. Adapted from (Crispino, Cousins, & Roberts-	

Wollmann, Anchorage Zone Design for Pretensioned Precast Bulb-T Bridge Girders in Virginia, 2009).....	221
Figure 5-13: Typical bridge cross section including BT-72 Bulb-Tee girders used for finite element simulation. Adapted from <i>PCI Bridge Design Manual</i> (PCI, 2003).	222
Figure 5-14: Typical AASHTO/PCI bulb-tee (BT-72) used for the analytical purposes of this research. Adapted from <i>PCI Bridge Design Manual</i> (PCI, 2003).....	224
Figure 5-15: Typical strands patterns for the proposed AASHTO/PCI bulb-tee (BT-72) used for the analytical purposes of this research. The proposed strands are 1/2-in.diameter low-relaxation, seven-wire. Adapted from <i>PCI Bridge Design Manual</i> (PCI, 2003): (a) Typical elevation showing the configuration of the straight and draped strands as well as the location of the harping points, (b) Typical cross-section at the mid-span of the proposed BT-72 showing the straight strands, and (c) Typical cross-section at the end face of the proposed BT-72 showing the straight and draped strands.	227
Figure 5-16: Typical cross-section of BT-72 girder: (a) Typical cross-section including the strands, end zone and confinement reinforcement, (b) Typical No.5 end zone rebar to be spaced in sets of two per design (double No.4 shear reinforcement have the same configuration), and (c) Typical No.3 confinement rebar spaced with end zone and shear reinforcement but not more than 6 in. on center.	233
Figure 5-17: Typical elevation view of the BT-72 girders showing the spacing of the end zone reinforcement (EZR) as well as shear and confinement reinforcement in accordance with AASHTO LRFD Specifications.	234

Figure 5-18: Typical elevation view of the BT-72 girders showing the spacing of the end zone reinforcement (EZR) as well as shear and confinement reinforcement in accordance with NCHRP Report 654 referred to as Nebraska Detail in this document. 236

Figure 5-19: Typical end zone reinforcing detail required by IDOT for equivalent BT-72 girders. Adapted from NCHRP Report 654 (Tadros, Badie, & Tuan, 2010). 238

Figure 5-20: Typical components of a finite element model of a BT-72 girder using embedment technique: (a) Solid concrete continuum simulating the girder, (b) truss elements simulating the straight and draped strands, (c) Beam elements simulating the end zone and shear reinforcement, and (d) beam elements simulating the confinement bars embedded inside the bottom flange..... 243

Figure 5-21: A typical Finite element model of BT-72 girder cambering over the casting bed upon the release of pretensioning due to eccentricity of the pretensioned strands. 245

Figure 5-22: Comparison of the stress-strain relationships obtained by the constitutive model with the theoretical stress-strain curves assumed for a concrete with initial compressive strength of $f'_c = 5,800$ psi: a) subject due to uniaxial compression, and (b) subject to uniaxial tension. 247

Figure 5-23: Longitudinal stresses (S33) in a typical BT-72 girder without end zone, shear and confinement reinforcement immediately after the release of pretensioned strands: (a) Extreme top fiber, and (b) extreme bottom fiber. 252

Figure 5-24: Longitudinal stresses (S33) along the height of a typical BT-72 girder without end zone, shear and confinement reinforcement immediately after the release

of pretensioned strands and based on the elasto-plastic response of the specimen.

Note: "h" is measured relative to the bottom face of the bottom flange assumed as

datum..... 253

Figure 5-25: Vertical stress (S22) distribution along the height of a typical BT-72 girder without end zone, shear and confinement reinforcement measured at: (a) 3 in. from girder end face, (b) 9 in. from the girder end face, (c) 33 in. from the girder end face, and (d) 51 in. from the girder end face. 255

Figure 5-26: Pressure distribution along the height of a typical BT-72 girder without end zone, shear and confinement reinforcement measured at: (a) 3 in. from girder end face, (b) 9 in. from the girder end face, (c) 33 in. from the girder end face, and (d) 51 in. from the girder end face. 256

Figure 5-27: Elasto-plastic response of a typical BT-72 girder without end zone, shear and confinement reinforcement near the member end face: (a) Maximum principal stress contour along the end zone, (b) Vertical stress (S22) contour at member end face and (c) Vertical stress (S22) contour along the end zone..... 258

Figure 5-28: Lateral stress (S11) distribution of a typical BT-72 girder without end zone, shear and confinement reinforcement within the bottom flange (elasto-plastic response). 259

Figure 5-29: Longitudinal stresses (S33) along the height of a typical BT-72 girder with AASHTO LRFD end zone reinforcing details in addition to shear and confinement reinforcement immediately after the release of pretensioned strands and based on the elasto-plastic response of the specimen. Note: "h" is measured relative to the bottom face of the bottom flange assumed as datum. 263

Figure 5-30: Vertical stress (S22) distribution along the height of a typical BT-72 girder with AASHTO LRFD end zone rebar in addition to shear and confinement reinforcement measured at: (a) 3 in. from girder end face, (b) 9 in. from the girder end face, (c) 33 in. from the girder end face, and (d) 51 in. from the girder end face. ... 265

Figure 5-31: Pressure distribution along the height of a typical BT-72 girder with AASHTO LRFD end zone rebar in addition to shear and confinement reinforcement measured at: (a) 3 in. from girder end face, (b) 9 in. from the girder end face, (c) 33 in. from the girder end face, and (d) 51 in. from the girder end face..... 266

Figure 5-32: Elasto-plastic response of a typical BT-72 girder with AASHTO LRFD end zone rebar in addition to shear and confinement reinforcement immediately after the release of pretensioning: (a) Maximum principal vector contour along the end zone, (b) Maximum principal stress contour at member end face and (c) Maximum principal stress contour along the end zone. 268

Figure 5-33: Vertical stress (S22) contours along the end zone of a typical BT-72 girder with AASHTO LRFD end zone rebar in addition to shear and confinement reinforcement immediately after the release of pretensioning shown at: (a) outside face of the web, (b) 1 in. into the web towards the centerline of the member, (c) 2 in. into the web towards the centerline of the member, and d) at the centerline of the member. 270

Figure 5-34: Planar shear stress (S23) distribution along the span of a typical BT-72 girder with AASHTO LRFD end zone rebar in addition to shear and confinement reinforcement immediately after the release of pretensioning: (a) Average shear stress

across the width of the web, and (b) Shear stress contour at the outside face of the web base don elasto-plastic response.....	272
Figure 5-35: Axial stress (S11) in the end zone reinforcing bars of a typical BT-72 girder with AASHTO LRFD end zone rebar in addition to shear and confinement reinforcement immediately after the release of pretensioning: (a) Numerical results obtained by the nonlinear finite element simulation and (b) maximum stress per each end zone rebar.....	275
Figure 5-36: Axial stress (S11) in the confinement reinforcement of a typical BT-72 girder with AASHTO LRFD end zone rebar in addition to shear and confinement reinforcement immediately after the release of pretensioning: (a) Numerical results obtained by nonlinear finite element simulation and (b) maximum stress per each confinement rebar.....	276
Figure 5-37: Lateral stress (S11) distribution of a typical BT-72 girder with AASHTO LRFD end zone reinforcement in addition to shear and confinement reinforcement within the bottom flange (elasto-plastic response).....	277
Figure 5-38: Longitudinal stresses (S33) along the height of a typical BT-72 girder with Nebraska end zone reinforcing details in addition to shear and confinement reinforcement immediately after the release of pretensioned strands and based on the elasto-plastic response of the specimen. Note: "h" is measured relative to the bottom face of the bottom flange assumed as datum.....	281
Figure 5-39: Vertical stress (S22) distribution along the height of a typical BT-72 girder with Nebraska end zone rebar in addition to shear and confinement reinforcement	

measured at: (a) 3 in. from girder end face, (b) 9 in. from the girder end face, (c) 33 in. from the girder end face, and (d) 51 in. from the girder end face.....	283
Figure 5-40: Pressure distribution along the height of a typical BT-72 girder with Nebraska end zone rebar in addition to shear and confinement reinforcement measured at: (a) 3 in. from girder end face, (b) 9 in. from the girder end face, (c) 33 in. from the girder end face, and (d) 51 in. from the girder end face.....	284
Figure 5-41: Elasto-plastic response of a typical BT-72 girder with Nebraska end zone rebar in addition to shear and confinement reinforcement immediately after the release of pretensioning: (a) Maximum principal vector contour along the end zone, (b) Maximum principal stress contour at member end face and (c) Maximum principal stress contour along the end zone.	287
Figure 5-42: Vertical stress (S22) contours along the end zone of a typical BT-72 girder with Nebraska end zone rebar in addition to shear and confinement reinforcement immediately after the release of pretensioning shown at: (a) outside face of the web, (b) 1 in. into the web towards the centerline of the member, (c) 2 in. into the web towards the centerline of the member, and d) at the centerline of the member.	288
Figure 5-43: Planar shear stress (S23) distribution along the span of a typical BT-72 girder with Nebraska end zone rebar in addition to shear and confinement reinforcement immediately after the release of pretensioning: (a) Average shear stress across the width of the web, and (b) Shear stress contour at the outside face of the web base don elasto-plastic response.....	290
Figure 5-44: Axial stress (S11) in the end zone reinforcing bars of a typical BT-72 girder with Nebraska end zone rebar in addition to shear and confinement reinforcement	

immediately after the release of pretensioning: (a) Numerical results obtained by the nonlinear finite element simulation and (b) maximum stress per each end zone rebar.	293
Figure 5-45: Axial stress (S11) in the confinement reinforcement of a typical BT-72 girder with Nebraska end zone rebar in addition to shear and confinement reinforcement immediately after the release of pretensioning: (a) Numerical results obtained by nonlinear finite element simulation and (b) maximum stress per each confinement rebar.	294
Figure 5-46: Lateral stress (S11) distribution of a typical BT-72 girder with Nebraska end zone reinforcement in addition to shear and confinement reinforcement within the bottom flange (elasto-plastic response).	295
Figure 5-47: Longitudinal stresses (S33) along the height of a typical BT-72 girder with IDOT end zone reinforcing details in addition to shear and confinement reinforcement immediately after the release of pretensioned strands and based on the elasto-plastic response of the specimen. Note: "h" is measured relative to the bottom face of the bottom flange assumed as datum.	299
Figure 5-48: Vertical stress (S22) distribution along the height of a typical BT-72 girder with IDOT end zone rebar in addition to shear and confinement reinforcement measured at: (a) 3 in. from girder end face, (b) 9 in. from the girder end face, (c) 33 in. from the girder end face, and (d) 51 in. from the girder end face.....	301
Figure 5-49: Pressure distribution along the height of a typical BT-72 girder with IDOT end zone rebar in addition to shear and confinement reinforcement measured at: (a) 3	

in. from girder end face, (b) 9 in. from the girder end face, (c) 33 in. from the girder end face, and (d) 51 in. from the girder end face.....	302
Figure 5-50: Elasto-plastic response of a typical BT-72 girder with IDOT end zone rebar in addition to shear and confinement reinforcement immediately after the release of pretensioning: (a) Maximum principal vector contour along the end zone, (b) Maximum principal stress contour at member end face and (c) Maximum principal stress contour along the end zone.	305
Figure 5-51: Vertical stress (S22) contours along the end zone of a typical BT-72 girder with IDOT end zone rebar in addition to shear and confinement reinforcement immediately after the release of pretensioning shown at: (a) outside face of the web, (b) 1 in. into the web towards the centerline of the member, (c) 2 in. into the web towards the centerline of the member, and d) at the centerline of the member.	306
Figure 5-52: Planar shear stress (S23) distribution along the span of a typical BT-72 girder with IDOT end zone rebar in addition to shear and confinement reinforcement immediately after the release of pretensioning: (a) Average shear stress across the width of the web, and (b) Shear stress contour at the outside face of the web base don elasto-plastic response.	308
Figure 5-53: Axial stress (S11) in the end zone reinforcing bars of a typical BT-72 girder with IDOT end zone rebar in addition to shear and confinement reinforcement immediately after the release of pretensioning: (a) Numerical results obtained by the nonlinear finite element simulation and (b) maximum stress per each end zone rebar.	311

- Figure 5-54: Axial stress (S11) in the confinement reinforcement of a typical BT-72 girder with IDOT end zone rebar in addition to shear and confinement reinforcement immediately after the release of pretensioning: (a) Numerical results obtained by nonlinear finite element simulation and (b) maximum stress per each confinement rebar. 312
- Figure 5-55: Lateral stress (S11) distribution of a typical BT-72 girder with IDOT end zone reinforcement in addition to shear and confinement reinforcement within the bottom flange (elasto-plastic response). 313
- Figure 5-56: Longitudinal stresses (S33) along the height of a typical BT-72 girder with Modified IDOT-AASHTO end zone reinforcing details in addition to shear and confinement reinforcement immediately after the release of pretensioned strands and based on the elasto-plastic response of the specimen. Note: "h" is measured relative to the bottom face of the bottom flange assumed as datum. 317
- Figure 5-57: Vertical stress (S22) distribution along the height of a typical BT-72 girder with Modified IDOT-AASHTO end zone rebar in addition to shear and confinement reinforcement measured at: (a) 3 in. from girder end face, (b) 9 in. from the girder end face, (c) 33 in. from the girder end face, and (d) 51 in. from the girder end face. ... 319
- Figure 5-58: Pressure distribution along the height of a typical BT-72 girder with Modified IDOT-AASHTO end zone rebar in addition to shear and confinement reinforcement measured at: (a) 3 in. from girder end face, (b) 9 in. from the girder end face, (c) 33 in. from the girder end face, and (d) 51 in. from the girder end face. ... 320
- Figure 5-59: Elasto-plastic response of a typical BT-72 girder with Modified IDOT-AASHTO end zone rebar in addition to shear and confinement reinforcement

immediately after the release of pretensioning: (a) Maximum principal vector contour along the end zone, (b) Maximum principal stress contour at member end face and (c) Maximum principal stress contour along the end zone.	323
Figure 5-60: Vertical stress (S22) contours along the end zone of a typical BT-72 girder with Modified IDOT-AASHTO end zone rebar in addition to shear and confinement reinforcement immediately after the release of pretensioning shown at: (a) outside face of the web, (b) 1 in. into the web towards the centerline of the member, (c) 2 in. into the web towards the centerline of the member, and d) at the centerline of the member.	324
Figure 5-61: Planar shear stress (S23) distribution along the span of a typical BT-72 girder with IDOT end zone rebar in addition to shear and confinement reinforcement immediately after the release of pretensioning: (a) Average shear stress across the width of the web, and (b) Shear stress contour at the outside face of the web base don elasto-plastic response.	326
Figure 5-62: Axial stress (S11) in the end zone reinforcing bars of a typical BT-72 girder with IDOT end zone rebar in addition to shear and confinement reinforcement immediately after the release of pretensioning: (a) Numerical results obtained by the nonlinear finite element simulation and (b) maximum stress per each end zone rebar.	329
Figure 5-63: Axial stress (S11) in the confinement reinforcement of a typical BT-72 girder with IDOT end zone rebar in addition to shear and confinement reinforcement immediately after the release of pretensioning: (a) Numerical results obtained by	

nonlinear finite element simulation and (b) maximum stress per each confinement rebar.	330
Figure 5-64: Lateral stress (S11) distribution of a typical BT-72 girder with Modified IDOT-AASHTO end zone reinforcement in addition to shear and confinement reinforcement within the bottom flange (elasto-plastic response).....	331
Figure 5-65: Comparison of axial stresses (S11) in the end zone rebar in accordance with AASHTO LRFD, Nebraska, IDOT and Modified IDOT-AASHTO schemes based on elasto-plastic finite element simulations of a typical BT-72 girder.....	334
Figure 5-66: Comparison of axial stresses (S11) in the end zone rebar based on elasto-plastic finite element simulations of a typical BT-72 girder, reported at $h = 36$ in. along the height of the member (bottom of bottom flange is assumed as datum): (a) Elasto-plastic response, and (b) Linear-elastic response.	337
Figure 5-67: Comparison of axial stresses (S11) in the end zone rebar based on elasto-plastic finite element simulations of a typical BT-72 girder, reported at $h = 32$ in. along the height of the member (bottom of bottom flange is assumed as datum): (a) Elasto-plastic response, and (b) Linear-elastic response.	338
Figure 5-68: Comparison of axial stresses (S11) in the end zone rebar based on elasto-plastic finite element simulations of a typical BT-72 girder, reported at $h = 28$ in. along the height of the member (bottom of bottom flange is assumed as datum): (a) Elasto-plastic response, and (b) Linear-elastic response.	339
Figure 5-69: Comparison of axial stresses (S11) in the end zone rebar based on elasto-plastic finite element simulations of a typical BT-72 girder, reported at $h = 24$ in.	

along the height of the member (bottom of bottom flange is assumed as datum): (a) Elasto-plastic response, and (b) Linear-elastic response.	340
Figure 5-70: Comparison of vertical stress (S22) distribution along the height of finite element models of a typical BT-72 girder with end zone reinforcing details in accordance with AASHTO LRFD, Nebraska, IDOT and Modified IDOT-AASHTO schemes and based on elasto-plastic simulations. The results are reported at 3 in. from the member end face.	341
Figure 5-71: Comparison of planar shear stress (S23) distribution along the span of finite element models of a typical BT-72 girder with end zone reinforcing details in accordance with AASHTO LRFD, Nebraska, IDOT and Modified IDOT-AASHTO schemes and based on elasto-plastic simulations. The results are reported at the interface between the web and bottom flange.....	342
 Chapter 6	
Figure 6-1: Map of the Alaskan Way Viaduct replacement project (WSDOT, 2011). ..	345
Figure 6-2: Staggered No.3 tie bars (301 series) hooked between the vertical legs of end zone and shear rebars: (a) Typical end section (CTC, 2010), and (b) typical strain gage mounted tie bar.	349
Figure 6- 3: 0.6-in. diameter strands with strain gages staggered over different rows...	349
Figure 6-4: Fabrication shop drawings for BWF100 G93C girders (CTC, 2010).....	351
Figure 6-5: Fabrication shop drawings for BWF100 G94C girders (CTC, 2010).....	352
Figure 6-6: Fabrication shop drawings for BWF100 G95C girders (CTC, 2010).....	353
Figure 6-7: Prestressing layout (CTC, 2010).....	355

Figure 6-8: Bunking configuration of the specimens at the release of straight strands (CTC, 2010).....	356
Figure 6-9: Test specimen No.1: (a) Reinforcement cage, and (b) Girder stored in the casting yard.....	357
Figure 6-10: Test specimen No.5: (a) Typical end face, (b) Typical web reinforcement with strain gages, and (c) Typical bottom flange reinforcement.....	358
Figure 6-11: Typical bunking configuration: (a) Specimen No.2 lifted from the casting bed after the release of pretensioning, and (b) Typical lifting details including the overhead cranes.....	360
Figure 6-12: A typical FLA-1-5LT strain gage by Texas Measurements, Inc (Texas Measurements, Inc., 2010).....	362
Figure 6-13: A typical hand-held grinder required for surface preparation.....	362
Figure 6-14: M-Bond 200 adhesive kit by Vishay Precision Group (Vishay Precision Group, 2010).....	363
Figure 6-15: A three-part coating mechanism recommended by Texas Measurements, Inc. (Texas Measurements, Inc., 2010).....	364
Figure 6-16: SB Tape by Texas Measurements, Inc. (Texas Measurements, Inc., 2010).	365
Figure 6-17: Araldite standard coating agent by Texas Measurements, Inc. (Texas Measurements, Inc., 2010).....	365
Figure 6-18: A typical seven wire 0.6-in. diameter strand after being grinded to host a strain gage.....	366

Figure 6-19: Installation of a typical FLA-1-350-11-5LT strain gage on a 0.6-in. diameter seven-sire prestressing strand: (a) Strain gage temporarily mounted on the strand using scotch tape and (b) Strain gage wrapped by electric tape during the curing of the surface bind agent.	367
Figure 6-20: Lead wires attached to the strand using a typical plastic strap while allowing adequate slack in the wire adjacent to the gage.	367
Figure 6-21: Application of the epoxy resin (the first layer of coating) over a FLA-5-11-5LT strain gage mounted on a vertical leg of a typical No.5 end zone rebar.	368
Figure 6-22: Application of the second layer of coating protection, SB tape.....	368
Figure 6-23: Araldite as the third layer of coating protection: (a) application of Araldite after the two agents are properly mixed, and (b) the final the assembly after Araldite coating has cured.....	369
Figure 6-24: Data acquisition: (a) typical wire management through the straight strands beyond the girder bottom flange, and (b) on-site DAQ setup.....	371
Figure 6-25: Girder No.1 (G93C) field log. Courtesy of Concrete Technology Corporation (CTC, 2010).....	372
Figure 6-26: Girder No.2 (G94C) field log. Courtesy of Concrete Technology Corporation (CTC, 2010).....	373
Figure 6-27: Girder No.3 (G94C) field log. Courtesy of Concrete Technology Corporation (CTC, 2010).....	374
Figure 6-28: Girder No.4 (G94C) field log. Courtesy of Concrete Technology Corporation (CTC, 2010).....	375

Figure 6-29: Girder No.5 (G94C) field log. Courtesy of Concrete Technology Corporation (CTC, 2010).....	376
Figure 6-30: Girder No.6 (G94C) field log. Courtesy of Concrete Technology Corporation (CTC, 2010).....	377
Figure 6-31: Girder No.7 (G94C) field log. Courtesy of Concrete Technology Corporation (CTC, 2010).....	378
Figure 6-32: Girder No.8 (G95C) field log. Courtesy of Concrete Technology Corporation (CTC, 2010).....	379
Figure 6-33: Girder No.1 (G93C) R1 thru R8 axial strain data at the end zone reinforcing bars.....	381
Figure 6-34: Girder No.1 (G93C) S1 thru S8 axial strain data at the prestressing strands.	381
Figure 6-35: Hydraulic abutment utilized for release of pretensioned strands: (a) typical anchorage of the draped strands at the abutments, and (b) pressure gage for control of detensioning. Courtesy of Concrete Technology Corporation (CTC, 2010).	382
Figure 6-36: Girder No.1 (G93C) summary of stresses at the reinforcing bars and the prestressing strands. Note that the stresses at the prestressing strands indicate the pretensioning loss immediately after the release of pretensioning measured at the dead end. Courtesy of Concrete Technology Corporation (CTC, 2010).	383
Figure 6-37: Girder No.2 (G94C) R1 thru R8 axial strain data at the end zone reinforcing bars.....	384
Figure 6-38: Girder No.2 (G94C) S1 thru S8 axial strain data at the prestressing strands.	384

Figure 6-39: Girder No.2 (G94C) summary of stresses at the reinforcing bars and the prestressing strands. Note that the stresses at the prestressing strands indicate the pretensioning loss immediately after the release of pretensioning measured at the dead end. Courtesy of Concrete Technology Corporation (CTC, 2010).	385
Figure 6-40: Girder No.3 (G94C) R1 thru R8 axial strain data at the end zone reinforcing bars.....	387
Figure 6-41: Girder No.3 (G94C) S1 thru S8 axial strain data at the prestressing strands.	387
Figure 6-42: Girder No.3 (G94C) summary of stresses at the reinforcing bars and the prestressing strands. Note that the stresses at the prestressing strands indicate the pretensioning loss immediately after the release of pretensioning measured at the dead end. Courtesy of Concrete Technology Corporation (CTC, 2010).	388
Figure 6-43: Girder No.4 (G94C) R1 thru R8 axial strain data at the end zone reinforcing bars.....	389
Figure 6-44: Girder No.4 (G94C) S1 thru S8 axial strain data at the prestressing strands.	389
Figure 6-45: Girder No.4 (G94C) summary of stresses at the reinforcing bars and the prestressing strands. Note that the stresses at the prestressing strands indicate the pretensioning loss immediately after the release of pretensioning measured at the dead end. Courtesy of Concrete Technology Corporation (CTC, 2010).	390
Figure 6-46: Girder No.5 (G94C) R1 thru R8 axial strain data at the end zone reinforcing bars.....	391

Figure 6-47: Girder No.5 (G94C) S1 thru S8 axial strain data at the prestressing strands.	391
Figure 6-48: Girder No.5 (G94C) summary of stresses at the reinforcing bars and the prestressing strands. Note that the stresses at the prestressing strands indicate the pretensioning loss immediately after the release of pretensioning measured at the live end. Courtesy of Concrete Technology Corporation (CTC, 2010).....	392
Figure 6-49: Girder No.6 (G94C) R1 thru R8 and S1 thru S4 axial strain data at the end zone reinforcing bars.....	394
Figure 6-50: Girder No.6 (G94C) S5 thru S8 axial strain data at the prestressing strands.	394
Figure 6-51: Girder No.6 (G94C) summary of stresses at the reinforcing bars and the prestressing strands. Note that the stresses at the prestressing strands indicate the pretensioning loss immediately after the release of pretensioning measured at the live end. Courtesy of Concrete Technology Corporation (CTC, 2010).....	395
Figure 6-52: Girder No.7 (G94C) R1 thru R8 and S1 thru S4 axial strain data at the end zone reinforcing bars.....	396
Figure 6-53: Girder No.7 (G94C) S5 thru S8 axial strain data at No.3 tie bars.	396
Figure 6-54: Girder No.7 (G94C) summary of stresses at the reinforcing bars and the prestressing strands. Note that the stresses at the prestressing strands indicate the pretensioning loss immediately after the release of pretensioning measured at the live end. Courtesy of Concrete Technology Corporation (CTC, 2010).....	397
Figure 6-55: Girder No.8 (G95C) R1 thru R7 axial strain data at the end zone reinforcing bars.....	398

Figure 6-56: Girder No.8 (G95C) summary of stresses at the reinforcing bars. Note that the strain gages S1 thru S2 did report any data due to malfunctioning. Courtesy of Concrete Technology Corporation (CTC, 2010).	399
Figure 6-57: Typical end zone cracks: (a) Specimen No.1 end zone (live end) showing spalling and bursting-splitting cracks at web and web-bottom flange interface, respectively, (b) close-up of a typical spalling crack at Specimen No.1 web (dead end), and (c) typical bursting and splitting cracks at Specimen No.6 web-bottom flange (live end) relative to the location of the strain gages shown in red dots.....	401
Figure 6-58: Transfer length normalized over the magnitude of pretensioning stresses.	402
Figure 6-59: Girder No.7 (G94C): (a) web reinforcement cage showing the location of strain gages at the vertical rebar and No.3 web tie bars, and (b) close-up of a typical No.3 tie bar.....	404
Figure 6-60: Distribution of longitudinal stresses (S33) along the height of the BWF100 specimens at the theoretical transfer length. Note that positive stresses denote state of compression.	406
Figure 6-61: Distribution of internal moments along the height of the member at the theoretical transfer length based on Gregly-Sozen method.	408
Figure 6-62: The double-tie, strut-and-tie model utilized for end anchorage analysis of Girders No.1 thru No.8. Adapted from (Crispino, Cousins, & Roberts-Wollmann, Anchorage Zone Design for Pretensioned Precast Bulb-T Bridge Girders in Virginia, 2009).	411
Figure 6-63: Partial cross section of the BWF100 girder required to resist the pretensioning force by the straight strands with equivalent compression force at the	

distance $h = 100$ in. from the member end face, immediately after the release of the prestressed strands.	413
Figure 6-64: Typical components of a finite element model of a typical G94C girder using embedment technique: (a) Solid concrete continuum simulating the girder, (b) truss elements simulating the straight, draped, and temporary strands, and (c) beam elements simulating the end zone, shear reinforcement, and the confinement bars embedded inside the bottom flange.	419
Figure 6-65: Comparison of the stress-strain relationships obtained by the constitutive model with the theoretical stress-strain curves assumed for a concrete with initial compressive strength of $f'_{ci} = 8,000$ psi: a) subject due to uniaxial compression, and (b) subject to uniaxial tension.	421
Figure 6-66: Vertical stress (S22) distribution along the height of a typical G94C girder with AASHTO LRFD end zone rebar in addition to shear and confinement reinforcement in accordance with Figure 6-5.	423
Figure 6-67: Pressure distribution along the height of a typical G94C girder with AASHTO LRFD end zone rebar in addition to shear and confinement reinforcement in accordance with Figure 6-5.	424
Figure 6-68: Elasto-plastic response of a typical G94C girder with end zone rebar, shear and confinement reinforcement in accordance with Figure 6-5 immediately after the release of pretensioning: (a) Maximum principal vector contour along the end zone, (b) Maximum principal stress contour at member end face and (c) Maximum principal stress contour along the end zone.	426

Figure 6-69: Planar shear stress (S23) distribution along the span of a typical G94C girder with zone rebar, shear and confinement reinforcement in accordance with Figure 6-5 immediately after the release of pretensioning: (a) Average shear stress across the width of the web, and (b) Shear stress contour at the outside face of the web base don elasto-plastic response.....	428
Figure 6-70: Axial stress (S11) in the end zone reinforcing bars of a typical G94C girder with end zone rebar, shear and confinement reinforcement in accordance with Figure 6-5 immediately after the release of pretensioning: (a) Numerical results obtained by the nonlinear finite element simulation and (b) maximum stress at both legs of the first end zone bars closest to the member end face.....	431
Figure 6-71: Axial stress (S11) in the confinement reinforcement of a typical G94C girder with end zone rebar, shear and confinement reinforcement in accordance with Figure 6-5 immediately after the release of pretensioning: (a) Numerical results obtained by nonlinear finite element simulation and (b) maximum stress per each confinement rebar.	432
Figure 6-72: Lateral stress (S11) distribution within the bottom flange (elasto-plastic response) of a typical G94C girder with end zone rebar, shear and confinement reinforcement in accordance with Figure 6-5.	433
Figure 6-73: Axial stress (S11) in the longitudinal No.7 bars embedded in the web (one side only) of a typical G94C girder with end zone rebar, shear and confinement reinforcement in accordance with Figure 6-5 immediately after the release of pretensioning: (a) Numerical results obtained by nonlinear finite element simulation and (b) maximum/minimum stresses per each rebar.	435

Figure 6-74: Comparison of the axial stresses (S11) at the three end zone rebar closest to the end face of a typical G94C girder with end zone rebar, shear and confinement reinforcement in accordance with Figure 6-5 based on the analytical solutions versus the experimental observations..... 437

Figure 6-75: Comparison of the axial stress (S11) at the three end zone rebar closest to the end face of a typical G94C girder with end zone rebar, shear and confinement reinforcement in accordance with Figure 6-5 based on analytical solutions versus experimental observations. 438

List of Tables

Chapter 3

Table 3-1: Material models used in the finite element analysis of concrete sleepers by Kaewunruen and Remennikov (2006).	54
Table 3-2: Prestressing stages utilized in the finite element modeling of prestressed concrete girders proposed by Ayoub and Filippou (2010).	58
Table 3-3: Recommended parameters by AASHTO LRFD for shear friction design (AASHTO LRFD, 2010).	64
Table 3-4: Summary of constitutive parameters used in finite element analyses.	99
Table 3-5: Summary of stresses obtained by the concentrically pretensioned finite element model.	105
Table 3-6: Summary of stresses obtained by the eccentrically pretensioned finite element model.	111

Chapter 4

Table 4-1: Characteristic properties of the specimens used in the experimental verification of transfer length and the corresponding effect of confinement reinforcement. Adapted from (Akhnoukh, 2008).	119
Table 4-2: Log of finite element models.	124
Table 4-3: Comparative analysis of the analytical results obtained from the finite element models with embedded strands against the closed form solutions. Negative stresses indicate compression.	136

Table 4-4: Comparative analysis of the analytical results obtained from the finite element models with extruded strands and contact friction coefficient of $\mu_f = 0.7$ against the closed form solutions. Negative stresses indicate compression.....	137
Table 4-5: Comparative analysis of the analytical results obtained from the finite element models with extruded strands and contact friction coefficient of $\mu_f = 1.4$ against the closed form solutions. Negative stresses indicate compression.....	137
Table 4-6: Log of Class I finite element models comprised of nine extruded strands spaced at 2.80 in. on center and contact friction coefficient of $\mu_f = 0.70$	143
Table 4-7: Log of Class I finite element models comprised of nine extruded strands spaced at 2.80 in. on center and contact friction coefficient of $\mu_f = 1.40$	144
Table 4-8: Log of Class II finite element models comprised of nine extruded strands spaced at 2.00 in. on center and contact friction coefficient of $\mu_f = 0.70$	149
Table 4-9: Log of Class II finite element models comprised of nine extruded strands spaced at 2.00 in. on center and contact friction coefficient of $\mu_f = 1.40$	150
Table 4-10: Comparative analysis of the analytical results obtained from the finite element models with nine extruded strands spaced at 2.80 in. on center and contact friction coefficient of $\mu_f = 0.70$ against the closed form solutions. Negative stresses indicate compression.....	158
Table 4-11: Comparative analysis of the analytical results obtained from the finite element models with nine extruded strands spaced at 2.80 in. on center and contact friction coefficient of $\mu_f = 1.40$ against the closed form solutions. Negative stresses indicate compression.....	159

Table 4-12: Comparative analysis of the analytical results obtained from the finite element models with nine extruded strands spaced at 2.00 in. on center and contact friction coefficient of $\mu_f = 0.70$ against the closed form solutions. Negative stresses indicate compression.....	159
Table 4-13: Comparative analysis of the analytical results obtained from the finite element models with nine extruded strands spaced at 2.00 in. on center and contact friction coefficient of $\mu_f = 1.40$ against the closed form solutions. Negative stresses indicate compression.....	160
Chapter 5	
Table 5-1: Basic sectional properties of the non-composite BT-72 bulb-tee (PCI, 2003).....	226
Table 5-2: BT-72 top and bottom fiber stresses at the release of prestressed strands based on elastic beam theory (PCI, 2003).....	228
Table 5-3: NCHRP Report 654 acceptance criteria for the pretensioned members with web cracking during the production (Tadros, Badie, & Tuan, 2010).	237
Table 5-4: Results of the finite element analysis of a typical BT-72 girder without end zone, shear and confinement reinforcement as well as those by the closed form solutions included in PCI BDM Example 9.4. The results are reported immediately after the release of pretensioning.	249
Table 5-5: Comparison of the results obtained by the finite element analysis of a typical BT-72 girder without end zone, shear and confinement reinforcement versus the closed form solutions in reference to Table 5-4.....	250

Table 5-6: Results of the finite element analysis of a typical BT-72 girder with AASHTO LRFD end zone reinforcing details in addition to shear and confinement reinforcement as well as those by the closed form solutions included in PCI BDM Example 9.4. The results are reported immediately after the release of pretensioning.	261
Table 5-7: Comparison of the results obtained by the BT-72 finite element model with AASHTO LRFD end zone, shear and confinement reinforcement versus the closed form solutions in reference to Table 5-6.	262
Table 5-8: Summary of the maximum tensile stresses in the end zone reinforcing bars obtained from the nonlinear numerical simulations of a typical BT-72 girder with AASHTO LRFD end zone rebar in addition to shear and confinement reinforcement immediately after the release of pretensioning.	274
Table 5-9: Results of the finite element analysis of a typical BT-72 girder with Nebraska end zone reinforcing details in addition to shear and confinement reinforcement as well as those by the closed form solutions included in PCI BDM Example 9.4. The results are reported immediately after the release of pretensioning.	279
Table 5-10: Comparison of the results obtained by the BT-72 finite element model with Nebraska end zone, shear and confinement reinforcement versus the closed form solutions in reference to Table 5-9.	280
Table 5-11: Summary of the maximum tensile stresses in the end zone reinforcing bars obtained from the nonlinear numerical simulations of a typical BT-72 girder with Nebraska end zone rebar in addition to shear and confinement reinforcement immediately after the release of pretensioning.	292

Table 5-12: Results of the finite element analysis of a typical BT-72 girder with IDOT end zone reinforcing details in addition to shear and confinement reinforcement as well as those by the closed form solutions included in PCI BDM Example 9.4. The results are reported immediately after the release of pretensioning.	297
Table 5-13: Comparison of the results obtained by the BT-72 finite element model with IDOT end zone, shear and confinement reinforcement versus the closed form solutions in reference to Table 5-12.....	298
Table 5-14: Summary of the maximum tensile stresses in the end zone reinforcing bars obtained from the nonlinear numerical simulations of a typical BT-72 girder with IDOT end zone rebar in addition to shear and confinement reinforcement immediately after the release of pretensioning.	310
Table 5-15: Results of the finite element analysis of a typical BT-72 girder with Modified IDOT-AASHTO end zone reinforcing details in addition to shear and confinement reinforcement as well as those by the closed form solutions included in PCI BDM Example 9.4. The results are reported immediately after the release of pretensioning.	315
Table 5-16: Comparison of the results obtained by the BT-72 finite element model with Modified IDOT-AASHTO end zone, shear and confinement reinforcement versus the closed form solutions in reference to Table 5-12.....	316
Table 5-17: Summary of the maximum tensile stresses in the end zone reinforcing bars obtained from the nonlinear numerical simulations of a typical BT-72 girder with Modified IDOT -AASHTO end zone rebar in addition to shear and confinement reinforcement immediately after the release of pretensioning.....	328

Table 5-18: Summary of the maximum tensile stresses in the end zone reinforcing bars near the end face of the member, obtained from the nonlinear numerical simulations of typical BT-72 girders with AASHTO LRFD, Nebraska, IDOT and Modified IDOT -AASHTO end zone reinforcing details in addition to shear and confinement reinforcement immediately after the release of pretensioning.....	334
---	-----

Chapter 6

Table 6-1: Proposed 2011 comprehensive budget outline for Alaskan Way Viaduct projects (WSDOT, 2011).....	347
Table 6-2: Basic material properties for BWF100 specimens.....	354
Table 6-3: Sectional properties of BWF100 specimens.	354
Table 6-4: Test specimens.	356
Table 6- 5: Normalized transfer length.....	403
Table 6-6: Summary of the internal moments for BWF100 specimens immediately after the release of pretensioning based on the assumption that the specimens are bunched at 8-ft from both ends during the release. The results include the effects of strands relaxation and member elastic shortening.....	407
Table 6-7: Summary of the extreme top and bottom fiber stresses immediately after the release of pretensioning based on the assumption that the specimens are bunched at 8-ft from both ends during the release. The results include the effects of strands relaxation and member elastic shortening.....	407
Table 6-8: Summary of constitutive parameters used in finite element analyses.....	417
Table 6-9: Comparison of the results obtained by the G94C finite element model with versus the closed form solutions summarized in Appendix J.....	422

Table 6-10: Summary of the maximum tensile stresses in the first three end zone reinforcing bars closest to the member end face, obtained from the nonlinear numerical simulations of a typical G94C girder with end zone rebar, shear and confinement reinforcement in accordance with Figure 6-5 immediately after the release of pretensioning. 430

Chapter 1 - Introduction

1.1. Research Objectives

Prestressing is one of the most common practices for overcoming the weakness of concrete in resisting tension. Two common methods of prestressing include pre- or post-tensioning methods. In pretensioned members, concrete is cast around the already prestressed strands. Once concrete matures enough to reach a prescribed target compressive strength (i.e., 80% of the 28-day compressive strength), pretensioned strands are released while chemically and mechanically bonded with the host concrete.

Two issues pertaining to the current state of pretensioning industry are investigated in this research:

- Optimized spacing of 0.7-in. diameter prestressing strands
- Remedial reinforcing details to address the problem of end zone cracking immediately after the release of pretensioning, and

In the U.S., the use of 0.7-in. diameter strands is generally limited to non-bridge applications except in cable-stayed configurations. One of the main obstacles against more usage of 0.7-in. diameter strands in pretensioned concrete members is the minimum center-to-center spacing of the 0.7-in. diameter strands. Due to the lack of historical data and past experience, the corresponding minimum spacing is defined by the current specifications as four times the strand diameter (2.80 in.). This requires costly and time-consuming changes to the precasting yard including the end plates and abutments, which are typically adjusted for 2-in. center-to-center spacing. Therefore, if it is shown, numerically and practically, that reduced spacing of 2-in. on-center is also potentially

applicable to 0.7-in. diameter strands, this will be a great incentive for the industry to promote the use of the corresponding strands.

End zone cracking is a persistent problem for the pretensioned concrete members more significantly for the member with relative slender cross-sections such as I-girders. The advancement of the precasting industry including the economic feasibility of high concrete allows for new generation of pretensioned members which are notably larger than the predecessors. The new super members are still anticipated to be prone to end zone cracking specially given the unprecedented magnitude of pretensioning they can host compared to before. Past studies of remedial approaches for end zone cracking reveal that the current details possess state-specific characteristics dictated by the local experience of state agencies as well as the precasters. Formal knowledge sharing among the state departments of transportation can greatly help the optimization of remedial steps towards confining the problem of end zone cracking within unified set of guidelines. As an academic step towards such goals, various end zone reinforcing details are comparatively investigated in this research to study their effectiveness.

As implied above, the introduction of the new generation of super members to the market has drawn the attention of the owners, precasters and academicians towards possible behaviors not previously known or observed. Therefore, through a collaborative effort with Washington Department of Transportation and a local precaster, Concrete Technology Corporation, eight production girders are monitored during the casting to investigate the response of the members immediately after the release of prestressed strands.

Given the current economic restraints coupled with the limitations of testing facilities, rarely academic and research institutions can afford or accommodate testing of the super members such as those studied in this research. Once verified and validated, reliable simulations can be used to complement the experimental observations, providing the researchers with additional tools towards research and development. While numerous commercial packages are available in the market that are capable of performing advance finite element simulations, the current state of analysis and design of pretensioned concrete members indicates a serious lack of reliable and unified guidelines for analytical simulation of precast prestressed concrete members. This re-emphasizes the great need for development of validated methodological approaches which can adequately simulate the behavior of pretensioned concrete members during various stages of construction and service life. In addition, as it is discussed in the next chapters, the elastoplastic behavior of concrete is an important factor essential for accurate and reliable simulation of end zone of pretensioned concrete girders, generally compromised due to tensile cracking. Therefore, the basic significance of this research is the proposal for finite element techniques that are outside the domain of structural engineering.

Thus, the fundamental objective of this research is careful evaluation of two different modeling approaches that can be utilized for simulation and analysis of the response of pretensioned concrete member immediately after the release of prestressing strands. This requires simulation of pretensioning mechanism as well as inelastic response of concrete which can assist in prediction of potential cracking immediately after the release of prestressing. In the next step, the proposed simulation techniques are need verified and validated to ensure their reliability before further application.

The objectives of this research are summarized as follows:

1. Evaluation of two finite element simulation approaches based on embedment and extrusion techniques for modeling the pretensioning mechanisms;
2. Verification of the proposed finite element methodological approaches versus the closed-form solutions commonly used in practice such as elastic beam theory;
3. Analysis of the effect of 0.7-in. diameter strands on the response of pretensioned concrete members based on the extrusion technique:
 - a. Verification of the finite element analysis versus the closed-form solutions based on elastic beam theory
 - b. Validation of the numerical simulations through comparison with the experimental observations obtained by rectangular, mono-strand test specimens
 - c. Analysis of the group effect including the spacing of the strands
4. Analysis of the end zone cracking of pretensioned concrete girders immediately after the release of prestressed strands by utilizing the embedment technique:
 - a. Finite element simulation of a typical AASHTO/PCI Bulb-tee girder and comparison of the results versus the closed-form solutions by elastic beam theory
 - b. Investigation of various end zone reinforcing details and their effectiveness

5. Investigation of end zone cracking in Washington Department of Transportation Super I-girders:
 - a. Instrumentation of eight (8) WF100 production girders to investigate the tensile stresses at the end zone reinforcing bars immediately after the release of pretensioning
 - b. Instrumentation of the same specimens to investigate the transfer length of the prestressing strands immediately after the release of pretensioning
 - c. Estimation of the tensile stresses in the end zone reinforcing bars based on the current closed-form solutions including Gregly-Sozen and Strut-&-Tie methods
 - d. Estimation of the tensile stresses in the end zone reinforcing bars based on the application of shear-friction theory as a closed-form solution
 - e. Nonlinear finite element simulation of the test specimens and comparison of the results versus closed-form solutions and the experimental results

1.2. Research Significance

With the advent of high strength concrete coupled with the technological advances in the prestressing industry, the new generation of pretensioned concrete girders is significantly longer and larger in cross-sectional dimensions in comparison with the previous generations of AASHTO and PCI girders. Consequently, larger members are able to host considerably more pretesting strands. Nebraska NU-girders and Washington Super-girders are common examples of the new generation of the large concrete girders which have been successfully implemented in practice. As the result, the current state of industry implies a great need for academic study of the new generation of the

pretensioned concrete members which have been observed to have certain characteristics different from the previous generations.

The need for reliable and unified simulation techniques is particularly important since the economic constraints and limitations of testing facilities generally prohibit academic and research institutions from extensive study of actual production girders.

One of the significances of this research is the careful evaluation of different simulation techniques for numerical evaluation of pretensioned concrete girders immediately after the release of prestressed strands. Two finite element approaches for simulation of pretensioned concrete girders are evaluated for the applicability, accuracy and reliability: embedment and extrusion techniques. Embedment and extrusion techniques provide lower and upper bound solutions coupled with simulation complexities, respectively. It is shown that each technique can lead to acceptable results if calibrated and appropriately implemented and depending on the purposes of intended research as well as the level of accuracy required.

Another important aspect of this research to show the vital role of material constitutive modeling of concrete when analyzing the response of pretensioned concrete girders immediately after the release of prestressing. The analytical findings of this research indicate potential inadequacies of conventional linear-elastic assumptions in proper estimation of the response of pretensioned members to the release of prestressing. It is shown that elasto-plastic material models can significantly enhance the prediction of potential cracking and the compromised areas due to overstressing and subsequent stress redistribution.

In addition to numerical techniques, this research suggests a closed-form solution for investigation of potential cracking along the interface of web and bottom flange of pretensioned concrete I-girders. The proposed solution is based on shear-friction analogy which provides the designer with an additional tool without requiring extensive modeling and higher-order computations.

1.3. Dissertation Outline

As shown in Figure 1- 1, the structure of this research is based on the following general scheme:

- Two finite element modeling approaches are proposed, which are theoretically capable of simulating the response of pretensioned concrete members immediately after the release of prestressing.
- The proposed numerical approaches are numerically verified against theoretical closed-form solutions such as elastic beam theory as well as similar experimental observations.
- Similarly, the proposed simulation techniques are validated based on experimental observations.
- Once verified and validated, each modeling approach is utilized for an application as outlined below:
 - Extrusion technique is utilized for the study of spacing and groups effect of 0.70-in. diameter strands.
 - Embedment technique is used for end zone cracking in pretensioned concrete girders.

- Eight unprecedented production super-girders are instrumented and monitored during the fabrication and release. The experimental observations are then analyzed versus two closed-form solutions and finite element simulations based on embedment technique.
- A new closed-form solution based on shear-friction theory is developed as an alternative analytical tool to estimate the tensile stresses in the end zone reinforcement at the web-bottom flange interface.

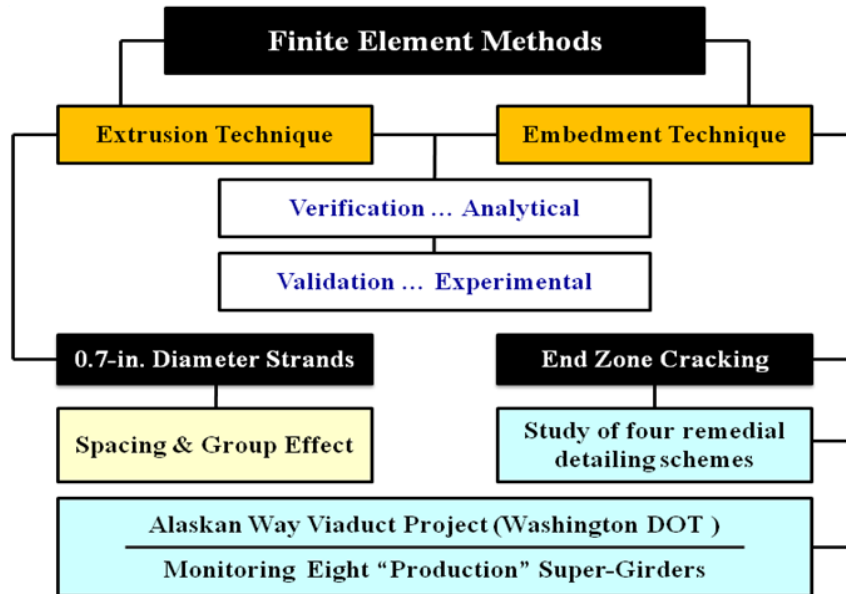


Figure 1- 1: Research outline

Accordingly, the present research is organized in seven chapters which include the pertinent literature review and past researches which provide fundamental support for the basic assumptions used in this research, analytical approaches and finally theoretical and experimental verification of the proposed methodologies.

Chapter 1 presents a general introduction about the main objectives and the significance of this research.

Chapter 2 includes a summary of notation and definitions of the parameters used throughout this document with proper reference to the corresponding sections of the dissertation.

Chapter 3 includes a detail evaluation of two finite element techniques for simulation of pretensioned concrete girders immediately after the release of prestressed strands: i) embedment and ii) extrusion techniques. The evaluation includes the study of the past related researches, basic characteristics of concrete and fundamentals of fracture mechanics. In addition, the chapter includes a thorough study of Concrete Damage Plasticity as the elasto-plastic constitutive model selected for the analytical purposes of this research. Final section of the chapter is dedicated to detail verification of the proposed finite element techniques. This section includes the comparative study of the finite element analysis of a series of concrete beam-column specimens with rectangular cross-sections versus the closed-form solutions based on elastic beam-theory. The specimens are concentrically and eccentrically pretensioned with one 0.6-in. diameter strands. In addition, the effect of confining reinforcement is studied.

Chapter 4 includes an application of the proposed extrusion technique for the study of 0.7-in. diameter prestressing strands. The first part of the chapter includes evaluation of

mono-strand concrete beam-column members with different levels of confining reinforcement. The analytical results are then compared with the experimental observations previously obtained by another research team at the University of Nebraska-Lincoln. Once the analytical simulations of the mono-strand members are validated, the mono-strand specimens are expanded to include concentric nine strands. The first class of specimens host strands spaced at equal horizontal and vertical grid spacing equivalent to four times the strand diameter. In the second class of the specimens, the strands are positioned at reduced spacing of 2 in. The main purpose of this study is to examine potential adverse effect of the reduced spacing. In addition, the effect of confining reinforcement is investigated similar to the mono-strand specimens.

Chapter 5 includes the numerical simulation of a typical AASHTO-PCI bulb-tee girder. The finite element model is constructed using the embedment technique. The finite element results are validated against the closed form solutions based on the elastic beam theory. Upon validation of the simulation, four different end zone reinforcement schemes are investigated in accordance with the following criteria:

- AASHTO LRFD Specifications
- NCHRP Report 654
- Illinois Department of Transportation (IDOT)
- Modified IDOT-AASHTO LRFD

The final section of the chapter includes a comparative study of the various schemes pertaining to efficiency and other factors such as constructability.

Chapter 6 includes study of six production girders as part of the Alaskan Way Viaduct project in state of Washington. The production girders are 100-in. deep super-

girders spanning over 200 ft. The chapter is divided into four main sections. The first section includes the details of instrumentation of the girders and data collection in the casting yard. In the second section, three closed-form solutions are applied in order to investigate the end zone cracking of the corresponding members. Two of the closed-form solutions are based on Gregly-Sozen and strut-&-tie methods previously established and widely used in practice. The third closed-form solution is based on shear-friction analogy proposed as the result of this research. The third section of the chapter includes the details of finite element modeling of a typical specimen using the embedment technique. And the last section of the chapter is dedicated to the comparison of the finite element results versus the closed-form solutions as well as the experimental observations.

Finally Chapter 7 includes the overall conclusions as well as recommendations for future research.

Chapter 2 - Notation & Definitions

$\delta \mathbf{D}$		Symmetric component of the virtual velocity gradient δL , representing the virtual rate of deformation (3.4)
δL		Virtual velocity gradient (3.4)
δW		Antisymmetric component of the virtual velocity gradient δL , representing the virtual rate of spin (3.4)
$\delta \mathbf{v}$		Virtual field (3.4)
ε		Strain tensor (3.4)
$\dot{\varepsilon}$		Total strain rate (3.4.1)
$\dot{\varepsilon}^{el}$		Elastic part of the total strain rate (3.4.1)
$\dot{\varepsilon}^{pl}$		Plastic part of the total strain rate (3.4.1)
σ		Stress tensor (3.4)
$\bar{\sigma}$		Effective cohesion stress tensor (0)
$\bar{\sigma}_c$		Effective compressive cohesion stress (3.4.1.2)

$\bar{\sigma}_t$	Effective tensile cohesion stress (3.4.1.2)
$\hat{\sigma}_{\max}$	Algebraic maximum principal stress (3.4.1)
σ_0	Initial pretensioning stress at the release, equivalent to f_{pi} (5.2.1)
σ_b	Stress in the extreme bottom fiber of the prestressed concrete BWF100 girder measured immediately after the release of pretensioning (6.4.1.2)
σ_{bp}	Bursting stress (5.2.1)
σ_c^{Harp}	Compressive stress in the extreme bottom fiber of the prestressed concrete BT-72 girder measured immediately after the release of pretensioning at the harping point of pretensioned strands (5.5.2)
$\sigma_c^{Midspan}$	Compressive stress in the extreme bottom fiber of the prestressed concrete BT-72 girder measured immediately after the release of pretensioning at the midspan (5.5.2)

$\sigma_{r,r}$	Radial compressive stress at the interface between strand and concrete upon the release of pretensioning (5.2.1)
σ_{sp}	Spalling stress (5.2.1)
σ_t	Stress in the extreme top fiber of the prestressed concrete BWF100 girder measured immediately after the release of pretensioning (6.4.1.2)
$\sigma_{t,avg}$	Average spalling tensile stress in reaction to the radial compressive stresses, $\sigma_{r,r}$, at the interface between strand and concrete upon the release of pretensioning (5.2.1)
σ_t^{Harp}	Tensile stress in the extreme top fiber of the prestressed concrete BT-72 girder measured immediately after the release of pretensioning at the harping point of pretensioned strands (5.5.2)
$\sigma_t^{Midspan}$	Compressive stress in the extreme bottom fiber of the prestressed concrete BT-72 girder measured immediately after the release of pretensioning at the midspan

(5.5.2)

$\sigma_{t,r}$	Tensile stress in reaction to the radial compressive stresses, $\sigma_{r,r}$, at the interface between strand and concrete upon the release of pretensioning (5.2.1)
\bar{f}_c	Concrete Damage Plasticity constitutive model: effective compressive stress (0)
\bar{f}_t	Concrete Damage Plasticity constitutive model: effective tensile stress (0)
$\ s\ $	Norm of deviatoric tensor (0)
\hat{x}^s	Position of fully constrained slave node (3.4.2.2)
A_{cv}	Area of the concrete anticipated to be involved in shear friction transfer (6.4.1.3)
A_{vf}	Area of reinforcement crossing the shear interface (6.4.1.3)
$c_c(\kappa)$	Concrete Damage Plasticity Constitutive Model - compressive cohesion parameter (3.4.1)

$c_t(\kappa)$	Concrete Damage Plasticity Constitutive Model: tensile cohesion parameter (3.4.1)
$\mathbf{C}(\phi^m)$	Rotation matrix of master node (3.4.2.2)
$\frac{e_0 - k}{d}$	Relative eccentricity of the strand group in relation to the centroidal axis of the member (5.2.1)
J	Jacobian matrix used in the Newton's formulation for solving nonlinear problems (3.4)
P_c	Permanent compressive force acting normal to the shear plane, contributed by self-weight and vertical component of draped strands (6.4.1.3)
ΔV_{shear}	Shear lag at the web-bottom flange interface due to the unequal pretensioning imposed by the straight, draped and temporary strands (if any) at release (6.4.1.3)
V_{ni}	Nominal shear resistance at the interface (6.4.1.3)

x/d	Longitudinal position of bursting or spalling stresses relative to the overall member height, d (5.2.1)
θ	Similarity angle measured from positive principal stress σ_l and lies in the deviatoric plane (3.2.4.1)
κ	Multiplier for development length of prestressing strands (3.3.2)
α	Concrete Damage Plasticity Constitutive Model : dimension constant (3.4.1)
β	Concrete Damage Plasticity Constitutive Model: dimension constant (3.4.1)
Π	Virtual work (3.4.2.1.2)
β	Matrix of strain variations relative to the variations of the kinematic variables (3.4)
ε'	Strain corresponding to the compressive stress f_c
ε_c	Tensile strain of concrete corresponding to rupture modulus (5.2.2)

κ_c	Concrete Damage Plasticity Constitutive Model : damage parameter due to compressive stresses (3.4.1)
ν_c	Poisson's ration of concrete (4.3.2) (4.4.2)
τ^c	Conjugate stress (3.4)
ε'_{cf}	Strain corresponding to the maximum compressive stress f'_c (3.2.2)
μ_f	Coefficient of friction (3.4.2.1.1) (4.3.1) (4.3.3) (4.4.1) (4.4.4.2) (6.4.1.3)
$(f_{EZR,s})_{average}$	Average tensile stress imposed on the end zone rebar (A_{EZR}) immediately after the release of prestensioned strands at service limit state (5.3.2.1) (6.4.1.3)
γ_i	Elastic slip (3.4.2.1.1)
ξ^M	M^{th} variable of a generalized nonlinear finite element analysis (3.4)
ν_p	Poisson's ration of prestressing strands (4.3.2) (4.4.2)

α_p	Concrete Damage Plasticity Constitutive Model : dilatancy parameter (0)
κ_t	Concrete Damage Plasticity Constitutive Model : damage parameter due to tensile stresses (3.4.1)
A_c	Gross cross sectional area of concrete member (4.3.2) (4.4.2) (5.2.1)
A_{EZR}	Vertical reinforcement located within anchorage zone of pretensioned member (5.2.2) (5.3.2.1) (6.4.1.2)
$A_{EZR,IDOT}$	End zone reinforcement required by IDOT for equivalent BT-72 girders (5.3.2.3)
$A_{EZR,IDOT_AASHTO}$	End zone reinforcement required by AASHTO while configured in accordance with IDOT requirements for equivalent BT-72 girders (5.5.6)
$A_{EZR,prov'd}$	Provided end zone reinforcement (5.3.2.1)
$A_{EZR,req'd}$	Minimum required end zone reinforcement (5.3.2.1)

$A_{EZR,Zone1}$	Vertical reinforcement located between member end face and $h_{nc}/8$ referred to as <i>Zone 1</i> (5.3.2.2)
$A_{EZR,Zone2}$	Vertical reinforcement located between $h_{nc}/8$ and $h_{nc}/2$ referred to as <i>Zone 2</i> (5.3.2.2)
A_{nc}	Non-composite cross-sectional area of precast BT-72 bulb-tee (6.2)
A_p	Area of one prestressing strand (4.3.2) (4.4.2)
b	Member width (5.2.1)
B	Strain-displacement transformation matrix to convert nodal displacement to strain at any given point (3.4)
$BT-72$	72-in. deep AASHTO/PCI Bulb-Tee girder (5.3.1)
c	Clear cover to prestressing strands (5.2.1); Vertical distance between the bottom of the bottom flange and the potential end

		zone crack (5.2.2.1) (6.4.1.3)
C	Compression component of Gergley-Sozen equilibrium model, imposed by the moment due to pretensioning eccentricity (5.2.2.1)
CDP	Concrete Damage Plasticity constitutive model (3.4.1)
d	Concrete Damage Plasticity constitutive model: scalar degradation variable (0); Overall member height of a pretensioned concrete member (5.2.1); Non-composite height of a typical BT-72 girder, same as h_{nc} (5.5.2) (5.5.3)
$D(\kappa)$	Concrete Damage Plasticity constitutive model: single degradation damage response (0)
d_c	Concrete Damage Plasticity constitutive model: scalar degradation damage variable due to compressive stresses (0)
d_p	Diameter of prestressing strands (4.3.1)

		(4.3.2) (4.4.2) (6.2) (6.3.5.2)
d_t	Concrete Damage Plasticity constitutive model: scalar degradation damage variable due to tensile stresses (0)
e	Eccentricity of the strand group used in Gergley-Sozen equilibrium model (5.2.2.1)
e_0	Eccentricity of the strand group relative to the centroidal axis of the member (5.2.1)
\mathbf{E}_0	Concrete Damage Plasticity model: initial-elastic stiffness tensor (0)
E_c	Tangent modulus of elasticity corresponding to compressive strength at 28 days (3.2.1)
E'_c	Secant modulus of elasticity corresponding to compressive strength at 28 days (5.3.1) (6.2)
E_{ci}	Modulus of elasticity corresponding to initial compressive strength at release of pretensioning (4.3.2) (4.4.2) (5.2.2)

E_p	Modulus of elasticity of prestressing strands (4.3.2) (4.4.2) (6.2)
$e_{p,draped}$	Eccentricity of the draped strands relative to the bottom of the bottom flanges of WSDOT BWF100 Girders No.1 thru No.8 (6.4.1.1)
$e_{p,straight}$	Eccentricity of the straight strands (including the temporary strands) relative to the bottom of the bottom flanges of WSDOT BWF100 Girders No.1 thru No.8 (6.4.1.1) (6.4.1.2)
EZR	End zone reinforcement (5.3.2.1)
f	Force per unit volume at a given time (3.4)
F	External loads acting on a system (3.4)
f_{b0}	Concrete Damage Plasticity constitutive model: initial biaxial yield compressive stress
f_c	Compressive stress (3.2.2)

f_c	Compressive stress @ 28 days (4.3.2) (4.4.2) (5.3.1) (6.2)
f_{c0}	Concrete Damage Plasticity constitutive model: initial uniaxial yield compressive stress
f_{ci}	Concrete Damage Plasticity constitutive model: initial compressive strength (4.3.2) (4.4.2) (5.3.1) (6.2)
$f_{EZR,allowable}$	Allowable tensile stress in the end zone reinforcement based on Article 5.10.10.1 of AASHTO LRFD (AASHTO LRFD, 2010) (5.3.2) (6.4.1.1) (6.4.1.2)
$f_{EZR,s}$	Tensile stress imposed on the end zone rebar (A_{EZR}) immediately after the release of pretensioned strands at service limit state (5.3.2.1) (6.4.1.2)
F_f	Slip tolerance (3.4.2.1.1)
f_j	Jacking stresses imposed on strands at the release of pretensioning (4.4.1)
F^N	Force component conjugate to N^{th} variable

(3.4)

f_{pe}	Compressive stress in concrete due to effective pretensioning stress including all the applicable losses (3.3.2)
f_{pi}	Prestressing at the strands immediately after release of pretensioning, including the losses due to elastic shortening and relaxation of strands (if any) (6.3.5.2)
f_{pj}	Jacking stress of prestressing strands (4.3.2) (4.4.2)
f_{pu}	Ultimate tensile strength of prestressing strands (4.3.2) (4.4.2) (5.3.1)
f_{py}	Yield strength of prestressing strands (4.3.2) (4.4.2) (5.3.1):

In accordance with AASHTO LRFD Table 5.4.4.1-1, the yield strength of low-relaxation strands is approximated to be 90% the ultimate tensile strength (f_{pu}). generally, this threshold is used for design purposes unless more specific information

is available by the Manufacturer
(AASHTO LRFD, 2010).

f_r	Modulus of rupture defined in accordance with Article 5.4.2.6 of AASHTO LRFD (AASHTO LRFD, 2010) (5.3.1) (5.5.2)
f_{ri}	Initial modulus of rupture at the time of pretensioning release (5.2.2)
f_{se}	Effective stress in prestressing strands including all the applicable losses (3.3.2)
f_{sm}	Axial service in the end zone reinforcing bars upon the release of pretensioning (5.2.2)
f_t	Tensile stress in the prestressed strands upon release of pretensioning (4.4.1)
F_t	Limit of tensile stresses in members with reinforcement (4.4.4.2)
f_y	Yield strength of steel reinforcing bars (3.5.2.1) (6.4.1.3) (6.4.2.1)
G	Out-of-balance or residual forces in a

		system of nonlinear equations (3.4)
h	Overclosure (3.4.2.1.2). Distance along the height of BT-72 girder, measured relative to the bottom of the bottom flange (5.2.2) (5.5.2) (5.5.3) (5.2.2.2) (6.4.1.2)
h_{max}	Vertical location along the height of the member corresponding to the maximum internal moment due to the combined effects of self-weight and prestressing strands in the end zone region of BWF100 specimens (6.4.1.1)
h_{nc}	Overall height of the non-composite BT-72 girder (5.3.2.1) (5.3.2.2)
HPC	High performance concrete (4.2.1)
I	Rank 4 identity matrix
I_I	First invariant defined as the trace of the stress tensor (σ_{ij}) (3.2.4.1)
I_c	Gross moment of inertia (5.2.1)
$IDOT$	Illinois Department of Transportation

(5.1) (5.3.2.3)

I_{nc}	Non-composite moment of inert about the centroid of the precast BT-72 bulb-tee (6.2)
J_2	Second invariant of the deviatoric stress tensor defined as $\frac{1}{2} s_{ij} s_{ij}$ (3.2.4.1)
K_1	Correction factor applicable to modulus of elasticity of concrete, related to aggregate stiffness (3.2.1)
k_c	Decay factor controlling the post-crack response of concrete to uniaxial compression (3.2.2)
ksf	Kips per square foot
ksi	Kips per square inch
L	The distance between the tension (T) and compression (C) components of Gergley-Sozen equilibrium model (5.2.2.1) (6.4.1.1)

L_{beam}	Span length of the concrete member (CL-CL support) (4.3.2) (4.4.2)
lbs	Pounds
L_d	Development length defined as the length required for an embedded reinforcement, including prestressing strands, develop the design strength per at a critical section as identified by design (3.3.2)
l_i	Characteristic length (3.4.2.1.1) (5.4.4)
L_t	Transfer length defined as the length required for an embedded pretensioned strand to transfer effective pretensioning to concrete (4.3.1) (5.2.2)
L_{total}	Total length of BT-72 girder (end face - end face) (5.3.1)
M_{DL}	Internal moment due to the self-weight of BWF100 specimens immediately after the release of pretensioning (6.4.1.1)
M_{max}	Maximum internal moment due to the combined effects of self-weight and

		prestressing strands in the end zone region of BWF100 specimens (6.4.1.1)
M_{pi}	Internal moment due to total prestressed force imposed by the straight, draped and temporary strands immediately after the release of pretensioning (6.4.1.1)
$M_{pi, straight}$	Internal moment due to prestressed force imposed by the straight strands including the temporary strands immediately after the release of pretensioning (6.4.1.1)
$M_{pidraped,}$	Internal moment due to prestressed force imposed by the draped strands immediately after the release of pretensioning (6.4.1.1)
n	Outward normal vector at any point on a given unit area, S (3.4)
N	Reference configuration position (3.4.2.2)
\mathbf{N}	Shape function (3.4)
$NCHRP$	National Cooperative Highway Research Program (5.1)

<i>NDOR</i>	Nebraska Department of Roads (4.2.1)
<i>o.c.</i>	On center (5.3.2.1)
<i>p</i>	Contact pressure (3.4.2.1.2)
<i>pcf</i>	Pounds per cubic foot
<i>PCI BDM</i>	<i>PCI Bridge Design Manual</i> (PCI, 2003) (5.3) (5.3.1) (5.3.1.2) (5.3.1.3) (5.3.2.1) (5.5.2) (5.5.3) (5.5.4) (5.5.5) (5.5.6)
$P_{EZR,r}$	Bursting resistance of the anchorage zone of pretensioned member at service limit state (5.3.2.1)
P_i	Initial pretensioning force upon the release of the strands including the losses due to elastic shortening and strands relaxation (5.2.2) (6.4.1.1) (6.4.1.2)
<i>PPC</i>	Precast pretensioned concrete (5.1)
<i>psf</i>	Pounds per square foot
<i>psi</i>	Pounds per square inch
r	Position vector (3.4)

<i>S</i>	Unit area of a material at a given time (3.4); Concrete Damage Plasticity constitutive model: scalar controlling tensile damage parameter under cyclic loading (3.4.1)
<i>S11</i>	Lateral stress conforming with the local axis of member, defined as follows (4.4.4.2) (5.5.2) (6.4.4) (6.5): Axis 1 - The axis parallel with the lateral orientation Axis 2 - The axis parallel with the vertical orientation Axis 3 - The axis parallel with the longitudinal orientation
<i>S22</i>	Vertical stress conforming with the local axis of member, defined as follows (4.4.4.2) (5.5.2) (6.4.4): <ul style="list-style-type: none"> ▪ Axis 1 - The axis parallel with the lateral orientation ▪ Axis 2 - The axis parallel with the

vertical orientation

- Axis 3 - The axis parallel with the longitudinal orientation

S23

.....

Planar shear stress conforming with the local axis of member, defined as follows

(5.5.2) (5.5.3) (5.5.4) (5.5.5) (5.5.6)
(6.4.4) (6.5):

- Axis 1 - The axis parallel with the lateral orientation
- Axis 2 - The axis parallel with the vertical orientation
- Axis 3 - The axis parallel with the longitudinal orientation

S33

.....

Longitudinal stress conforming with the local axis of member, defined as follows

(4.4.4.2) (5.5.2) (5.5.3) (5.5.4) (5.5.5)
(5.5.6) (6.4.4):

- Axis 1 - The axis parallel with the lateral orientation
- Axis 2 - The axis parallel with the vertical orientation

- Axis 3 - The axis parallel with the longitudinal orientation

$S_{nc,b}$	Non-composite section modulus for the extreme bottom fiber of the precast BT-72 bulb-tee (6.2)
$S_{nc,t}$	Non-composite section modulus for the extreme top fiber of the precast BT-72 bulb-tee (6.2)
s_p	Spacing of prestressing strands (4.4.1)
$Spac.$	Spaced (5.3.2.1)
t	Force per unit area of a material at a given time (3.4)
T	Tension component of Gergley-Sozen equilibrium model, imposed by the moment due to pretensioning eccentricity (5.2.2.1)
$T1 \& T2$	Tension ties within the end zone of pretensioned members based in accordance with Crispino's double-tie, strut-and-tie mode (5.2.2.2)

T_{max}	Maximum tension component of Gergley-Sozen equilibrium model, imposed by the moment due to pretensioning eccentricity (5.2.2.1) (6.4.1.1)
\mathbf{u}	Displacement vector (3.4)
\mathbf{u}_e	Nodal displacement vector (3.4)
v	Velocity of neighboring particles inside a given body (3.4)
V	Volume of material at given point of time (3.4)
w_c	Weight density of concrete (3.2.1) (4.3.2) (4.4.2) (6.2)
w_{cr}	Crack width (5.3.2.2)
w_p	Weight density of prestressing strands (4.3.2) (4.4.2)
$WSDOT$	Washington Department of Transportation (6.1)
x	Distance along the longitudinal axis of the member, measured from the member end

		face (6.4.1.1)
\mathbf{X}^m	Position vector of master node (3.4.2.2)
\mathbf{X}^s	Position vector of slave node (3.4.2.2)
y	Vertical position of bursting or spalling stresses at the member end face, relative to the overall member height, d (5.2.1); Vertical distance between the applied pretensioning and the resultant force in accordance with Crispino's double-tie, strut-and-tie mode (5.2.2.2) (6.4.1.2)
y_c	The centroid of the partial cross section of a typical BWF100 girder required to resist the axial pretensioning force imposed by the straight strands with equivalent compression force at the distance $h = 100$ in. from the member end face, measured from the bottom of the bottom flange (6.4.1.2)
$y_{nc,b}$	Distance from the extreme bottom fiber to the centroid of the non-composite precast

BT-72 bulb-tee (6.2)

$y_{nc,t}$

.....

Distance from the extreme top fiber to the centroid of the non-composite precast BT-72 bulb-tee (6.2)

Chapter 3 - A Methodological Approach for Finite Element Modeling of Pretensioned Concrete Girders

3.1. Objectives

The current state of analysis and design of pretensioned concrete members indicates a serious lack of unified and practical guidelines for analytical simulation of precast prestressed concrete members. There is a need for development of a validated methodological approach to analytically simulate the behavior of pretensioned concrete members during various stages of construction and service life. This chapter represents modeling methodologies which primarily focus on the response of the members immediately after the release of the pretensioning.

The main objective of this research is careful evaluation of modeling approaches that can adequately simulate the pretensioning mechanism and predict the inelastic response of a pretensioned member immediately after the release of the pretensioning.

Once a reliable analytical method is developed and validated against the available closed-form solutions, a series of comparative analyses are conducted to verify the simulation of concentrically pretensioned concrete prisms against experimental data. The comparative analyses not only show conformance of the analytical results with the test data, they also indicate the sensitivity of the simulated models to passive confinement in the form of close stirrups along the length of the member. It is important to note that availability of analytical procedures to simulate the pretensioning mechanism can have direct impact on future research in the area of precast/prestressed concrete considering the costly laboratory experiments using full or scaled specimens.

3.2. Literature Review

3.2.1. Concrete: Fundamental Properties

Modulus of elasticity of concrete is generally estimated based on the recommendations of the ACI codes as follows (ACI, 2008):

$$E_c = 33 w_c^{1.5} \sqrt{f'_c} \quad (3.1)$$

where weight density of concrete, w_c , and compressive strength, f'_c , shall be given in pounds per cubic feet (pcf) and pounds per square inches (psi).

AASHTO LRFD recommends a similar expression for modulus of elasticity concrete specimens with addition of a correction factor, K_1 , for the stiffness of the aggregate (AASHTO LRFD, 2010):

$$E_c = 33 K_1 w_c^{1.5} \sqrt{f'_c} \quad (3.2)$$

The correction factor, K_1 , is generally taken as 1.0 unless physical test data shows otherwise. Equation (3.2) is applicable to concrete specimens with weight density ranging from 90 pcf to 155 pcf and compressive strengths up to 15 ksi.

Equations (3.1) and (3.2) are based on the secant stiffness which defines the slope between the origin and the stress-strain curve at $0.4 f'_c$ where concrete response is expected to enter inelastic regime. Since the difference between the secant modulus, E'_c , and the initial tangent modulus, E_c , is negligible for normal-weight concrete, Equation (3.3) can be simplified to the following form (Collins & Mitchell, 1997):

$$E_c = 57000 \sqrt{f'_c} \quad (3.3)$$

where secant modulus is defined as

$$E'_c = \frac{f'_c}{\varepsilon'_c} \quad (3.4)$$

In Equation (3.5), ε'_c represents the maximum strain corresponding to the peak compressive stress, f'_c .

Past research indicates that when compressive strength of concrete exceeds the threshold of 6000 psi, Equations (3.1) and (3.2) may significantly overestimate the modulus of elasticity of concrete. Alternatively, the stiffness of normal-weight concrete with compressive strengths exceeding 6000 psi may be estimated using Equation (3.5) (Carrasquillo, Nilson, & Slate, 1981):

$$E_c = 40,000\sqrt{f'_c} + 1,000,000 \text{ psi} \quad (3.5)$$

Collins and Mitchell (1997) recommend the secant modulus of elasticity of normal-weight concrete be estimated using Equation (3.5) in order to prevent potential overestimation as mentioned above.

3.2.1. Poisson's Ratio

The Poisson's ratio, ν_c , for concrete ranges from 0.15 to 0.22 while the representative values are 0.19 or 0.20 (Chen, Plasticity in Reinforced Concrete, 2007). Past researches show that ν_c remains constant under uniaxial compression until 80% f'_c . Figure 3-1 shows that above the stress-strength ratios of 80%, Poisson's ratio begins to increase towards 0.5 regardless of the different compressive strengths and initial Poisson's ratios ranging 0.19 to 0.24.

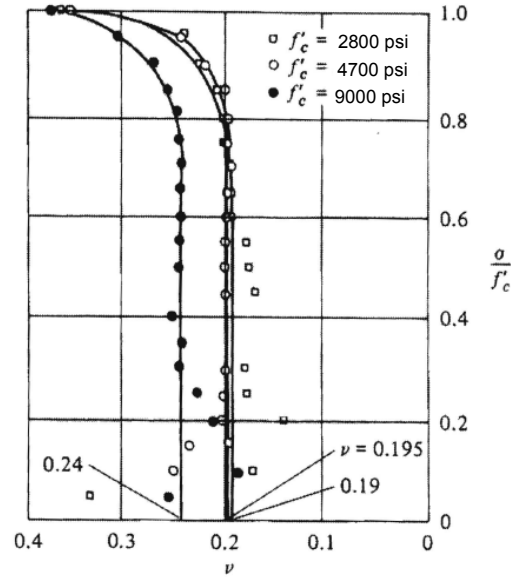


Figure 3-1: Relationship between stress-strength and Poisson's ration (Chen, Plasticity in Reinforced Concrete, 2007).

3.2.2. Concrete in Uniaxial Compression

The basic constituents of concrete are aggregate and cement paste. Although both of these constituents have linear response to uniaxial compression., the response of concrete is nonlinear. The nonlinearity of concrete's response to uniaxial compression is mainly due to the interaction between the aggregate and cement paste. At relatively low compressive stresses, concrete develops micro-cracks at the aggregate-cement paste interface. As the compressive stress increases, the cracks propagate further, resulting in "softening" of the concrete. As concrete reaches compressive failure, significant longitudinal cracking will dominate the specimen coupled with lateral expansion (Collins & Mitchell, 1997).

While several expressions have been introduced to describe the compressive stress-strain response of concrete, the generalized relationship of Equation (3.6) derived by

Thorenfeldt et. al. (Thorenfeldt, Tomaszewicz, & Jensen, June 1987) is widely used as a reference for concretes with various compressive strengths. The corresponding stress-strain relationship was derived to represent a wide domain of stress-strain curves pertaining to concretes of different strengths:

$$f_c = \left[\frac{n_c \left(\frac{\varepsilon'_{cf}}{\varepsilon'_c} \right)}{(n-1) + \left(\frac{\varepsilon'_{cf}}{\varepsilon'_c} \right)^{n_c k_c}} \right] f'_c \quad (3.6)$$

Note that in Equation (3.6), ε'_{cf} represents the strain corresponding to the compressive stress f_c . Similarly, ε'_c represents the strain as the compressive stress, f_c , reaches the maximum compressive stress f'_c .

In reference to Equation (3.6), n_c is the curve-fitting factor defined as the ratio of E_c/E'_c , ranges from 4 for low-strength concrete to 1.3 for high-strength concrete (Popovics, 1970). Collins and Mitchell (Collins & Mitchell, 1997) introduce a mathematical relationship for n_c as defined below:

$$n_c = 0.8 + \frac{f'_c (psi)}{2,500} \quad (3.7)$$

Subsequently, the maximum compressive strain, ε'_c , can be expressed as follows:

$$\varepsilon'_c = \left(\frac{f'_c}{E_c} \right) \frac{n_c}{n_c - 1} \quad (3.8)$$

Additionally, k_c is defined as a post-peak decay factor which increases as the concrete strength increases, ranging from 1.0 for f'_c equal or less than 3000 psi to about 2.0 for f'_c of 12,000 psi. The post-peak decay factor, k_c , is defined as:

$$k_c = 0.6 + \frac{f'_c (psi)}{9,000} \quad (3.9)$$

Figure 3-2 shows typical stress-strain curves derived by Collins and Mitchell for concrete samples with various compressive strengths ranging from 2,000 psi to 12,000 psi (Collins & Mitchell, 1997). It is observed that as the compressive strength increases, the potential for brittle failure of concrete increase:

- The threshold for linear-elastic response of concrete $\left(\frac{f_c}{f'_c}\right)$ increases from 0.45 at lower strengths to nearly 0.85 at high strength specimens, and
- The plateau of softening degradation significantly decreases as the compressive strength increases.

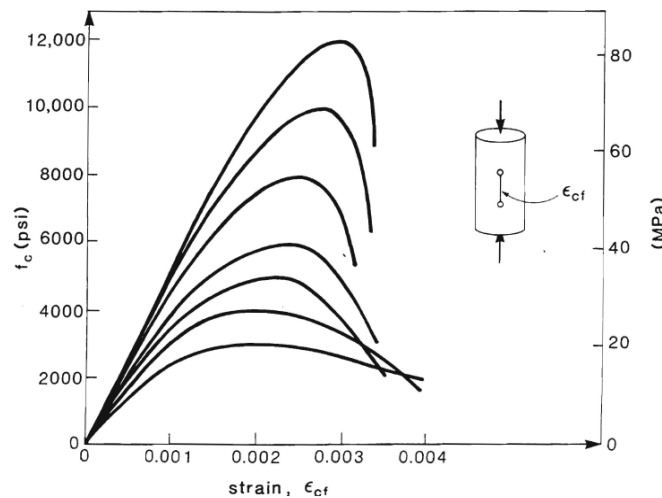


Figure 3-2: Typical compressive stress-strain curves for concretes with various compressive strengths (Collins & Mitchell, 1997).

3.2.3. Concrete in Uniaxial Tension

It is widely accepted that the stress-strain relationship of concrete to uniaxial tension is linear up to cracking. Response of concrete to pure tension is very difficult to measure

due to the brittle nature of tensile failure. Figure 3-3 shows comparison of experimental and theoretical stress-strain relationships for 4 in. x 8 in. cylindrical concrete samples with compressive strengths of 6,000 psi, 10,000 psi, and 15,000 psi.

The tensile strength of concrete is usually measured by indirect tests. For instance, the modulus of rupture, f_r , can be determined from the response of specimens to pure bending. Alternatively, the splitting strength, f_{sp} , can be measured by splitting a cylindrical test specimen subject to line loading. Tensile strength of concrete is influenced by a number of parameters such as the volume factor. Past researches indicate as the concrete volume increases, the cracking stress will be reduced inversely proportional to approximately the fourth root of the size (Collins & Mitchell, 1997).

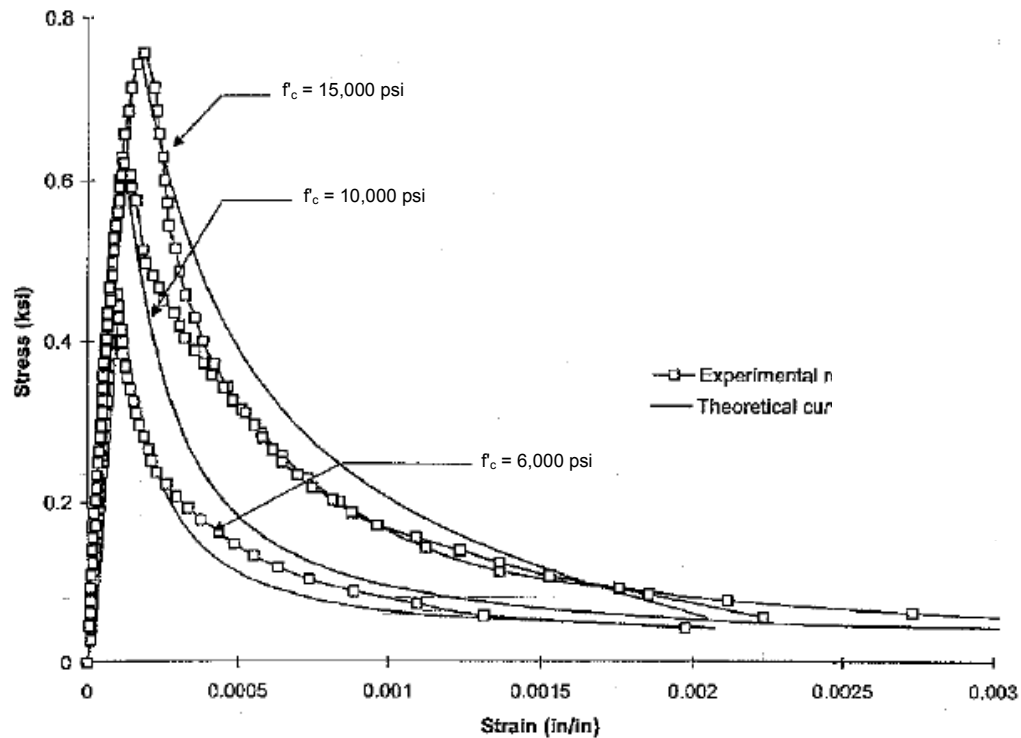


Figure 3-3: Stress-strain relationships for high-strength concrete in uniaxial tension (Li & Ansari, 1999).

Therefore, if the depth of a girder is doubled, the tensile cracking stress is anticipated to be reduced by a factor of 0.84. Collins and Mitchell (1997) recommend that members with large strain gradients are anticipated to withstand higher local tensile stresses prior to failure. This is an important factor affecting the behavior of large girders such as bulb-tee and super-girders used in the current highway construction.

Therefore, larger members are subject to cracking at relatively lower tensile stresses compared with smaller members with the same concrete properties. This is an important factor affecting the end zone cracking of the I-girders studied in Chapter 6. Past experiments show that the direct tensile strength of concrete is related to the compressive strength, f'_c , as follows (Collins & Mitchell, 1997):

$$f_{cr} = 4.00 \lambda \sqrt{f'_c} \text{ (psi)} \quad (3.10)$$

where λ represents the factor that accounts for the density of concrete as listed below:

$$\lambda = \begin{cases} 1.00 \cdots \text{normal - weight concrete} \\ 0.85 \cdots \text{sand - lightweight concrete} \\ 0.75 \cdots \text{all - lightweight concrete} \end{cases}$$

Modulus of rupture, f_r , is widely used for estimation of the flexural cracking strength of concrete. The most common expression for f_r is defined by ACI Code as follows:

$$f_r = 7.5 \lambda \sqrt{f'_c} \text{ (psi)} \quad (3.11)$$

Figure 3-4 shows different test methods and the approximate relationships that are commonly used in order to estimate cracking strength of concrete by means of correlation of the obtained experimental results.

Smearred crack is one of the common methods of simulating the tension stiffening effect. In this approach, the cracked section is treated as continuum instead of discrete

cracked sub-sections. Once the first crack is initiated, concrete will be assumed as orthotropic material. This enables the constitutive law to approximate gradual or sudden drop of strength as cracks propagate. While concrete loses strength in the direction of tension, shear strength can be reserved due to aggregate interlocking as long as a positive shear modulus is retained in the analysis (Chen, Plasticity in Reinforced Concrete, 2007).

When a nonlinear stress-strain relationship is coupled with smeared crack approach, concrete is allowed to retain certain amount of tension beyond cracking strength. Among the various tensile stress-strain relationships, the curvilinear tension softening is commonly used since it also allows for better numerical convergence (see Figure 3-5).

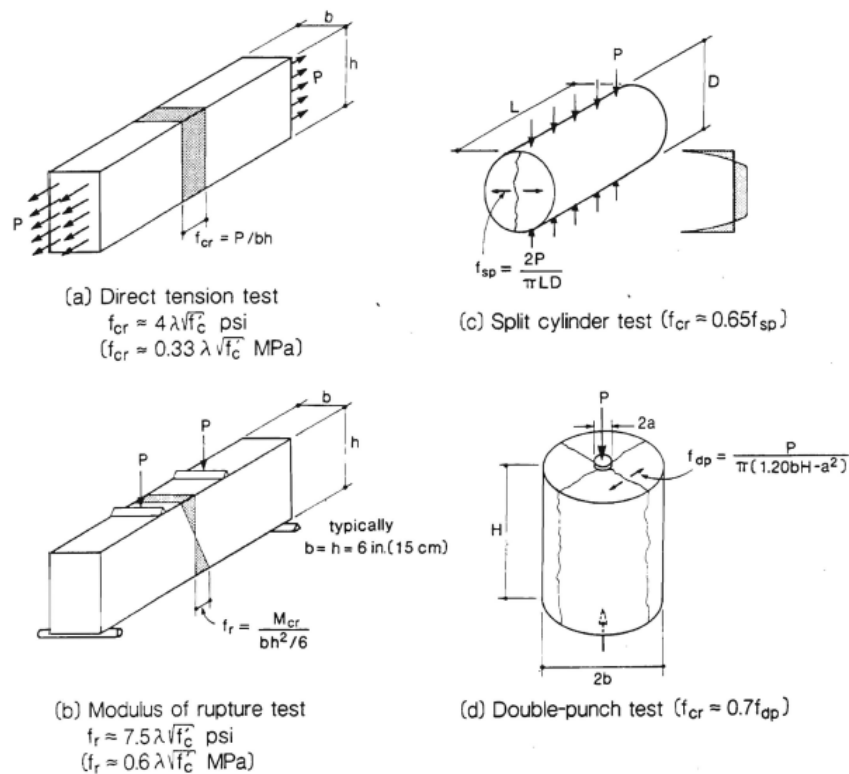


Figure 3-4: Common methods of estimating tensile strength of concrete (Collins & Mitchell, 1997).

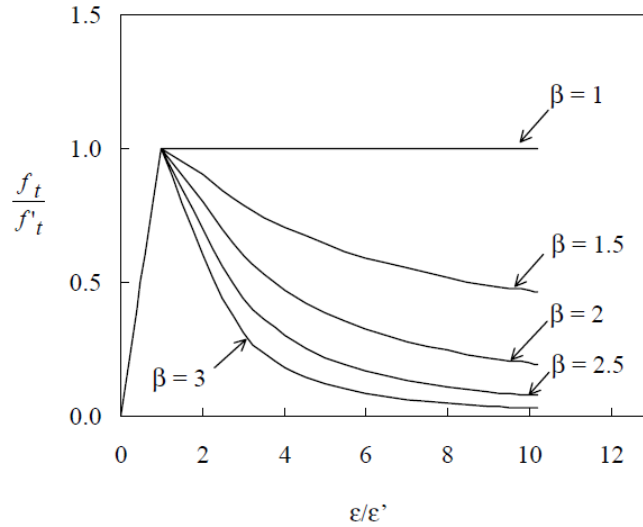


Figure 3-5: Tensile stress-strain relationship for concrete with curvilinear tension softening (Piyasena, 2002).

The response of concrete to uniaxial tension (Figure 3-5) can be expressed as follows

(Piyasena, 2002):

$$f_t = \begin{cases} f'_t \left(\frac{\varepsilon}{\varepsilon'} \right) \cdots \text{if } \left(\frac{\varepsilon}{\varepsilon'} \right) \leq 1.0 \\ \frac{\beta f'_t \left(\frac{\varepsilon}{\varepsilon'} \right)}{\beta - 1 + \left(\frac{\varepsilon}{\varepsilon'} \right)^\beta} \cdots \text{if } \left(\frac{\varepsilon}{\varepsilon'} \right) > 1.0 \end{cases} \quad (3.12)$$

where ε denotes the tensile straining of concrete at the instance of loading, f_t is the tensile stress corresponding to ε , and f'_t and ε' represent the tensile strength of concrete and the corresponding peak tensile strain. The parameter β controls the rate of decline of tension stiffening with the increase of loading. In accordance with Prakhya and Morley, β is dependent on the various parameters such as member sectional properties and depth of neutral axis at the state of cracking (Prakhya & Morley, 1990). Additionally, β indirectly simulates the effect of bond slippage; the steeper the descending branch of stress-strain relationship, the more the loss of tension stiffening at smaller slips (Piyasena, 2002).

3.2.4. Fracture Mechanics

As shown in Figure 3-6, the 3D failure envelope for concrete is deemed to follow a cone-like path in the space of principal stresses. Two distinct levels of response characterize the triaxial failure space of concrete continuum as an isotropic material (Chen, Plasticity in Reinforced Concrete, 2007):

- *Elastic Limit* - stable onset of crack propagation
- *Failure Limit* - Instability as the result of crack propagation

Referring to Figure 3-6, hydrostatic axis is defined as a line along which all three principal stresses are equal:

$$\sigma_1 = \sigma_2 = \sigma_3 \quad (3.13)$$

A deviatoric section is defined as a plane perpendicular to the hydrostatic axis. As the hydrostatic compression increases, the deviatoric planes tend to follow circular patterns. This is an indication that the failure is independent of the third invariant of stress tensor. On the contrary, when the hydrostatic pressure decreases, the deviatoric planes tend to transform to convex (non-circular) patterns (Chen, Plasticity in Reinforced Concrete, 2007). Deviatoric pressure is defined as

$$p = \frac{1}{3} \sum_{i=1}^3 \sigma_i \quad (3.14)$$

where state of tension and compression is accordingly determined by the following conditions:

$p > 0$ Compression

$p < 0$ Tension

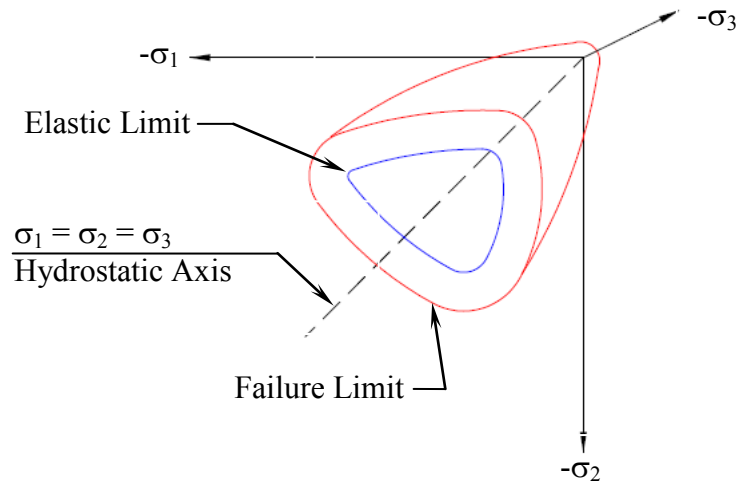


Figure 3-6: Theoretical triaxial failure space of concrete. Adapted from (Chen, Plasticity in Reinforced Concrete, 2007).

The fracture caused by hydrostatic compression is deemed to form closed surfaces around the coarser aggregates. As the hydrostatic pressure increases, the compaction of the cement paste consequently increases without subsequent interruption in the material. Chin and Zimmerman (1965) show that as the uniaxial hydrostatic compression is unloaded and then reloaded, the uniaxial compressive strength will be anticipated to be reduced down to 60% of the original value.

The following includes a brief overview of the common criteria for evaluation tensile and compressive failure in concrete. A more elaborate discussion of the constitutive law selected for the analytical purposes of this research is presented in Section 3.4.1.

3.2.4.1. Maximum-Tensile-Stress Criterion (Rankine)

The maximum-tensile-stress criterion by Rankine dating back to 1876 is still a generally accepted tool to evaluate whether the nature of failure is due to tension or compression (Chen, Plasticity in Reinforced Concrete, 2007). Based on Rankine's criterion, brittle fracture of concrete occurs when the maximum principal stress (σ_i) inside the material reaches the tensile strength (f'_t). Per Rankine's argument, such failure

will happen regardless of the state of normal and/or shearing stresses. The fracture surfaces defined by Rankine's criterion are expressed in terms of maximum principal stress:

$$\text{Max}(\sigma_1, \sigma_2, \sigma_3) = f'_{t,\text{max}} \quad (3.15)$$

Equation (3.15) defines three planes orthogonal to the principal axes, commonly referred to as fracture-cutoff surfaces defined as below (Chen, Plasticity in Reinforced Concrete, 2007):

$$f(I_1, J_2, \theta) = \left(2\sqrt{3}\right) \frac{\sqrt{J_2}}{\sqrt{3}} \cos(\theta) + I_1 - 3f'_t = 0 \quad (3.16)$$

where I_1 and J_2 represent the first invariant (trace of stress tensor) and the second invariant of the deviatoric tensor, respectively. Additionally, θ is defined as the angle of similarity which is measured from positive σ_1 and lies in the deviatoric plane as shown in Figure 3-7 where σ_1 , σ_2 and σ_3 correspond to principal stresses.

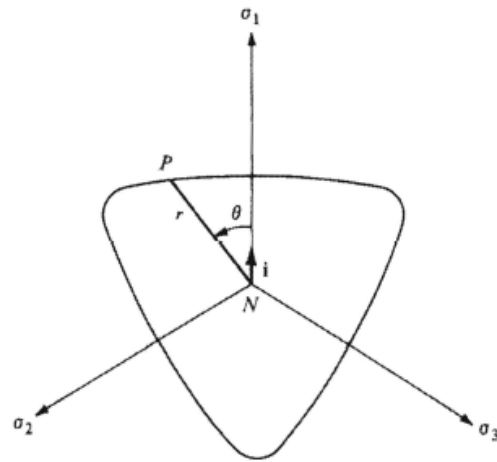


Figure 3-7: Definition of angle of similarity, θ (Chen, Plasticity in Reinforced Concrete, 2007).

3.2.4.2. Shearing-Stress Criterion (Tresca & Von Mises)

Tresca yield-criterion (dating back to 1864) is based on the premise that yielding is initiated once shearing stress reaches a critical value (τ_{cr}). Tresca criterion is mathematically defined as follows (Chen, Plasticity in Reinforced Concrete, 2007):

$$\max\left(\frac{1}{2}|\sigma_1 - \sigma_2|, \frac{1}{2}|\sigma_2 - \sigma_3|, \frac{1}{2}|\sigma_3 - \sigma_1|\right) = \tau_{cr} \quad (3.17)$$

As mentioned above, τ_{cr} represents a critical shearing stress which is commonly referred to as yielding stress in pure shear:

$$f(J_2, \theta) = \sqrt{J_2} \sin\left(\theta + \frac{\pi}{3}\right) - \tau_{cr} = 0 \quad (3.18)$$

Figure 3-8 shows Tresca and Van Mises shearing stress criteria as matched in tension on a deviatoric plane. As shown, Tresca's yielding surface is confined inside Von Mises octahedral yield criteria which is defined as follows (Chen, Plasticity in Reinforced Concrete, 2007):

$$f(J_2) = J_2 - \tau_{cr} = 0 \quad (3.19)$$

In uniaxial tension, Van Mises yield occurs when σ_1 reaches the yielding stress (σ_y) while σ_2 and σ_3 are null. This is mathematically equivalent to

$$\sigma_y^{Van\ Mises} = \sqrt{3} \tau_{cr} \quad (3.20)$$

while under similar conditions, Tresca's criteria results in

$$\sigma_y^{Tresca} = 2 \tau_{cr} \quad (3.21)$$

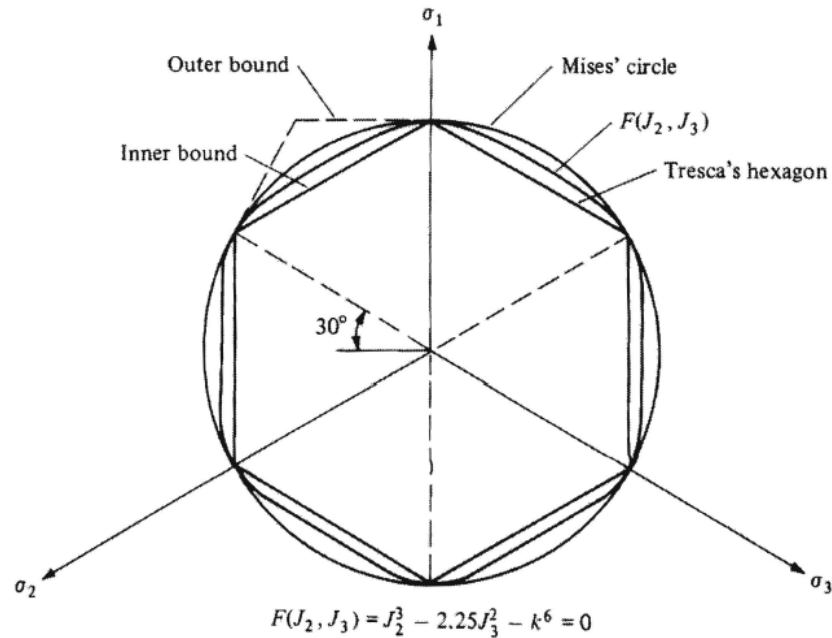


Figure 3-8: Tresca and Van Mises shearing stress criteria with inner and outer bounds (Chen, Plasticity in Reinforced Concrete, 2007).

3.2.5. Finite Element Modeling of Pretensioned Concrete Members

In the past 30 years, many attempts have been made to propose finite element models which can capture the response of pretensioned concrete members. Dating back to 1978, Mirza and Tawfik (1978) presented a one-dimensional mathematical modeling which included a stiffness analysis for detensioning (release) process. This model required the system stiffness matrix and load vectors to be updated upon the releasing of each individual strands, resulting in a time consuming process.

Kannel et al. (Kannel, French, & Stolarski, 1997) utilized a three-dimensional finite element model to investigate the effect of the release methodologies on the end cracking in the pretensioned concrete. This model included continuum elements to model the concrete girder and truss elements to model the strands. The transfer length was indirectly modeled using two methodologies: 1) cross-sectional areas of the strands were

linearly varied from zero (at the end face of the girder) to the maximum (at the end of the theoretical transfer length), and 2) truss elements were constrained to the continuum elements using rigid-plastic springs. The validation of the analytical results was done through field observations. The numerical simulations were performed using ABAQUS software. The study indicated that the results obtained by the models with ramped-area strands and spring transfer methods did not significantly differ. The finite element models showed a significant concentration of horizontal shear stresses at the interface between the web and bottom flange at the full release along the first 18 in. of the specimens from the end face. This was attributed to the transfer of the prestressing force from the bottom flange to the web. The results of the study complemented the earlier conclusions by Mirza and Tawfik (1978) with additional emphasis on the three-dimensional characteristics of the stresses in the end zone of pretensioned concrete members. The finite element models were not expected to capture the complex nature of the pretensioning mechanism and the resulting stress field; however, they were judged to be accurate enough for the study of the response of the members to different pattern of strands release using flame-cutting.

A nonlinear finite element model using a commercial code (ANSYS) was used by Kaewunruen and Remennikov to analyze railway prestressed concrete sleepers (Kaewunruen & Remennikov, 2006). This model included brick elements to represent the concrete matrix with embedded three-dimensional truss elements simulating the prestressing. Four different finite element models were used with characteristics summarized in Table 3-1. The bottom and top fiber stresses of the finite element simulations of the sleepers were observed to be identical to the closed form solutions.

As shown in Figure 3-9, the finite element simulations indicated that MAT2 and MAT3 concrete models seemed to well represent the hardening segment of the nonlinear load-deflection curve obtained by the experimental observations while neither models could capture the softening behavior. However, MAT2 and MAT3 concrete models very well approximated the maximum loads corresponding to peak deflections within 4.5% and 5.3% of the experimental observations, respectively.

Table 3-1: Material models used in the finite element analysis of concrete sleepers by Kaewunruen and Remennikov (2006).

Model	Concrete Model		Pretensioning Wire Model	
	Tension	Compression	Distribution	Material Properties
MAT1	Linear Elastic	Linear Elastic	Discrete	Linear Elastic
MAT2	Linear Elastic	Multi-linear Isotropic	Discrete	Linear Elastic
MAT3	Linear Elastic	Multi-linear Isotropic	Discrete	Multi-linear Isotropic
MAT4	Cracking	Multi-linear Crushing	Discrete	Multi-linear Isotropic

Multi-linear stress-strain curve of concrete

Multi-linear stress-strain curve of wires

Note: 1 in. = 25.4 mm; 1 psi = 6.89 kPa.

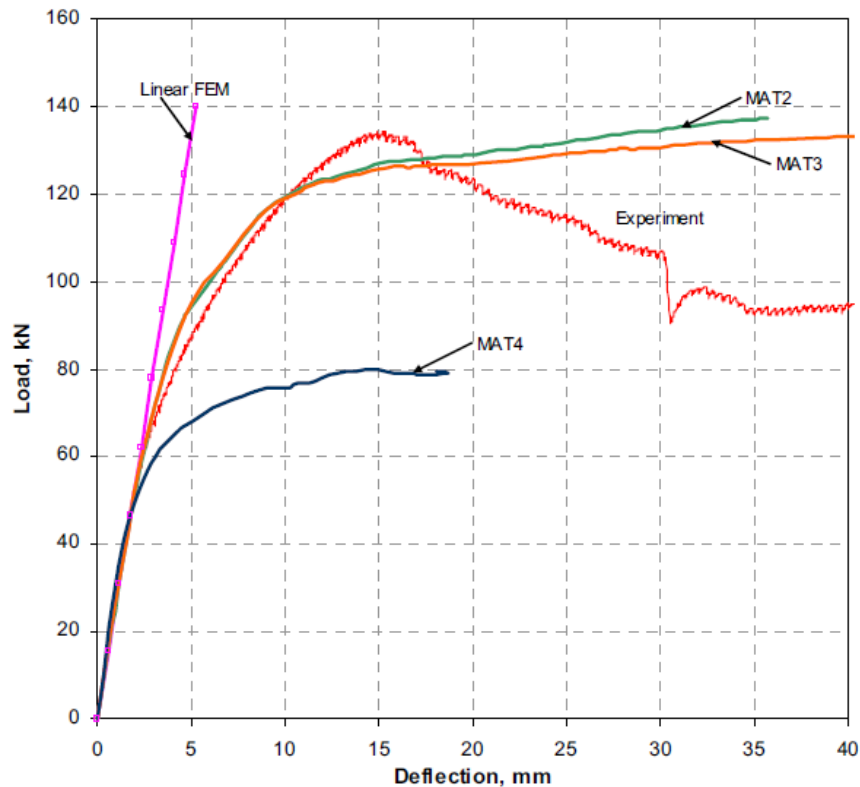


Figure 3-9: Finite element solutions for load-deflection responses of pretensioned concrete railway sleepers by Kaewunruen and Remennikov (2006).

Note: 1 in. = 25.4 mm; 1 kip = 4.448 kN.

Stephen (2006) used a comprehensive three-dimensional finite element model utilizing ABAQUS to simulate the long-term behavior of precast/prestressed concrete bridges. This model included elastoplastic material modeling capable of capturing the nonlinear behavior of various concrete members (e.g., deck slab, pretensioned concrete girders) due to long term effects such as creep and shrinkage. The model required an external subroutine to facilitate specific operations such as prestressing and application of the long term effects. The finite element simulations were validated against the data collected during an earlier study of Route 104 Bridge over the Newfound River in

Bristol, New Hampshire, conducted by Federal Highway Administration (FHWA). The validation process included analytical modeling of a similar composite deck-girder system and comparison of the results with field observations based on the strain readings at the midspan of the bottom flanges of the pretensioned concrete girders. The main focus of the study was on the progression of the strain and deflection as the result of aging of the concrete. The numerical simulations were simplified for a simple-span girder as opposed to the actual continuous configuration. Meanwhile, the finite element predicted the potential cracking of the deck slab due to restraints by the by the girder and reinforcement. The conclusion was then extended to the response of the same composite de-girder system but in a continuous superstructure configuration.

The elasto-plastic characteristics of the concrete deck slab were simulated using the Concrete Damage Plasticity (CDP) model which is discussed in Section 3.4.1. Meanwhile, CDP was not used to model the pretensioned girders since it only allowed for isotropic properties. This was deemed to conflict with the effects of creep which was applied as orthotropic thermal expansion strain. Instead, the age dependency of elastic modulus as well as compressive and tensile strengths of concrete was controlled by a field variable enforced through a user subroutine.

Rabczuk and Eibl (2004) proposed a coupled element free Galerkin method to analyze prestressed concrete beams under quasi-static loading. The constitutive law governing the concrete medium was based on a coupled damage-plasticity model. The reinforcement was modeled as discrete beam elements so that the interaction between concrete and reinforcement can be modeled. The bond model included two modes of failure: pullout failure, and splitting failure. The formulation of the bond model was

based on the radial stress-radial strain relation with three distinct domains: the nonlinear material behavior including the initiation and propagation of cracks, linear softening, and residual strength. The proposed method of simulating pretensioned concrete girders requires that concrete be discretized with particles. As shown in Figure 3-10, the finite element modeling approach was able to approximate the behavior of two beams with different failure modes: Beam I with bending failure and Beam II with shear failure.

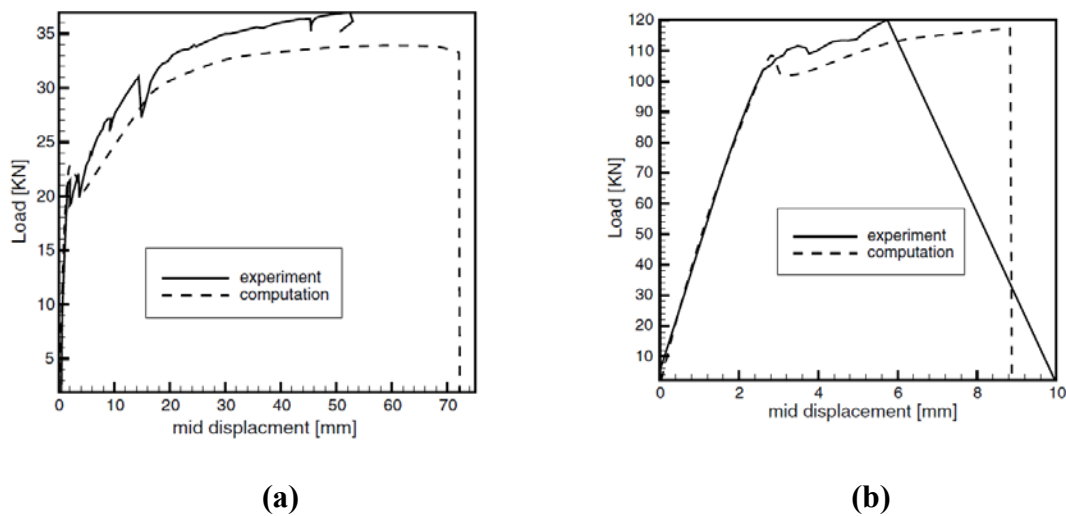


Figure 3-10: Load mid displacement curve by Rabczuk and Eibl (2004): (a) Beam I with bending failure and (b) Beam II with shear failure.

Note: 1 in. = 25.4 mm; 1 kip = 4.448 kN

It was observed that a two-dimensional plane stress analysis seemed to be adequate to simulate the response of members with constant thickness as the in the case of Beam I. However, when the failure mode is a combination of shear and pullout as in the case of Beam II, the proposed approach is not able to completely capture the actual failure. A discrete crack model and three -dimensional analysis were recommended as potential solutions to be considered for future research.

More recently, Ayoub and Filippou (2010) proposed a nonlinear model for simulation of the pretensioned prestressed concrete girders. The model was derived from a two-field mixed formulation with independent approximation of: i) forces and ii) displacements. The simulation approach consisted of three main components: i) concrete girder simulated as a beam-column, ii) prestressing strands modeled as truss elements, and iii) a bond element to model the prestress transfer between the concrete and strands. The constitutive laws governing the nonlinear response of concrete and strands were based on discretization of the mediums into fibers with uniaxial hysteric models. The bond model at the interface between the concrete and strand was formulated using special bond stress-slip relations. The pretensioning mechanism was divided into discrete time steps representing various stages of the operation as summarized in Table 3-2:

Table 3-2: Prestressing stages utilized in the finite element modeling of prestressed concrete girders proposed by Ayoub and Filippou (2010).

Time	Operation	Model
t_0	Prestressing of strands in the casting bed	Beam-column elements simulating concrete are inactive; Bond elements are inactive; Strands are active, and Prestressing is applied to strands.
t_1	Load transfer to concrete	Beam-column elements simulating concrete are active; Bond elements are active; Strands are active, Bedding element is removed.

The finite element models were based on the specimens previously tested by Michell et. al. (1993) for the effect of high strength concrete of the transfer and development length of prestressing strands as scheme as shown in Figure 3-11:

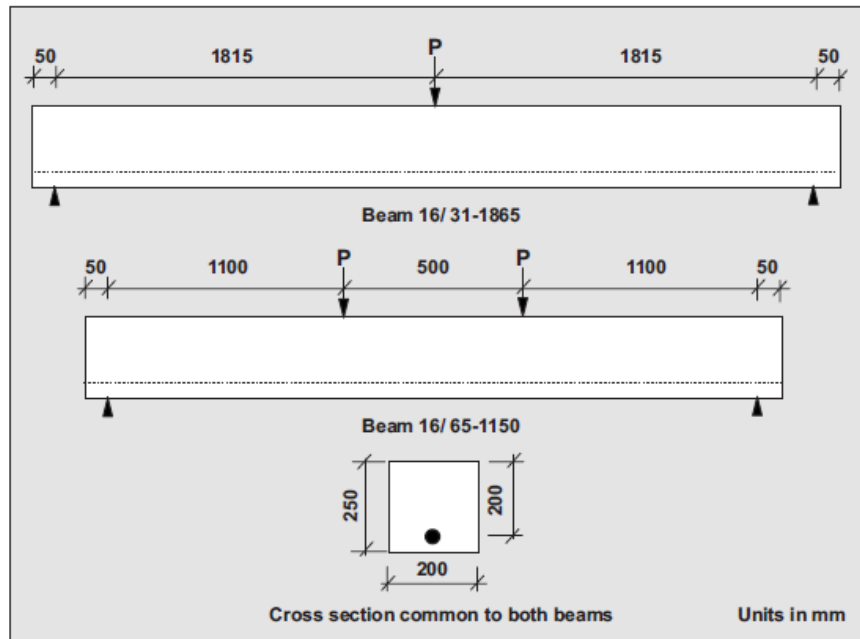


Figure 3-11: Test specimens used for the analytical purposes by Ayoub and Filippou (2010)

Note: 1 in. = 25.4 mm

Figure 3-12 shows the distribution of the tensile force in the strands during the analytical simulation of prestressing:

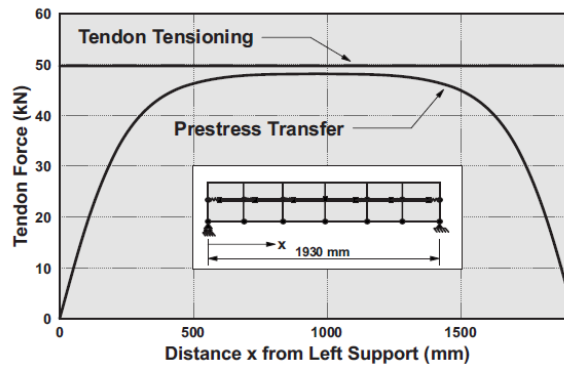


Figure 3-12: Analytical distribution of tensile force in the strands during the prestressing by Ayoub

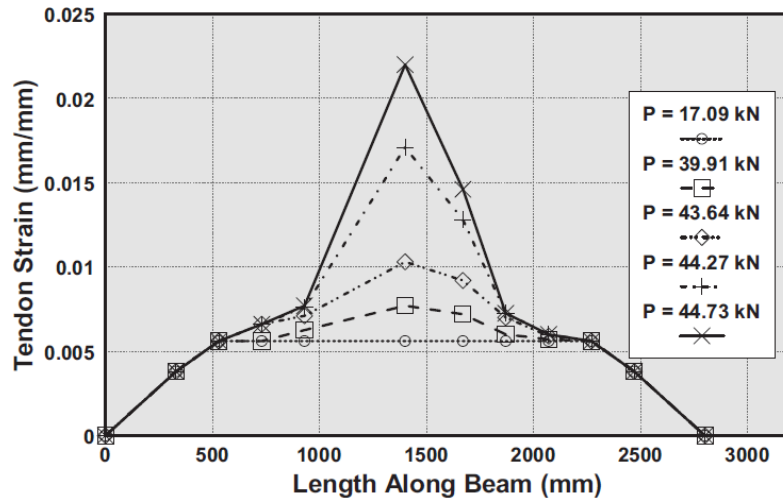
and Filippou (2010)

Note: 1 in. = 25.4 mm; 1 kip = 4.448 kN

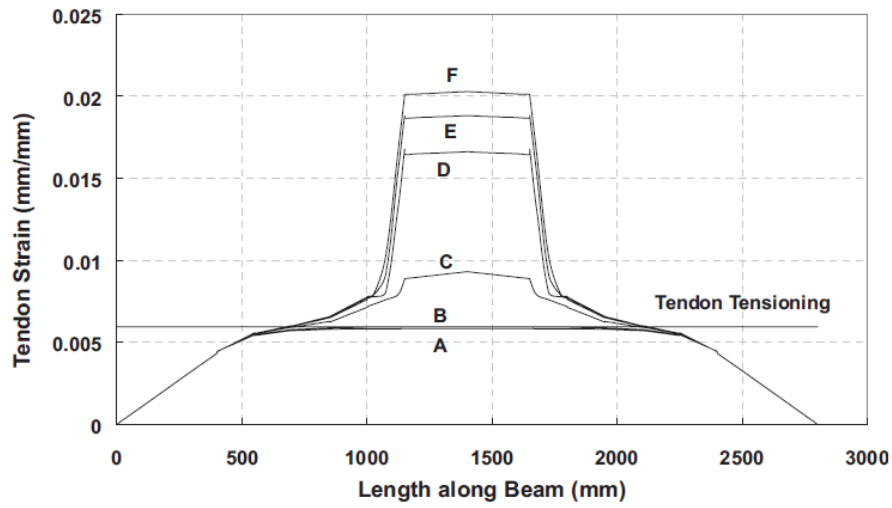
The bond between the strands and concrete host is modeled utilizing distributed interface elements that simulate the bond-slip relations. Figure 3-13 (a) and (b) show the comparison of the strains in the strands as obtained by the experimental observations versus the corresponding finite element simulations. It is observed that the transfer and development lengths are very well captures by the finite element simulations.

The correlation between the analytical results and the experimental observations confirmed the accuracy and efficiency of the proposed finite element approach for modeling of pretensioned concrete girders.

This research includes evaluation of alternative methodologies that use three-dimensional finite element modeling of pretensioned members, which are suitable for predicting elastoplastic response of concrete immediately after the release of pretensioning. Since concrete is modeled as a 3D continuum hosting the pretensioned strands, the global and local effects of pretensioning can be assessed in full details.



(a)



(b)

Figure 3-13: Comparison of straining of strands by Ayoub and Filippou (2010): (a) the experimental results and (b) the corresponding finite element simulations.

Note: 1 in. = 25.4 mm

3.3. Overview of Pretensioning Mechanism

Pretensioning of concrete members refers to the practice where prestressing strands are tensioned prior to casting concrete. Once concrete attains adequate strength (commonly referred to as initial compressive strength), strands are released while bonded with the host concrete. The process of load transfer between the pretensioned strands and concrete host is based on the following mechanisms: 1) Adhesion at the interface between strands and concrete, 2) Hoyer (wedging) effect, and 3) Mechanical interlocking between strands and concrete. The analytical techniques proposed in this paper simulate the combined effects of these factors. Figure 3-14 shows the schematic interrelationship among the factors affecting the pretensioning mechanism:

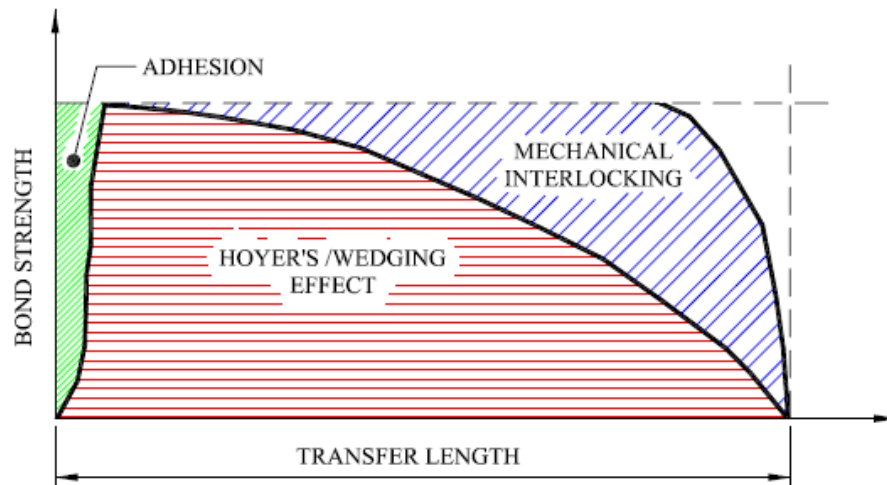


Figure 3-14: Schematic stages of bond strength provided by adhesion between prestressing strands and concrete before and after slippage. Adapted from (Russell & Burns, 1996).

3.3.1. Adhesion

The adhesion between the prestressed strands and concrete matrix is the result of the chemical and physical bonding developed at the interface of the two media. The adhesive bond is primarily controlled by the shear strength of the weaker material

(cementitious matrix) and greatly affected by the surface condition of the strands. Table 3- 1 includes the current cohesion values recommended by AASHTO LRFD (AASHTO LRFD, 2010) applicable to shear-friction interfaces.

Immediately after the release of the prestressing strands, the adhesion between strands and concrete medium is expected to fail in the vicinity of the member end faces. Once the adhesive bonding between strands and concrete is overcome, strands experience slippage inside the concrete host along the length of adhesion failure. The contribution of adhesion to the overall bond strength is generally negligible in magnitude and will be terminated at the onset of slippage. Therefore, adhesion may be ignored when analyzing the ultimate bond strength between strands and concrete after initiation of slippage.

Past experience indicates that the contribution of the adhesion between the prestressing strands and concrete matrix to the overall bond strength is negligible in magnitude and therefore, will be terminated at the onset of slippage. Figure 3- 15 schematically shows the effect of adhesion on the bond strength at the interface between the prestressing strands and concrete host. As shown herein, once the stresses (primarily shear) developed at the interface between strands and concrete reach a critical state, adhesion fails and slippage of strands within the concrete host will be initiated along the length of bond failure. Upon the onset of slippage of the strands through the concrete continuum, the load transfer mechanism will mainly rely on Hoyer's effect and mechanical interlock. Therefore, adhesion will be ignored when analyzing the ultimate bond strength between the strands and concrete after initiation of slippage.

Table 3-3: Recommended parameters by AASHTO LRFD for shear friction design (AASHTO LRFD, 2010).

Categorization of Shear Interface	Cohesion (psi)	Friction Coefficient
Normal weight concrete cast monolithically	400	1.4
Light weight concrete cast monolithically	240	1.0
Normal weight concrete cast against clean (free of laitance) concrete surface intentionally roughened to a minimum amplitude of ¼ inch	280	1.0
Light weight concrete cast against clean (free of laitance) concrete surface intentionally roughened to a minimum amplitude of ¼ inch	240	1.0
Normal\Light weight concrete cast against clean (free of laitance) concrete surface not intentionally roughened	75	0.6
Normal\Light weight concrete cast against clean steel surface Norma\Light weight concrete anchored to structural steel by means of headed studs or reinforcing bars	25	0.7

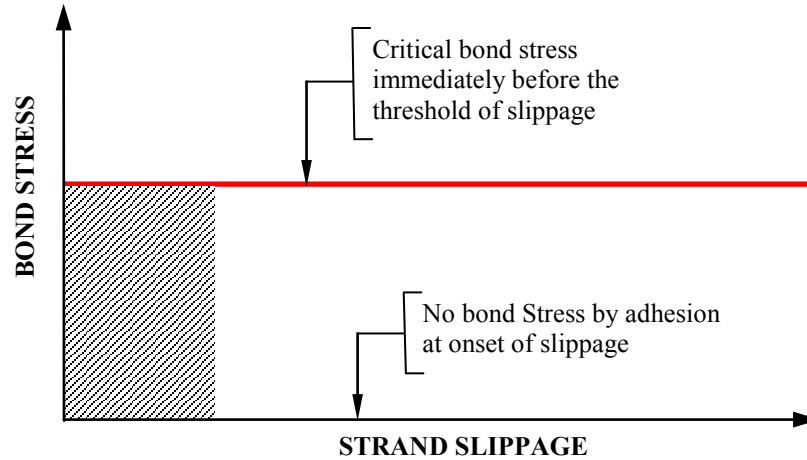


Figure 3- 15: Schematic stages of bond strength provided by adhesion between prestressing strands and concrete before and after slippage. Adapted from (Russell & Burns, 1996).

3.3.2. Hoyer's (Wedging) Effect

Upon jacking, the diameter of the pretensioned strands will be reduced in direct correlation with the Poisson's ratio (ν_c), resulting the reduction of cross sectional area of the strands. In accordance with the pretensioning practices, concrete will be cast after the strands are pretensioned to a target tensile stage. When concrete gains the minimum required compressive strength, commonly known as initial compressive strength (f'_{ci}), strands will be released. Once the pretensioned strands are released, the strands tend to retreat to the original diameter due to the elastic response while restraining the adjacent concrete matrix. As the result, a compromise is achieved between the strand and the concrete host: the strand diameter will go back to the original dimension at the end of the member while varying down to the reduced diameter due pretensioning at a distance away from the member end. This distance is referred to as *Transfer Length, L_t* , along which the pretensioning after release will increase from zero (at the end of the pretensioned member) to the target stress (after the losses). Thus, two wedged regions

are anticipated to be imposed at the girder ends along the transfer length (Akhnoukh, 2008). Currently, AASHTO LRFD assumes a linear variation of the pretensioning stresses along the transfer length (AASHTO LRFD, 2010).

As shown in Figure 3-16, the current state of practice assumes a linear approximation of Hoyer's effect. In other words, it is deemed that incremental decrease in the diameter of the prestressing strands (after release) approximately follows a linear contour from the released end of the strand towards the inner limits of the transfer length.

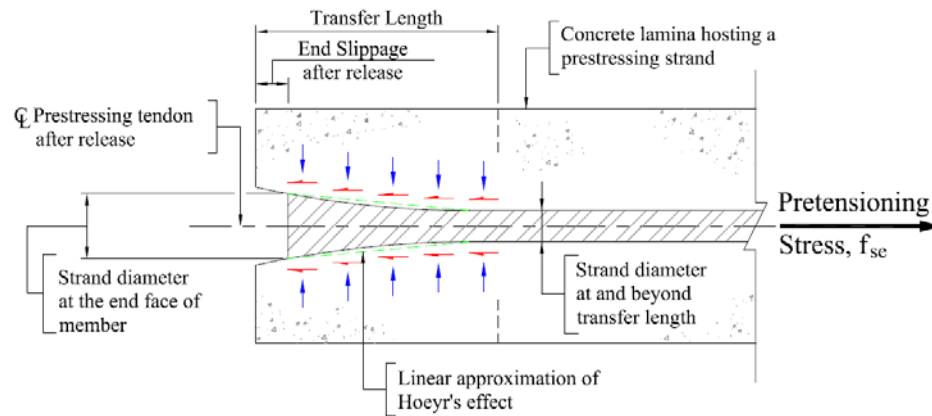


Figure 3-16: Pretensioning mechanism - Hoyer's (wedging) effect. Adapted from (Russell & Burns, 1996).

This approximation is further translated into linear stress variation from zero to the maximum effective pretensioning stress, f_{pe} , in the vicinity of the theoretical transfer length. The above is consistent with the current AASHTO LRFD specifications which recommend an idealized linear stress variation for analytical and design purposes. The approximate magnitude of transfer length as prescribed by AASHTO LRFD specifications is as follows (AASHTO LRFD, 2010):

$$L_t \geq 60 d_b \quad (3.22)$$

The definition of the transfer length, L_t , by ACI code indicates a linearization approximation as shown below (ACI, 2008):

$$L_t = \frac{f_{se}}{3} d_b \quad (3.23)$$

Figure 3-17 shows a schematic correlation between the stress in the strands and the length of bonding between strands and the concrete matrix (host) over which the linear regime is idealized. The linearized idealization of Figure 3-17 is in accordance with AASHTO LRFD specifications as discussed above indicating that starting from the end of the member or the released end of the prestensioned strand, three distinct zones can be identified:

- *Zone 1* - dominated by transfer length (L_t)
- *Zone 2* - dominated by development length (L_d)
- *Zone 3* - dominated by the nominal strength of the member at the failure

Development length, L_d , refers to the length required for an embedded prestressing strand to develop the design strength as defined below (AASHTO LRFD, 2010):

$$L_d \geq \kappa \left(f_{ps} - \frac{2}{3} f_{pe} \right) d_b \quad (3.24)$$

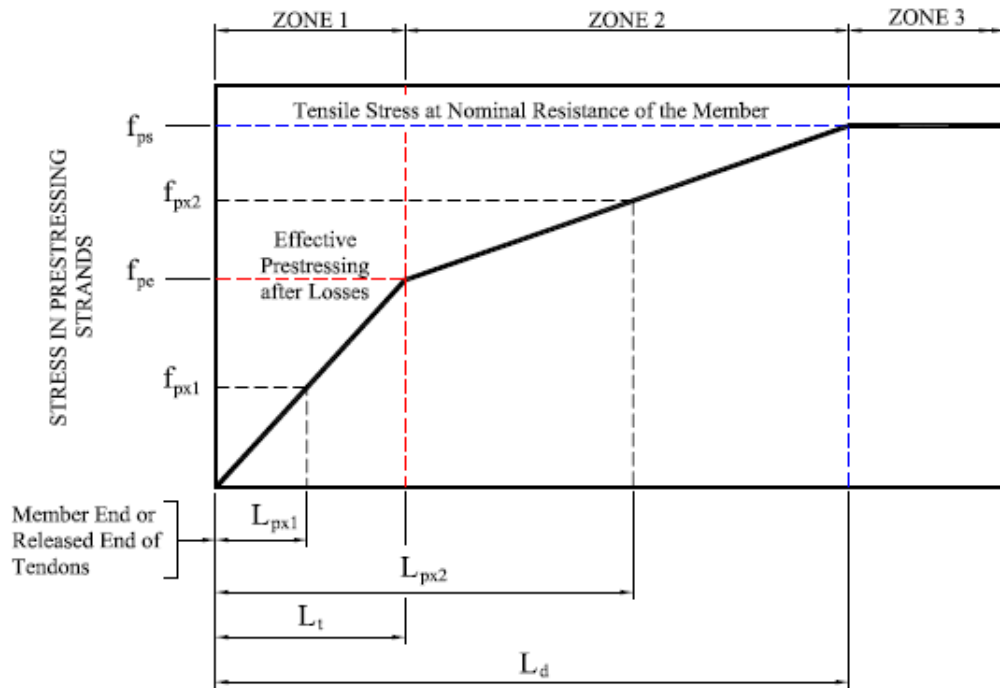


Figure 3-17: Idealized transfer and development lengths in accordance with AASHTO LRFD. Adapted from (AASHTO LRFD, 2010).

The parameter κ is defined by AASHTO LRFD Specifications as follows (AASHTO LRFD, 2010):

$\kappa = 1.0$ Applicable to pretensioned panels, piling and other pretensioned members with a depth of less than or equal to 24.0 in.

$\kappa = 1.6$ Applicable to pretensioned members with a depth greater than 24.0 in.

The three zones mentioned above are mathematically expressed as follows based on Figure 3-17 (AASHTO LRFD, 2010):

$$f_{px1} = \frac{f_{pe} L_{px1}}{60 d_b} \quad (\text{Zone 2}) \quad (3.25)$$

$$f_{px2} = f_{pe} + \frac{(L_{px2} - 60 d_b)}{(L_d - 60 d_b)} (f_{ps} - f_{pe}) \quad (\text{Zone 2}) \quad (3.26)$$

As implied by Equations (3.25) and (3.26), the current practice assumes that the pretensioning mechanism is based on linear transformations initiating from the free end of the released strand. However, the actual transfer of pretensioning is anticipated to follow a parabolic path as shown in Figure 3- 18:

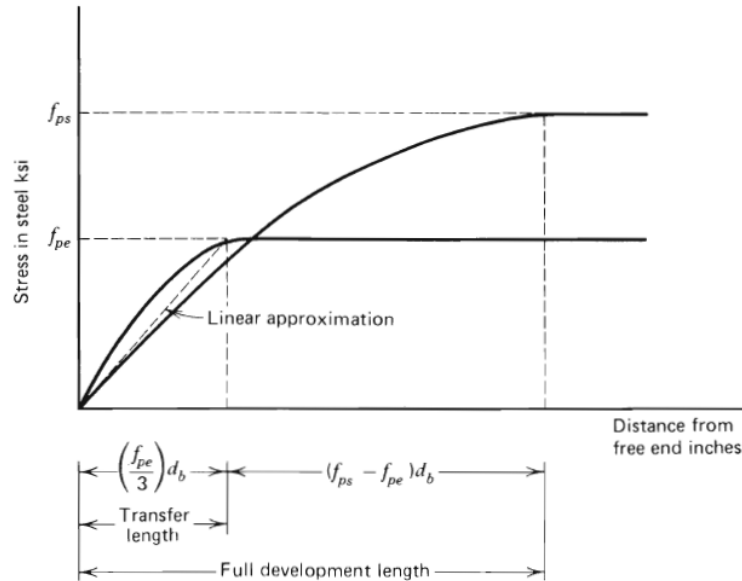


Figure 3- 18: Transfer and development lengths for pretensioned concrete members (Nilson, 1987).

3.3.3. Mechanical Interlocking

Currently low-relaxation seven-wire strands are the most common type of prestressing used in the market (Figure 3- 19). Mechanical interlocking is the result of the chemical and physical bonding between the strand and concrete host once the concrete is cast and hardens. Once a pretensioned seven-wire strand is released, it will

twist and subsequently slips inside the concrete host due to the helical formation. As the result of this phenomenon, non-uniform stresses are developed at the interface with the concrete host as shown in Figure 3-20.

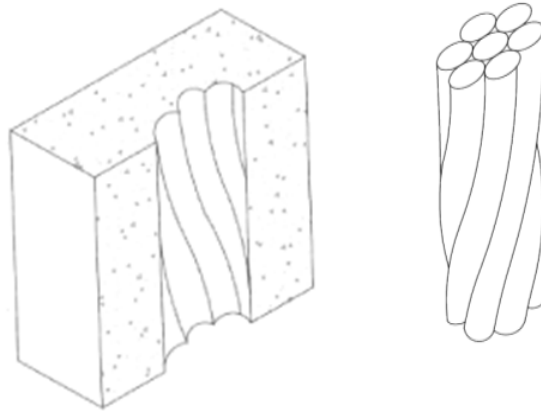


Figure 3- 19: Typical 7-wire strands with helical formation.

Mechanical interlocking is proved to be difficult to predict and measure due its complex nature. Nevertheless, past experience and researches indicate that mechanical interlocking is a multi-parameter phenomenon which is dependent on various factors such as (Akhnoukh, 2008):

- Compressive strength of concrete
- Surface condition of the strand in contact with concrete
- Number of strands
- Spacing of strands
- Level of confinement at the girder end zones

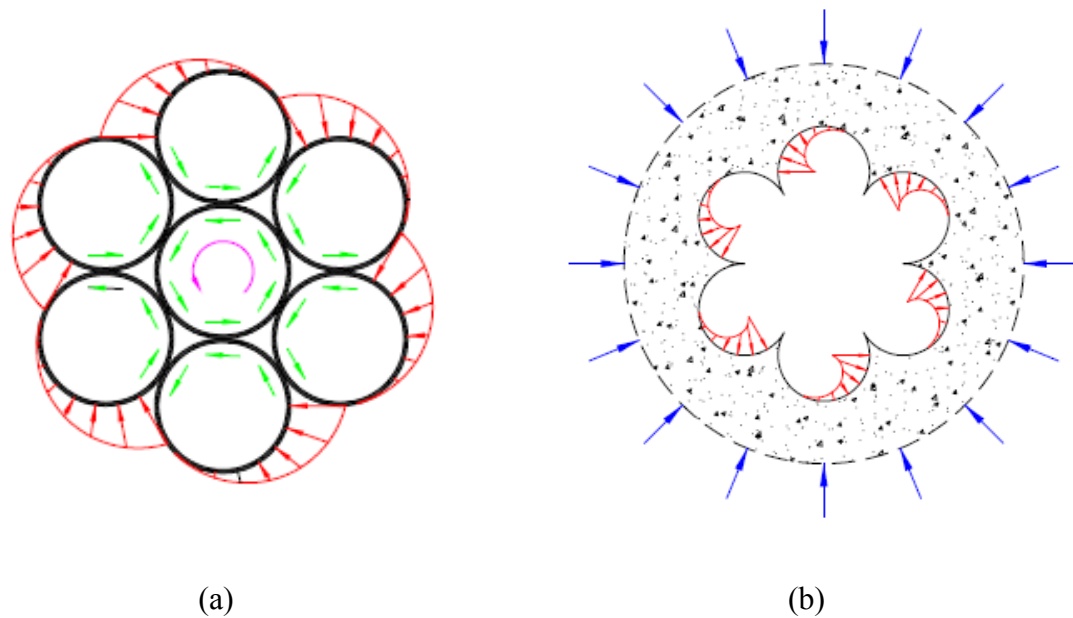


Figure 3-20: Mechanical interlocking between concrete host and pretensioned strand upon being released: (a) Typical seven-wire strand undergoing twisting immediately after being released, and (b) Concrete matrix in the vicinity of the released strand under radial stresses imposed by the twisted strand.

Mechanical interlocking at the interface between a released strand and concrete host is a complex phenomenon which can be affected by multiple parameters as mentioned above. In addition, mechanical interlocking is interrelated to the Hoyer's effect. Therefore, the numerical simulation of this phenomenon is anticipated to pose significant challenges.

3.4. Modeling Approaches

Numerical modeling of pretensioned concrete members generally consists of the following analytical foundations:

- Material constitutive modeling, and
- Finite element techniques to simulate the anticipated pretensioning mechanism.

Material constitutive models control the elastoplastic response of the simulated specimen immediately after the release of the pretensioned strands. The constitutive model for concrete must be able to correctly estimate the response of the member to compressive and tensile stresses. This is an essential element of modeling which enables the analysis to predict the extent of the damaged regions (cracked or fractured). In addition to initiation of cracks, the numerical model should be able to realistically relieve the overstressed regions by redistributing the stresses within the continua.

For a given volume, V , of material at a specific point of time subjected to force t per unit area of S and force f per unit volume V , the basic force equilibrium can be written as follows (ABAQUS, 2010):

$$\int_S \mathbf{t} dS + \int_V \mathbf{f} dV = 0 \quad (3.27)$$

Based on the definition of Cauchy stress matrix, $\boldsymbol{\sigma}$, Equation (3.27) can be rewritten as follows:

$$\int_S \mathbf{n} \boldsymbol{\sigma} dS + \int_V \mathbf{f} dV = 0 \quad (3.28)$$

where \mathbf{n} represents the outward normal vectors at any point on S .

Similarly, the moment equilibrium can be described as

$$\int_S (\mathbf{x} \times \mathbf{t}) dS + \int_V (\mathbf{r} \times \mathbf{f}) dV = 0 \quad (3.29)$$

where \mathbf{r} represents the position vector. Applying Gauss's theorem, we can rewrite

Equation (3.28) as follows:

$$\int_S \mathbf{n} \boldsymbol{\sigma} dS = \int_V \left(\frac{\delta}{\delta \mathbf{r}} \right) \boldsymbol{\sigma} dV \quad (3.30)$$

Since Equation (3.30) is derived over an arbitrary volume, V , it needs to be applied as a pointwise function inside the body of the material and therefore, the translational equilibrium shall satisfy the following condition:

$$\left(\frac{\partial}{\partial \mathbf{r}}\right) \cdot \boldsymbol{\sigma} + \mathbf{f} = 0 \quad (3.31)$$

Integrating Equation (3.30) over the entire volume, V , we can write:

$$\int_V \left[\left(\frac{\partial}{\partial \mathbf{r}}\right) \cdot \boldsymbol{\sigma} + \mathbf{f} \right] \cdot \delta \mathbf{v} dV = 0 \quad (3.32)$$

where \mathbf{v} indicates the velocity of neighboring particles in the body. Equation (3.32) can then be further expanded to the following form based on the application of chain rule:

$$\int_V \left[\left(\frac{\partial}{\partial \mathbf{r}}\right) \cdot \boldsymbol{\sigma} \right] \cdot \delta \mathbf{v} dV = \int_S \mathbf{n} \cdot \boldsymbol{\sigma} \cdot \delta \mathbf{v} dS - \int_V \boldsymbol{\sigma} : \left(\frac{\partial \delta \mathbf{v}}{\partial \mathbf{r}}\right) dV \quad (3.33)$$

Equation (3.33) can be rewritten to represent the virtual work in its most basic form:

$$\int_S \mathbf{n} \boldsymbol{\sigma} \cdot \boldsymbol{\delta} dS + \int_V \mathbf{f} \cdot \boldsymbol{\delta} dV = \int_V \boldsymbol{\sigma} : \left(\frac{\partial \delta \mathbf{v}}{\partial \mathbf{r}}\right) dV \quad (3.34)$$

Based on the rate of deformation, the virtual velocity gradient $\delta \mathbf{L}$ can be defined as follows:

$$\delta \mathbf{L} = \frac{\partial \delta \mathbf{v}}{\partial \mathbf{r}} = \delta \mathbf{D} + \delta \mathbf{W} \quad (3.35)$$

which is decomposed into a symmetric part, $\delta \mathbf{D}$, and an antisymmetric part $\delta \mathbf{W}$ representing virtual rate of deformation and spin, respectively (ABAQUS, 2010). Since Cauchy stress matrix, $\boldsymbol{\sigma}$, is symmetric:

$$\boldsymbol{\sigma} : \delta \mathbf{L} = \boldsymbol{\sigma} : \delta \mathbf{D} + \boldsymbol{\sigma} : \delta \mathbf{W} = \boldsymbol{\sigma} : \delta \mathbf{D} \quad (3.36)$$

Therefore, Equation (3.34) can be rewritten in the following general form:

$$\int_V \boldsymbol{\sigma} : \delta \mathbf{D} dV = \int_S \delta \mathbf{v} \cdot \mathbf{t} dS + \int_V \delta \mathbf{v} \cdot \mathbf{f} dV \quad (3.37)$$

In accordance with the generalized Hooke's law, the fundamental relationship between stress and the corresponding strain tensors can be expressed as follows:

$$\boldsymbol{\sigma} = \mathbf{E}_0 : (\boldsymbol{\varepsilon} - \boldsymbol{\varepsilon}^{pl}) \quad (3.38)$$

where $\boldsymbol{\sigma}$ and \mathbf{E}_0 denote the stress and the initial-elastic stiffness; $\boldsymbol{\varepsilon}$ is the strain tensor and $\boldsymbol{\varepsilon}^{pl}$ is the plastic part of the strain tensor..

Given \mathbf{N} as the shape function, the displacement vector \mathbf{u} can be written as

$$\mathbf{u} = \mathbf{N} \mathbf{u}_e \quad (3.39)$$

where \mathbf{u}_e denotes vector of nodal displacement (McHugh, 2007). Therefore, the general finite element approximation results in the simplification of principle of virtual work as follows:

$$\delta \mathbf{u} = \mathbf{N} \delta \mathbf{u}_e \quad (3.40)$$

$$\boldsymbol{\varepsilon} = \frac{1}{2} \left(\frac{\partial \mathbf{u}}{\partial \mathbf{x}} + \frac{\partial \mathbf{u}^T}{\partial \mathbf{x}} \right) = \mathbf{B} \mathbf{u}_e \quad (3.41)$$

Therefore,

$$\delta \boldsymbol{\varepsilon} = \mathbf{B} \delta \mathbf{u}_e \quad (3.42)$$

$$\int_V \delta \boldsymbol{\varepsilon}^T \boldsymbol{\sigma} dV = \int_S \delta \mathbf{u}^T \mathbf{f} dS \quad (3.43)$$

$$\int_V \delta \mathbf{u}_e^T \mathbf{B}^T dV = \int_S \delta \mathbf{N}_e^T \mathbf{f}^T dS \quad (3.44)$$

Thus,

$$\int_V \mathbf{B}^T \boldsymbol{\sigma} dV = \int_S \mathbf{N} \bar{\mathbf{f}} dS \quad (3.45)$$

which leads to the a fundamental form of finite element equation:

$$\int_V \mathbf{B}^T(\mathbf{u}_e) dV = \mathbf{F} \quad (3.46)$$

where \mathbf{F} is the vector of external forces acting on the element and \mathbf{B} is the transformation matrix which translate displacement to strain at any given point within the element.

In general, nonlinearity can be attributed to the following factors (McHugh, 2007):

- Geometric nonlinearity such as kinematic problems with large deformations

$$\boldsymbol{\varepsilon} = \frac{1}{2} \left(\frac{\partial \mathbf{u}}{\partial \mathbf{x}} + \frac{\partial \mathbf{u}^T}{\partial \mathbf{x}} + \frac{\partial \mathbf{u}}{\partial \mathbf{x}} \frac{\partial \mathbf{u}^T}{\partial \mathbf{x}} \right) \quad (3.47)$$

or nonlinear strain-displacement relationships:

$$\boldsymbol{\varepsilon} = \mathbf{B}(\mathbf{u}_e) \mathbf{u}_e \quad (3.48)$$

- Material nonlinearity such as elastoplastic constitutive law or nonlinear stress-strain relationships:

$$\boldsymbol{\sigma} = \boldsymbol{\sigma}(\mathbf{u}_e) \quad (3.49)$$

- Nonlinear boundary conditions such as contact formulations

Therefore, the basic finite element Equation (3.46) can be rewritten as follows for general nonlinearities (McHugh, 2007):

$$\int_V \mathbf{B}(\boldsymbol{\sigma}_e)^T \mathbf{u}(\mathbf{u}_e) dV - \mathbf{G}(\mathbf{u}_e) = \mathbf{0} \quad (3.50)$$

where \mathbf{G} represents the out-of-balance or residual forces and $\mathbf{G}(\mathbf{u}_e) = \mathbf{0}$ is a set of nonlinear equations in \mathbf{u}_e .

The nonlinear finite element Equation (3.50) can be solved using an implicit or explicit approach. The implicit approach requires an initial value to start the iterative solution. Once Equation (3.50) is solved for a time t , the next step is to iterate for solution at time $t + \Delta t$ (McHugh, 2007):

$$\mathbf{G}(\mathbf{u}^{t+\Delta t}) = \mathbf{0} \quad (3.51)$$

The implicit approach results in accurate solutions while it may require timely iterative solutions. ABAQUS/Standard solves nonlinear finite element problems based on the implicit approach.

Explicit approach uses the state at time t to solve for the state at time $t+\Delta t$. As the result, no iteration and convergence check are required leading to a robust process (McHugh, 2007).

Now, the equilibrium statement is rewritten as follows in reference to Equation (3.37):

$$\int_V \boldsymbol{\sigma} : \delta \mathbf{D} dV = \int_S \mathbf{t}^T \cdot \delta \mathbf{v} dS + \int_V \mathbf{f}^T \cdot \delta \mathbf{v} dV \quad (3.52)$$

The left-hand side of Equation (3.60) corresponds to the rate of internal virtual work and can be replaced conjugate pairing of the corresponding stresses and strains as below:

$$\int_{V^0} \boldsymbol{\tau}^c : \delta \boldsymbol{\varepsilon} dV^0 = \int_S \mathbf{t}^T \cdot \delta \mathbf{v} dS + \int_V \mathbf{f}^T \cdot \delta \mathbf{v} dV \quad (3.53)$$

where $\boldsymbol{\tau}^c$ and $\boldsymbol{\varepsilon}$ denote the conjugate pairing of material stress and corresponding strain.

Defined as the virtual field, $\delta \mathbf{v}$ is compelled to conform to all the kinematic constraints. Therefore, in reference to Equation (3.39), the virtual field $\delta \mathbf{v}$ shall have the same form as the displacement field $\delta \mathbf{u}$:

$$\delta \mathbf{v} = \mathbf{N} \delta \mathbf{v}_e \quad (3.54)$$

Subsequently, the virtual rate of material straining, $\delta \boldsymbol{\varepsilon}$, can be defined as a linear function of $\delta \mathbf{v}$:

$$\delta \boldsymbol{\varepsilon} = \boldsymbol{\beta} \delta \mathbf{v}_e \quad (3.55)$$

where $\boldsymbol{\beta}$ defines the strain variations relative to the variations of the kinematic variables, depending on the current position of the referenced material point. Therefore, Equation (3.53) can be written as

$$\delta \mathbf{v}_e \int_{V^0} \boldsymbol{\beta} : dV^0 = \delta \left(\int_S \mathbf{N}^T \cdot \mathbf{t}^T dS + \int_V \mathbf{N}^T \cdot \mathbf{f}^T dV \right) \quad (3.56)$$

And since $\delta \mathbf{v}_e$ includes independent variables, each one can be assumed non-zero while all others are zero (ABAQUS, 2010). Therefore,

$$\int_{V^0} \boldsymbol{\tau}^c : \boldsymbol{\beta} dV^0 = \int_S \mathbf{N}^T \cdot \mathbf{t}^T dS + \int_V \mathbf{N}^T \cdot \mathbf{f}^T dV \quad (3.57)$$

The equilibrium statement of Equation (3.57) results in a systems equations which can be discretized in the following form (ABAQUS, 2010):

$$F^N(\xi^M) = 0 \quad (3.58)$$

where F^N corresponds to the force components conjugate to N^{th} variable. Additionally, ξ^M indicates the M^{th} involved in the problem. Many nonlinear problems, including numerical simulations utilized in this research, are history dependent and therefore, require iterative solutions over relatively small increments. ABAQUS generally uses Newton's method for numerical solution of the nonlinear equilibrium equations. Based on Newton's formulation, an approximate solution ξ_i^M is obtained at i^{th} iteration. Thus, $\Delta \xi_{i+1}^M$ is calculated as the difference between the approximate solution ξ_i^M and the exact solution for the discretized equilibrium Equation (3.58). Therefore,

$$F^N(\xi_i^M + \Delta \xi_{i+1}^M) = 0 \quad (3.59)$$

The left-hand side of Equation (3.59) can be expanded using Taylor's series as follows:

$$F^N(\xi_i^M) + \frac{\partial F^N}{\partial \xi^P}(\xi_i^M) \Delta \xi_{i+1}^P + \frac{\partial^2 F^N}{\partial \xi^P \partial \xi^Q}(\xi_i^M) \Delta \xi_{i+1}^P \Delta \xi_{i+1}^Q + \dots = 0 \quad (3.60)$$

As ξ_i^M converges towards the solution, $\Delta \xi_{i+1}^M$ becomes smaller and therefore, all but the first two left-hand side terms of Equation (3.60) can be neglected. Thereafter, Equation (3.60) will be converted to a system of linear equations characterized by Equation (3.61):

$$F_i^N + J_i^{NP}(\Delta \xi_{i+1}^P) = 0 \quad (3.61)$$

where J_i^{NP} is the Jacobian matrix defined as

$$J_i^{NP} = \frac{\partial F^N}{\partial \xi^P}(\xi_i^M) \quad (3.62)$$

and

$$F_i^N = F^N(\xi_i^M) \quad (3.63)$$

The above iteration continues until the target convergence is fulfilled.

3.4.1. Material Simulation: Concrete Damage Plasticity Constitutive Model

The elastoplastic response of pretensioned members is predicted in accordance with the Concrete Damage Plasticity (CDP) constitutive model. This constitutive model was first developed by Lee and Fenves in 1998 (Lee & Fenves, 1998). CDP is generally capable of analyzing the behavior of quasi-brittle materials under cyclic and/or dynamic loading, including concrete. In the absence of adequate confining pressure, concrete is anticipated to behave in a brittle manner. Under such conditions, the failure modes are either tensile cracking or crushing due to excessive compression. When adequate

confining pressure applied, the failure mechanism will be due to the collapse of the microstructure of concrete, which results in global macroscopic failure similar to those of ductile materials (ABAQUS, 2010). The CDP model has sepecific macroscopic characteristics which are summarized as follows (ABAQUS, 2010):

- i. The yield strength is different under tension and compression;
- ii. The tensile failure is characterized with a softening behavior as opposed to a two-step (hardening-softening) compressive failure;
- iii. The degradation of the elastic stiffness is different under tension and compression failure;
- iv. Under cyclic loading, stiffness undergoes partial recovery as the material oscillates between the states of tension and compression, and
- v. Mechanical properties, including strength, is rate sensitive.

In reference to Item v above, CDP assumes additive strain rate decomposition for the rate independent constitutive model as follows:

$$\dot{\epsilon} = \dot{\epsilon}^{el} + \dot{\epsilon}^{pl} \quad (3.64)$$

where $\dot{\epsilon}$ corresponds to the total strain rate comprised of $\dot{\epsilon}^{el}$ and $\dot{\epsilon}^{pl}$ which indicate the elastic and plastic parts of the strain rate, respectively.

The initiation of cracks in concrete is based on a continuous formation during which the micro-cracks are connected. This phenomenon leads to the softening of concrete, during which redistribution of stress occurs from the localized damaged areas to the neighboring elements. In addition to fracture and micro-cracking, concrete will experience significant stiffness degradation. The complexity of this phenomena arises from the fact that concrete will be able to recover some of the degraded stiffness as it is

reloaded from tensile to compressive range while the previously initiated cracks will closed up under compression (Reinhardt, 1984). The Concrete Damage Plasticity model is based on two main concepts:

- Fracture-energy-based damage, and
- Stiffness degradation.

The fracture-energy-based damage is similar to the Barcelona Model previously developed by Lubliner (Lubliner, Oliver, & Onate, 1990), which is an extension of J_2 plasticity as shown in Figure 3-21.

Chen defines CDP as a geometric combination of two different types of Drucker-Prager functions (Chen, Plasticity in Reinforced Concrete, 2007). In other words, CDP can be described as a modified Barcelona Model with multi-variable failure condition as defined below (Lee & Fenves, 1998):

$$\bar{F}(\sigma, \kappa) = \frac{1}{1-\alpha} \left(\alpha I_1 + \sqrt{3J_2} + \beta \langle \hat{\sigma}_{\max} \rangle \right) - c_c(\kappa) \quad (3.65)$$

I_1 and J_2 correspond to the trace of the stress tensor (First invariant) and the second invariant of the deviatoric stress tensor, respectively. In addition, $\hat{\sigma}_{\max}$ indicates the algebraic maximum principle stress. The parameters α and β are dimensionless coefficients related to the initial uniaxial and biaxial yield compressive stress (f_{c0} and f_{b0} , respectively), defined as follows:

$$\alpha = \frac{f_{b0} - f_{c0}}{2f_{b0} - f_{c0}}, [0 \leq \alpha \leq 0.5] \quad (3.66)$$

$$\beta(\kappa) = \frac{c_c(\kappa)}{c_t(\kappa)} (1 - \alpha) + (1 + \alpha) \quad (3.67)$$

In Equation (3.67), f_{b0} and f_{c0} correspond to initial biaxial and uniaxial yield compressive stresses. Past experimental results indicate that the typical values for f_{b0}/f_{c0} ranges from 1.10 to 1.16 for concrete (Lubliner, Oliver, & Onate, 1990). Additionally, the variable $c_t(\kappa)$ represents the tensile cohesion and $c_c(\kappa)$ represents the compressive cohesion, indicating the shear resistance of concrete as a cohesive, frictional medium. The evolution of the yield function for CDP model as defined by Equation (3.65) is partially based on the relationship between cohesion and damage variables at the states of tension and compression. This is particularly important since the evolution of compressive strength hardly affects tensile strength and vice versa. As shown in Figure 3-21, the yield function consists of two Drucker-Prager type functions corresponding to compression and tension where $c_0 = -f_{c0}$, and f_{by} and f_{ty} correspond to the states of biaxial compression and tension, respectively.

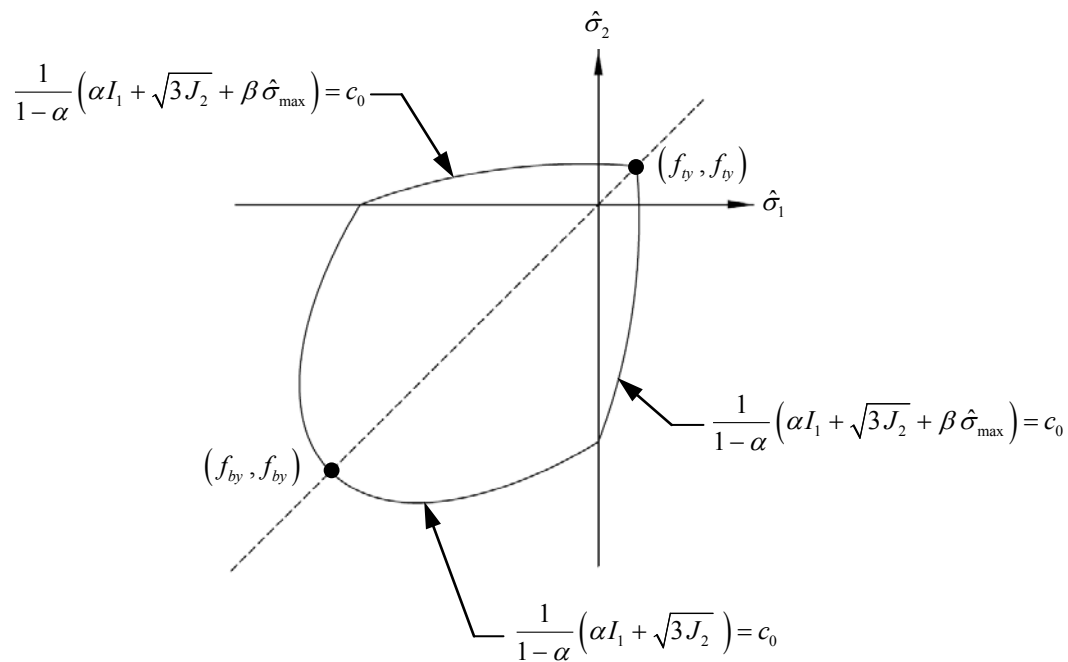


Figure 3-21: Barcelona yield function in plane stress state.

3.4.1.1. Degradation Damage

Given d , a scalar degradation damage variable, the degradation strain relationship is described as follows:

$$\boldsymbol{\sigma} = (1 - D) \mathbf{E}_0 : (\boldsymbol{\varepsilon} - \boldsymbol{\varepsilon}^{Pl}) \quad 0 \leq D \leq 1 \quad (3.68)$$

In isotropic form, damage can be described as

$$\mathbf{D} = \frac{1}{1 - d} \mathbf{I} \quad (3.69)$$

Since concrete is a frictional material, non-associative flow rule is required to properly control the dilatancy. Thus, CDP is based on a plastic potential function as defined below (Lee & Fenves, 1998):

$$\Phi = \|\mathbf{s}\| + \alpha_p \mathbf{I} \quad (3.70)$$

where $\|\mathbf{s}\|$ corresponds to the norm of the deviatoric tensor and α_p denotes the dilatancy parameter.

Thus, the plastic strain rate, $\dot{\boldsymbol{\varepsilon}}^{Pl}$, is defined as

$$\dot{\boldsymbol{\varepsilon}}^{Pl} = \dot{\lambda} \left(\frac{\mathbf{s}}{\|\mathbf{s}\|} + \alpha_p \mathbf{I} \right) \quad (3.71)$$

The state of damage in CDP model is controlled by the following internal variables:

- Plastic strain, $\boldsymbol{\varepsilon}^{Pl}$, as defined by Equation (3.71)
- Damage variable, $\dot{\boldsymbol{\kappa}}$, as defined by Equation (3.72)

$$\dot{\boldsymbol{\kappa}} = \dot{\lambda} \mathbf{H}(\bar{\boldsymbol{\sigma}}, \boldsymbol{\kappa}) \quad (3.72)$$

where \mathbf{H} is a function related to the plastic dissipation and $\bar{\boldsymbol{\sigma}}$ denotes the effective stress defined as

$$\bar{\sigma} = \mathbf{E}_0 : (\boldsymbol{\varepsilon} - \boldsymbol{\varepsilon}^p) \quad (3.73)$$

where \mathbf{E}_0 corresponds to the initial-elastic stiffness tensor.

In the current form of Concrete Plasticity Damage Model, two damage parameters are utilized to address damage under tension (κ_t) and compression (κ_c). Therefore, under uniaxial loading, the tensile and compressive responses can be decoupled as:

$$f_t(\kappa_t) = [1 - d_t(\kappa_t)] \bar{f}_t \quad 0 \leq d_t \leq 1 \quad (3.74)$$

$$f_c(\kappa_c) = [1 - d_c(\kappa_c)] \bar{f}_c \quad 0 \leq d_c \leq 1 \quad (3.75)$$

where \bar{f}_t and \bar{f}_c denote the effective tensile and compressive stresses, and d_t and d_c represent the scalar degradation damage variables due to tensile and compressive stresses, respectively.

Based on the above discussion, a single degradation formulation $D(\boldsymbol{\kappa})$ is assembled to include damage due to both tension and compression (Lee & Fenves, 1998):

$$D(\boldsymbol{\kappa}) = 1 - (1 - d_t)(1 - d_c) \quad (3.76)$$

Therefore, Equation (3.68) can be written in terms of the effective stress and single degradation damage response as follows:

$$\boldsymbol{\sigma} = [1 - D(\boldsymbol{\kappa})] \bar{\boldsymbol{\sigma}} \quad (3.77)$$

3.4.1.2. Stiffness Degradation and Recovery Under Cyclic Loading

One of the most important and complex capabilities of CDP is its ability to control stiffness degradation and recovery under cyclic loading. As previously discussed, micro-cracks will be initiated once a specimen reaches the tensile capacity. Upon continuation of tensioning, these cracks will propagate and further open, resulting into stiffness degradation. Once the specimen is unloaded and reloaded to the state of compression, the

micro-cracks will close, resulting in recovery of a certain degree of stiffness lost during the state of tensioning.

In order to predict the above behavior, CDP includes a scalar, s , which will control the change of the tensile damage parameter, d_t , as the state of loading oscillates between compression and tension:

$$\sigma = [1 - d_c(\kappa)][1 - s d_t(\kappa)] \mathbf{E}_0 : (\boldsymbol{\varepsilon} - \boldsymbol{\varepsilon}^{pl}) \quad 0 \leq s \leq 1 \quad (3.78)$$

Figure 3-22 shows the theoretical stiffness degradation of concrete when subject to uniaxial tensile and compressive loading (ABAQUS, 2010). When unloaded from any point within the strain-softening state, the elastic stiffness is observed to be degraded and the reversal unloading will be dictated by slopes smaller than the elastic modulus. The tensile and compressive degradations undergo different regimes as indicated in Figure 3-22, dictated the tension (D_t) and compression (D_c) damage variables. Given the initial elastic stiffness, E_0 , the uniaxial tensile and compressive stress-strain relationships can be estimated as follows (ABAQUS, 2010):

$$\sigma_t = (1 - D_t) E_0 (\varepsilon_t - \tilde{\varepsilon}_t^{pl}) \quad 0 \leq D_t \leq 1 \quad (3.79)$$

$$\sigma_c = (1 - D_c) E_0 (\varepsilon_c - \tilde{\varepsilon}_c^{pl}) \quad 0 \leq D_c \leq 1 \quad (3.80)$$

where plastic tensile ($\tilde{\varepsilon}_t^{pl}$) and compressive strains ($\tilde{\varepsilon}_c^{pl}$) indicate the permanent deformations after the member is unloaded from the state of tension or compression, respectively.

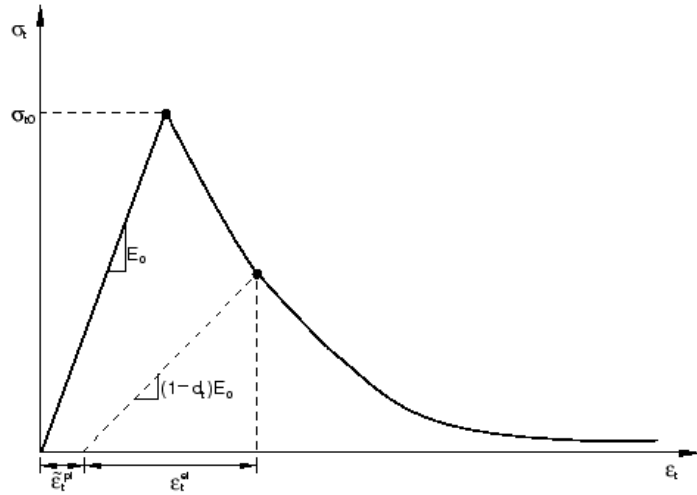
Under uniaxial tension, tensile cracks generally propagate transverse to the direction of loading. As the result, the load-carrying area will be reduced resulting in an increase in the effective stress. On the other hand, cracks due to uniaxial compression normally run parallel with the direction of loading and therefore, the resulting stiffness degradation

is not as severe as the state of uniaxial tension. However, the load-carrying area can also be significantly compromised if concrete is crushed under excessive compression. The following shows the effective uniaxial tensile and compressive cohesion stresses affected by the degradation as discussed above:

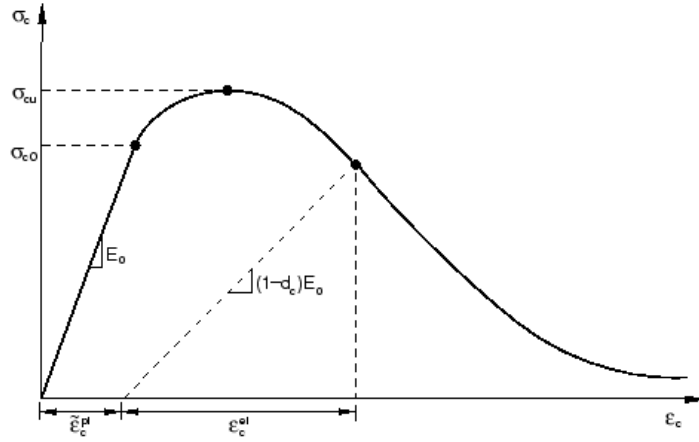
$$\bar{\sigma}_t = \frac{\sigma_t}{(1-D_t)} = E_0 (\varepsilon_t - \tilde{\varepsilon}_t^{pl}) \quad 0 \leq D_t \leq 1 \quad (3.81)$$

$$\bar{\sigma}_c = \frac{\sigma_c}{(1-D_c)} = E_0 (\varepsilon_c - \tilde{\varepsilon}_c^{pl}) \quad 0 \leq D_c \leq 1 \quad (3.82)$$

When subject to triaxial loading ($\sigma_2 = \sigma_3$), Past researches show that the confining pressure has significant effect on the deformational behavior of concrete (Chen & Han, 1988). Figure 3-23 shows response of sample concrete cylinders to compressive loading with simultaneous equal confining pressures. The samples are subjected to five levels of lateral confining pressure: 0, 2, 4, 6 and 8 ksi. The figure shows the axial and lateral strains versus the concurrent axial stress. It is observed that the up to confining pressure of $\sigma_2 = \sigma_3 = 4 \text{ ksi}$, axial and lateral strains significantly increase with the increasing confining pressure. Beyond this threshold, increasing the lateral stresses will decrease the axial and lateral strains. However, compared with the response of the samples subject to uniaxial compression, the confining pressure is anticipated to increase the strains and impose noticeable ductility before failure (Chen & Han, 1988).



(a)



(b)

Figure 3-22: Stiffness degradation of concrete under uniaxial: (a) tension and (b) compression (ABAQUS, 2010).

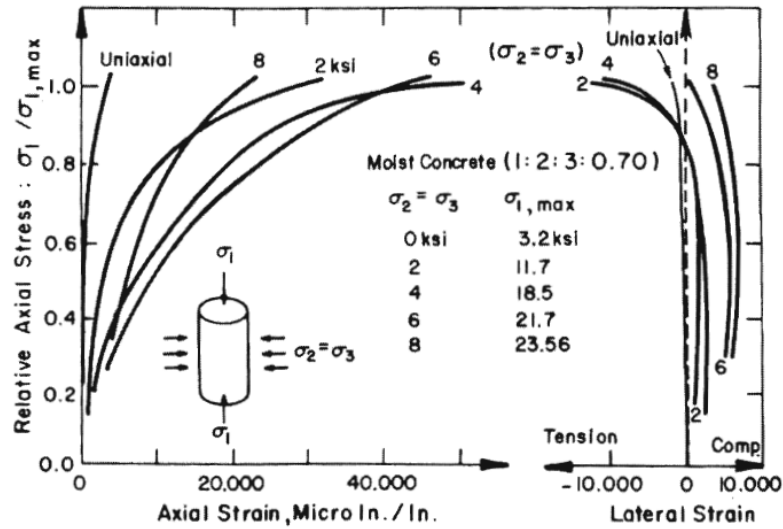


Figure 3-23: Response of concrete to triaxial compressive loading (Palaniswamy & Shah, 1974).

Figure 3-24 shows the volumetric changes of concrete under biaxial (σ_1, σ_2) versus uniaxial (σ_1) compressive loadings (Kupfer, Hilsdorf, & Rusch, 1969). It is observed that the volumetric strain decreases as the biaxial compressive stresses approach 75% to 90% of the ultimate compressive strength. Beyond the above threshold of biaxial compression, a reverse tendency is observed as the loading increases. Past research by Shah and Chandra (1968) indicates that cement paste is not the primary factor contributing to the increase in the volumetric straining of concrete due to excessive compression. On the contrary, cement paste continues to become consolidated up to compression failure of concrete. Instead, the composite nature of cement paste mixed with aggregates is primarily responsible for the augmentation of microcracks in the mortar. Furthermore, this leads to unstable crack propagation and volume increase as concrete approaches compressive failure.

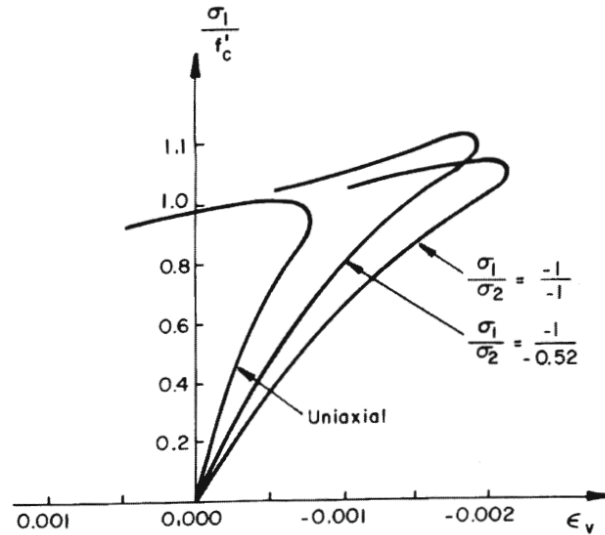


Figure 3-24: Volumetric strain of concrete under biaxial compression (Kupfer, Hilsdorf, & Rusch, 1969).

3.4.2. Finite Element Techniques

The analytical models presented in this research are constructed using a commercial finite element package, ABAQUS (ABAQUS, 2010). The features and functions utilized in this research are also offered in some other commercially available finite element packages.

3.4.2.1. Extrusion Technique

The extrusion technique is based on modeling the interface between strands and concrete using friction contact formulations. This is facilitated by modeling the strands within an extruded concrete matrix as solid elements (e.g., 8-node elements, Figure 3-25) with common surfaces. An extruded model will require various contact properties in order to optimize the simulation of the composite interaction between concrete and strands, including friction, slippage, pressure dependency and over-closure.

The contact surfaces of extruded models will require various sub-modules in order to accurately simulate the interaction between strands and concrete matrix during the

pretensioning mechanism. A friction-based model is utilized to simulate the collective effects of the pretensioning mechanisms as previously discussed. Based on the preliminary examinations by the author, it was decided that the built-in features in ABAQUS could adequately facilitate such simulations while requiring proper calibrations.

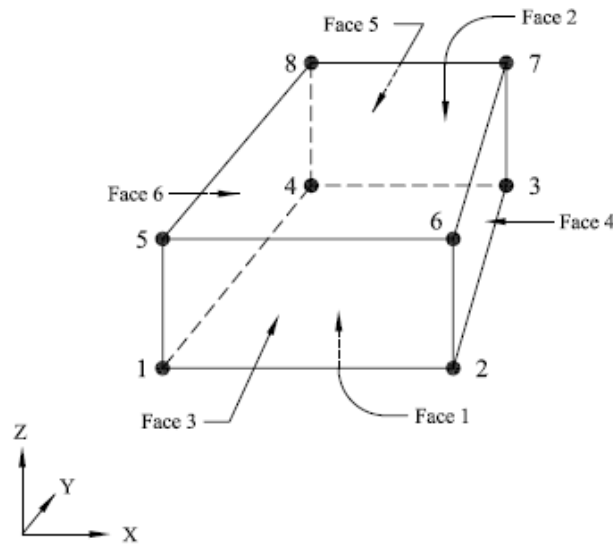


Figure 3-25: Typical three-dimensional 8-node linear brick element used for simulation of concrete continua.

Based on the fundamental definition of friction-dominated interfaces, it is anticipated that shear and normal stresses will be developed at the interface between strands and concrete host. Consequently, the proposed friction contact model shall be comprised of the following components: 1) Tangential Behavior and 2) Normal Behavior.

The mechanical properties of the interaction between strands and concrete matrix are modeled using the friction-based contact surface algorithms.

The surface interaction is further coupled with the contact algorithms to enforce additional controls for the simulation of tangential and normal interactions at the

interfaces. Figure 3- 26 shows a typical scheme for finite element modeling of pretensioned concrete members using extrusion technique.

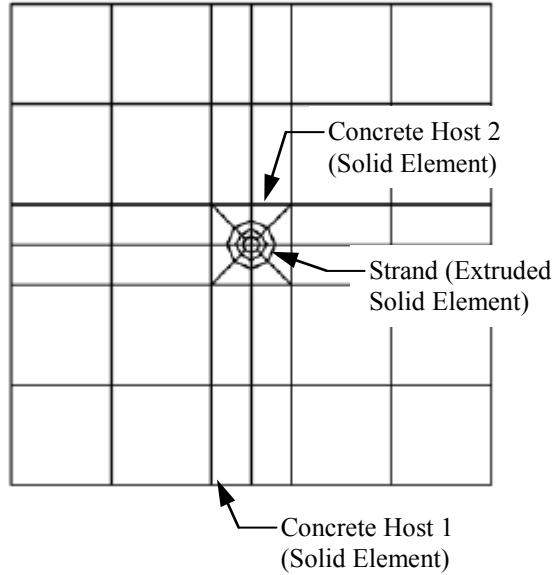


Figure 3- 26: Typical schemes of finite element modeling of pretensioned concrete members using extrusion technique.

3.4.2.1.1. Contact Formulation: Tangential Behavior

The tangential behavior of the proposed contact model is governed by coefficient of friction, μ_f , which is treated as a variable parameter for the parametric studies of this research, while the target values are based on the AASHTO LRFD recommendations for shear friction design as summarized in Table 3-3 (AASHTO LRFD, 2010).

Slip tolerance is further defined as the ratio of allowable maximum elastic slip to characteristic contact surface dimension (ABAQUS, 2010):

$$\gamma_i = F_f l_i \quad (3.83)$$

where l_i corresponds to the characteristic contact surface length. The elastic slip, γ_i , will be controlled by the slip tolerance, F_f , which is set at the default value of 0.005 for an optimized balance between computational accuracy and efficiency.

Moreover, a parametric investigation is performed in order to identify efficient while accurate methods to simulate the slippage of the strands within the concrete continuum based on the following techniques (see Figure 3-27):

Technique 1: Tie prestressing strand to the concrete host (extruded to host the strand), and model the interfaces of the concrete host to allow for slippage.

Technique 2: Model the interface of the strand and concrete host to allow for direct slippage of strands within the concrete matrix.

3.4.2.1.2. Contact Formulation: Normal Behavior

The normal behavior at the interface between strands and concrete matrix is simulated using “hard” pressure-overclosure relationship, which minimizes the penetration of slave nodes into the master surface at the onset of contact. This formulation also prevents the transfer of tensile stresses within the contact interface. The applicable contact constraints are mathematically enforced using a Lagrange multiplier technique, which is related to the magnitude of contact pressure (p) as a function of overclosure (h). The contribution of virtual work ($\delta \Pi$) can be described in the following linearized form (ABAQUS, 2010):

$$d\delta \Pi = (\delta p)dh + dp(\delta h) \quad (3.84)$$

where $p = 0$ when $h < 0$ (No contact), and $h = 0$ when $p > 0$ (Contact initiated). This contact formulation includes no physical softening, preventing separation once contact is initiated between the adjacent surfaces. More specifically, the no-separation condition is applicable for the simulation of the contact interaction between the strands and the

extruded concrete host, maintaining the continuous transfer of pretensioning between the strands and concrete upon the release.

3.4.2.2. Embedment Technique

Embedment is a powerful finite element technique, which enables one or more elements to be embedded inside a host element. One of the most significant advantages of the embedment technique is the fact it does not require modeling of contact surfaces, and therefore, eliminates the numerically expensive iterations associated with surface formulations.

An embedded element needs to be geometrically confined within the host element. The degrees of freedom at the nodes of the embedded element will be eliminated and the nodes will become “embedded nodes” while constrained to the interpolated values of the corresponding degrees of freedom of the host element. The constraint rules governing the relationship between master and slave nodes can be theoretically described as follows. Given \mathbf{X}^m and \mathbf{X}^s as position of the master and slave nodes, respectively, the reference configuration position, \mathbf{N} , is defined as (ABAQUS, 2010):

$$\mathbf{N} = \mathbf{X}^m - \mathbf{X}^s \quad (3. 85)$$

Consequently, the position of the fully constrained slave node at any instance is found as

$$\hat{\mathbf{X}}^s = \mathbf{X}^m + \mathbf{C}(\phi^m)\mathbf{N} \quad (3. 86)$$

where $\mathbf{C}(\phi^m)$ corresponds to the rotation matrix of the master node. Figure 3- 28 shows a typical scheme for the finite element modeling of pretensioned concrete members using the embedment technique.

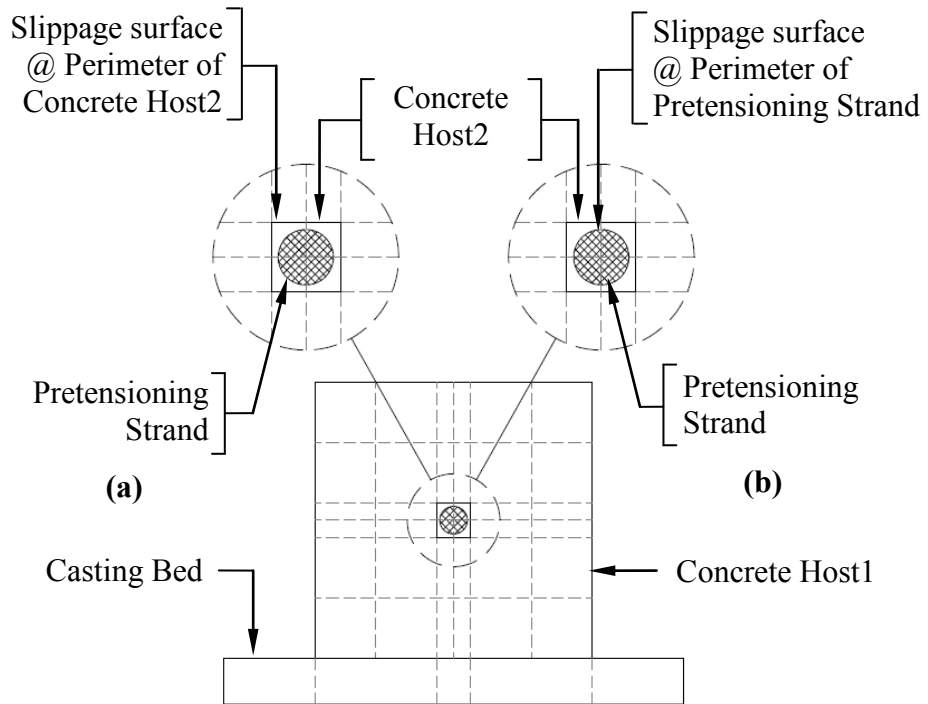


Figure 3-27: Schematic presentation of the techniques used for simulation of slippage surface upon releasing the strands: (a) Concrete-over-concrete slippage and (b) Steel-over-concrete slippage.

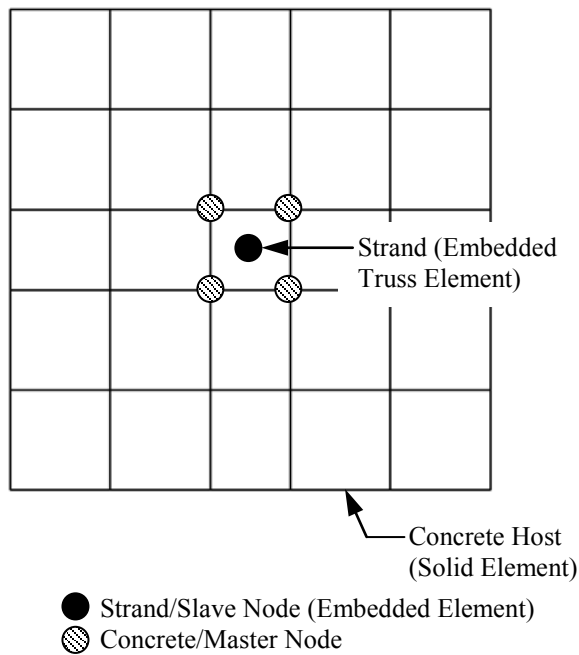


Figure 3-28: Schematic presentation of finite element modeling of pretensioned concrete members using embedment technique.

3.4.3. Simulation of Pretensioning

Pretensioning of strands and the releasing mechanism can be simulated using various modeling techniques. One effective technique is based on the strain-compatibility between strand and concrete (the default pretensioning methodology used in this work). The strain-compatibility technique includes various steps as outlined below with sample ABAQUS commands:

- Step 1: Pretension the strands as initial conditions before any relationship is established between the strands and concrete host:
** Initial Conditions, Type=STRESS*
Element Number or Element Set, PRESTRESSING MAGNITUDE
Repeat as many lines as necessary.
Element or element set per each line can be assigned different prestressing values if desired.
- Step 2: Deactivate the strain-compatibility in order to decouple the strands and concrete host while pretensioning is applied; this ensures that concrete is not strained while the strands are pretensioned:
**MODEL CHANGE, REMOVE*
List all elements except the pressing strands.
- Step 3: Apply strain-compatibility which simulates the release of the strands while the constraints to the concrete host are established:
**MODEL CHANGE, ADD=WITH STRAIN*
List all elements except the prestressing strands.

3.4.4. Simulation of Casting Bed

In order to capture the effect of the self-weight of the specimens simultaneously applied with prestressing, the simulated models are supported on a casting bed (steel) which provides rigid support without restraining the longitudinal and transverse movements of the pretensioned member. The interface between the pretensioned member and the casting bed is modeled as a friction-based surface (coefficient of friction is set at zero in this work), using the “hard” pressure-overclosure relationship as previously discussed with the exception that complete separation is allowed at the interface upon the cambering of the pretensioned member.

Alternatively, the effect of the casting bed may be simulated by modifying the boundary conditions as follows: 1) Provide rollers at the release ends, 2) Provide symmetry conditions at the mid-span (if a half-symmetric model is used), and 3) Apply the self-weight of the member simultaneously with activation of strain compatibility. The advantage of this methodology is the elimination of contact surface formulations which generally require complex numerical iterations upon cambering of the member over the casting bed.

3.5. Method Verification Based on Simulation of Mono-Strand Rectangular Beams

3.5.1. Introduction

The following section includes the verification of the methodologies for finite element simulation of pretensioned concrete members as proposed in the previous sections. The method verification is based on the comparative analysis of the numerical results obtained for beam-column specimens with rectangular cross sections and one prestressing strand versus the applicable closed-form solutions. The geometric characteristics of the models are: Concrete Beam (6 in. x 6in. x 96 in.) and 0.6-in.

diameter seven-wire low relaxation strands. The main objectives of this simulation are: 1) material calibration (concrete, steel and prestressing strands), 2) model calibration based on extrusion technique, 3) model calibration based on embedment technique, and 4) comparison of responses between the embedment and extruded models as well as the closed form solutions based on beam theory.

Two independent classes of models will be discussed to address the effect of eccentricity of the strand on the behavior of the concrete beam at the time of release. The simulation presented in this example investigates the response of pretensioned concrete beams immediately after the release of pretensioning without consideration of any time-dependent effects such as creep and shrinkage.

3.5.2. Calibration of Constitutive Models

3.5.2.1. Calibration of Concrete Constitutive Model

Table 3-4 includes the summary of the elastoplastic parameters used in the finite element analyses discussed in this section. In addition to the elastoplastic parameters, the uniaxial stress-strain behavior under tension and compression need to be included in the constitutive model. Figure 3-29 (a) and (b) show the compressive and tensile stress-strain models used for the analytical purposes of this research based on initial compressive strength of 5,800 (psi) at the time of release.

The calibration of the concrete constitutive model was performed by analyzing the response of a 2 in. x 8 in. finite element prism subject to uniaxial compressive and tensile straining. This process involves iteration of the following plastic parameters until the response of the test specimen in uniaxial tension and compression converges towards the prescribed theoretical stress-strain curves:

- Dilation Angle (ψ)
- Flow potential eccentricity (ε_c)
- Ratio of the initial equibiaxial compressive yield stress to initial uniaxial compressive yield stress (σ_{bo}/σ_{00})
- Ratio of the second stress invariant to that of the compressive meridian at the initial yield (K_c)
- Viscosity Parameter (μ_c)

The dilation angle (ψ) and the ratio of the second stress invariant to that of the compressive meridian at the initial yield (K_c) are estimated based on the following closed form relationships (Stephen, 2006):

$$\psi = \arctan \left[\frac{6 \sin(\phi)}{3 - \sin(\phi)} \right] \leq 56.3^\circ \quad (3.87)$$

$$\phi = \arcsin \left[\frac{f'_{ci} - f_{ti}}{f'_{ci} + f_{ti}} \right] \quad (3.88)$$

$$0.5 < K_c = \frac{3 - \sin(\phi)}{3 + \sin(\phi)} \leq 1.0 \quad (\text{default value @ } 2/3) \quad (3.89)$$

where f'_{ci} and f_{ti} denote the initial compressive and tensile strength of concrete at release.

Table 3-4 includes the final constitutive parameters that ensure the best convergence towards the anticipated (theoretical) response of concrete with initial compressive strength (f'_c) of 5,800 psi to uniaxial compression and tension based on the constitutive models discussed in Sections 3.2.2 and 3.2.3. Figure 3-29 (a) and (b) show the convergence of the response of the calibrated models towards the theoretical uniaxial compressive and tensile stress-strain curves, respectively, after several iterations. In

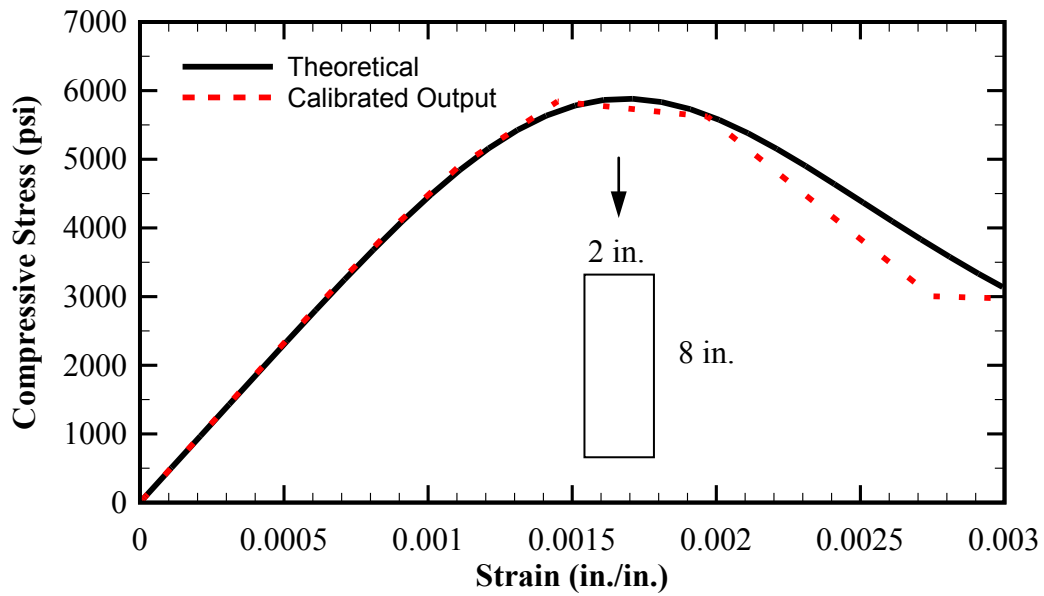
addition, Table 3-4 includes the constitutive parameters pertaining to prestressing strands and mild reinforcement, which are discussed in Section 3.5.2.2 in more details.

Figure 3-29 (a) shows an overall close convergence between the theoretical compressive stress-strain curve and the corresponding finite element solution. However, the finite element simulation based on CDP shows a steeper rate of softening in comparison with the closed form behavior.

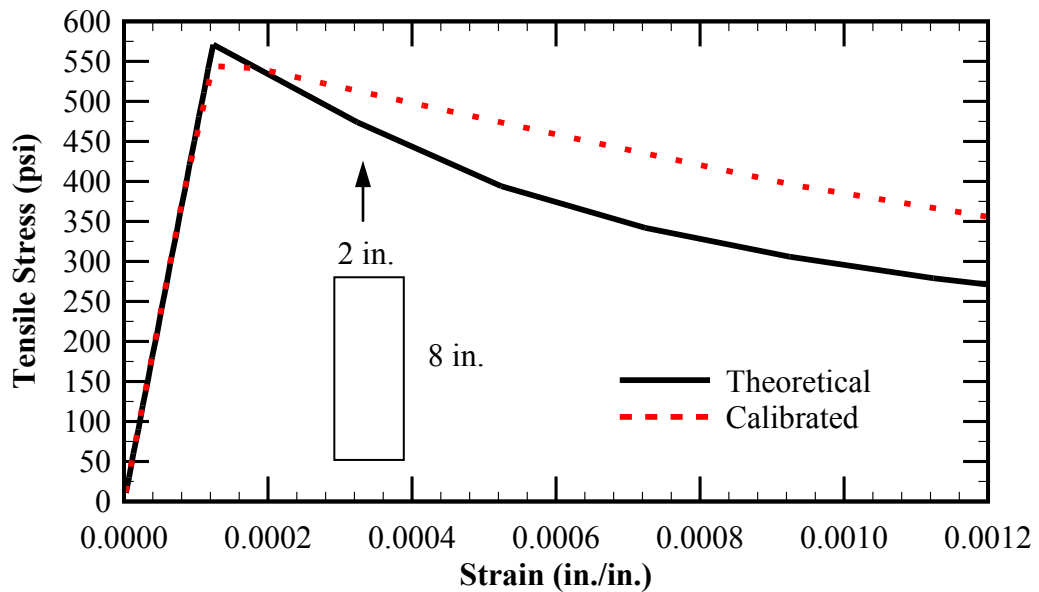
Similarly, Figure 3-29 (b) shows a comparison between the theoretical tensile stress-strain relationship and the corresponding finite element simulation. A more pronounced deviation is observed between the closed form and numerical solutions and mainly due to the difference in the initial elastic stiffness. In spite of the observed differences, both solutions indicate acceptable similarities in response to uniaxial tension, adequate for the analytical purposes of this research.

Table 3-4: Summary of constitutive parameters used in finite element analyses.

Parameter	Value Used in Analysis
Concrete	
Compressive strength at time of release (f_{ci}')	5.800 (ksi)
Tensile [Rupture] strength at time of release (f_{ti})	0.578 (ksi)
Density (w_c)	150 (lb/ft ³)
Young's Elastic Modulus (E_{ci})	4617 (ksi)
Poisson's Ratio (ν_c)	0.2
Dilation Angle (ψ)	52.9°
Flow potential eccentricity (ε_c)	0.1
Ratio of the initial equibiaxial compressive yield stress to initial uniaxial compressive yield stress (σ_{bo}/σ_{00})	1.16
Ratio of the second stress invariant to that of the compressive meridian at the initial yield (K_c)	0.778
Viscosity Parameter (μ_c)	0.0
Prestressing Strands	
Ultimate tensile strength (f_{pu})	270 (ksi)
Density (w_p)	490 (lb/ft ³)
Young's Elastic Modulus (E_p)	28,500 (ksi)
Poisson's Ratio (ν_p)	0.2
Non-Prestressed Reinforcement	
Yield Strength (f_y)	60 (ksi)
Density (w_p)	490 (lb/ft ³)
Young's Elastic Modulus (E_p)	29,000 (ksi)
Poisson's Ratio (ν_p)	0.2
Other Structural Steel (Casting Bed)	
Yield Strength (f_y)	36 (ksi)
Density (w_p)	490 (lb/ft ³)
Young's Elastic Modulus (E_p)	29,000 (ksi)
Poisson's Ratio (ν_p)	0.2



(a)



(b)

Figure 3-29: Comparison of the stress-strain relationships obtained by the constitutive model with the theoretical stress-strain curves assumed for a concrete with initial compressive strength of $f'_{ci} = 5,800$ psi: a) subject due to uniaxial compression, and (b) subject to uniaxial tension.

3.5.2.2. Constitutive Parameters for Prestressing Strands and Other Structural Steel

Table 3-4 gives the summary of the constitutive parameters based on the default values used in the current practice of bridge engineering in the U.S. (AASHTO LRFD, 2010). The prestressing strands will be stressed to a maximum threshold of

$$f_{p0} = f_j \leq 0.75 f_{pu} \quad (3.90)$$

where f_{p0} (f_j) is commonly referred to as jacking stress, and f_{pu} corresponds to ultimate tensile capacity of the prestressing. Since the yield strength (f_{py}) of 270-ksi pretensioned strands is approximately 90% f_{pu} , the prestressing strands are anticipated to remain elastic throughout the analysis.

The application of the structural steel will be limited to non-prestressed reinforcement as well as casting beds (when applicable). It is assumed that the reinforcing bars and casting bed will remain within the elastic regime and the material characteristics are consequently limited to the elastic parameters. The analysis of stresses in the casting bed is not relevant to the objectives of this research.

3.5.3. Finite Element Models

The extruded models are divided into two categories: 1) concentrically pretensioned, and 2) eccentrically pretensioned. The rectangular beams are modeled using linear 8-node cube elements (refer to Figure 3-25). The linear brick elements possess only translational degrees of freedom. The simulation of the prestressing strands depends on the modeling technique as previously discussed: i) extrusion, where prestressing strands are simulated using three-dimensional linear brick elements, and ii) embedment, where prestressing strands are simulated using one-dimensional truss elements. Figure 3-30

shows the typical finite element models of the concentrically pretensioned rectangular beams.

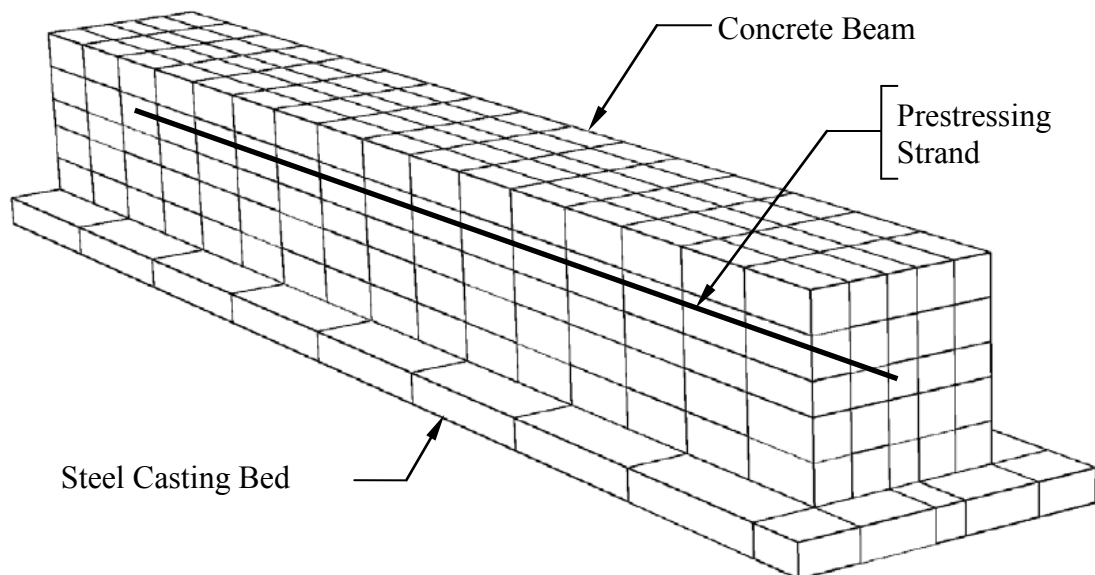
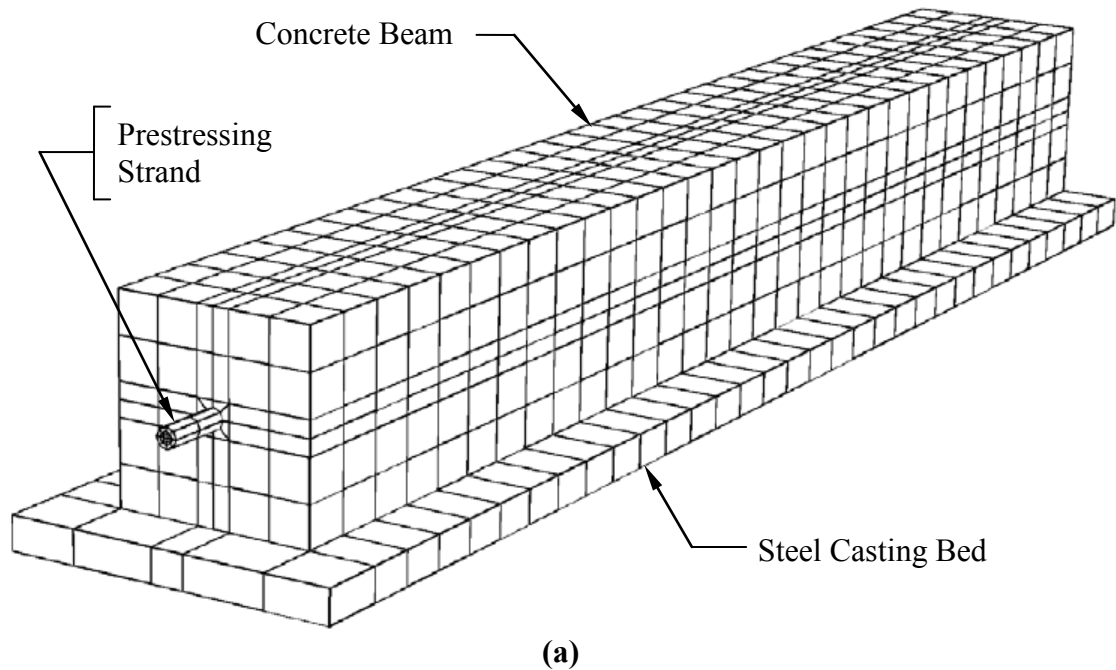
The concentrically pretensioned models include the interaction between the concrete medium and the casting bed. In the eccentrically pretensioned models, the effect of casting beds are simulated using the boundary conditions as previously discussed in Section 3.4.4.

Based on the earlier discussion, the slippage of the strands is modeled using the following techniques: 1) Slippage of concrete (with tied strand) over concrete host, and 2) Direct slippage of strands over concrete host.

The concentric models are pretensioned using one 0.6-in. diameter low-relaxation seven-wire strand positioned at the center of gravity of the concrete beams. Therefore, the concrete member will be subjected to axial compression stress upon releasing of the strand. Appendices A and B includes sample finite element simulations for concentrically pretensioned specimens based on the extrusion and embedment techniques, respectively.

At the time of release, losses due to relaxation of strands and elastic shortening are only considered. The anticipated relaxation of strands up to the time of release is already considered in the threshold of jacking stresses (input parameter). Elastic shortening is automatically taken into account through strain compatibility between the pretensioned strand and concrete host. Alternatively, the theoretical loss due to elastic shortening may be estimated in accordance with the provision of AASHTO LRFD. Given the characteristics of the concrete beams combined with the level of pretensioning, the elastic shortening losses are anticipated to be 7,500 psi.

The eccentric models are also pretensioned using one 0.6-in. diameter low-relaxation seven-wire strand positioned 1.556 in. below the center of gravity of the concrete beams. Therefore, the concrete member is subjected to axial compression combined with bending upon releasing of the strand. Figure 3-31 schematically shows the composite configuration of the rectangular beams with one eccentric strand.



(b)

Figure 3-30: Typical finite element models for simulation of rectangular beams with one prestressing strand supported on casting bed: (a) Extruded model, and (b) Embedded model.

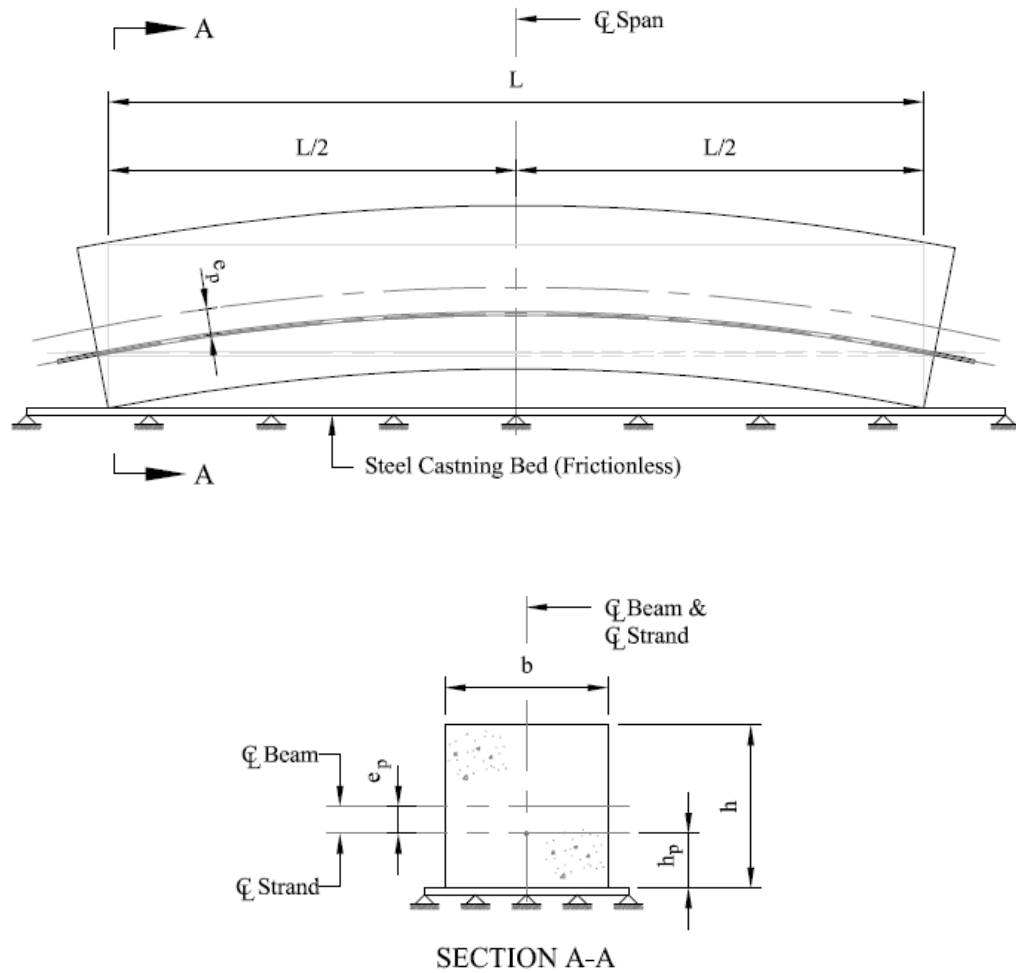


Figure 3-31: Schematic presentation of the analytical model with strand eccentricity parameter (e_p) relative to the center of gravity of the member.

3.6. Discussion of Results

3.6.1. Rectangular Beam with One Concentric Strand

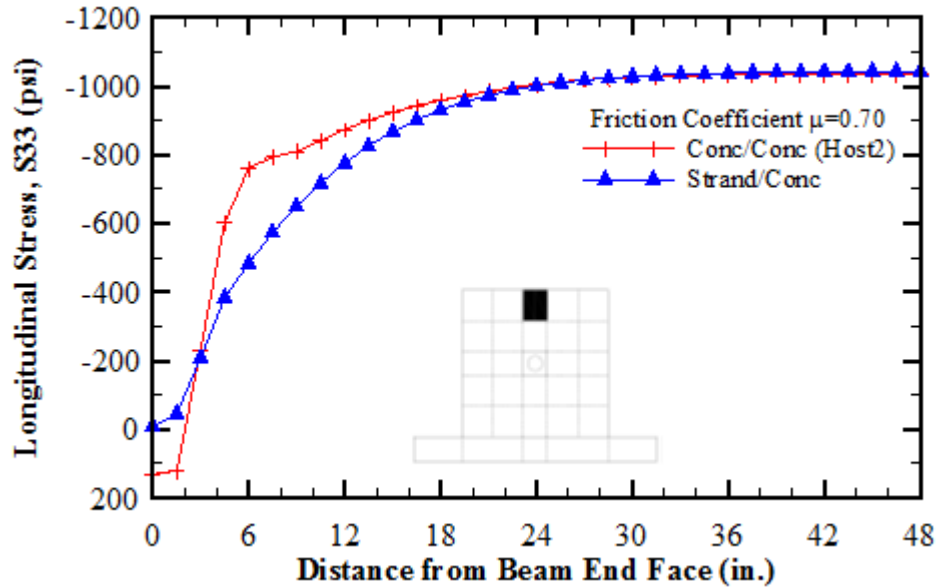
Based on the available closed form solutions (elastic beam analysis), the maximum anticipated compressive stress in the beam slightly varies depending on whether gross, net or transferred cross section is considered. The estimated compressive stresses are summarized in Table 3-5.

Table 3-5: Summary of stresses obtained by the concentrically pretensioned finite element model.

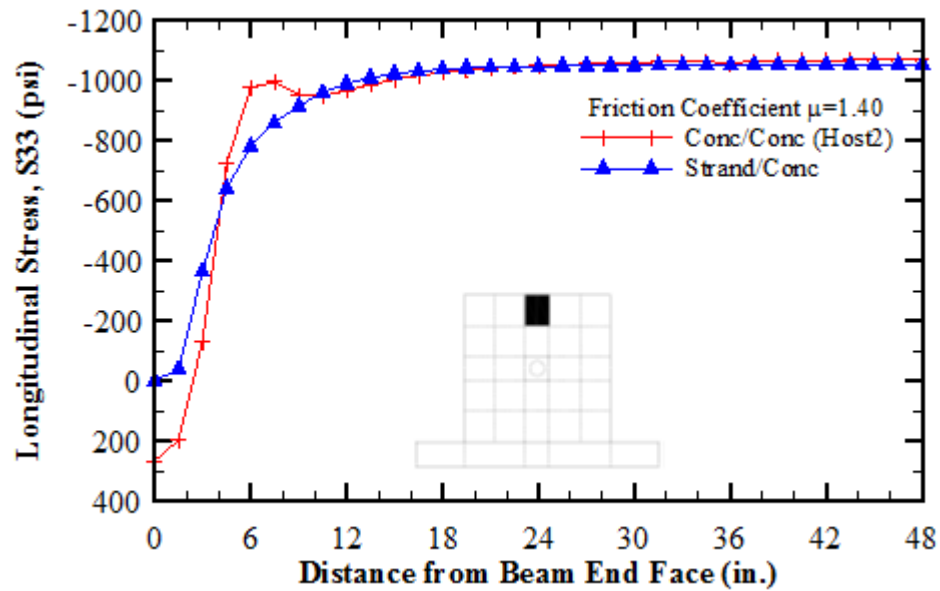
Model	Compressive Stress (psi)	Tensile Stress (psi)
Extruded Models		
$\mu = 0.70$	1043	0
$\mu = 1.40$	1054	0
Embedded Models		
Linear transfer length	1173	0
Nonlinear transfer length	1177	0
Nonlinear transfer length	1183	0
Closed Form Solution (Beam Theory)		
Gross section	1165	0
Net section	1154	0
Transferred section	1184	0

Appendix I includes the details of the corresponding closed form solutions based on elastic beam theory corresponding to the gross, net and transformed sectional properties of the concrete host.

Figure 3-32 shows the simulated response of the concentrically pretensioned concrete specimen in accordance with: i) concrete-over-concrete slippage, and ii) strand-over-concrete slippage based on lower and upper boundary friction coefficients of 0.70 and 1.40, respectively.



(a)



(b)

Figure 3-32: Response of extruded models to concentric pretensioning based on various coefficients of friction at the slippage surface: (a) Coefficient of friction of $\mu=0.70$ and (b) Coefficient of friction of $\mu=1.40$.

The main objectives of these parametric studies are to identify: i) the optimized simulation of the slippage based on concrete-over-concrete versus strand-over-concrete, and ii) the optimized coefficients of friction providing lower and upper bounds for

pretensioning stress path over the simulated slippage surface (transfer length). Figure 3-33 shows the axial stresses developed in the strands immediately after the release of pretensioning for two extruded models with coefficients of friction of 0.70 and 1.40, respectively. It can be observed that both models converge towards the theoretical transfer length along a nonlinear stress variation path as opposed to the linear stress path assumed in current practice.

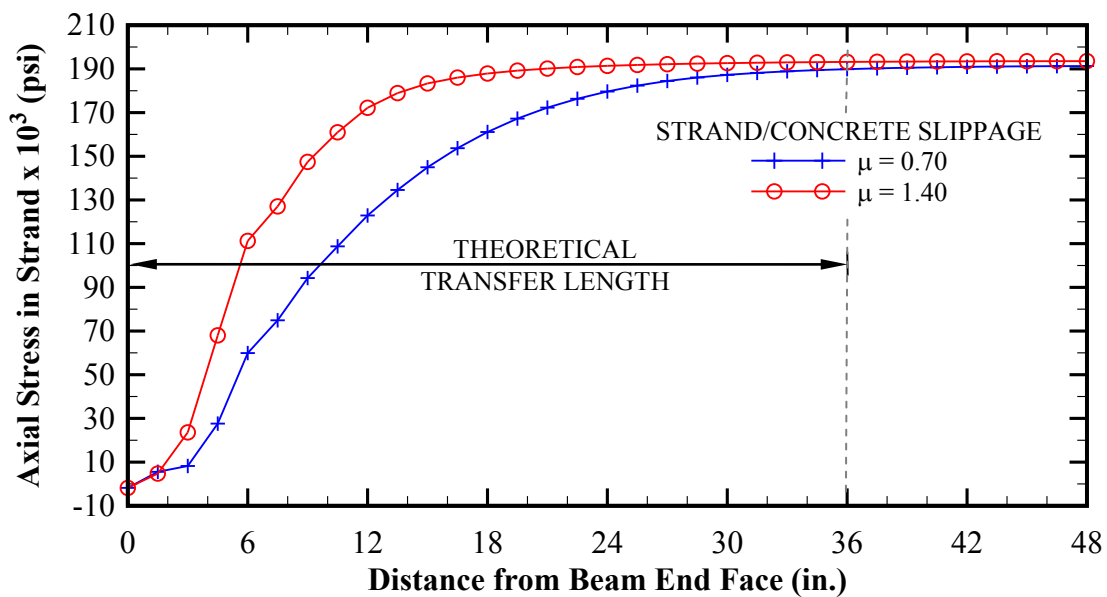


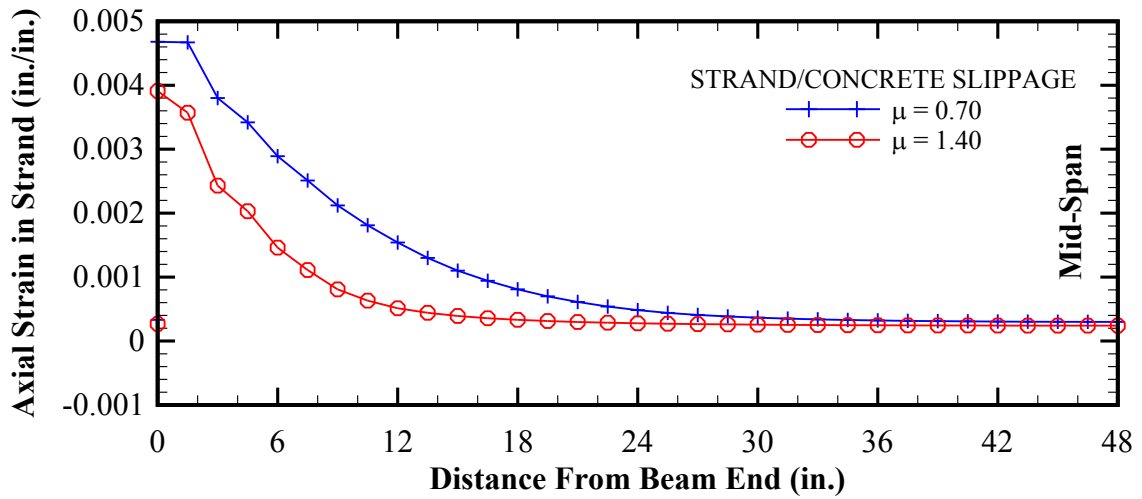
Figure 3-33: Axial pretensioning stress in the concentric strands immediately after the release (including elastic shortening losses).

As previously discussed, the embedded models are not capable of predicting the bond stresses at the interface between the concrete and strand(s) since they simulate the pretensioning mechanism based on nodal constraints rather than contact formulation. However, the extruded models are capable of estimating the bond stresses based on contact formulation. Figure 3-34 shows typical results corresponding to the friction-based contact formulations, including the straining of the pretensioned strand, pressure

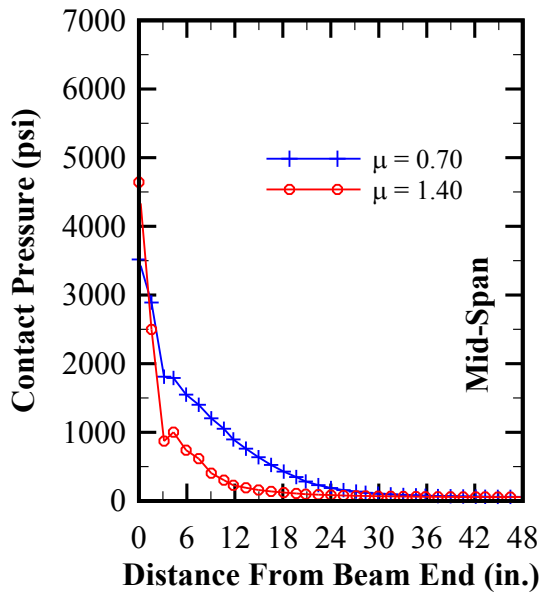
and shear stresses developed at the interface between the concrete and strand and the corresponding strains immediately after release.

Since the concentrically pretensioned specimens are globally in compression, optimized accuracy can be achieved within numerical efficiency. The optimized characteristic length of the solid elements simulating the concrete medium is reached at 3 in., evaluated against the closed form solutions. The optimization of the concrete Host2 (Figure 3-27) is studied in order to verify the effect of the mesh sensitivity on the contact formulation used in the extruded models. Figure 3-35 shows the convergence of the longitudinal stresses based on the size of the concrete elements representing the zone of interface with the pretensioned strand (applicable to the extruded models only).

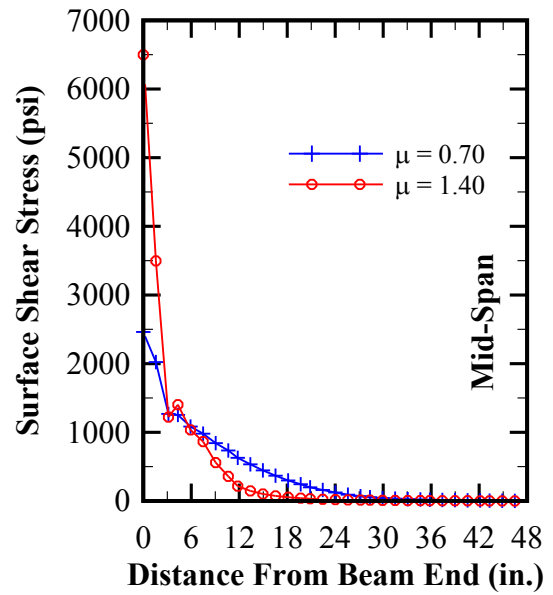
As indicated in Table 3-5, the compressive stresses resulted by the embedded models are also consistent with the closed form solutions (based on beam theory).



(a)



(b)



(c)

Figure 3-34: Sample results for concentrically pretensioned specimens with friction-based contact formulation: (a) axial strain the strand after the release, (b) contact pressure at the interface between concrete host and strand, and (c) surface shear stresses at the interface between concrete and strand.

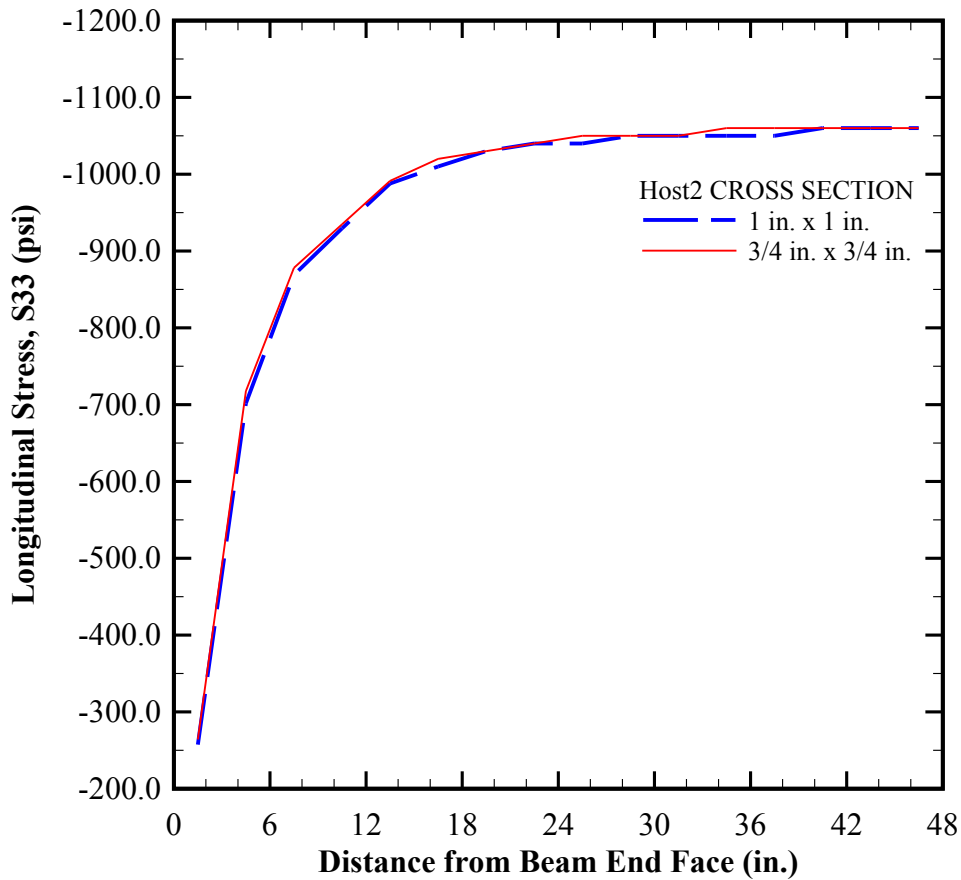


Figure 3-35: Concrete mesh sensitivity at interface with the pretensioned strand (extruded model with one concentric strand).

3.6.2. Rectangular Beam with One Eccentric Strand

Table 3-6 includes the summary of top and bottom fiber stresses at the mid-span of the eccentrically pretensioned specimens. Appendix I includes the details of the corresponding closed form solution based on elastic beam theory.

It is observed that the results of the simulation with embedded models agree with the closed form solutions within a 5% range. In the case of the extruded models, the results are generally lower than those obtained by the closed form solutions and/or embedded.

Due to the flexural demand at top fibers of the concrete beam, the acceptable

convergence of the model requires denser meshing with the optimized characteristic length 1 in.

Table 3-6: Summary of stresses obtained by the eccentrically pretensioned finite element model.

Model	Compressive Stress (psi)	Tensile Stress (psi)
Extruded Models		
$\mu = 0.70$	2739	485
$\mu = 1.40$	2751	492
Embedded Models		
Linear transfer length simulation	2803	513
Closed Form Solution (Beam Theory)		
Gross section	2871	541
Net section	2854	536
Transferred section	2848	533

Figure 3-36 shows the longitudinal stress profiles, measured at the top fiber, along the span of the pretensioned extruded models. The results correspond to two different cases based on the slippage coefficients (μ_f) of 0.70 and 1.40 for friction at the interface between the strand and concrete. Additionally, identical results corresponding to the embedded models with linear approximation of transfer length as prescribed by AASHTO LRFD are included in Figure 3-36. It can be observed that the longitudinal stresses by the extruded models generally hover over the idealized linear approximation of the stress variation within the end regions of the beam towards the location of the theoretical transfer length. Beyond the transfer length, the results from the extruded models converge towards similar plateau obtained from the embedded models.

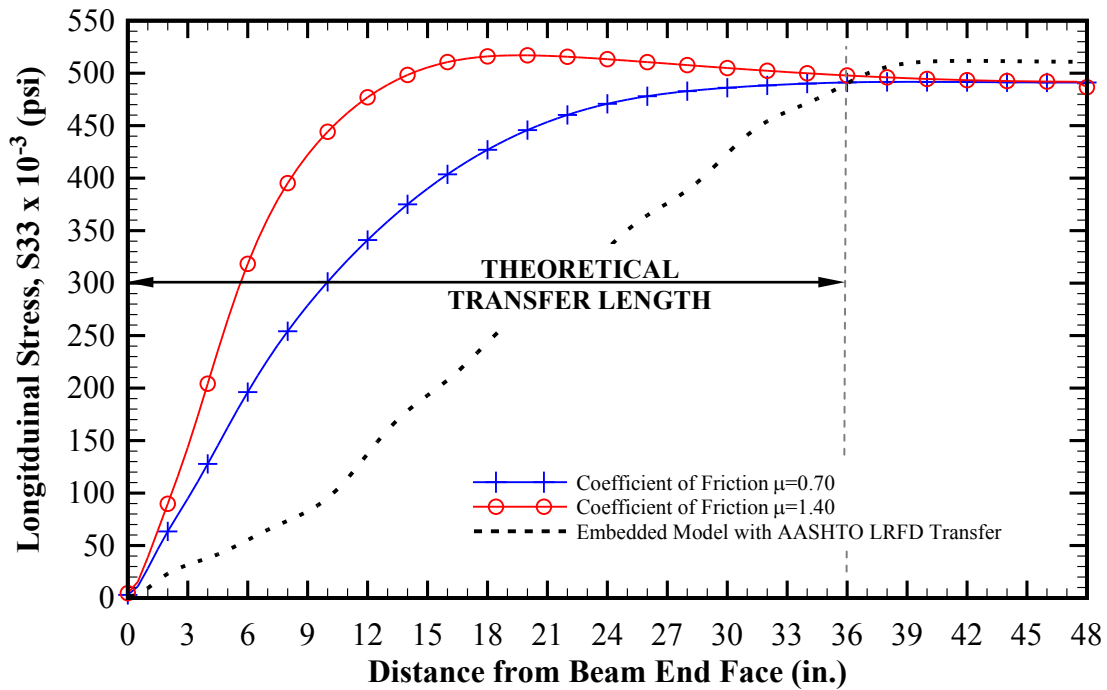


Figure 3-36: Longitudinal stress S33 measured at the extreme top fiber along the extruded member, corresponding to two levels of contact friction at the interface between the strand and concrete host: $\mu_f = 0.70$ and 1.40 . Response of an equivalent embedded model is also shown based on AASHTO LRFD linearized pretensioning.

Three-dimensional finite element models of the pretensioned concrete members are able to capture stress redistributions once the specimens enter the inelastic regimes. As previously discussed, the extrusion technique is capable of direct simulation of the stress transfer mechanism at the interface between concrete and pretensioned strands by utilizing friction-based contact formulations. This facilitates more detail prediction of elastoplastic response of concrete as well as potentials for cracking, crushing, and stress redistributions in the zones near the released strands. Figure 3-37 and Figure 3-38 show the distribution of the vertical stresses immediately after the release of the axial pretensioning for extruded models with friction coefficients of 0.7 and 1.4, respectively. The areas with high stress concentrations are identifiable near the extrusion. Figure 3-39 similarly shows the distribution of the vertical stresses immediately after the release of

the axial pretensioning for embedded model. As it can be observed, the extruded models provide more details related to slippage and the local stress distributions in the areas adjacent to the strand in comparison with the embedded model.

Since the primary objectives of the extruded finite element models are the evaluation of the flexural stresses and identifying the areas with high stress concentrations, the results are observed to be highly mesh sensitive. Consequently, the extruded models generally become very numerically expensive, affected by the convergence of the friction-based contact formulations. On the contrary, the embedded models are generally numerically efficient since the convergence of the densely meshed models is not nearly as demanding as the complex interface solutions required in the extrusion technique. In addition, a linear elastic analysis is not capable of estimating the potentials for plastic response of the zones with high stress concentrations. One example of such areas includes the interface between concrete and pretensioned strands as previously discussed in this paper. Additionally, past experience indicates that end zones of pretensioned members are subject to cracking due to effects such as bursting and splitting immediately after the release of pretensioning. Therefore, inclusion of an elastoplastic constitutive model is deemed essential for accurate simulation of response of concrete members to pretensioning depending on the objectives of analysis.

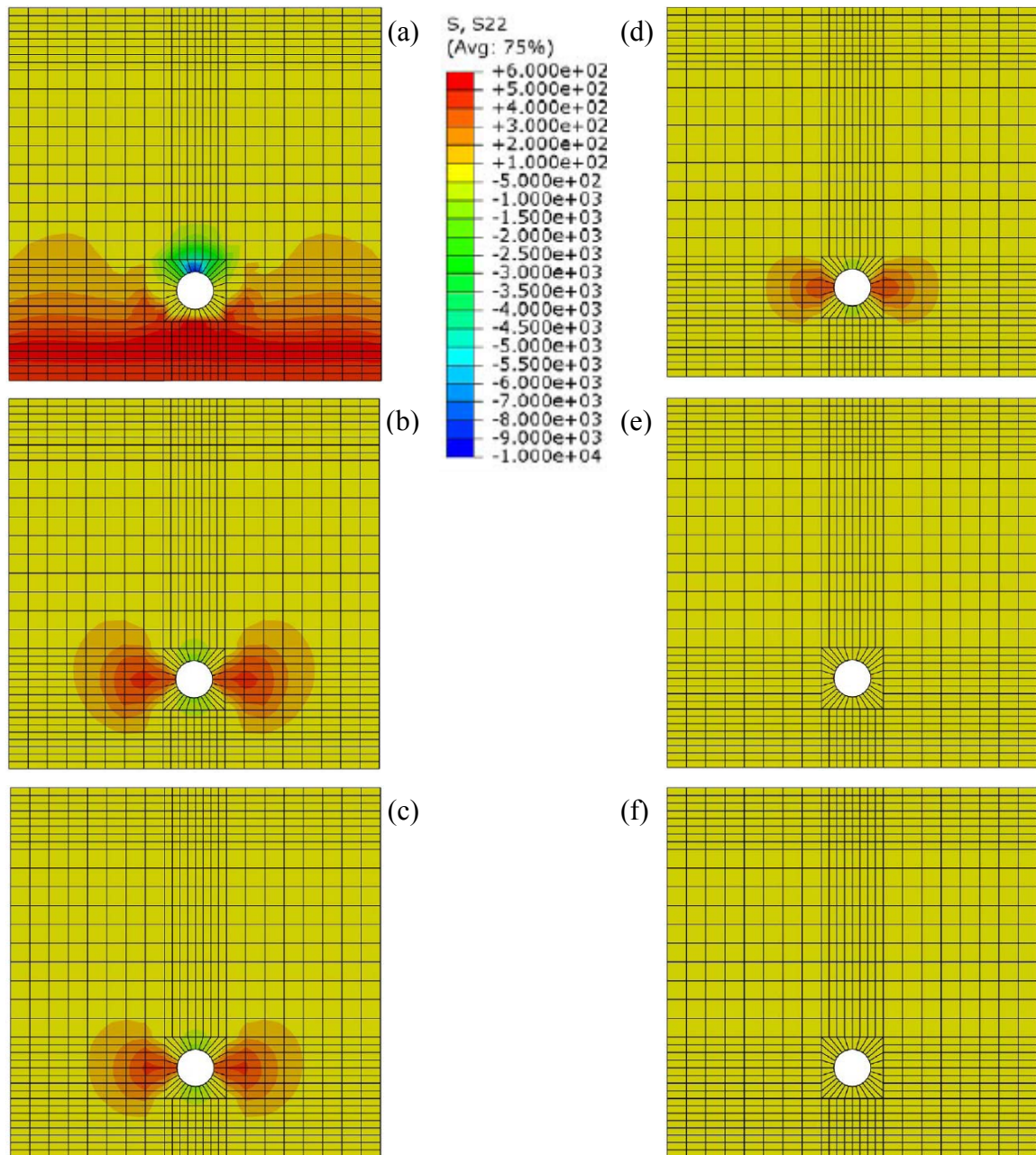


Figure 3-37: Vertical stress contours for embedded model with one eccentric strand with coefficient of friction $\mu = 0.7$ at the following distances from the end face of the rectangular beam: (a) 0 in., (b) 3 in., (c) 6 in., (d) 12 in., (e) 36 in. (Theoretical Transfer Length) and (f) 48 in. (Mid-span)

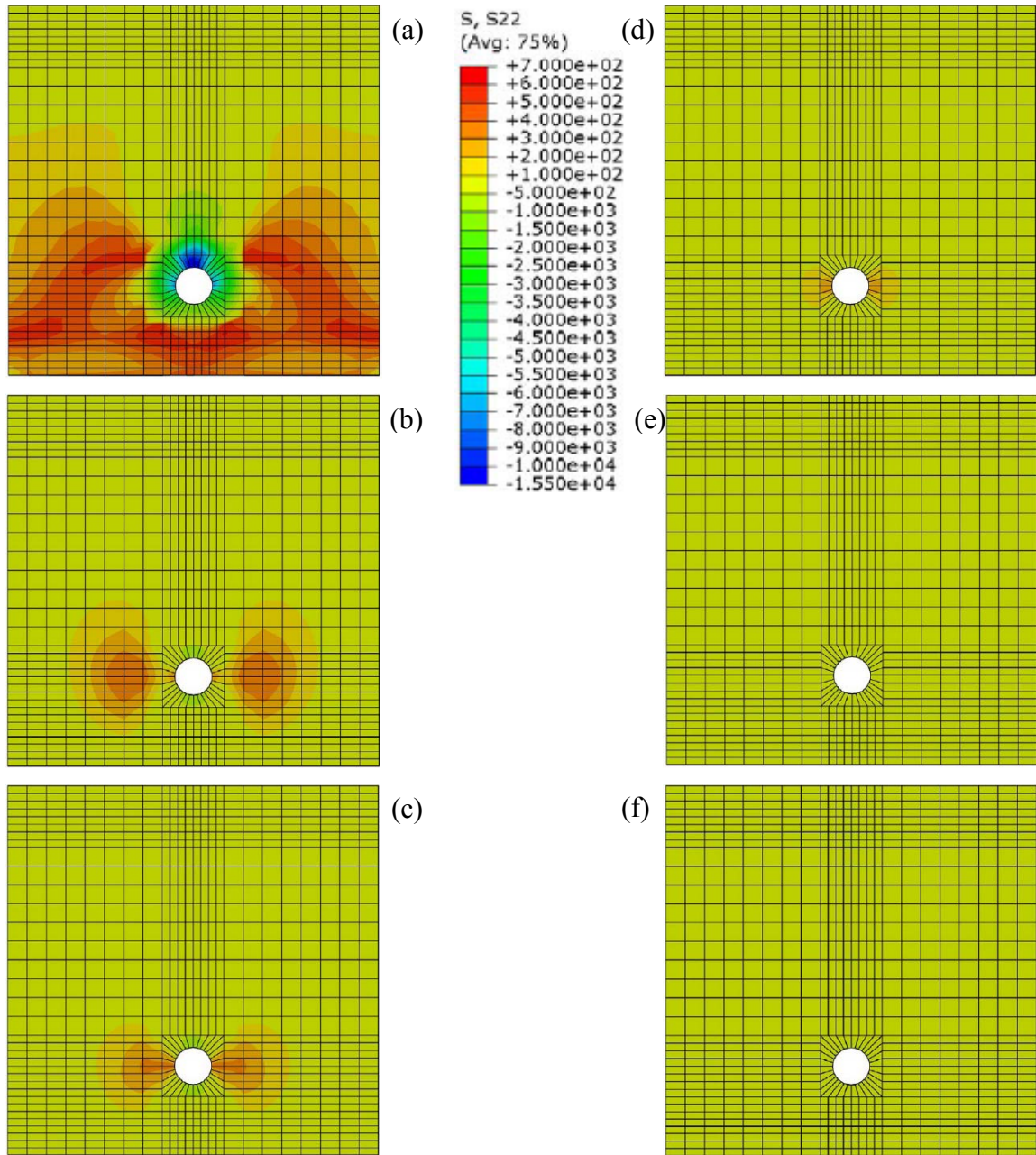


Figure 3-38: Vertical stress contours for embedded model with one eccentric strand with coefficient of friction $\mu = 1.4$ at the following distances from the end face of the rectangular beam: (a) 0 in., (b) 3 in., (c) 6 in., (d) 12 in., (e) 36 in. (Theoretical Transfer Length) and (f) 48 in. (Mid-span)

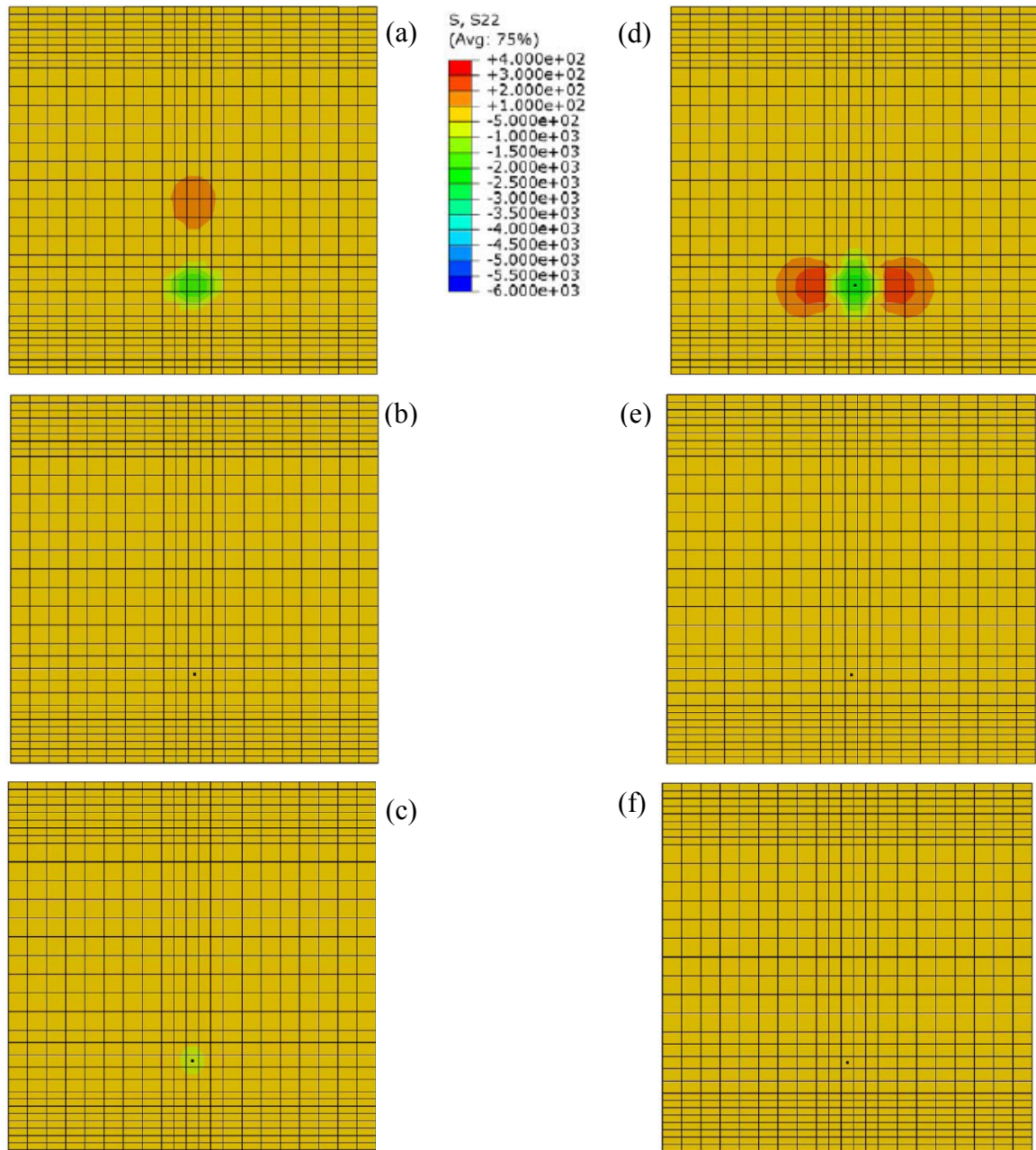


Figure 3-39: Vertical stress distribution for embedded model with one eccentric strand along the span and at the following distances from the end face of the rectangular beam: (a) 0 in., (b) 3 in., (c) 6 in., (d) 12 in., (e) 36 in. (Theoretical Transfer Length) & (f) 48 in. (Mid-span)

Chapter 4 - Response of Pretensioned Concrete Beams to 0.7-in. Diameter Prestressing Strands with Experimental Verification

4.1. Objectives & Research Background

The main objectives of this chapter are summarized as follows:

1. Experimental verification of the methodological approach for finite element modeling of pretensioned concrete members as previously presented;
2. Evaluation of response of rectangular beams to pretensioning enforced by one concentric 0.7-in. diameter low-relaxation seven-wire strand;
3. The effect of confinement on the response of the above specimens to the imposed pretensioning;
4. The group effect of strands as well as their spacing on the transfer length;
5. The effect of spacing of the strands on the imposed stresses at the core of the specimens, in the vicinity of the central strand, and
6. The effect of confinement reinforcement (amount and spacing) on the response of the specimens to pretensioning imposed by nine 0.7--in. diameter strands.

The experimental data used for the analytical purposes of this research are based on the previous research by Akhnoukh (Akhnoukh, 2008). One of the main objectives of Akhnoukh's research was to investigate the effect of confinement on transfer length of prestressing strands, and more specifically 0.7-in. diameter strands. The experiments utilized four 7-in. x 7-in. rectangular beams, 8-ft long (each). Each specimen was concentrically pretensioned using one 0.7-in. diameter low-relaxation seven-wire prestressing strand. Four classes of specimens were then created based on the following confinement schemes (Akhnoukh, 2008):

- *Class I* - No.3 closed stirrup confinement reinforcement spaced at 3 in. on center
- *Class II* - No.3 closed stirrup confinement reinforcement spaced at 6 in. on center
- *Class III* - No.3 closed stirrup confinement reinforcement spaced at 9 in. on center
- *Class IV* - No.3 closed stirrup confinement reinforcement spaced at 12 in. on center

DEMEC discs were used in order to measure the compressive strains imposed by the pretensioning. The discs were installed on the outside faces of the concrete prisms (each face) parallel with the centroid of the beam and the prestressing strand (concentric pretensioning). The first measurement control point was set at 2 in. from the end face of the beam. Figure 4-1 shows a typical experimental beam hosting DEMEC discs on the outside faces.

In accordance with the research documents, the prestressing strands were released using flame-cut process after the initial DEMEC readings were recorded 24 hours after the casting. Upon releasing of pretensioning, DEMEC measurements were repeated at 1, 3, 7, 14 and 28-day intervals. Since DEMEC measurements corresponded to surface straining of the concrete beam due to pretensioning, a direct correlation was established between the recorded measurements and the transfer length of the 0.7-in. diameter strands. For the analytical purposes of this research, the strain readings obtained by Akhnoukh's experiments are normalized and compared with the corresponding finite element results also normalized.

Table 4-1 includes the summary of the specimens used by Akhnoukh in order to establish transfer length of 0.7-in. diameter low-relaxation seven-wire strands and the effect of confinement.



Figure 4-1: Typical experimental specimen with DEMEC discs on the outside faces to facilitate measurement of straining after the release of pretensioning (Akhnoukh, 2008).

Table 4-1: Characteristic properties of the specimens used in the experimental verification of transfer length and the corresponding effect of confinement reinforcement. Adapted from (Akhnoukh, 2008).

Specimen	Geometric Properties	Confinement	
		Reinforcement	Spacing
1-L8-3	7-in. x 7-in. x 8-ft (long)	No.3 Close Stirrup	3 in. on center
1-L8-6	7-in. x 7-in. x 8-ft (long)	No.3 Close Stirrup	6 in. on center
1-L8-9	7-in. x 7-in. x 8-ft (long)	No.3 Close Stirrup	9 in. on center
1-L8-12	7-in. x 7-in. x 8-ft (long)	No.3 Close Stirrup	12 in. on center

Once Objectives 1 through 3 are fulfilled, the mono-strand finite element models are expanded to include nine 0.7-in. diameter strands hosted within prisms with larger cross-sectional areas in the later portion of this chapter. The analytical results obtained by the multi-strand finite element models are normalized and compared with the corresponding experimental readings by Akhnoukh. The analytical results are then investigated to evaluate the effects of strand groups and spacing on transfer length.

4.2. Literature Review

4.2.1. 0.7-in. Diameter Prestressing Strands: Transfer Length and Confinement

During the past few years, 0.7-in. diameter low-relaxation seven-wire strands have been reported to be used the U.S. but mainly in the cable-stayed bridges and mining applications (Morcou, Hanna, & Tadros, 2010). With increasing applications in post-tensioning tendons reported in Europe and Japan, it is anticipated that sooner or later 0.7-in. diameter strands will find their way to more widespread bridge applications in the U.S. The Pacific Street Bridge over I-680 in Omaha, Nebraska, is recorded as the first bridge in the world that the utilized 0.7-in. diameter strands for pretensioning of the project I-girders (Schuler, 2009). In accordance with Schuler, the precast I-girders used in the Pacific Street Bridge utilized 10,000 psi concrete while pretensioned with total of thirty 0.7-in. diameter strands spaced at 2 in. horizontally and 2.5 in. vertically. The use of 0.7-in. diameter strands with nominal area of 0.294 in.² resulted in significant savings in the number of strands compared to 0.5-in. and 0.6-in. diameter strands (75% and 50%, respectively) (Schuler, 2009). Such levels of reduction in the number of prestressing strands can directly be translated to significant labor and material cost savings.

On the other hand, 0.7-in. diameter strands can deliver significantly larger amount of pretensioning compared with 0.5-in. and 0.6-in. diameter strands, directly proportioned to the larger cross-sectional area as follows:

- 192% over 0.5-in. diameter strands, and
- 135% over 0.6-in. diameter strands

The Pacific Street project included total of twenty 98'-4" long NU 900 girders weighing 90,000 lbs each. Due to the lack of previous data related to the use of 0.7-in. diameter strands as pretensioning elements, full-scale testing was performed prior to the

production of the girders in order to ensure that the potential cracks at the time release were similar to the usual end zone cracking of the pretensioned girders. Based on the full-scale test results, it was eventually decided that the end zone design and details recommended by the AASHTO LRFD Bridge Specifications were adequate for the purposes of the project. The main challenges of the production of the corresponding girders were the market availability of 0.7-in. diameter strands at the time and the need for larger hold-down devices (Schuler, 2009).

Russell et. al. performed one of the first comprehensive studies of optimized sections for high-performance-concrete (HPC) girders (Russell, Volz, & Bruce, 1997). In spite of unavailability of 0.7-in. diameter strands in the U.S. market at the time of the study, Russell et. al. showed that the use of 0.7-in. diameter strands in combination with 10,000 psi concrete can result in the longest and most economical precast girders in comparison with the similar sections pretensioned with 0.5-in. and 0.6-in. diameter strands.

Following the construction of the Pacific Street Bridge over I-680, Morcoux et. al. conducted extensive experimental studies of the use of 0.7-in. diameter strands at the University of Nebraska-Lincoln (Morcoux, Hanna, & Tadros, 2010). One of the objectives of this research was to show that 0.7-in. diameter strands could be spaced at 2-in. x 2-in. horizontal and vertical grids without detrimental effects on the members. The 2-in. x 2-in. horizontal and vertical spacing layout is similar to practice of pretensioning using 0.6-in. diameter strands. Therefore, if similar spacing can be used for 0.7-in. diameter strands, fabricators will be more willing to use 0.7-in. diameter strands without the need for costly retooling and modifications of the casting beds and abutments. In addition, the experimental data showed that the measured transfer and development

lengths of 0.7-in. diameter strands were below the corresponding recommendations by the AASHTO LRFD Design Specifications (Morcou, Hanna, & Tadros, 2010).

Based on the study performed in a collaboration between the Nebraska Department of Roads (NDOR) and the University of Nebraska-Lincoln, Morcou and Tadros recommend that a minimum of 10,000 psi concrete (28-day compressive strength) be used for the precast girders pretensioned using 0.7-in. diameter strands spaced at 2 -in. x 2-in. horizontal and vertical spacing in order to ensure conformance with the AASHTO LRFD recommendations for transfer and development lengths (Morcou & Tadros, 2011). In addition, the same study recommends that the confinement reinforcement recommended by AASHTO LRFD be considered as the minimum while additional confinement is recommended for enhancement of member ductility (Morcou & Tadros, 2011).

As discussed in details in Section 4.1, Akhnoukh also conducted a series of parametric studies with experimental tests on mono-strand prisms concentrically pretensioned using one 0.7-in. diameter strand (Akhnoukh, 2008). One of the objectives of Akhnoukh's research was to determine an optimized transfer length for 0.7-in. diameter strands. Additionally, Akhnoukh investigated the effect of confinement reinforcement on the transfer length of the specimens. As previously discussed, the experimental results by Akhnoukh are used for the comparative purposes of this chapter.

4.2.2. 0.7-in. Diameter Prestressing Strands: Spacing of prestressing strands

As discussed in the previous section, the experimental studies by Morcou et. al. at the University of Nebraska-Lincoln shows that 0.7-in. diameter strands may be spaced at 2 in. on center (both horizontal and vertical grids) if combined 10,000 psi (min.) concrete.

Similar studies at the University of Tennessee-Knoxville examined AASHTO Bulb-Tee girders pretensioned with 0.7-in. diameter strands (Vadivelu, 2009). While the strands were spaced at 2 in. on center (both horizontally and vertically), the analytical and experimental results reported that no cracking due to closer spacing of the strands were observed. The same study concludes that since 0.7-in. diameter strands generally are observed to have shorter transfer length compared with smaller diameter strands, larger splitting stresses are anticipated within the end zone of the member. This subsequently increases the probability of cracking of the end zones of the member due to higher splitting forces.

4.3. Rectangular Beams with One Concentric Pretensioned 0.7-inch Diameter Strand

4.3.1. Finite Element Models

In conformance with the experimental procedures as described in Section 4.1, four classes of finite element models are constructed to correspond to the test specimens. Table 4-2 includes the summary of the finite element models used for the analytical purposes of this section. As discussed later on this section, Class IV models will be ignored for the analytical purposes of this research due to disparity of the experimental data. Figure 4-2 thru Figure 4-5 show typical properties of Class I thru IV finite element models as summarized in Table 4-2, respectively.

Table 4-2: Log of finite element models.

Model		Sectional Properties	Pretensioning	Confinement
Class	I.D.			
I	1-L8-3	7-in. x 7-in. x 8-ft (long)	1-0.7 in. diameter strand (concentric)	No.3 confinement rebar spaced at 3 in. on center
II	1-L8-6	7-in. x 7-in. x 8-ft (long)	1-0.7 in. diameter strand (concentric)	No.3 confinement rebar spaced at 6 in. on center
III	1-L8-9	7-in. x 7-in. x 8-ft (long)	1-0.7 in. diameter strand (concentric)	No.3 confinement rebar spaced at 9 in. on center
IV	1-L8-12	7-in. x 7-in. x 8-ft (long)	1-0.7 in. diameter strand (concentric)	No.3 confinement rebar spaced at 12 in. on center

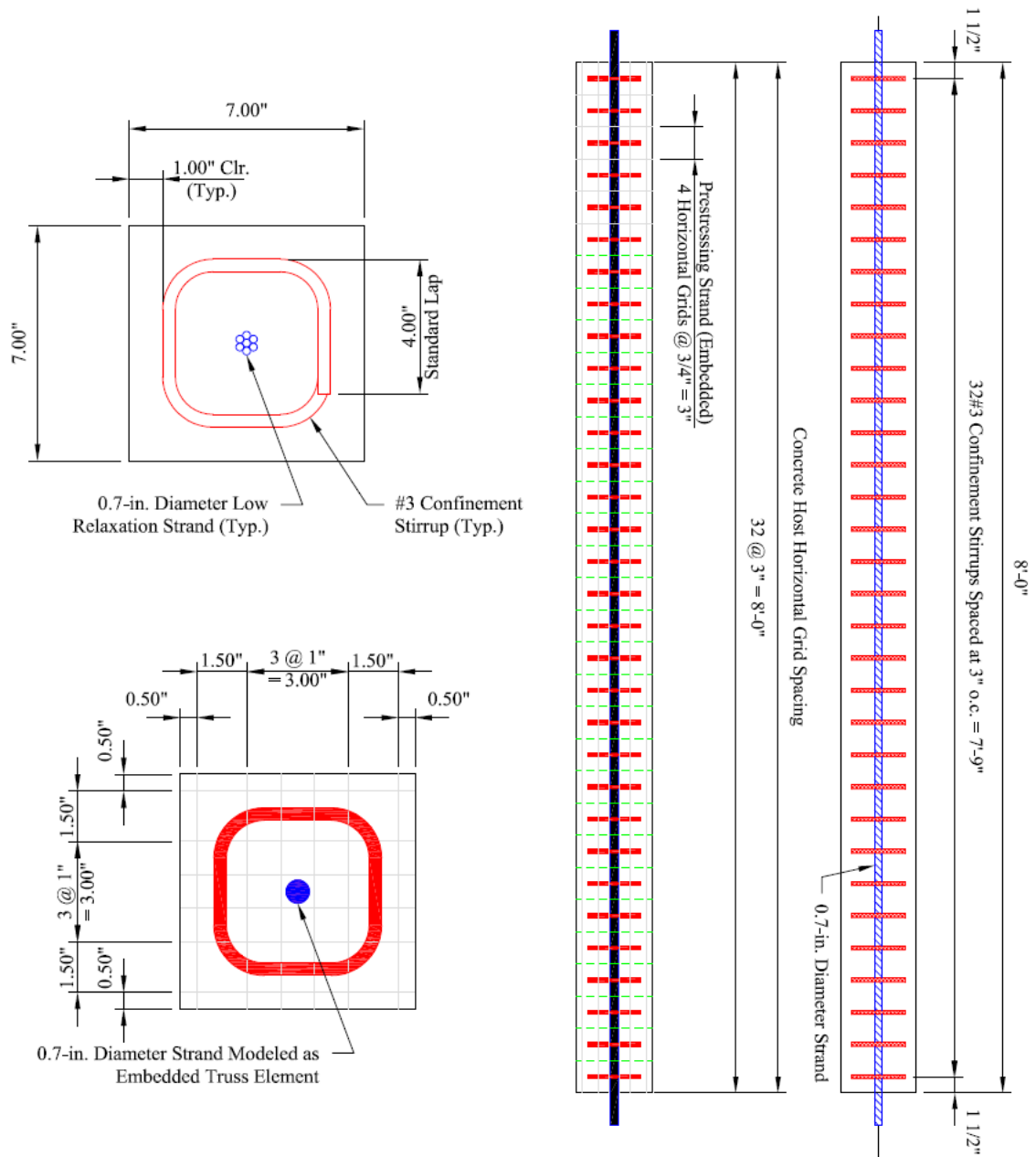


Figure 4-2: Details of Class I [1-8L-3] finite element models.

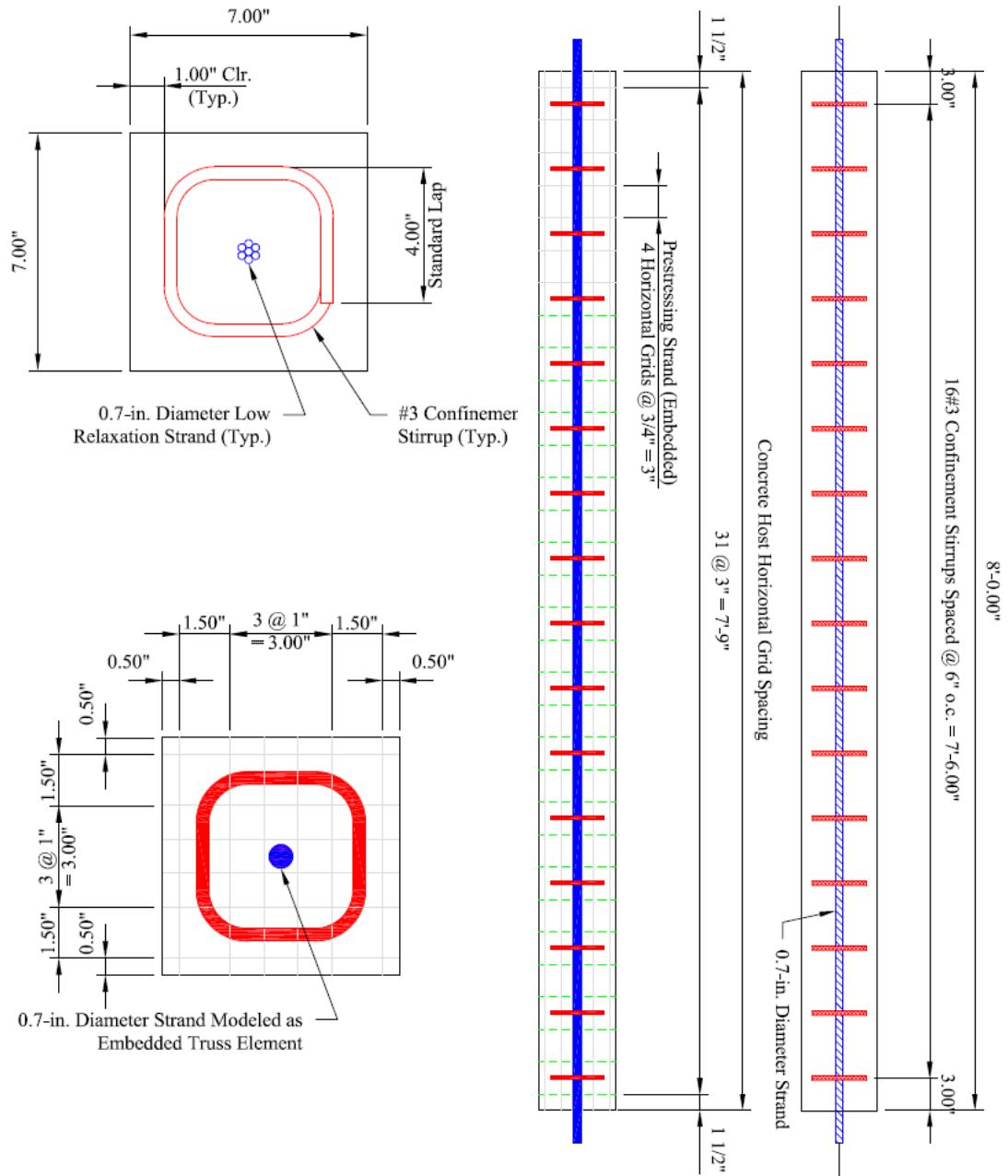


Figure 4-3: Details of Class I [1-8L-6] finite element models.

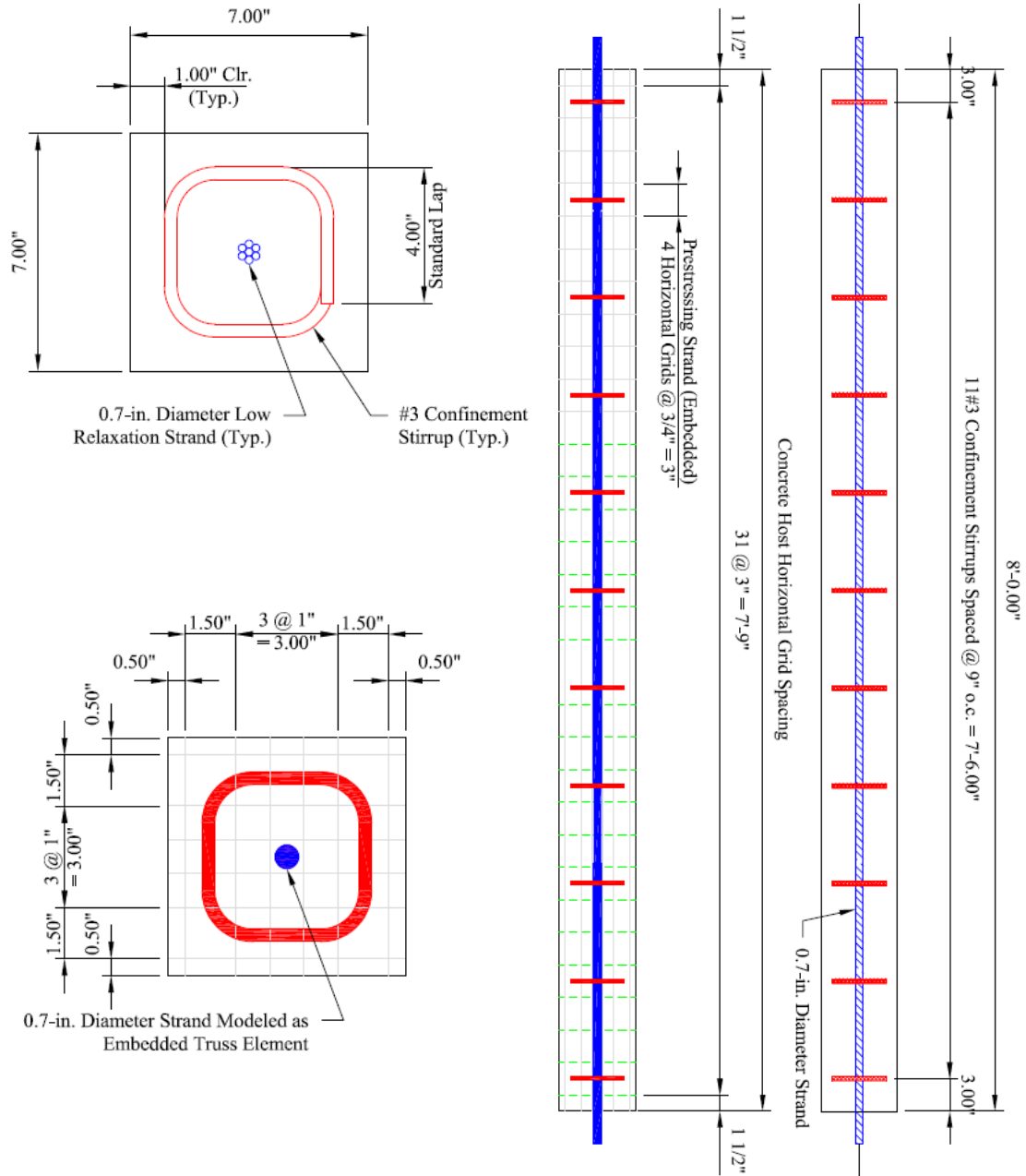


Figure 4-4: Details of Class I [1-8L-9] finite element models.

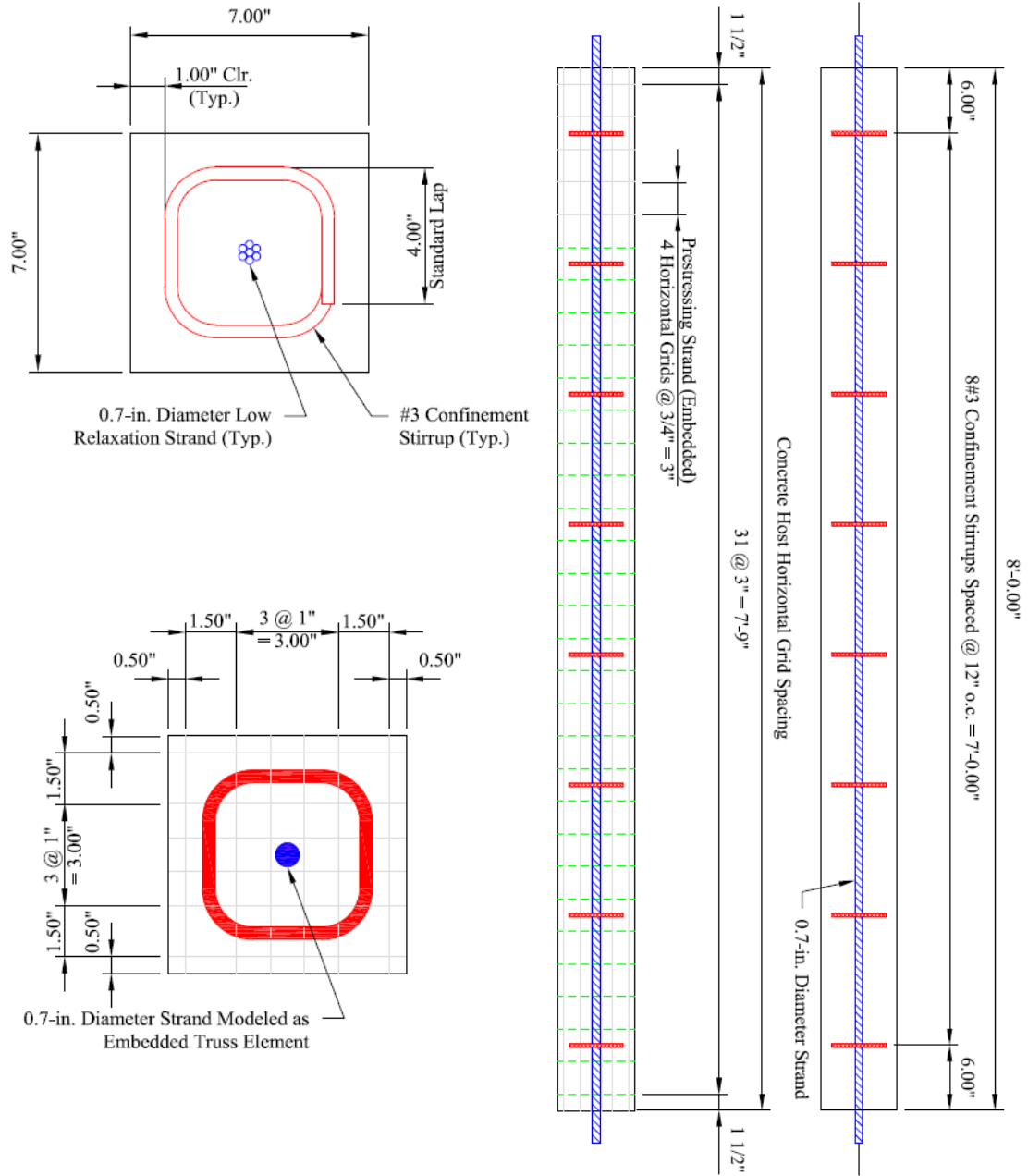
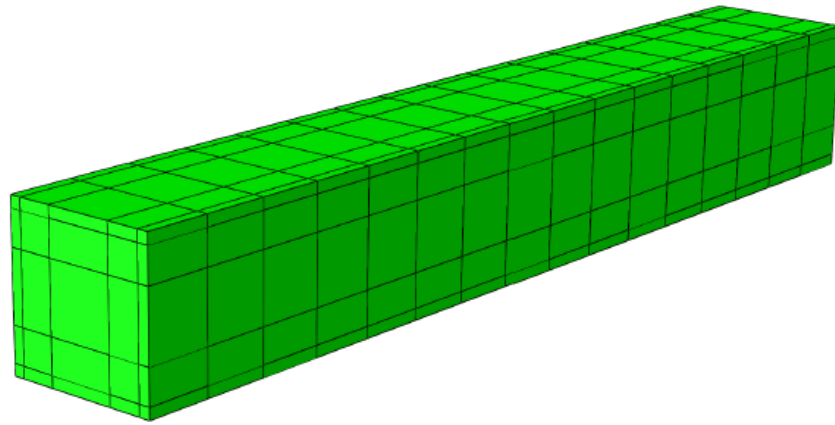
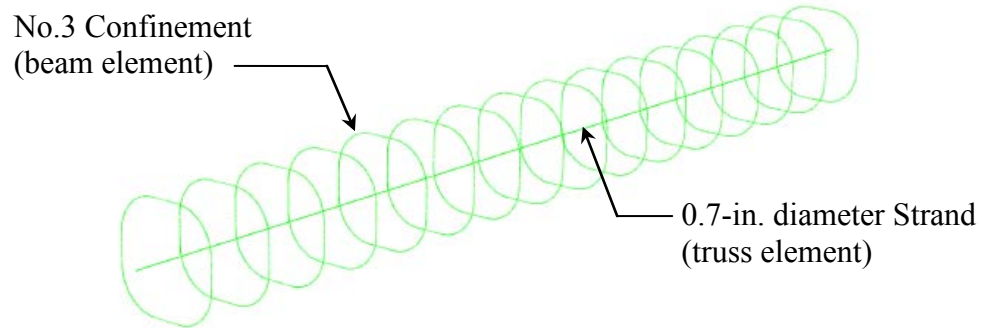


Figure 4-5: Details of Class I [1-8L-12] finite element models.

Figure 4-6 and Figure 4-7 show typical finite element models for Class I specimens based on embedment and extruded techniques, respectively. Based on the previous discussions, the extruded models are more densely meshed compared with the embedded models in order to facilitate numerical convergence in combination with analytical accuracy.

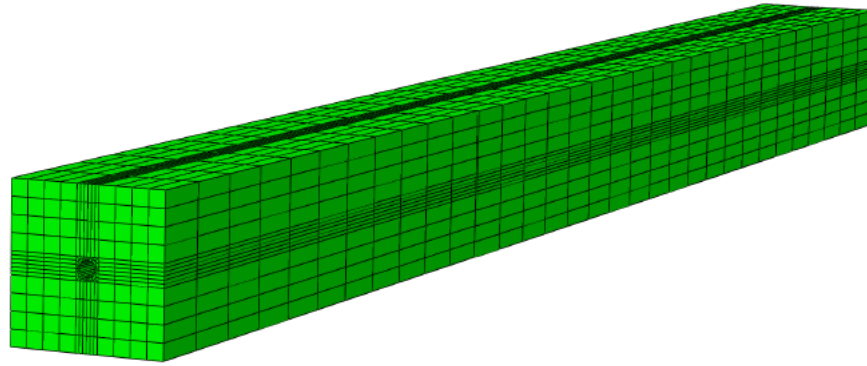


(a)

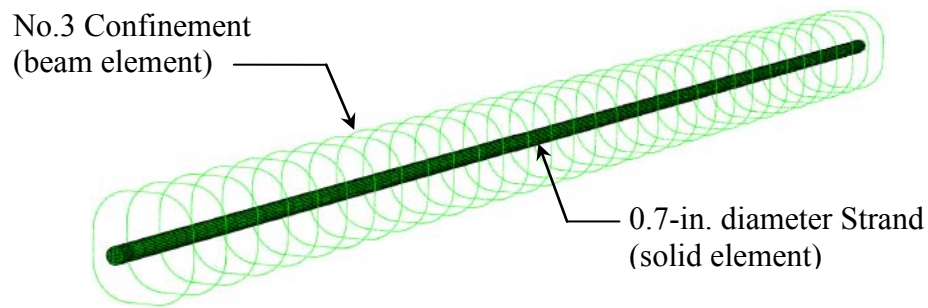


(b)

Figure 4-6: Typical finite element model with embedded pretensioned strands and ties: (a) Concrete beam modeled as continuum elements, and (b) strands and ties modeled as truss and beam elements, respectively.



(a)



(b)

Figure 4-7: Typical finite element model with extruded pretensioned strands and embedded ties: (a) Concrete beam modeled as continuum elements, and (b) strands and ties modeled as solid and beam elements, respectively.

When embedded, strands are modeled as truss (tension-compression only) elements which slaved with the translational degrees of freedom (only) of the solid host (concrete). As discussed in the previous chapter, the pretensioning mechanism (including transfer length) for the embedded model is controlled by input parameters. Therefore, the pretensioning load path is determined, calibrated and applied to the model based on the available experimental data. Figure 4-8 (a), (b), (c) and (d) shows the simulated transfer length based on the experimental data for the finite element models with one (1) embedded strand and No.3 confinement reinforcement spaced at 3 in., 6 in., 9 in. and 12 in., respectively.

In addition, Figure 4-8 shows the linear transfer length based on AASHTO LRFD as assumed in current state of practice in the U.S., estimated by Equation as follows:

$$L_t \approx 60 d_p = 42 \text{ in.} \quad (4.1)$$

where,

$$d_p = 0.7 \text{ in.} \quad (4.2)$$

As it can be observed, the linear approximation of stress path by Equation (4.1) can result in significant underestimation of the tensile stresses in the strands along the transfer length.

Besides, as indicated by Figure 4-8 (d), an acceptable correlation could not be established between the experimental data obtained from the beams (1-8L-12) with confinement spacing of 12 in. and the rest of the test specimens (1-8L-3, 1-8L-6 and 1-8L-9). Therefore, the test data obtained from the corresponding specimens (1-8L-12) will be ignored for the purposes of this research.

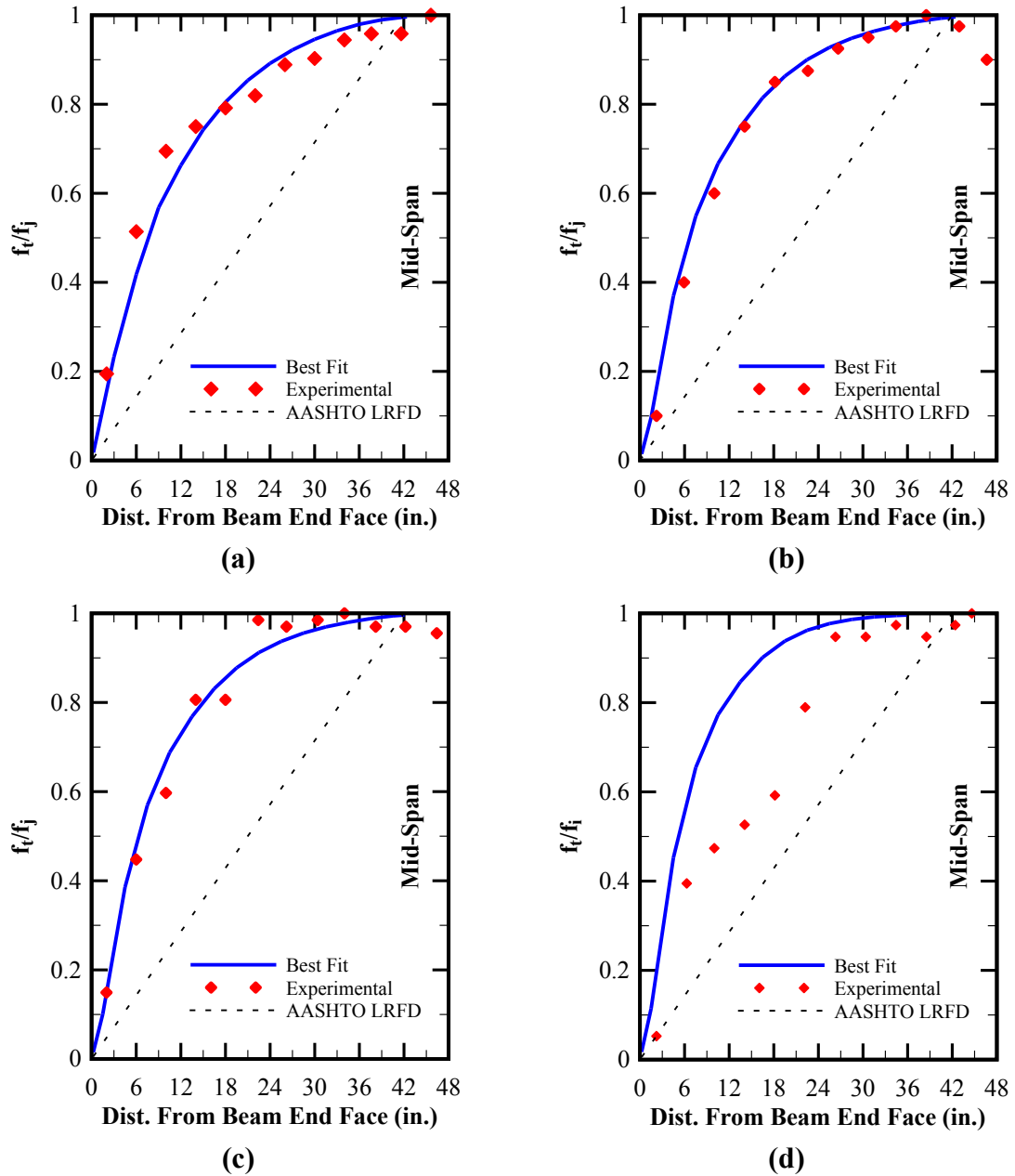


Figure 4-8: Transfer length simulation for the finite element models with embedded strands: (a) 1-L8-3, (b) 1-8L-6, (c) 1-8L-9, and (d) 1-8L-12.

When extruded, strands are modeled as solid elements which are constrained with the host (concrete) through friction-based contact formulation which allows for slippage.

The extruded modeled are further subdivided to the following two groups:

- Group 1 (*Slip_Max*): Minimum coefficient of contact friction $\mu_f = 0.7$ at the interface between the strand and concrete host, resulting in maximum slippage of strand upon release of pretensioning
- Group 2 (*Slip_Min*): Minimum coefficient of contact friction $\mu_f = 1.4$ at the interface between the strand and concrete host, resulting in minimum slippage of strand upon release of pretensioning

No.3 close stirrup ties are modeled as embedded beam elements in all models. Since the embedment technique constrains the translational degrees of freedom of the ties with the host element (concrete), there is no need to model the lap details to account for development length. Instead, development length of rebar is accounted for through mathematical formulation of translational constraints.

4.3.2. Material Calibration & Sectional Properties

The material and sectional characteristics of the concrete beams are summarized as follows:

$$\text{Cross sectional dimensions} \dots\dots\dots A_c = 7 \text{ in.} \times 7 \text{ in.} = 49 \text{ in.}^2 \quad (4.3)$$

$$\text{Span Length} \dots\dots\dots L_{beam} = 8 \text{ ft} \quad (4.4)$$

$$\text{Compressive strength @ 28}^{\text{th}} \text{ day} \dots\dots f'_c = 8,000 \text{ psi} \quad (4.5)$$

$$\text{Compressive strength @ Release} \dots\dots f'_{ci} = 3,000 \text{ psi} \quad (4.6)$$

$$\text{Modulus of Elasticity @ Release} \dots\dots E_{ci} = 33 w_c^{1.5} \sqrt{f'_c} = 5,422,453 \text{ psi} \quad (4.7)$$

$$\text{Weight Density} \dots\dots\dots w_c = 150 \text{ lbs/ft}^3 \quad (4.8)$$

$$\text{Poisson's Ratio} \dots\dots\dots \nu_c = 0.20 \quad (4.9)$$

The following includes the summary of the assumptions for the prestressing strands utilized for the analytical purposes of this research:

$$\text{Nominal diameter of strands} \dots\dots\dots d_p = 0.70 \text{ in.} \quad (4.10)$$

$$\text{Nominal cross sectional area of strands} \dots A_p = 0.294 \text{ in.}^2 \quad (4.11)$$

$$\text{Ultimate tensile strength of strands} \dots\dots\dots f_{pu} = 270,000 \text{ psi} \quad (4.12)$$

$$\text{Yield strength of strands} \dots\dots\dots f_{py} \approx 80\% f_{pu} = 216,000 \text{ psi} \quad (4.13)$$

$$\text{Max. Jacking Stress} \dots\dots\dots f_{pj} = 75\% f_{pu} = 202,500 \text{ psi} \quad (4.14)$$

$$\text{Modulus of Elasticity of strands} \dots\dots\dots E_p = 28,500,000 \text{ psi} \quad (4.15)$$

$$\text{Weight Density} \dots\dots\dots w_p = 590 \text{ lbs/ft}^3 \quad (4.16)$$

$$\text{Poisson's Ratio} \dots\dots\dots \nu_p = 0.20 \quad (4.17)$$

As discussed in Section 4.3.3, it is anticipated that the concrete beams as well as the strand and tie reinforcement will stay within the elastic stage. Therefore, the material constitutive parameters are limited to linear-elastic behavior of concrete and steel as described above.

4.3.3. Comparative Analysis of Results Based on Closed Form Solutions

The closed form solution for the concentrically pretensioned concrete beams with the sectional properties similar to the specimens (see Table 4-2 for the basic properties) is based on the elastic response of the specimens to the induced pressure resulted by pretensioning. In addition, the closed form solution accounts for the loss of pretensioning due to elastic shortening of the member immediately after the release of strands. Appendix J includes the details of the closed form solution as discussed above, summarized below:

$$f_c = -1162 \text{ psi} \quad \dots\dots\dots \text{Compressive stress in concrete after initial loss} \quad (4.18)$$

due to elastic shortening

$$\varepsilon_c = -3.5 \times 10^{-4} \quad \dots\dots\dots \text{Compressive strain corresponding to } f_c \quad (4.19)$$

$$\frac{f_c}{f'_{ci}} = 0.387 \quad \dots\dots\dots \text{Ratio of compressive stress } (f_c) \text{ due to} \quad (4.20)$$

pretensioning to the compressive strength of
concrete at the time of release (f'_{ci})

It is anticipated that response of concrete to compressive stresses stays within elastic stage up to threshold of 40% f'_c (Collins & Mitchell, 1997). Additionally, the imposed compressive stress is below the threshold of $0.6 f'_{ci}$ as required by AASHTO LRFD (AASHTO LRFD, 2010). Thus, Equation (4.20) indicates that the concrete specimens respond linear-elastically in response to the compressive stresses induced by the release of the pretensioned strands.

In addition, the compressive stress induced in the beams includes the effect of elastic shortening losses immediately after the release of pretensioning. The effect of elastic shortening included in Appendix J (closed form solution) is based on the approximation by AASHTO LRFD (AASHTO LRFD, 2010). Instead, the finite element models will directly account for the losses due to elastic shortening through numerical solutions.

Table 4-3 includes the summary of concrete stresses obtained from the finite element models with strand simulated using the embedment technique. As it can be observed the analytical results obtained by all three classes of the models (1-8L-3, 1-8L-6 and 1-8L-9) are in close conformance with the theoretical value based on the closed form solution presented in Appendix J. Similar to the theoretical solutions, the volume of concrete is

not replaced with the embedded strand. Therefore, close conformance is expected between the finite element results and the theoretical solution when strands are embedded inside the concrete continuum.

Table 4-4 and Table 4-5 include the concrete stresses obtained from the finite element models including strands simulated using the extrusion technique and with contact friction coefficients of 0.7 and 1.4, respectively. While still within acceptable ranges, the finite element results clearly show more pronounced differences with the theoretical solution. The following factors may explain the above observation:

- Due to extrusion, the cross sectional area engaged against the imposed pressure upon release of the strands is different in comparison with the embedded models, and
- The straining of the concrete host is facilitated through the contact friction at the interface between the strand and concrete. While this allows for slippage of strand inside the host, the embedded strands impose strain compatibility on the host through nodal constraints. Therefore, the higher the coefficient of friction (μ), the higher the degrees of load transfer.

Table 4-3: Comparative analysis of the analytical results obtained from the finite element models with embedded strands against the closed form solutions. Negative stresses indicate compression.

Model I.D.	$f_c^{Finite-Element}$	$f_c^{Closed Form}$	$f_c^{Finite Element} / f_c^{Closed Form}$
1-8L-3	-1157	-1162	99.6%
1-8L-6	-1152	-1162	99.1%
1-8L-9	-1156	-1162	99.5%

Table 4-4: Comparative analysis of the analytical results obtained from the finite element models with extruded strands and contact friction coefficient of $\mu_f = 0.7$ against the closed form solutions. Negative stresses indicate compression.

Model I.D.	$f_c^{Finite-Element}$	$f_c^{Closed Form}$	$f_c^{Finite Element} / f_c^{Closed Form}$
1-8L-3	-1124	-1162	96.7%
1-8L-6	-1103	-1162	94.9%
1-8L-9	-1120	-1162	96.4%

Table 4-5: Comparative analysis of the analytical results obtained from the finite element models with extruded strands and contact friction coefficient of $\mu_f = 1.4$ against the closed form solutions. Negative stresses indicate compression.

Model I.D.	$f_c^{Finite-Element}$	$f_c^{Closed Form}$	$f_c^{Finite Element} / f_c^{Closed Form}$
1-8L-3	-1104	-1162	95.0%
1-8L-6	-1073	-1162	92.4%
1-8L-9	-1087	-1162	93.6%

4.3.4. Comparative Analysis of Results Based on Experimental Data

In order to further verify the modeling approaches presented in the previous chapter, the family of numerical solutions of Section 4.3.3 will be compared with the experimental data based on a series of parametric tests by Akhnoukh (Akhnoukh, 2008). As previously discussed, Akhnoukh's research was focused on the investigation of transfer length of 0.7-in. diameter strands and the effect of confinement reinforcement on the transfer length. For the comparative purposes of this study, the DEMEC readings are normalized with respect to their corresponding maximum values. This allows the comparisons to focus on the trend of stress variation over the transfer length.

Figure 4-9, Figure 4-10 and Figure 4-11 show the comparison of the analytical results obtained by the embedded and extruded finite element models 1-8L-3, 1-8L-6 and 1-8L-9, respectively, versus the experimental data. As previously discussed, the above three classes of models correspond to 7-in. x 7-in. x 96-in. prisms concentrically pretensioned with one 0.7-in. diameter low-relaxation seven-wire strand and confined with No.3 closed stirrups spaced at 3 in., 6 in. and 9 in. on center, respectively.

The normalized axial strains correspond to the response of the concrete prism immediately after the release of pretensioning, corresponding to the transfer length established between the released strand and the concrete host. The results indicate that the assumption of linear stress (strain) path as assumed in the current practice significantly underestimate the actual transfer length.

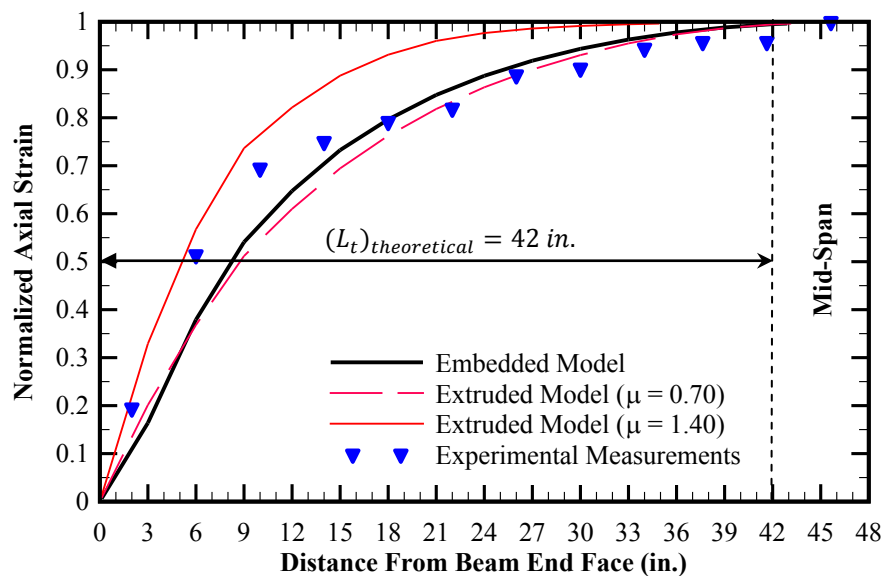


Figure 4-9: Comparison of experimental measurements for strains versus the corresponding finite element results for 7-in. prisms confined with No.3 close stirrups spaced at 3 in. on center (Model 1-8L-3).

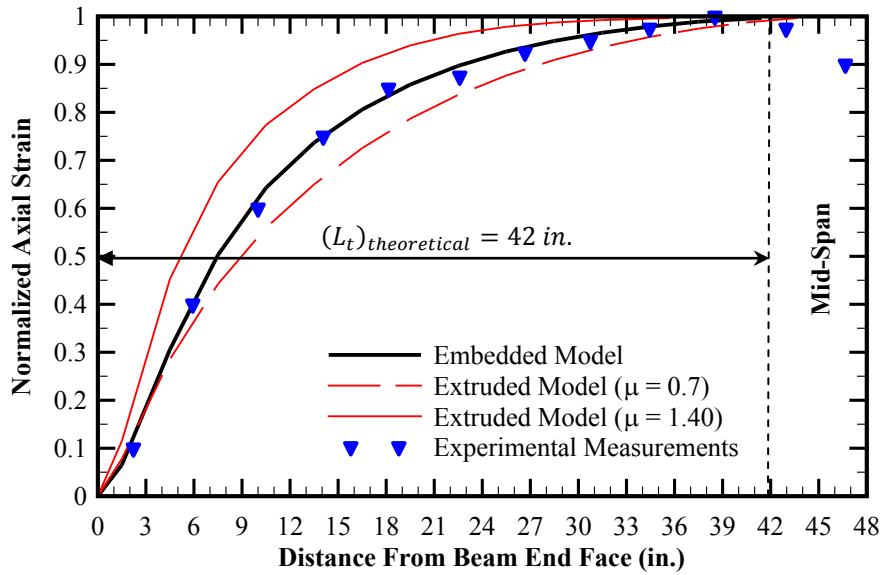


Figure 4-10: Comparison of experimental measurements for strains versus the corresponding finite element results for 7-in. prisms confined with No.3 close stirrups spaced at 6 in. on center (Model 1-8L-6).

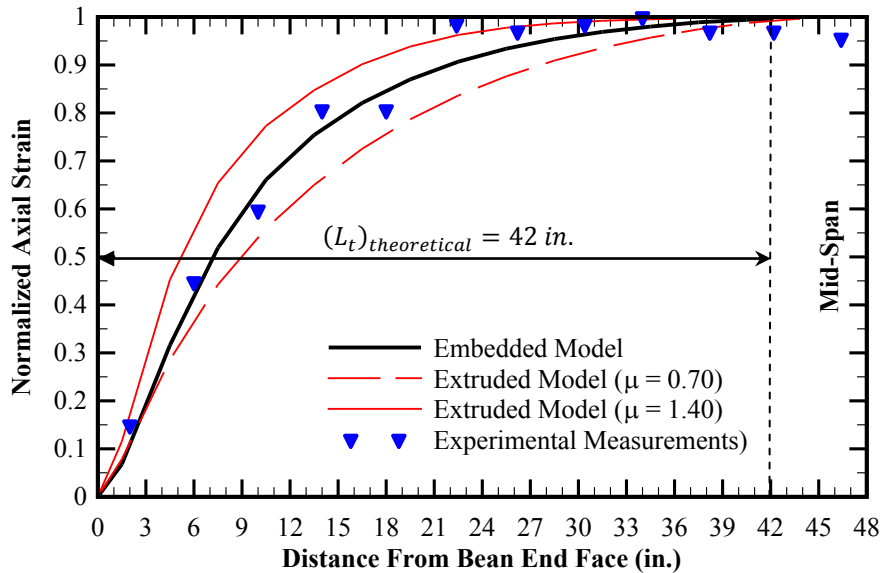


Figure 4-11: Comparison of experimental measurements for strains versus the corresponding finite element results for 7-in. prisms confined with No.3 close stirrups spaced at 9 in. on center (Model 1-8L-9).

Additionally, the embedded models are calibrated such that the initial pretensioning conditions (model input) result in stress (strain) variations that provide best-fit to the experimental data as discussed in Section 4.3.1.

Parametric studies also show that: i) direct slippage of strand-over-concrete using the friction simulation provides an acceptable approximation of the pretensioning mechanism, including the transfer length phenomenon, ii) friction coefficients of 0.70 and 1.4 , in combination with Poisson’s effect and other contact parameters, appear to adequately provide lower and upper bound interface interactions between the strands and concrete host immediately after the release of pretensioning, and iii) the variation of axial stresses in the strands along the transfer length zone is found to be of nonlinear (parabolic) nature rather than the linear approximation recommended by the codes and guidelines used in current practice.

As shown in Figure 4-12, the analytical results indicate that the finite element models are sensitive to the effect of the confinement on the transfer length although such effects are not significant. This is also consistent with the experimental findings by Akhnoukh (Akhnoukh, 2008).

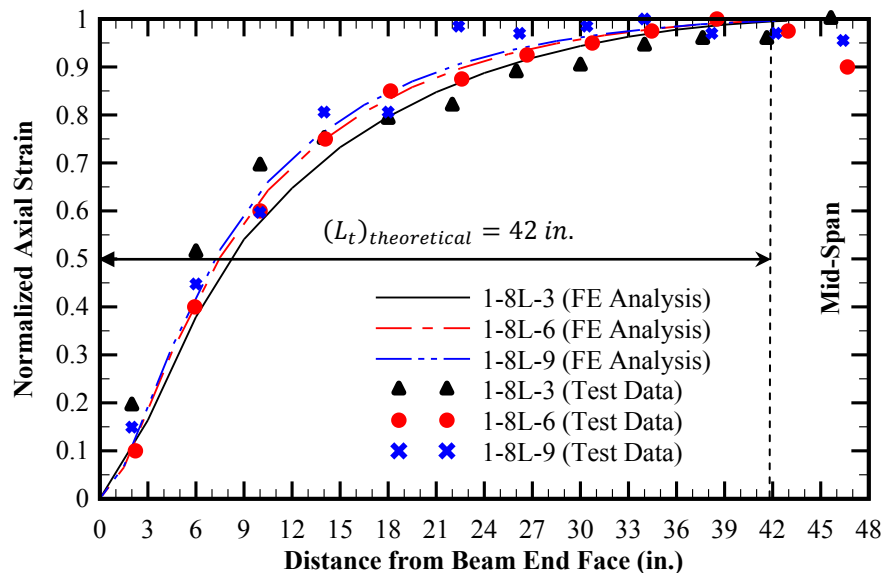


Figure 4-12: Effect of confinement on transfer length (results of finite element models with embedded strands versus test data)

4.4. Rectangular Beams with Nine Pretensioned 0.7-inch Diameter Strands

In the previous chapter, two approaches were presented for finite element modeling of pretensioned concrete member based on embedment and extrusion techniques. Results obtained from the analytical models were compared against available closed form solutions (e.g., beam theory) for verification. Further, the validity of the proposed approaches was evaluated against experimental results for concentrically pretensioned concrete prisms using one concentric 0.7-in. diameter low-relaxation strand as discussed Section 4.3.

In this section, the extrusion technique is utilized to expand the pretensioned concrete prisms analyzed in Section 4.3 to host nine 0.7-in. diameter low-relaxation strands instead of one. The application of the pretensioning is concentric similar to the mono-strand test specimens discussed in Section 4.3. The main objective of the parametric studies of this section is to investigate the effect of the spacing of the strands on the response of the concrete members. In addition, the effect of the confinement reinforcement (amount and spacing) on the localized and the global behavior of the member are investigated similar to Section 4.3.

4.4.1. Finite Element Models

The finite element models used for the analytical purposes of this section are based on 11-in. x 11-in. concrete prisms. The models are 20 ft long (each) hosting nine extrusions to host 0.70-in. diameter low-relaxation strands modeled as solid elements. The strands are symmetrically located around the centroid of the members in both horizontal and vertical grid spacing.

Two main classes of finite elements are constructed to include concentrically positioned nine 0.7-in. diameter low-relaxation strands with the following variations of the strands spacing:

- Class I - Prestressing strands are spaced at four times the strand diameter in accordance with ACI requirements (ACI, 2008):

$$s_p = 4 d_p = 2.80 \text{ in.} \quad (4.21)$$

- Class II - Prestressing strands are spaced at 2.00 in. on center in conformance with the current standards of fabrication for pretensioned members with 0.6-in. diameter strands.

Similar to the parametric studies presented in Section 4.3, each class of the finite element models mentioned above are subdivided for two levels of contact friction at the interface between the strands and the concrete host. The boundary friction coefficients selected for the analytical purposes of this section are based on the conclusions of Section 4.3 as summarized below:

- Upper bound slippage at lowest contact friction coefficient of $\mu_f = 0.70$
- Lower bound slippage at highest contact friction coefficient of $\mu_f = 1.40$

In addition, the finite element models are investigated for the effect of the confinement reinforcement on the response of the specimens to the release of pretensioning. Thus, the response of the models to the same magnitude of pretensioning is evaluated when the specimens are confined with No.3 closed stirrups (modeled as embedded beam elements) spaced at 3 in., 6 in., 9 in. and 12 in. on center as well as when no confinement is present. Table 4-6 and Table 4-7 include the basic properties of Class I finite element models, utilizing the extrusion technique and contact formulation to

simulate the interface between the strands and concrete host utilizing friction coefficients of 0.70 (upper slippage boundary) and 1.40 (lower slippage boundary).

Figure 4-13 through Figure 4-16 show the details of Class I finite elements with No.3 confinement closed stirrups spaced at 3 in., 6 in., 9 in. and 12 in. on center, respectively. The details of the models without confinement reinforcement (S280-u070-conf0-W0-L-P and S280-u140-conf0-W0-L-P) are similar while excluding the embedded beam elements simulating the closed stirrups.

Table 4-6: Log of Class I finite element models comprised of nine extruded strands spaced at 2.80 in. on center and contact friction coefficient of $\mu_f = 0.70$.

Model I.D.	Sectional Properties	Pretensioning	Confinement
S280-U070-C0	11-in. x 11-in. x 20-ft (long)	9-0.7 in. diameter strands (concentric) spaced at 2.80 in. on center	No confinement reinforcement
S280-U070-C3	11-in. x 11-in. x 20-ft (long)	9-0.7 in. diameter strands (concentric) spaced at 2.80 in. on center	No.3 confinement rebar spaced at 3 in. on center
S280-U070-C6	11-in. x 11-in. x 20-ft (long)	9-0.7 in. diameter strands (concentric) spaced at 2.80 in. on center	No.3 confinement rebar spaced at 6 in. on center
S280-U070-C9	11-in. x 11-in. x 20-ft (long)	9-0.7 in. diameter strands (concentric) spaced at 2.80 in. on center	No.3 confinement rebar spaced at 9 in. on center
S280-U070-C12	11-in. x 11-in. x 20-ft (long)	9-0.7 in. diameter strands (concentric) spaced at 2.80 in. on center	No.3 confinement rebar spaced at 12 in. on center
Coefficient of friction for contact formulation at the interface between each strand and the concrete host $\mu_f = 0.70$.			

Table 4-7: Log of Class I finite element models comprised of nine extruded strands spaced at 2.80 in. on center and contact friction coefficient of $\mu_f = 1.40$.

Model I.D.	Sectional Properties	Pretensioning	Confinement
S280-U140-C0	11-in. x 11-in. x 20-ft (long)	9-0.7 in. diameter strands (concentric) spaced at 2.80 in. on center	No confinement reinforcement
S280-U140-C3	11-in. x 11-in. x 20-ft (long)	9-0.7 in. diameter strands (concentric) spaced at 2.80 in. on center	No.3 confinement rebar spaced at 3 in. on center
S280-U140-C6	11-in. x 11-in. x 20-ft (long)	9-0.7 in. diameter strands (concentric) spaced at 2.80 in. on center	No.3 confinement rebar spaced at 6 in. on center
S280-U140-C9	11-in. x 11-in. x 20-ft (long)	9-0.7 in. diameter strands (concentric) spaced at 2.80 in. on center	No.3 confinement rebar spaced at 9 in. on center
S280-U140-C12	11-in. x 11-in. x 20-ft (long)	9-0.7 in. diameter strands (concentric) spaced at 2.80 in. on center	No.3 confinement rebar spaced at 12 in. on center
Coefficient of friction for contact formulation at the interface between each strand and the concrete host $\mu_f = 1.40$.			

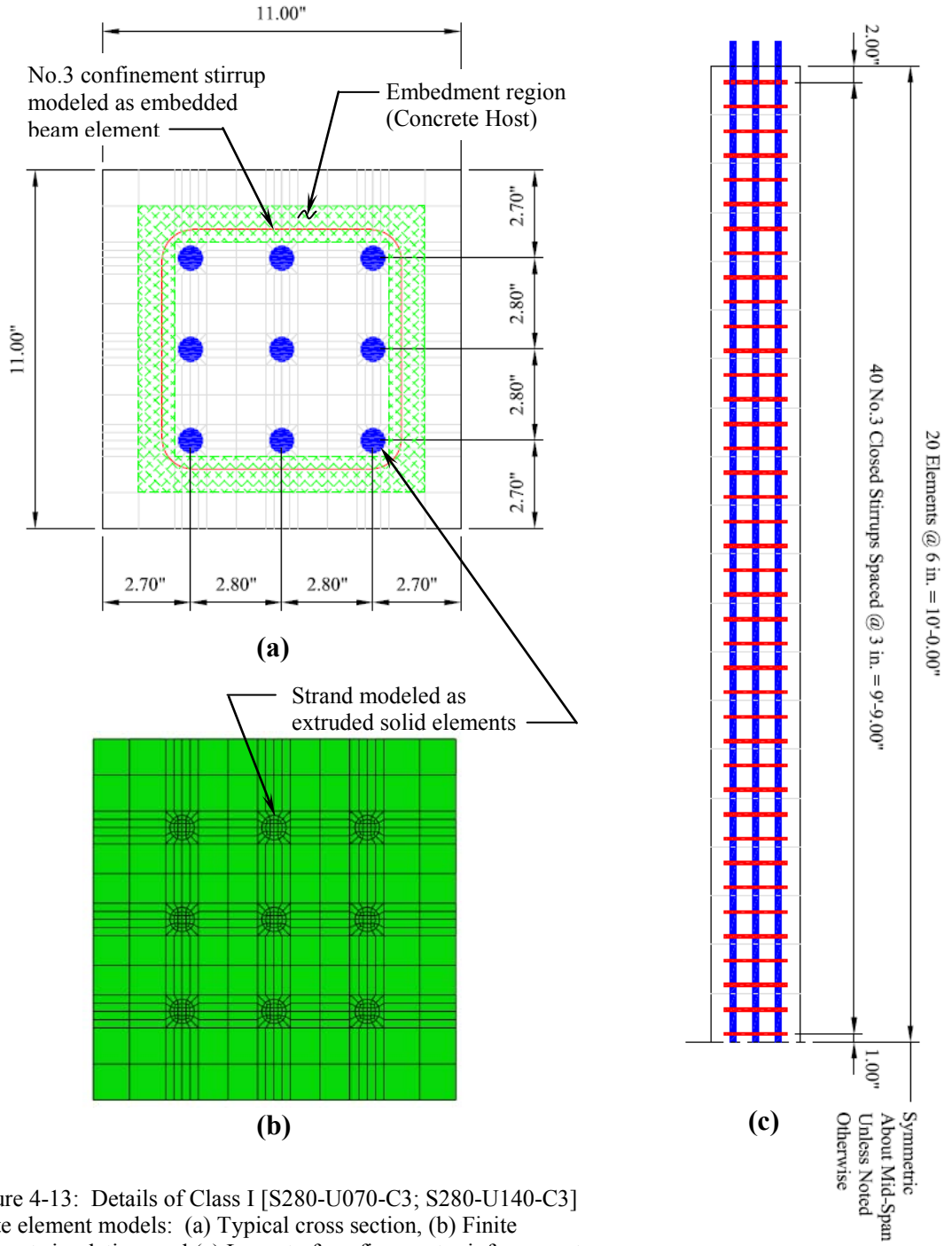


Figure 4-13: Details of Class I [S280-U070-C3; S280-U140-C3] finite element models: (a) Typical cross section, (b) Finite element simulation, and (c) Layout of confinement reinforcement (No.3 closed stirrups spaced at 3 in. on center)

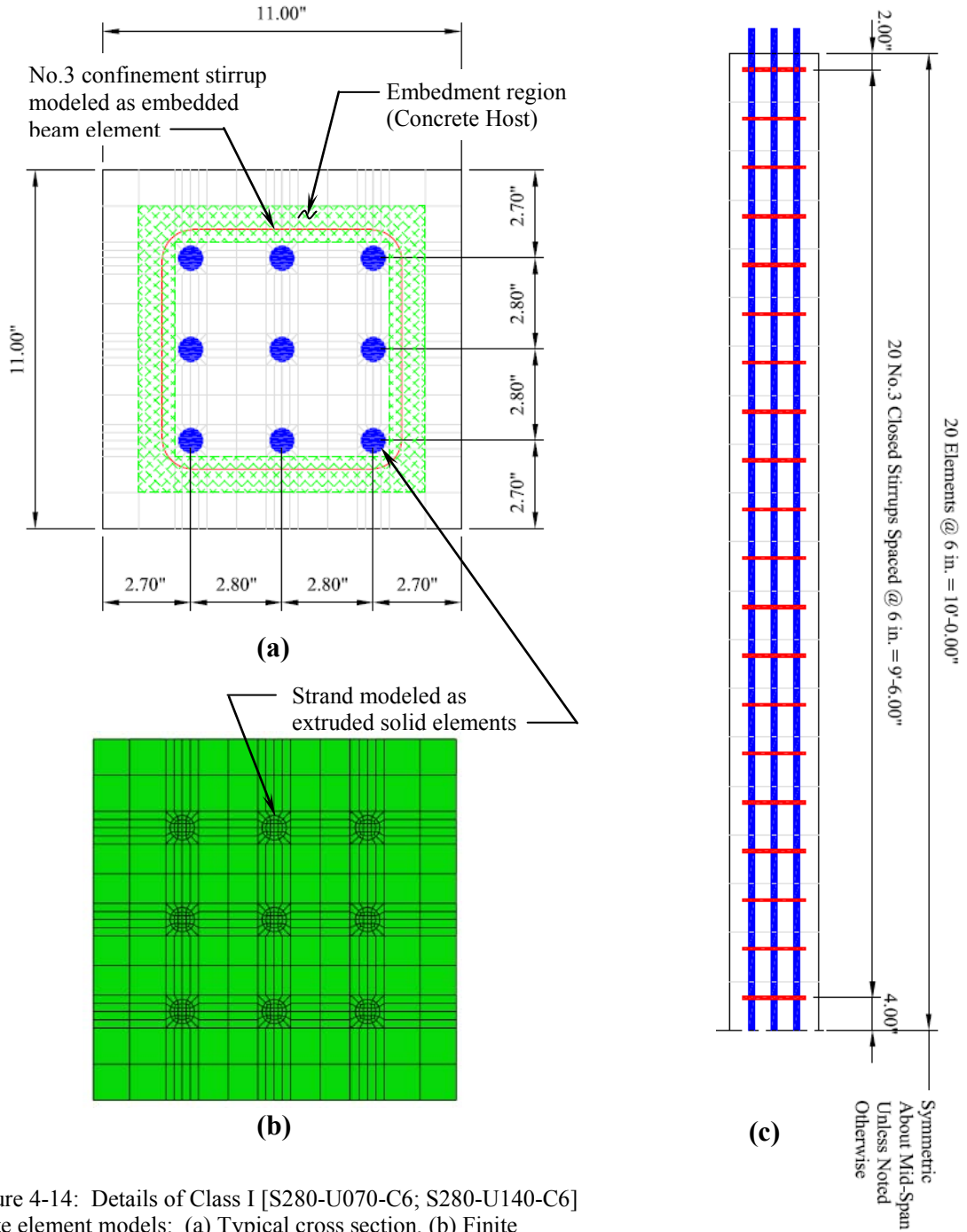


Figure 4-14: Details of Class I [S280-U070-C6; S280-U140-C6] finite element models: (a) Typical cross section, (b) Finite element simulation, and (c) Layout of confinement reinforcement (No.3 closed stirrups spaced at 6 in. on center)

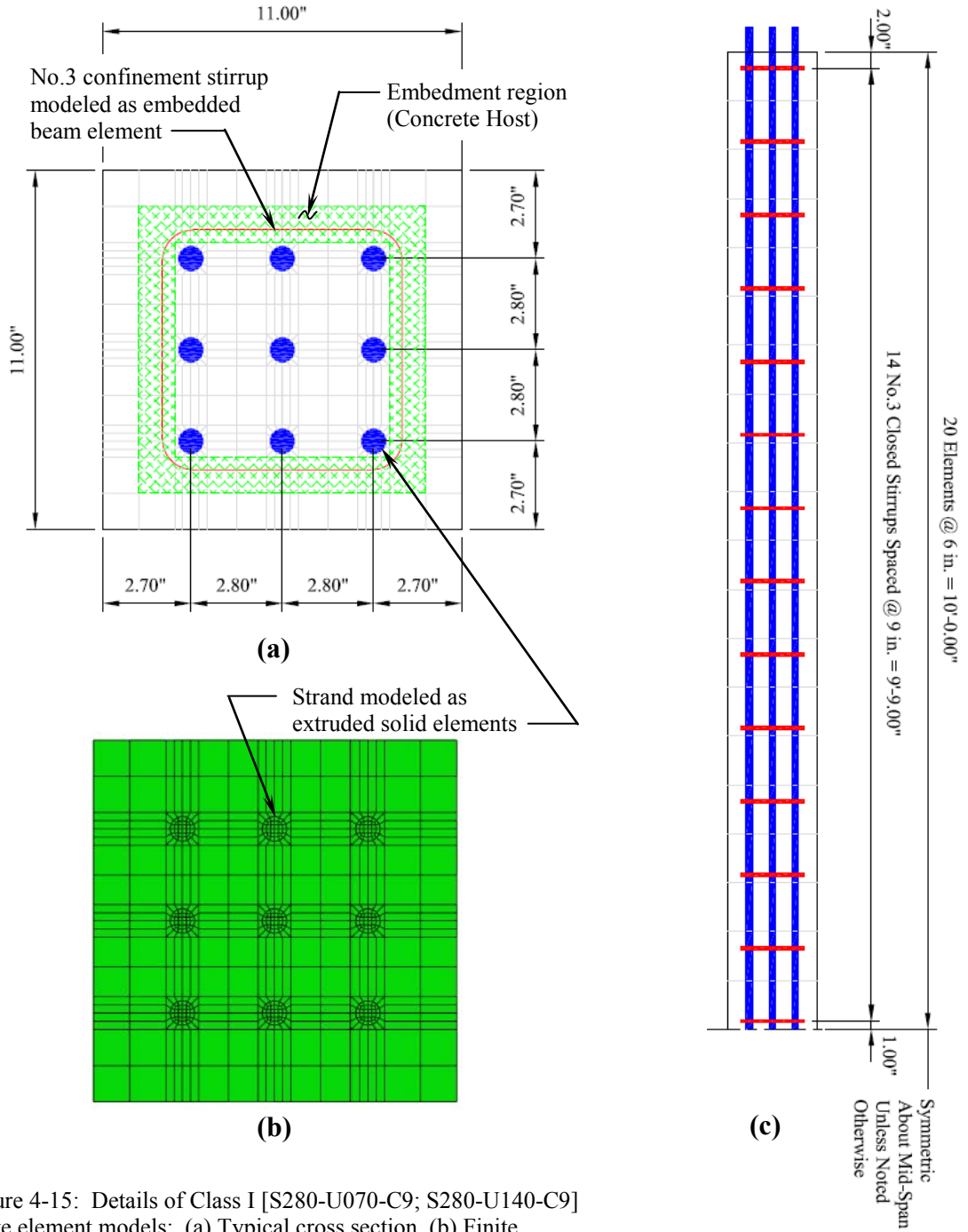


Figure 4-15: Details of Class I [S280-U070-C9; S280-U140-C9] finite element models: (a) Typical cross section, (b) Finite element simulation, and (c) Layout of confinement reinforcement (No.3 closed stirrups spaced at 9 in. on center)

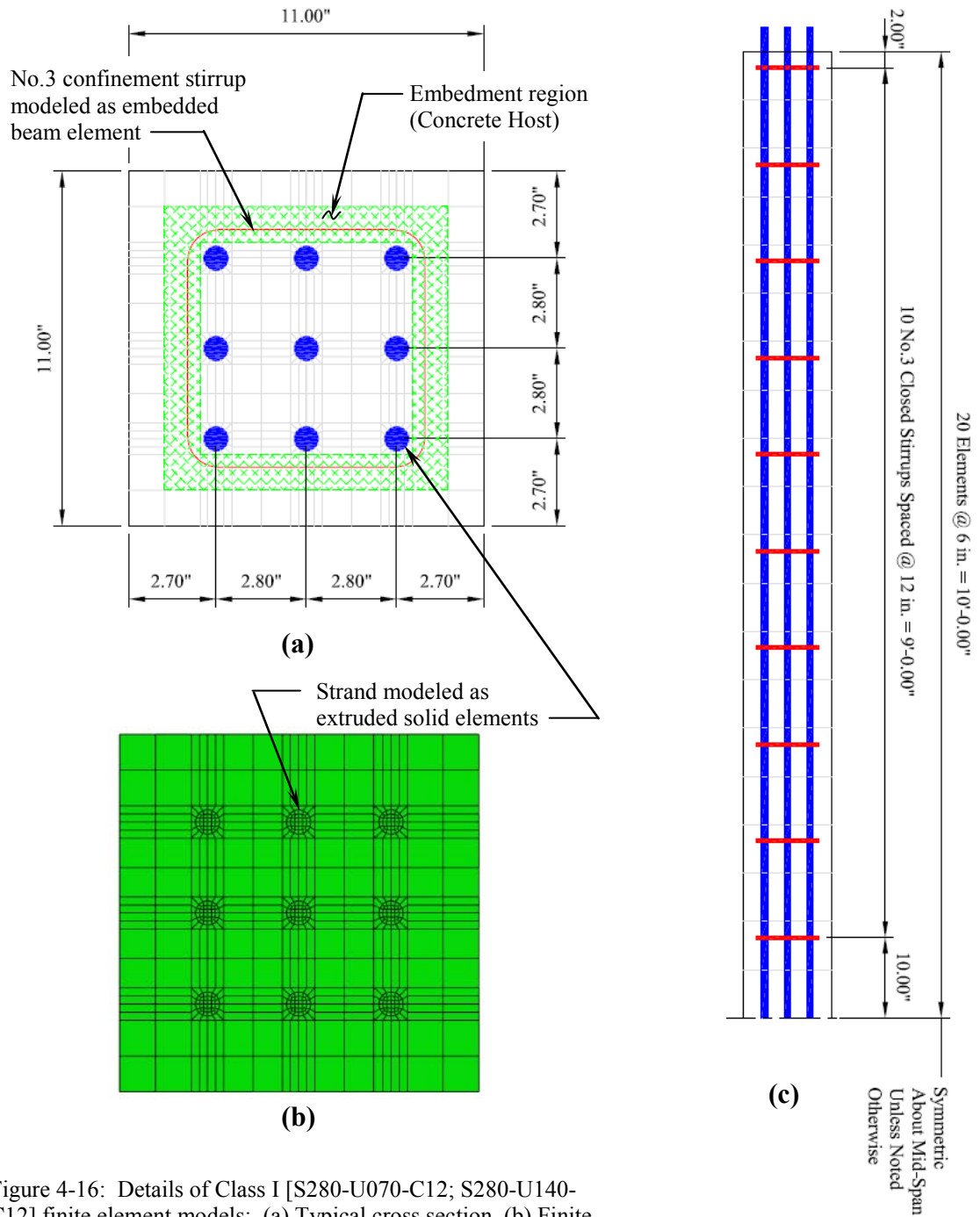


Figure 4-16: Details of Class I [S280-U070-C12; S280-U140-C12] finite element models: (a) Typical cross section, (b) Finite element simulation, and (c) Layout of confinement reinforcement (No.3 closed stirrups spaced at 12 in. on center)

Similarly, Table 4-8 and Table 4-9 include the basic properties of Class II finite element models, utilizing the extrusion technique and contact formulation to simulate the interface between the strands and concrete host utilizing friction coefficients of 0.70 (upper slippage boundary) and 1.40 (lower slippage boundary).

Table 4-8: Log of Class II finite element models comprised of nine extruded strands spaced at 2.00 in. on center and contact friction coefficient of $\mu_f = 0.70$.

Model I.D.	Sectional Properties	Pretensioning	Confinement
S200-U070-C0	11-in. x 11-in. x 20-ft (long)	9-0.7 in. diameter strands (concentric) spaced at 2.00 in. on center	No confinement reinforcement
S200-U070-C3	11-in. x 11-in. x 20-ft (long)	9-0.7 in. diameter strands (concentric) spaced at 2.00 in. on center	No.3 confinement rebar spaced at 3 in. on center
S200-U070-C6	11-in. x 11-in. x 20-ft (long)	9-0.7 in. diameter strands (concentric) spaced at 2.00 in. on center	No.3 confinement rebar spaced at 6 in. on center
S200-U070-C9	11-in. x 11-in. x 20-ft (long)	9-0.7 in. diameter strands (concentric) spaced at 2.00 in. on center	No.3 confinement rebar spaced at 9 in. on center
S200-U070-C12	11-in. x 11-in. x 20-ft (long)	9-0.7 in. diameter strands (concentric) spaced at 2.00 in. on center	No.3 confinement rebar spaced at 12 in. on center
Coefficient of friction for contact formulation at the interface between each strand and the concrete host $\mu_f = 0.70$.			

Table 4-9: Log of Class II finite element models comprised of nine extruded strands spaced at 2.00 in. on center and contact friction coefficient of $\mu_f = 1.40$.

Model I.D.	Sectional Properties	Pretensioning	Confinement
S200-U140-C0	11-in. x 11-in. x 20-ft (long)	9-0.7 in. diameter strands (concentric) spaced at 2.00 in. on center	No confinement reinforcement
S200-U140-C3	11-in. x 11-in. x 20-ft (long)	9-0.7 in. diameter strands (concentric) spaced at 2.00 in. on center	No.3 confinement rebar spaced at 3 in. on center
S200-U140-C6	11-in. x 11-in. x 20-ft (long)	9-0.7 in. diameter strands (concentric) spaced at 2.00 in. on center	No.3 confinement rebar spaced at 6 in. on center
S200-U140-C	11-in. x 11-in. x 20-ft (long)	9-0.7 in. diameter strands (concentric) spaced at 2.00 in. on center	No.3 confinement rebar spaced at 9 in. on center
S200-U140-C12	11-in. x 11-in. x 20-ft (long)	9-0.7 in. diameter strands (concentric) spaced at 2.00 in. on center	No.3 confinement rebar spaced at 12 in. on center
Coefficient of friction for contact formulation at the interface between each strand and the concrete host $\mu_f = 1.40$.			

Figure 4-17 through Figure 4-20 show the details of Class II finite elements with No.3 confinement closed stirrups spaced at 3 in., 6 in., 9 in. and 12 in. on center, respectively. The details of the models without confinement reinforcement (S200-u070-conf0-W0-L-P and S200-u140-conf0-W0-L-P) are similar while excluding the embedded beam elements simulating the closed stirrups.

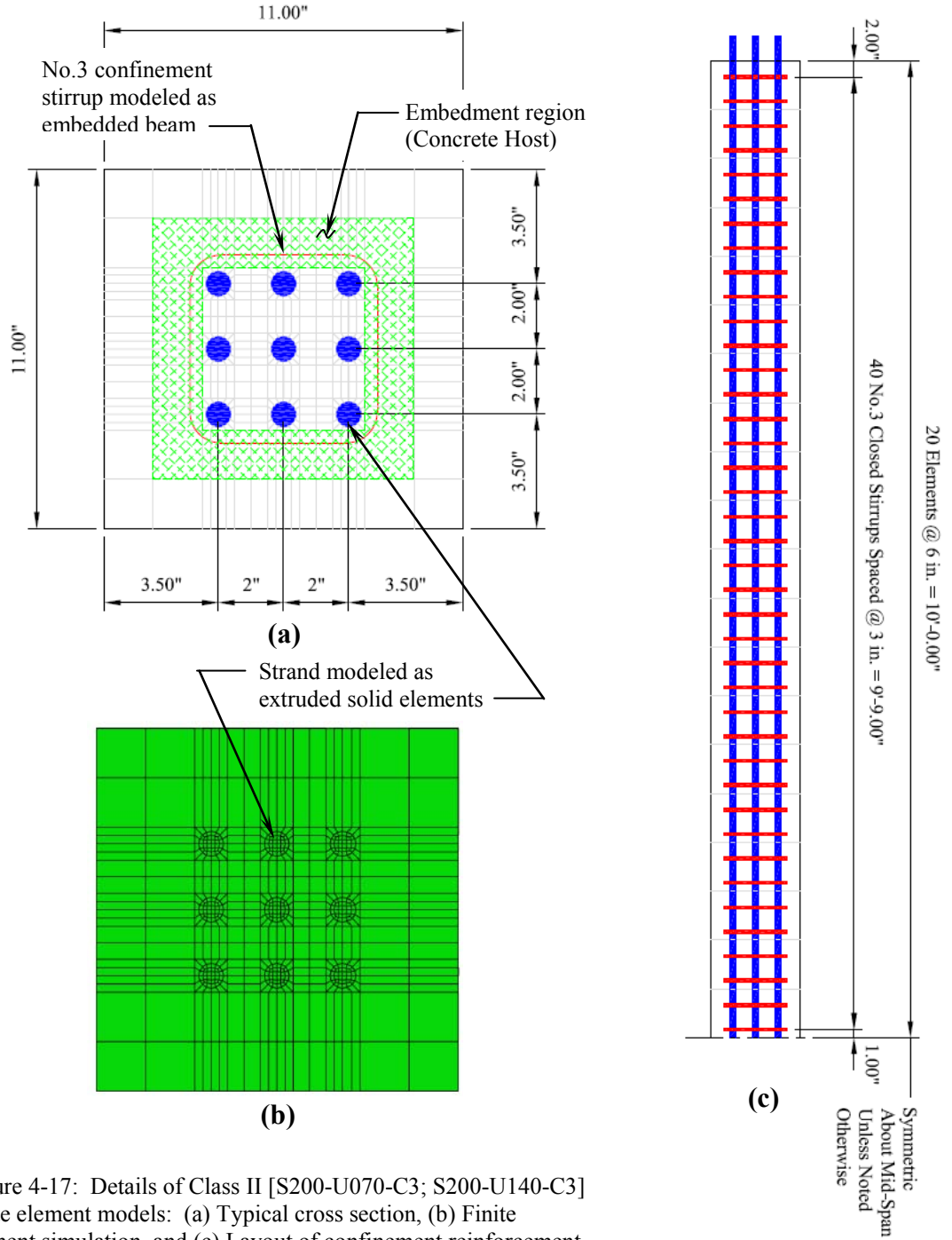


Figure 4-17: Details of Class II [S200-U070-C3; S200-U140-C3] finite element models: (a) Typical cross section, (b) Finite element simulation, and (c) Layout of confinement reinforcement (No.3 closed stirrups spaced at 3 in. on center)

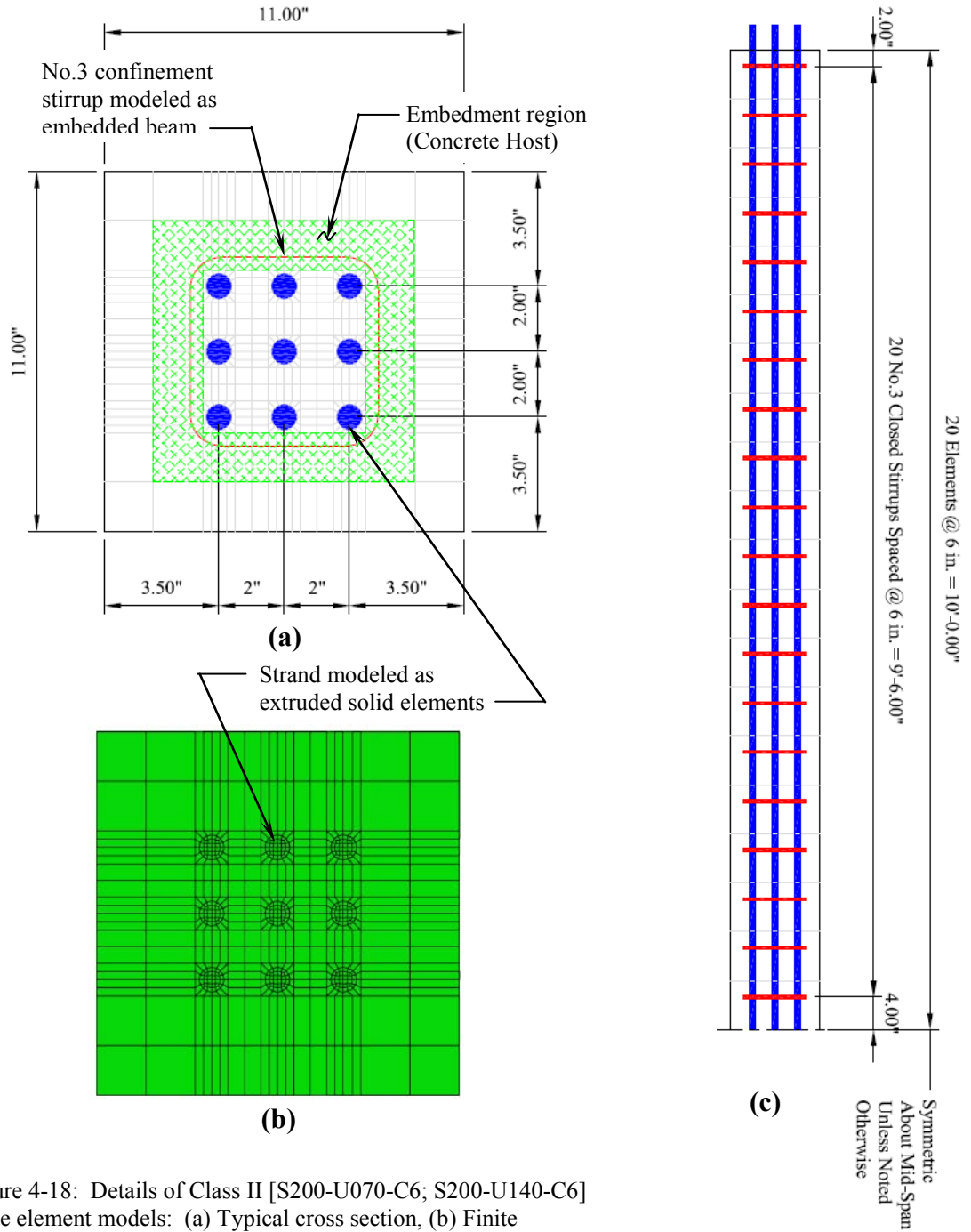


Figure 4-18: Details of Class II [S200-U070-C6; S200-U140-C6] finite element models: (a) Typical cross section, (b) Finite element simulation, and (c) Layout of confinement reinforcement (No.3 closed stirrups spaced at 6 in. on center)

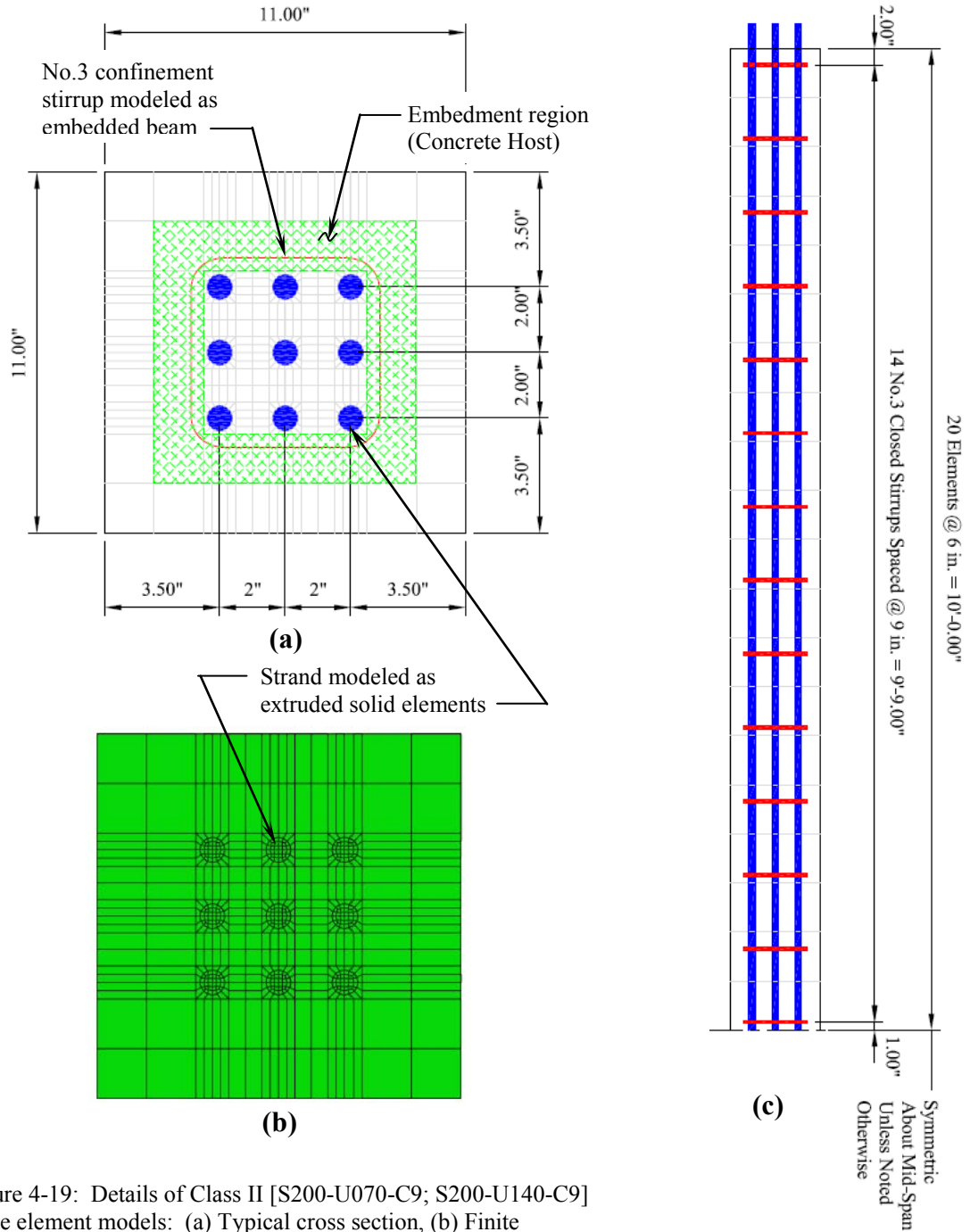


Figure 4-19: Details of Class II [S200-U070-C9; S200-U140-C9] finite element models: (a) Typical cross section, (b) Finite element simulation, and (c) Layout of confinement reinforcement (No.3 closed stirrups spaced at 9 in. on center)

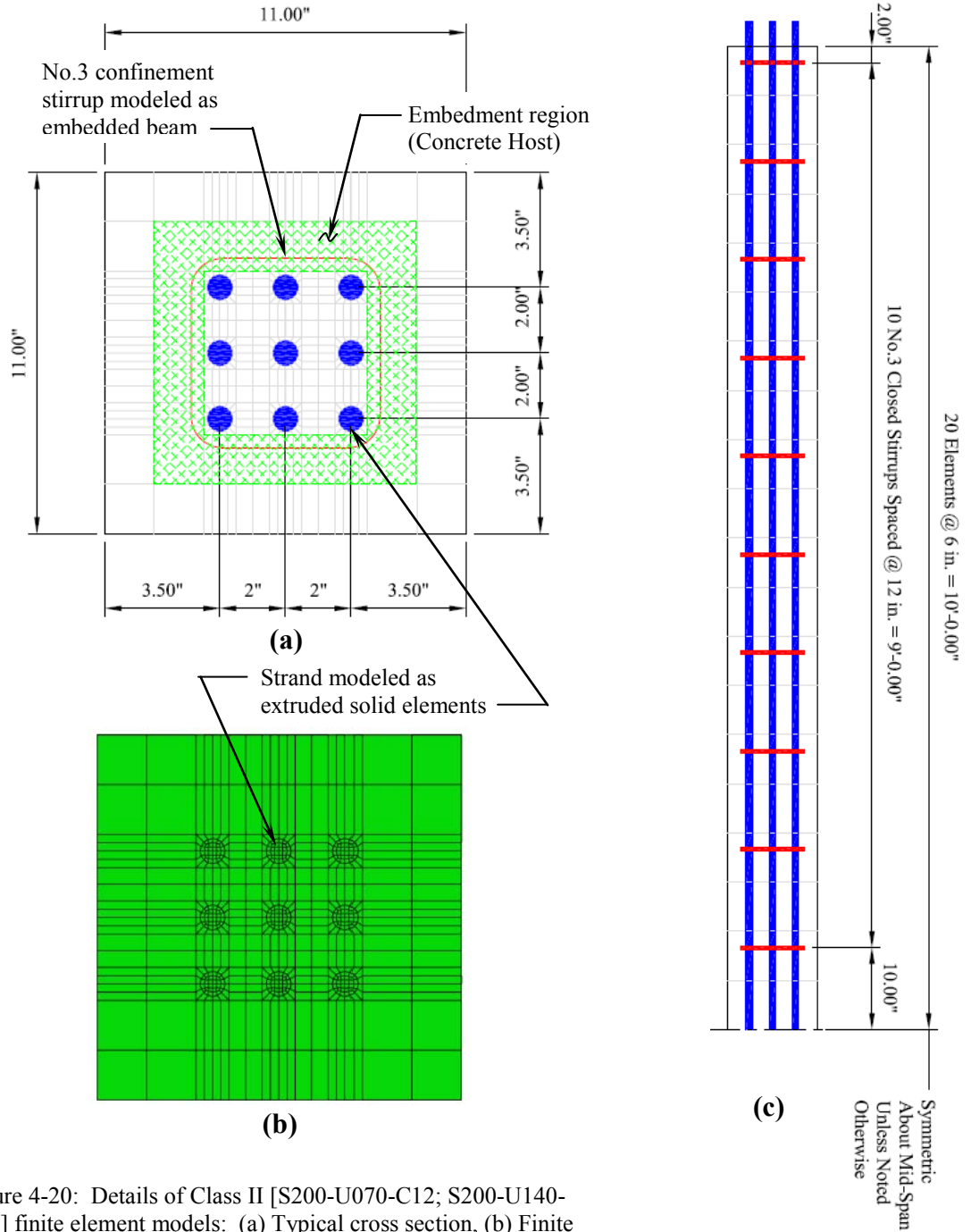


Figure 4-20: Details of Class II [S200-U070-C12; S200-U140-C12] finite element models: (a) Typical cross section, (b) Finite element simulation, and (c) Layout of confinement reinforcement (No.3 closed stirrups spaced at 12 in. on center)

For the analytical purposes of this section, the pretensioning process is based on the assumption that the prestressed strands are released while the specimens fully rest on the casting bed. Since the pretensioning is applied concentrically (e.g., all the strands are simultaneously released), the effect of the self-weight on the response of beams to the pretensioning will be ignored.

In addition, the transfer length between the strands and concrete host is directly simulated using the extrusion technique based on the upper- and lower-bound contact formulations as previously discussed.

4.4.2. Material Calibration & Sectional Properties

The material and sectional characteristics of the concrete beams are summarized as follows:

$$\text{Cross sectional dimensions} \dots\dots\dots A_c = 11 \text{ in.} \times 11 \text{ in.} = 121 \text{ in.}^2 \quad (4.22)$$

$$\text{Span Length} \dots\dots\dots L_{beam} = 20 \text{ ft} \quad (4.23)$$

$$\text{Compressive strength @ 28}^{\text{th}} \text{ day} \dots\dots f'_c = 10,000 \text{ psi} \quad (4.24)$$

$$\text{Compressive strength @ Release} \dots\dots f'_{ci} = 8,000 \text{ psi} \quad (4.25)$$

$$\text{Modulus of Elasticity @ Release} \dots\dots E_{ci} = 33 w_c^{1.5} \sqrt{f'_c} = 5,422,453 \text{ psi} \quad (4.26)$$

$$\text{Weight Density} \dots\dots\dots w_c = 150 \text{ lbs/ft}^3 \quad (4.27)$$

$$\text{Poisson's Ratio} \dots\dots\dots \nu_c = 0.20 \quad (4.28)$$

The following includes the summary of the assumptions for the prestressing strands utilized for the analytical purposes of this research:

$$\text{Nominal diameter of strands} \dots\dots\dots d_p = 0.70 \text{ in.} \quad (4.29)$$

$$\text{Nominal cross sectional area of strands} \dots A_p = 0.294 \text{ in.}^2 \quad (4.30)$$

$$\text{Ultimate tensile strength of strands} \dots f_{pu} = 270,000 \text{ psi} \quad (4.31)$$

$$\text{Yield strength of strands} \dots f_{py} \approx 80\% f_{pu} = 216,000 \text{ psi} \quad (4.32)$$

$$\text{Max. Jacking Stress} \dots f_{pj} = 75\% f_{pu} = 202,500 \text{ psi} \quad (4.33)$$

$$\text{Modulus of Elasticity of strands} \dots E_p = 28,500,000 \text{ psi} \quad (4.34)$$

$$\text{Weight Density} \dots w_p = 590 \text{ lbs/ft}^3 \quad (4.35)$$

$$\text{Poisson's Ratio} \dots \nu_p = 0.20 \quad (4.36)$$

As discussed in Section 4.3.3, it is anticipated that the concrete beams as well as the prestressing strands and tie reinforcement will stay within the elastic regime. Therefore, the material constitutive parameters are limited to linear-elastic behavior of concrete and steel as described above.

4.4.3. Comparative Analysis of Results Based on Closed Form Solutions

The closed form solution for the concentrically pretensioned concrete beams with the sectional properties similar to the specimens (see Table 4-6 through Table 4-9 for the basic properties) is based on the elastic response of the specimens to the induced pressure resulted by pretensioning. In addition, the closed form solution accounts for the loss of pretensioning due to elastic shortening of the member immediately after the release of strands. Appendix I includes the details of the corresponding closed-form solution based on the gross sectional properties of the concrete body, summarized below:

$$f_c = -4383 \text{ psi} \quad \dots \text{Compressive stress in concrete after initial loss} \quad (4.37)$$

due to elastic shortening

$$\varepsilon_c = -8.083 \times 10^{-4} \quad \dots\dots\dots \text{Compressive strain corresponding to } f_c \quad (4.38)$$

$$\frac{f_c}{f'_{ci}} = 0.548 \quad \dots\dots\dots \text{Ratio of compressive stress } (f_c) \text{ due to} \quad (4.39)$$

pretensioning to the compressive strength of
concrete at the time of release (f'_{ci})

Given the ratio of the compressive stress in the beam to the compressive strength of concrete at the time of release ($f'_{ci} = 8,000 \text{ psi}$) as indicated by Equation (4.39), it is anticipated that the response of the specimens is within the elastic regime. Additionally, the imposed compressive stress is below the threshold of $0.6 f'_{ci}$ as required by AASHTO LRFD (AASHTO LRFD, 2010). Therefore, the constitutive parameters for simulation of the concrete prisms will be limited to elastic properties as previously discussed in Section 4.4.2.

The compressive stress induced in the beams includes the effect of elastic shortening losses immediately after the release of pretensioning. The effect of elastic shortening included in Appendix I (closed form solution) is based on the approximation method recommended by AASHTO LRFD (AASHTO LRFD, 2010). Instead, the finite element models will directly account for the losses due to elastic shortening through numerical solutions.

Table 4-10 and Table 4-11 show the maximum compressive stresses at the mid-span of Class I models (9 strands spaced at 2.80 in on center) with contact friction coefficients of 0.70 and 1.40, respectively. The results indicate a close conformance between the analytical models and the closed form solution. Besides, it appears that the slippage of the strands due to the contact friction formulation does not affect the compressive stresses

at the mid-span of the specimens. Finally, although the models show sensitivity to the spacing of the confinement reinforcement, the variation of the compressive stresses at the mid-span of the beams is negligible.

Table 4-12 and Table 4-13 show the maximum compressive stresses at the mid-span of Class II models (9 strands spaced at 2.00 in on center) with contact friction coefficients of 0.70 and 1.40, respectively. The results indicate a close conformance between the analytical models and the closed form solution. In addition, it appears that the slippage of the strands due to the contact friction formulation does not affect the compressive stresses at the mid-span of the specimens. Finally, although the models show sensitivity to the spacing of the confinement reinforcement, the variation of the compressive stresses at the mid-span of the beams is negligible.

Table 4-10: Comparative analysis of the analytical results obtained from the finite element models with nine extruded strands spaced at 2.80 in. on center and contact friction coefficient of $\mu_f = 0.70$ against the closed form solutions. Negative stresses indicate compression.

Model I.D.	$f_c^{Finite-Element}$	$f_c^{Closed Form}$	$f_c^{Finite Element} / f_c^{Closed Form}$
S280-U070-C0	-4359	-4383	99.4%
S280-U070-C3	-4364	-4383	99.6%
S280-U070-C6	-4361	-4383	99.5%
S280-U070-C9	-4361	-4383	99.5%
S280-U070-C12	-4360	-4383	99.5%

Table 4-11: Comparative analysis of the analytical results obtained from the finite element models with nine extruded strands spaced at 2.80 in. on center and contact friction coefficient of $\mu_f = 1.40$ against the closed form solutions. Negative stresses indicate compression.

Model I.D.	$f_c^{Finite-Element}$	$f_c^{Closed Form}$	$f_c^{Finite Element} / f_c^{Closed Form}$
S280-U140-C0	-4360	-4383	99.5%
S280-U140-C3	-4364	-4383	99.6%
S280-U140-C6	-4362	-4383	99.5%
S280-U140-C9	-4362	-4383	99.5%
S280-U140-C12	-4361	-4383	99.5%

Table 4-12: Comparative analysis of the analytical results obtained from the finite element models with nine extruded strands spaced at 2.00 in. on center and contact friction coefficient of $\mu_f = 0.70$ against the closed form solutions. Negative stresses indicate compression.

Model I.D.	$f_c^{Finite-Element}$	$f_c^{Closed Form}$	$f_c^{Finite Element} / f_c^{Closed Form}$
S200-U070-C0	-4358	-4383	99.4%
S200-U070-C3	-4364	-4383	99.6%
S200-U070-C6	-4361	-4383	99.5%
S200-U070-C9	-4361	-4383	99.5%
S200-U070-C12	-4359	-4383	99.5%

Table 4-13: Comparative analysis of the analytical results obtained from the finite element models with nine extruded strands spaced at 2.00 in. on center and contact friction coefficient of $\mu f = 1.40$ against the closed form solutions. Negative stresses indicate compression.

Model I.D.	$f_c^{Finite-Element}$	$f_c^{Closed Form}$	$f_c^{Finite Element} / f_c^{Closed Form}$
S200-U140-C0	-4359	-4383	99.5%
S200-U140-C3	-4364	-4383	99.6%
S200-U140-C6	-4361	-4383	99.5%
S200-U140-C9	-4361	-4383	99.5%
S200-U140-C12	-4360	-4383	99.5%

Moreover, the analytical results obtained by Class I and Class II finite element models indicate that the spacing of the pretensioned strands does not have a significant effect on the compressive stresses at the mid-span of the specimens. This is consistent with the assumptions of the beam theory used in the analysis and design of pretensioned concrete members used in current practice.

4.4.4. Discussion of Results

The following section includes a comparative analysis of the analytical results obtained from Class I (nine 0.7-in. diameter strands spaced at 2.80 in. on center) and Class II (nine 0.7-in. diameter strands spaced at 2.00 in. on center) (see Table 4-6 through Table 4-9 for the basic properties of Class I and Class II finite element models). The main objective of this comparative analysis is to show the differential response of the models immediately after the release of pretensioning as the spacing of the released strands decreases from 2.80 in. to 2.00 in. Such comparison is intended to provide analytical insight for optimization of the strands spacing as the industry moves towards the use of larger diameter strands.

In addition, the effect of the confinement reinforcement (the amount and spacing) will be evaluated for each class of the finite element models similar to Section 4.3.

4.4.4.1. Transfer Length

The following includes the evaluation of the transfer length obtained by Class I and Class II finite element models. In addition, the analytical results will be compared with the experimental data by Akhnoukh, discussed in Section 4.3.

As previously discussed, Akhnoukh's experimental results are based on specimens with different cross sectional dimensions and span length compared with the Class I and Class II finite element models used for the analytical purposes of this section. Besides, Akhnoukh's specimens are pretensioned with one concentric 0.7-in. diameter strands in contrast with the nine-strand configurations (concentric and all 0.7-in. diameter).

Nevertheless, the comparison of the analytical results obtained by Class I and Class II simulated specimens with Akhnoukh's experimental results is merely intended to show the affect of number and spacing of the strands on the transfer length and the stress path. In addition, as indicated by Equation (4.1), the current standard of practice assumes a linear transfer length based on the strand diameter regardless of the number and spacing of the strands.

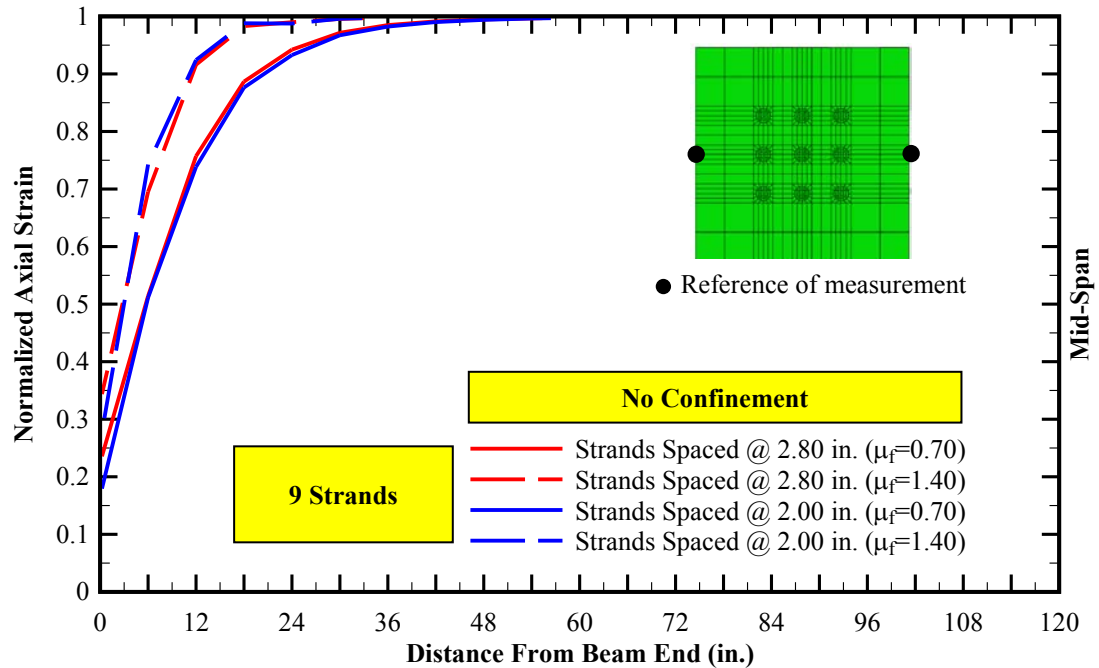


Figure 4-21: Comparison of axial strains (transfer length) of Class I (nine 0.7-in. diameter strands spaced at 2.80 in. on center) and Class II finite element simulation of concrete beams (nine 0.7-in. diameter strands spaced at 2.00 in. on center) with no confinement reinforcement.

Figure 4-21 shows the comparison of the axial (compressive) strains of the concrete beams in response to nine 0.7-in. diameter strands spaced at 2.80 in. and 2.00 in. on center. The strains are measured along the mid-side of the finite element models. In addition, the analytical results correspond to lower and upper boundary contact friction coefficients of 0.70 and 1.40, respectively, similar to the discussion of Section 0. As indicated by the analytical results, the closer spacing of the strands (2.00 in versus 2.80 in.) does not significantly affect the axial (compressive) strains of the pretensioned concrete specimens with no confinement reinforcement.

Similarly, Figure 4-22 shows the comparison of the axial strains of Class I and Class II finite element models confined with No.3 closed stirrups spaced at 3.00 in. on center. Based on the finite element simulation, the spacing of the strands does not significantly

affect the compressive strains of the specimens. However, the number of the strands and consequently the magnitude of pretensioning affect the pretensioning path (transfer length mechanism) within the end zone of the member. Nevertheless, the linearization of the prestressing shows convergence between 24 and 42 in. from the member ends, as the lower and upper boundary solutions, respectively. The obtained boundary values for transfer length are less than or equal to 60 times the strand diameter limit recommended by AASHTO LRFD (AASHTO LRFD, 2010).

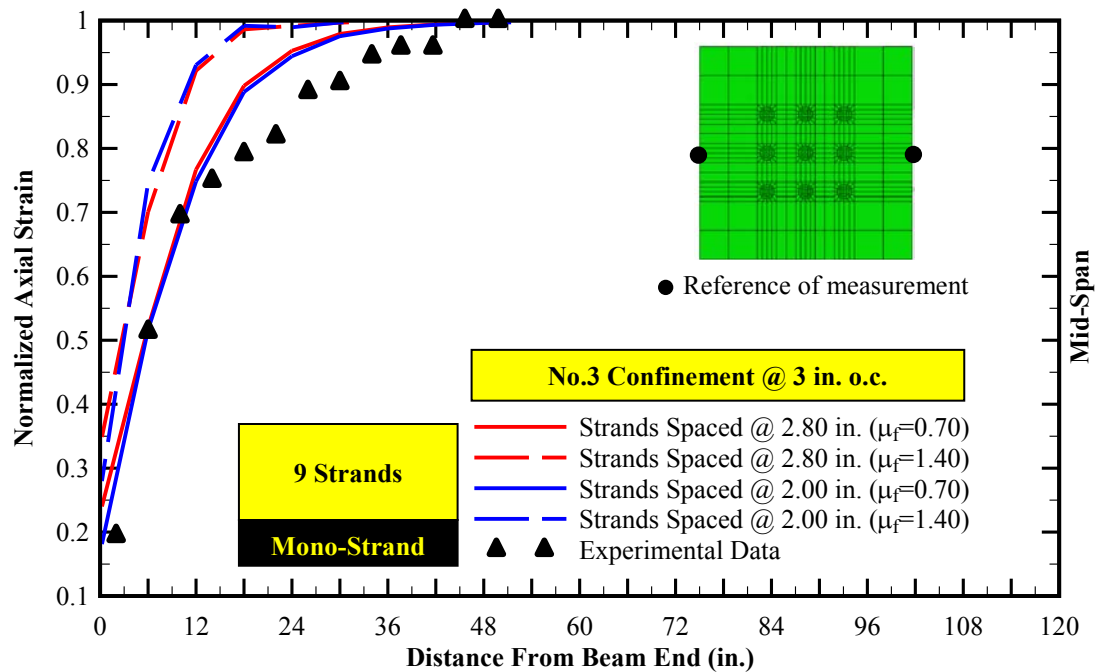


Figure 4-22: Comparison of axial strains (transfer length) of Class I (nine 0.7-in. diameter strands spaced at 2.80 in. on center) and Class II finite element simulation of concrete beams (nine 0.7-in. diameter strands spaced at 2.00 in. on center) confined with No.3 closed stirrups spaced at 3.00 in. on center. Note that the experimental data corresponds to 7 in. x 7 in. x 8 ft prisms with one concentric 0.7-in. diameter strand (Akhnoikh, 2008).

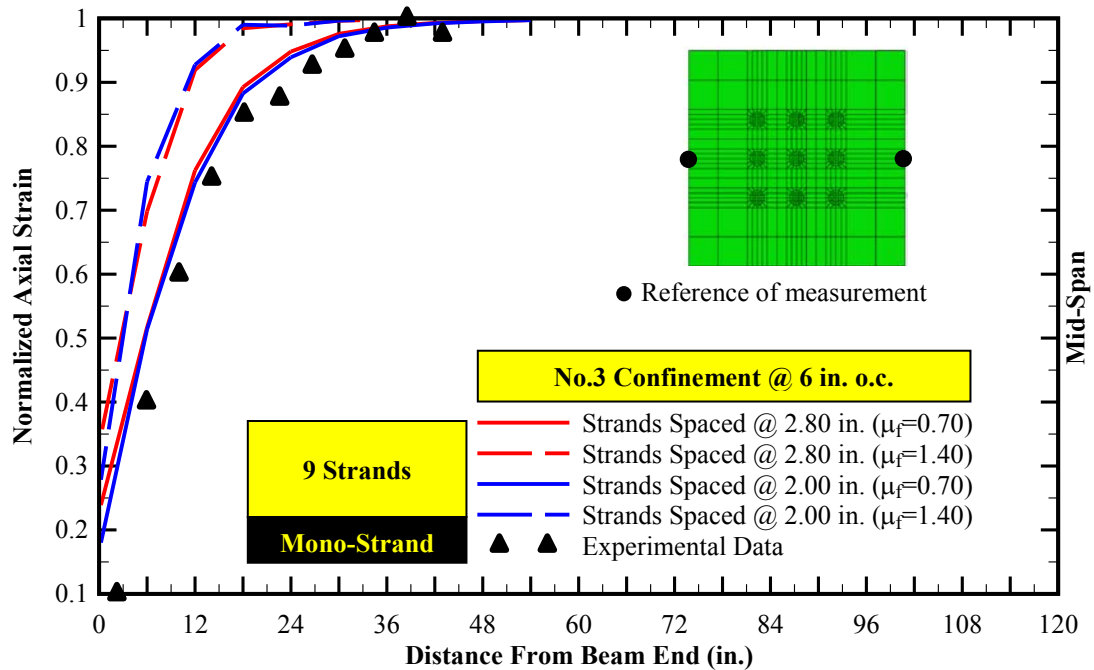


Figure 4-23: Comparison of axial strains (transfer length) of Class I (nine 0.7-in. diameter strands spaced at 2.80 in. on center) and Class II finite element simulation of concrete beams (nine 0.7-in. diameter strands spaced at 2.00 in. on center) confined with No.3 closed stirrups spaced at 6.00 in. on center. Note that the experimental data corresponds to 7 in. x 7 in. x 8 ft prisms with one concentric 0.7-in. diameter strand (Akhnoukh, 2008).

Figure 4-23 shows the comparison of the axial strains of Class I and Class II finite element models confined with No.3 closed stirrups spaced at 6.00 in. on center. Based on the finite element simulation, the spacing of the strands does not significantly affect the compressive strains of the specimens. However, the number of the strands and consequently the magnitude of pretensioning affect the pretensioning path (transfer length mechanism) within the end zone of the member. Nevertheless, the obtained boundary values for transfer length are less than or equal to 60 times the strand diameter limit recommended by AASHTO LRFD (AASHTO LRFD, 2010).

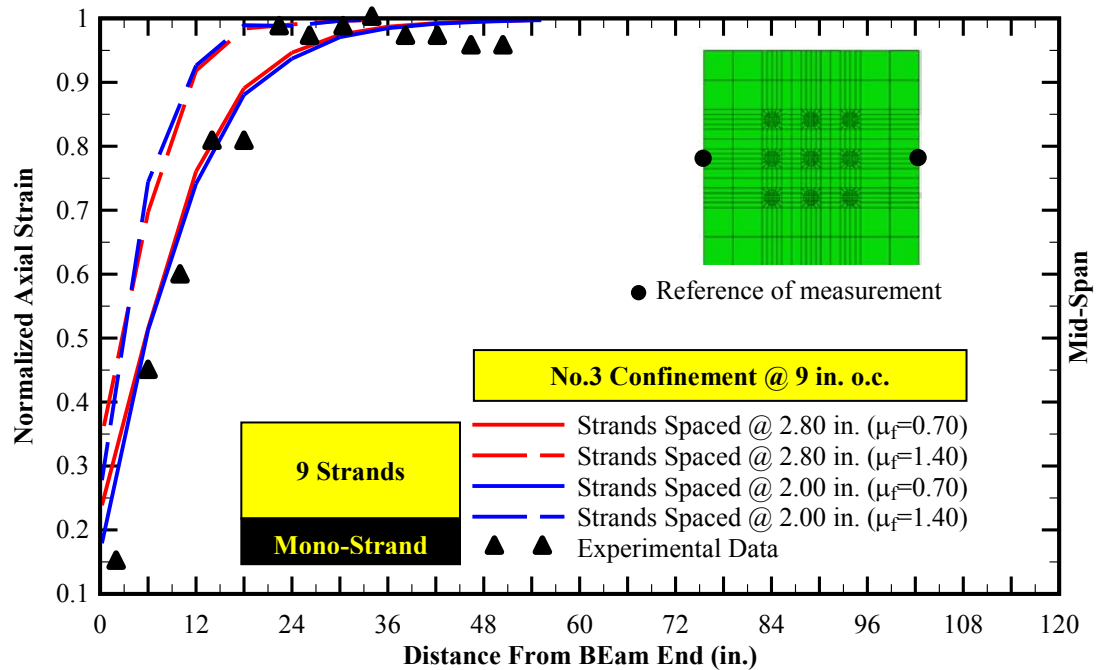


Figure 4-24: Comparison of axial strains (transfer length) of Class I (nine 0.7-in. diameter strands spaced at 2.80 in. on center) and Class II finite element simulation of concrete beams (nine 0.7-in. diameter strands spaced at 2.00 in. on center) confined with No.3 closed stirrups spaced at 9.00 in. on center. Note that the experimental data corresponds to 7 in. x 7 in. x 8 ft prisms with one concentric 0.7-in. diameter strand (Akhnoukh, 2008).

Figure 4-24 shows the comparison of the axial strains of Class I and Class II finite element models confined with No.3 closed stirrups spaced at 9.00 in. on center. Based on the finite element simulation, the spacing of the strands does not significantly affect the compressive strains of the specimens. However, the number of the strands and consequently the magnitude of pretensioning affect the pretensioning path (transfer length mechanism) within the end zone of the member. Nevertheless, The obtained boundary values for transfer length are less than or equal to 60 times the strand diameter limit recommended by AASHTO LRFD (AASHTO LRFD, 2010).

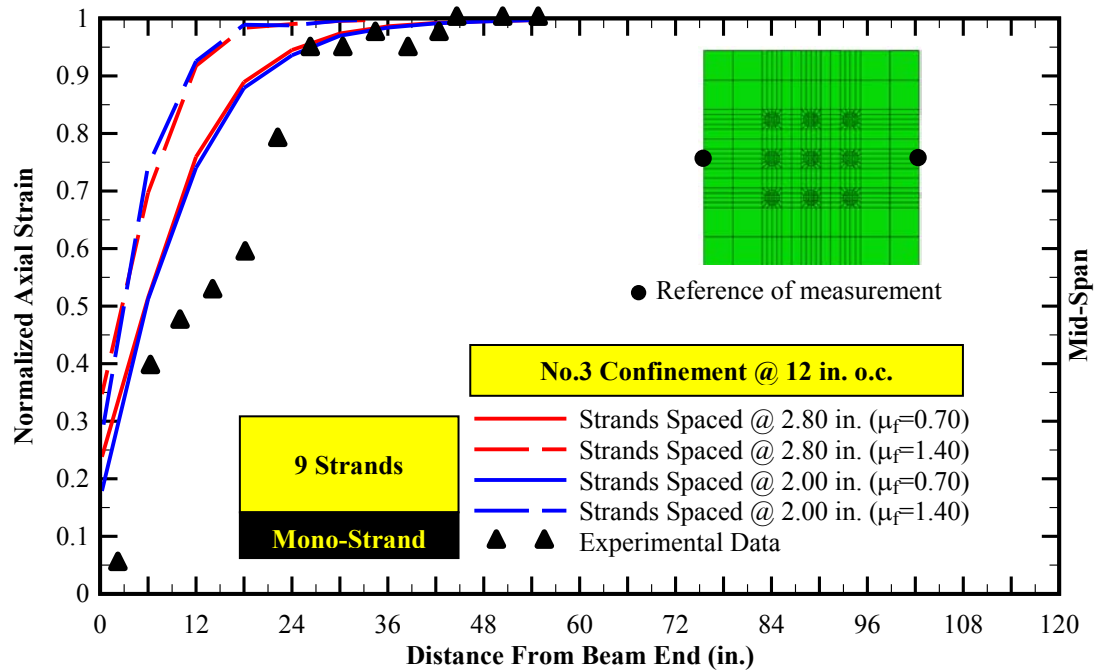


Figure 4-25: Comparison of axial strains (transfer length) of Class I (nine 0.7-in. diameter strands spaced at 2.80 in. on center) and Class II finite element simulation of concrete beams (nine 0.7-in. diameter strands spaced at 2.00 in. on center) confined with No.3 closed stirrups spaced at 12.00 in. on center. Note that the experimental data corresponds to 7 in. x 7 in. x 8 ft prisms with one concentric 0.7-in. diameter strand (Akhnoukh, 2008).

As previously discussed in Section 4.3.1, the experimental data for the specimens confined with No.3 closed stirrups spaced at 12.00 in. on center were ignored for the purposes of this research due to nonconforming nature of the information. Nevertheless, Figure 4-25 shows the comparison of the axial strains of Class I and Class II finite element models confined with No.3 closed stirrups spaced at 12.00 in. on center. Based on the finite element simulation, the spacing of the strands does not significantly affect the compressive strains of the specimens. Nonconformity of the analytical results with the experimental data is non-conclusive as discussed above. However, the trend of the analytical results obtained by the simulated specimens is similar to those confined with No.3 closed stirrups spaced at 3.00, 6.00, and 9.00 in. as well as non-confined models.

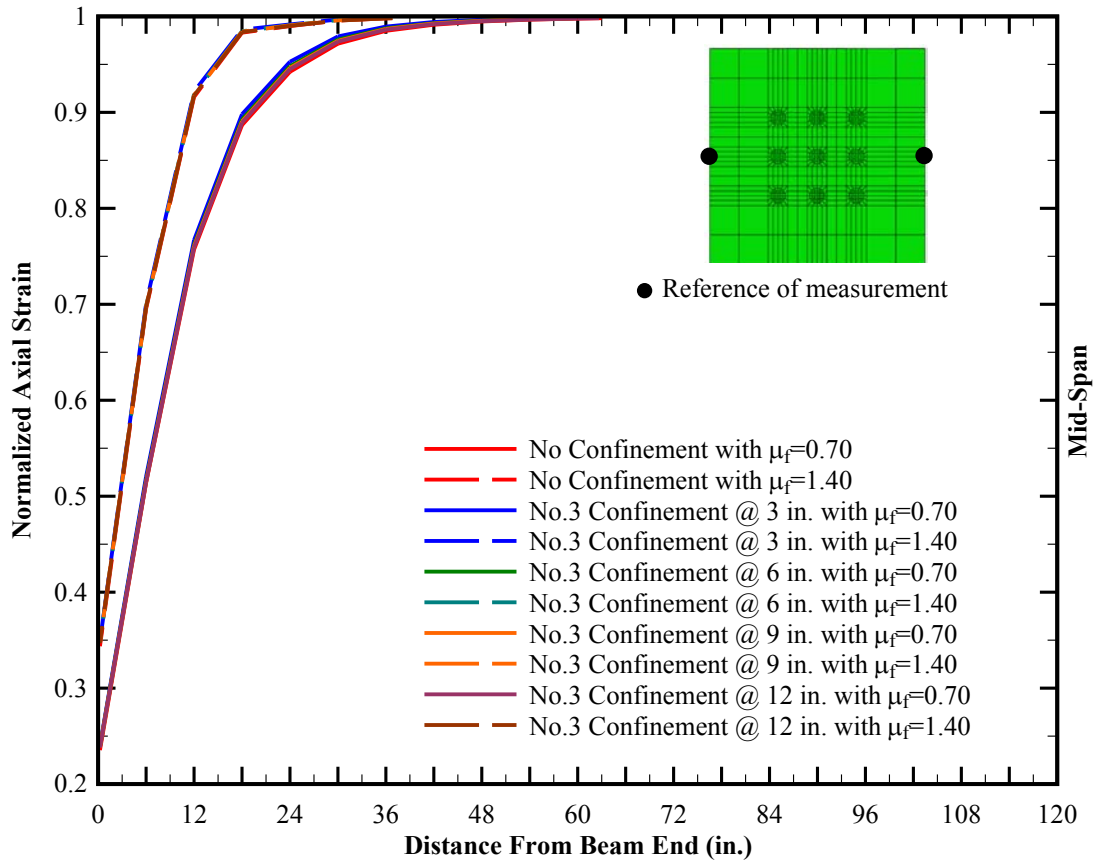


Figure 4-26: Comparison of axial strains (transfer length) of Class I (nine 0.7-in. diameter strands spaced at 2.80 in. on center) with various configurations of confinement reinforcement.

Figure 4-26 and Figure 4-27 show the comparison of axial strain for Class I and Class II finite element models with various configurations of confinement reinforcement considering the effect of the strands spacing, respectively. Based on the analytical results, both classes of the finite element models indicate that the amount and spacing of the confinement rebars (No.3 closed stirrups for the analytical purposes of this research) do not significantly affect the transfer and the pretensioning stress path regardless of the strands spacing.

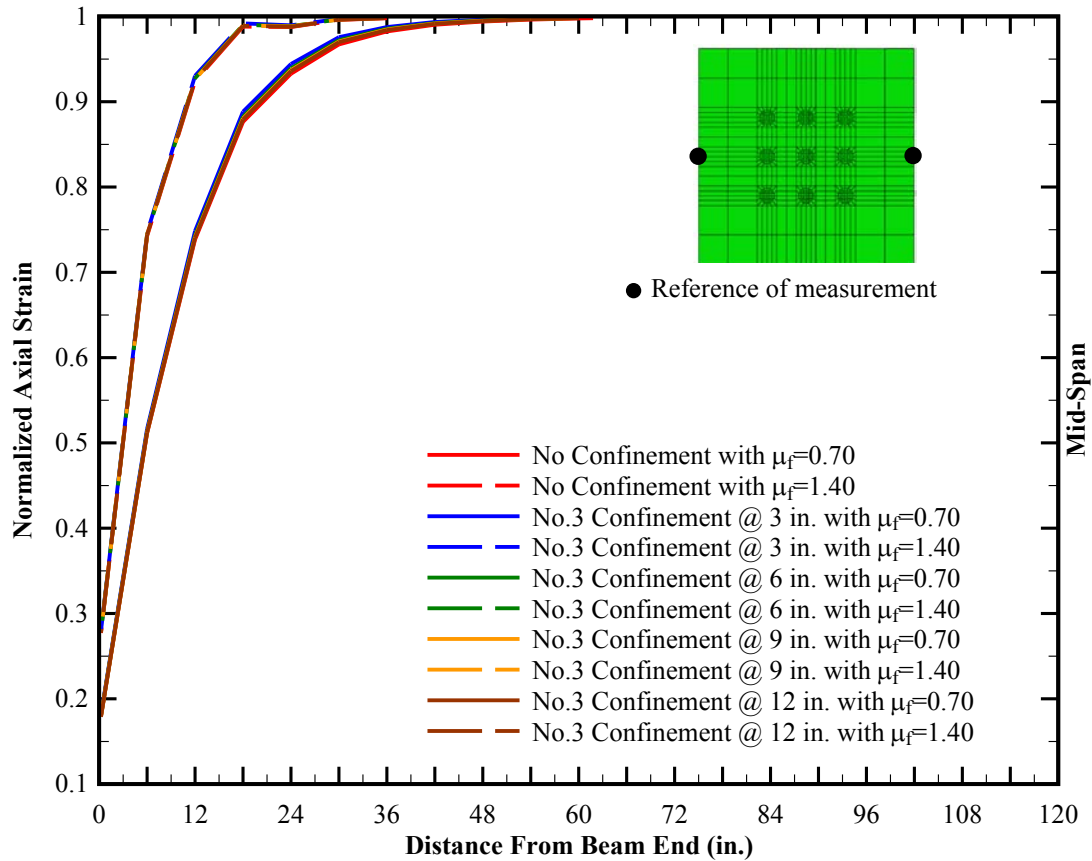


Figure 4-27: Comparison of axial strains (transfer length) of Class II (nine 0.7-in. diameter strands spaced at 2.00 in. on center) with various configurations of confinement reinforcement.

4.4.4.2. Stress Analysis

When 0.7-in. diameter strands are spaced closer than four times the diameter, one of the major concerns is the tensile failure of the concrete between the strands due to lack of adequate clearance. During the following section, Class I and Class II finite element models will be analyzed with the aim of comparing the internal stresses developed between the strands while spaced at 2.80 in. (Class I; four times the strand diameter) and 2.00 in. (Class II; optimized practice of fabrication). Additionally, the effect of the confinement reinforcement (amount and spacing) will be comparatively analyzed similar to the previous sections.

In accordance with AASHTO LRFD, the limit of tensile stresses in prestressed members is estimated as follows (AASHTO LRFD, 2010):

$$F_t = 6\sqrt{f'_{ci}} = 537 \text{ psi} \quad (4.40)$$

Note that Equation (4.40) is applicable only if bonded tendons or reinforcement are readily available to withstand the imposed tensile stresses. In case of the prestressed members, the confinement as well as vertical end zone and shear reinforcement are assumed to provide a basis for the applicability of the allowable tensile limits of Equation (4.40).

On the other hand, since the simulation of the specimens is based on linear elastic analysis as described in Section 4.4.2, the level of obtained tensile stresses will indicate possible violation of the allowable limits without subsequent stress redistribution.

The following includes the definition of the local axis convention for the three-dimensional finite element models as shown in Figure 4-28:

- Local Axis 1: The axis parallel with the lateral orientation of the member
- Local Axis 2: The axis parallel with the vertical orientation of the member
- Local Axis 3 : The axis parallel with the longitudinal orientation of the member

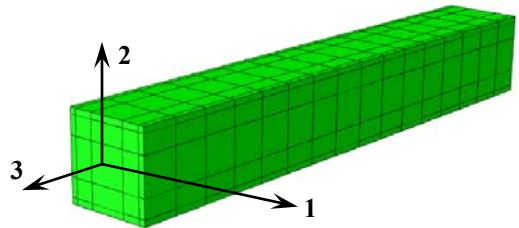


Figure 4-28: Typical local axis convention for the three-dimensional finite element models

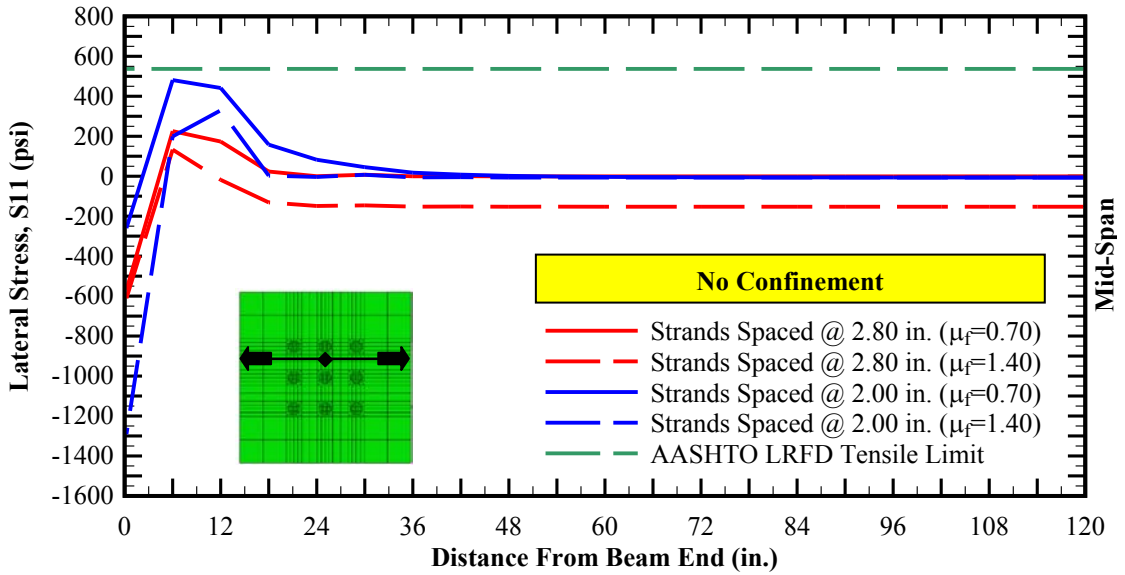
Subsequently, the following stress components are delineated in conformance with the local axes defined above:

- Lateral Stress (S11): Component of stress acting along Local Axis 1
- Vertical Stress (S22): Component of stress acting along Local Axis 2
- Longitudinal Stress (S33): Component of stress acting along Local Axis 3

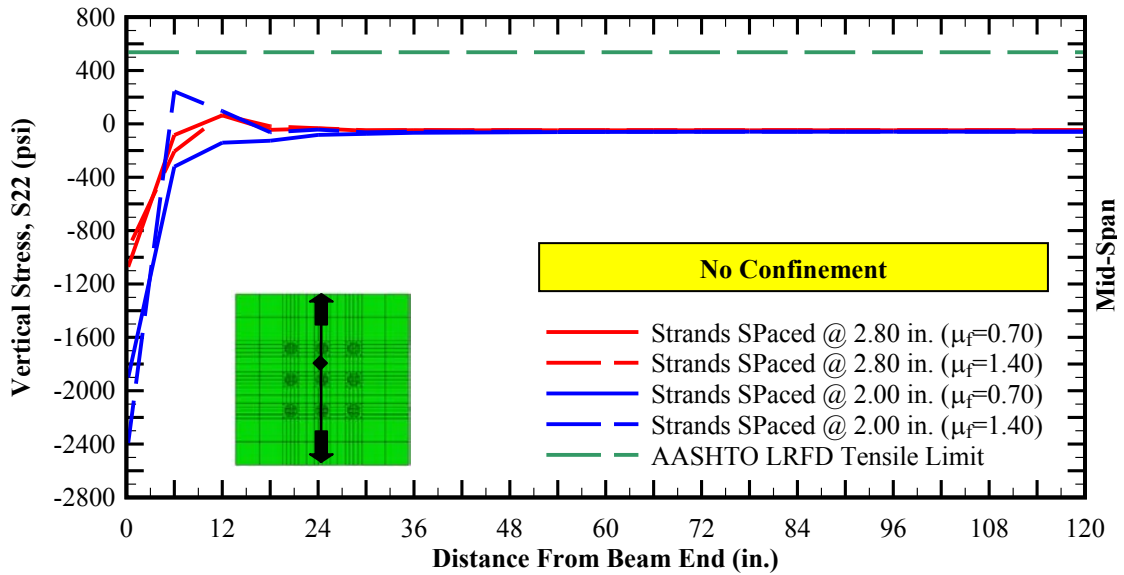
Figure 4-29 shows the comparison of the lateral (S11) and vertical (S22) stresses imposed in the region located at the mid-distance between the central strand and the exterior strand immediately above it while the specimen is unconfined. As it can be observed, the level of lateral tensile stresses may significantly increase (by as much as 240%) as the strands spacing decreases from 2.80 in. to 2.00 in. on center, also affected by the level of strands slippage. Additionally, the upper boundary of tensile stresses approaches near the allowable limit recommended by AASHTO LRFD (AASHTO LRFD, 2010).

The vertical stresses show a different trend. When strands are spaced at four times the diameter (2.80 in.) and for both upper and lower slippage boundaries (0.70 and 1.40, respectively), it appears that the corresponding zone vertically fluctuates between the state of compression and negligible tension within the first 24 in. from the member end. Meanwhile, as the strands are spaced closer to each other (2.00 in. on center), the models show sensitivity to the slippage. The fluctuation between the states of compression and tension is much more pronounced for the strands spaced at 2.00 in. on center, corresponding to the upper and lower contact friction coefficients (1.40 and 0.70, respectively). While such spikes in the response of the finite element models are sometimes attributed to the numerical noises in the areas with sharp and/or sudden

variations of stresses, experimental verifications are required to establish more conclusive comments. Nevertheless, the mean response of both Class I (strands spaced at 2.80 in. on center) and Class II (strands spaced at 2.00 in. on center) indicates that the corresponding zone stays either completely under compression or is subject to negligible tensile stresses.



(a)



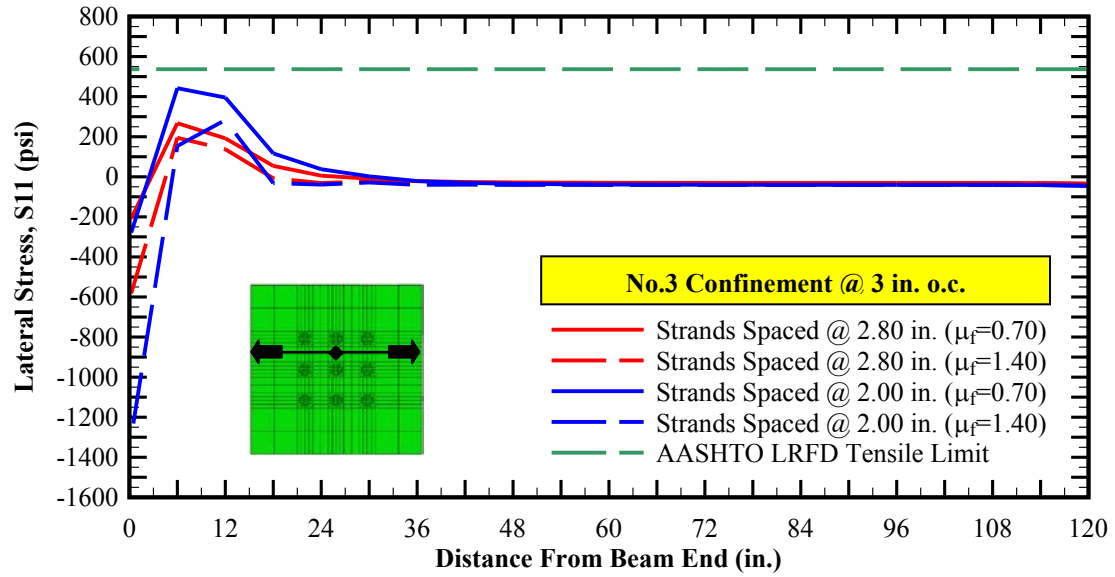
(b)

◆ Reference of measurement

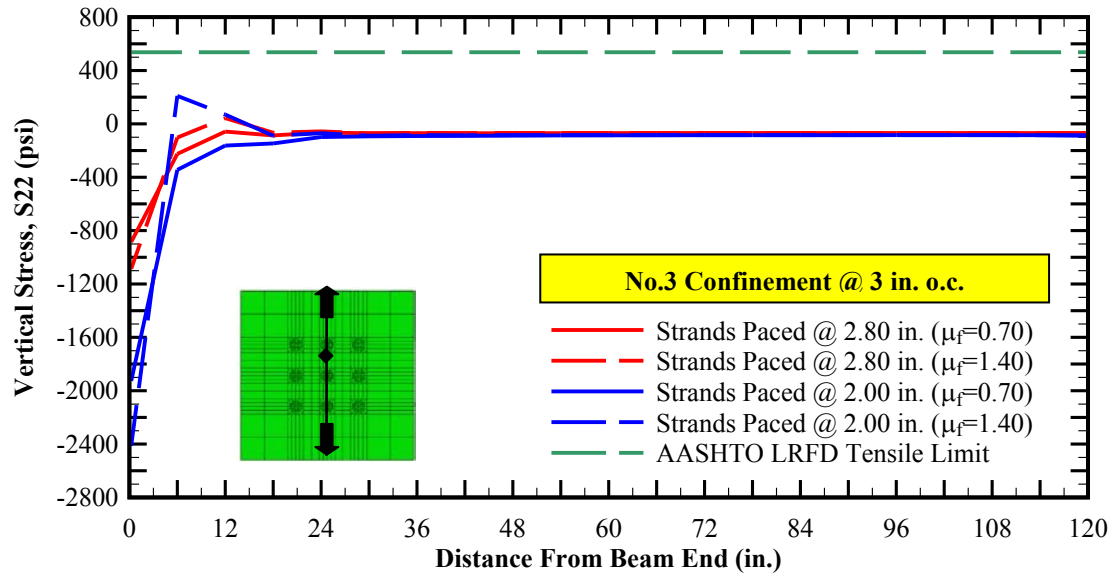
Figure 4-29: Comparison of stresses obtained by Class I (nine 0.7-in. diameter strands spaced at 2.80 in. on center) and Class II (nine 0.7-in. diameter strands spaced at 2.00 in. on center) with no confinement: (a) Lateral Stresses (S11), and Vertical Stresses (S22).

Figure 4-30 shows the comparison of the lateral (S11) and vertical (S22) stresses imposed in the region located at the mid-distance between the central strand and the exterior strand immediately above it while the specimen is confined with No.3 closed stirrups spaced at 3 in. on center. As it can be observed, the magnitude of the lateral tensile stresses may significantly increase (by as much as 165%) as the strands spacing decreases from 2.80 in. to 2.00 in. on center, affected by the level of strands slippage. Additionally, the upper boundary of tensile stresses approaches near the allowable limits recommended by AASHTO LRFD.

On the other hand, the vertical stresses show a different trend. When the strands are spaced at four times the diameter (2.80 in.) and for both upper and lower slippage boundaries (0.70 and 1.40, respectively), it appears that the corresponding zone vertically fluctuates between the state of compression and negligible tension within the first 24 in. from the member end. Meanwhile, as the strands are spaced closer to each other (2.00 in. on center), the models show sensitivity to the slippage. The fluctuation between the states of compression and tension is much more pronounced for the strands spaced at 2.00 in. on center, dictated by the contact friction coefficients. In reference to the previous discussion for the models without confinement reinforcement and regardless of the spikes in the response of the finite element models, the mean response of both Class I and Class II indicates that the corresponding zone stays either completely under compression or is subject to negligible tensile stresses.



(a)



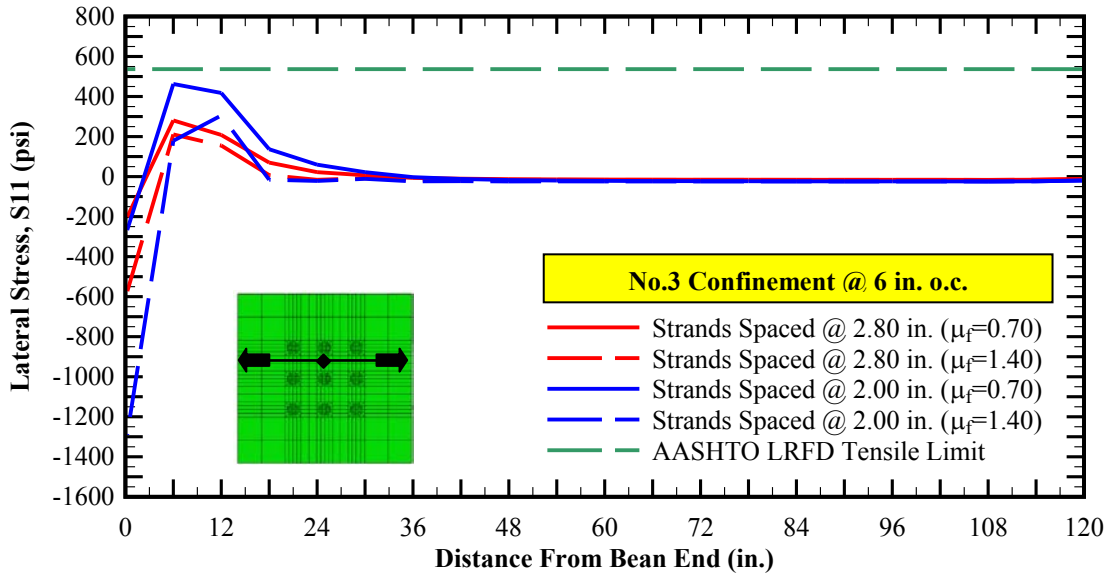
(b)

◆ Reference of measurement

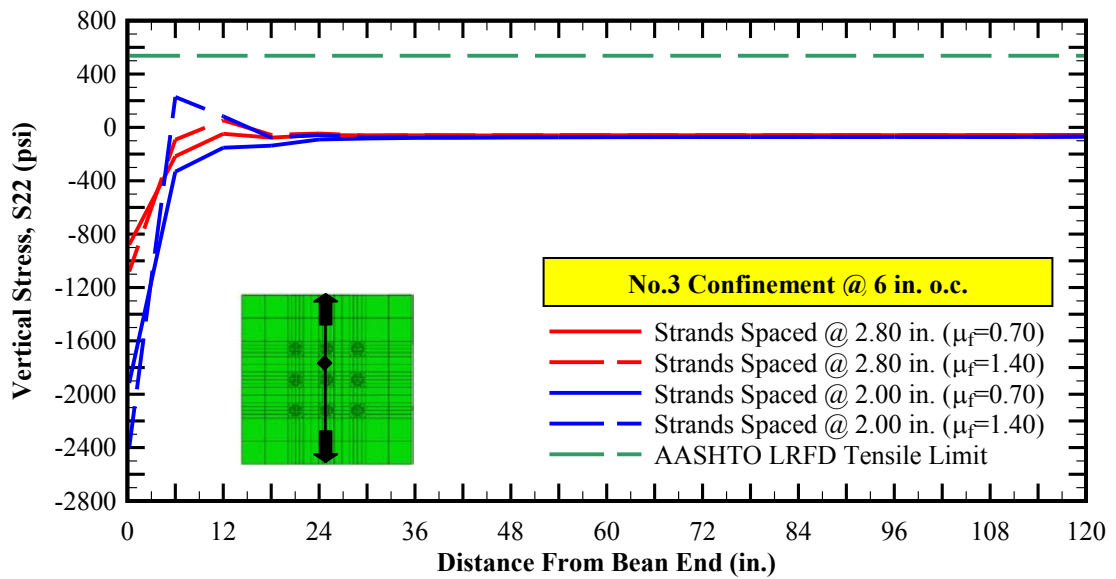
Figure 4-30: Comparison of stresses obtained by Class I (nine 0.7-in. diameter strands spaced at 2.80 in. on center) and Class II (nine 0.7-in. diameter strands spaced at 2.00 in. on center) confined with No.3 closed stirrups spaced at 3 in. on center: (a) Lateral Stresses (S11), and Vertical Stresses (S22).

Figure 4-31 shows the comparison of the lateral (S11) and vertical (S22) stresses imposed in the region located at the mid-distance between the central strand and the exterior strand immediately above it while the specimen is confined with No.3 closed stirrups spaced at 6 in. on center. As it can be observed, the level of lateral tensile stresses may significantly increase (by as much as 165%) as the strands spacing decreases from 2.80 in. to 2.00 in. on center, depending on the level of strands slippage. Additionally, the upper boundary of tensile stresses approaches the allowable limits recommended by AASHTO LRFD.

On the other hand, the vertical stresses show a different trend. When strands are spaced at four times the diameter (2.80 in.) and for both upper and lower slippage boundaries (0.70 and 1.40, respectively), it appears that the corresponding zone vertically fluctuates between the state of compression and negligible tension within the first 24 in. from the member end. Meanwhile, as the strands are spaced closer to each other (2.00 in. on center), the models show sensitivity to the slippage. The fluctuation between the states of compression and tension is much more pronounced for the strands spaced at 2.00 in. on center, dictated by the contact friction coefficients. In reference to the previous discussion for the models without confinement reinforcement and regardless of the spikes in the response of the finite element models, the mean response of both Class I and Class II indicates that the corresponding zone stays either completely under compression or is subject to negligible tensile stresses.



(a)



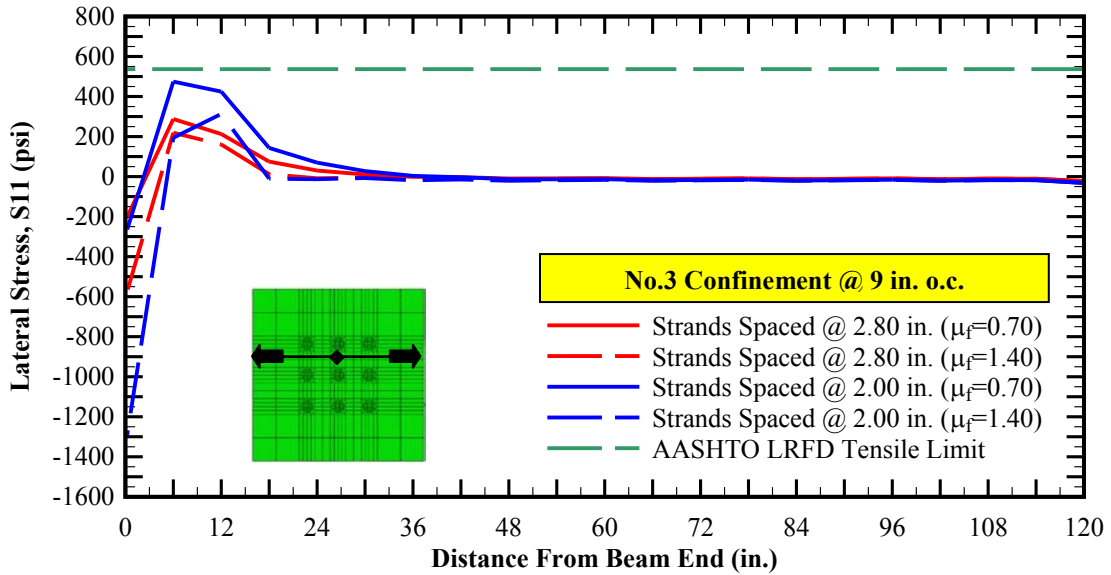
(b)

◆ Reference of measurement

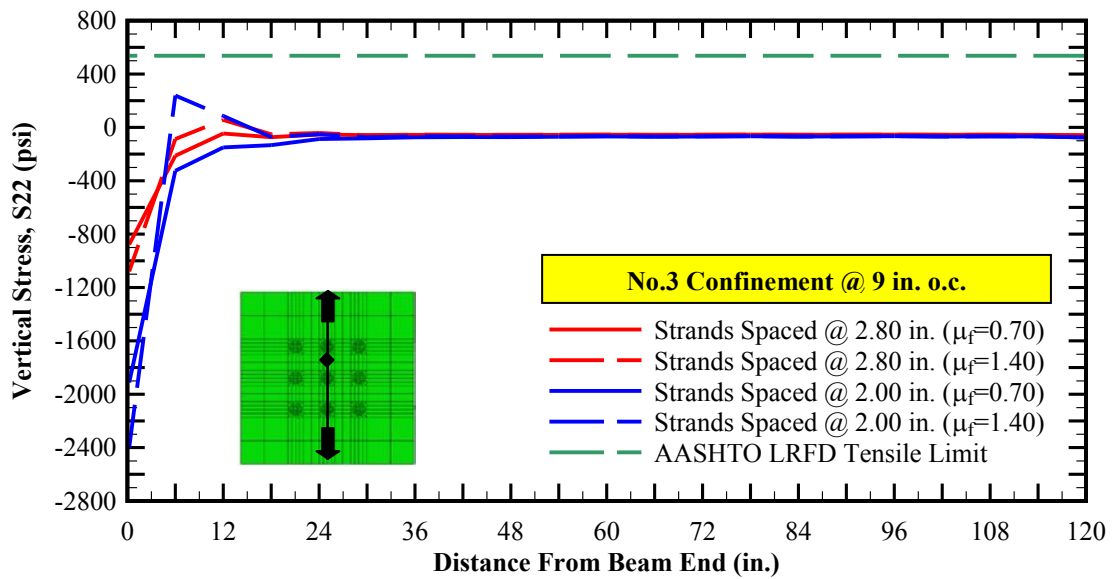
Figure 4-31: Comparison of stresses obtained by Class I (nine 0.7-in. diameter strands spaced at 2.80 in. on center) and Class II (nine 0.7-in. diameter strands spaced at 2.00 in. on center) confined with No.3 closed stirrups spaced at 6 in. on center: (a) Lateral Stresses (S11), and Vertical Stresses (S22).

Figure 4-32 shows the comparison of lateral (S11) and vertical (S22) stresses imposed in the region located at the mid-distance between the central strand and the exterior strand immediately above it while the specimen is confined with No.3 closed stirrups spaced at 9 in. on center. As it can be observed, the level of lateral tensile stresses may significantly increase (by as much as 165%) as the strands spacing decreases from 2.80 in. to 2.00 in. on center, depending on the level of strands slippage. Additionally, the upper boundary of tensile stresses approaches the allowable limits recommended by AASHTO LRFD.

On the other hand, the vertical stresses show a different trend. When strands are spaced at four times the diameter (2.80 in.) and for both upper and lower slippage boundaries (0.70 and 1.40, respectively), it appears that the corresponding zone vertically fluctuates between the state of compression and negligible tension within the first 24 in. from the member end. Meanwhile, as the strands are spaced closer to each other (2.00 in. on center), the models show sensitivity to the slippage. The fluctuation between the states of compression and tension is much more pronounced for the strands spaced at 2.00 in. on center, dictated by the contact friction coefficients. In reference to the previous discussion for the models without confinement reinforcement and regardless of the spikes in the response of the finite element models, the mean response of both Class I and Class II indicates that the corresponding zone stays either completely under compression or is subject to negligible tensile stresses.



(a)



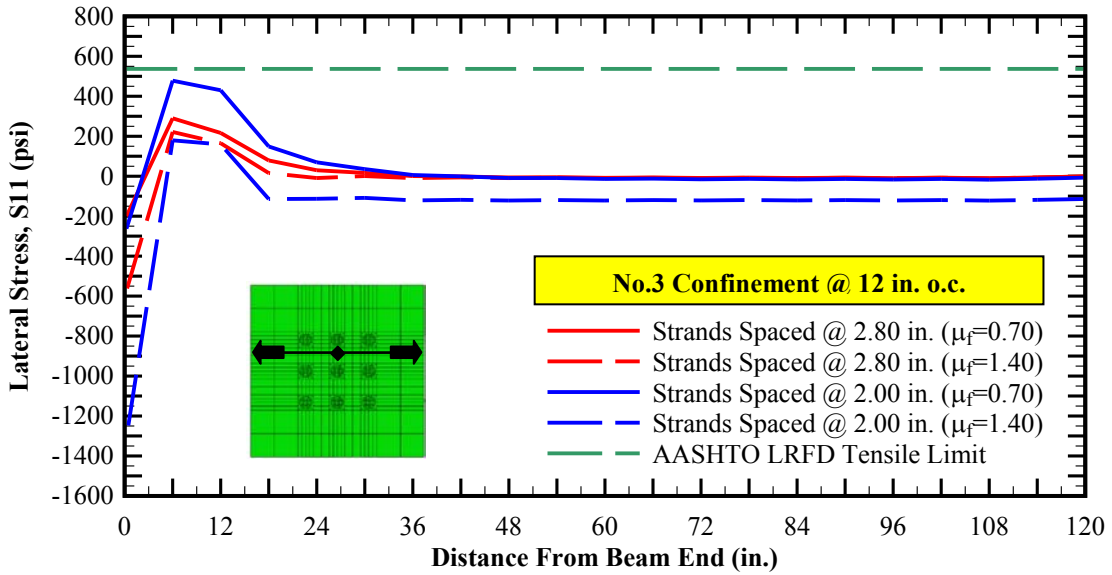
(b)

◆ Reference of measurement

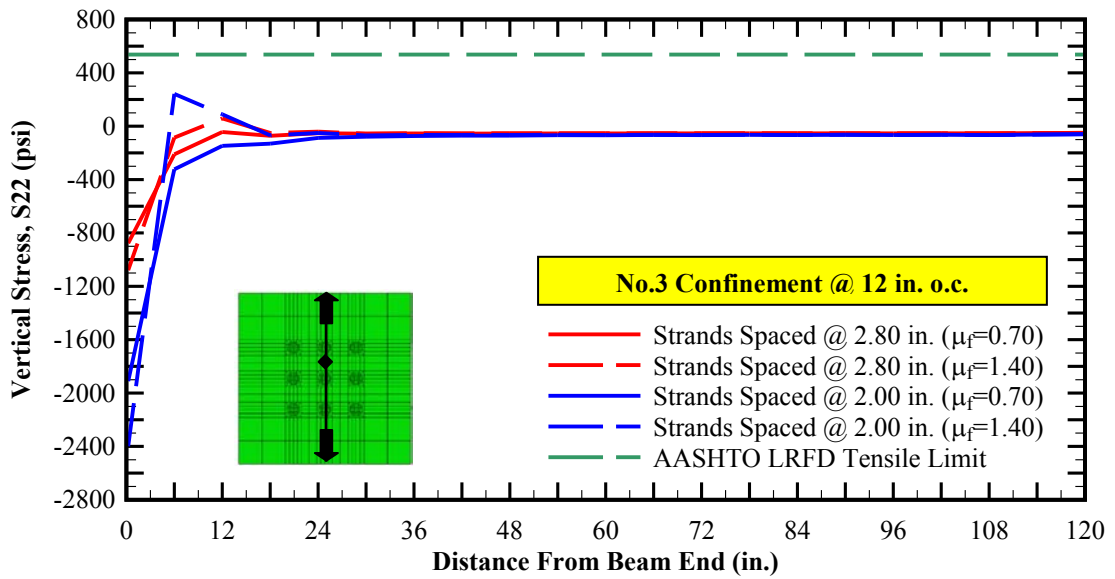
Figure 4-32: Comparison of stresses obtained by Class I (nine 0.7-in. diameter strands spaced at 2.80 in. on center) and Class II (nine 0.7-in. diameter strands spaced at 2.00 in. on center) confined with No.3 closed stirrups spaced at 9 in. on center: (a) Lateral Stresses (S11), and Vertical Stresses (S22).

Figure 4-33 shows the comparison of lateral (S11) and vertical (S22) stresses imposed in the region located at the mid-distance between the central strand and the exterior strand immediately above it while the specimen is confined with No.3 closed stirrups spaced at 12 in. on center. As it can be observed, the level of lateral tensile stresses may significantly increase (by as much as 165%) as the strands spacing decreases from 2.80 in. to 2.00 in. on center, depending on the level of strands slippage. Additionally, the upper boundary of tensile stresses approaches the allowable limits recommended by AASHTO LRFD.

On the other hand, the vertical stresses show a different trend. When strands are spaced at four times the diameter (2.80 in.) and for both upper and lower slippage boundaries (0.70 and 1.40, respectively), it appears that the corresponding zone vertically fluctuates between the state of compression and negligible tension within the first 24 in. from the member end. Meanwhile, as the strands are spaced closer to each other (2.00 in. on center), the models show sensitivity to the slippage. The fluctuation between the states of compression and tension is much more pronounced for the strands spaced at 2.00 in. on center, dictated by the contact friction coefficients. In reference to the previous discussion for the models without confinement reinforcement and regardless of the spikes in the response of the finite element models, the mean response of both Class I and Class II indicates that the corresponding zone stays either completely under compression or is subject to negligible tensile stresses.



(a)



(b)

◆ Reference of measurement

Figure 4-33: Comparison of stresses obtained by Class I (nine 0.7-in. diameter strands spaced at 2.80 in. on center) and Class II (nine 0.7-in. diameter strands spaced at 2.00 in. on center) confined with No.3 closed stirrups spaced at 12 in. on center: (a) Lateral Stresses (S11), and Vertical Stresses (S22).

As previously mentioned, it is observed that the amount and spacing of the confinement does not significantly affect the lateral and vertical stresses imposed around the central strand. However, the analytical results show that the absence of confinement may have further increase the magnitude of the imposed tensile stresses. As discussed above and in the absence confinement reinforcement, the analytical results indicate that the unidirectional tensile stresses are anticipated to increase by as much as 240% as the strands spacing is reduced from 2.80 in. to 2.00 in. on center. Meanwhile, similar simulations with confinement reinforcement comprised of No.3 closed stirrups show an increase of tensile stresses by as much as 165% regardless of the spacing of the confinement rebar.

Figure 4-34 shows the trend of the lateral stress changes around the central strand conforming to confinement reinforcement. It can be observed that the upper and lower levels of tensile stresses are enveloped between the zero confinement and closely spaced (3.00 in. on center) confinement reinforcement as expected.

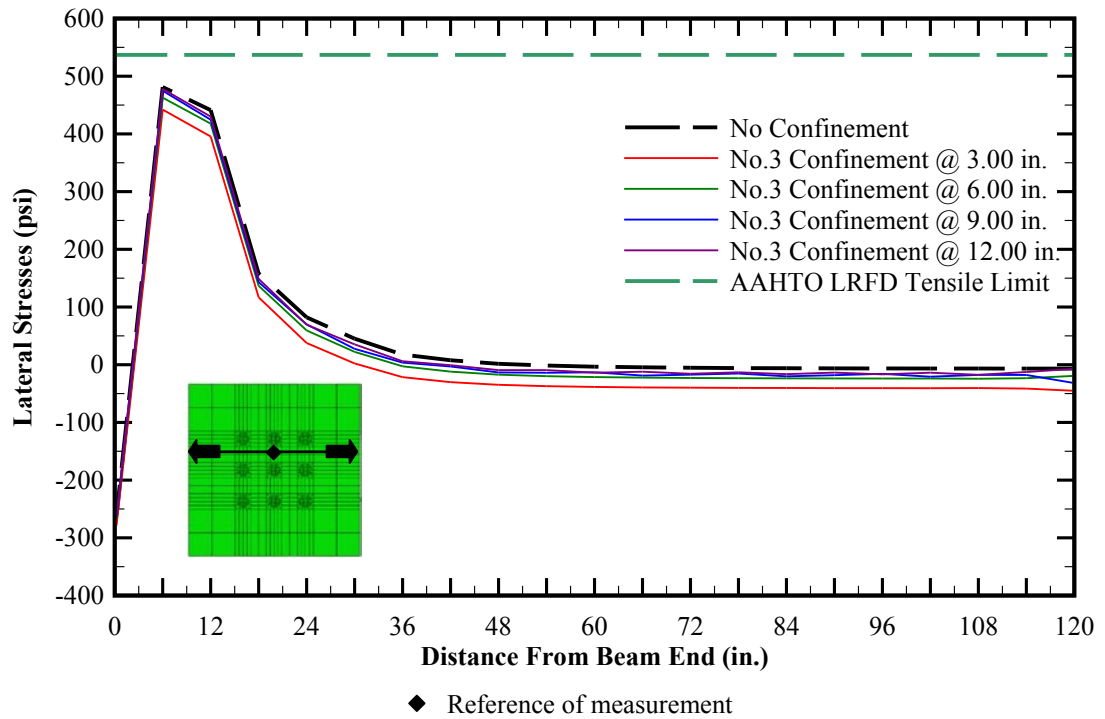


Figure 4-34: The effect of confinement on the lateral stresses obtained by Class II (nine 0.7-in. diameter strands spaced at 2.00 in. on center) with contact friction coefficient $\mu_f = 1.40$.

Figure 4-35 shows the comparison of maximum principal stresses obtained by Class I and Class II finite element models confined with No.3 closed stirrups spaced at 3 in. on center. Consistent with the previous results, the analytical results indicate that the state of tension may be significantly affected (increased) as the strands spacing is reduced from 2.80 in. to 2.00 in. Nevertheless, the anticipated changes of the tensile stresses are well below the allowable tensile limit recommended by AASHTO LRFD (AASHTO LRFD, 2010).

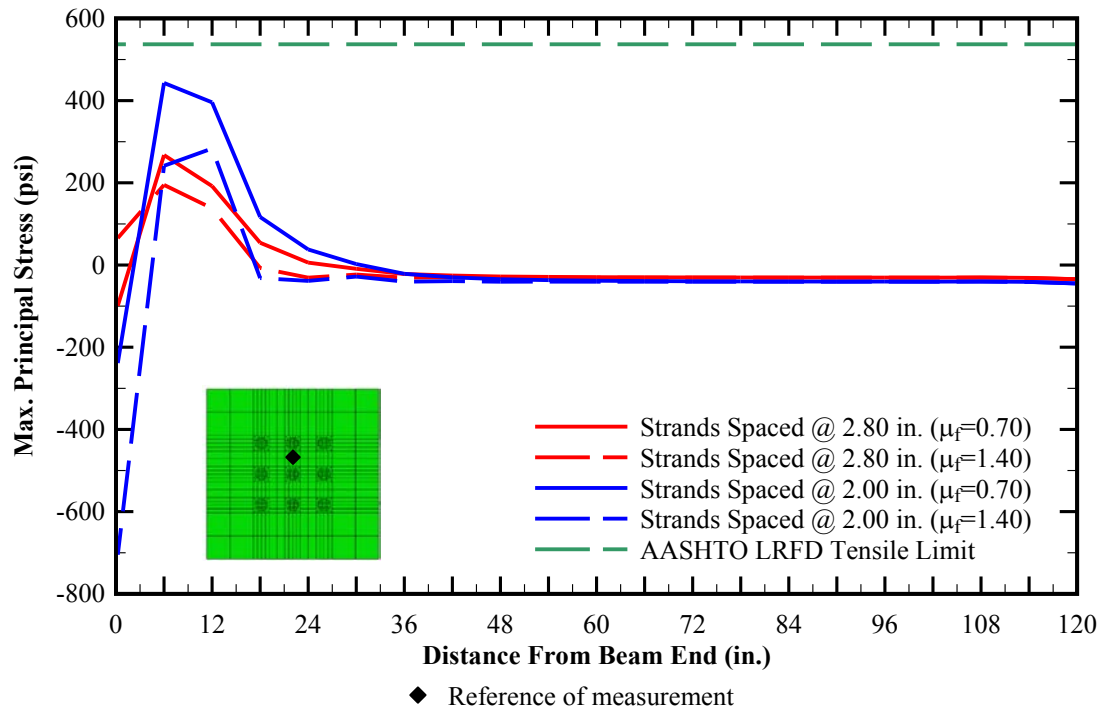


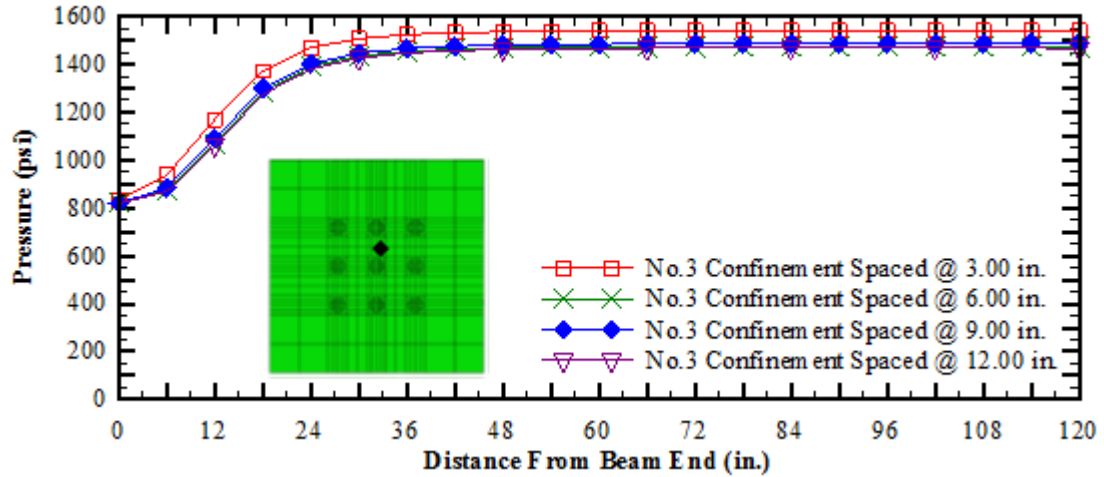
Figure 4-35: Comparison of maximum principal stresses obtained by Class I (nine 0.7-in. diameter strands spaced at 2.80 in. on center) and Class II (nine 0.7-in. diameter strands spaced at 2.00 in. on center) confined with No.3 closed stirrups spaced at 3 in. on center.

As previously discussed in Section 3.2.4, pressure is deviatoric characteristics of material, which is numerically defined as the average of lateral (S11), vertical (S22) and axial (S33) stress components at the point within the material matrix. The positive sign of deviatoric pressure indicates overall state of pressure. Under the state of positive pressure (compression) below the compressive strength of concrete (elastic regime), further compaction of cement paste within the concrete matrix is anticipated to be maintained.

Figure 4-36 and Figure 4-37 show the state of pressure around the central strand in response to the pretensioning release for Class I and Class II finite element models with upper boundary of strand slippage (minimum contact friction coefficient of $\mu_f = 0.70$), respectively. As it can be observed, the reduction of strands spacing from 2.800 in. to

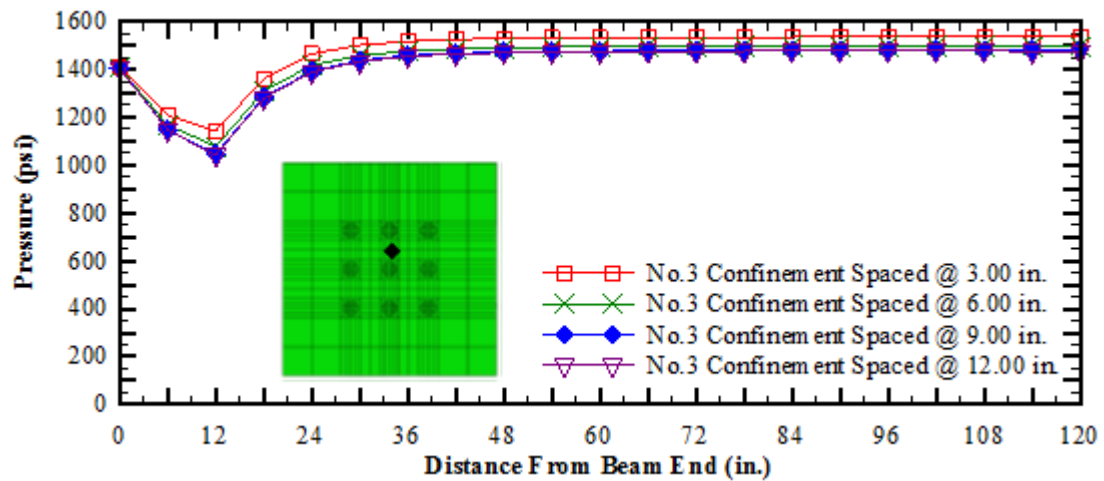
2.00 in. on center significantly improves the state of pressure within 24 in. from the beam end. Figure 4-36 indicates a smooth increase of pressure distribution starting from the lowest values at end face of the member towards maximum linearization near 42 in. from the member end face. Meanwhile, Figure 4-37 indicates as the strands are placed at closer spacing, the trend of pressure distribution becomes completely different. The end face of the member experiences high level of pressure close to the maximum values. Moving towards linearization near 42 in. from the end face, the region experiences a notable concave trend of decrease-increase of pressure.

It is important to note that the analytical results indicate that an overall state of compression (while varying in magnitude) is maintained around the central strands regardless of the spacing of the strands group. Meanwhile, the strands spacing is observed to result in notable alteration to the trend of pressure distribution along the end segments of the members. While pressure is not generally used as a design parameter in the current practice, it is an important elastoplastic measure of material dilation and volumetric changes. In general, areas experiencing moderate levels of pressure maintained below the compressive strength of concrete are less prone to tensile cracking due to sustained compaction of the cement around the aggregates.



◆ Reference of measurement

Figure 4-36: Comparison of pressure obtained by Class I (nine 0.7-in. diameter strands spaced at 2.80 in. on center) with various configuration of confinement reinforcement and upper slippage boundary ($\mu_f = 0.70$).



◆ Reference of measurement

Figure 4-37: Comparison of pressure obtained by Class II (nine 0.7-in. diameter strands spaced at 2.00 in. on center) with various configuration of confinement reinforcement and upper slippage boundary ($\mu_f = 0.70$).

Figure 4-38 (a) and (b) show the lateral stress (S11) contours obtained by Class I measured at the end face of the members with lower ($\mu_f = 0.70$) and upper ($\mu_f = 1.40$) contact friction coefficients, respectively. It is observed when strands are spaced at 2.80 in. on center, areas of high tensile and compressive stresses are localized in the vicinity of all the strands. Such high levels of stresses are anticipated at the interface between the strands and concrete host due to Poisson's effect in combination with the numerical convergence of the contact formulation used for the simulation purposes of this research. At lower levels of strands slippage ($\mu_f = 0.70$), the stress concentrations are more pronounced. Nevertheless, the zone under investigation (the mid-space of the central strand and the adjacent strands) remains either at neutral state (zero stress) or withstands moderate levels of tensile or compressive stresses well below the limits of the current state of practice.

Figure 4-38 (c) and (d) shows similar results obtained by Class II models. Analytical comparison of results corresponding to lower and upper levels of slippage indicate that closer spacing of the strands (2.00 in. versus 2.80 in.) does not significantly affect the state of stresses immediately around the strands. Figure 4-38 (c) shows moderate increase in the tensile stresses in the zone under investigation (the mid-space of the central strand and the adjacent strands) at upper boundary of slippage ($\mu_f = 0.70$). Meanwhile, Figure 4-38 (d) indicates larger compressive stresses in the corresponding zone at lower slippage boundary ($\mu_f = 1.40$).

Figure 4-39 (a), (b), (c) and (d) show lateral stress (S11) contours similar to Figure 4-38 but measured 6 in. from the end face of the specimens, where the significant difference in responses by Class I and Class II models are observed in reference to Figure

4-30. Comparative analysis of the results indicates that the zone under investigation (the mid-space of the central strand and the adjacent strands) may experience significant increase of the tensile stresses as the strands are spaced closer than four times the strand diameter. In addition, the slippage of the strands is observed to have a pronounced effect on the imposed stresses. Lower levels of slippage corresponding to higher contact friction coefficient of $\mu_f = 1.40$ results in relatively steeper pretensioning path along the anticipated transfer length as discussed in Section 4.3.4. Therefore, Figure 4-39 (d) shows upper levels of tensile stress increase as the spacing of the strands is decreased from 2.80 in. to 2.00 in. It is also observed that as the spacing of the strands reduces, the trend of increase in the tensile stresses around the central strand changes as follows: the zones near both sides of the central strand show significant increase of the tensile stresses while the zones above and below it show moderate increases as the top of the fibers of the member experience significant increase in the tensile stresses well above the allowable limit of AASHTO LRFD. Comparison of Figure 4-39 (b) and (d) more clearly indicates such behavioral differences affected by the spacing and group effects of the strands. Further experimental verification of this phenomenon is required in order to ensure that this observation is a behavioral characteristic of the continuum response.

As previously discussed, the analytical studies of this chapter are based on linear-elastic behavior of concrete. Thus, the over-stressed areas are identified within the gray-shaded zones, within which cracking of the member is anticipated. As indicated in Figure 4-39 (d), pockets of areas with tensile stresses over the allowable tensile limits by AASHTO LRFD (see Equation (4.40)) are concentrated adjacent to the central strand.

Similar magnitude and distribution of stresses are observed regardless of the reduction of the strand spacing from 2.80 in. to 2.00 in.

Figure 4-40 and Figure 4-41 show the vertical stress (S22) contours similar to Figure 4-38 and Figure 4-39 measured at beam end face and 6 in. from the end face, respectively. Due to the symmetric configuration of strands and applied pretensioning while ignoring the effect of the self-weight (refer to Section 4.4.1 for the related discussion), it is anticipated that the zones around the central strand experience vertical stresses (S22) similar to vertical lateral stressing (also refer to Figure 4-30 through Figure 4-33). Variation of the responses correlating to lateral (S11) and vertical (S22) stresses is contributed to the mathematical boundary conditions (restraints against lateral and vertical translations) imposed on the lower edge of the member end faces. Therefore, the observations regarding the lateral stresses (S11) can be accordingly extended to vertical axis of the specimens.

Figure 4-42 and Figure 4-43 show longitudinal stress (S33) contours similar to lateral and vertical stress components, measured at the beam end face and 6 in. from the end face of the specimens, respectively. As anticipated, the longitudinal component of the pretensioning imposes compression in both classes of the specimens and regardless of strands spacing. The effect of the strands group is observed to affect the transfer length and the slope of the pretensioning path. The analytical comparison of the responses by Class I (nine 0.7-in. diameter strands spaced at 2.80 in. on center) versus Class I (nine 0.7-in. diameter strands spaced at 2.00 in. on center) indicates faster rate of pretensioning transfer from the strands to the concrete. In addition, it is observed that as the contact becomes more enhanced (less slippage; higher value of contact friction) at the interface

between concrete and strand, the rate of pretensioning transfer increases. This observation is consistent with the previous discussion presented in Section 4.3.4.

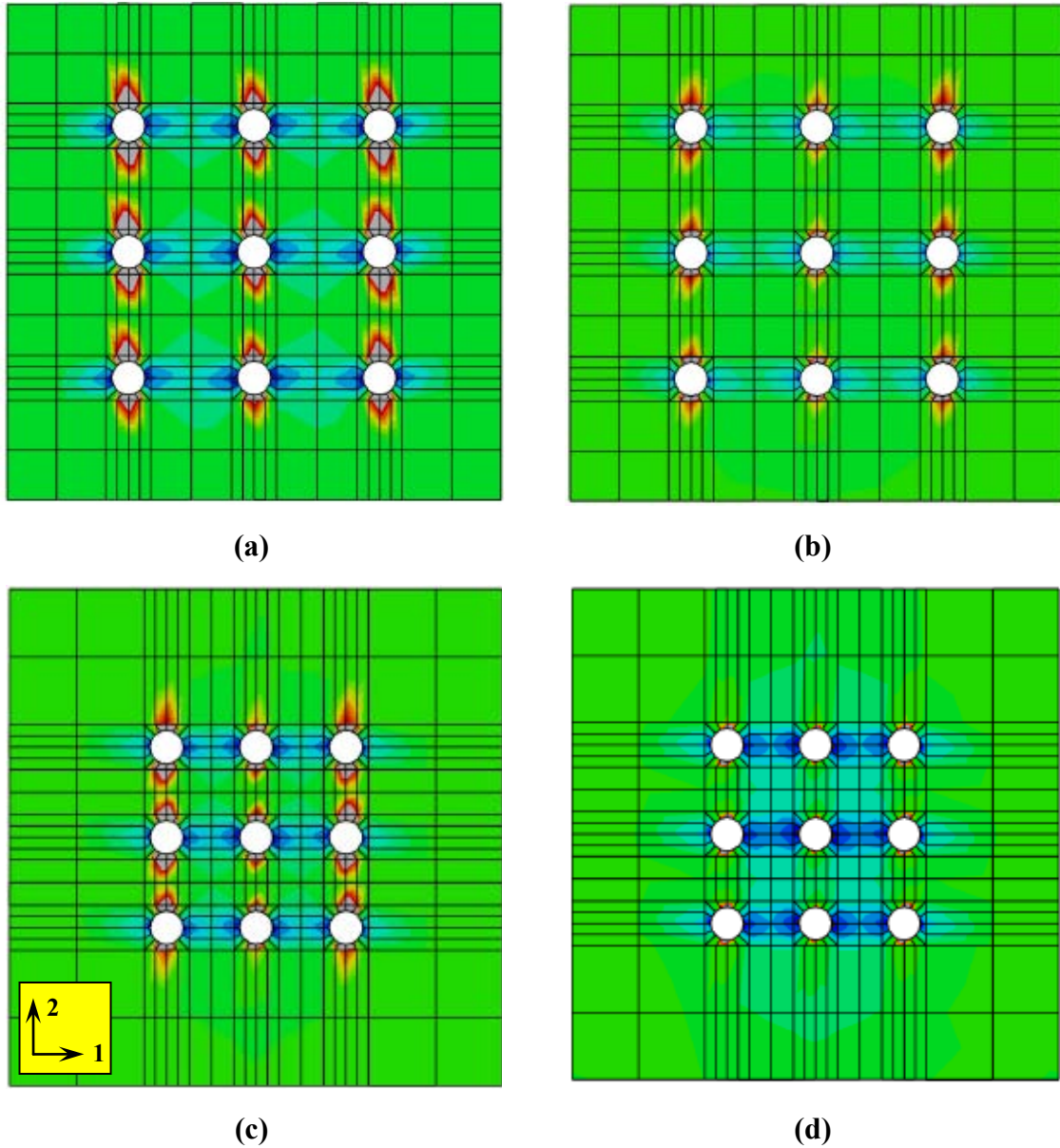
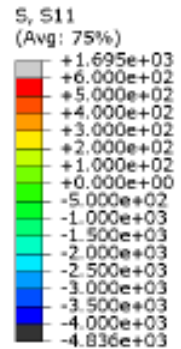


Figure 4-38: lateral stress (S11) contour at the end face of the specimens: (a) Class I Model (nine 0.7-in. diameter strands spaced at 2.80 in. on center) with contact friction coefficient of $\mu_f = 0.70$, (b) Class I Model (nine 0.7-in. diameter strands spaced at 2.80 in. on center) with contact friction coefficient of $\mu_f = 1.40$, (c) Class II Model (nine 0.7-in. diameter strands spaced at 2.00 in. on center) with contact friction coefficient of $\mu_f = 0.70$, and (d) Class II Model (nine 0.7-in. diameter strands spaced at 2.00 in. on center) with contact friction coefficient of $\mu_f = 1.40$.

Note: Stresses are reported in psi. Positive stress indicates state of tension; negative stress indicates state of compression.



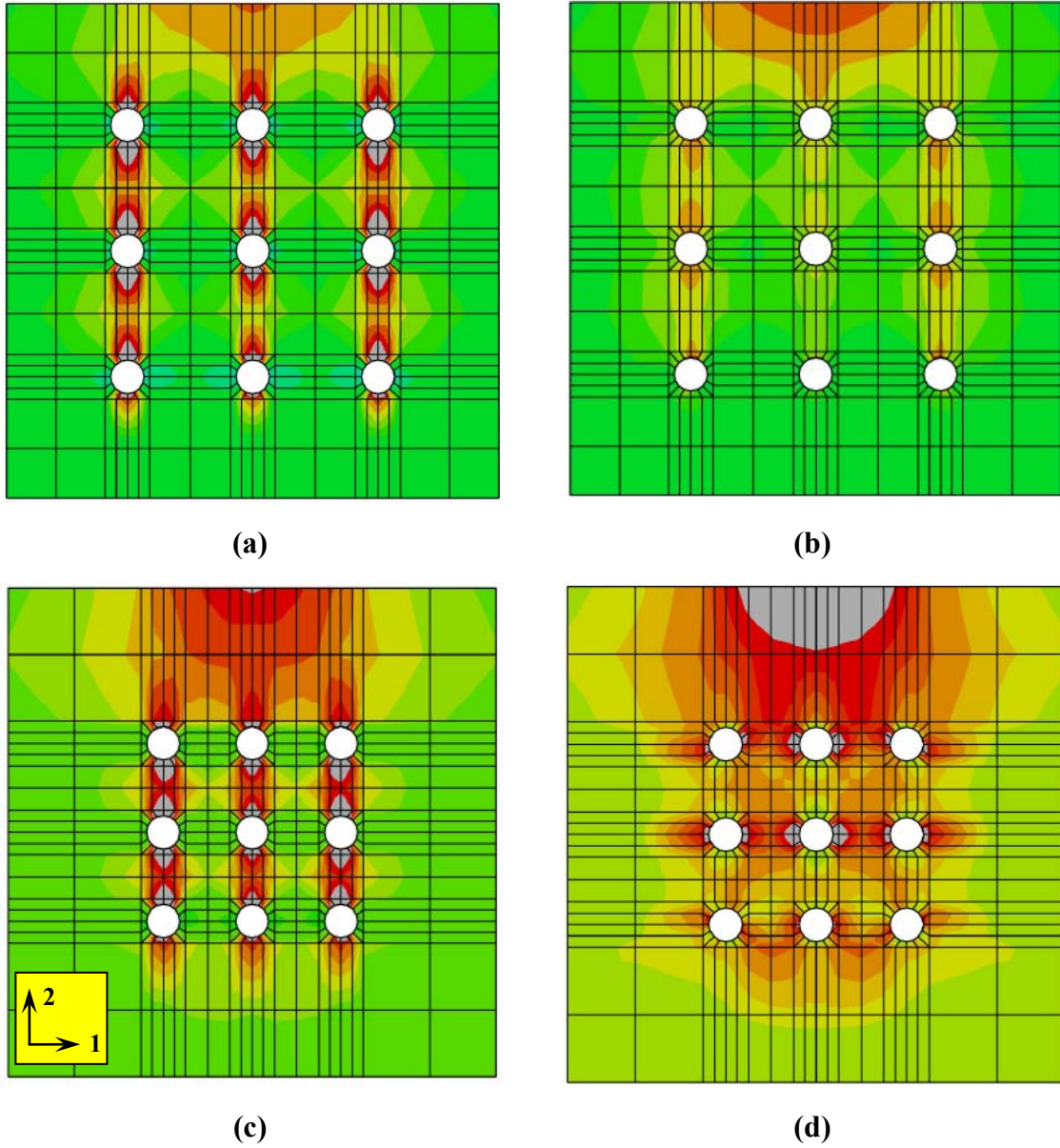
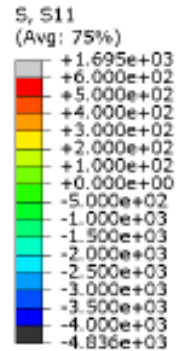


Figure 4-39: Lateral stress (S11.) contour at 6 in. from the end face of the specimens: (a) Class I Model (nine 0.7-in. diameter strands spaced at 2.80 in. on center) with contact friction coefficient of $\mu_f = 0.70$, (b) Class I Model (nine 0.7-in. diameter strands spaced at 2.80 in. on center) with contact friction coefficient of $\mu_f = 1.40$, (c) Class II Model (nine 0.7-in. diameter strands spaced at 2.00 in. on center) with contact friction coefficient of $\mu_f = 0.70$, and (d) Class II Model (nine 0.7-in. diameter strands spaced at 2.00 in. on center) with contact friction coefficient of $\mu_f = 1.40$.

Note: Stresses are reported in psi. Positive stress indicates state of tension; negative stress indicates state of compression.



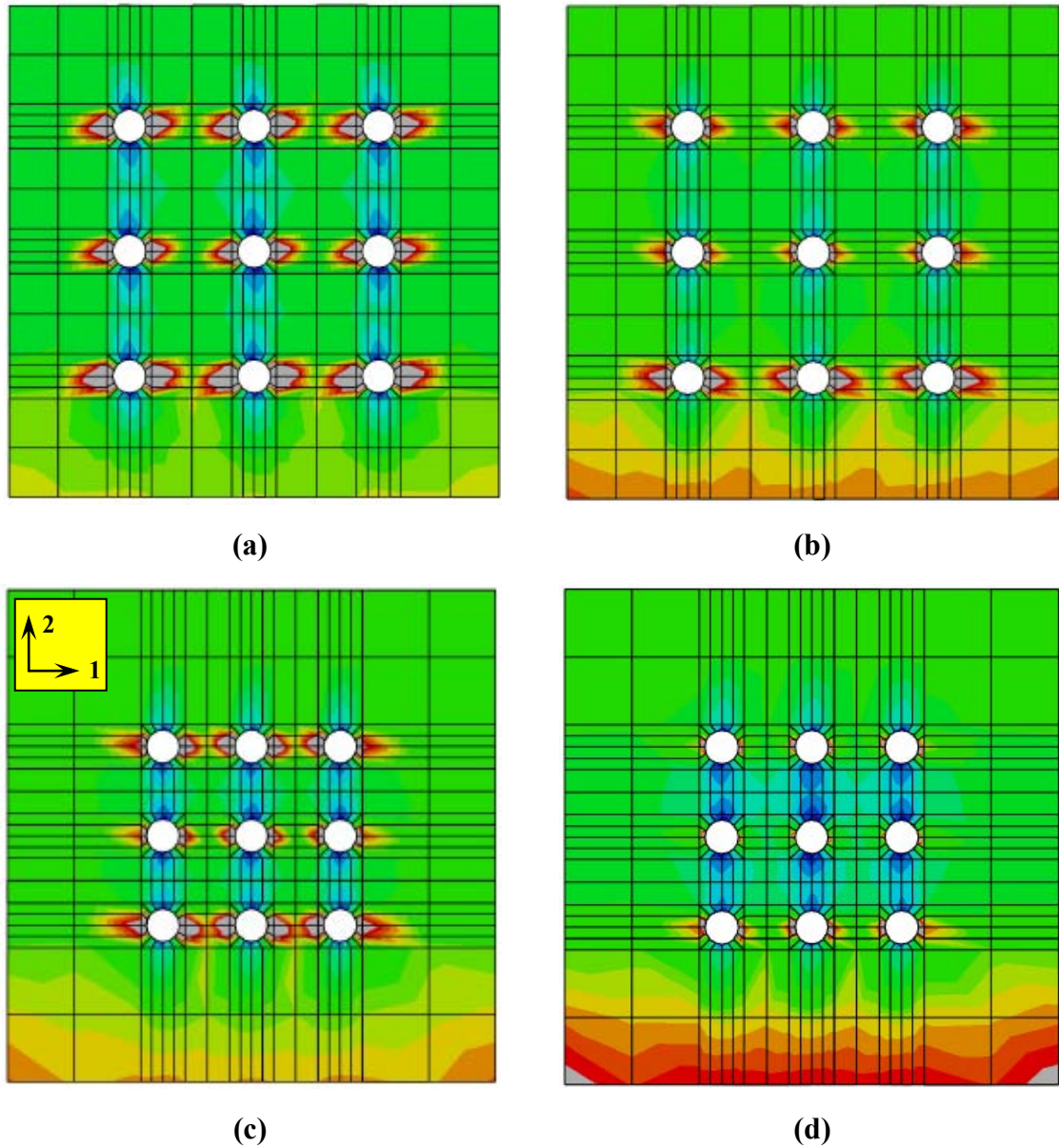
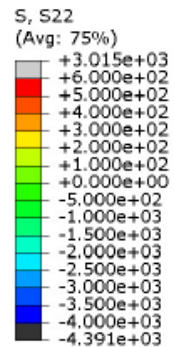


Figure 4-40: Vertical stress (S_{22}) contour at the end face of the specimens: (a) Class I Model (nine 0.7-in. diameter strands spaced at 2.80 in. on center) with contact friction coefficient of $\mu_f = 0.70$, (b) Class I Model (nine 0.7-in. diameter strands spaced at 2.80 in. on center) with contact friction coefficient of $\mu_f = 1.40$, (c) Class II Model (nine 0.7-in. diameter strands spaced at 2.00 in. on center) with contact friction coefficient of $\mu_f = 0.70$, and (d) Class II Model (nine 0.7-in. diameter strands spaced at 2.00 in. on center) with contact friction coefficient of $\mu_f = 1.40$.

Note: Stresses are reported in psi. Positive stress indicates state of tension; negative stress indicates state of compression.



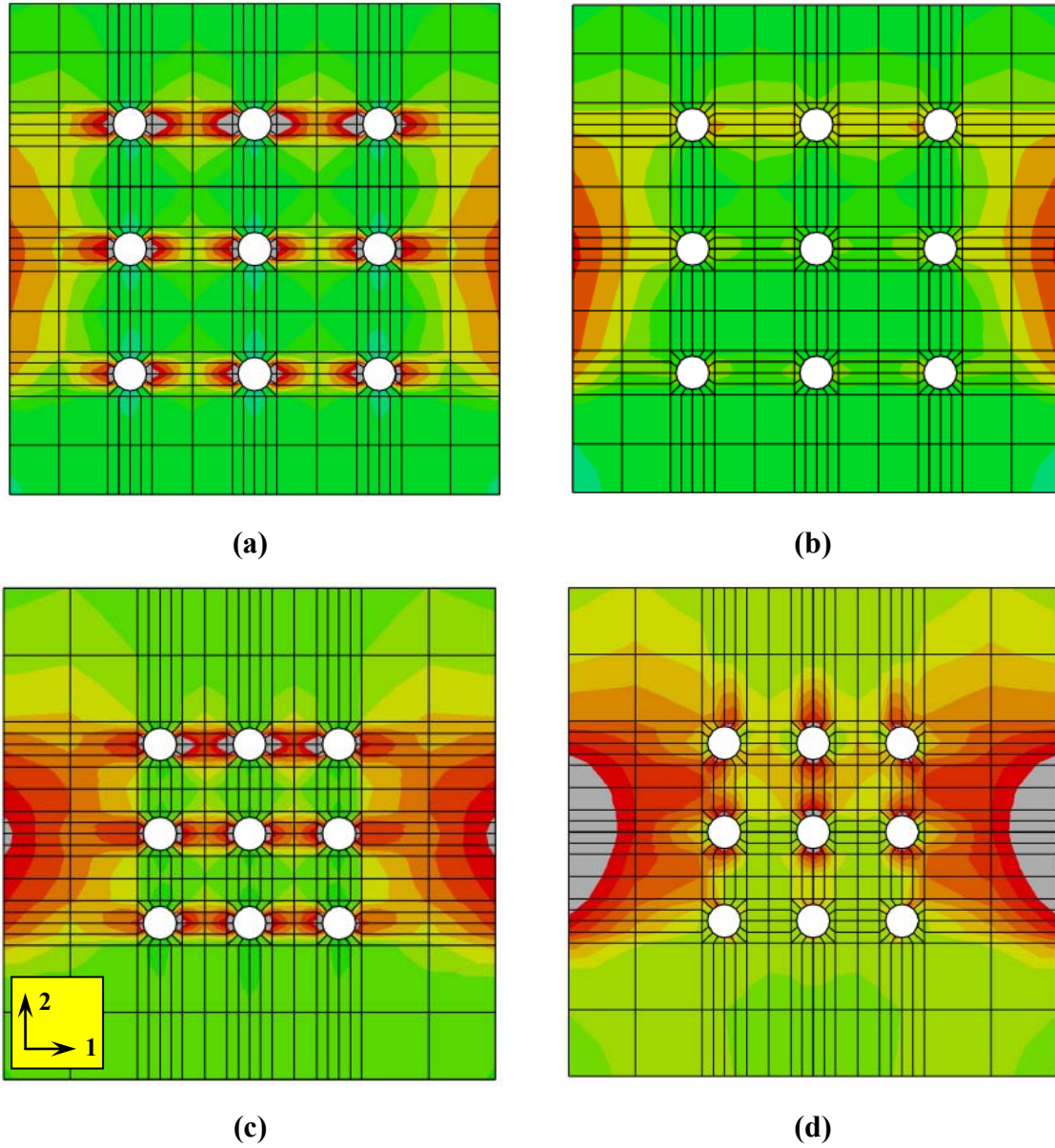
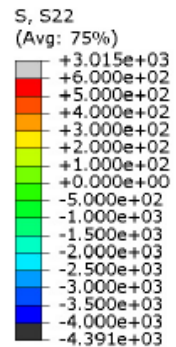


Figure 4-41: Vertical stress (S_{22}) contour at 6 in. from the end face of the specimens: (a) Class I Model (nine 0.7-in. diameter strands spaced at 2.80 in. on center) with contact friction coefficient of $\mu_f = 0.70$, (b) Class I Model (nine 0.7-in. diameter strands spaced at 2.80 in. on center) with contact friction coefficient of $\mu_f = 1.40$, (c) Class II Model (nine 0.7-in. diameter strands spaced at 2.00 in. on center) with contact friction coefficient of $\mu_f = 0.70$, and (d) Class II Model (nine 0.7-in. diameter strands spaced at 2.00 in. on center) with contact friction coefficient of $\mu_f = 1.40$.

Note: Stresses are reported in psi. Positive stress indicates state of tension; negative stress indicates state of compression.



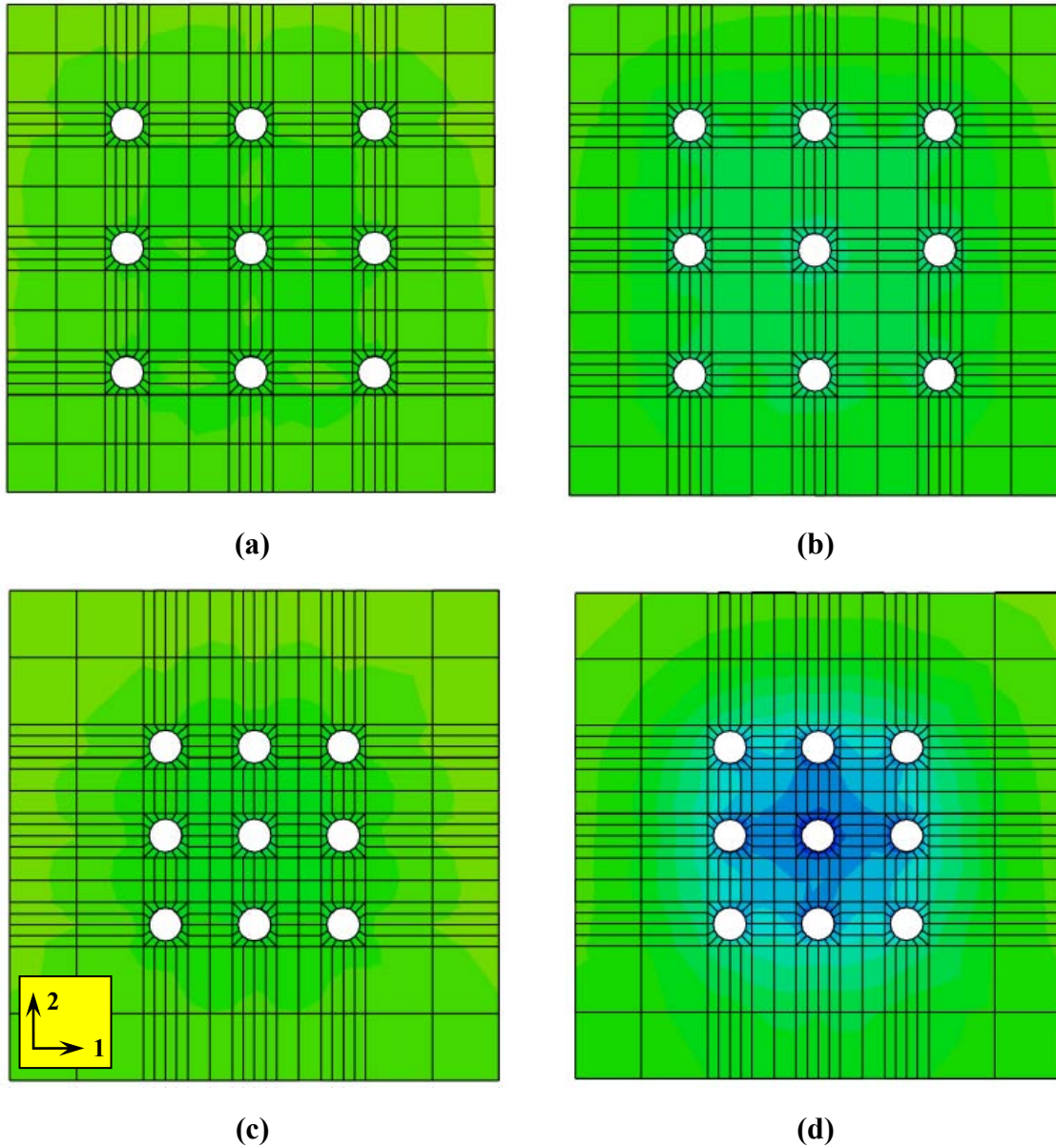
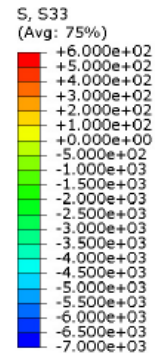


Figure 4-42: Longitudinal stress (S33) contour at the end face of the specimens: (a) Class I Model (nine 0.7-in. diameter strands spaced at 2.80 in. on center) with contact friction coefficient of $\mu_f = 0.70$, (b) Class I Model (nine 0.7-in. diameter strands spaced at 2.80 in. on center) with contact friction coefficient of $\mu_f = 1.40$, (c) Class II Model (nine 0.7-in. diameter strands spaced at 2.00 in. on center) with contact friction coefficient of $\mu_f = 0.70$, and (d) Class II Model (nine 0.7-in. diameter strands spaced at 2.00 in. on center) with contact friction coefficient of $\mu_f = 1.40$.

Note: Stresses are reported in psi. Positive stress indicates state of tension; negative stress indicates state of compression.



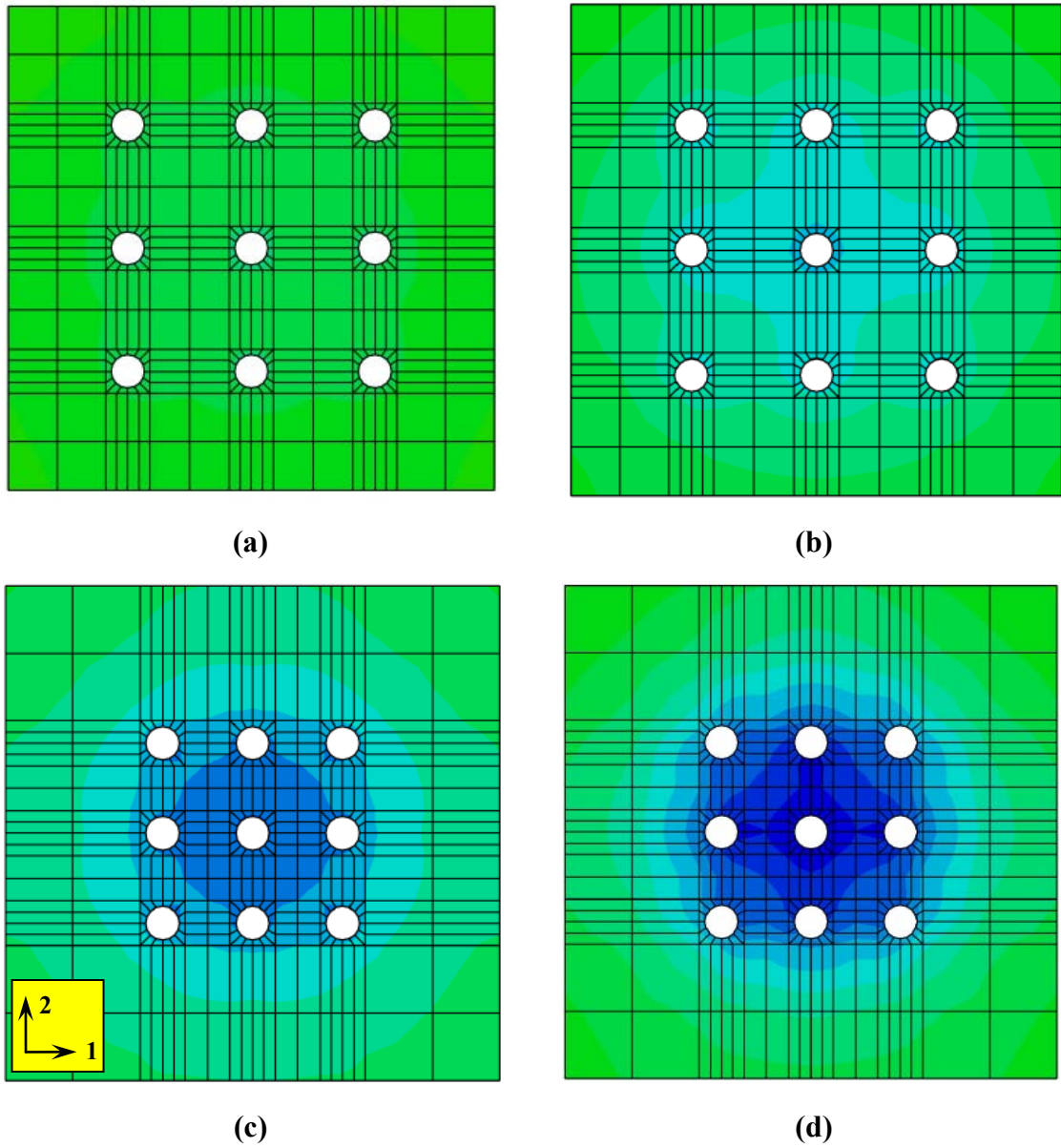
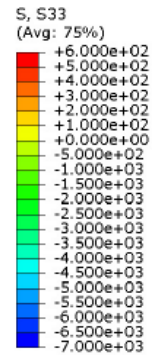


Figure 4-43: Longitudinal stress (S33) contour at 6 in. from the end face of the specimens: (a) Class I Model (nine 0.7-in. diameter strands spaced at 2.80 in. on center) with contact friction coefficient of $\mu_f = 0.70$, (b) Class I Model (nine 0.7-in. diameter strands spaced at 2.80 in. on center) with contact friction coefficient of $\mu_f = 1.40$, (c) Class II Model (nine 0.7-in. diameter strands spaced at 2.00 in. on center) with contact friction coefficient of $\mu_f = 0.70$, and (d) Class II Model (nine 0.7-in. diameter strands spaced at 2.00 in. on center) with contact friction coefficient of $\mu_f = 1.40$.

Note: Stresses are reported in psi. Positive stress indicates state of tension; negative stress indicates state of compression.



The analytical results indicate that the spacing of confinement reinforcement does not have significant effect on the response of the specimens regardless of the strands spacing. However, non-confined members show notable differences in the magnitude of the tensile stresses imposed by the pretensioned strands. Therefore, confinement reinforcement is observed to be a critical component of the pretensioned members as required by the current state of practice.

As the spacing of the strands decreases from 2.80 in. (four times the diameter) to 2.00 in., pronounced effects are observed in the stresses around the central strand. The analytical results show a notable increase (by as much as 165% for confined members) in the tensile stresses around the central strand as the strands are spaced closer four times the strand diameter. Meanwhile, depending on the strength of the concrete at the time of pretensioning release, the corresponding increase in the tensile stresses is observed to be below the acceptable limits of the current guidelines. In other words, initial compressive strength of concrete at the time of pretensioning release is observed to be a critical parameter for using 0.7-in. diameter strands at 2.00 in. spacing which is less than the recommended four times the strand diameter. These analytical observations are consistent with the analytical and experimental observations obtained from specimens with different geometric properties and pretensioning magnitude as discussed in Section 4.2.2.

In addition to the strands spacing, quality of the interface contact between concrete and strands is also observed to have notable effects on the level of the imposed stresses along the end segment of the specimens. As previously discussed, the simulation of pretensioning is based on the extrusion technique discussed in the previous chapter,

which utilizes a friction-based contact formulation to simulate the collective effects of adhesion, Hoyer's effect and mechanical interlocking (refer to Section 0). Therefore, as the contact interaction becomes more enhanced, lesser levels of strands slippage is anticipated within the concrete matrix, resulting in faster rate of stress transfer and higher levels stresses. As shown previously in this section, the analytical results are also observed to be in conformance with the above anticipation.

Chapter 5 - End Zone Cracking

5.1. Introduction

The past experience indicates that cracks frequently appear at the end regions of the prestressed members upon releasing of the strands. This phenomenon is particularly more severe for the members with narrow stems such as precast pretensioned concrete (PPC) I-girders. In some cases, the magnitude of the cracks imposed on the PPC members during the construction is such that the overall serviceability of the member may be compromised, resulting reduced service life (Koyuncu, Birgul, Ahlborn, & Aktan, 2003).

The high tensile stresses which are developed at the end faces of the PPC members (i.e., outside face of the web of I-girders) is the main cause of the horizontal cracks within the end regions.

During the past decade, significant advances have been achieved towards the academic and practical knowledge about the end zone cracking of PPC members supported by extensive research as well as the awareness of Fabricators. However, end zone cracking remains one of the main issues with fabrication of pretensioned concrete. In recent years, this problem has gained even more attention as the concept of Super-Girders has entered the routine practice of bridge engineers. Many states such as Nebraska and Washington have developed state-specific Super-Girders as well. With the introduction of high performance concrete in combination with the matured experience of local Fabricators, it is anticipated that Super-Girders will sooner or later become part of the widespread practice of bridge engineering throughout the U.S. Meanwhile, lack of experimental data , variety of the properties and details from state to state pose a

significant need for reliable analytical tools to complement cost-prohibited experimental data collection.

Chapter 3 of this dissertation included proposals for two general methodologies applicable to finite element modeling of pretensioned concrete members. As part of model verification, the analytical models were compared with the closed form solutions (such as beam theory) used in current practice. Subsequently, in Chapter 4 the adequacy and reliability of the finite element simulations were verified against experimental data based a series of parametric studies of pretensioned [mono-strand] concrete prisms previously performed by Akhnoukh (Akhnoukh, 2008).

The following chapter includes a detail analysis of finite element model of an AASHTO-PCI bulb-tee girder based on a design example included in PCI Bridge Design Handbook (PCI, 2003). The main objectives of this chapter are as follows:

1. To further show the applicability and reliability of the proposed methodologies for finite element simulation of a sample bulb-tee girder widely used in the practice of bridge engineering throughout the U.S., and
2. To perform an analytical comparison of four detailing schemes to address the problem of end zone cracking based on:
 - a) Current AASHTO LRFD recommendations
 - b) NCHRP Report 654 recommendations based on the experiments performed at the University of Nebraska-Lincoln
 - c) Current practice by Illinois Department of Transportation (IDOT)
 - d) Proposed combination of AASHTO-LRFD and IDOT details

5.2. Literature Review

Prestressed concrete was first introduced by the French Engineer Eugene Freyssinet in 1930's (Nilson, 1987). Introduction of prestressed concrete to the construction industry further facilitated the use of high strength concrete and steel. Since the introduction of prestressed concrete to the U.S. bridge industry in the 1950's, pretensioned concrete girders have offered cost-effective and low-maintenance solutions for increasing transportation needs.

While precast prestressed concrete members offer many advantages to other comparable structural members such as steel girders, they poses some challenges on design and fabrication. End zone cracking is one of the most challenging issues that designers as well as fabricators have been dealing with since the advent of pretensioning technology. The use of high strength concrete and larger diameter strands has eased the way for loner spans with slimmer cross-sections in the last two decades. While longitudinal web cracks have been one of the regular features of pretensioned concrete girder during the fabrication process, the use of high strength concrete in combination with larger magnitude of pretensioning and deeper member cross-sections have made the end zone cracking more prevalent due to more widespread and in some cases larger tensile cracks initiating at the release of the prestressed strands (Tadros, Badie, & Tuan, 2010).

Marshall and Mattock reported the problem of end zone cracking in 1960's (Marshall & Mattock, 1962). They had observed horizontal cracks in the end of the prestressed concrete I-beams on numerous occasions. The cracks were consistently observed near the centroidal axis of the member as well as the interface of the web and the bottom flange. At the time, the end zone cracking was contributed to the smaller horizontal

cross-sections of the concrete resisting the vertical tensile forces at the release. Further, Marshall and Mattock concluded that the end zone cracks were primarily initiated due to the concentration of the pretensioning forces immediately after the release of the prestressed strands. However, they would not likely widen or lengthen during the service life of the member since only minimal increase of tensile straining of the strands was anticipated after the application of the service loads.

The research by Tadros et. al. emphasized on the frequency of the cracks in the end zone of the modern prestressed concrete members at the time of release of pretensioning (Tadors, Tuan, Yehia, & Jongpitaksseel, 2004). Similar to the earlier observations by Marshall and Mattock, relatively narrow webs of I-girders and inverted-tee beams were identified to be susceptible to cracking along the height of the web and/or the interface of the web and bottom flange upon the release of the prestressed strands.

Figure 5-1 shows typical end zone cracking patterns in the modern pretensioned concrete I-girders. Figure 5-1 (a) shows the schematic patterns of end zone cracks commonly observed in the precast prestressed girders in state of Virginia (Crispino, Cousins, & Roberts-Wollmann, Anchorage Zone Design for Pretensioned Precast Bulb-T Bridge Girders in Virginia, 2009). Figure 5-1 (b) shows the typical bursting and spalling cracks observed in one of the production AASHTO Type VI girders included in the Galveston Causeway Expansion Project in state of Texas (O'Callaghan & Bayrak, 2008). The common practice requires that end cracks up to width of 0.01 in. shall be epoxy injected. Larger width of cracks and/or excessive number of end zone cracks may constitute rejection of the production girders. Section 5.2.1 includes the definition of the bursting and spalling cracks as related to end zone cracking of pretensioned members.

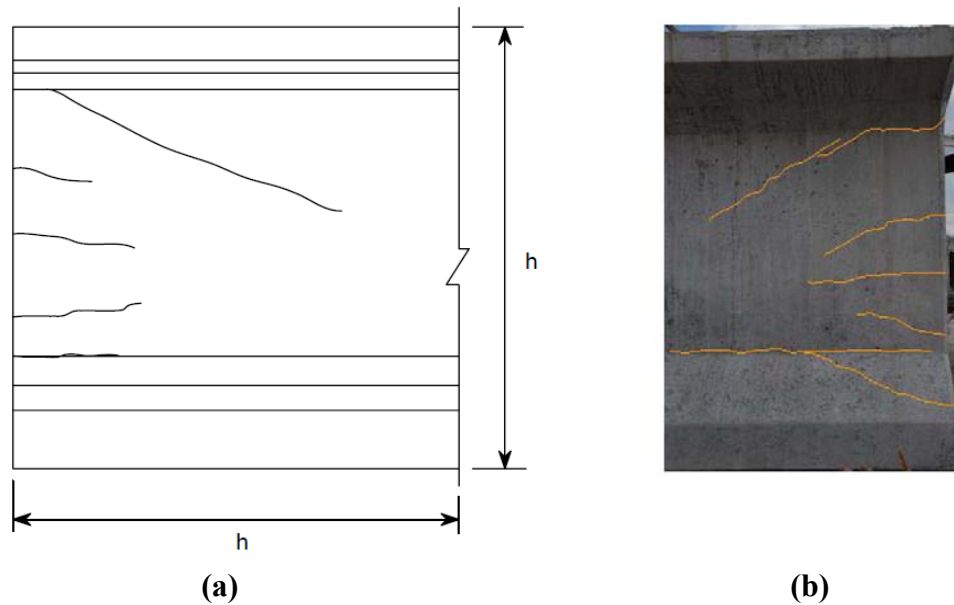


Figure 5-1: Typical end zone cracking in the modern precast pretensioned concrete I-girders: (a) Common patterns of end zone cracks observed in the precast prestressed girders in state of Virginia (Crispino, Cousins, & Roberts-Wollmann, Anchorage Zone Design for Pretensioned Precast Bulb-T Bridge Girders in Virginia, 2009), and (b) Typical bursting and spalling cracks in a production AASHTO Type VI girder included in the Galveston Causeway Expansion Project, Texas (O'Callaghan & Bayrak, 2008).

NCHRP Report 654 indicates several factors contributing to end zone cracking as summarized below (Tadros, Badie, & Tuan, 2010):

- *Methods of detensioning:* Flame cutting and hydraulic release are common methods of release of prestressed strands. Flame cutting requires individual release of the prestensioned strands, which may result in uneven internal forces in the member. This is further intensified if an optimized order of release of strands is not adequately developed. On the other hand, hydraulic releasing of the strands facilitates slow and gradual detensioning of the strands.
- *Release of the top straight and draped strands before the bottom straight strands:* Generally the top straight strands (if any) and the draped strands are released prior to detensioning of the straight strands in the bottom flange.

This process is anticipated to create tension in the bottom flange through stretching of the member. The restraints imposed by the casting bed such as surface friction may eventually cause vertical cracks at the bottom flanges.

- *Length of the free strands in the casting bed:* This phenomenon is also attributed to flame cutting technique during which individual strands are detensioned sequentially. Once a strand is released, the member experiences elastic shortening. During this stage, the remaining uncut strands shall stretch in order to accommodate the compressive straining of the member. Previous researches indicate that the shorter the length of the free strand is between member end face and the prestressing abutment, the lesser the corresponding effect will be.
- *Surface friction at the interface between the casting bed and the bottom face of the bottom flange:* As previously discussed above, the surface friction may develop at the interface between the girder and the bed. Consequently, if the casting bed is not properly oiled, frictional resistance can restrain the member against straining imposed by detensioning of the strands, which can result in vertical cracks in the bottom flange.
- *Concentration of heat during flame cutting:* Another adverse effect of flame cutting is sudden release of the strands due to concentration of excessive heat. Therefore, it is generally recommended that strands be heated over a long enough distance to allow for slow elongation.
- *Lifting of the girders off the casting bed:* Generally a centroidal eccentricity exists between the strands group and the concrete host. If so, the member will

camber up upon the release of pretensioned strands. The girders are then lifted from the casting bed to be shipped to the casting yard or the job site. The lifting points depend on the member length as much as 15 to 20 ft from the member end face. As it will be discussed in Chapter 6, some Precasters also prefer to lift the girders from the casting bed prior to the release of the straight strands in the bottom flange. This is primarily intended to break bond between the girder and bed, preventing surface friction from imposing unwanted restraints on the girder.

Lifting of the girders, either prior or after the release of all the strands, will impose new support conditions on the member, causing negative moments and stress reversals at the flanges due to prestressing force as well as the member self-weight. Past experience indicates that lifting of the girders may contribute to widening of the end zone cracks in addition to new downward diagonal cracks in the upper portion of the web.

- *Hoyer's effect:* In reference to discussion of Section 3.3.2, the Hoyer's effect is anticipated to project radial tensile stresses in the concrete volume. This potentially initiates radial cracks extending from the strands to the nearest concrete surface. Confinement reinforcement in the bottom flange is intended to control the potential cracking due to Hoyer's effect.
- *Inadequate strength of concrete at release:* Inadequate Initial strength of concrete is one of the trivial factors affecting the response of a member at the time of pretensioning release. As previously discussed, the compressive strength of concrete controls the flexural stiffness of the member by affecting

the modulus of elasticity. In addition, the rupture modulus is directly related to modulus of elasticity, which defines the tensile behavior of concrete at various stages of member life.

- *Distribution of strands:* Past observations indicate that members with no or fewer draped strands are susceptible to less cracking than those with larger number of draped strands. Draped strands contribute to larger bending of the section and resulting vertical stresses due to concentration of forces at the top of the web and the bottom flange.
- *Diameter and spacing of strands:* In reference to Section 4.4 of this document, the use of high strength and high performance concrete has enabled the precast industry to engage larger diameter strands at relatively smaller spacing. Therefore, members with slimmer cross-sections are expected much larger concentration of pretensioning in comparison with the previous generations. Introduction of larger diameter strands such as super-strands (0.62-in. diameter) or 0.7-in. diameter strands is anticipated to worsen the problem end zone cracking, requiring more in-depth investigation of the potential causes and remedies.

In accordance with NCHRP Report 654, strand distribution and detensioning are among the most commonly cited causes of end zone cracking (Tadros, Badie, & Tuan, 2010). However, as previously discussed in Chapter 3, the pretensioning transfer from the strands to the concrete host is a multi-parameter mechanism. Subsequently, the end zone cracking can be contributed to various factors that may individually or collectively affect the response of the member to the release of pretensioning.

5.2.1. Classification of End-Zone Tensile Cracks

In his research published in 1983, Ujil identifies three distinct classes of tensile stresses contributed to release of pretensioned strands as summarized below (Ujil, 1983):

- *Bursting*: Bursting stresses act along the axis of pretensioning while oriented orthogonal to it. Bursting stresses are maximized at a distance further away from the member end face.
- *Spalling*: Spalling stresses occur away from the axis of pretensioning and along the border of the member.
- *Splitting*: Splitting stresses are circumferential tensile reaction to the radial compressive stresses at the interface between the strand and concrete host.

Figure 5-2 shows the schematic classification of the above tensile stresses that can potentially occur in the end zone of prestressed members upon the release of pretensioned strands. Until recent years, splitting stresses were not subject of much investigation and research. However, it has become more apparent that splitting stresses significantly contribute to the end zone behavior of a member upon the release of pretensioning.

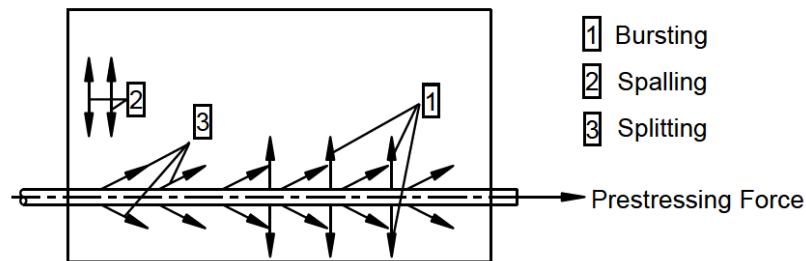


Figure 5-2: Classification of stresses contributed to end zone cracking by Ujil. Adapted from (O'Callaghan & Bayrak, 2008).

Ujil's research indicates that spalling stresses developed in the end zone of pretensioned girders are very similar to those of post-tensioned members. The research further established a relationship between the spalling stresses and the eccentricity of the pretensioning forces in respect to the centroidal axis of the member. Figure 5-3 (a) shows the relationship between the position of the maximum spalling stress and the eccentricity of pretensioning force relative to the centroidal axial of the member as derived by Ujil, where (Ujil, 1983):

- σ_0 represents the initial prestressing force including losses due to elastic shortening and relaxation of strands
- σ_{sp} represents spalling stress

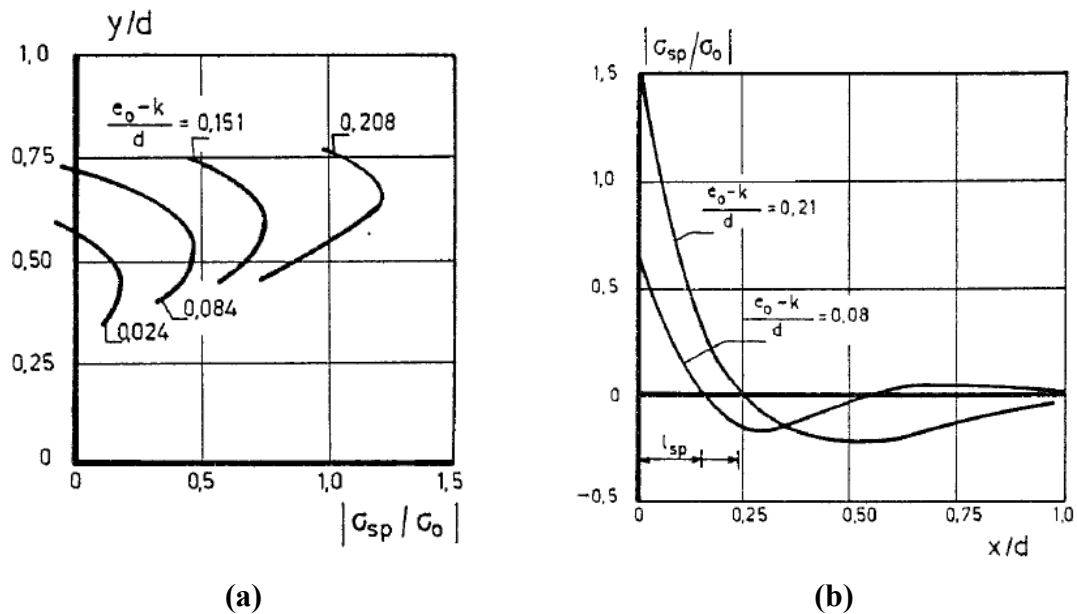


Figure 5-3: Spalling stresses: (a) Position of maximum spalling stresses along the face of the member as a function of pretensioning eccentricity, and (b) Distribution of spalling stresses along the member span, affected by eccentricity of pretensioning force. Adapted from (Ujil, 1983).

- y/d refers to the position of the spalling stress relative to the overall height of the member, and
- $\frac{e_0 - k}{d}$ indicates the relative eccentricity of the prestressing force, e_0 , in relation to the overall member height, d , where k corresponds to core radius, estimated as follows:

$$k \approx \frac{I_c}{0.5 d A_c} \quad (5.1)$$

and I_c represents the gross moment of inertia of the member.

Based on Ujil's observations, as the eccentricity of the prestressing forces increases in relationship to the centroidal axis of the member, the location of the maximum spalling stresses also moves upwards.

Figure 5-3 (b) shows the distribution of spalling stress along the span of the member, influenced by the relative eccentricity of the pretensioning force as defined above, where x/d indicates the longitudinal position of spalling stress relative to the overall height of the member, d . It can be observed that:

- i. The maximum spalling stresses are anticipated at the member end face;
- ii. As the relative eccentricity of the strand group (or pretensioning) increases, the magnitude of the spalling stresses also grows;
- iii. Spalling stresses are observed to reverse from tension to compression at a longitudinal distance from the member end face, equivalent to 25% of the overall member height ($0.25 d$), and

Spalling stresses are observed to resolve to state of neutral (zero stress) at a longitudinal distance from the member end face, equivalent to the overall height of the member ($1.0 d$).

Similarly, Ujil derives that the distribution of bursting stresses along the length of the member is directly influenced by the eccentricity of the pretensioning force relative to the centroidal axis of the member as shown in Figure 5-4 where σ_{bp} represents bursting stress. It is observed that:

- iv. The magnitude of bursting stress increases directly proportional to the relative eccentricity of the pretensioning force;
- v. At larger relative eccentricities, the bursting stress resolves faster into state of neutral (zero stress), and
- vi. Bursting stress, σ_{bp} , disappears at a longitudinal distance from the member end face, equivalent to the overall member height ($1.0 d$).

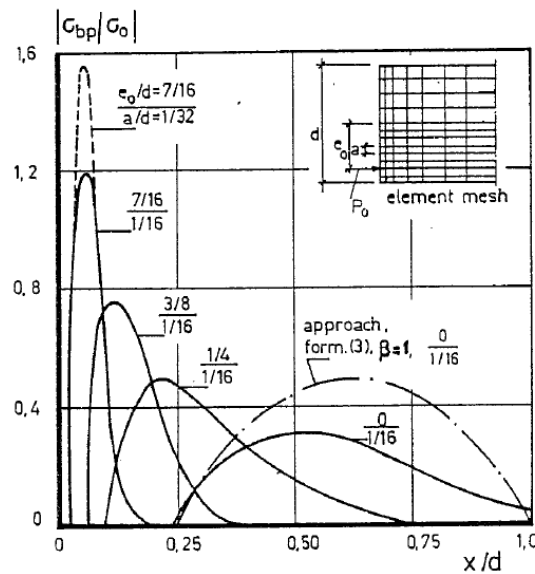


Figure 5-4: Distribution of bursting stresses along the axis of pretensioning. Adapted from (Ujil, 1983).

Figure 5-5 schematically shows the distribution of splitting stresses in the vicinity of an individual strand immediately after the release based on linear elastic material response. Note that $\sigma_{r,r}$ and $\sigma_{t,r}$ represent the radial compressive and tensile stresses, respectively, while $\sigma_{t,avg}$ indicates the average splitting stress. Finally, r_i and r_e refer to the strand diameter and the spacing of internal strands or edge distance of exterior strands, respectively.

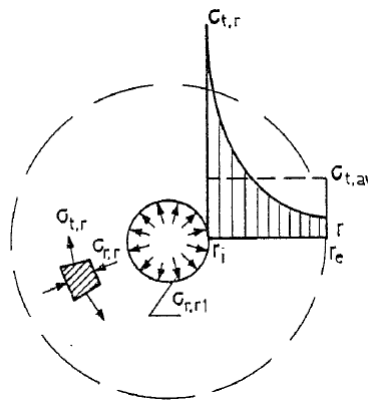


Figure 5-5: Distribution of circumferential splitting stresses based on linear-elastic material response by Ujil. Adapted from (Ujil, 1983).

Figure 5-6 shows the schematic distribution of splitting stresses along the row of prestressing strands at immediately after the release of pretensioning. The maximum splitting stresses are anticipated to occur between the strands where the stress overlap is expected due to the contribution by each strand (refer to Figure 5-5). Therefore, micro-cracks initiate in the vicinity of the strands, propagating to visible cracks extending between the strands and towards the nearest concrete surface (Ujil, 1983).

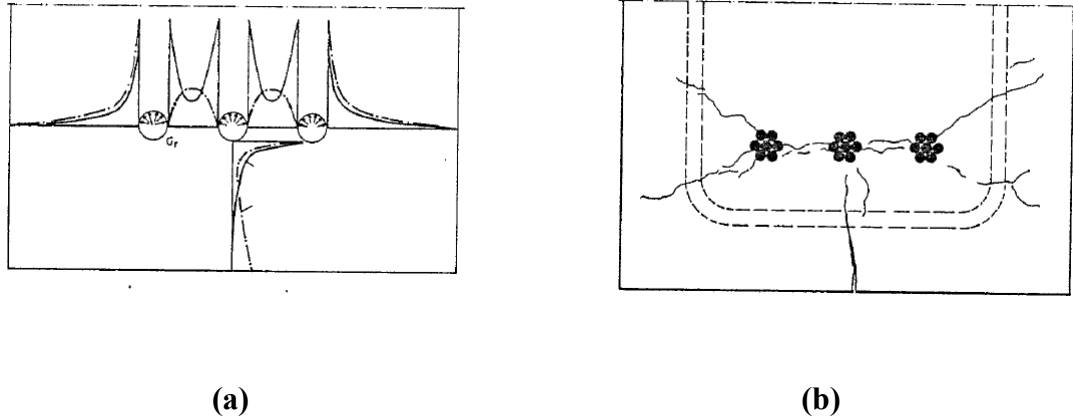


Figure 5-6: Splitting stresses: (a) Schematic distribution along a row of strands, and (b) Typical pattern of cracks due to excessive spalling stresses. Adapted from (Ujil, 1983).

The experimental investigations by Ujil indicate that some of the cracks in the bursting/splitting zone did not extend to the exterior faces of the specimens. He suggests that superposition of bursting and splitting stresses may impose state of compression on the end zone near the end face of the member as schematically shown in Figure 5-7.

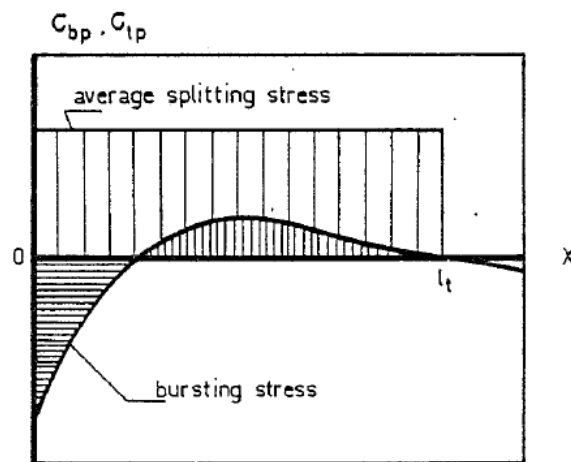


Figure 5-7: Superposition of bursting and splitting stresses near the member end face. Adapted from (Ujil, 1983).

As the result, Ujil suggests that bursting and splitting stresses cannot be clearly distinguished from one another and therefore, their effects on the member end zone may be collectively considered as follows (Ujil, 1983):

$$\sigma_{tp} = 0.05 \left(\frac{d_p}{c} \right) \sqrt{\sigma_0 f_{ci}} \dots\dots\dots \text{ Combined bursting/splitting stress} \quad (5.2)$$

where c represents the clear cover to strands, f_{ci}' indicates the initial compressive strength of concrete at the time of release, and σ_0 corresponds to the compressive stress imposed by the initial prestressing force immediately after the release defines as follows:

$$\sigma_0 = \frac{P_i}{bd} \dots\dots\dots (b \text{ corresponds to the width of the member}) \quad (5.3)$$

5.2.2. End Zone Design of Pretensioned Concrete Members

As previously mentioned, Marshall and Mattock conducted an extensive research on the end zone cracking of pretensioned concrete members in 1960's. Their investigations included examination of a number of I-girders divided into two test groups A and B as shown in Figure 5-8 through Figure 5-10. All the specimens were 10 ft long with cross-sectional heights ranging from 22-1/2" to 25" (Marshall & Mattock, 1962).

Test Group A included ten specimens, intended for measurement of concrete stresses in the member end zones at the release of pretensioning. The specimens were investigated for the effect of the following variables:

- a. Web thickness
- b. Arrangement of prestressing strands
- c. Surface condition of the prestressing strands

Test Group B included twenty five specimens which were instrumented for measurement of axial stresses developed in the vertical stirrups at the transfer length upon the release of pretensioning.

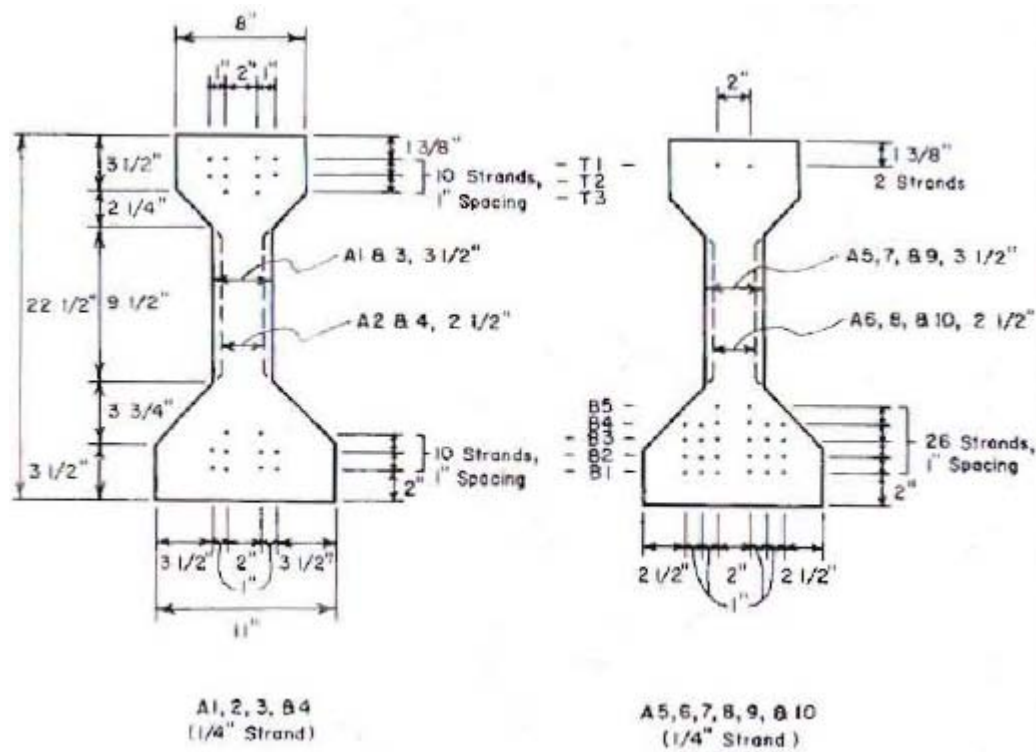


Figure 5-8: Test Group A - specimens A1 thru A14, investigated by Marshall and Mattock. Adapted from (Marshall & Mattock, 1962).

The following variables were considered in the investigation of Test Group B specimens:

- d. I-girders with two different cross-sectional properties
- e. Two different sizes of vertical stirrups
- f. Size and location of prestressing strands
- g. Different magnitude of pretensioning

The initial compressive strength of concrete at the time release ranged from 3,715 psi to 7,190 psi. The prestressing strands used for the purposes of the research included:

- h. 1/4-in. diameter strands with ultimate tensile strength of 280 ksi
- i. 3/8-in. diameter strands with ultimate tensile strength of 286 ksi
- j. 1/2-in. diameter strands with ultimate tensile strength of 254 ksi

Investigation of Test Group A specimens indicated that the maximum vertical tensile stresses occurred near the mid-height of web near the end face of the member. Moving away from the girder end face, the tensile stresses disappeared. Marshall and Mattock then concluded that the vertical stirrups for control of end zone cracking were the most effective if placed as close as practically possible to the member end face.

Among the twenty five Test Group B specimens, seven did not crack and four showed cracking away from the end zone area. Consequently, only fourteen specimens were considered for data collection and other analytical purposes. All fourteen specimens showed similar responded to the release of pretensioning including tensile cracking in the lower segment of the web near centroidal axis of the members. The width of cracks was observed to range from 0.001 in. to 0.004 in., extending 2 in. to 4 in. away from the girders end face. Based on the rupture modulus of concrete, Marshall and Mattock assumed the following strain of concrete as the potential extent of tensile cracking (Marshall & Mattock, 1962):

$$\begin{aligned}
 \varepsilon_c &= f_{ri} / E_{ci} && (5.4) \\
 &= 7.5 \sqrt{f'_{ci} \text{ (psi)}} / 60,000 \sqrt{f'_{ci}} \\
 &= 125 \text{ micro in./in.}
 \end{aligned}$$

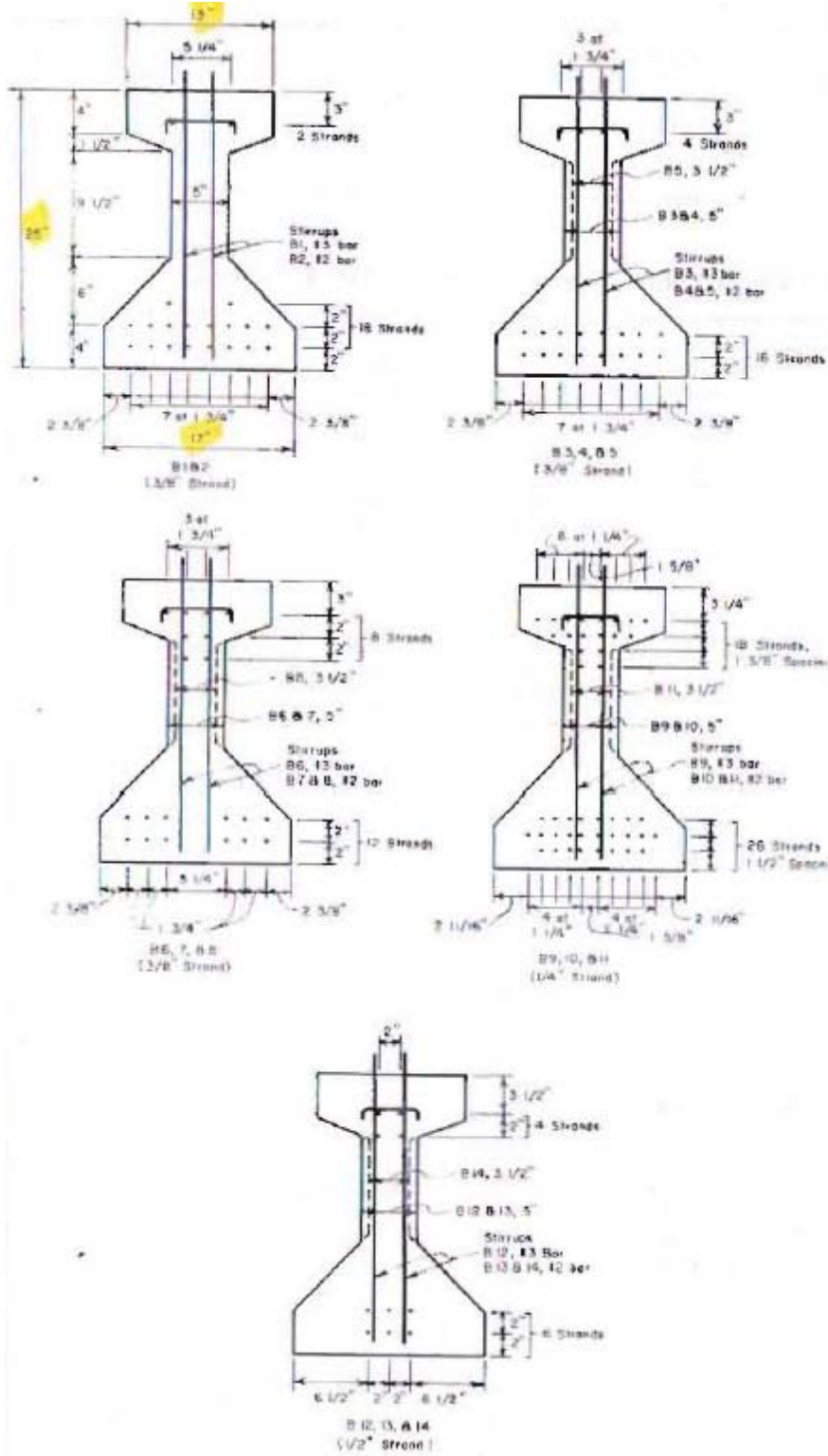


Figure 5-9: Test Group B, specimens B1 thru B14, investigated by Marshall and Mattock. Adapted from (Marshall & Mattock, 1962).

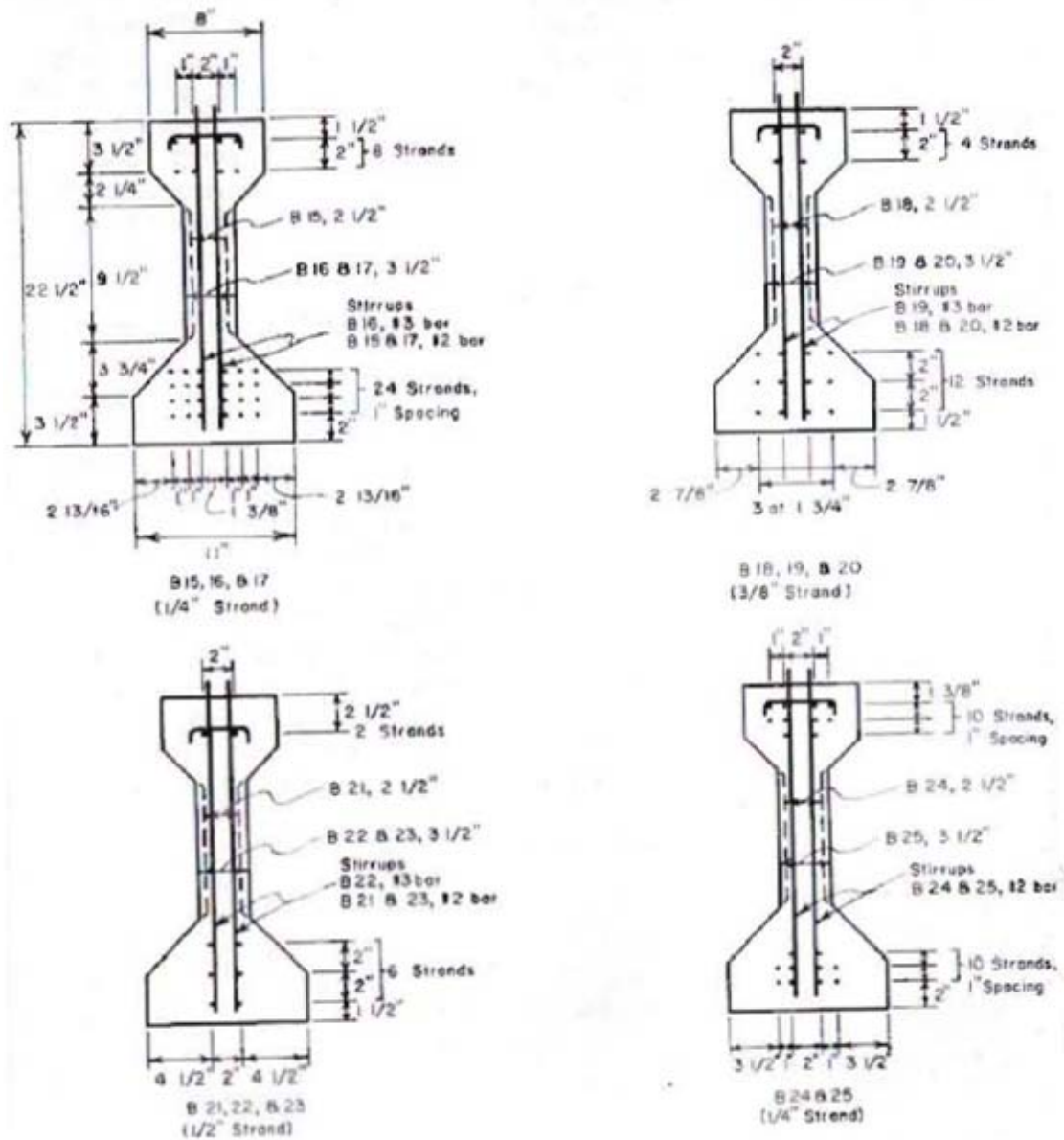


Figure 5-10: Test Group B, specimens B15 thru B25, investigated by Marshall and Mattock. Adapted from (Marshall & Mattock, 1962).

The experimental results by Marshall and Mattock indicated at given member cross-sections, the magnitude of the vertical stresses in the end zone vertical stirrups at the time of release was a function of transfer length and prestressing force as follows:

$$A_{EZR} = 0.021 \left(\frac{P_i}{f_{sm}} \frac{h}{L_t} \right) . \quad (5.5)$$

where A_{EZR} is the total cross-sectional area of vertical stirrups within the end zone; P_i represents initial prestressing force; h is the overall member height; f_{sm} refers to the service stress in the end zone rebar upon the release of pretensioning, and L_t indicates the transfer length.

Equation (5.5) was deemed accurate for girders that met the condition of $h/L_t \leq 2$ while yielding conservative results for members with $h/L_t > 2$ (Tadors, Tuan, Yehia, & Jongpitaksseel, 2004). This conclusion forms the basis for the current AASHTO LRFD specifications which require that end zone reinforcement be capable of withstanding at least 4% of the applied pretensioning while not exceeding allowable service stress of 20 ksi upon the release of the prestressed strands (AASHTO LRFD, 2010).

In addition to the closed-form approach by AASHTO LRFD to end zone design of pretensioned concrete members, other analytical methods are available. Finite element analysis is one of the alternatives that is the main focus of this research. Besides, Gergley-Sozen model and Strut-and-Tie truss analogy are among the most commonly methods of approximating the response of member end zone to pretensioning release.

5.2.2.1. Gergley-Sozen Model

Gergley-Sozen model is based on a linear-elastic approach of analyzing the equilibrium conditions of the cracked end zone upon the release of pretensioning. Figure 5-11 shows the typical equilibrium model based on Gergley-Sozen approach where c represents the height from the bottom flange to the potential end zone crack, and L indicates the distance required for resolution of the moment (M) due to pretensioning

eccentricity (e) into tension (T) and compression (C) couples. Moment (M) is mathematically derived as follows (Gergley & Sozen, 1967):

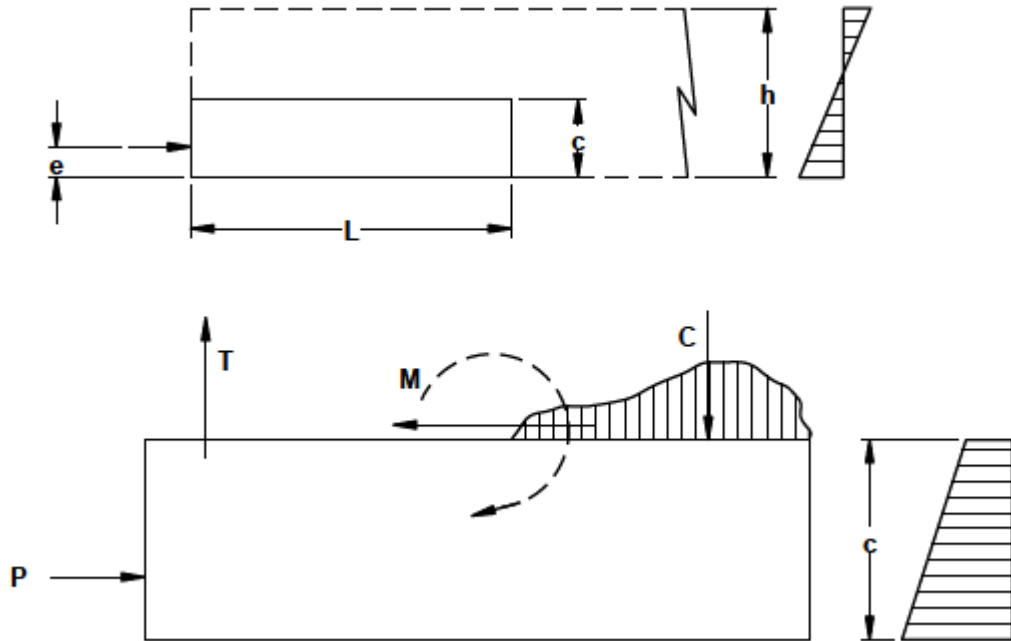


Figure 5-11: Gergley-Sozen equilibrium model. Adapted from (Gergley & Sozen, 1967).

$$M = P_i \left[c - e - \left(\frac{c}{h} \right)^2 \left(2h - 3e - c + \frac{2ec}{h} \right) \right] \quad (5.6)$$

Moment (M) is dependent on the height of the end zone crack (c) and is maximized by the following two values of c :

$$c_1 = \frac{h^2}{3(h - 2e)} \quad (5.7)$$

$$c_2 = h \quad (5.8)$$

Equation (5.9) results in the maximum moment along the height of the member while Equation (5.10) leads to zero moment on the top surface of the top flange:

$$M_{\max} = P_i \left[\frac{h^2}{27} \frac{4h - 9e}{(h - 2e)^2} - e \right]. \quad (5.9)$$

Another potential solution for Gergley-Sozen equilibrium model is to maximize the moment along the axis of pretensioning where $e = c$:

$$M_{\max,e} = 2P_i \frac{e^2}{h^3} (h - e)^2. \quad (5.10)$$

5.2.2.2. Strut-and-Tie Model

Strut-and-tie model is based on strength limit state, commonly used for the anchorage design of post-tensioned concrete members. A strut-and-tie model needs to satisfy force equilibrium rather than strain compatibility where it is assumed that concrete has cracked (no tension state) and uniform-intensity compression bands are present within the concrete continuum. Pats researches indicate that since large number possible trusses can be attributed to the same problem while strain compatibility does not have to be satisfied, strut-and-tie models generally predict the upper bound stresses at the end zones of pretensioned members (Tadors, Tuan, Yehia, & Jongpitaksseel, 2004).

In a typical strut-and-tie model, external forces are applied as point loads. This enables the strut-and-tie methodology to realistically approximate the stress fields within end anchorages of post-tensioned concrete members. However, in pretensioned concrete members the prestress transfer occurs through a more complex mechanism as discussed in Section 0. Nevertheless, strut-and-tie is still considered by many designers as a

practical means for approximation of tensile stresses in the end zone of pretensioned concrete girders.

Figure 5-12 shows a double-tie, strut-and-tie model developed by Crispino et. al. based on field observations of Virginia bulb-tee girders (Crispino, Cousins, & Roberts-Wollmann, Anchorage Zone Design for Pretensioned Precast Bulb-T Bridge Girders in Virginia, 2009). One of the challenges of double-tie strut-and-tie models is that upper and lower bound models are solved independently. The parametric studies by Crispino et. al. indicated that the required area of end zone reinforcement within $h/4$ from the end member end face and between $h/4$ to $3h/4$ are very similar. Therefore, the compression stress bands are positioned such that the tension ties $T1$ and $T2$ are equal. Another characteristic of Crispino's model is that the compression strut is located at a distance equivalent to $3h/4$ from the member end face as opposed to h . Equation (5.11) shows the solution of the double-tie, strut-and-tie model proposed by Crispino et. al. (Crispino, Cousins, & Roberts-Wollmann, Anchorage Zone Design for Pretensioned Precast Bulb-T Bridge Girders in Virginia, 2009):

$$T1 = T2 = \frac{8P_1 y}{7h} . \quad (5.11)$$

where y represents the vertical distance between the resultant force and applied prestress force and $P1$ and $P2$ are equivalent to the initial prestress forces P_i at straight and draped strands, respectively.

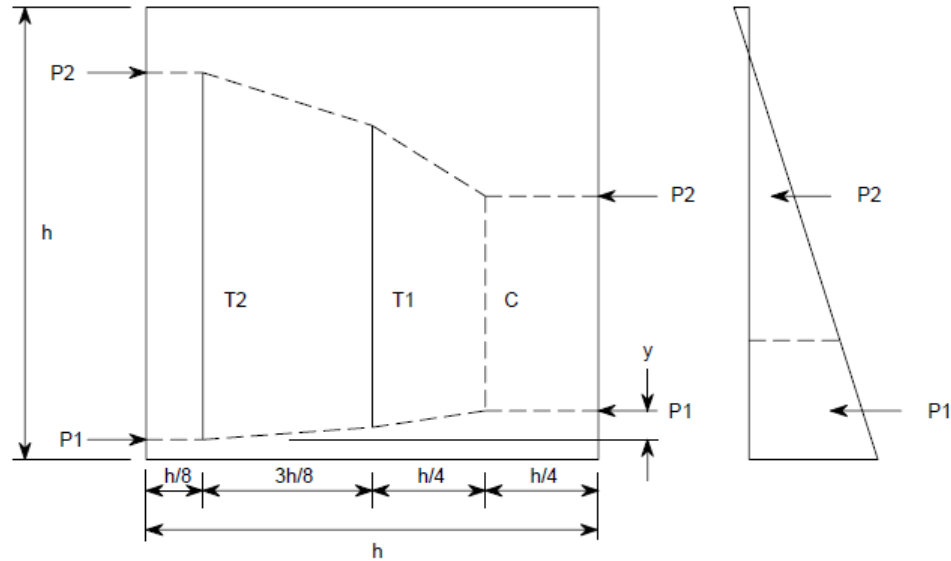


Figure 5-12: A sample double-tie, strut-and-tie model for end anchorage design of pretensioned concrete members. Adapted from (Crispino, Cousins, & Roberts-Wollmann, Anchorage Zone Design for Pretensioned Precast Bulb-T Bridge Girders in Virginia, 2009).

5.3. Problem Statement

As previously mentioned in Section 5.1, the following section includes a finite element simulation of an AASHTO/PCI Bulb-Tee girder based on Example 9.4 of PCI *Bridge Design Manual* (PCI, 2003) (PCI BDM Example 9.4). The corresponding example presents the general steps required for the design of 72-in. deep, precast pretensioned Bulb-Tee girder which will be referred to as BT-72 for the rest of this chapter. The referenced girder is designed as part of a six-girder composite superstructure system to fit a single-span of 120-ft as shown in Figure 5-13.

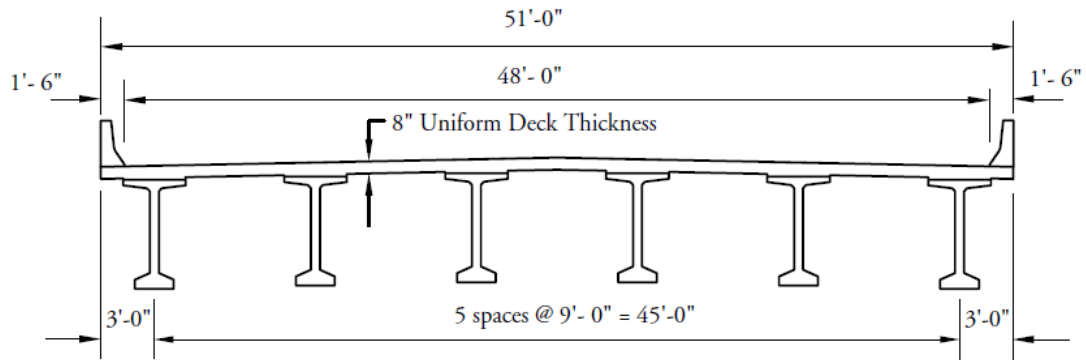


Figure 5-13: Typical bridge cross section including BT-72 Bulb-Tee girders used for finite element simulation. Adapted from *PCI Bridge Design Manual* (PCI, 2003).

In order to fulfill the objectives of this research, first a finite element model of one of the typical BT-72 bulb-tee girders will be constructed. The response of the numerical simulation to combined effects of self-weight and pretensioning will be verified in comparison with the customary closed form solutions such as beam theory. Once the validity of the finite element solutions is confirmed, the application of the proposed numerical simulations will be extended to examine the response of the members to various end zone details.

5.3.1. AASHTO/PCI Bulb-Tee

The BT-72 girder selected for the analytical purposes of this research is a typical AASHTO/PCI bulb-tee. The proposed BT-72 are designed in accordance with the AASHTO LRFD Specifications for design of highway bridges (AASHTO LRFD, 2010).

Figure 5-14 shows a typical cross section (including geometric properties) of the referenced BT-72 girder. One of the main characteristics of such girders is the relatively narrow web and top flanges in comparison with the member depth and span length.

Table 5-1 includes the basic sectional properties of the referenced BT-72. Since the main focus of this research is on the response of the member immediately after the release of pretensioning, the properties are reported at the non-composite stage of the member life.

The following includes the compressive strengths of concrete at the time of release as well as 28 days. As previously mentioned, the focus of this research is the response of the BT-72 girders to the release of pretensioning when the concrete is at the initial age of maturity:

$$f'_c = 6,500 \text{ (psi)} \dots\dots\dots \text{Compressive strength at 28 days} \quad (5.12)$$

$$f'_{ci} = 5,800 \text{ (psi)} \dots\dots\dots \text{Initial compressive strength at the} \quad (5.13)$$

release of pretensioning

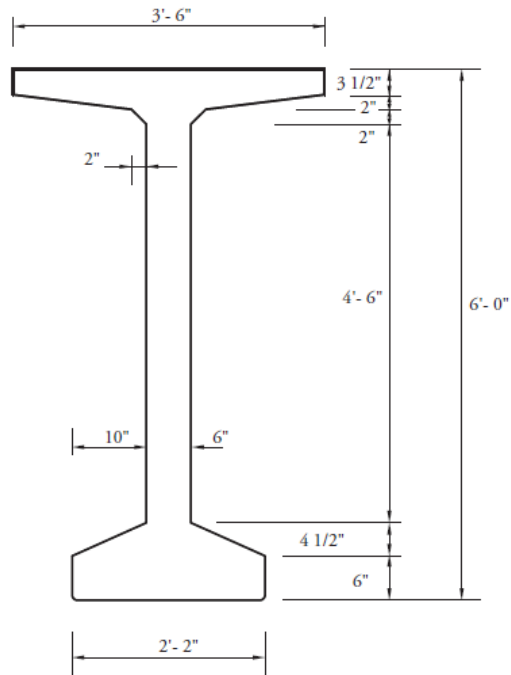


Figure 5-14: Typical AASHTO/PCI bulb-tee (BT-72) used for the analytical purposes of this research. Adapted from *PCI Bridge Design Manual* (PCI, 2003).

In accordance with the design steps presented in PCI BDM Example 9.4, forty eight 1/2-in. diameter low-relaxation, seven-wire strands are required for pretensioning of the proposed BT-72 girders in order to satisfy the applicable service and strength limit states (PCI, 2003). As shown , the top twelve strands are draped at two harping points symmetrically located from the mid-span of the girders at a distance equal to 10% of the design span (12 ft, each). The following includes the basic properties of the prestressing strands utilized for pretensioning of the proposed BT-72 girders:

$$A_p = 0.153 \text{ (in.}^2\text{)} \dots\dots\dots \text{Area of one 1/2-in. diameter} \quad (5.14)$$

prestressing strand

$$f_{pu} = 270,000 \text{ (psi)} \dots\dots\dots \text{Ultimate tensile strength of the} \quad (5.15)$$

proposed strands (each)

$$f_{py} \approx 90\% f_{pu} = 243,000 \text{ (psi)} \dots\dots\dots \text{Approximate yield strength of the} \quad (5.16)$$

strands in accordance

$$E_p = 28,500 \text{ (ksi)} \dots\dots\dots \text{Modulus of elasticity of the} \quad (5.17)$$

proposed strands

Figure 5-15 (a) shows a typical elevation of the BT-72 girders, including the longitudinal profile of the straight and draped strands. Figure 5-15 (b) and (c) show the typical cross-sections at the mid-span and end face of the girders, respectively.

Table 5-1: Basic sectional properties of the non-composite BT-72 bulb-tee (PCI, 2003).

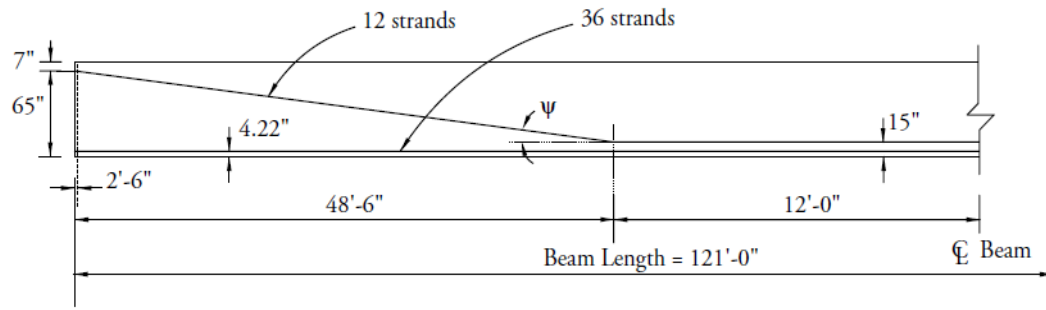
Cross-sectional area (A_{nc})	767 in. ²
Weight of the non-composite member (w_{nc})	799 lbs/ft
Non-composite moment of inert about the centroid of the member (I_{nc})	545,894 in. ⁴
Distance from the extreme bottom fiber to the centroid of the non-composite member ($y_{nc,b}$)	36.60 in.
Distance from the extreme top fiber to the centroid of the non-composite member ($y_{nc,t}$)	35.40 in.
Non-composite section modulus for the extreme bottom fiber ($S_{nc,b}$)	14,915 in. ³
Non-composite section modulus for the extreme top fiber ($S_{nc,t}$)	15,421 in. ³
Overall girder length (L_{total})	121.0 ft
Design span length (L_{span})	120.0 ft

5.3.1.1. Jacking Stresses

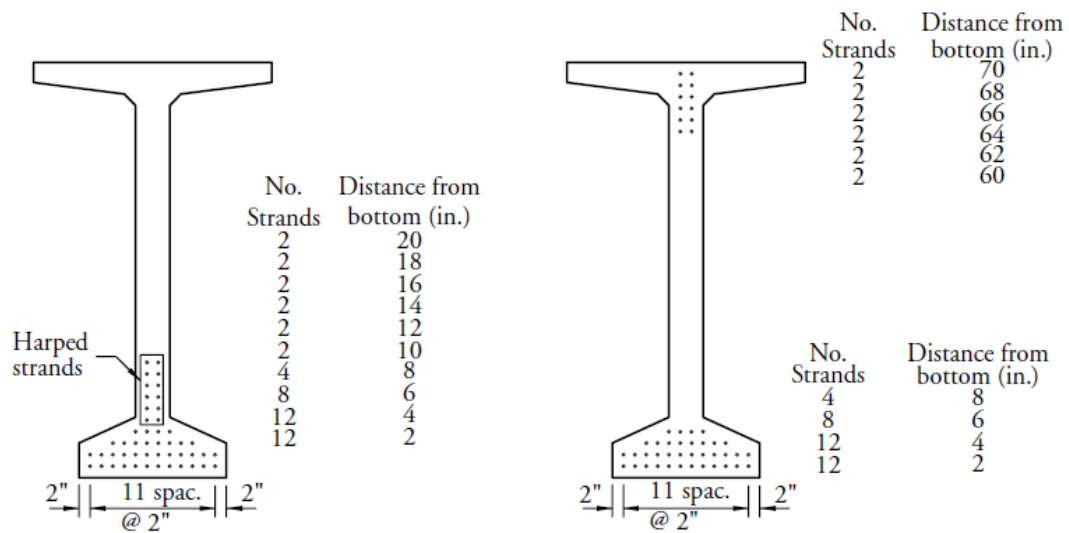
In accordance with Article 5.9.3 of AASHTO LRFD, the low-relaxation strands can be stressed up to the following threshold:

$$f_{pj} = 75\% f_{pu} = 202.5 \text{ ksi} \dots\dots\dots \text{Maximum allowable jacking stress} \quad (5.18)$$

immediately before release of
pretensioning



(a)



(b)

(c)

Figure 5-15: Typical strands patterns for the proposed AASHTO/PCI bulb-tee (BT-72) used for the analytical purposes of this research. The proposed strands are 1/2-in.diameter low-relaxation, seven-wire. Adapted from *PCI Bridge Design Manual* (PCI, 2003): (a) Typical elevation showing the configuration of the straight and draped strands as well as the location of the harping points, (b) Typical cross-section at the mid-span of the proposed BT-72 showing the straight strands, and (c) Typical cross-section at the end face of the proposed BT-72 showing the straight and draped strands.

5.3.1.2. Prestress Losses at Transfer

The applicable prestress losses immediately after the release of pretensioning are as follows:

- Losses due to relaxation of strands prior to being released
- Losses due to elastic shortening immediately after the release of the strands

For the analytical purposes of this research, the prestress losses due to relaxation of the strands prior to the release of pretensioning will be ignored in accordance with PCI BDM Example 9.4 and consistent with Article 5.9.5.1 of AASHTO LRFD (AASHTO LRFD, 2010).

The other component of the prestress losses at the transfer correlates to elastic shortening, which is estimated to be approximately 9%. The loss due to elastic shortening will be accounted for by the finite element analysis.

5.3.1.3. Top and Bottom Fiber Stresses Immediately After Release of Pretensioning

As it was previously discussed, the top and bottom fiber stresses immediately after the release of pretensioning are generally estimated based on the elastic closed-form solutions. Table 5-2 shows the summary of the top and bottom fiber stresses while PCI BDM Example 9.4 includes the corresponding computational details:

Table 5-2: BT-72 top and bottom fiber stresses at the release of prestressed strands based on elastic beam theory (PCI, 2003).

	Top Fiber Stress, σ_t (psi)	Bottom Fiber Stress, σ_b (psi)
At transfer length section	- 291	- 3276
At harp points	- 256	- 3313
At mid-span	- 301	- 3266

The current practice of designing pretensioned concrete girders is based on elastic response of uncracked members. Although the end zone of prestressed members may undergo cracking immediately after the release of pretensioning, the rest of the member is anticipated to withstand tensile and compressive stresses below the allowable limits. Therefore, the top and bottom fiber stresses of Table 5-2 are anticipated to be unaffected by end zone cracking except at those at the transfer length.

5.3.2. End Zone Reinforcement

Currently in the U.S., the design of the end zone reinforcement for the precast/prestressed concrete girders consists of three distinct steps:

Step 1 - Estimation of the bursting forces resulting in vertical tensile stresses within the end zone of the members;

Step 2 - Identifying the allowable level of the tensile stresses due to the bursting action upon the release of the pretensioned strands in order to limit the potential cracks within acceptable range, and

Step 3 - Distributing the required end zone reinforcement to conform to the tensile stress and crack width limits of Step 2.

As it will be discussed later in the following sections, the estimation of the bursting forces is generally based on 4% of the total prestressing force. As previously discussed in Section 5.2, the corresponding design limit is based on the research performed in 1960's by Marshall and Mattock, limited to prestressed girders heights ranging from 22.5 in. to 25 in. (Marshall & Mattock, 1962). With the introduction of modern prestressed girders (e.g., Super-girders), it is deemed necessary that the bursting as well as other effects such as spalling forces be revisited.

In addition to the magnitude of the bursting force, the distribution of the end zone reinforcement is another important factor which affects the response of the member and the size of the potential cracks. In the following sections, four different schemes of end zone reinforcing details are introduced all based on the bursting forces equivalent to 4% of the total pretensioning.

The current AASHTO LRFD specifications define the maximum limit of the tensile stress in the end zone reinforcement as follows:

$$f_{EZR,allowable} = 20.0 \text{ ksi} \quad (5.19)$$

As previously discussed, the tensile stresses imposed on the end zone of the pretensioned members upon the release of pretensioning are correlated to the potential cracking and subsequent crack width. The allowable tensile stress as stated by Equation (5.19) was used in the earlier research by Marshall and Mattock based on the experimental observation of end zone crack widths up to 0.004 in. (Marshall & Mattock, 1962). However, later on this section other acceptance/rejection criteria for members undergone end zone cracking will be discussed.

5.3.2.1. AASHTO LRFD Details

Article 5.10.10.1 of AASHTO LRFD states that the bursting resistance of anchorage zones of pretensioned girders ($P_{EZR,r}$) shall satisfy the following service limit state (AASHTO LRFD, 2010):

$$P_{EZR,r} \geq f_{EZR,s} A_{EZR} \quad (5.20)$$

where $f_{EZR,s}$ indicates the tensile stress of end zone rebars, A_{EZR} , immediately after the release of pretensioning at service limit state. The current state of practice limits $f_{EZR,s}$ to 20 ksi to control the crack width. In addition, A_{EZR} shall consist of vertical reinforcement to be located within a distance equivalent to 25% of the overall height of the proposed BT-72 girder as follows:

$$h_{nc}/4 = 72 \text{ in.}/4 = 18 \text{ in.} \quad (5.21)$$

In accordance with AASHTO LRFD Specifications, the bursting resistance of the pretensioned anchorage zone shall meet the following condition:

$$\begin{aligned} P_{EZR,r} &\geq 4\% f_{pj} \sum A_p \\ &= 4\% (202.5 \text{ ksi}) (48 \text{ Strands} \times 0.153 \text{ in.}^2) \\ &= 59.5 \text{ kips} \end{aligned} \quad (5.22)$$

Therefore, the following minimum reinforcement required within the 18 in. of the each end of the BT-72 girders is estimated based on the allowable tensile stress as follows:

$$\begin{aligned} A_{EZR,req'd} &\geq \frac{59.5 \text{ kips}}{f_{EZR,allowable} = 20 \text{ ksi}} \\ &= 2.97 \text{ in.}^2 \end{aligned} \quad (5.23)$$

As shown in PCI BDM Example 9.4, five double legs of No.5 vertical bars will be provided at an equal spacing of 4 in. The first rebar is located 2 in. from the member end face. Thus,

$$\begin{aligned} A_{EZR,prov'd} &= 5 \times 2 \times 0.31 \text{ in.}^2 \\ &= 3.1 \text{ in.}^2 \geq A_{EZR,req'd} \end{aligned} \quad (5.24)$$

In accordance with PCI BDM Example 9.4, double No.4 stirrups will be provided along the remaining girder length at maximum spacing of 12 in. in order to satisfy AASHTO LRFD shear requirements.

In addition to bursting reinforcement, Article 5.10.10.2 of AASHTO LRFD requires that confinement reinforcement be provided in the bottom flanges at a distance not less than 1.5 times the effective depth of the non-composite member, d_{nc} , (AASHTO LRFD, 2010). As shown in PCI BDM Example 9.4, the effective depth, d_{nc} , is usually assumed to be equal to the overall height of the non-composite member, h_{nc} . In the current design practice and fabrication of pretensioned girders, the confinement rebar consists of No.3 bars bent to fit inside the bottom flange of the member with adequate clearance from the outside faces while confining the entire strands group. AASHTO LRFD requires that the confinement reinforcement be specified at a maximum spacing of 6 in. on center.

Figure 5-16 shows typical cross-section of the BT-72 girders including the strands, end zone and confinement reinforcement. The shape of the end zone reinforcement is generally similar to shear rebar. Both end zone and shear reinforcement extend above the top flange and into the deck slab. This will provide for the composite action between the girders and slabs. The confinement reinforcement is provided at a maximum spacing of 6 in. on center for a distance of approximately 9 ft, equivalent to 1.5 times the member depth, d .

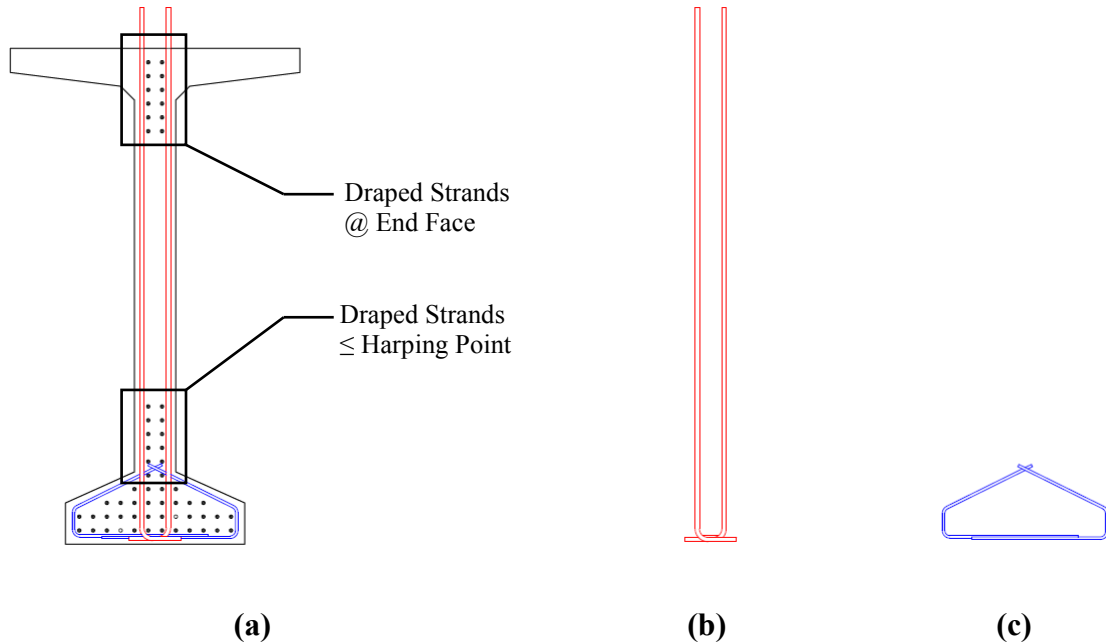


Figure 5-16: Typical cross-section of BT-72 girder: (a) Typical cross-section including the strands, end zone and confinement reinforcement, (b) Typical No.5 end zone rebar to be spaced in sets of two per design (double No.4 shear reinforcement have the same configuration), and (c) Typical No.3 confinement rebar spaced with end zone and shear reinforcement but not more than 6 in. on center.

Figure 5-17 shows the typical elevation of the BT-72 girders including the spacing of the end zone reinforcement (EZR) as well as the shear and confinement reinforcement. It can be observed that the EZR is spaced over a distance equivalent to $h_{nc}/4$ in accordance with Equation (5.22). Subsequently, the shear reinforcement (double #4 stirrups) is located at maximum spacing of 12 in. on center. In addition, the confinement reinforcement is spaced at 6 in. on center over a distance equivalent to $1.458 h_{nc}$ ($\approx 1.5 h_{nc}$) where h_{nc} corresponds to the non-composite depth of the BT-72 girder.

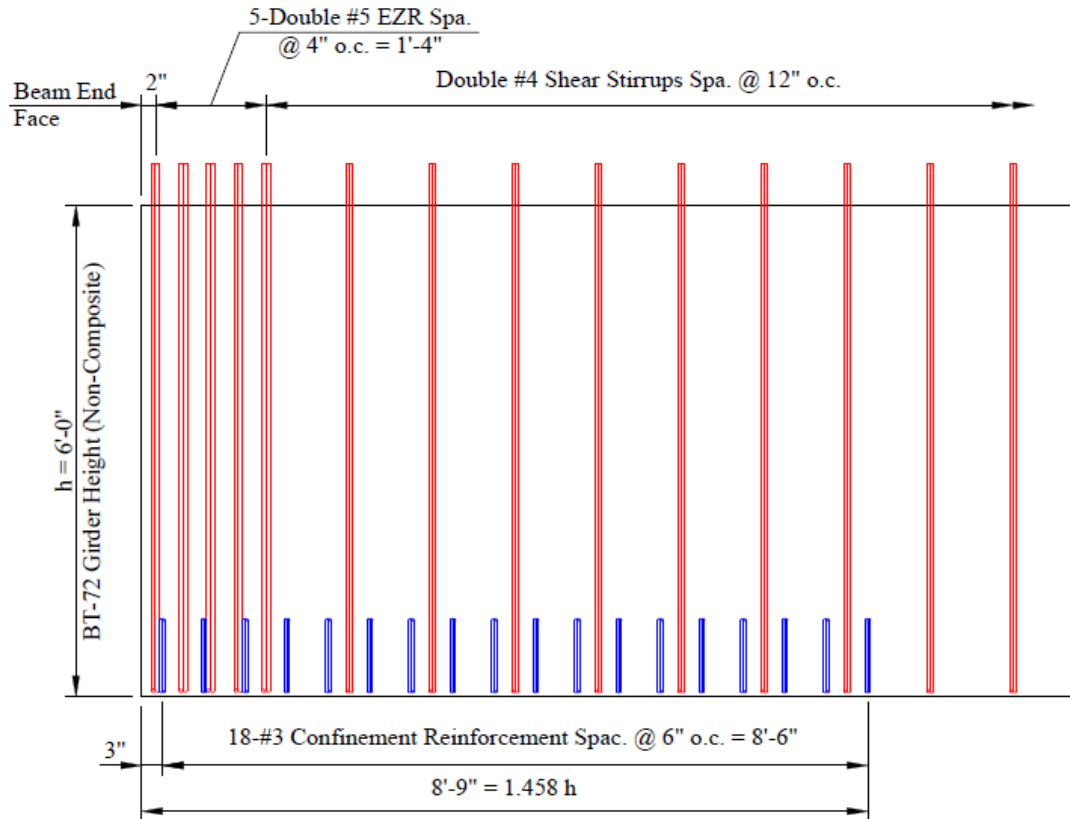


Figure 5-17: Typical elevation view of the BT-72 girders showing the spacing of the end zone reinforcement (EZR) as well as shear and confinement reinforcement in accordance with AASHTO LRFD Specifications.

5.3.2.2. Nebraska Details

The Nebraska end zone reinforcing detail is based on the recommendations by Tadros et. al. included in NCHRP Report 654 (Tadros, Badie, & Tuan, 2010). Based on the referenced research, the magnitude of bursting force and the limit of allowable tensile stress in the end zone reinforcement are similar to those specified by AASHTO LRFD. However, the experimental results indicate a very high concentration of the tensile stresses in the vicinity of the member end face rather than the uniform distribution as assumed by current AASHTO LRFD specifications. Therefore, NCHRP Report 654 recommends (Tadros, Badie, & Tuan, 2010):

- At least 50% of the required end zone reinforcement be placed within $\frac{h_{nc}}{8} = 9 \text{ in.}$ (Zone 1) from the member end face
- The remaining end zone rebar shall then be placed from $\frac{h_{nc}}{8}$ to $\frac{h_{nc}}{2} = 36 \text{ in.}$ (Zone 2). This zone shall also be checked for the critical shear requirements. The larger of the reinforcing requirements will govern since the corresponding demands do not occur simultaneously.
- In order to satisfy the allowable tensile stress limits, the end zone rebar shall be adequately embedded into the top (or cast in-place slab) and bottom flanges such that they can develop to threshold of Equation (5.20) at the interface between the web and the bottom flange.

Based on the above, the Nebraska end zone reinforcing for the BT-72 girders is detailed as follows:

Zone 1 - Provide two sets of No.6 bars:

$$A_{EZR,Zone1} = 4 \times 0.44 \text{ in.}^2 = 1.76 \text{ in.}^2 \quad \left(\text{Member End Face, } \frac{h_{nc}}{8} = 9 \text{ in.} \right) \quad (5.25)$$

Zone 2 - Provide five sets of No.4 bars:

$$A_{EZR,Zone2} = 10 \times 0.20 \text{ in.}^2 = 2.00 \text{ in.}^2 \quad \left(\frac{h_{nc}}{8} = 9 \text{ in.}, \frac{h_{nc}}{2} = 36 \text{ in.} \right) \quad (5.26)$$

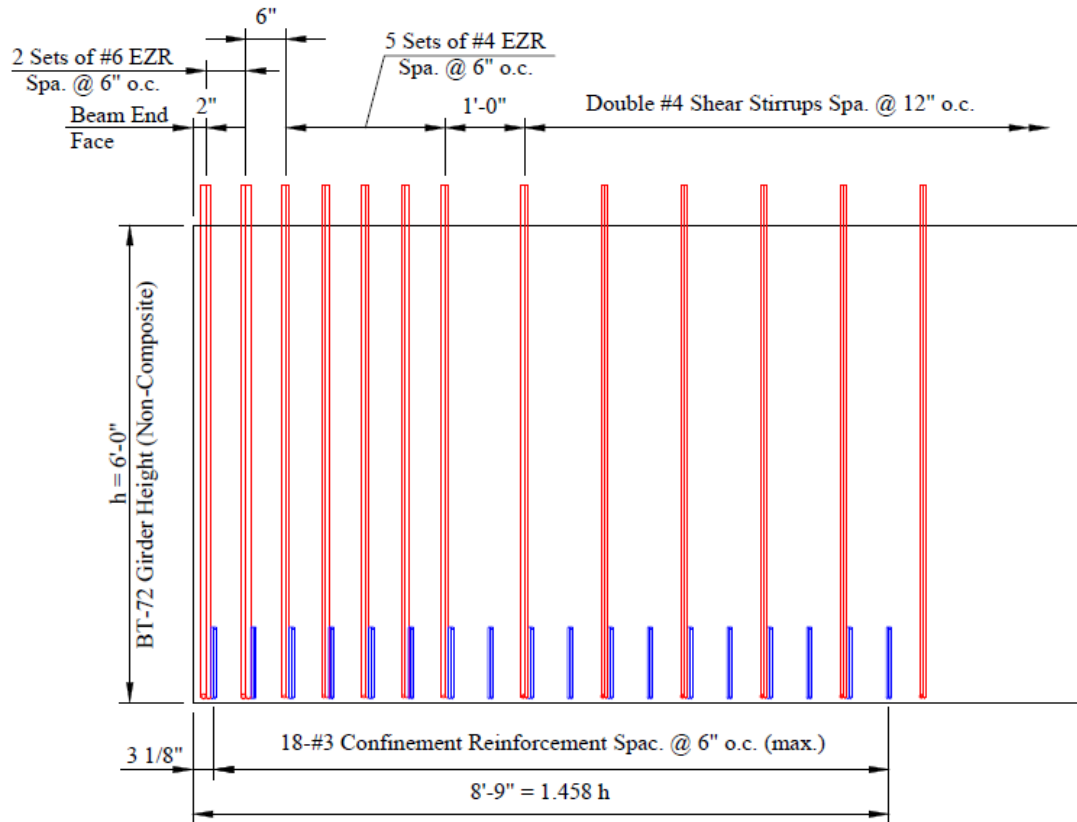


Figure 5-18: Typical elevation view of the BT-72 girders showing the spacing of the end zone reinforcement (EZR) as well as shear and confinement reinforcement in accordance with NCHRP Report 654 referred to as Nebraska Detail in this document.

Table 5-3 includes the summary of the acceptance criteria proposed by NCHRP Report 654. As previously discussed, one of the principal objectives of any design and detailing scheme for end zone of pretensioned members is to confine the cracks during the production process (e.g., release of prestressed strands) within a tolerance without compromising the local and/or global structural capacity as well as the long-term durability of the member. Therefore, the approach proposed by NCHRP Report 654 correlates the above to the crack width. As it observed, the criteria summarized in Table 5-3 provides the precaster, the client and the designer with sequential options and action items when dealing with end zone cracking.

Table 5-3: NCHRP Report 654 acceptance criteria for the pretensioned members with web cracking during the production (Tadros, Badie, & Tuan, 2010).

Criterion	Crack Width, w_{cr} (in.)	Action
1	$w_{cr} < 0.012$	No action
2	$0.012 \leq w_{cr} < 0.025$	Cracks need to be filled and subsequently, the end 4 ft of the member should receive proper surface sealant
3	$0.025 \leq w_{cr} < 0.050$	Cracks need to be epoxy-injected and subsequently, the end 4 ft of the member should receive proper surface sealant
4	$0.050 \leq w_{cr}$	Member need to be rejected unless further detailed analysis can show that structural capacity and long-term durability have not been compromised

5.3.2.3. IDOT Details

Illinois Department of Transportation (IDOT) is among the state departments of transportation that enforce specific end zone detailing for the pretensioned girders. In accordance to IDOT, the end zone reinforcing of pretensioned concrete girders statewide shall consist of 3/4-in. diameter threaded rods that are welded to a 1-in, thick plate embedded inside near the outside face of the bottom flange. At the top flange, the threaded rods are mechanically fastened to a 3/4-in. thick plate partially embedded near the outside face of the top flange. Please note that the threaded rods are not pre- or post-tensioned and are just mechanically fastened in-place with nuts.

Figure 5-19 shows a typical end zone reinforcing detail required by IDOT for pretensioned girders with properties equivalent to BT-72 girders. Please note that the

prescribed detail, including the amount and spacing of the threaded rods, are based on the Department's past experience statewide and may provide more reinforcement than required by AASHTO LRFD specifications as in the case of the BT-72 girders:

$$A_{EZR, IDOT} = 10 \times 0.334 \text{ in.}^2 = 3.340 \text{ in.}^2 = 112\% A_{EZR, req'd} \quad (5.27)$$

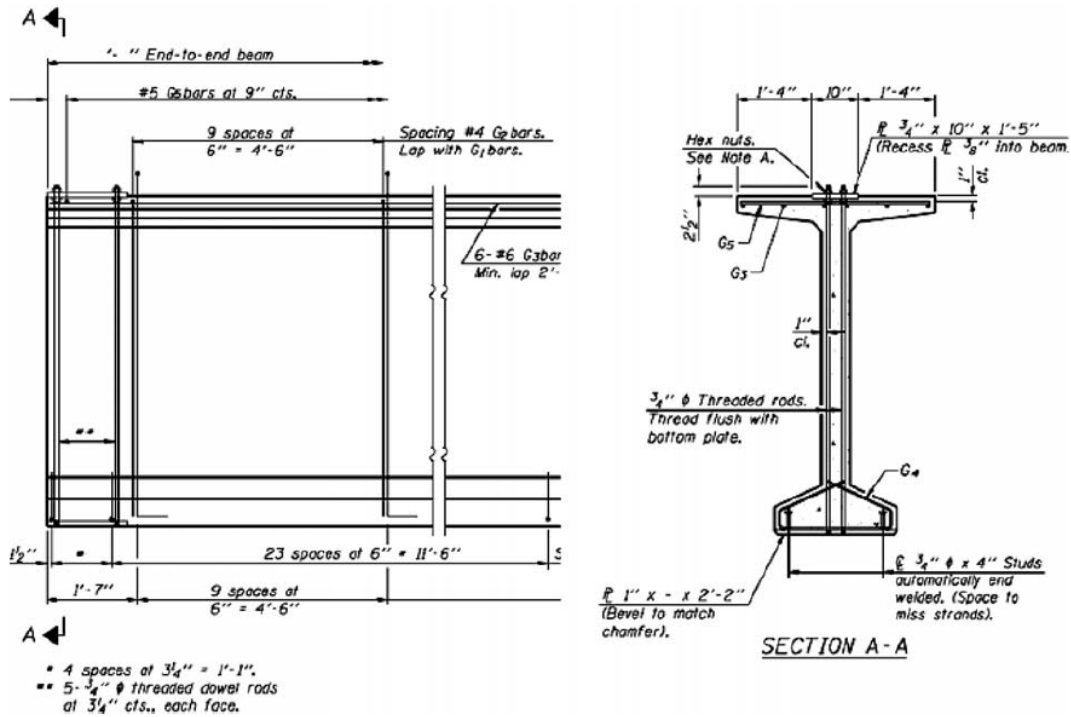


Figure 5-19: Typical end zone reinforcing detail required by IDOT for equivalent BT-72 girders. Adapted from NCHRP Report 654 (Tadros, Badie, & Tuan, 2010).

As indicated in Equation (5.27) and Figure 5-19, the IDOT end zone detail requires that ten 3/4-in. diameter threaded bars be provided along a distance of 19 in. regardless of the amount of prestressing force. Beyond this segment, shear reinforcement is provided at maximum spacing of 6 in. along a distance of 11'-6". In addition, the top flange of the member hosts an orthogonal grid of No.5 longitudinal and transverse reinforcement as shown in Figure 5-19.

5.3.2.4. Modified IDOT-AASHTO Details

As mentioned in the previous section, it is anticipated that the IDOT end zone detail results in more reinforcement than required by the AASHTO LRFD specifications. In the case of the BT-72 girder under investigation, Equation (5.27) indicates that IDOT EZR detail provides 12% more reinforcement than required by the AASHTO LRFD. Therefore, for the sake of comparative studies of this research, a fourth EZR scheme is also investigated, which includes a modification to the IDOT EZR by maintaining similar amount of reinforcement. In other words, in reference to Figure 5-19, the 3/4-in. threaded rods are replaced with equivalent No.5 stirrups while other details remain the same including the top and bottom plates as well as the distance over which the EZR is provided:

$$A_{EZR,IDOT_AASHTO} = 10 \times 0.31 \text{ in.}^2 = 3.10 \text{ in.}^2 = 104\% A_{EZR,req'd} \quad (5.28)$$

5.4. Numerical Modeling

The numerical modeling of the referenced BT-72 girders is based on finite element analysis of the composite behavior of the concrete host, prestressing strands and the non-prestressed reinforcement. The girders are modeled and analyzed as three-dimensional continuum elements while the prestressing strands are treated as truss (tension-compression only) members. Non-prestressed reinforcement such as end zone rebar, shear and confinement bars are simulated using beam elements which also provide shear stiffness.

Chapter 3 provides a detail discussion of two proposed methodologies for simulation of pretensioned concrete members based on Embedment and Extrusion techniques.

Based on the characteristics of the BT-72 members, Embedment technique is used for the analytical purposes of this chapter.

The following section gives a discussion of the key steps required for the simulation of the BT-72 girders using Embedment technique.

5.4.1. Constitutive Models

In reference to Section 3.4.1, Concrete Damage Plasticity constitutive model is utilized for the simulation of the linear elastic as well as elastoplastic response of concrete. The concrete properties at the time of prestressing release are similar to the specimens used in the numerical examples of Chapter 3. Therefore, the corresponding constitutive parameters will be similar to those summarized in Table 3-4.

In addition, Table 3-4 includes the fundamental elastic properties of the prestressing strands, non-prestressed rebar as well as the steel casting bed.

5.4.2. Simulation of the Composite Interaction between Concrete and Prestressing Strands and Other Reinforcement

The prestressing strands are modeled as truss elements which are embedded inside the concrete continuum serving as host. Additionally, a typical host can include multiple embedded elements. Therefore, the embedment technique facilitates simulation of a composite system as the referenced BT-72 girders which include a concrete host and multiple levels of embedded elements including straight and draped strands, end zone and shear stirrups, and confinement rebar in the bottom flange.

The non-prestressed reinforcing bars such as the end zone, shear and confinement reinforcement are simulated using three-dimensional beam elements. This ensures that the corresponding elements provide the shear stiffness based on individual material and geometric properties.

The commercial finite element package ABAQUS is used for the analytical purposes of this research (ABAQUS, 2010). Other commercial packages are also currently available in the market with similar capabilities. The following includes a sample ABAQUS command structure for embedment of a prestressing strand inside the BT-72 as the host. The embedment schemes follow a similar structure in ABAQUS environment (ABAQUS, 2010)

```
*Embedded Element, host elset=BT-72.SD_2_1_2  
SD_2_1.SD_2_2
```

where *BT-72.SD_2_1_2* represents a typical host [solid] element and *SD_2_1.SD_2_2* is an embedded truss element simulating a portion of the typical draped prestressing strands.

Figure 5-20 shows a typical finite element simulation of the BT-72 girders using the embedment technique. The basic components of such simulation are the solid elements representing the girder, truss elements simulating each individual straight or draped strand, and beam elements modeling the end zone, shear and confinement reinforcing bars.

5.4.3. Simulation of Pretensioning

In reference to Section 0, the process of pretensioning release is simulated through initial conditions and based on strain compatibility between concrete as the host and the prestressing strands as the embedded elements. First, the pretensioning is imposed on the strands as initial conditions (ABAQUS, 2010):

```
*Initial Conditions, Type=STRESS  
Element Number or Element Set, PRESTRESSING MAGNITUDE
```

→ Repeat as many lines as necessary.

→ Element or element set per each line can be assigned different prestressing values if desired.

Then the strain compatibility is applied through a two part process as listed below (ABAQUS, 2010):

**MODEL CHANGE, REMOVE*

→ List all elements except the pressing strands.

**MODEL CHANGE, ADD=WITH STRAIN*

→ List all elements except the prestressing strands.

The experience shows that imposing nodal boundary conditions on the girder elements during the first step of *Model Change* (Removal) greatly enhances the numerical convergences. If such conditions are implemented, they shall be removed during the second step of *Model Change* (Addition).

5.4.4. Transfer Length

As previously discussed, one of the characteristics of the embedment technique is that the transfer length is treated as a model input. In other words, once the prestressing strands are meshed into smaller units, each unit can be stresses by a different level through initial conditions. Therefore, to accomplish the comparative objectives of this chapter, the pretensioning scheme is based on the linear distribution as prescribed by AASHTO LRFD specifications. Based on Equation (3.22), the transfer length for the 0.5-in. diameter prestressing is estimated as

$$L_t \approx 60 \times 0.5 = 30 \text{ in.} \quad (5.29)$$

In reference to Figure 3-17, it is assumed that the pretensioning path follows a linear trend starting from the beam end face at a value of zero linearly increasing to the

maximum initial prestress (including the effects of the initial losses upon the release of strands) at a distance equal to 30 in. from the member end face.

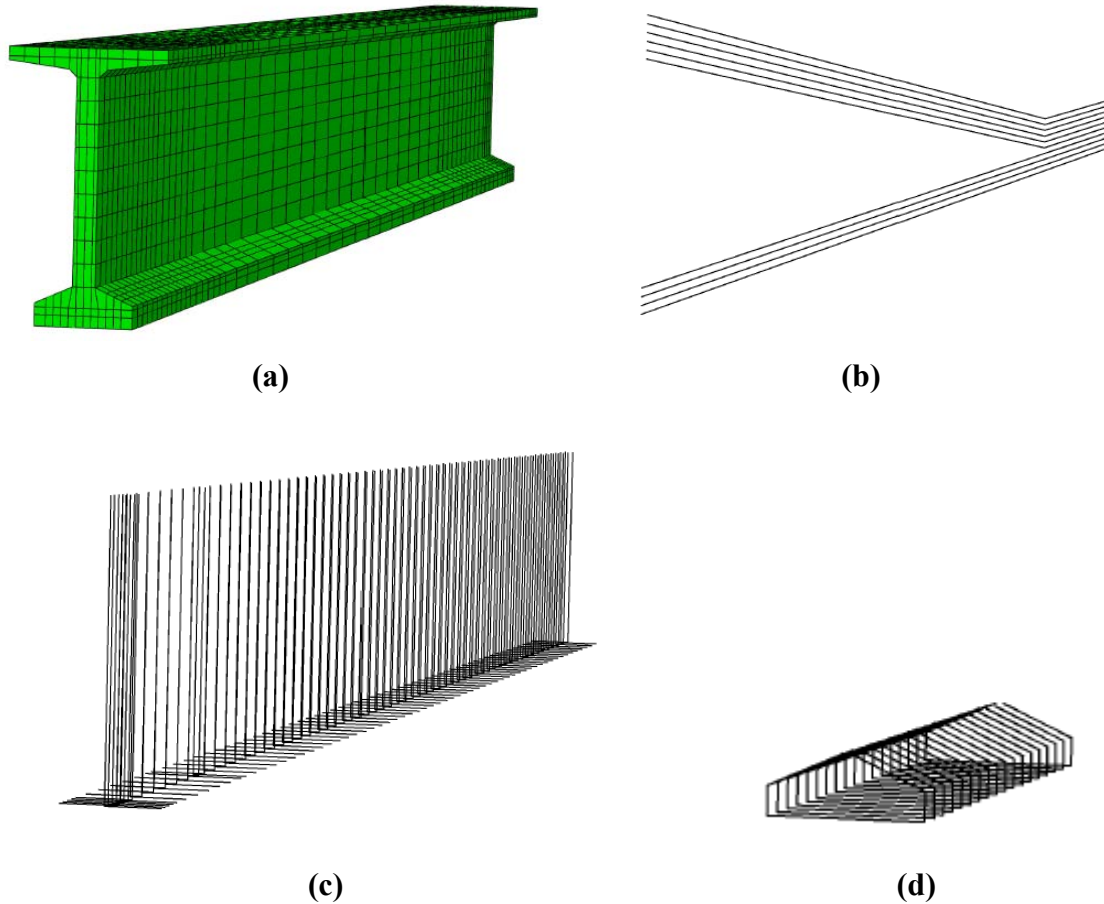


Figure 5-20: Typical components of a finite element model of a BT-72 girder using embedment technique: (a) Solid concrete continuum simulating the girder, (b) truss elements simulating the straight and draped strands, (c) Beam elements simulating the end zone and shear reinforcement, and (d) beam elements simulating the confinement bars embedded inside the bottom flange.

5.4.5. Simulation of Casting Bed

In Section 3.4.4, several techniques were discussed for simulation of the casting bed. For the analytical purposes of this chapter, the casting bed is modeled using solid elements, supporting the BT-72 girder on the top surface. The casting bed is simulated with linear-elastic steel properties (please refer to Table 3-4). In addition, the casting bed

is assumed to be fully supported in order to provide the BT-72 girder a rigid planar support.

The interface between the casting bed and outside face of the bottom flange is simulated with hard pressure contact properties while allowing complete separation of the paired elements (ABAQUS, 2010):

Definition of surfaces at girder

**Surface, type=ELEMENT, name=Girder*

_Girder_S1, S1

Definition of surfaces at casting bed

**Surface, type=ELEMENT, name=Bed*

_Bed_S1, S1

Definition of interaction properties

**** INTERACTION PROPERTIES**

**Surface Interaction, name=Bed_Girder*

1.,

**Friction*

0.,

**Surface Behavior, pressure-overclosure=HARD*

Please note that the above simulation allows for imposing a desired coefficient of friction at the contact interface between the girder and casting bed. For the analytical purposes of this research, it is assumed that the casting bed is properly greased to prevent any significant frictional effects (coefficient of friction of zero).

In addition, the preliminary analysis and simulation of the referenced girders indicated that the nodes along the centerline of the top flange had to be restrained against lateral translation in order to enhance numerical convergence.

Figure 5-21 shows a typical finite element model of a BT-72 girder cambering over the supporting casting bed immediately after the release of pretensioned strands.

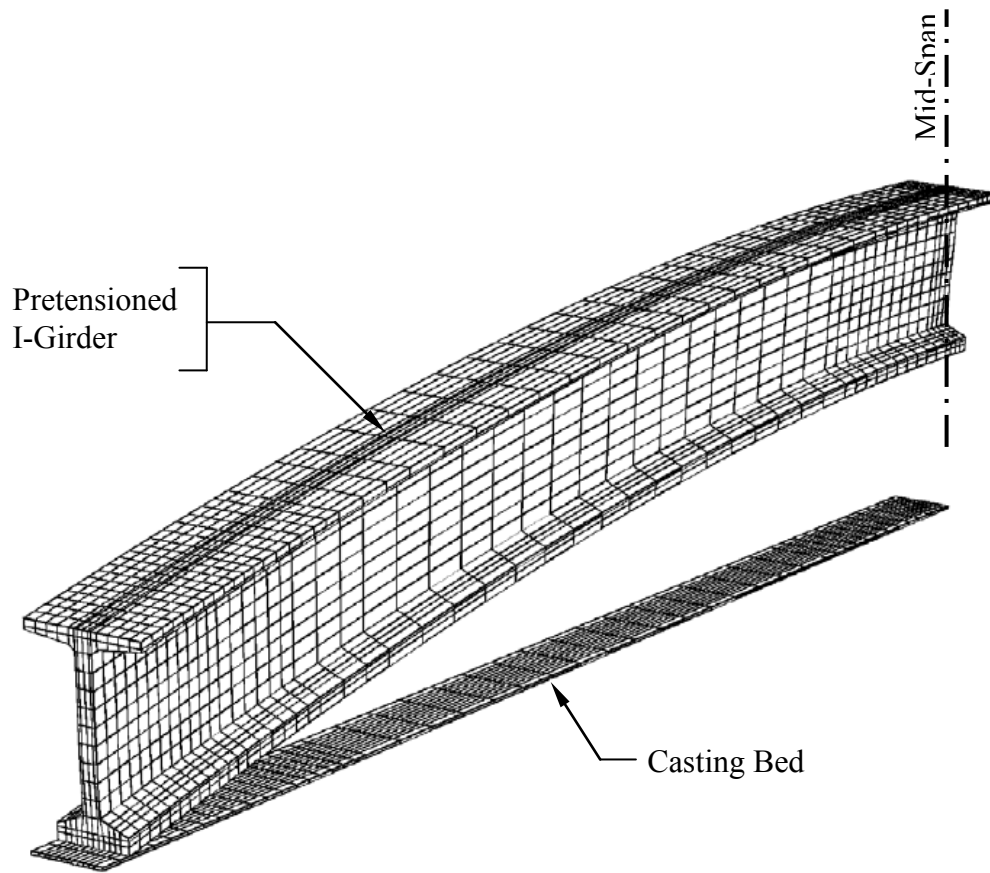
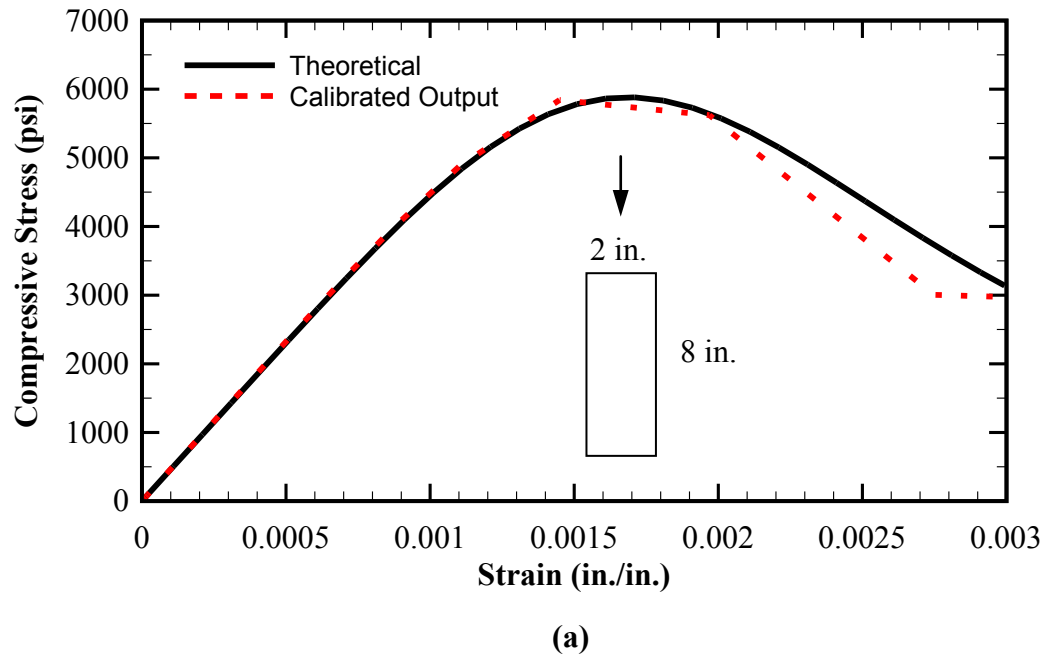


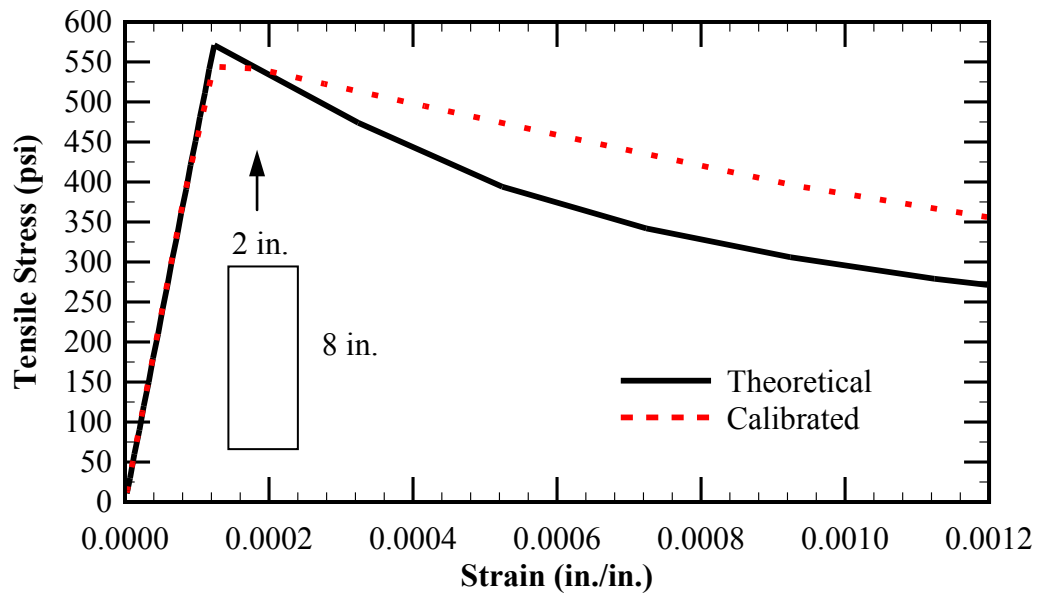
Figure 5-21: A typical Finite element model of BT-72 girder cambering over the casting bed upon the release of pretensioning due to eccentricity of the pretensioned strands.

5.5. Numerical Simulations

5.5.1. Calibration of Material Constitutive Models

As mentioned in Section 5.4.1, the properties of concrete at time of prestress release are similar to specimens used for the analytical purposes of Chapter 3. Section 3.5.2 includes the detailed discussion of the calibration process for the Concrete Damage Plasticity constitutive model including the uniaxial compressive and tensile stress-strain relations as shown in Figure 3-29 and repeated in Figure 5-22.





(b)

Figure 5-22: Comparison of the stress-strain relationships obtained by the constitutive model with the theoretical stress-strain curves assumed for a concrete with initial compressive strength of $f'_c = 5,800$ psi: a) subject due to uniaxial compression, and (b) subject to uniaxial tension.

5.5.2. BT-72 FE Model without End Zone, Shear and Confinement Reinforcement

The first class of numerical simulations includes the finite element model of the referenced BT-72 girder without end zone, shear and confinement reinforcement. This class of models includes two sub-categories: i) models with linear-elastic material response, and ii) models with elasto-plastic material response.

For the purpose of model verification, the following key results are compared between the finite element models and the corresponding values obtained from the closed form solutions as included in PCI BDM Example 9.4 (PCI, 2003):

- BT-72 girder top and bottom fiber stresses at the harping point of the strands
- BT-72 girder top and bottom fiber stresses at the member midspan

- Maximum camber of BT-72 girder at the midspan immediately after the release of pretensioned strands

Please note that it is anticipated that the end zone of the member, including the areas in the vicinity of the transfer length, undergoes potential cracking and nonlinear stress redistribution. Therefore, the end zone will be investigated separately and will not be considered as a parameter for model verification.

Table 5-4 includes the top and bottom fiber stresses at the harping point and midspan of the member. At each control location, three independent sets of results are reported based on the material behavior (linear-elastic or elasto-plastic) as well as those obtained by closed form solutions of PCI BDM Example 9.4. In addition, the maximum camber is reported at the midspan of the girder. The reported camber is based on the collective effects of self-weight of the girder and pretensioning immediately after the release of the strands.

Table 5-4: Results of the finite element analysis of a typical BT-72 girder without end zone, shear and confinement reinforcement as well as those by the closed form solutions included in PCI BDM Example 9.4. The results are reported immediately after the release of pretensioning.

	Linear-elastic Response	Elasto-plastic Response	Closed Form Solution
Tensile stress in the extreme top fiber at harping point, σ_t^{Harp} (psi)	-238.6	-231.6	-256
Compressive stress in the extreme bottom fiber at harping point, σ_c^{Harp} (psi)	-3683.5	-3671.9	-3313
Tensile stress in the extreme top fiber at mid-span, $\sigma_t^{Midspan}$ (psi)	-272.4	-265.9	-301
Compressive stress in the extreme bottom fiber at mid-span, $\sigma_c^{Midspan}$ (psi)	-3606.6	-3592.2	-3266
Maximum deflection at mid-span, $\Delta_{max}^{Midspan}$ (in.)	2.56 ↑	2.58↑	2.28 ↑
<p>Notes:</p> <ol style="list-style-type: none"> 1. Positive stresses correspond to the state of tension.. 2. Negative stresses correspond to the state of compression. 3. ↑ denotes positive camber (upward deflection). 4. ↓ denotes negative camber (downward deflection). 			

Table 5-5 shows the comparison between the linear-elastic and elasto-plastic results versus the closed form solutions. It can be observed that the closed form solutions overestimate the top fiber stresses at the midspan by maximum of 10% and 12% in comparison with linear and nonlinear simulations, respectively. On the other hand, the bottom fiber stresses are underestimated by maximum of 11% by the closed form solutions. The maximum midspan camber is also underestimated by the closed form

solutions by 12% and 13% relative to the models with linear-elastic and elasto-plastic material behavior, respectively.

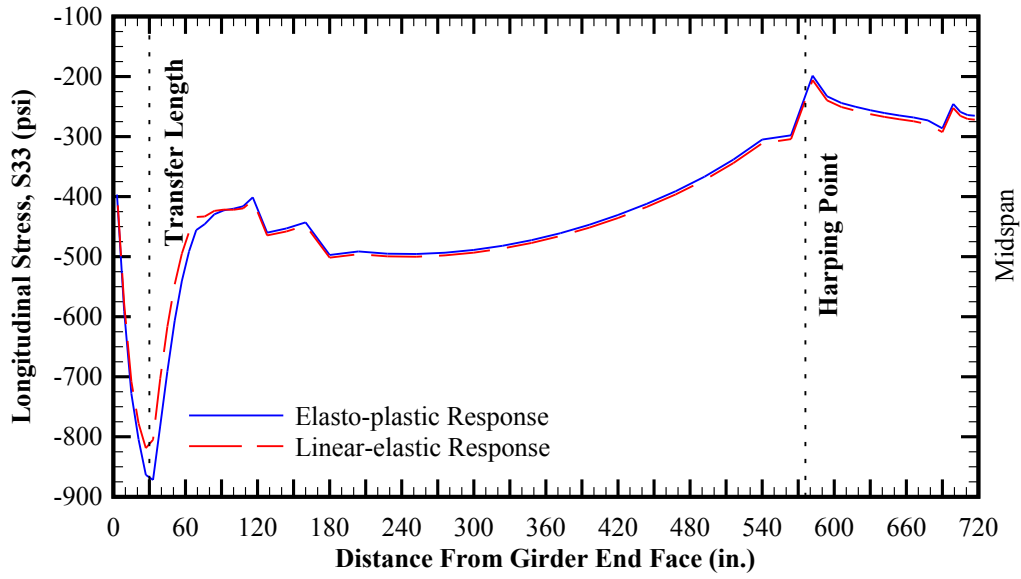
The results depict an acceptable convergence between the numerical simulations (linear-elastic and elasto-plastic models) and the close form solutions. It should be noted that the closed form solutions ignore the three-dimensional response of the concrete continuum. Meanwhile, the embedded finite element models overestimate the stiffness of the girder by addition of the strands and other reinforcing bars to the global stiffness without subtracting the corresponding concrete volume occupied by the embedded elements. Additionally, the obtained results indicate that current closed form solutions based on beam theory adequately capture the behavior of pretensioned concrete girders in the vicinity of the member midspan which predominantly stays within linear-elastic stage.

Table 5-5: Comparison of the results obtained by the finite element analysis of a typical BT-72 girder without end zone, shear and confinement reinforcement versus the closed form solutions in reference to Table 5-4.

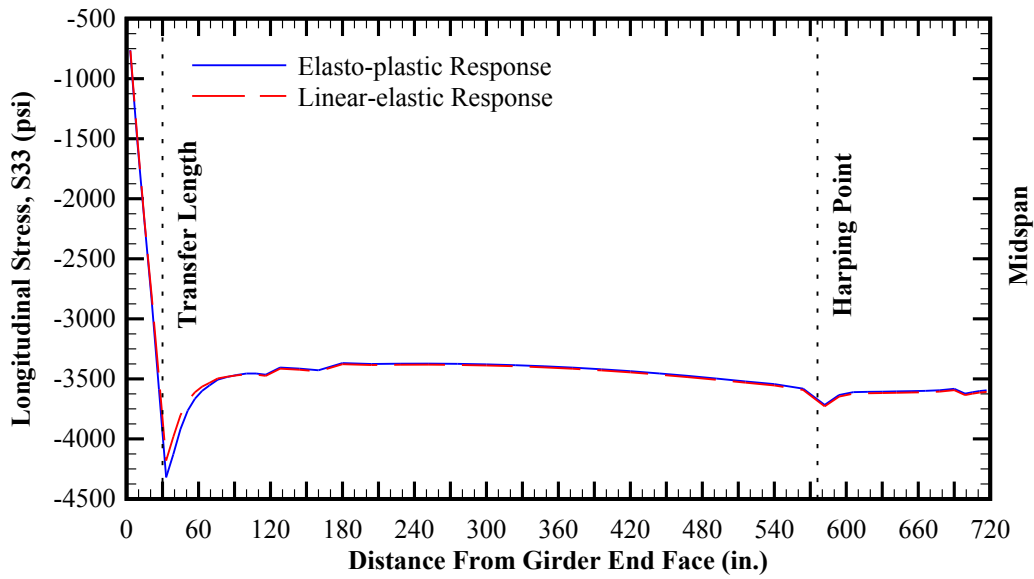
	<i>Linear – elastic</i> <i>Closed Form Sloution</i>	<i>Elasto – plastic</i> <i>Closed Form Sloution</i>
Tensile stress in the extreme top fiber at harping point, σ_t^{Harp}	93%	90%
Compressive stress in the extreme bottom fiber at harping point, σ_c^{Harp}	111%	111%
Tensile stress in the extreme top fiber at mid-span, $\sigma_t^{Midspan}$	90%	88%
Compressive stress in the extreme bottom fiber at mid-span, $\sigma_c^{Midspan}$	110%	110%
Max. deflection at mid-span, $\Delta_{max}^{Midspan}$	112%	113%

Figure 5-23 shows the longitudinal stresses in extreme top and bottom concrete fibers immediate after the release of pretensioned strands. It also depicts the linear-elastic response versus the elasto-plastic behavior. Figure 5-24 shows the longitudinal stress (S33) distribution along the span of the member while measured at various heights of the BT-72 girder with elasto-plastic response. Subsequently, the following important observations are made:

1. The top and bottom fibers show noticeable stress peaks along the transfer length. As previously discussed in Chapter 3, the embedment technique requires that the strands be incrementally stressed in order to simulate the transfer length. Therefore, it is anticipated that the corresponding stress peaks may be partially due to numerical convergence of along the strands with stepped initial conditions of stress type.
2. The "numerical noises" described in Item 1 above are also observed in the vicinity of the harping points but in smaller magnitude.
3. In reference to Figure 5-24, the stress peaks are confined along the top and bottom flanges. Within the girder web, the longitudinal stress path is smooth.
4. Based on Item 4 above, it is anticipated that the section changes due to the top and bottom flanges may disturb the longitudinal stress path in addition to potential numerical noises. At the top flange with relatively thinner thickness while wider in planar dimension, the magnitude of stress peaks are more pronounced in comparison with the bottom flange.



(a)



(b)

Figure 5-23: Longitudinal stresses (S_{33}) in a typical BT-72 girder without end zone, shear and confinement reinforcement immediately after the release of pretensioned strands: (a) Extreme top fiber, and (b) extreme bottom fiber.

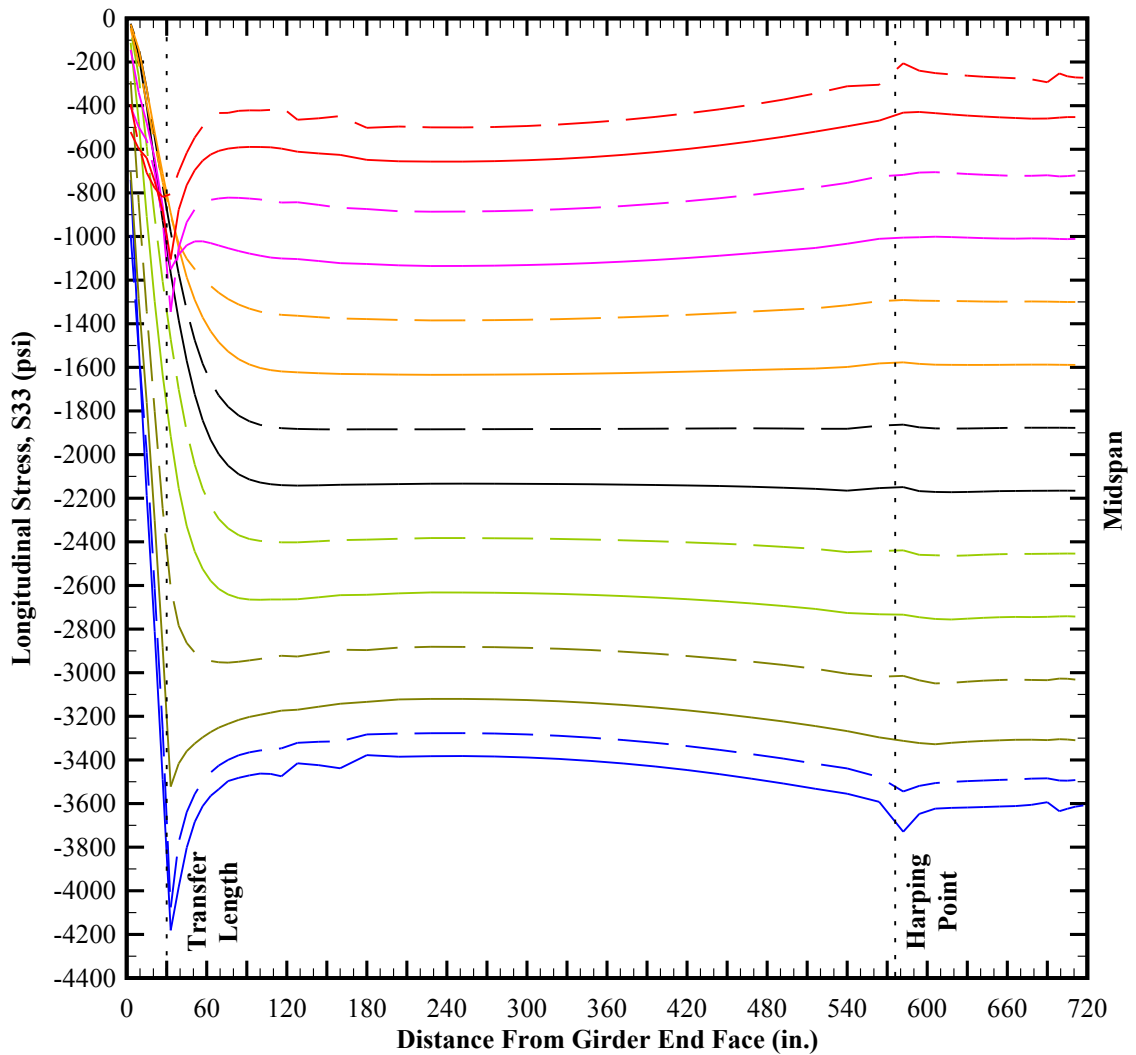


Figure 5-24: Longitudinal stresses (S33) along the height of a typical BT-72 girder without end zone, shear and confinement reinforcement immediately after the release of pretensioned strands and based on the elasto-plastic response of the specimen. Note: "h" is measured relative to the bottom face of the bottom flange assumed as datum.

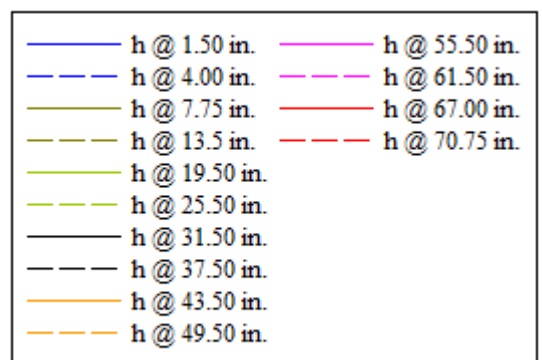


Figure 5-25 (a) thru (d) show the distribution of the vertical stresses (S22) along the height of the BT-72 girder, measured at 3 in., 9 in., 33 in. and 51 in. from the girder end face, respectively. In addition, the elasto-plastic and linear-elastic responses are superimposed on each graph in order to show the effect of nonlinearity and softening (potential cracking) at each interval.

It is observed that significant softening of concrete host occurs within a domain confined between the member end face and 9 in. away from the girder end. The magnitude of the vertical tensile stresses indicates that potential cracking is anticipated along the height of the mid-section of the girder web. Beyond the corresponding domain, the numerical solutions indicate that results obtained by the nonlinear and linear models begin to converge. Beyond the theoretical transfer length (30 in. from the girder end face), the response of the BT-72 girder predominantly remains within elastic regime.

Similarly, Figure 5-26 includes the pressure distribution along the height of the BT-72 girder, measured at 3 in., 9 in., 33 in. and 51 in. from the girder end face, respectively. The trend of pressure is very similar to the longitudinal stress (S33) as described above. In accordance with the results obtained by the nonlinear finite element analysis, the girder web along 9 in. from the girder end face is susceptible to cracking immediately after the release of pretensioned strands.

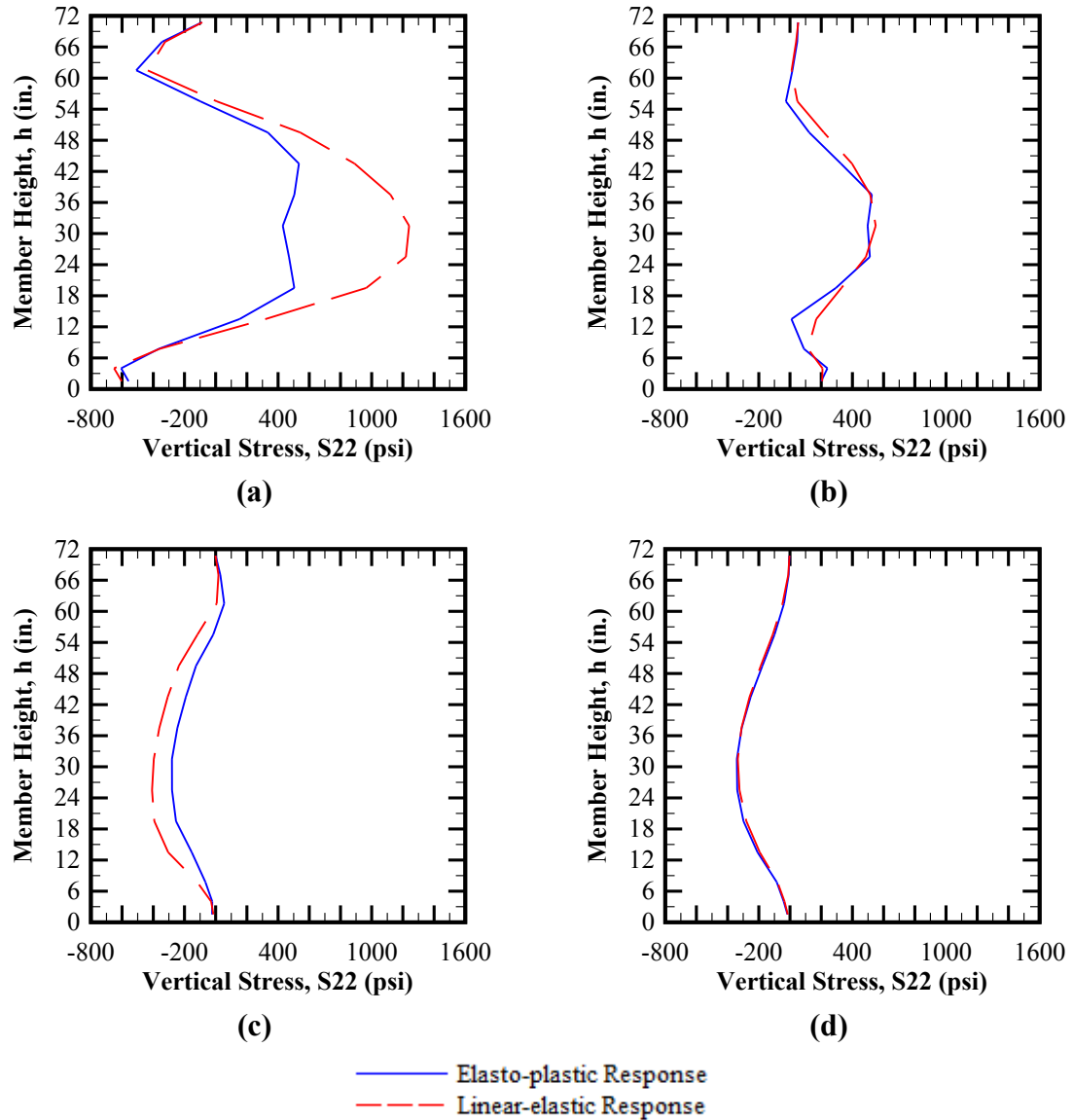


Figure 5-25: Vertical stress (S22) distribution along the height of a typical BT-72 girder without end zone, shear and confinement reinforcement measured at: (a) 3 in. from girder end face, (b) 9 in. from the girder end face, (c) 33 in. from the girder end face, and (d) 51 in. from the girder end face.

Note: Positive stresses indicate state of tension; negative stresses indicate state of compression.

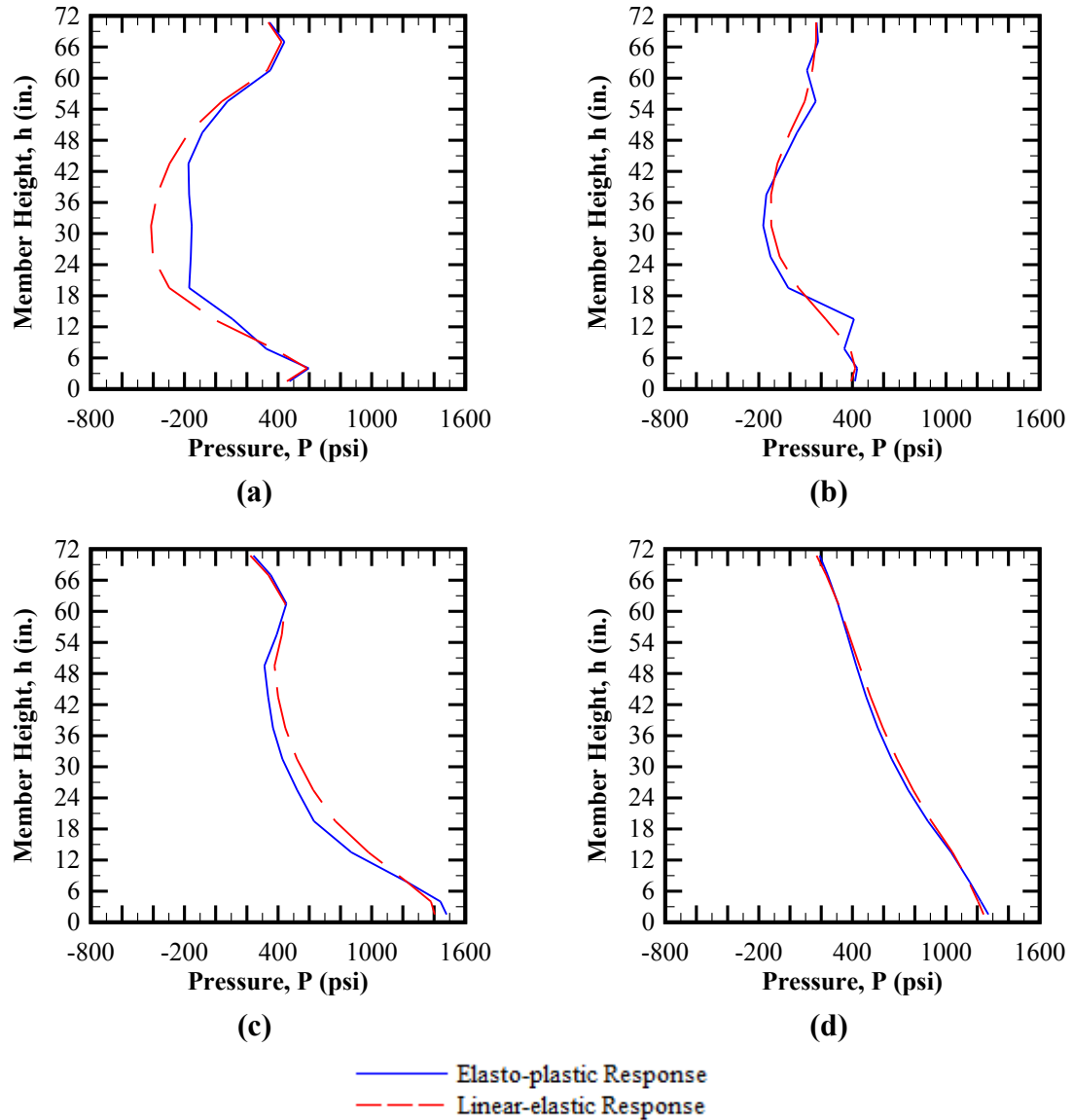


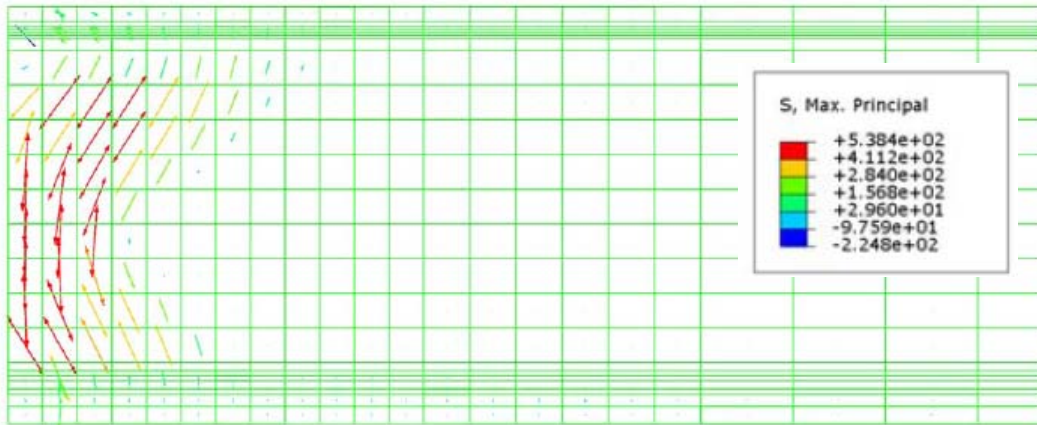
Figure 5-26: Pressure distribution along the height of a typical BT-72 girder without end zone, shear and confinement reinforcement measured at: (a) 3 in. from girder end face, (b) 9 in. from the girder end face, (c) 33 in. from the girder end face, and (d) 51 in. from the girder end face.

Note: Positive pressure indicates state of compression; negative pressure indicates state of tension.

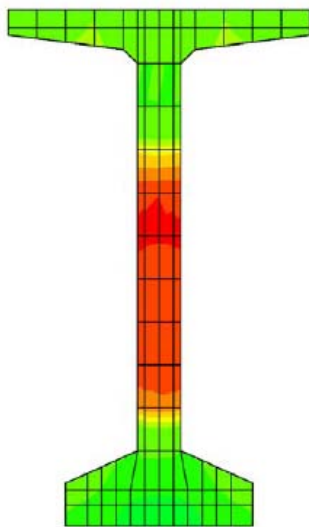
Figure 5-27 shows sample stress contours along the end zone BT-72 based on nonlinear (e.g., elasto-plastic concrete response) simulation. Figure 5-27 (a) shows the maximum principal stress contour near the girder end face, indicating the tensile stresses near rupture strength (f_r) initiating from the interface between the web and bottom flange. Therefore, the web is potentially vulnerable to cracking not only along the mid height but also along the areas in the vicinity of the interface with the bottom flange. This important observation will be discussed in more details in Chapter 6.

Figure 5-27 (b) shows the vertical stress (S22) distribution at the member end face. The finite element results indicate that a zone immediately above the mid-height of the girder will potentially crack upon release of pretensioning. As indicated by the cross section, the potential tensile crack is anticipated to extend well into the thickness of the web.

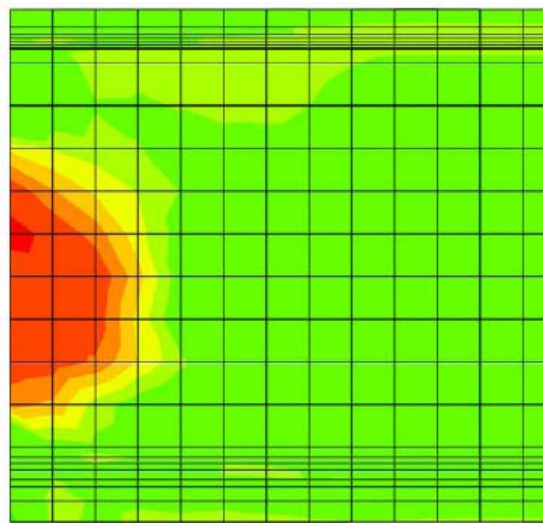
Figure 5-27 (c) shows the vertical stress (S22) distribution along the end zone of the specimen. As previously discussed, the corresponding stress contour indicates that the potential tensile cracking of the girder web is confined to an area extending 9 in. from the member end face. In addition, the effect of the tensile stressing due to the release of prestressed strands is more skewed towards the bottom flange.



(a)

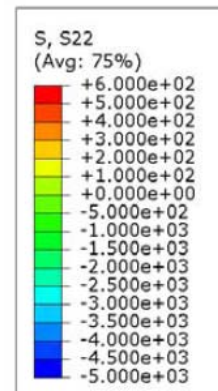


(b)



(c)

Figure 5-27: Elasto-plastic response of a typical BT-72 girder without end zone, shear and confinement reinforcement near the member end face: (a) Maximum principal stress contour along the end zone, (b) Vertical stress (S22) contour at member end face and (c) Vertical stress (S22) contour along the end zone.



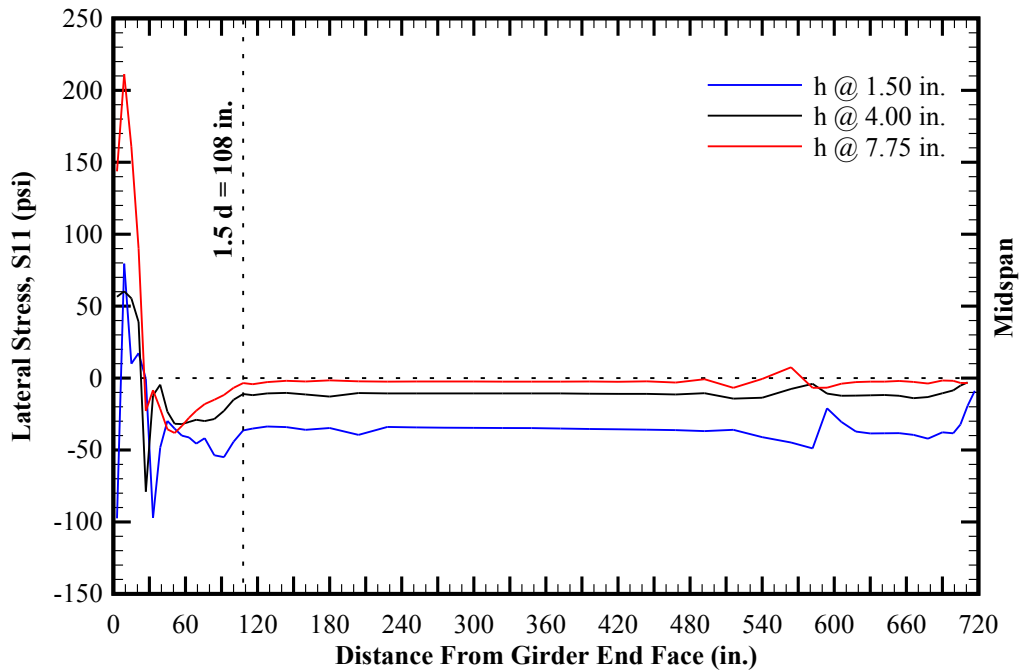


Figure 5-28: Lateral stress (S11) distribution of a typical BT-72 girder without end zone, shear and confinement reinforcement within the bottom flange (elasto-plastic response).

Note: Positive pressure indicates state of compression; negative pressure indicates state of tension.

Figure 5-28 shows the lateral stress (S11) distribution within the bottom flange of a typical BT-72 girder with elasto-plastic response. As previously discussed, the current AASHTO LRFD specifications require confinement reinforcement to extend over a distance equal to 1.5 times the height of the precast member. The numerical simulations show a maximum lateral tensile stress of 211 psi near the top of the bottom flange at approximately 9 in. from the member end face. However, the lateral tensile stresses are resolved into state of compression at a distance approximately 27 in. from the girder end face.

5.5.3. BT-72 FE Model with AASHTO LRFD End Zone Reinforcing Details in Addition to Shear and Confinement Reinforcement

The second class of the finite element models correspond to the simulation of a typical BT-72 girder with end zone reinforcing details in accordance with AASHTO LRFD specifications as shown in Figure 5-17. Additionally, the finite element models include the shear and confinement reinforcement in accordance with the design requirements as shown in PCI BDM Example 9.4.

Table 5-6 includes the top and bottom fiber stresses at the harping point and midspan of the member. At each control location, three independent sets of results are reported based on the material behavior (linear-elastic or elasto-plastic) as well as those obtained by closed form solutions of PCI BDM Example 9.4. In addition, the maximum camber is reported at the midspan of the girder. The reported camber is based on the combined effect of self-weight of the girder and pretensioning immediately after the release of the strands.

Table 5-7 shows the comparison between the linear-elastic and elasto-plastic results versus the closed form solutions. Similar to the results of Section 5.5.2, the comparison of the results indicates overestimation of top fiber stresses and underestimation of the bottom fiber stress by the close form solutions. It is also observed that the inclusion of the end zone, shear and confinement reinforcement does not significantly affect the longitudinal stresses at the top and bottom fibers as well as the camber. This is consistent with the assumptions of the beam theory used as the basis for the closed form solutions.

The comparative study of the results obtained by the numerical simulations and the closed form solution indicates an acceptable conformance between the two

methodologies. In other words, the two-dimensional beam theory is deemed adequately capable of estimating the flexural response of the pretensioned BT-72 girder.

Table 5-6: Results of the finite element analysis of a typical BT-72 girder with AASHTO LRFD end zone reinforcing details in addition to shear and confinement reinforcement as well as those by the closed form solutions included in PCI BDM Example 9.4. The results are reported immediately after the release of pretensioning.

	Linear-elastic Response	Elasto-plastic Response	Closed Form Solution
Stress in the extreme top fiber at harping point, σ_t^{Harp} (psi)	-238.6	-231.7	-256
Stress in the extreme bottom fiber at harping point, σ_c^{Harp} (psi)	-3683.5	-3672.1	-3313
Stress in the extreme top fiber at mid-span, $\sigma_t^{Midspan}$ (psi)	-272.4	-266.0	-301
Stress in the extreme bottom fiber at mid-span, $\sigma_c^{Midspan}$ (psi)	-3606.0	-3592.3	-3266
Maximum deflection at mid-span, $\Delta_{max}^{Midspan}$ (in.)	2.56 ↑	2.59 ↑	2.28 ↑
Notes:			
5. Positive stresses correspond to the state of tension..			
6. Negative stresses correspond to the state of compression.			
7. ↑ denotes positive camber (upward deflection).			
8. ↓ denotes negative camber (downward deflection).			

Table 5-7: Comparison of the results obtained by the BT-72 finite element model with AASHTO LRFD end zone, shear and confinement reinforcement versus the closed form solutions in reference to Table 5-6.

	<i>Linear – elastic</i>	<i>Elasto – plastic</i>
	<i>Closed Form Sloution</i>	<i>Closed Form Sloution</i>
Stress in the extreme top fiber at harping point, σ_t^{Harp}	93%	91%
Stress in the extreme bottom fiber at harping point, σ_c^{Harp}	111%	111%
Stress in the extreme top fiber at mid-span, $\sigma_t^{Midspan}$	90%	88%
Stress in the extreme bottom fiber at mid-span, $\sigma_c^{Midspan}$	110%	110%
Maximum deflection at mid-span, $\Delta_{max}^{Midspan}$	112%	114%

Figure 5-29 shows the longitudinal stress (S33) distribution along the span of the member, measured at various heights of the BT-72 girder with elasto-plastic response. The magnitude and trend of the longitudinal stress distribution are similar to the results obtained in 5.5.2 with similar observations. Thus, the inclusion of the end zone, shear and confinement reinforcement does not affect the longitudinal stresses at top and bottom fibers along the span of the member, including the peaks affected by the sectional transition between the web and flanges as previously observed in the plain model without end zone, shear and confinement reinforcing bars.

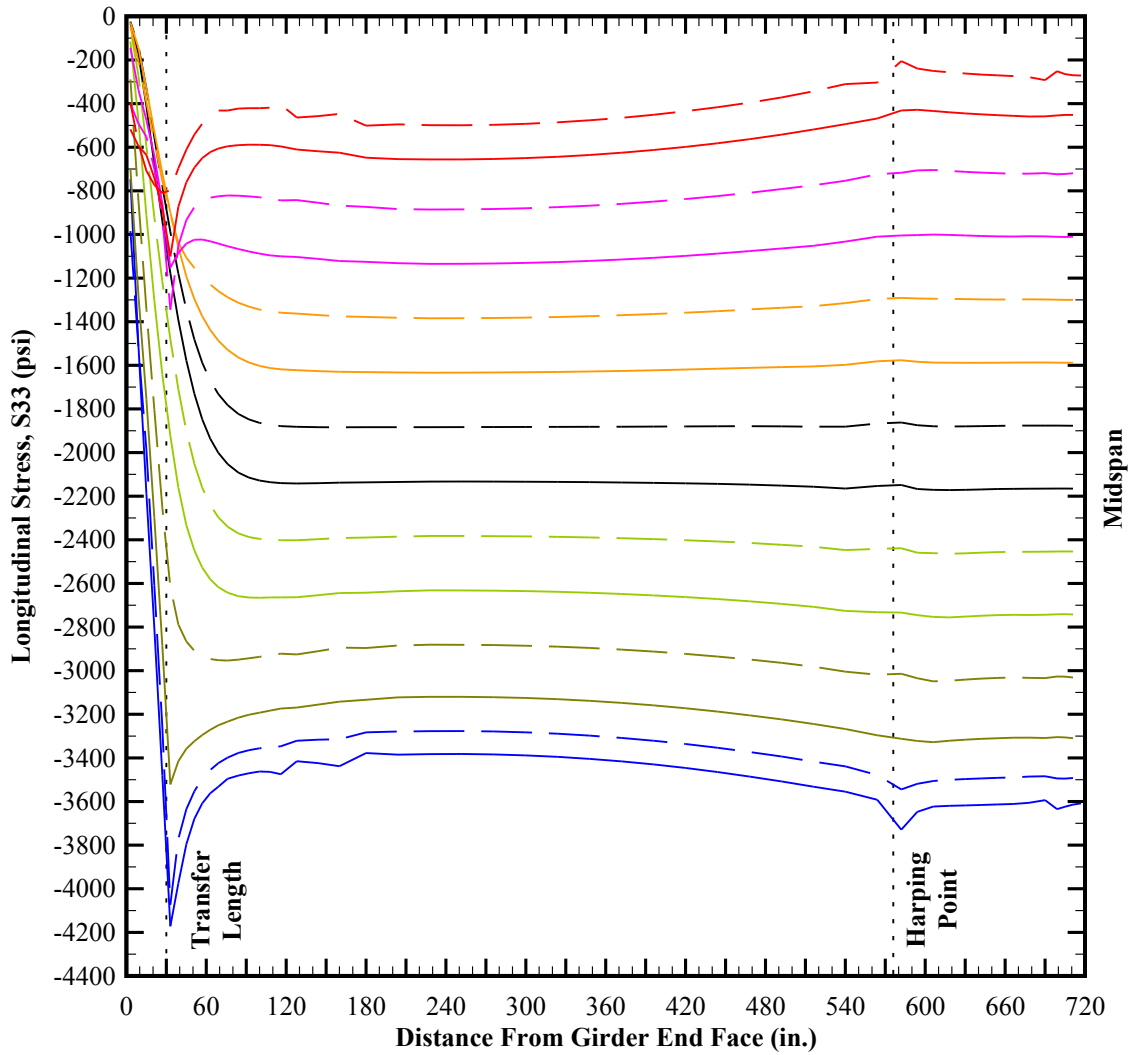


Figure 5-29: Longitudinal stresses (S33) along the height of a typical BT-72 girder with AASHTO LRFD end zone reinforcing details in addition to shear and confinement reinforcement immediately after the release of pretensioned strands and based on the elasto-plastic response of the specimen. Note: "h" is measured relative to the bottom face of the bottom flange assumed as datum.

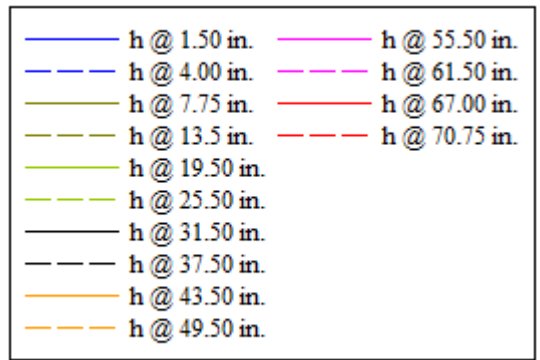


Figure 5-30 (a) thru (d) show the distribution of the vertical stresses (S22) along the height of the BT-72 girder, measured at 3 in., 9 in., 33 in. and 51 in. from the girder end face, respectively. In addition, the elasto-plastic and linear-elastic responses are superimposed on each graph in order to show the effect of nonlinearity and material softening (e.g., potential cracking) at each interval.

It is observed that significant softening of concrete occurs within a domain confined between the member end face and 9 in. away from the girder end. The magnitude of the vertical tensile stresses indicate that potential cracking is anticipated along the mid-height of the girder web. Along the next domain confined between domain 9 in from the girder end and the theoretical transfer length (30 in. from the girder end face), the numerical solutions indicate that results obtained by the nonlinear and linear models begin to converge, indicating that the response of the member tends to stay and remain within the elastic regime. Beyond the theoretical transfer length, the response of the BT-72 girder predominantly remains within the elastic regime.

Similarly, Figure 5-31 includes the pressure distribution along the height of the BT-72 girder, measured at 3 in., 9 in., 33 in. and 51 in. from the girder end face, respectively. The trend of pressure is very similar to the longitudinal stresses (S33) as described above. In accordance with the results obtained by the nonlinear finite element analysis, the girder web along 9 in. from the girder end face is susceptible to cracking immediately after the release of pretensioned strands.

The obtained numerical solutions re-emphasize the importance of utilizing elasto-plastic material behavior when analyzing the effect of pretensioning along the member

end zone, adequately capable of estimating material softening and the resulting stress redistribution within the areas susceptible to tensile cracking.

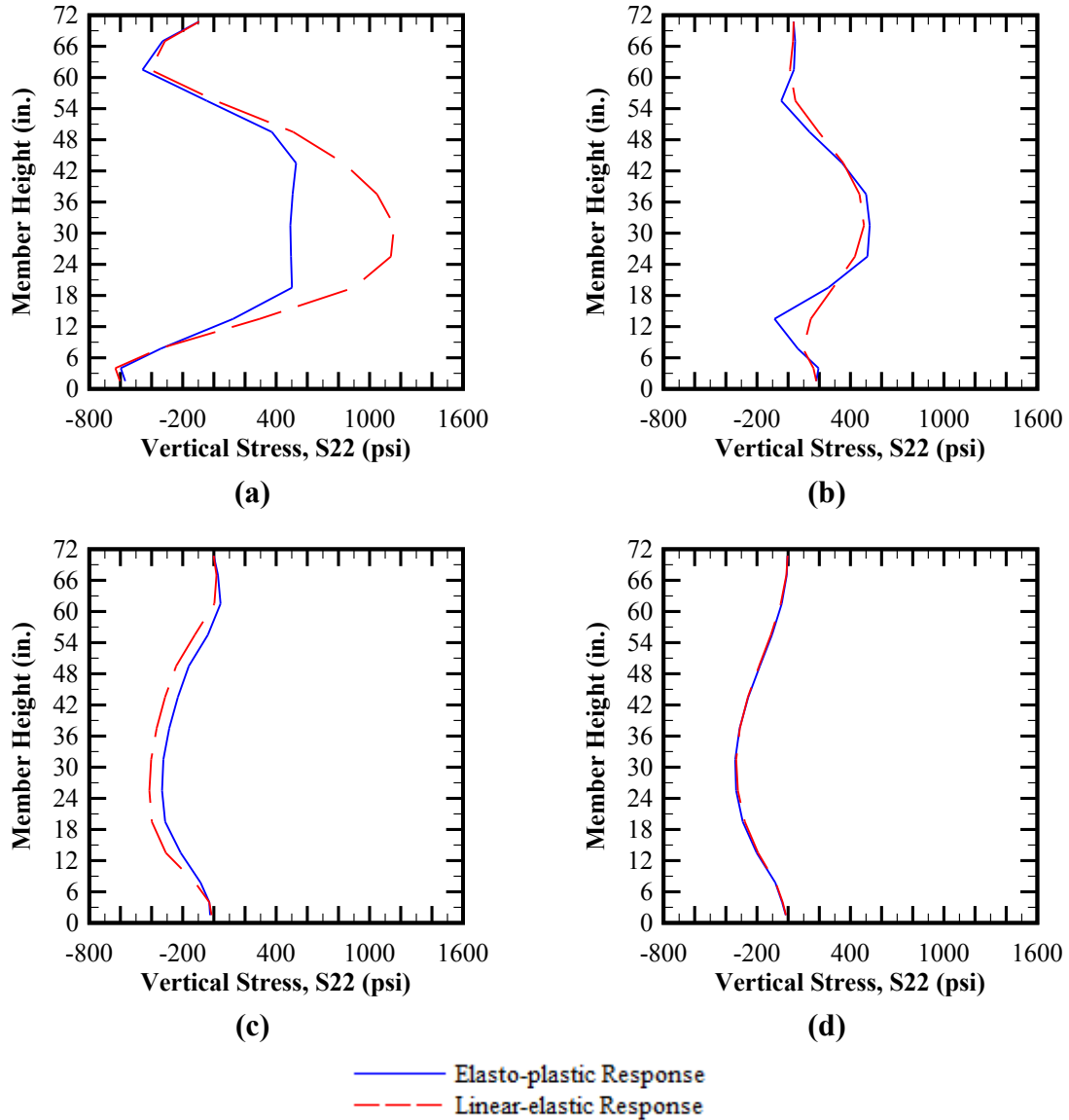


Figure 5-30: Vertical stress (S22) distribution along the height of a typical BT-72 girder with AASHTO LRFD end zone rebar in addition to shear and confinement reinforcement measured at: (a) 3 in. from girder end face, (b) 9 in. from the girder end face, (c) 33 in. from the girder end face, and (d) 51 in. from the girder end face.

Note: Positive stresses indicate state of tension; negative stresses indicate state of compression.

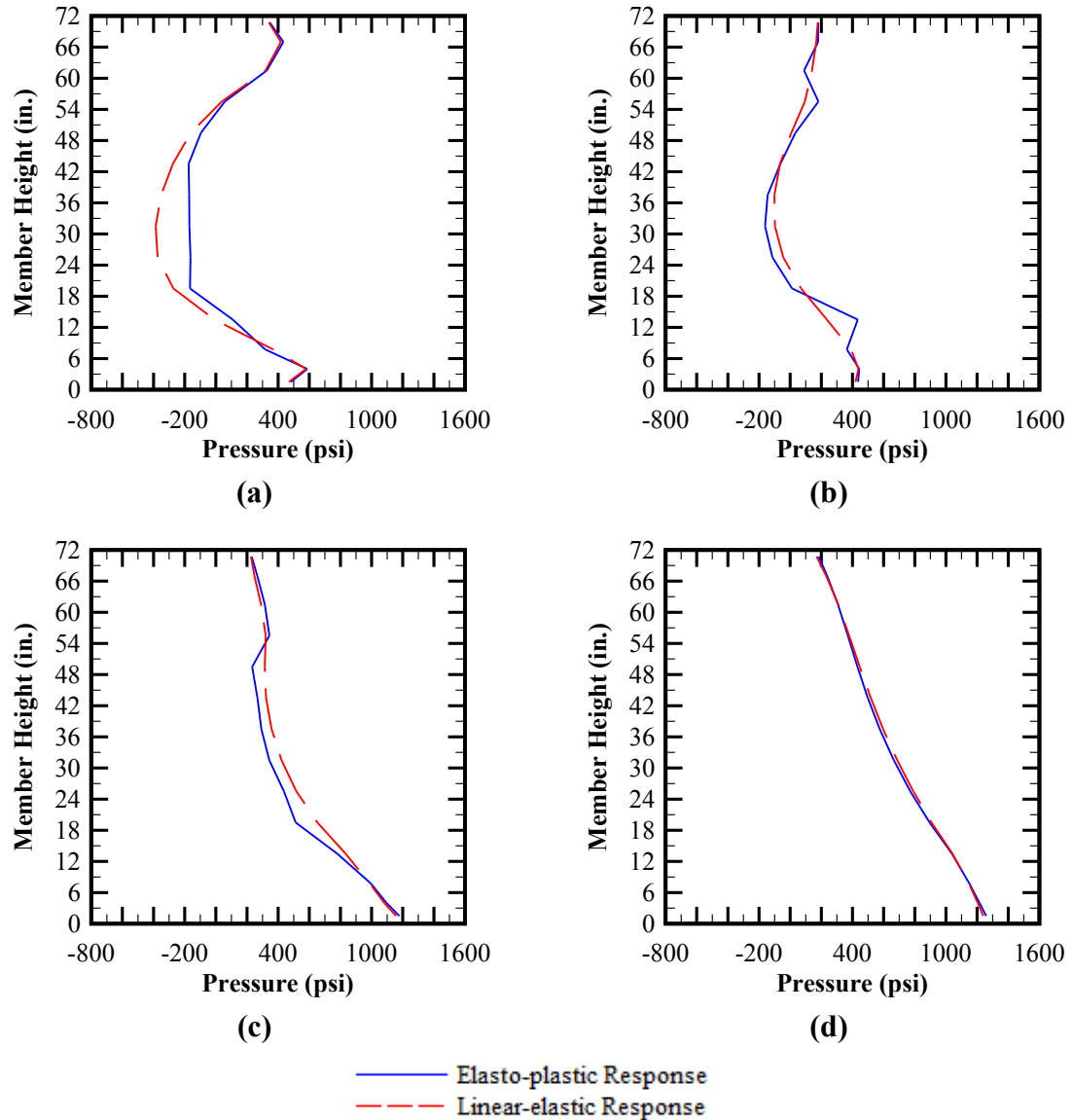


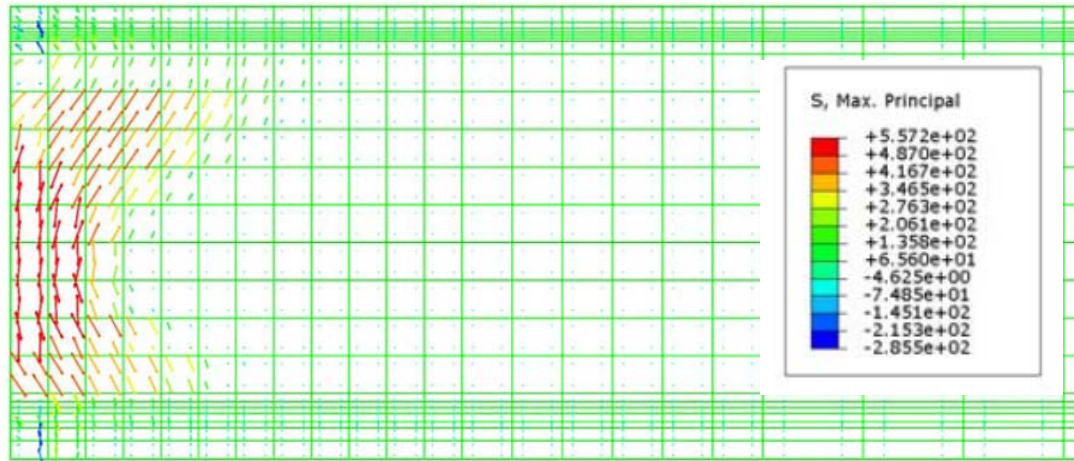
Figure 5-31: Pressure distribution along the height of a typical BT-72 girder with AASHTO LRFD end zone rebar in addition to shear and confinement reinforcement measured at: (a) 3 in. from girder end face, (b) 9 in. from the girder end face, (c) 33 in. from the girder end face, and (d) 51 in. from the girder end face.

Note: Positive pressure indicates state of compression; negative pressure indicates state of tension.

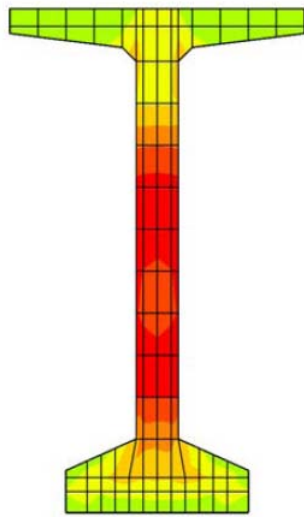
Figure 5-32 shows the state of maximum principal stress along the end zone of the BT-72 girder based on nonlinear (e.g., elasto-plastic concrete response) simulation. Figure 5-32 (a) shows the maximum principal vector contours near the girder end face, indicating the tensile stresses near rupture strength (f_r) initiating in a zone immediately above the interface between the web and bottom flange. Therefore, the web is potentially vulnerable to cracking not only along the mid height but also along the areas in the vicinity of the interface with the bottom flange. Although in comparison with Figure 5-27, the tensile stresses tend to decrease near the bottom flange interface with the web.

Figure 5-32 (b) shows the maximum principal stress distribution at the member end face. The finite element results indicate that a zone immediately above the mid-height of the girder will potentially crack upon release of pretensioning. As indicated by the cross section, the potential tensile crack is anticipated to extend well into the thickness of the web. As described above, the same observation is made in the vicinity of the bottom flange interface with the web.

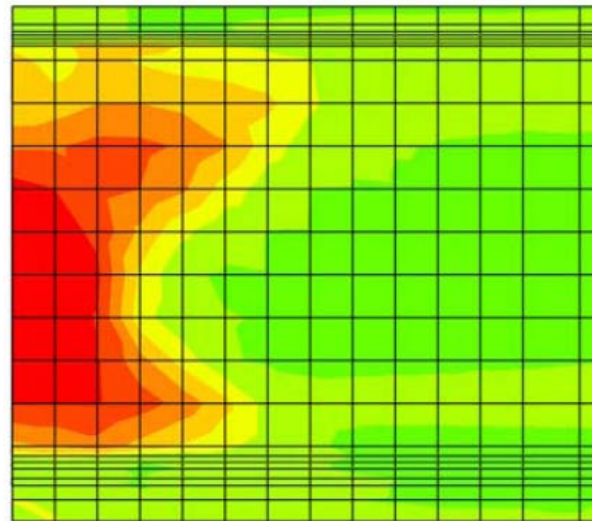
Figure 5-32 (c) shows the maximum principal stress distribution along the end zone of the specimen. The stress contour indicates that the potential tensile cracking of the girder web is confined to an area extending 6 in. from the member end face. The numerical results indicate that the addition of the end zone reinforcement retracts the tensile zone vulnerable to cracking by 3 in. in comparison with the finite element simulations without end zone rebar.



(a)



(b)



(c)

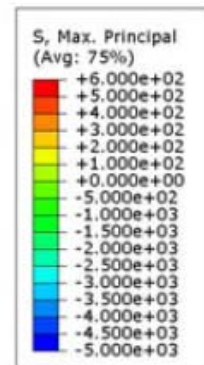


Figure 5-32: Elasto-plastic response of a typical BT-72 girder with AASHTO LRFD end zone rebar in addition to shear and confinement reinforcement immediately after the release of pretensioning: (a) Maximum principal vector contour along the end zone, (b) Maximum principal stress contour at member end face and (c) Maximum principal stress contour along the end zone.

Figure 5-33 (a) thru (d) show the vertical stress (S22) distribution along the end zone of the specimen shown at the various cross sections including the outside face of the web, 1 in. into the web thickness, 2 in. into the web thickness and the centerline of the member, respectively. Figure 5-33 (a) indicates a zone with tensile stresses near the rupture strength, initiating at about 3 in. from the girder end face at about the mid-height of the member. Based on Figure 5-33 (b) thru (d), the corresponding zone diminishes at about 1 in. into the web thickness.

Additionally, the numerical simulations indicate that the three-dimensional continuum analysis is capable of estimating not only the location and length but also the approximate depth of the potential tensile cracks immediately after the release of pretensioning.

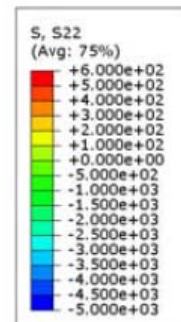
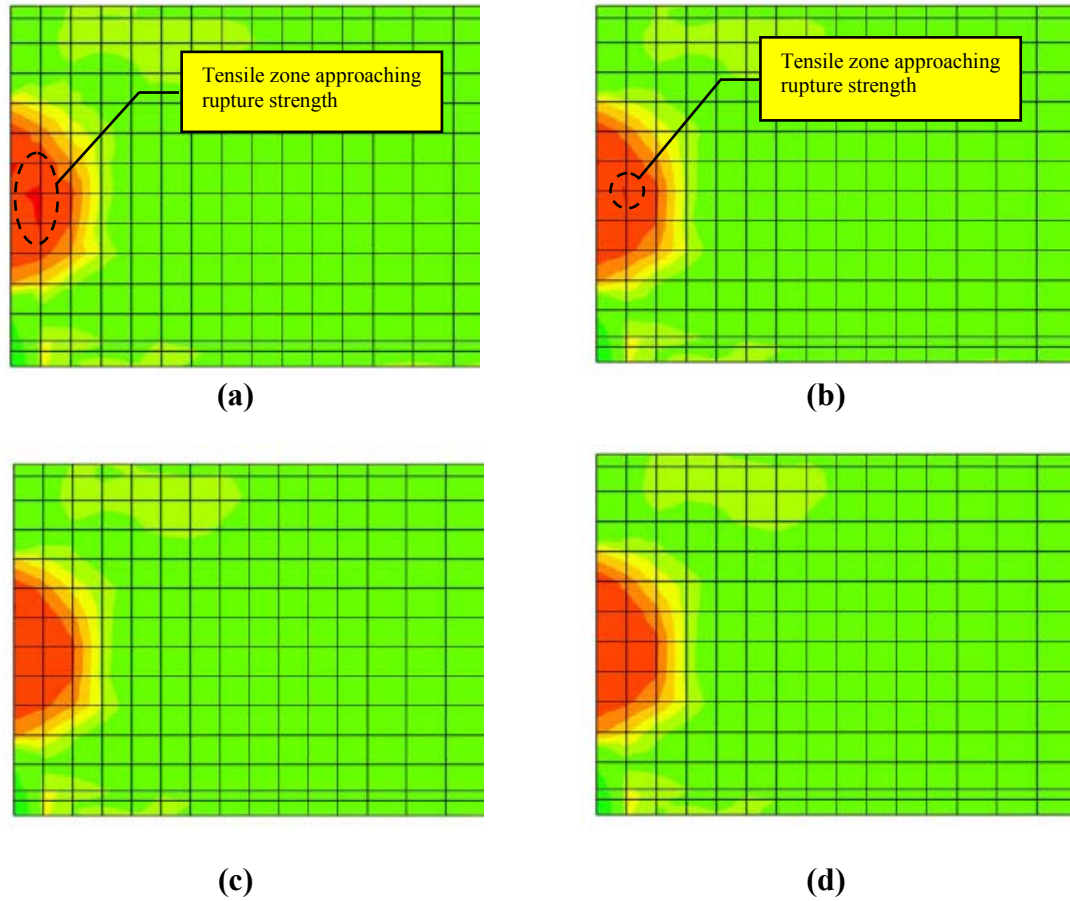


Figure 5-33: Vertical stress (S22) contours along the end zone of a typical BT-72 girder with AASHTO LRFD end zone rebar in addition to shear and confinement reinforcement immediately after the release of pretensioning shown at: (a) outside face of the web, (b) 1 in. into the web towards the centerline of the member, (c) 2 in. into the web towards the centerline of the member, and d) at the centerline of the member.

Figure 5-34 (a) shows the distribution of the planar shear stress (S23) averaged across the thickness of the web, along the span of the girder based on elasto-linear and elasto-plastic responses. The numerical simulations indicate tensile softening along the first 30 in. of the girder immediately after the release of pretensioning: maximum shear stress of 746 (psi) at 24 in. versus 830 (psi) at 18 in. from the girder end face based on elasto-plastic and linear-elastic responses, respectively.

Figure 5-34 (b) shows the planar shear stress (S23) contour at the outside face of the web based on elasto-plastic response of concrete. It is observed that the transfer of the axial pretensioning from the bottom flange upwards into the web results in significant concentration of shear stress at the bottom flange interface with the web. This shear transfer mechanism is anticipated to be due to the shear-lag caused by the difference in the magnitude of pretensioning in the bottom flange and web. The shear concentration is eventually resolved into the web over a distance approximately equal to the transfer length.

As it will be discussed in more details in Chapter 6, the above shear lag phenomenon may contribute to equivalent shear-friction cracking in the vicinity of the web and bottom flange, increasing the tensile stresses in the end zone reinforcement along the corresponding zone.

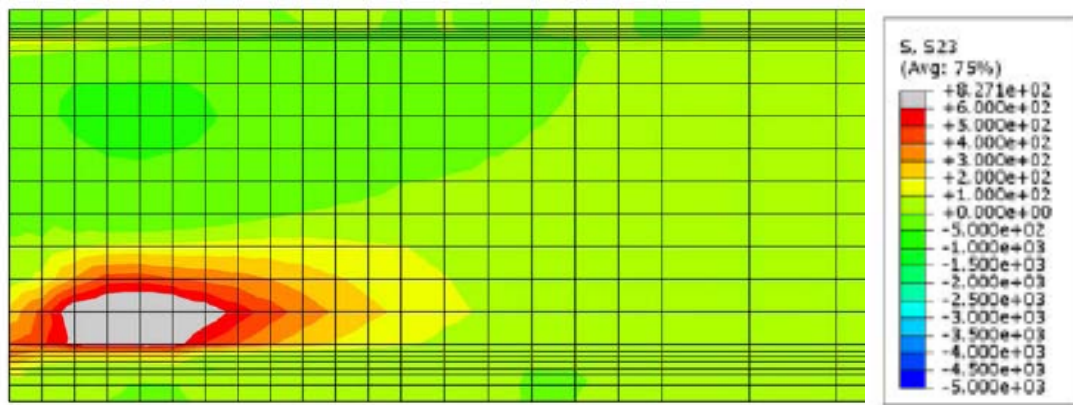
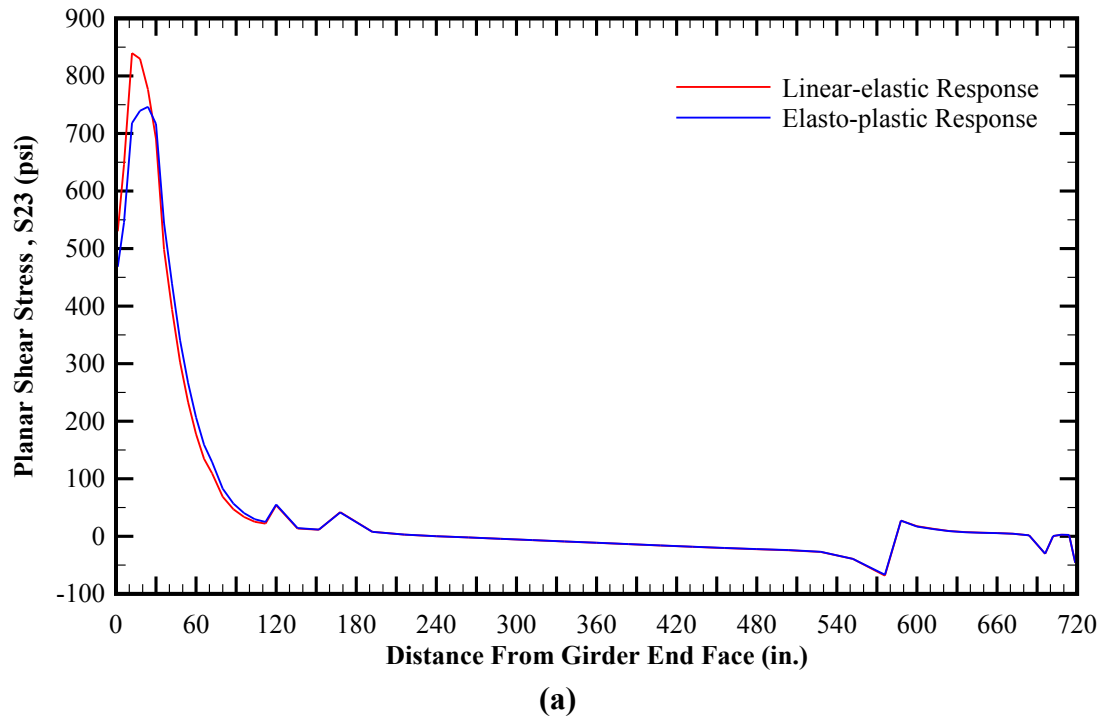


Figure 5-34: Planar shear stress (S23) distribution along the span of a typical BT-72 girder with AASHTO LRFD end zone rebar in addition to shear and confinement reinforcement immediately after the release of pretensioning: (a) Average shear stress across the width of the web, and (b) Shear stress contour at the outside face of the web base on elasto-plastic response.

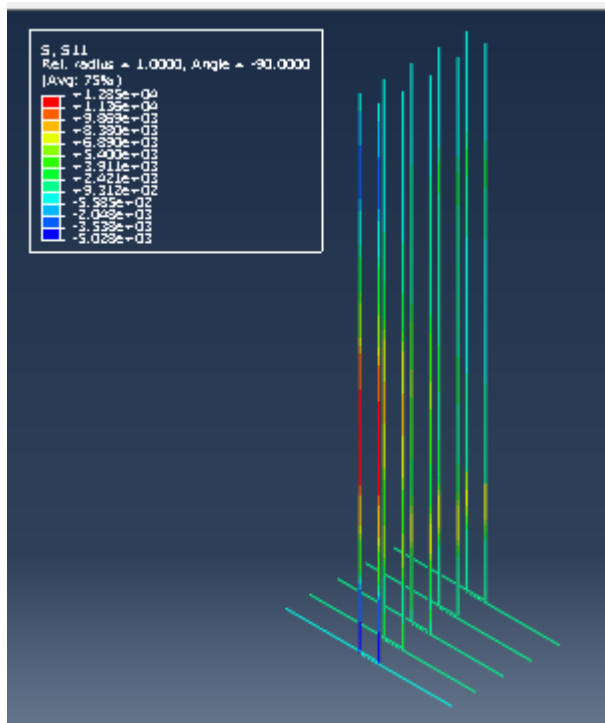
Figure 5-35 shows the state of axial stresses (S11) in the end zone reinforcing bars immediately after the release of pretensioning and based on elasto-plastic (e.g., nonlinear) response of concrete. As shown in Figure 5-35 (a), the magnitude of axial stresses in the end zone rebar reaches the maximum near the end face of the girder. Figure 5-35 (b) comparatively shows the maximum axial stress (S11) per each rebar in accordance with the location relative to the member end face. It shall be noted that positive axial stress indicates state of tension; negative axial stress indicates compression in the bars. The numerical results indicate that the maximum tensile stress is observed near the end face of the member. Travelling away from the end face, the magnitude of the tensile stress significantly decreases. This observation is consistent with the discussion of Section 5.5.4. Additionally, the axial stress distributions shown in Figure 5-35 (a) indicate that the location of the maximum tensile stresses shifts downwards from approximately the mid-height of EZR No.1 to the vicinity of the bottom flange interface with the web at EZR Nos. 3, 4, and 5. Table 5-8 shows the summary of the maximum tensile stresses in the end zone reinforcing bars obtained from the nonlinear numerical simulations of a typical BT-72 girder with AASHTO LRFD end zone rebar in addition to shear and confinement reinforcement immediately after the release of pretensioning, including the stress magnitude as well as the location along the height of the bar measured in relation to the bottom of the girder bottom flange assumed as datum.

The numerical results indicate that the maximum tensile stresses observed by the finite element simulations (12.8 ksi) is well below the allowable limit (20.0 ksi) specified by AASHTO LRFD in reference to Equation (5.20).

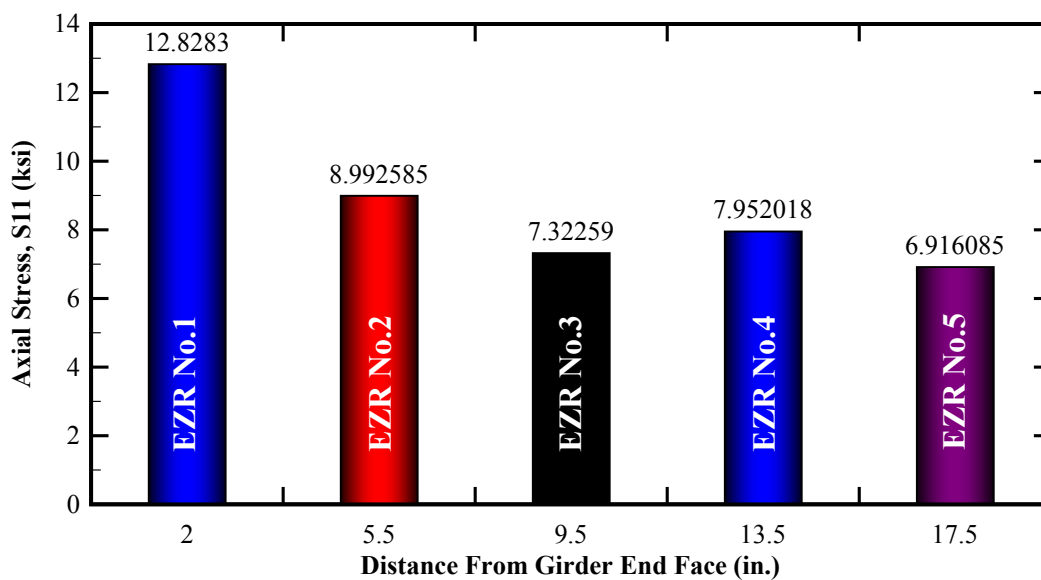
Table 5-8: Summary of the maximum tensile stresses in the end zone reinforcing bars obtained from the nonlinear numerical simulations of a typical BT-72 girder with AASHTO LRFD end zone rebar in addition to shear and confinement reinforcement immediately after the release of pretensioning.

I.D.	Max. Axial Stress at EZR (ksi)	Height along the Rebar (in.)
EZR #1	12.80	24.625
EZR #2	8.99	30.625
EZR #3	7.32	12.625
EZR #4	7.95	11.125
EZR #5	6.92	12.625

Similarly, Figure 5-36 (a) and (b) shows the axial stress (S11) distribution in the confinement reinforcement and the maximum stress per each rebar, respectively. The maximum tensile stress of 4.8 ksi is observed at a distance equivalent to 0.39 d (39% of the member height). Beyond a distance equivalent to 0.75 d (75% of the member height), the axial stresses in the confinement reinforcing bars stabilize on a constant magnitude of approximately 3.6 ksi.



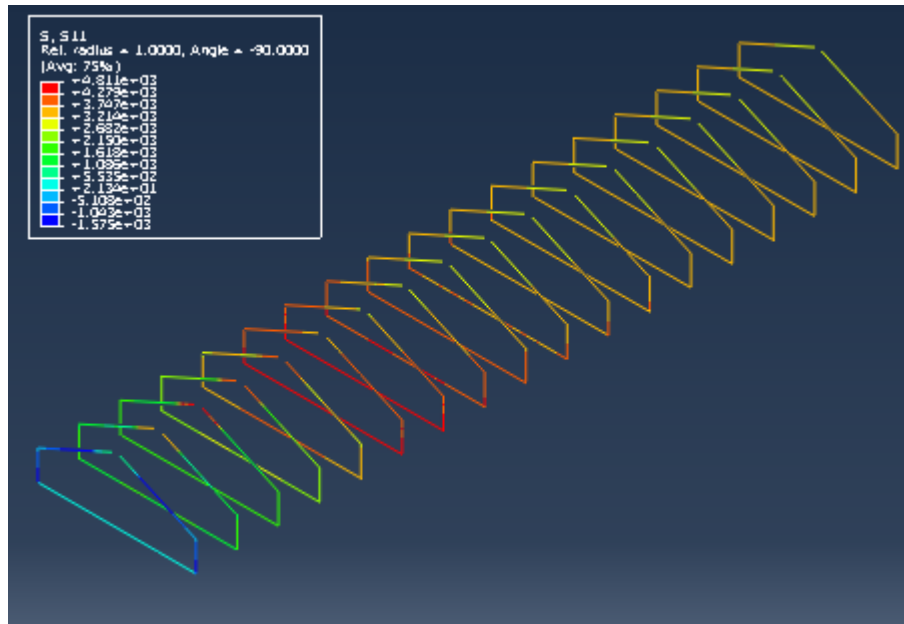
(a)



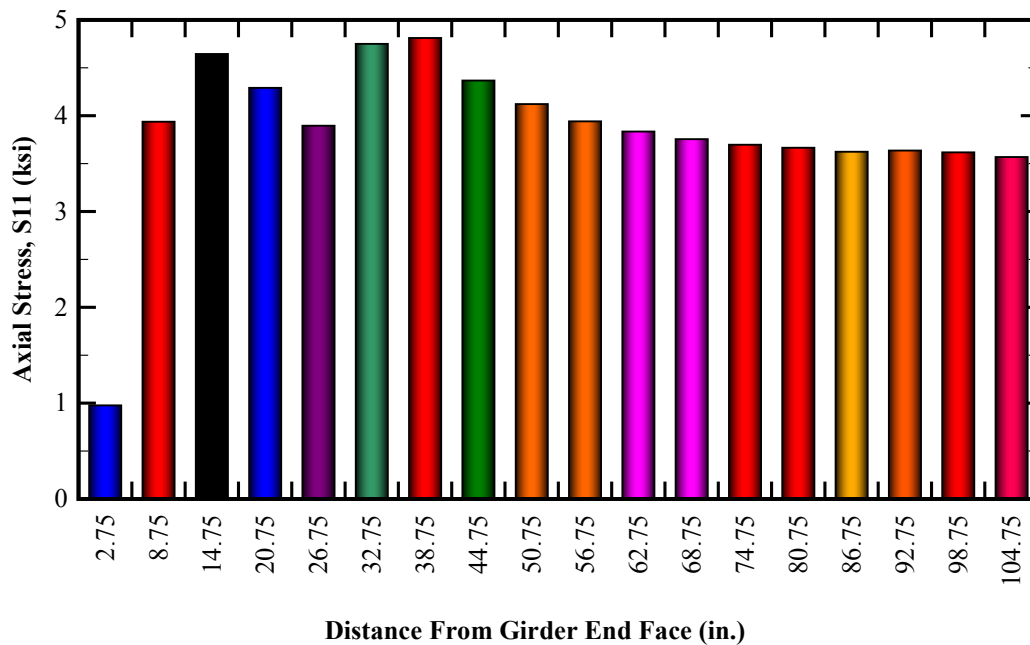
(b)

Figure 5-35: Axial stress (S11) in the end zone reinforcing bars of a typical BT-72 girder with AASHTO LRFD end zone rebar in addition to shear and confinement reinforcement immediately after the release of pretensioning: (a) Numerical results obtained by the nonlinear finite element simulation and (b) maximum stress per each end zone rebar.

Note: Positive axial stress indicates tension; negative axial stress indicate compression



(a)



(b)

Figure 5-36: Axial stress (S11) in the confinement reinforcement of a typical BT-72 girder with AASHTO LRFD end zone rebar in addition to shear and confinement reinforcement immediately after the release of pretensioning: (a) Numerical results obtained by nonlinear finite element simulation and (b) maximum stress per each confinement rebar.

Note: Positive axial stress indicates tension; negative axial stress indicates compression.

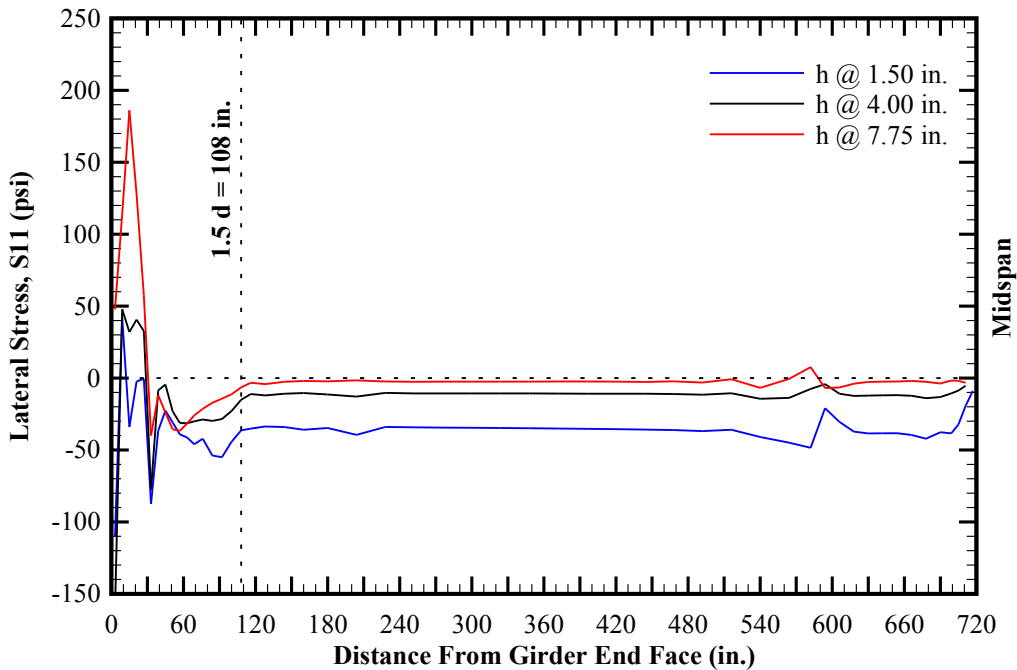


Figure 5-37: Lateral stress (S11) distribution of a typical BT-72 girder with AASHTO LRFD end zone reinforcement in addition to shear and confinement reinforcement within the bottom flange (elasto-plastic response).

Note: Positive pressure indicates state of compression; negative pressure indicates state of tension.

Figure 5-37 shows the lateral stress (S11) distribution within the bottom flange of a typical BT-72 girder with elasto-plastic response. As previously discussed, the current AASHTO LRFD specifications require confinement reinforcement to extend over a distance equal to 1.5 times the height of the precast member. The numerical simulations show a maximum lateral tensile stress of 186 psi near the top of the bottom flange at approximately 15 in. from the member end face. However, the lateral tensile stresses are resolved into state of compression at a distance approximately 33 in. from the girder end face.

5.5.4. BT-72 FE Model with Nebraska End Zone Reinforcing Details in Addition to Shear and Confinement Reinforcement

The third class of the finite element models correspond to the simulation of a typical BT-72 girder with end zone reinforcing details in accordance with the recommendations of NCHRP Report 654 as shown in Figure 5-18. The corresponding end zone reinforcement configurations will be referred as Nebraska details in reference to the supporting background research by Tadros et. al. (Tadros, Badie, & Tuan, 2010). Additionally, the finite element models include the shear and confinement rebars in accordance with the design requirements as shown in PCI BDM Example 9.4.

Table 5-9 includes the top and bottom fiber stresses at the harping point and midspan of the member. At each control location, three independent sets of results are reported based on the material behavior (linear-elastic or elasto-plastic) as well as those obtained by closed form solutions of PCI BDM Example 9.4. In addition, the maximum camber is reported at the midspan of the girder. The reported camber is based on the combined effect of self-weight of the girder and pretensioning immediately after the release of the strands.

Table 5-10 shows the comparison between the linear-elastic and elasto-plastic results versus the closed form solutions. Similar to the results of Section 5.5.2, the comparison of the results indicates overestimation of top fiber stresses and underestimation of the bottom fiber stress by the close form solutions. It is also observed that the inclusion of the end zone, shear and confinement reinforcement does not significantly affect the longitudinal stresses at the top and bottom fibers as well as the camber. This is consistent with the assumptions of the beam theory used as the basis for the closed form solutions.

The comparative study of the results obtained by the numerical simulations and the closed form solution indicates an acceptable conformance between the two methodologies. In other words, the two-dimensional beam theory is deemed adequately capable of estimating the flexural response of the pretensioned BT-72 girder.

Table 5-9: Results of the finite element analysis of a typical BT-72 girder with Nebraska end zone reinforcing details in addition to shear and confinement reinforcement as well as those by the closed form solutions included in PCI BDM Example 9.4. The results are reported immediately after the release of pretensioning.

	Linear-elastic Response	Elasto-plastic Response	Closed Form Solution
Stress in the extreme top fiber at harping point, σ_t^{Harp} (psi)	-238.6	-231.6	-256
Stress in the extreme bottom fiber at harping point, σ_c^{Harp} (psi)	-3683.5	-3672.1	-3313
Stress in the extreme top fiber at mid-span, $\sigma_t^{Midspan}$ (psi)	-272.4	-265.9	-301
Stress in the extreme bottom fiber at mid-span, $\sigma_c^{Midspan}$ (psi)	-3606.0	-3592.4	-3266
Maximum deflection at mid-span, $\Delta_{max}^{Midspan}$ (in.)	2.55 ↑	2.58 ↑	2.28 ↑
Notes: 9. Positive stresses correspond to the state of tension.. 10. Negative stresses correspond to the state of compression. 11. ↑ denotes positive camber (upward deflection). 12. ↓ denotes negative camber (downward deflection).			

Table 5-10: Comparison of the results obtained by the BT-72 finite element model with Nebraska end zone, shear and confinement reinforcement versus the closed form solutions in reference to Table 5-9.

	<i>Linear – elastic</i>	<i>Elasto – plastic</i>
	<i>Closed Form Sloution</i>	<i>Closed Form Sloution</i>
Stress in the extreme top fiber at harping point, σ_t^{Harp}	93%	90%
Stress in the extreme bottom fiber at harping point, σ_c^{Harp}	111%	111%
Stress in the extreme top fiber at mid-span, $\sigma_t^{Midspan}$	90%	88%
Stress in the extreme bottom fiber at mid-span, $\sigma_c^{Midspan}$	110%	110%
Maximum deflection at mid-span, $\Delta_{max}^{Midspan}$	112%	113%

Figure 5-38 shows the longitudinal stress (S33) distribution along the span of the member, measured at various heights of the BT-72 girder with elasto-plastic response. The magnitude and trend of the longitudinal stress distribution are similar to the results obtained in Section 5.5.2 with similar observations. Thus, the inclusion of the end zone, shear and confinement reinforcement does not affect the longitudinal stresses at top and bottom fibers along the span of the member, including the peaks affected by the sectional transition between the web and flanges as previously observed in the plain model without end zone, shear and confinement reinforcing bars.

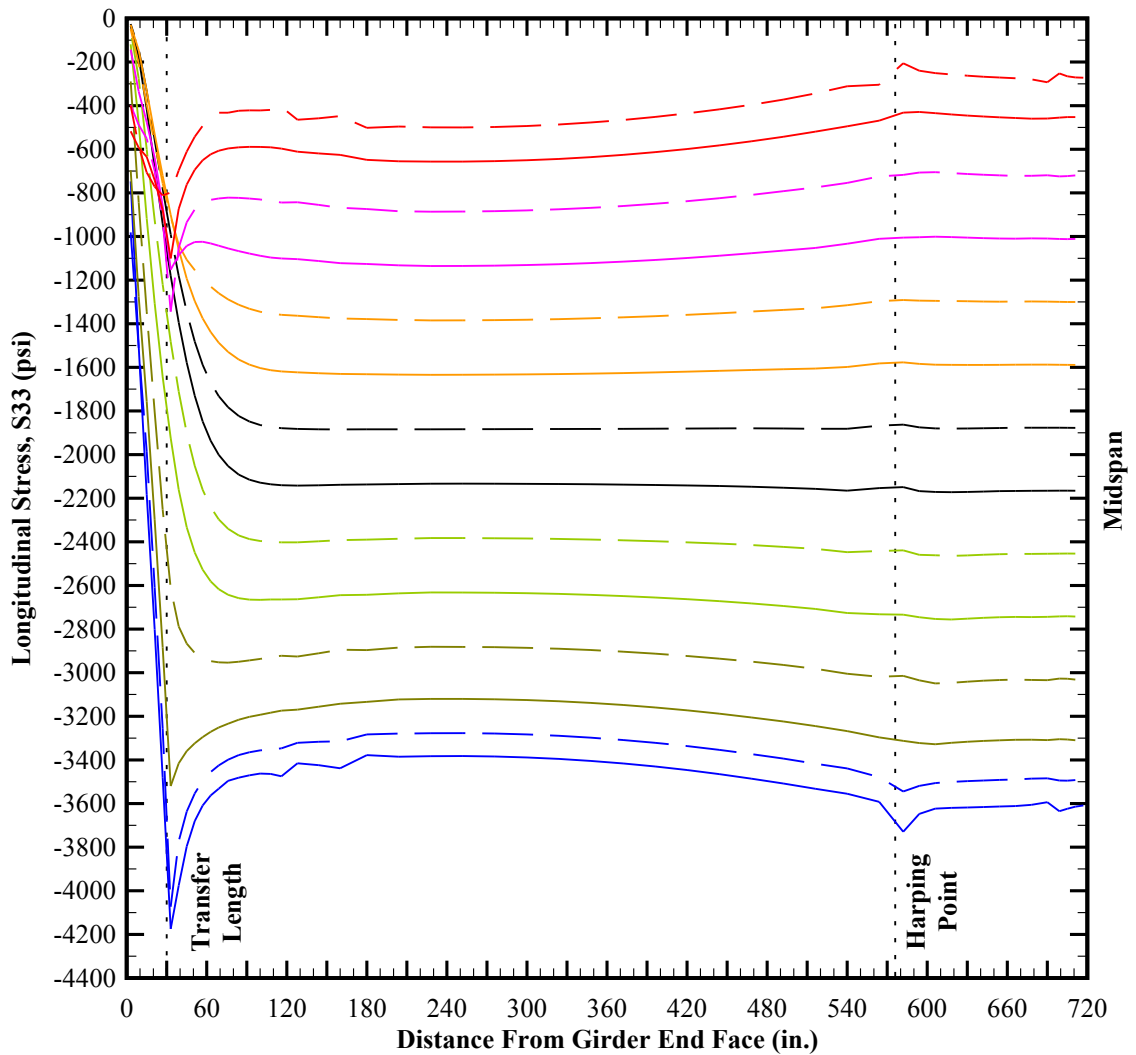


Figure 5-38: Longitudinal stresses (S33) along the height of a typical BT-72 girder with Nebraska end zone reinforcing details in addition to shear and confinement reinforcement immediately after the release of pretensioned strands and based on the elasto-plastic response of the specimen. Note: "h" is measured relative to the bottom face of the bottom flange assumed as datum.

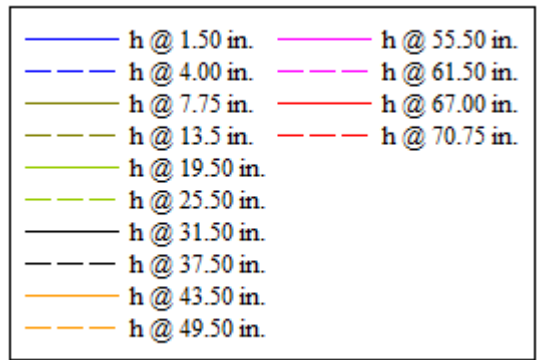


Figure 5-39 (a) thru (d) show the distribution of the vertical stresses (S_{22}) along the height of the BT-72 girder, measured at 3 in., 9 in., 33 in. and 51 in. from the girder end face, respectively. In addition, the elasto-plastic and linear-elastic responses are superimposed on each graph in order to show the effect of nonlinearity and material softening (e.g., potential cracking) at each interval.

It is observed that significant softening of concrete occurs within a domain confined between the member end face and 9 in. away from the girder end. The magnitude of the vertical tensile stresses indicates that potential cracking is anticipated along the mid-height of the girder web. Along the next domain confined between domain 9 in from the girder end and the theoretical transfer length (30 in. from the girder end face), the numerical solutions indicate that results obtained by the nonlinear and linear models begin to converge, indicating that the response of the member tends to stay and remain within the elastic regime. Beyond the theoretical transfer length, the response of the BT-72 girder predominantly remains within the elastic regime.

Similarly, Figure 5-40 includes the pressure distribution along the height of the BT-72 girder, measured at 3 in., 9 in., 33 in. and 51 in. from the girder end face, respectively. The trend of pressure is very similar to the longitudinal stresses (S_{33}) as described above. In accordance with the results obtained by the nonlinear finite element analysis, the girder web along 9 in. from the girder end face is susceptible to cracking immediately after the release of pretensioned strands.

The obtained numerical solutions re-emphasize the importance of utilizing elasto-plastic material behavior when analyzing the effect of pretensioning along the member

end zone, adequately capable of estimating material softening and the resulting stress redistribution within the areas susceptible to tensile cracking.

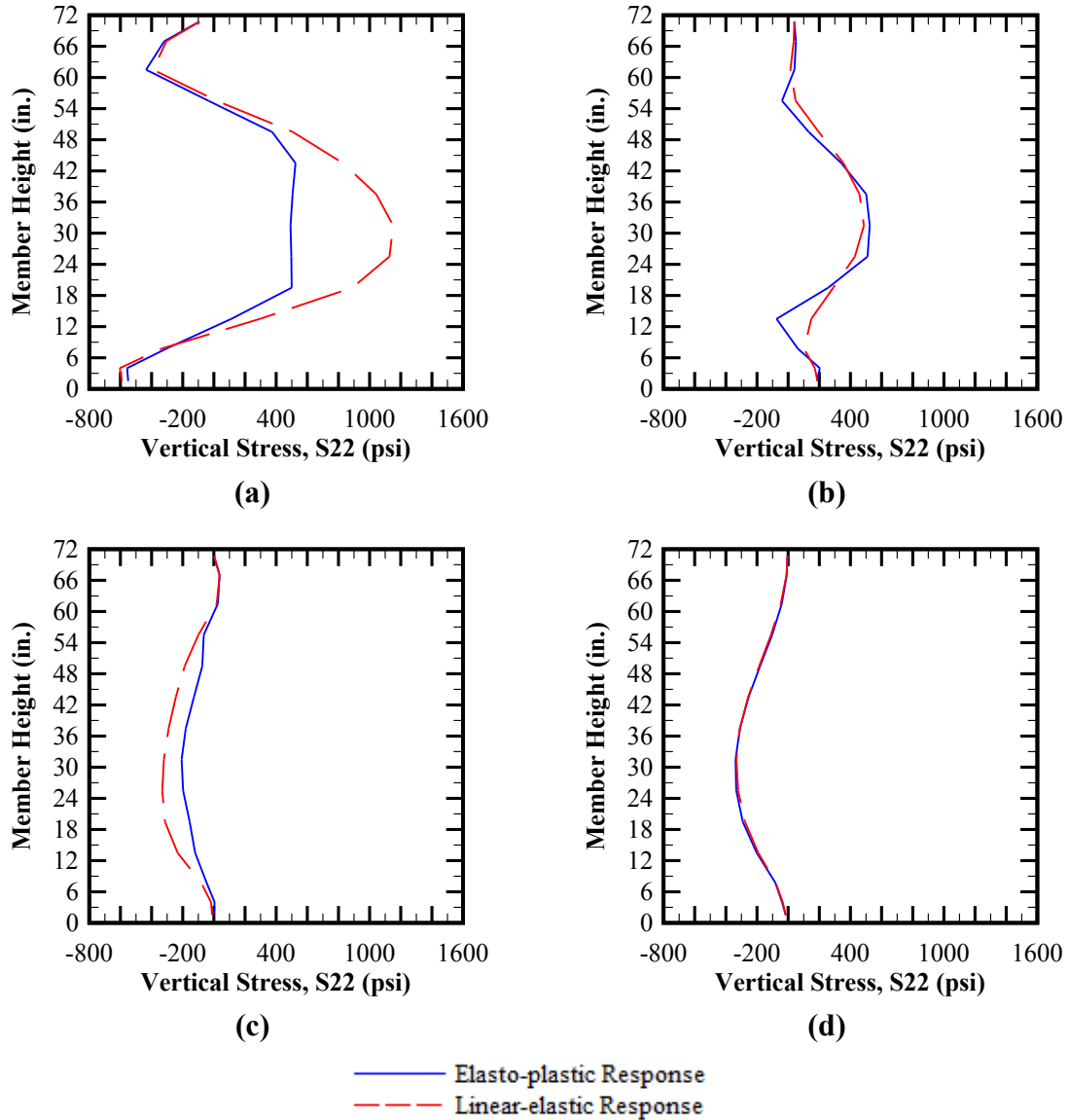


Figure 5-39: Vertical stress (S22) distribution along the height of a typical BT-72 girder with Nebraska end zone rebar in addition to shear and confinement reinforcement measured at: (a) 3 in. from girder end face, (b) 9 in. from the girder end face, (c) 33 in. from the girder end face, and (d) 51 in. from the girder end face.

Note: Positive stresses indicate state of tension; negative stresses indicate state of compression.

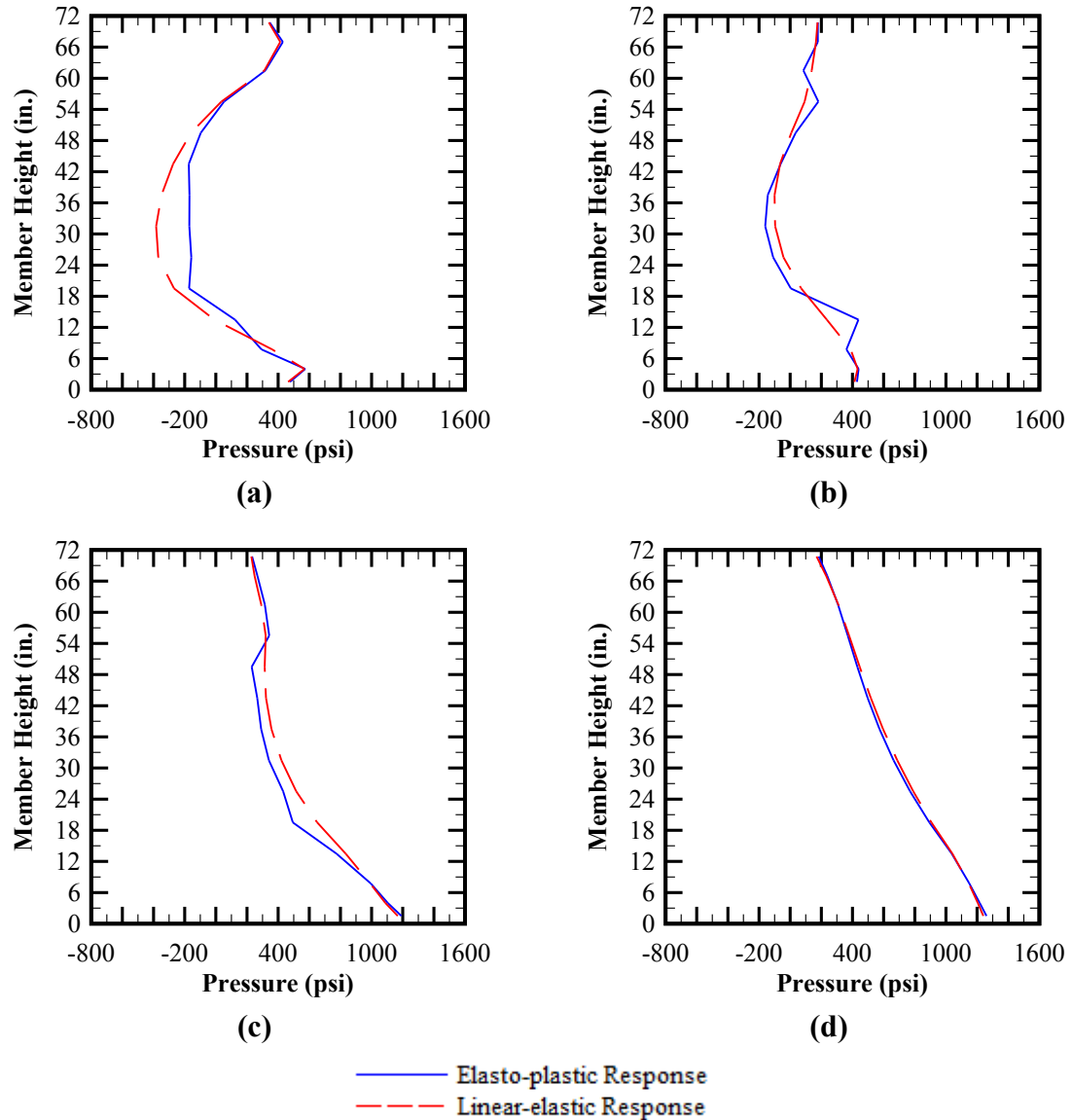


Figure 5-40: Pressure distribution along the height of a typical BT-72 girder with Nebraska end zone rebar in addition to shear and confinement reinforcement measured at: (a) 3 in. from girder end face, (b) 9 in. from the girder end face, (c) 33 in. from the girder end face, and (d) 51 in. from the girder end face.

Note: Positive pressure indicates state of compression; negative pressure indicates state of tension.

Figure 5-41 shows the state of maximum principal stress along the end zone of the BT-72 girder based on nonlinear (e.g., elasto-plastic concrete response) simulation. Figure 5-41 (a) shows the maximum principal vector contours near the girder end face, indicating the tensile stresses near rupture strength (f_r) initiating in a zone immediately above the interface between the web and bottom flange. Therefore, the web is potentially vulnerable to cracking not only along the mid height but also along the areas in the vicinity of the interface with the bottom flange. Although in comparison with Figure 5-27, the tensile stresses tend to decrease near the bottom flange interface with the web.

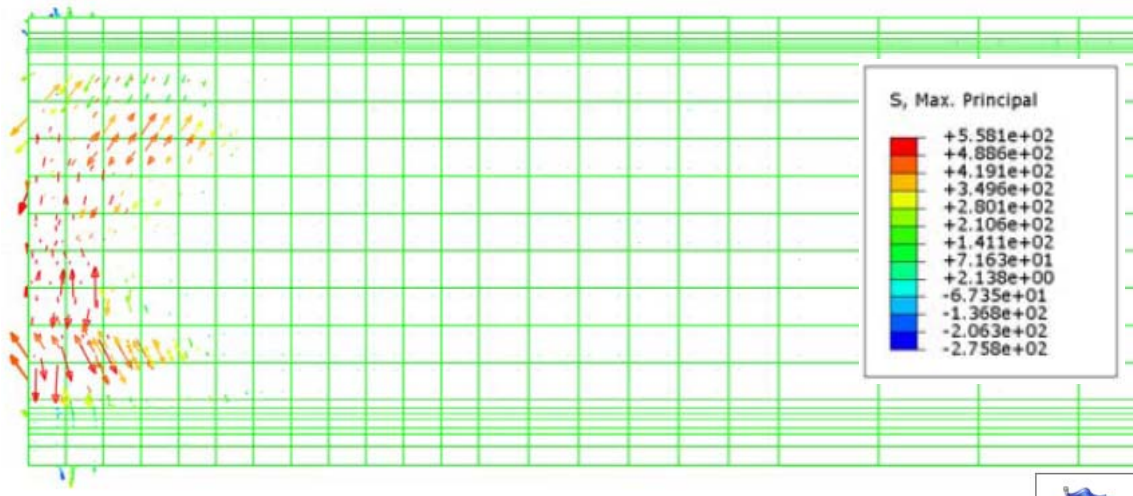
Figure 5-41 (b) shows the maximum principal stress distribution at the member end face. The finite element results indicate that a zone immediately above the mid-height of the girder will potentially crack upon release of pretensioning. As indicated by the cross section, the potential tensile crack is anticipated to extend well into the thickness of the web. As described above, the same observation is made in the vicinity of the bottom flange interface with the web.

Figure 5-41 (c) shows the maximum principal stress distribution along the end zone of the specimen. The stress contour indicates that the potential tensile cracking of the girder web is confined to an area extending 6 in. from the member end face. The numerical results indicate that the addition of the end zone reinforcement retracts the tensile zone vulnerable to cracking by 3 in. in comparison with the finite element simulations without end zone rebar.

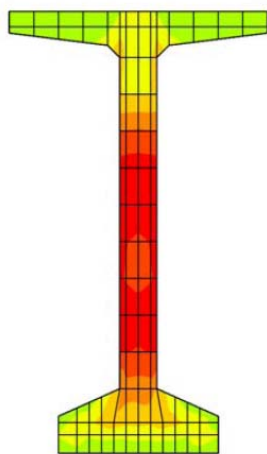
The comparison of the numerical results versus Section 5.5.3 indicates that similar maximum principal stresses are observed near the end face of the member: 558 psi (tensile) with Nebraska details versus 558 psi (tensile) with AASHTO LRFD details.

However, the concentration of the larger Nebraska end zone rebars near the end face of the member is shown to contain the areas susceptible to cracking in a smaller zone between the mid-height of the web and the bottom flange interface with web.

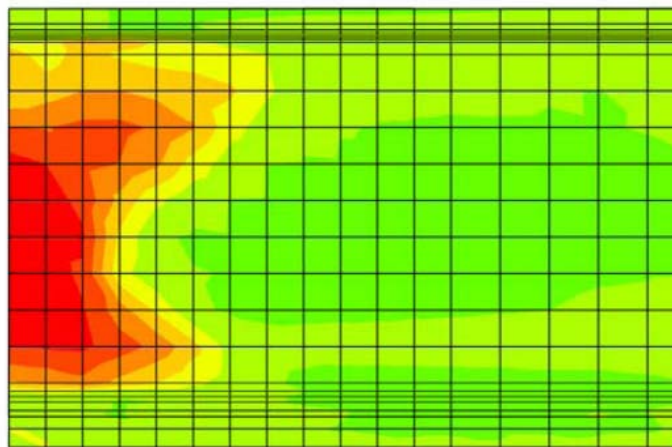
Figure 5-42 (a) thru (d) show the vertical stress (S22) distribution along the end zone of the specimen shown at the various cross sections including the outside face of the web, 1 in. into the web thickness, 2 in. into the web thickness and the centerline of the member, respectively. Figure 5-42 (a) indicates a zone with tensile stresses near the rupture strength, initiating at about 3 in. from the girder end face at about the mid-height of the member. Based on Figure 5-42 (b) thru (d), the tensile cracking is anticipated to be localized over the exterior face of the web versus the deeper cracks observed in finite element models with AASHTO LRFD end zone rebar (see Figure 5-33).



(a)



(b)



(c)

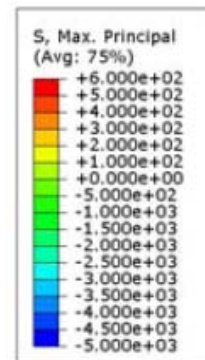


Figure 5-41: Elasto-plastic response of a typical BT-72 girder with Nebraska end zone rebar in addition to shear and confinement reinforcement immediately after the release of pretensioning: (a) Maximum principal vector contour along the end zone, (b) Maximum principal stress contour at member end face and (c) Maximum principal stress contour along the end zone.

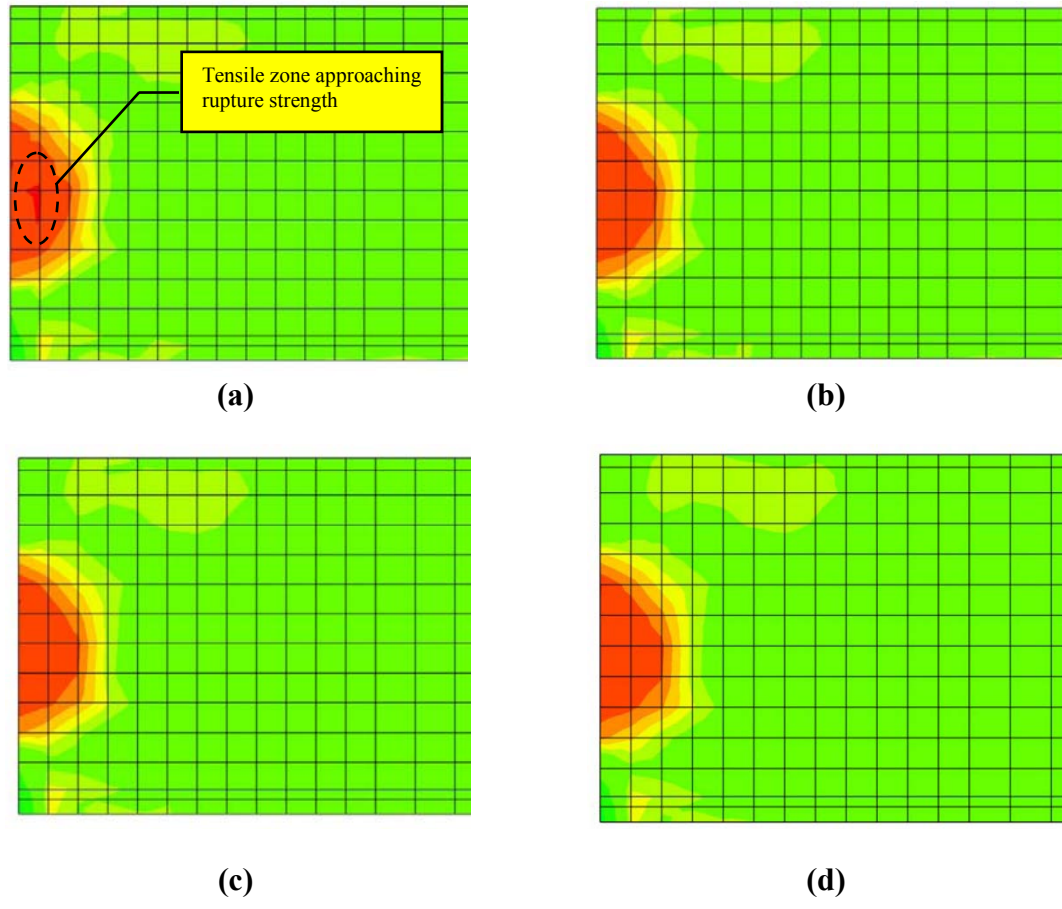


Figure 5-42: Vertical stress (S22) contours along the end zone of a typical BT-72 girder with Nebraska end zone rebar in addition to shear and confinement reinforcement immediately after the release of pretensioning shown at: (a) outside face of the web, (b) 1 in. into the web towards the centerline of the member, (c) 2 in. into the web towards the centerline of the member, and d) at the centerline of the member.

Figure 5-43 (a) shows the distribution of the planar shear stress (S23) averaged across the thickness of the web, along the span of the girder based on elasto-linear and elasto-plastic responses. The numerical simulations indicate tensile softening along the first 30 in. of the girder immediately after the release of pretensioning: maximum shear stress of 740 (psi) at 24 in. versus 828 (psi) at 18 in. from the girder end face based on elasto-plastic and linear-elastic responses, respectively.

Figure 5-43 (b) shows the planar shear stress (S23) contour at the outside face of the web based on elasto-plastic response of concrete. It is observed that the transfer of the axial pretensioning from the bottom flange upwards into the web results in significant concentration of shear stress at the bottom flange interface with the web. This shear transfer mechanism is anticipated to be due to the shear-lag caused by the difference in the magnitude of pretensioning in the bottom flange and web. The shear concentration is eventually resolved into the web over a distance approximately equal to the transfer length. The trend of the observed shear-lag is similar to the simulations utilizing AASHTO LRFD end zone rebar while the magnitude is slightly increased from 827 psi to 832 psi. As it was previously mentioned, the shear-lag phenomenon and the resulting shear-friction cracks at the interface between the web and bottom flange will be discussed in more details in Chapter 6.

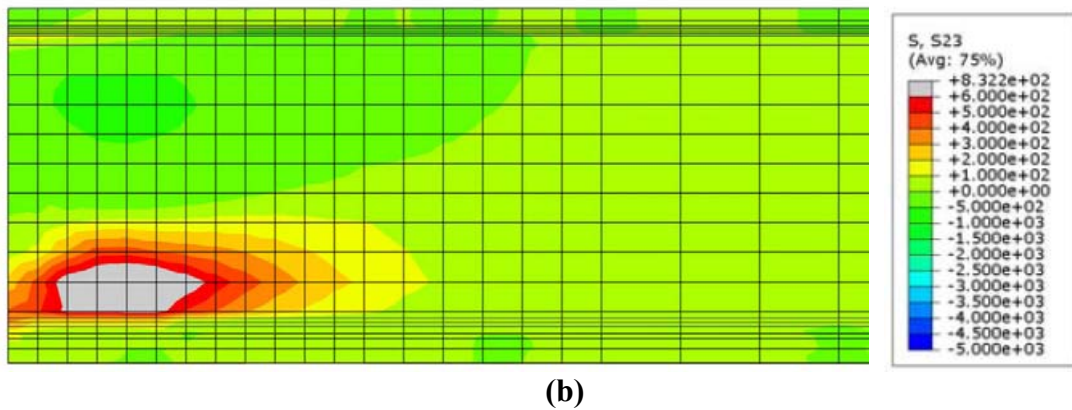
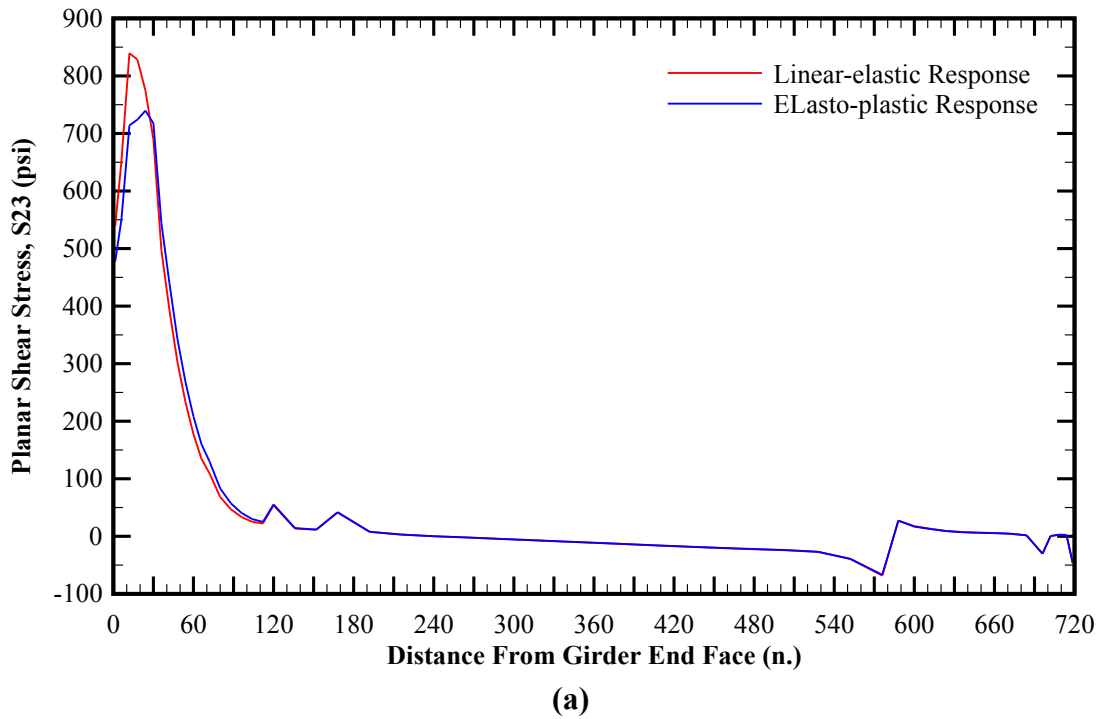


Figure 5-43: Planar shear stress (S23) distribution along the span of a typical BT-72 girder with Nebraska end zone rebar in addition to shear and confinement reinforcement immediately after the release of pretensioning: (a) Average shear stress across the width of the web, and (b) Shear stress contour at the outside face of the web base don elasto-plastic response.

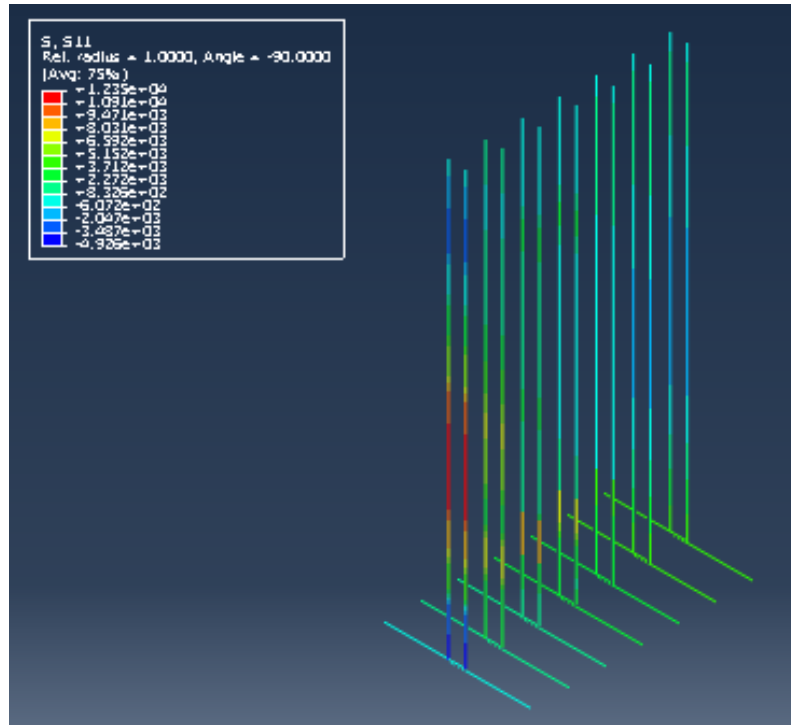
Figure 5-44 shows the state of axial stresses (S11) in the end zone reinforcing bars immediately after the release of pretensioning and based on elasto-plastic (e.g., nonlinear) response of concrete. As shown in Figure 5-44 (a), the magnitude of axial stresses in the end zone rebar reaches the maximum near the end face of the girder. Figure 5-44 (b) comparatively shows the maximum axial stress (S11) per each rebar in accordance with the location relative to the member end face. It shall be noted that positive axial stress indicates state of tension; negative axial stress indicates compression in the bars. The numerical results indicate that the maximum tensile stress is observed near the end face of the member. Travelling away from the end face, the magnitude of the tensile stress significantly decreases. This observation is consistent with the recommendations of NCHRP Report 654. Additionally, the axial stress distributions shown in Figure 5-44 (a) indicate that the location of the maximum tensile stresses shifts downwards from the mid-height of EZR No.1 to the vicinity of the bottom flange interface with the web at EZR Nos. 3 and 4. Table 5-11 shows the summary of the maximum tensile stresses in the end zone reinforcing bars obtained from the nonlinear numerical simulations of a typical BT-72 girder with Nebraska end zone rebar in addition to shear and confinement reinforcement immediately after the release of pretensioning, including the stress magnitude as well as the location along the height of the bar measured in relation to the bottom of the girder bottom flange assumed as datum.

Table 5-11: Summary of the maximum tensile stresses in the end zone reinforcing bars obtained from the nonlinear numerical simulations of a typical BT-72 girder with Nebraska end zone rebar in addition to shear and confinement reinforcement immediately after the release of pretensioning.

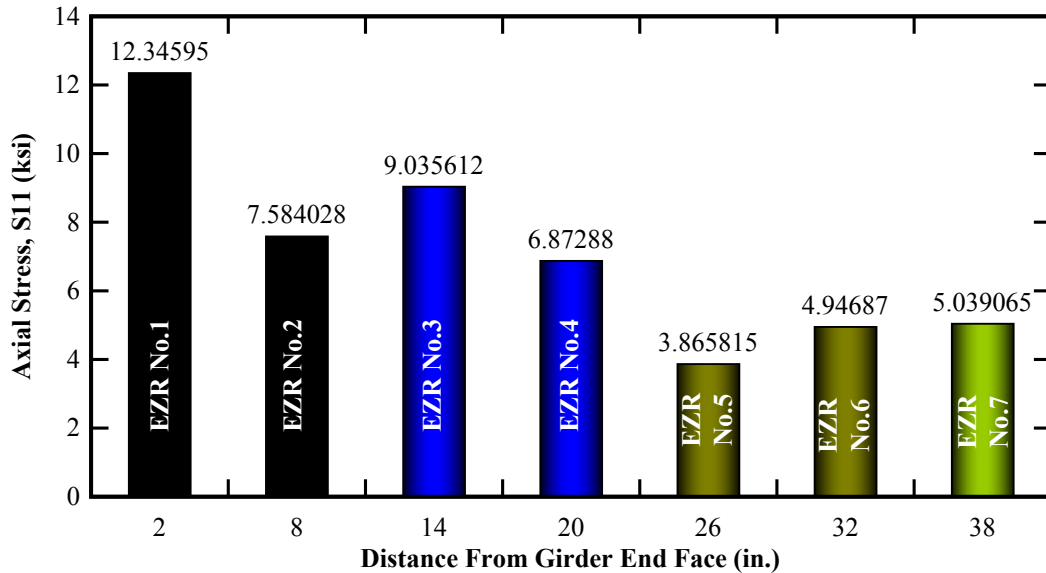
I.D.	Max. Axial Stress at EZR (ksi)	Height along the Rebar (in.)
EZR #1	12.34	30.625
EZR #2	7.58	11.125
EZR #3	9.04	14.125
EZR #4	6.87	12.625
EZR #5	3.87	11.125
EZR #6	4.95	1.203
EZR #7	5.04	0.859

The numerical results indicate that the maximum tensile stresses observed by the finite element simulations (12.3 ksi) is well below the allowable limit (20.0 ksi) specified by AASHTO LRFD in reference to Equation (5.20). In addition, the maximum tensile stress in the end zone near the end face of the member is approximately 96% of the maximum tension observed in the AASHTO LRFD end zone rebar at the same location.

Similarly, Figure 5-45 (a) and (b) shows the axial stress (S11) distribution in the confinement reinforcement and the maximum stress per each rebar, respectively. The maximum tensile stress of 4.9 ksi is observed at a distance equivalent to 0.15 d (15% of the member height). Beyond a distance equivalent to 0.75 d (75% of the member height), the axial stresses in the confinement reinforcing bars stabilize on a constant magnitude of approximately 3.6 ksi.



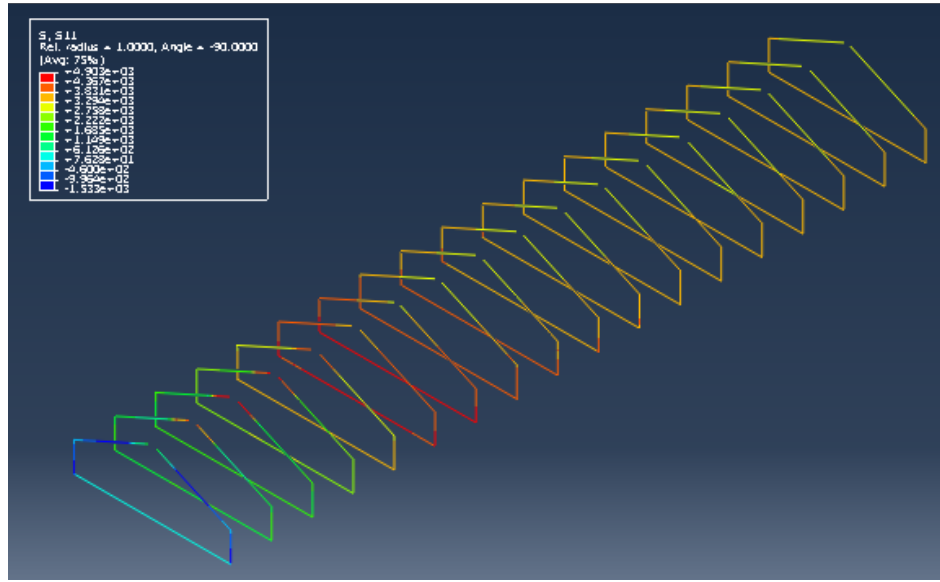
(a)



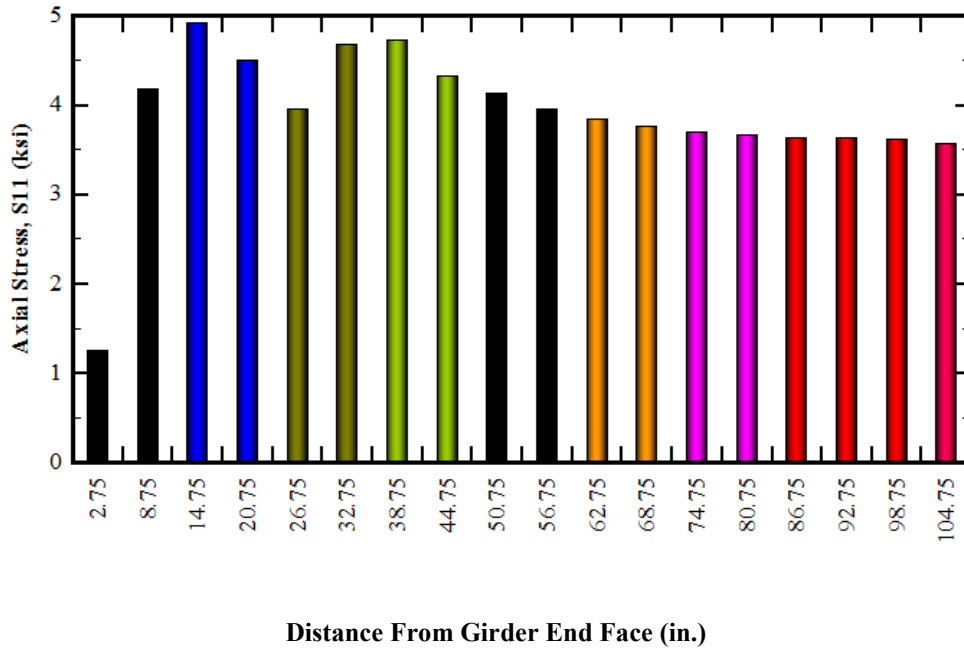
(b)

Figure 5-44: Axial stress (S11) in the end zone reinforcing bars of a typical BT-72 girder with Nebraska end zone rebar in addition to shear and confinement reinforcement immediately after the release of pretensioning: (a) Numerical results obtained by the nonlinear finite element simulation and (b) maximum stress per each end zone rebar.

Note: Positive axial stress indicates tension; negative axial stress indicate compression



(a)



(b)

Figure 5-45: Axial stress (S11) in the confinement reinforcement of a typical BT-72 girder with Nebraska end zone rebar in addition to shear and confinement reinforcement immediately after the release of pretensioning: (a) Numerical results obtained by nonlinear finite element simulation and (b) maximum stress per each confinement rebar.

Note: Positive axial stress indicates tension; negative axial stress indicates compression.

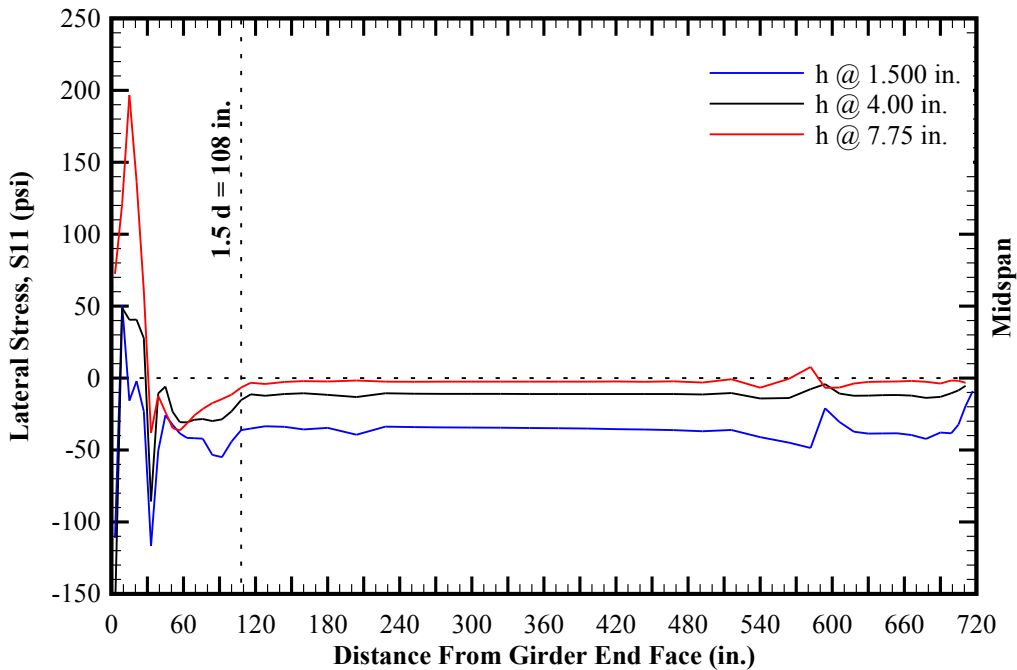


Figure 5-46: Lateral stress (S11) distribution of a typical BT-72 girder with Nebraska end zone reinforcement in addition to shear and confinement reinforcement within the bottom flange (elasto-plastic response).

Note: Positive pressure indicates state of compression; negative pressure indicates state of tension.

Figure 5-46 shows the lateral stress (S11) distribution within the bottom flange of a typical BT-72 girder with elasto-plastic response. As previously discussed, the current AASHTO LRFD specifications require confinement reinforcement to extend over a distance equal to 1.5 times the height of the precast member. The numerical simulations show a maximum lateral tensile stress of 197 psi near the top of the bottom flange at approximately 15 in. from the member end face. However, the lateral tensile stresses are resolved into state of compression at a distance approximately 33 in. from the girder end face.

5.5.5. BT-72 Model with IDOT End Zone Reinforcing Details in Addition to Shear and Confinement Reinforcement

The fourth class of the finite element models corresponds to the simulation of a typical BT-72 girder with end zone reinforcing details in accordance with the current requirements by Illinois Department of Transportation (IDOT) as shown in Figure 5-19. As previously discussed in Section 5.3.2.3, the IDOT end zone reinforcing configuration is comprised of 5 sets of 2-3/4 in. diameter threaded rods spaced at 3-1/4" on center. Further, the threaded rods are mechanically fastened to top and bottom steel plates (no pre- or post-tensioning), sandwiching the end zone along the vertical axis of the member. Additionally, the finite element models include the shear and confinement reinforcement in accordance with the design requirements as shown in PCI BDM Example 9.4.

Table 5-12 includes the top and bottom fiber stresses at the harping point and midspan of the member. At each control location, three independent sets of results are reported based on the material behavior (linear-elastic or elasto-plastic) as well as those obtained by closed form solutions of PCI BDM Example 9.4. In addition, the maximum camber is reported at the midspan of the girder. The reported camber is based on the combined effect of self-weight of the girder and pretensioning immediately after the release of the strands.

Table 5-13 shows the comparison between the linear-elastic and elasto-plastic results versus the closed form solutions. Similar to the results of Section 5.5.2, the comparison of the results indicates overestimation of top fiber stresses and underestimation of the bottom fiber stress by the close form solutions. It is also observed that the inclusion of the end zone, shear and confinement reinforcement does not significantly affect the

longitudinal stresses at the top and bottom fibers as well as the camber. This is consistent with the assumptions of the beam theory used as the basis for the closed form solutions.

The comparative study of the results obtained by the numerical simulations and the closed form solution indicates an acceptable conformance between the two methodologies. In other words, the two-dimensional beam theory is deemed adequately capable of estimating the flexural response of the pretensioned BT-72 girder.

Table 5-12: Results of the finite element analysis of a typical BT-72 girder with IDOT end zone reinforcing details in addition to shear and confinement reinforcement as well as those by the closed form solutions included in PCI BDM Example 9.4. The results are reported immediately after the release of pretensioning.

	Linear-elastic Response	Elasto-plastic Response	Closed Form Solution
Stress in the extreme top fiber at harping point, σ_t^{Harp} (psi)	-238.6	-231.7	-256
Stress in the extreme bottom fiber at harping point, σ_c^{Harp} (psi)	-3683.5	-3672.0	-3313
Stress in the extreme top fiber at mid-span, $\sigma_t^{Midspan}$ (psi)	-272.4	-266.0	-301
Stress in the extreme bottom fiber at mid-span, $\sigma_c^{Midspan}$ (psi)	-3606.0	-3592.3	-3266
Maximum deflection at mid-span, $\Delta_{max}^{Midspan}$ (in.)	2.55 ↑	2.58 ↑	2.28 ↑
Notes: 13. Positive stresses correspond to the state of tension.. 14. Negative stresses correspond to the state of compression. 15. ↑ denotes positive camber (upward deflection). 16. ↓ denotes negative camber (downward deflection).			

Table 5-13: Comparison of the results obtained by the BT-72 finite element model with IDOT end zone, shear and confinement reinforcement versus the closed form solutions in reference to Table 5-12.

	<i>Linear – elastic</i>	<i>Elasto – plastic</i>
	<i>Closed Form Sloution</i>	<i>Closed Form Sloution</i>
Stress in the extreme top fiber at harping point, σ_t^{Harp}	93%	91%
Stress in the extreme bottom fiber at harping point, σ_c^{Harp}	111%	111%
Stress in the extreme top fiber at mid-span, $\sigma_t^{Midspan}$	90%	88%
Stress in the extreme bottom fiber at mid-span, $\sigma_c^{Midspan}$	110%	110%
Maximum deflection at mid-span, $\Delta_{max}^{Midspan}$	112%	113%

Figure 5-47 shows the longitudinal stress (S33) distribution along the span of the member, measured at various heights of the BT-72 girder with elasto-plastic response. The magnitude and trend of the longitudinal stress distribution are similar to the results obtained in Section 5.5.2 with similar observations. Thus, the inclusion of the end zone, shear and confinement reinforcement does not affect the longitudinal stresses at top and bottom fibers along the span of the member, including the peaks affected by the sectional transition between the web and flanges as previously observed in the plain model without end zone, shear and confinement reinforcing bars.

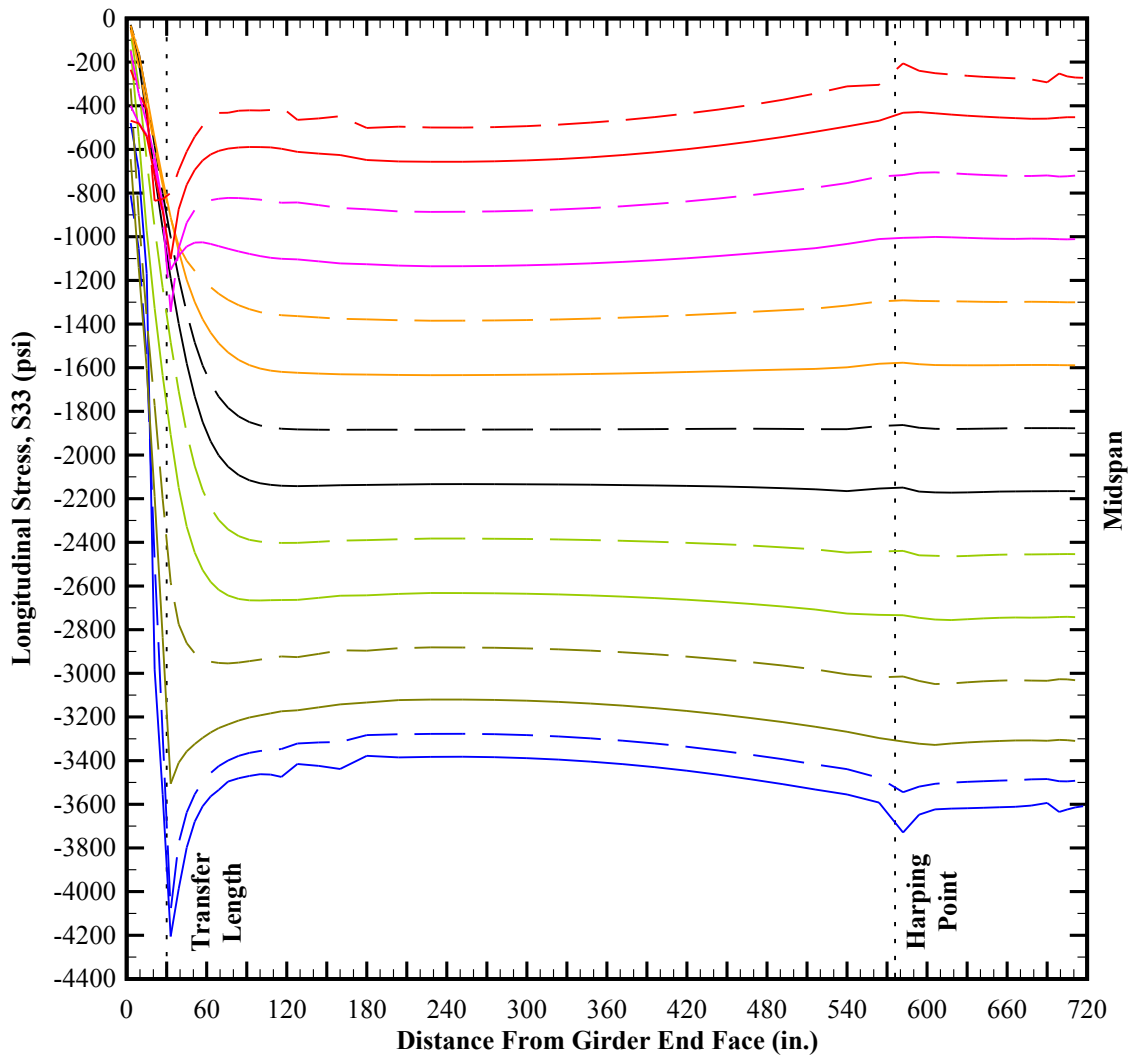


Figure 5-47: Longitudinal stresses (S33) along the height of a typical BT-72 girder with IDOT end zone reinforcing details in addition to shear and confinement reinforcement immediately after the release of pretensioned strands and based on the elasto-plastic response of the specimen. Note: "h" is measured relative to the bottom face of the bottom flange assumed as datum.

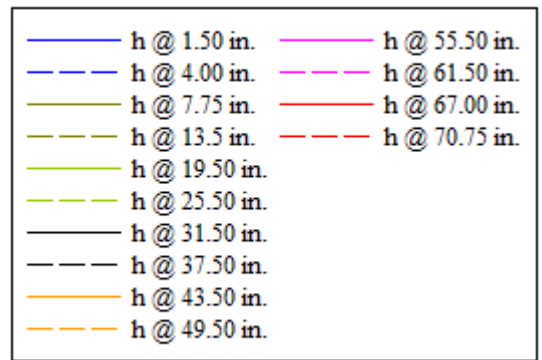


Figure 5-48 (a) thru (d) show the distribution of the vertical stresses (S_{22}) along the height of the BT-72 girder, measured at 3 in., 9 in., 33 in. and 51 in. from the girder end face, respectively. In addition, the elasto-plastic and linear-elastic responses are superimposed on each graph in order to show the effect of nonlinearity and material softening (e.g., potential cracking) at each interval.

It is observed that significant softening of concrete occurs within a domain confined between the member end face and 9 in. away from the girder end. The magnitude of the vertical tensile stresses indicates that potential cracking is anticipated along the mid-height of the girder web. Along the next domain confined between domain 9 in from the girder end and the theoretical transfer length (30 in. from the girder end face), the numerical solutions indicate that results obtained by the nonlinear and linear models begin to converge, indicating that the response of the member tends to stay and remain within the elastic regime. Beyond the theoretical transfer length, the response of the BT-72 girder predominantly remains within the elastic regime.

Similarly, Figure 5-49 includes the pressure distribution along the height of the BT-72 girder, measured at 3 in., 9 in., 33 in. and 51 in. from the girder end face, respectively. The trend of pressure is very similar to the longitudinal stresses (S_{33}) as described above. In accordance with the results obtained by the nonlinear finite element analysis, the girder web along 9 in. from the girder end face is susceptible to cracking immediately after the release of pretensioned strands.

The obtained numerical solutions re-emphasize the importance of utilizing elasto-plastic material behavior when analyzing the effect of pretensioning along the member

end zone, adequately capable of estimating material softening and the resulting stress redistribution within the areas susceptible to tensile cracking.

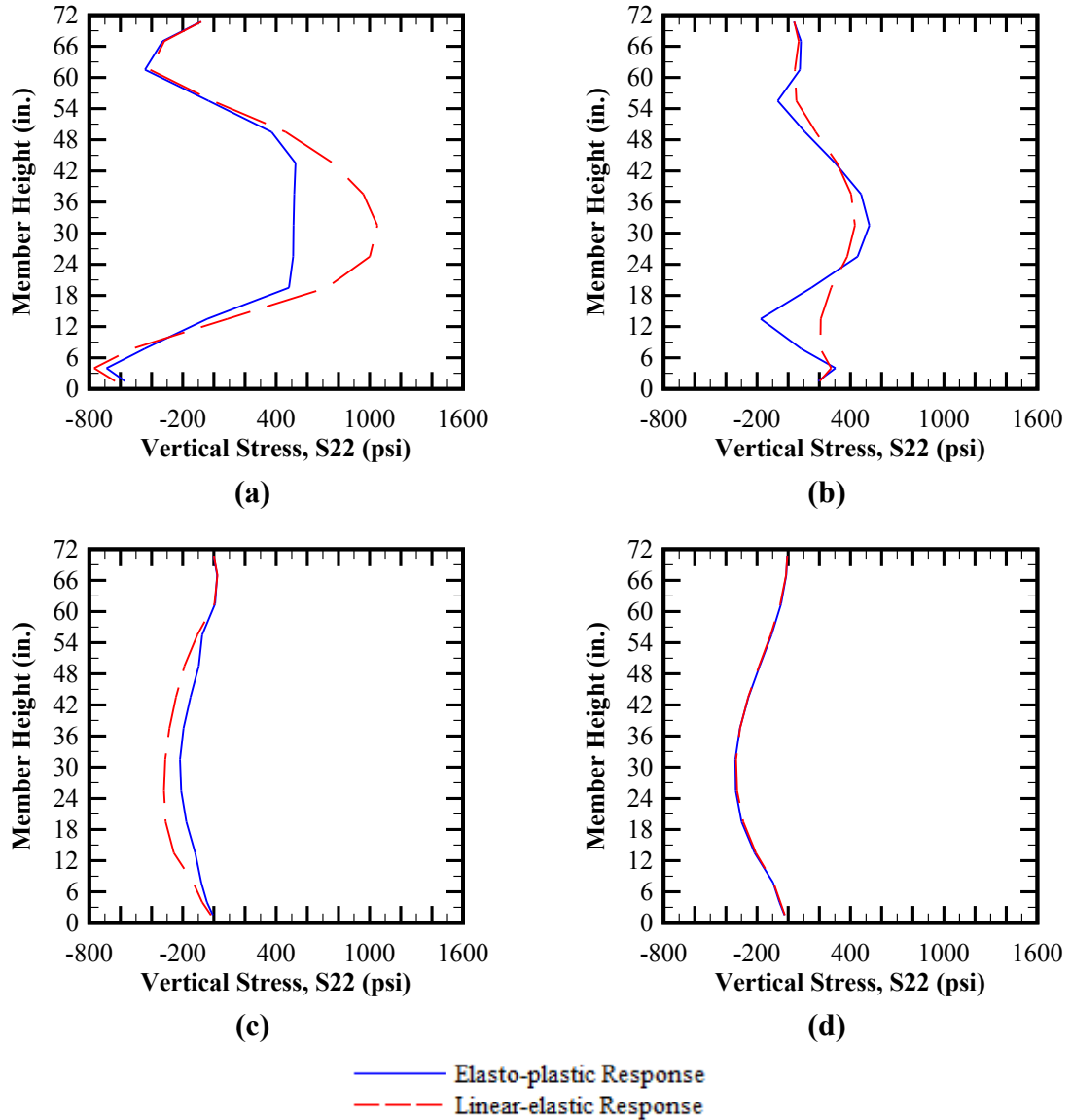


Figure 5-48: Vertical stress (S22) distribution along the height of a typical BT-72 girder with IDOT end zone rebar in addition to shear and confinement reinforcement measured at: (a) 3 in. from girder end face, (b) 9 in. from the girder end face, (c) 33 in. from the girder end face, and (d) 51 in. from the girder end face.

Note: Positive stresses indicate state of tension; negative stresses indicate state of compression.

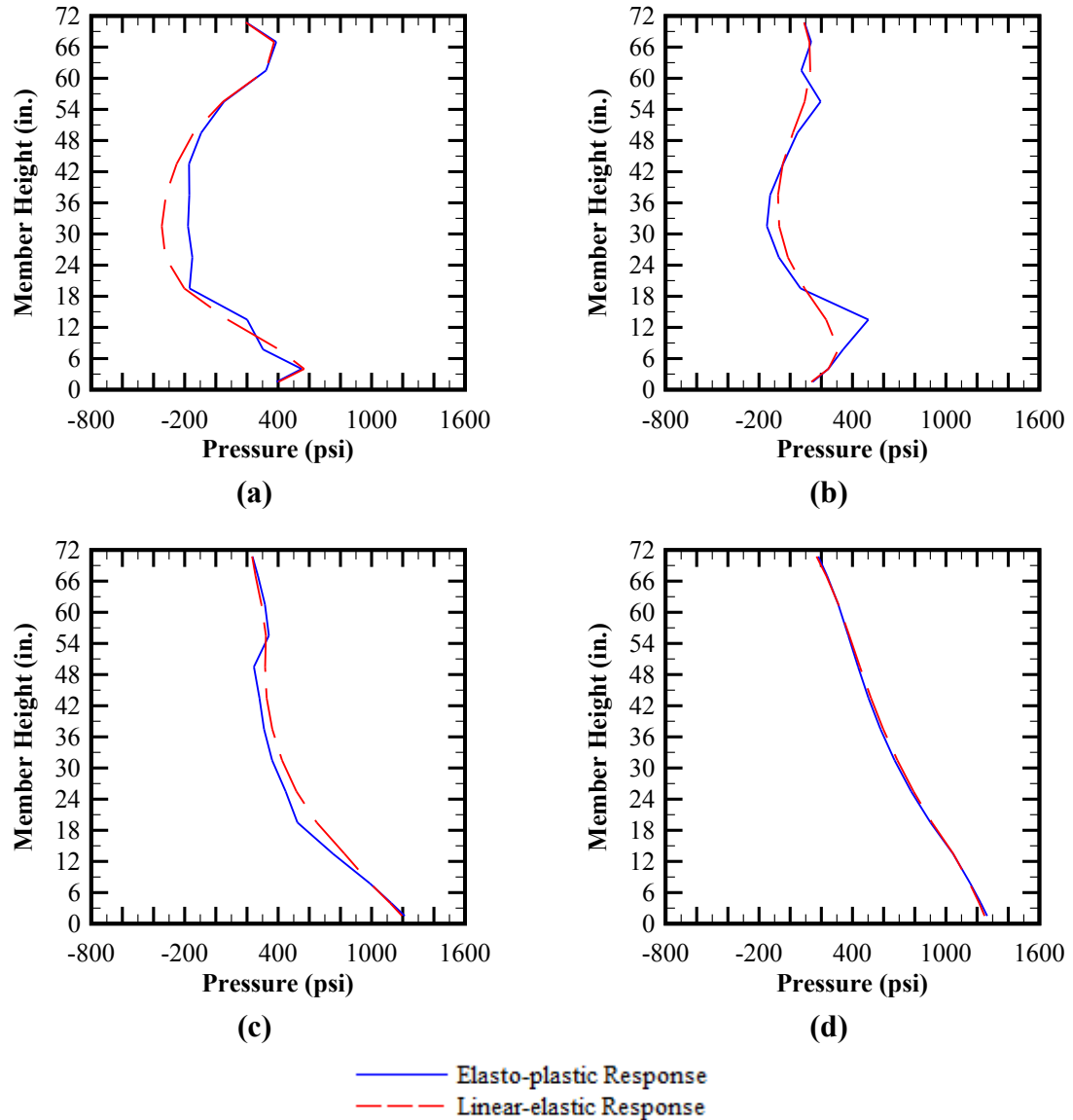


Figure 5-49: Pressure distribution along the height of a typical BT-72 girder with IDOT end zone rebar in addition to shear and confinement reinforcement measured at: (a) 3 in. from girder end face, (b) 9 in. from the girder end face, (c) 33 in. from the girder end face, and (d) 51 in. from the girder end face.

Note: Positive pressure indicates state of compression; negative pressure indicates state of tension.

Figure 5-50 shows the state of maximum principal stress along the end zone of the BT-72 girder based on nonlinear (e.g., elasto-plastic concrete response) simulation. Figure 5-50 (a) shows the maximum principal vector contours near the girder end face, indicating the tensile stresses near rupture strength (f_r) initiating in a zone in the vicinity of the mid-height of the web. In comparison with the response of the members with AASHTO LRFD and Nebraska details, the simulations utilizing the IDOT end zone configurations indicate that the areas susceptible to tensile cracking are more concentrated near mid-height of the web.

Figure 5-50 (b) shows the maximum principal stress distribution at the member end face. The finite element results indicate that a zone near the mid-height of the girder will potentially crack upon release of pretensioning. As indicated by the cross section, the potential tensile crack is anticipated to extend through the entire web thickness.

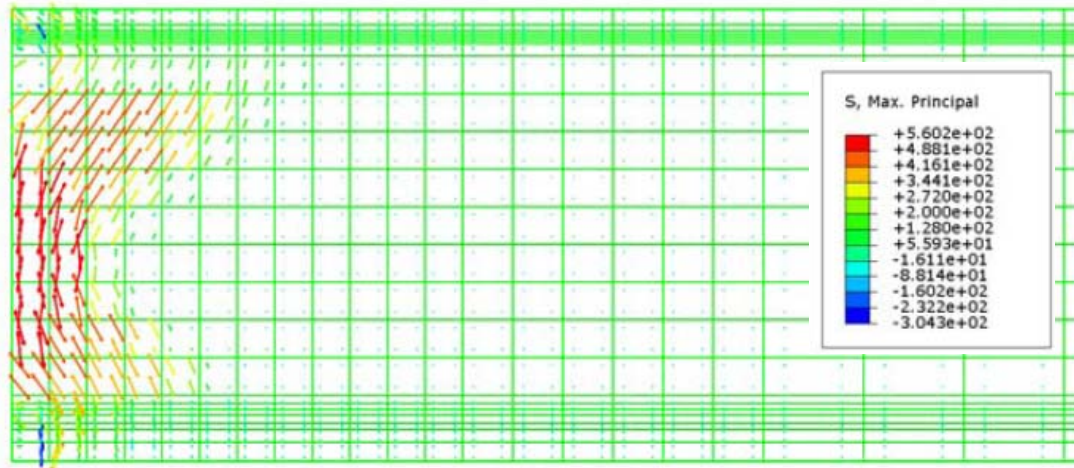
Figure 5-50 (c) shows the maximum principal stress distribution along the end zone of the specimen. The stress contour indicates that the potential tensile cracking of the girder web is confined to an area approximately extending 4 in. from the member end face. The numerical results indicate that the IDOT end zone reinforcing details further retracts the concentration of the tensile stresses in comparison with the members including AASHTO LRFD and Nebraska details.

The comparison of the numerical results versus Section 5.5.3 indicates slight increase in the magnitude of the maximum principal stresses near the end face of the member: 560 psi (tensile) versus 558 psi (tensile) with AASHTO LRFD details. However, the IDOT end zone scheme is shown to contain the areas susceptible to cracking in a smaller zone

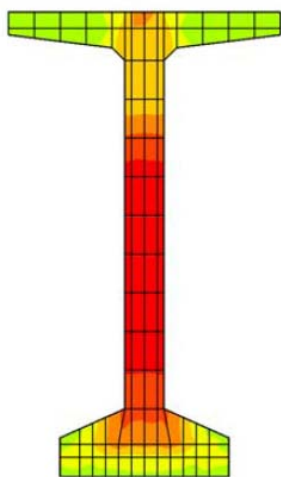
between the mid-height of the web and the bottom flange interface with web as mentioned above.

Figure 5-51 (a) thru (d) show the vertical stress (S22) distribution along the end zone of the specimen shown at the various cross sections including the outside face of the web, 1 in. into the web thickness, 2 in. into the web thickness and the centerline of the member, respectively. The numerical results indicate areas susceptible to tensile cracking extending from the outside face of the web towards the centerline of the member immediately after the release of pretensioning. The corresponding response is different from both the members with AASHTO LRFD and Nebraska end zone details which show shallower tensile cracks.

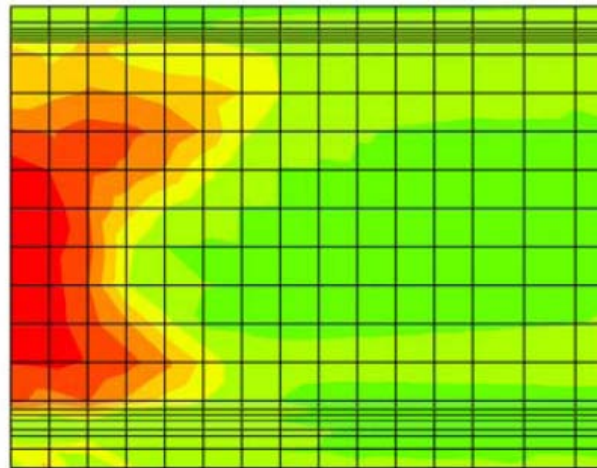
On the other hand, the areas exposed to tensile stresses near the rupture strength are shifted towards the mid-height of the web in the simulations utilizing the IDOT end zone details. However, the extent of the areas susceptible to tensile cracking is stays closer to the member end face in comparison with the members with AASHTO LRFD and IDOT end zone details.



(a)

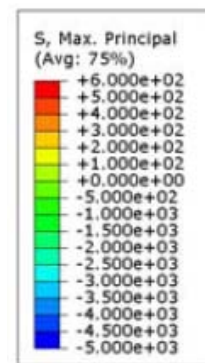


(b)



(c)

Figure 5-50: Elasto-plastic response of a typical BT-72 girder with IDOT end zone rebar in addition to shear and confinement reinforcement immediately after the release of pretensioning: (a) Maximum principal vector contour along the end zone, (b) Maximum principal stress contour at member end face and (c) Maximum principal stress contour along the end zone.



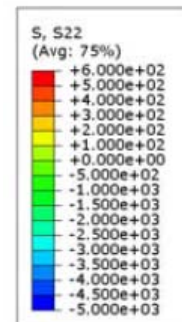
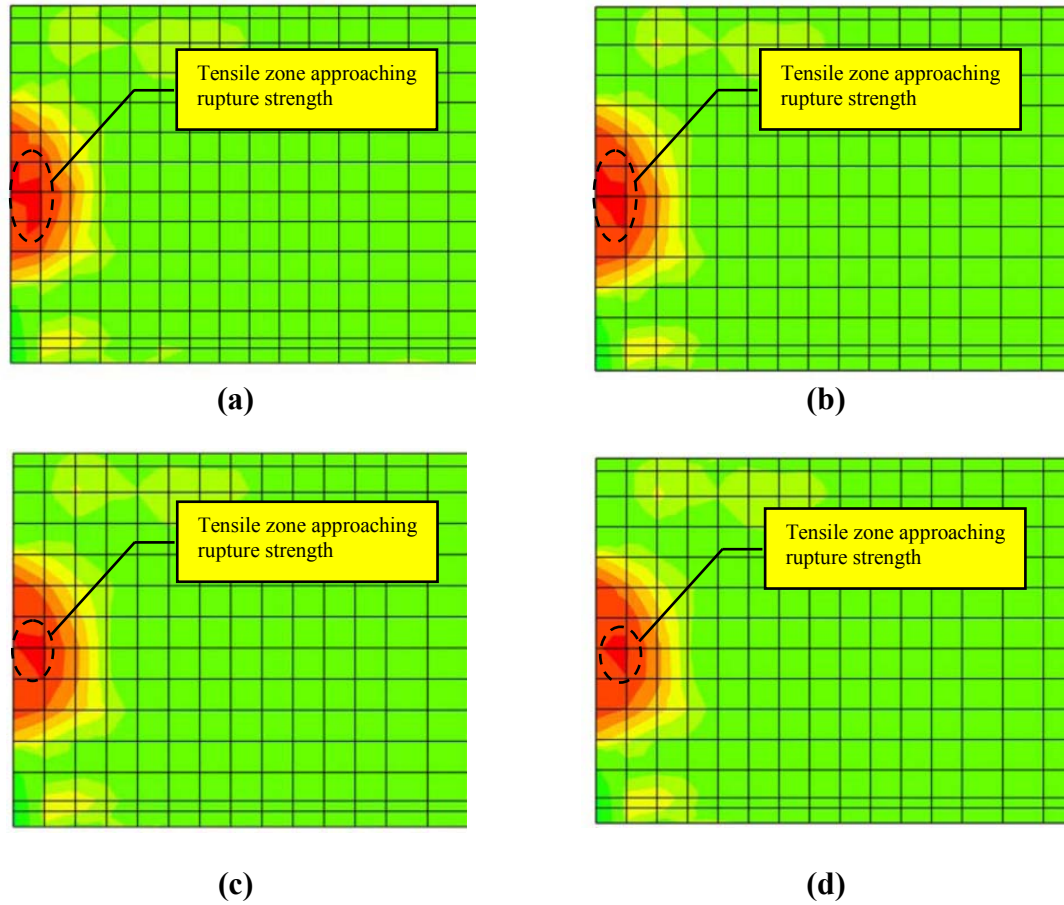


Figure 5-51: Vertical stress (S22) contours along the end zone of a typical BT-72 girder with IDOT end zone rebar in addition to shear and confinement reinforcement immediately after the release of pretensioning shown at: (a) outside face of the web, (b) 1 in. into the web towards the centerline of the member, (c) 2 in. into the web towards the centerline of the member, and d) at the centerline of the member.

Figure 5-52 (a) shows the distribution of the planar shear stress (S23) averaged across the thickness of the web, along the span of the girder based on elasto-linear and elasto-plastic responses. The numerical simulations indicate tensile softening along the first 30 in. of the girder immediately after the release of pretensioning: maximum shear stress of 718 (psi) at 24 in. versus 844 (psi) at 12 in. from the girder end face based on elasto-plastic and linear-elastic responses, respectively.

Figure 5-52 (b) shows the planar shear stress (S23) contour at the outside face of the web based on elasto-plastic response of concrete. It is observed that the transfer of the axial pretensioning from the bottom flange upwards into the web results in significant concentration of shear stress at the bottom flange interface with the web. This shear transfer mechanism is anticipated to be due to the shear-lag caused by the difference in the magnitude of pretensioning in the bottom flange and web. The shear concentration is eventually resolved into the web over a distance approximately equal to the transfer length. The trend of the observed shear-lag is similar to the simulations utilizing AASHTO LRFD end zone rebars while the magnitude is decreased from 827 psi to 800 psi. As it was previously mentioned, the shear-lag phenomenon and the resulting shear-friction cracks at the interface between the web and bottom flange will be discussed in more details in Chapter 6.

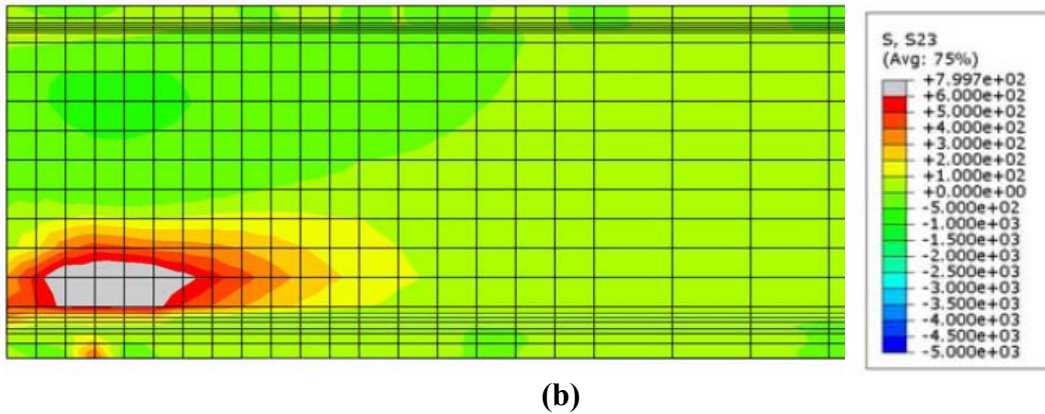
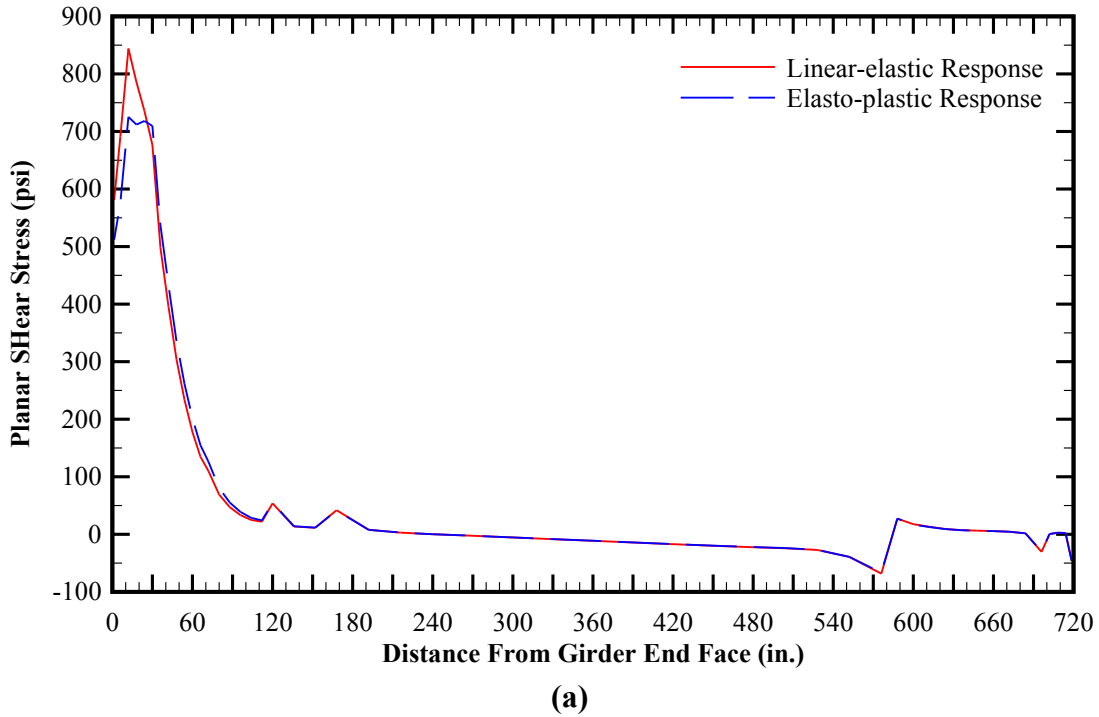


Figure 5-52: Planar shear stress (S23) distribution along the span of a typical BT-72 girder with IDOT end zone rebar in addition to shear and confinement reinforcement immediately after the release of pretensioning: (a) Average shear stress across the width of the web, and (b) Shear stress contour at the outside face of the web base on elasto-plastic response.

Figure 5-53 shows the state of axial stresses (S11) in the end zone reinforcing bars immediately after the release of pretensioning and based on elasto-plastic (e.g., nonlinear) response of concrete. As shown in Figure 5-53 (a), the magnitude of axial stresses in the end zone rebar reaches the maximum near the end face of the girder. Figure 5-53 (b)

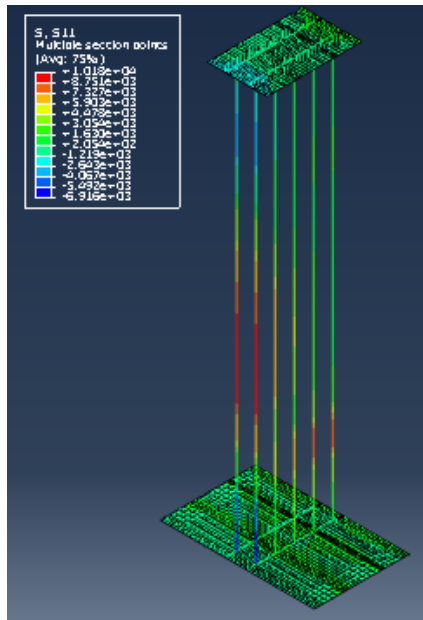
comparatively shows the maximum axial stress (S11) per each rebar in accordance with the location relative to the member end face. It shall be noted that positive axial stress indicates state of tension; negative axial stress indicates compression in the bars. The numerical results indicate that the maximum tensile stress is observed near the end face of the member. Travelling away from the end face, the magnitude of the tensile stress significantly decreases. This observation is consistent with the previous results obtained by the numerical simulations of the finite element models with AASHTO LRFD and Nebraska end zone details. Additionally, the axial stress distributions shown in Figure 5-53 (a) indicate that the location of the maximum tensile stresses shifts downwards from mid-height of EZR No.1 towards the bottom flange interface with the web at EZR No.5. Table 5-14 shows the summary of the maximum tensile stresses in the end zone reinforcing bars obtained from the nonlinear numerical simulations of a typical BT-72 girder with IDOT end zone rebar in addition to shear and confinement reinforcement immediately after the release of pretensioning, including the stress magnitude as well as the location along the height of the bar measured in relation to the bottom of the girder bottom flange assumed as datum.

The numerical results indicate that the maximum tensile stresses observed by the finite element simulations (10.1 ksi) is well below the allowable limit (20.0 ksi) specified by AASHTO LRFD in reference to Equation (5.20). In addition, the maximum tensile stress in the end zone near the end face of the member is approximately 80% of the maximum tension observed in the AASHTO LRFD end zone rebar at the same location. The stresses in the top and bottom plates are observed to be well below the anticipated yield strength.

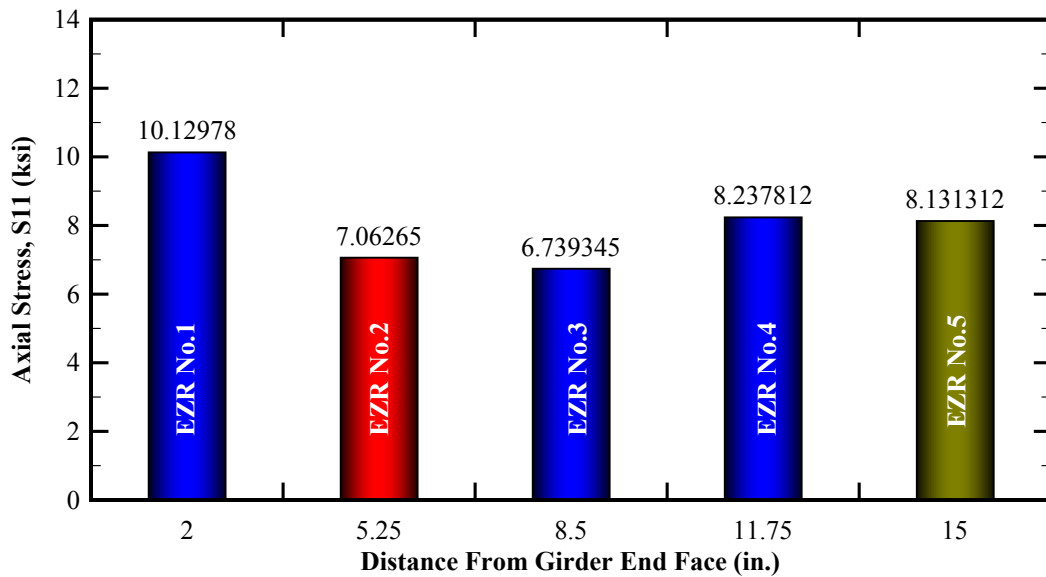
Table 5-14: Summary of the maximum tensile stresses in the end zone reinforcing bars obtained from the nonlinear numerical simulations of a typical BT-72 girder with IDOT end zone rebar in addition to shear and confinement reinforcement immediately after the release of pretensioning.

I.D.	Max. Axial Stress at EZR (ksi)	Height along the Rebar (in.)
EZR #1	10.13	27.25
EZR #2	7.06	30.25
EZR #3	6.74	12.25
EZR #4	8.24	12.25
EZR #5	8.13	10.75

Similarly, Figure 5-53 (a) and (b) show the axial stress (S11) distribution in the confinement reinforcement and the maximum stress per each rebar, respectively. The maximum tensile stress of 5.1 ksi is observed at a distance equivalent to 0.15 d (15% of the member height). Beyond a distance equivalent to 0.75 d (75% of the member height), the axial stresses in the confinement reinforcing bars stabilize on a constant magnitude of approximately 3.6 ksi.



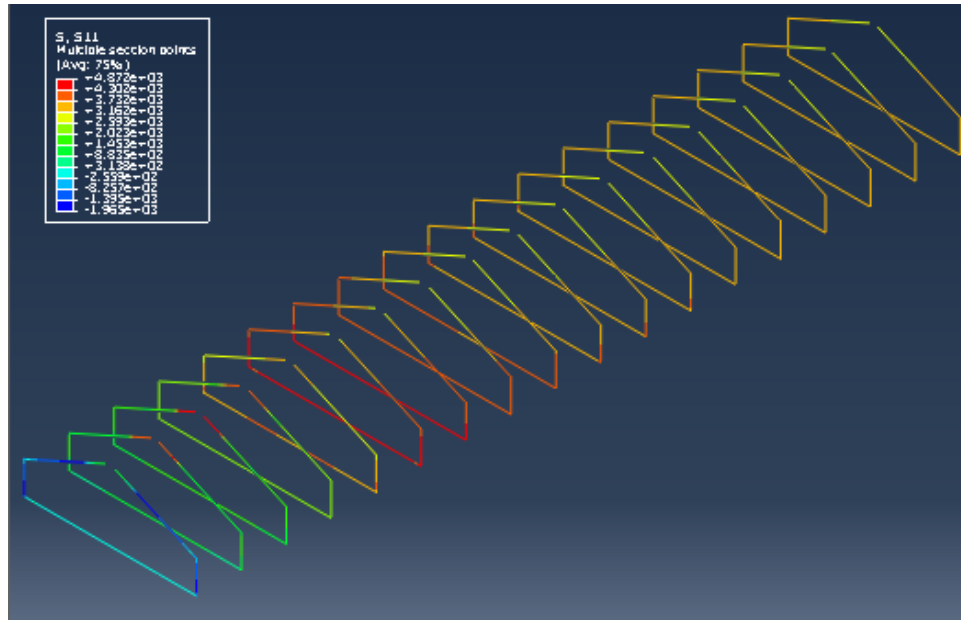
(a)



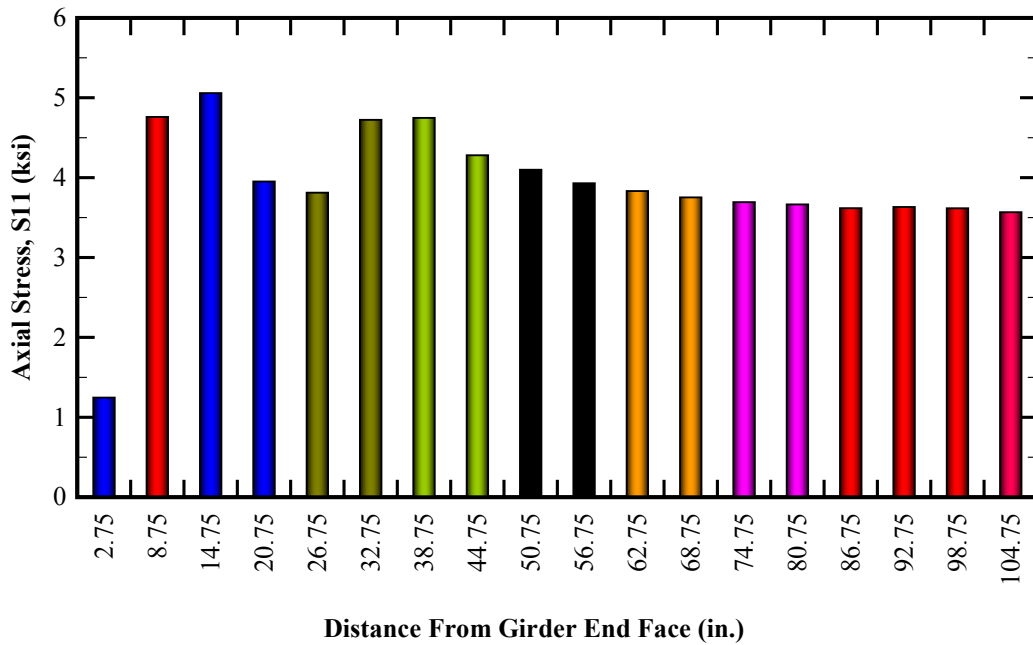
(b)

Figure 5-53: Axial stress (S11) in the end zone reinforcing bars of a typical BT-72 girder with IDOT end zone rebar in addition to shear and confinement reinforcement immediately after the release of pretensioning: (a) Numerical results obtained by the nonlinear finite element simulation and (b) maximum stress per each end zone rebar.

Note: Positive axial stress indicates tension; negative axial stress indicate compression



(a)



(b)

Figure 5-54: Axial stress (S11) in the confinement reinforcement of a typical BT-72 girder with IDOT end zone rebar in addition to shear and confinement reinforcement immediately after the release of pretensioning: (a) Numerical results obtained by nonlinear finite element simulation and (b) maximum stress per each confinement rebar.

Note: Positive axial stress indicates tension; negative axial stress indicates compression.

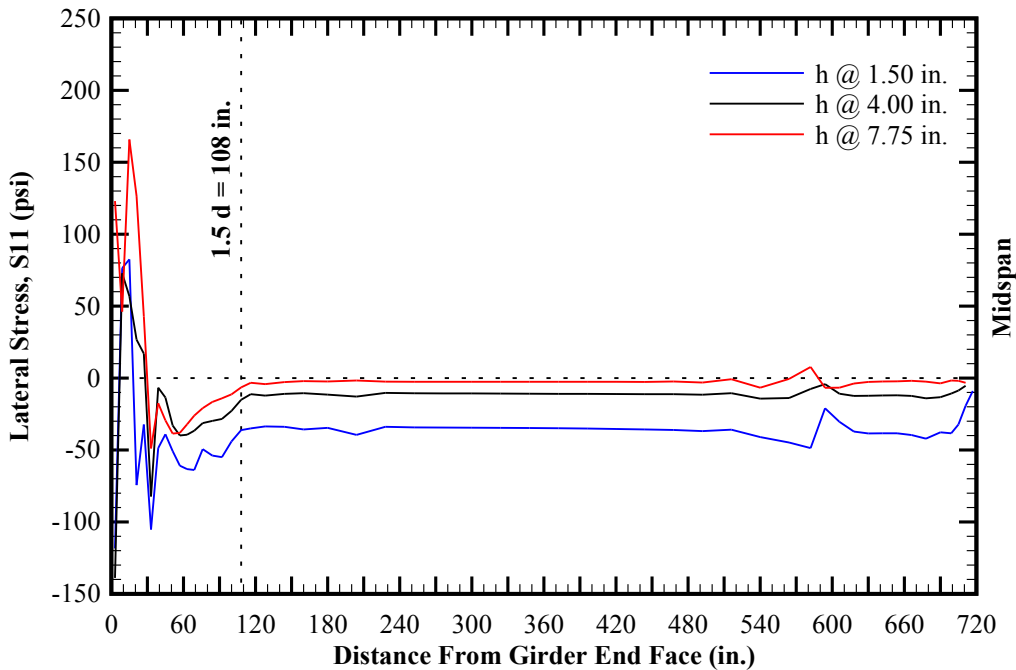


Figure 5-55: Lateral stress (S11) distribution of a typical BT-72 girder with IDOT end zone reinforcement in addition to shear and confinement reinforcement within the bottom flange (elasto-plastic response).

Note: Positive pressure indicates state of compression; negative pressure indicates state of tension.

Figure 5-55 shows the lateral stress (S11) distribution within the bottom flange of a typical BT-72 girder with elasto-plastic response. As previously discussed, the current AASHTO LRFD specifications require confinement reinforcement to extend over a distance equal to 1.5 times the height of the precast member. The numerical simulations show a maximum lateral tensile stress of 165 psi near the top of the bottom flange at approximately 15 in. from the member end face. However, the lateral tensile stresses are resolved into state of compression at a distance approximately 33 in. from the girder end face.

5.5.6. BT-72 Model with Modified IDOT-AASHTO End Zone Reinforcing Details in Addition to Shear and Confinement Reinforcement

The fifth class of the finite element models corresponds to the simulation of a typical BT-72 girder with modified IDOT end zone reinforcing details. As previously discussed in Section 5.3.2.3, the modified IDOT end zone reinforcing configuration is comprised of 5 sets of No.5 bars spaced at 3-1/4" on center, which are mechanically fastened to top and bottom steel plates, sandwiching the end zone along the vertical axis of the member. The corresponding end zone detail is a combination of the requirements by AASHTO LRFD and IDOT. Additionally, the finite element models include the shear and confinement reinforcement in accordance with the design requirements as shown in PCI BDM Example 9.4.

Table 5-15 includes the top and bottom fiber stresses at the harping point and midspan of the member. At each control location, three independent sets of results are reported based on the material behavior (linear-elastic or elasto-plastic) as well as those obtained by closed form solutions of PCI BDM Example 9.4. In addition, the maximum camber is reported at the midspan of the girder. The reported camber is based on the combined effect of self-weight of the girder and pretensioning immediately after the release of the strands.

Table 5-16 shows the comparison between the linear-elastic and elasto-plastic results versus the closed form solutions. Similar to the results of Section 5.5.2, the comparison of the results indicates overestimation of top fiber stresses and underestimation of the bottom fiber stress by the close form solutions. It is also observed that the inclusion of the end zone, shear and confinement reinforcement does not significantly affect the

longitudinal stresses at the top and bottom fibers as well as the camber. This is consistent with the assumptions of the beam theory used as the basis for the closed form solutions.

The comparative study of the results obtained by the numerical simulations and the closed form solution indicates an acceptable conformance between the two methodologies. In other words, the two-dimensional beam theory is deemed adequately capable of estimating the flexural response of the pretensioned BT-72 girder.

Table 5-15: Results of the finite element analysis of a typical BT-72 girder with Modified IDOT-AASHTO end zone reinforcing details in addition to shear and confinement reinforcement as well as those by the closed form solutions included in PCI BDM Example 9.4. The results are reported immediately after the release of pretensioning.

	Linear-elastic Response	Elasto-plastic Response	Closed Form Solution
Stress in the extreme top fiber at harping point, σ_t^{Harp} (psi)	-238.6	-231.7	-256
Stress in the extreme bottom fiber at harping point, σ_c^{Harp} (psi)	-3683.5	-3672.0	-3313
Stress in the extreme top fiber at mid-span, $\sigma_t^{Midspan}$ (psi)	-272.4	-266.0	-301
Stress in the extreme bottom fiber at mid-span, $\sigma_c^{Midspan}$ (psi)	-3606.0	-3592.3	-3266
Maximum deflection at mid-span, $\Delta_{max}^{Midspan}$ (in.)	2.55 ↑	2.58 ↑	2.28 ↑
Notes: 17. Positive stresses correspond to the state of tension.. 18. Negative stresses correspond to the state of compression. 19. ↑ denotes positive camber (upward deflection). 20. ↓ denotes negative camber (downward deflection).			

Table 5-16: Comparison of the results obtained by the BT-72 finite element model with Modified IDOT-AASHTO end zone, shear and confinement reinforcement versus the closed form solutions in reference to Table 5-12.

	<i>Linear – elastic</i> <i>Closed Form Sloution</i>	<i>Elasto – plastic</i> <i>Closed Form Sloution</i>
Stress in the extreme top fiber at harping point, σ_t^{Harp}	93%	91%
Stress in the extreme bottom fiber at harping point, σ_c^{Harp}	111%	111%
Stress in the extreme top fiber at mid-span, $\sigma_t^{Midspan}$	90%	88%
Stress in the extreme bottom fiber at mid-span, $\sigma_c^{Midspan}$	110%	110%
Maximum deflection at mid-span, $\Delta_{max}^{Midspan}$	112%	113%

Figure 5-56 shows the longitudinal stress (S33) distribution along the span of the member, measured at various heights of the BT-72 girder with elasto-plastic response. The magnitude and trend of the longitudinal stress distribution are similar to the results obtained in Section 5.5.2 with similar observations. Thus, the inclusion of the end zone, shear and confinement reinforcement does not affect the longitudinal stresses at top and bottom fibers along the span of the member, including the peaks affected by the sectional transition between the web and flanges as previously observed in the plain model without end zone, shear and confinement reinforcing bars.

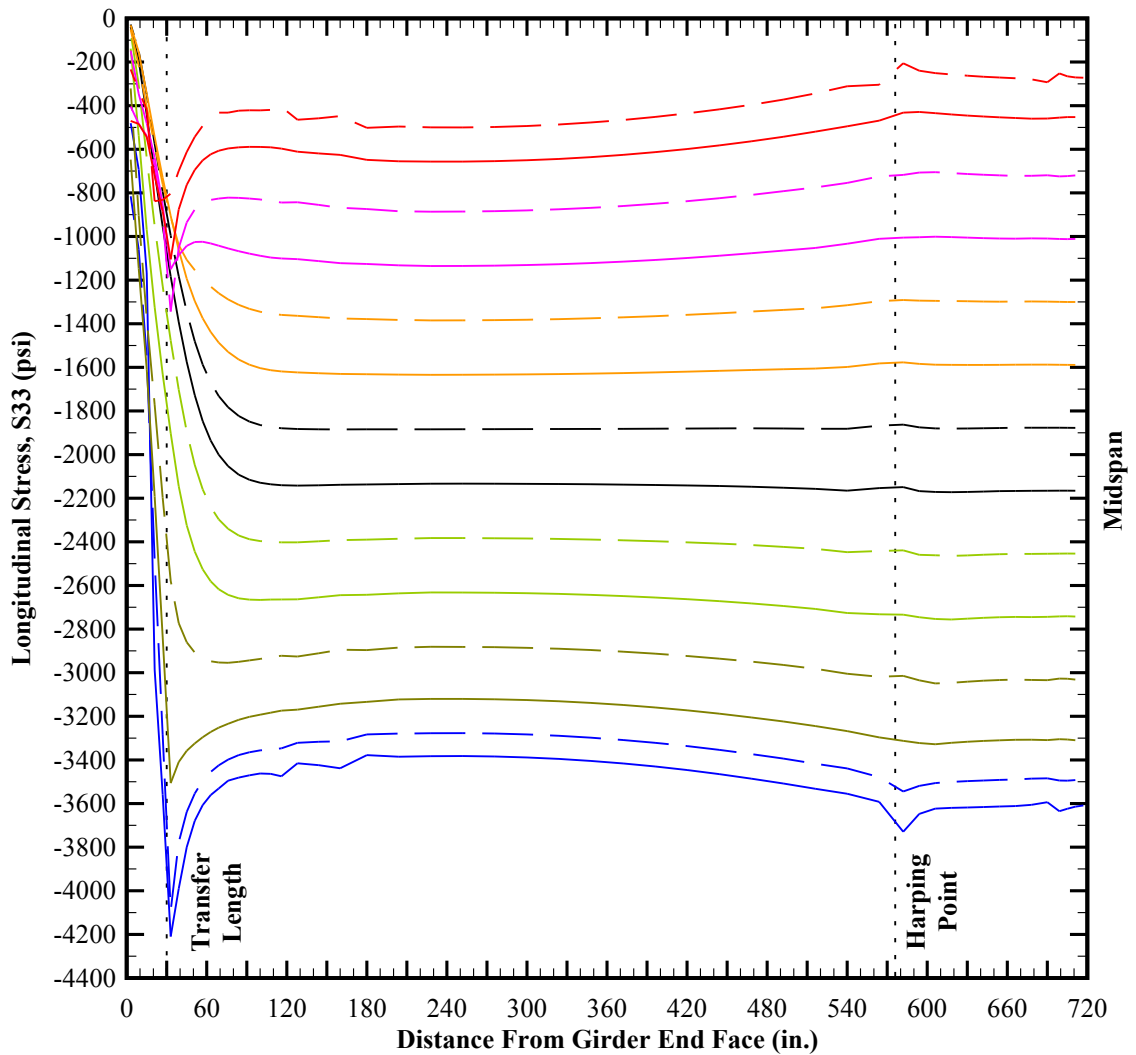


Figure 5-56: Longitudinal stresses (S33) along the height of a typical BT-72 girder with Modified IDOT-AASHTO end zone reinforcing details in addition to shear and confinement reinforcement immediately after the release of pretensioned strands and based on the elasto-plastic response of the specimen. Note: "h" is measured relative to the bottom face of the bottom flange assumed as datum.

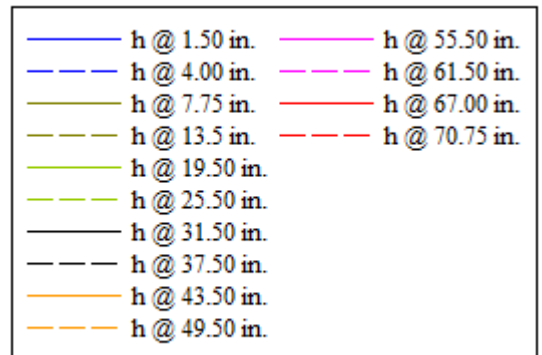


Figure 5-57 (a) thru (d) show the distribution of the vertical stresses (S_{22}) along the height of the BT-72 girder, measured at 3 in., 9 in., 33 in. and 51 in. from the girder end face, respectively. In addition, the elasto-plastic and linear-elastic responses are superimposed on each graph in order to show the effect of nonlinearity and material softening (e.g., potential cracking) at each interval.

It is observed that significant softening of concrete occurs within a domain confined between the member end face and 9 in. away from the girder end. The magnitude of the vertical tensile stresses indicates that potential cracking is anticipated along the mid-height of the girder web. Along the next domain confined between domain 9 in from the girder end and the theoretical transfer length (30 in. from the girder end face), the numerical solutions indicate that results obtained by the nonlinear and linear models begin to converge, indicating that the response of the member tends to stay and remain within the elastic regime. Beyond the theoretical transfer length, the response of the BT-72 girder predominantly remains within the elastic regime.

Similarly, Figure 5-58 includes the pressure distribution along the height of the BT-72 girder, measured at 3 in., 9 in., 33 in. and 51 in. from the girder end face, respectively. The trend of pressure is very similar to the longitudinal stresses (S_{33}) as described above. In accordance with the results obtained by the nonlinear finite element analysis, the girder web along 9 in. from the girder end face is susceptible to cracking immediately after the release of pretensioned strands.

The obtained numerical solutions re-emphasize the importance of utilizing elasto-plastic material behavior when analyzing the effect of pretensioning along the member

end zone, adequately capable of estimating material softening and the resulting stress redistribution within the areas susceptible to tensile cracking.

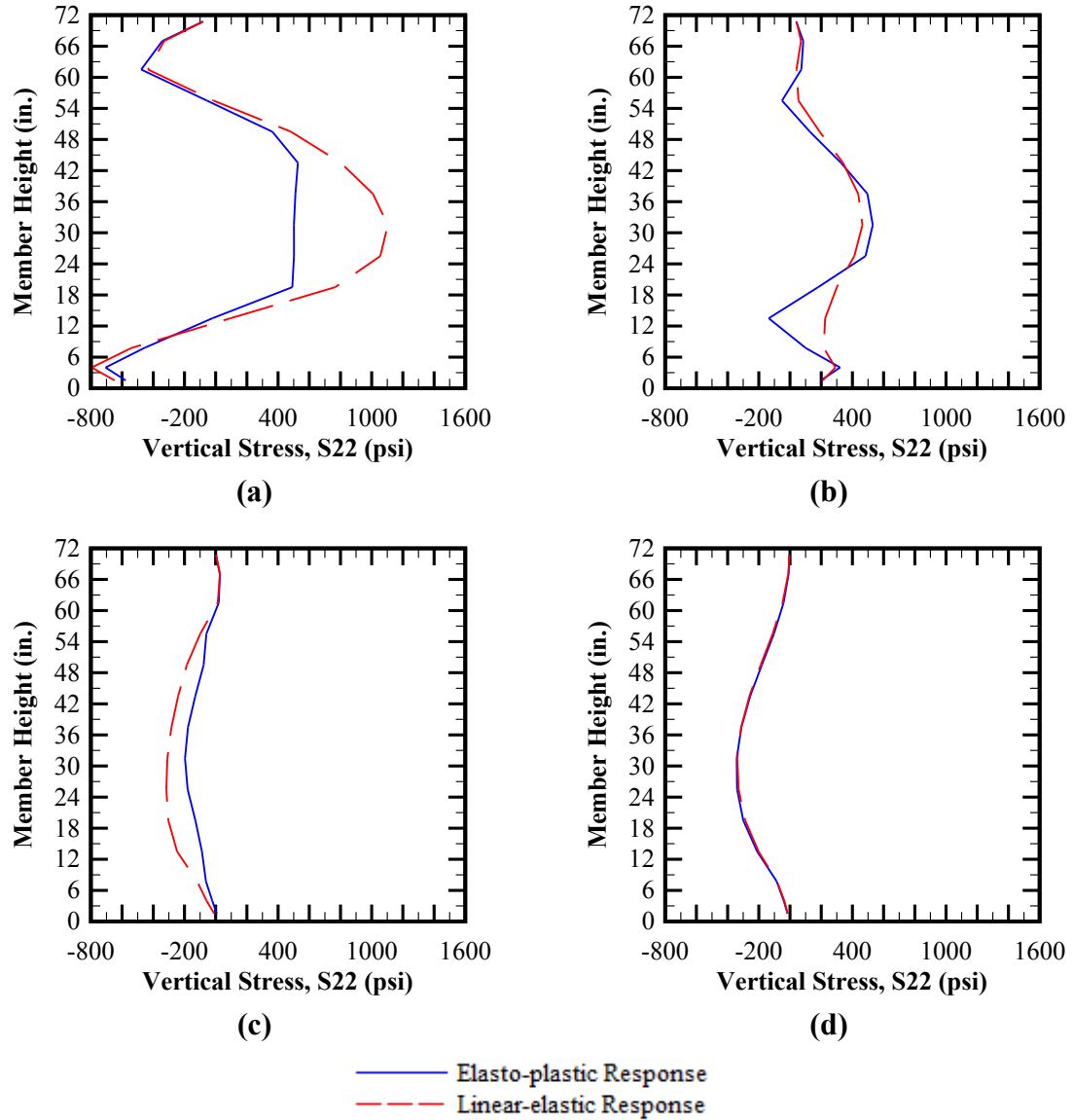


Figure 5-57: Vertical stress (S22) distribution along the height of a typical BT-72 girder with Modified IDOT-AASHTO end zone rebar in addition to shear and confinement reinforcement measured at: (a) 3 in. from girder end face, (b) 9 in. from the girder end face, (c) 33 in. from the girder end face, and (d) 51 in. from the girder end face.

Note: Positive stresses indicate state of tension; negative stresses indicate state of compression.

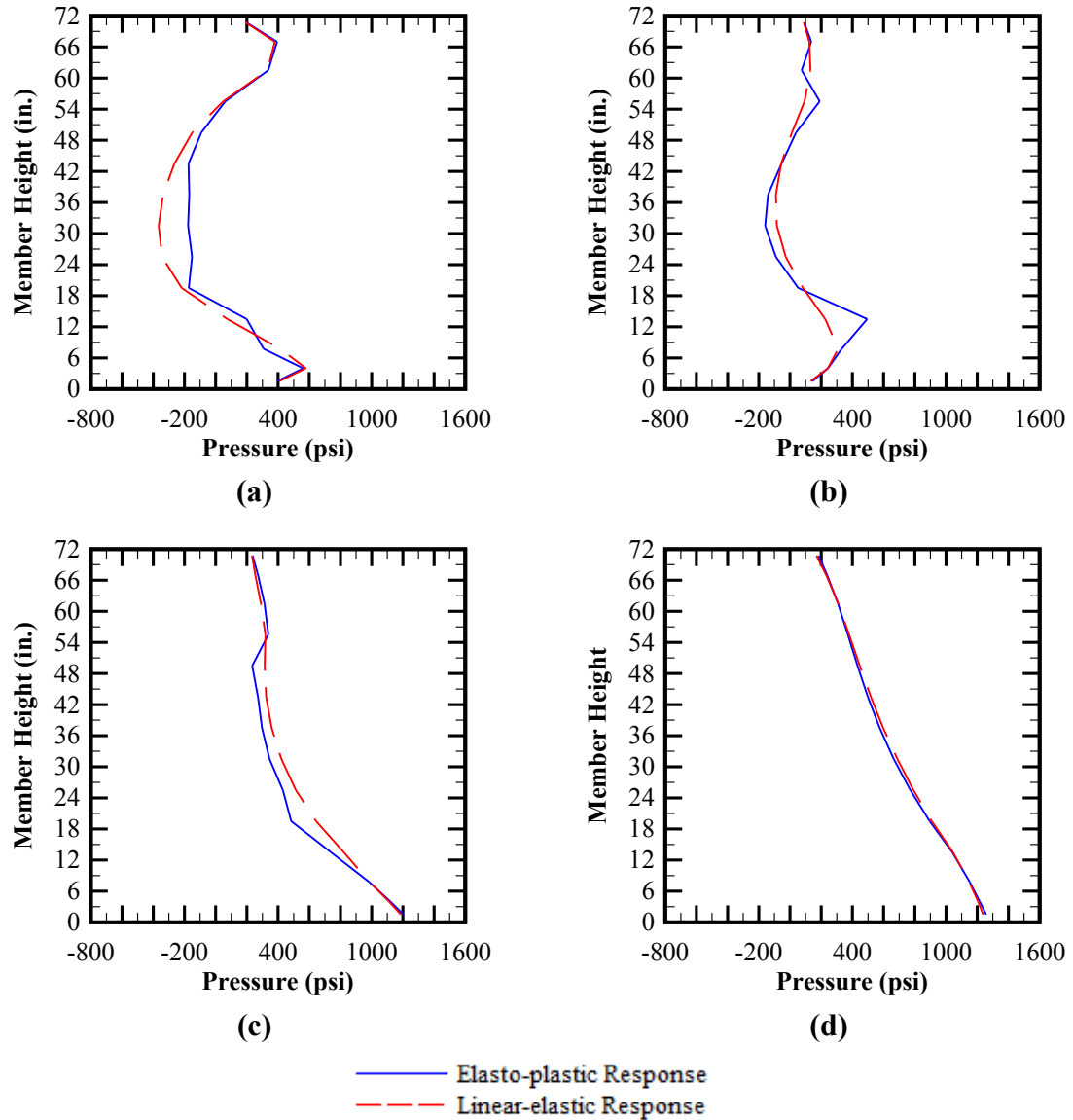


Figure 5-58: Pressure distribution along the height of a typical BT-72 girder with Modified IDOT-AASHTO end zone rebar in addition to shear and confinement reinforcement measured at: (a) 3 in. from girder end face, (b) 9 in. from the girder end face, (c) 33 in. from the girder end face, and (d) 51 in. from the girder end face.

Note: Positive pressure indicates state of compression; negative pressure indicates state of tension.

Figure 5-59 shows the state of maximum principal stress along the end zone of the BT-72 girder based on nonlinear (e.g., elasto-plastic concrete response) simulation. Figure 5-59 (a) shows the maximum principal vector contours near the girder end face, indicating the tensile stresses near rupture strength (f_r) initiating in a zone in the vicinity of the mid-height of the web. In comparison with the response of the members with AASHTO LRFD and Nebraska details, the simulations utilizing the IDOT end zone configurations indicate that the areas susceptible to tensile cracking are more concentrated near mid-height of the web.

Figure 5-59 (b) shows the maximum principal stress distribution at the member end face. The finite element results indicate that a zone near the mid-height of the girder will potentially crack upon release of pretensioning. As indicated by the cross section, the potential tensile crack is anticipated to extend through the entire web thickness.

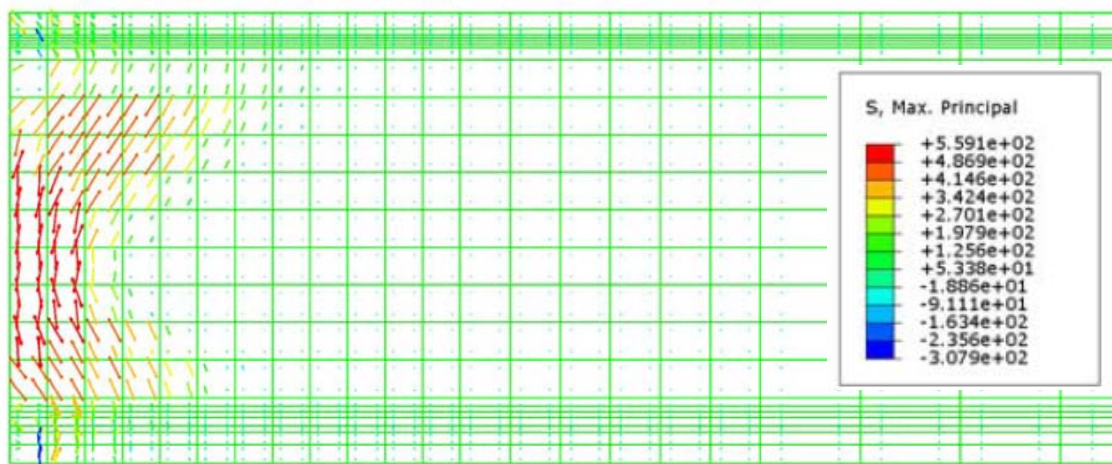
Figure 5-59 (c) shows the maximum principal stress distribution along the end zone of the specimen. The stress contour indicates that the potential tensile cracking of the girder web is confined to an area approximately extending 4 in. from the member end face. The numerical results indicate that the IDOT end zone reinforcing details further retracts the concentration of the tensile stresses in comparison with the members including AASHTO LRFD and Nebraska details similar to the simulations with IDOT end zone details.

The comparison of the numerical results versus Section 5.5.3 indicates slight increase in the magnitude of the maximum principal stresses near the end face of the member: 559 psi (tensile) versus 558 psi (tensile) with AASHTO LRFD details. However, the IDOT end zone scheme is shown to contain the areas susceptible to cracking in a smaller zone

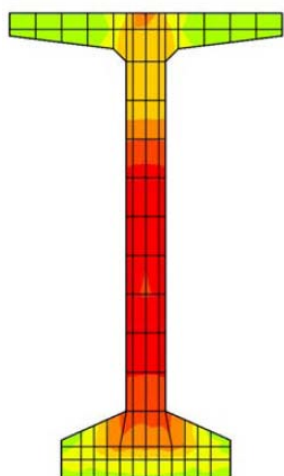
between the mid-height of the web and the bottom flange interface with web as mentioned above.

Figure 5-60 (a) thru (d) show the vertical stress (S22) distribution along the end zone of the specimen shown at the various cross sections including the outside face of the web, 1 in. into the web thickness, 2 in. into the web thickness and the centerline of the member, respectively. The numerical results indicate areas susceptible to tensile cracking extending from the outside face of the web towards the centerline of the member immediately after the release of pretensioning. The corresponding response is different from both the members with AASHTO LRFD and Nebraska end zone details which show shallower tensile cracks. Meanwhile, the simulations utilizing IDOT and Modified IDOT-AASHTO end zone details show similar responses with the exception that the zones susceptible to tensile cracking near the end face of the girder are confined to smaller areas, respectively.

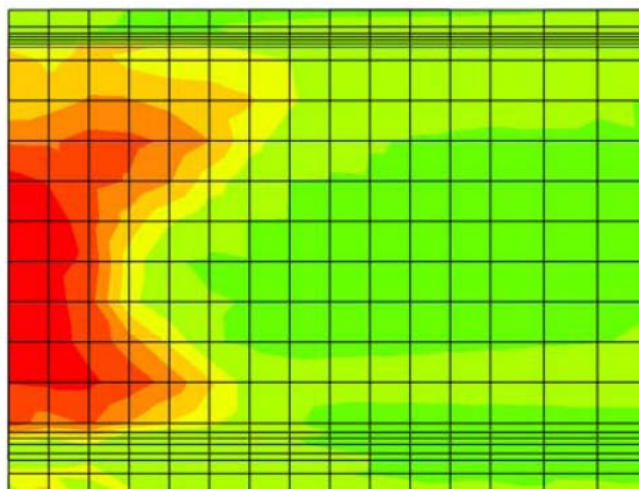
On the other hand, the areas exposed to tensile stresses near the rupture strength are shifted towards the mid-height of the web in the simulations utilizing the IDOT end zone details. However, the extent of the areas susceptible to tensile cracking is stays closer to the member end face in comparison with the members with AASHTO LRFD and IDOT end zone details.



(a)



(b)



(c)

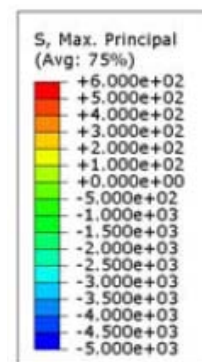


Figure 5-59: Elasto-plastic response of a typical BT-72 girder with Modified IDOT-AASHTO end zone rebar in addition to shear and confinement reinforcement immediately after the release of pretensioning: (a) Maximum principal vector contour along the end zone, (b) Maximum principal stress contour at member end face and (c) Maximum principal stress contour along the end zone.

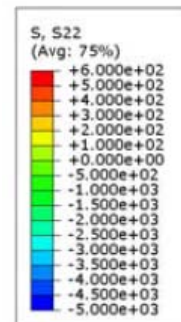
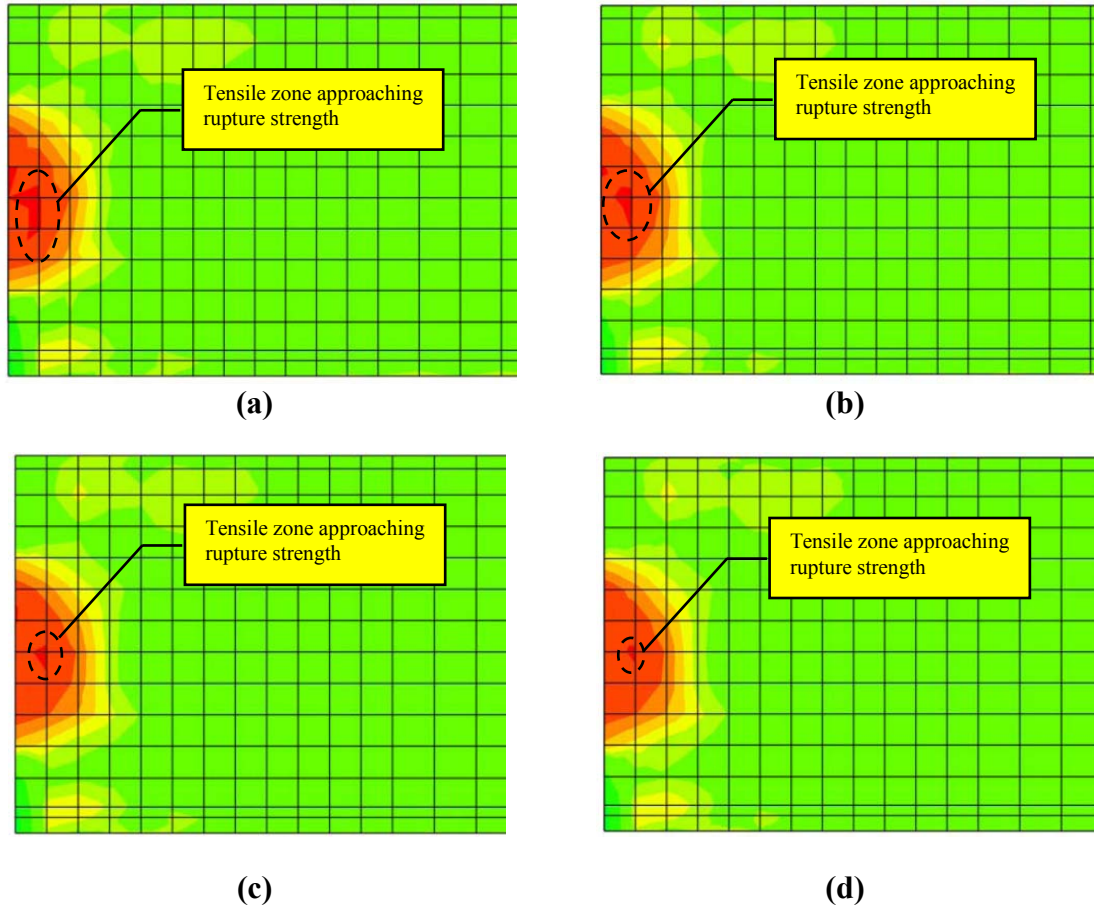


Figure 5-60: Vertical stress (S22) contours along the end zone of a typical BT-72 girder with Modified IDOT-AASHTO end zone rebar in addition to shear and confinement reinforcement immediately after the release of pretensioning shown at: (a) outside face of the web, (b) 1 in. into the web towards the centerline of the member, (c) 2 in. into the web towards the centerline of the member, and d) at the centerline of the member.

Figure 5-61 (a) shows the distribution of the planar shear stress (S23) averaged across the thickness of the web, along the span of the girder based on elasto-linear and elasto-plastic responses. The numerical simulations indicate tensile softening along the first 30 in. of the girder immediately after the release of pretensioning: maximum shear stress of 708 (psi) at 30 in. versus 841 (psi) at 12 in. from the girder end face based on elasto-plastic and linear-elastic responses, respectively.

Figure 5-61 (b) shows the planar shear stress (S23) contour at the outside face of the web based on elasto-plastic response of concrete. It is observed that the transfer of the axial pretensioning from the bottom flange upwards into the web results in significant concentration of shear stress at the bottom flange interface with the web. This shear transfer mechanism is anticipated to be due to the shear-lag caused by the difference in the magnitude of pretensioning in the bottom flange and web. The shear concentration is eventually resolved into the web over a distance approximately equal to the transfer length. The trend of the observed shear-lag is similar to the simulations utilizing AASHTO LRFD end zone rebar with maximum magnitude of 827 psi. As it was previously mentioned, the shear-lag phenomenon and the resulting shear-friction cracks at the interface between the web and bottom flange will be discussed in more details in Chapter 6. It is also observed that the magnitude of the planar shear stress (S23) increases by approximately 3% due to the modifications to IDOT end zone details by replacing the 3/4-in. diameter threaded bars with No.5 rebar.

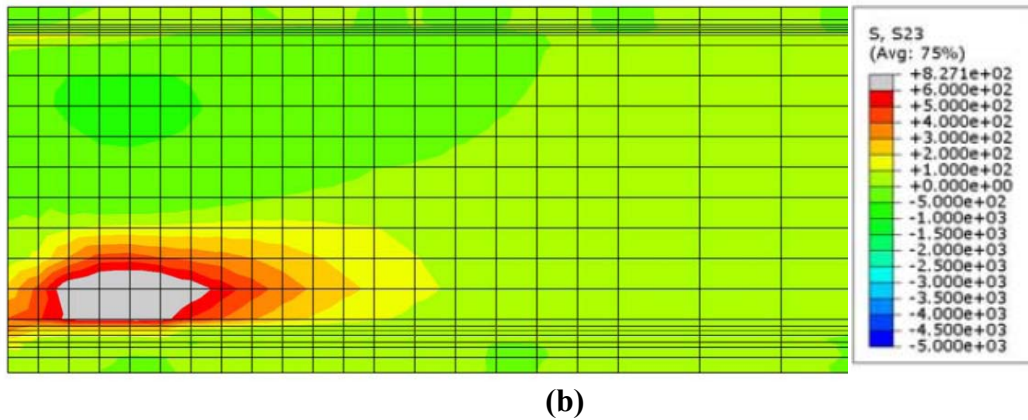
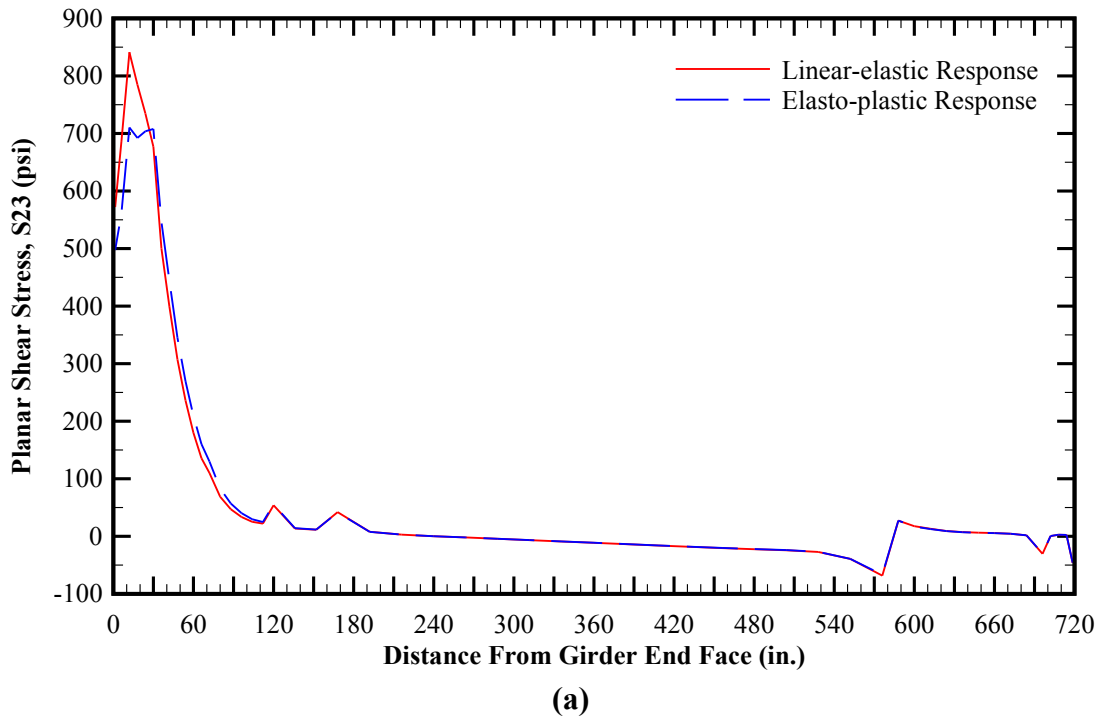


Figure 5-61: Planar shear stress (S₂₃) distribution along the span of a typical BT-72 girder with IDOT end zone rebar in addition to shear and confinement reinforcement immediately after the release of pretensioning: (a) Average shear stress across the width of the web, and (b) Shear stress contour at the outside face of the web base on elasto-plastic response.

Figure 5-62 shows the state of axial stresses (S11) in the end zone reinforcing bars immediately after the release of pretensioning and based on elasto-plastic (e.g., nonlinear) response of concrete. As shown in Figure 5-62 (a), the magnitude of axial stresses in the end zone rebar reaches the maximum near the end face of the girder. Figure 5-62 (b) comparatively shows the maximum axial stress (S11) per each rebar in accordance with the location relative to the member end face. It shall be noted that positive axial stress indicates state of tension; negative axial stress indicates compression in the bars. The numerical results indicate that the maximum tensile stress is observed near the end face of the member. Travelling away from the end face, the magnitude of the tensile stress significantly decreases. This observation is consistent with the previous results obtained by the numerical simulations of the finite element models with AASHTO LRFD and Nebraska end zone details. Additionally, the axial stress distributions shown in Figure 5-62 (a) indicate that the location of the maximum tensile stresses shifts downwards from the mid-height of EZR No.1 to the vicinity of the bottom flange interface with the web at EZR No.5. Table 5-17 shows the summary of the maximum tensile stresses in the end zone reinforcing bars obtained from the nonlinear numerical simulations of a typical BT-72 girder with Modified IDOT-AASHTO end zone rebar in addition to shear and confinement reinforcement immediately after the release of pretensioning, including the stress magnitude as well as the location along the height of the bar measured in relation to the bottom of the girder bottom flange assumed as datum.

The numerical results indicate that the maximum tensile stresses observed by the finite element simulations (11.7 ksi) is well below the allowable limit (20.0 ksi) specified by AASHTO LRFD in reference to Equation (5.20). In addition, the maximum tensile

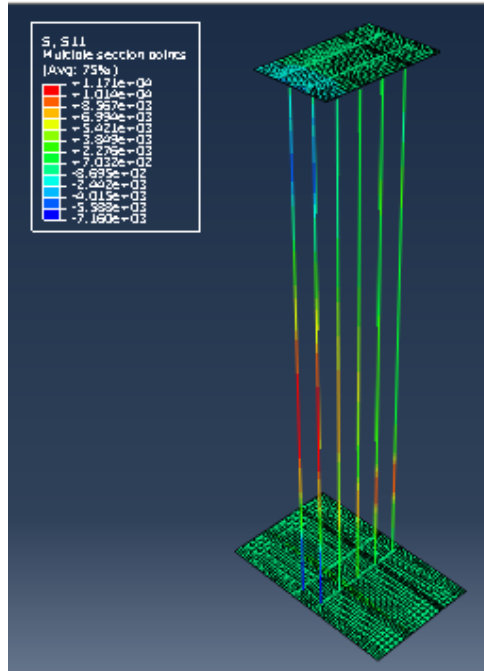
stress in the end zone near the end face of the member is approximately 91% of the maximum tension observed in the AASHTO LRFD end zone rebar at the same location. Meanwhile, the Modified IDOT-AASHTO end zone details are observed to withstand a 16% increase in the magnitude of the maximum axial stress upon the release of pretensioning. The stresses in the top and bottom plates are observed to be well below the anticipated yield strength.

Table 5-17: Summary of the maximum tensile stresses in the end zone reinforcing bars obtained from the nonlinear numerical simulations of a typical BT-72 girder with Modified IDOT -AASHTO end zone rebar in addition to shear and confinement reinforcement immediately after the release of pretensioning.

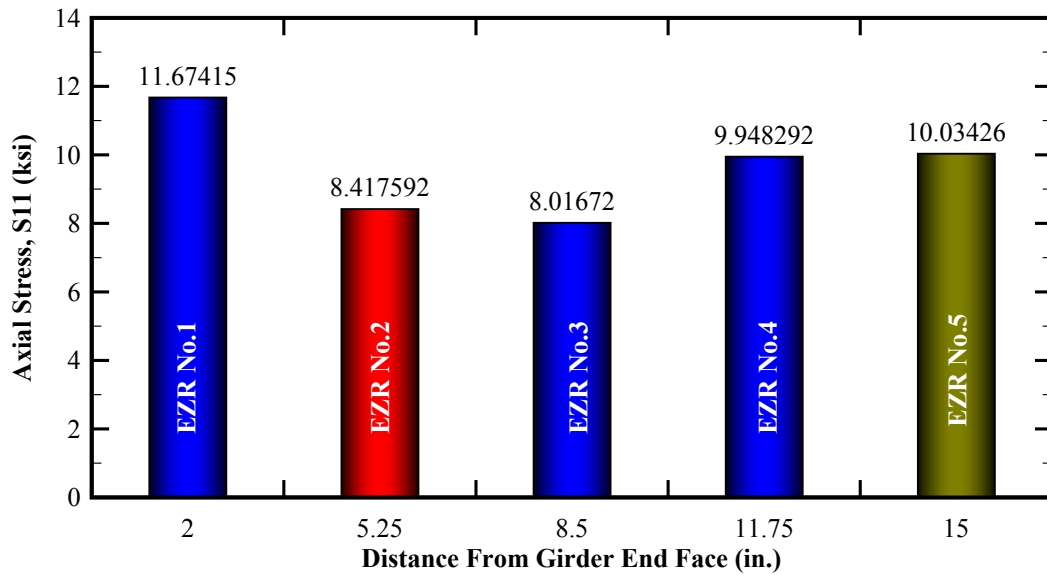
I.D.	Max. Axial Stress at EZR (ksi)	Height along the Rebar (in.)
EZR #1	11.67	22.75
EZR #2	8.42	31.75
EZR #3	8.02	12.25
EZR #4	9.95	15.25
EZR #5	10.03	10.75

Similarly, Figure 5-63 (a) and (b) show the axial stress (S11) distribution in the confinement reinforcement and the maximum stress per each rebar, respectively. The maximum tensile stress of 5.6 ksi is observed at a distance equivalent to 0.15 d (15% of the member height). Beyond a distance equivalent to 0.75 d (75% of the member height), the axial stresses in the confinement reinforcing bars stabilize on a constant magnitude of approximately 3.6 ksi.

Therefore, it is concluded that the modifications to IDOT end zone details by replacing the 3/4-in. diameter threaded bars with No.5 rebar does not affect the magnitude and trend of the axial stresses in the confinement reinforcement.



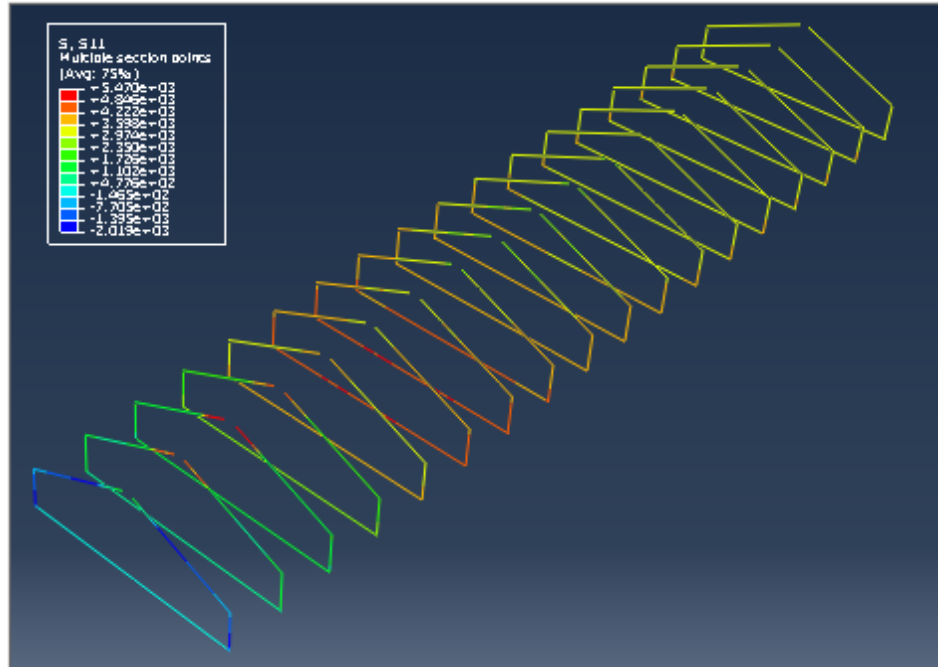
(a)



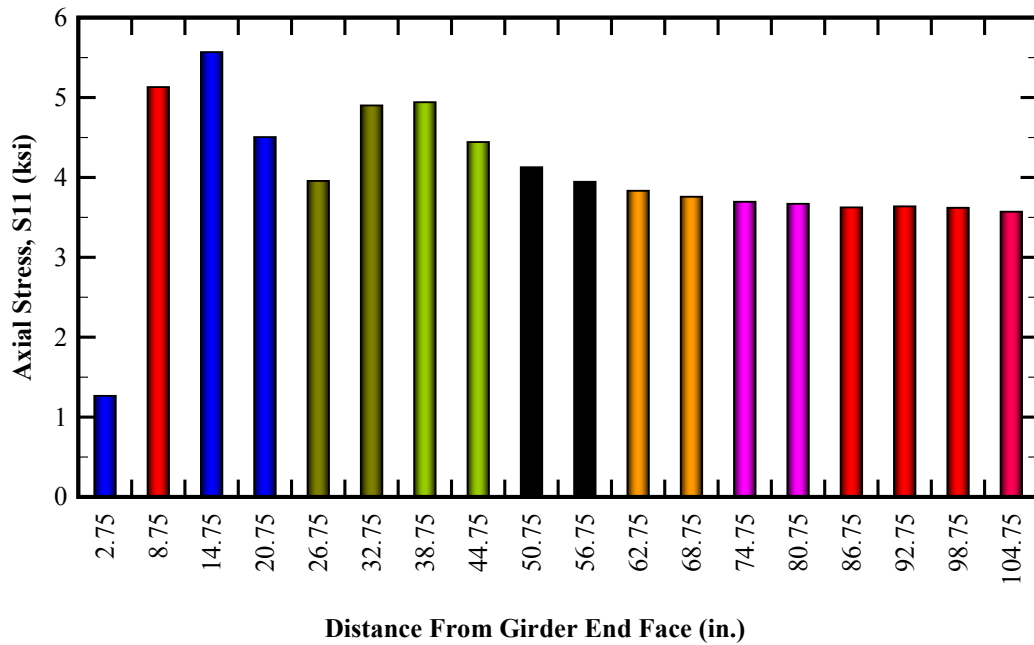
(b)

Figure 5-62: Axial stress (S11) in the end zone reinforcing bars of a typical BT-72 girder with IDOT end zone rebar in addition to shear and confinement reinforcement immediately after the release of pretensioning: (a) Numerical results obtained by the nonlinear finite element simulation and (b) maximum stress per each end zone rebar.

Note: Positive axial stress indicates tension; negative axial stress indicates compression.



(a)



(b)

Figure 5-63: Axial stress (S11) in the confinement reinforcement of a typical BT-72 girder with IDOT end zone rebar in addition to shear and confinement reinforcement immediately after the release of pretensioning: (a) Numerical results obtained by nonlinear finite element simulation and (b) maximum stress per each confinement rebar.

Note: Positive axial stress indicates tension; negative axial stress indicates compression.

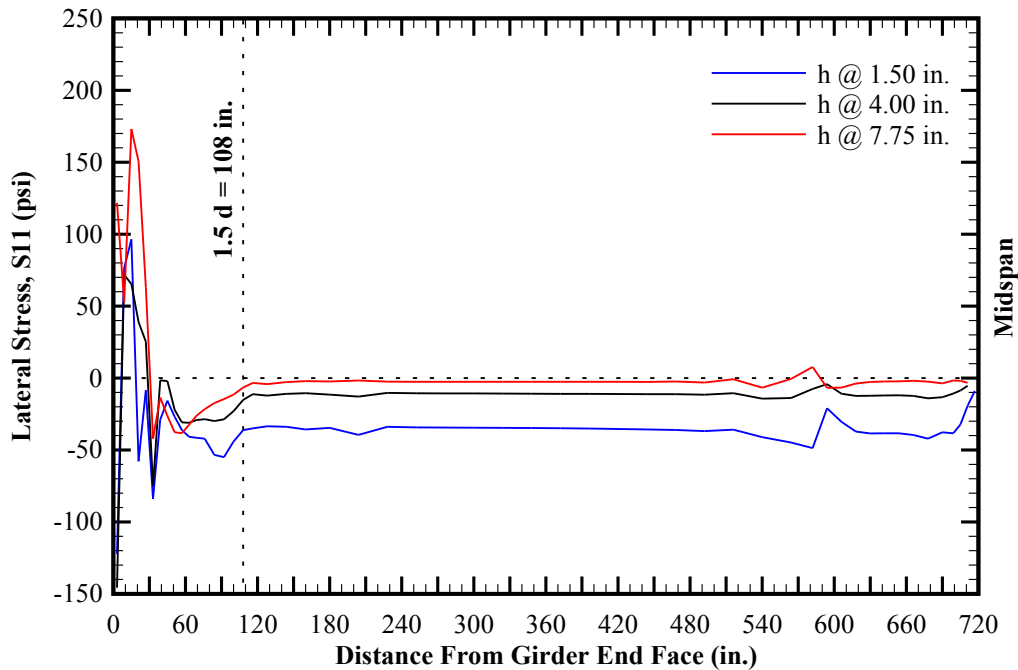


Figure 5-64: Lateral stress (S11) distribution of a typical BT-72 girder with Modified IDOT-AASHTO end zone reinforcement in addition to shear and confinement reinforcement within the bottom flange (elasto-plastic response).

Note: Positive pressure indicates state of compression; negative pressure indicates state of tension.

Figure 5-64 shows the lateral stress (S11) distribution within the bottom flange of a typical BT-72 girder with elasto-plastic response. As previously discussed, the current AASHTO LRFD specifications require confinement reinforcement to extend over a distance equal to 1.5 times the height of the precast member. The numerical simulations show a maximum lateral tensile stress of 173 psi near the top of the bottom flange at approximately 15 in. from the member end face. However, the lateral tensile stresses are resolved into state of compression at a distance approximately 33 in. from the girder end face.

5.6. Comparison of Results

The following section includes a comparative study of the numerical results obtained in Section 5.5. The main objectives of this section is to verify the effectiveness of the end zone details previously proposed in Section 5.5 in minimizing adverse effects such as potential tensile cracking of concrete upon the release of pretensioned strands.

As it was discussed in the previous sections, the current specifications for the design of prestressed members generally require conformance with allowable service limit states. Therefore, pretensioned concrete girders are designed as uncracked members with elastic response to longitudinal stresses (S33) based on linear-elastic beam theory.

On the other hand, pretensioned girders are susceptible to tensile cracking due to vertical stresses upon release of pretensioning in the vicinity of member end faces. Additionally, the numerical simulations of Section 5.5 indicate that the planar shear transfer (S23) between the bottom flange with the concentration of the straight strands and the relatively narrow web walls may cause a shear lag which can potentially cause cracking along the corresponding interface.

Figure 5-65 shows the comparison of maximum tensile stresses in the end zone rebar based on nonlinear finite element simulation of typical BT-72 girders with AASHTO LRFD, Nebraska, IDOT and Modified IDOT-AASHTO end zone reinforcing details. Table 5-18 includes the maximum tensile stresses in the end zone rebar near the end face of the girders, corresponding to Figure 5-65. The following observations are made:

1. The Nebraska end zone reinforcing detail experiences approximately the same tensile stress as AASHTO LRFD detail. However, the Nebraska detail requires the reinforcing bars be spaced at 6 in. on center versus 4 in. spacing required by AASHTO LRFD specifications:

$$\frac{\sigma_{t,\max}^{Nebraska}}{\sigma_{t,\max}^{AASHTO LRFD}} = 96\% \quad (5.30)$$

2. Item 1 above results in significantly less congestion of reinforcement within the end zone of the member, facilitating better placement of concrete.
3. The IDOT end zone detail significantly reduces the level of maximum tensile stresses in the rebar:

$$\frac{\sigma_{t,\max}^{IDOT}}{\sigma_{t,\max}^{AASHTO LRFD}} = 79\% \quad (5.31)$$

4. Addition of the top and bottom end plates to the end zone rebars required by AASHTO LRFD is observed to result in notable reduction in the magnitude of the tensile stresses in the end zone rebar:

$$\frac{\sigma_{t,\max}^{Modified IDOT-AASHTO}}{\sigma_{t,\max}^{AASHTO LRFD}} = 91\% \quad (5.32)$$

5. The numerical results indicate that magnitude of the tensile stresses in the end zone reinforcing bars is well below the allowable limit of 20.0 ksi by AASHTO LRFD specifications [please refer to Equation (5.20)].
6. The numerical results indicate that the area of web susceptible to tensile cracking is confined to a zone between 22 in. to 31 in. along the height of the member (measured from the bottom of the bottom flange), depending on the end zone reinforcing scheme.

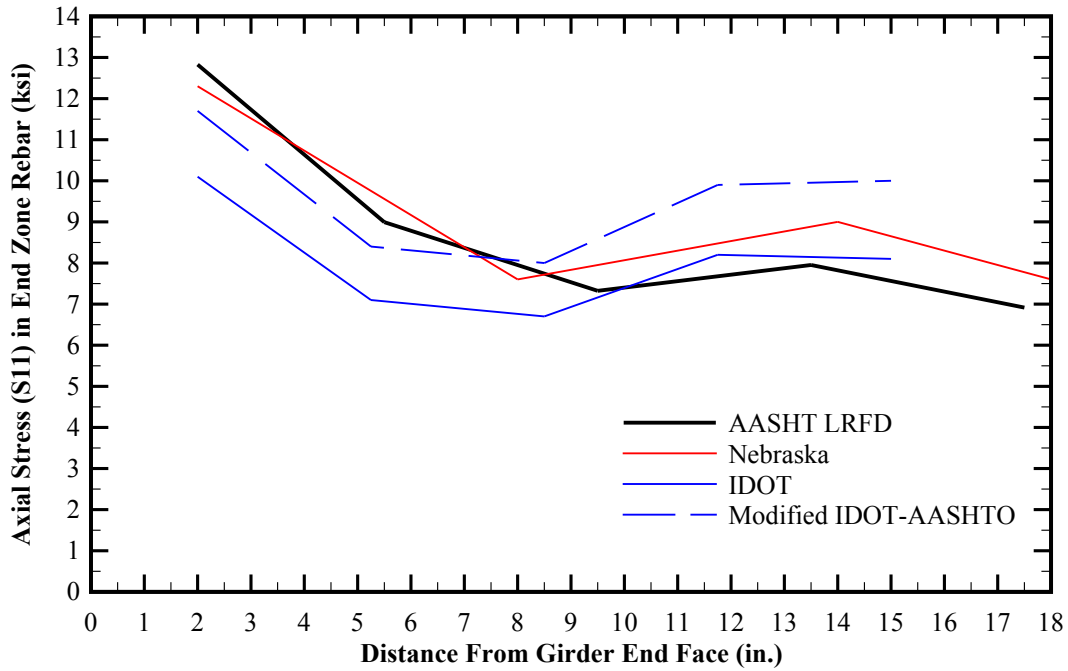


Figure 5-65: Comparison of axial stresses (S11) in the end zone rebar in accordance with AASHTO LRFD, Nebraska, IDOT and Modified IDOT-AASHTO schemes based on elasto-plastic finite element simulations of a typical BT-72 girder.

Table 5-18: Summary of the maximum tensile stresses in the end zone reinforcing bars near the end face of the member, obtained from the nonlinear numerical simulations of typical BT-72 girders with AASHTO LRFD, Nebraska, IDOT and Modified IDOT -AASHTO end zone reinforcing details in addition to shear and confinement reinforcement immediately after the release of pretensioning.

	Max. Axial Stress at EZR (ksi)	Height along the Rebar (in.)
AASHTO LRFD	12.80	24.625
Nebraska	12.34	30.625
IDOT	10.13	27.25
Modified IDOT-AASHTO	11.67	22.75

Figure 5-66 thru Figure 5-69 show the distribution of the axial stresses in the end zone and shear reinforcement located between the girder end face and 75 in. away, measured at 36 in., 32 in., 28 in. and 24 in. along the height of the member relative to the bottom of the bottom flange, respectively. In addition, each figure shows the stress distributions based on elasto-plastic versus linear-elastic finite element simulations. The following observations are made:

7. Maximum tensile stress of 12.8 ksi is observed in the first AASHTO LRFD end zone reinforcing bar at 28 in. along the height of the member, measured relative to the bottom of the girder bottom flanges.
8. Maximum tensile stress of 12.3 ksi is observed in the first Nebraska end zone reinforcing bars within a zone 24 in to 32 in. along the height of the member, measured relative to the bottom of the girder bottom flanges.
9. Maximum tensile stress of 10.1 ksi is observed in the first IDOT end zone rod within a zone 24 in to 32 in. along the height of the member, measured relative to the bottom of the girder bottom flanges.
10. Maximum tensile stress of 11.7 ksi is observed in the first Modified IDOT-AASHTO end zone reinforcing bar within a zone 24 in to 32 in. along the height of the member, measured relative to the bottom of the girder bottom flanges.
11. The linear-elastic models report approximately the same magnitude of axial tension (8 ksi \pm) in the AASHTO LRFD, Nebraska, IDOT and Modified IDOT-AASHTO end zone reinforcing bars. Such response is notably different from those resulted by the nonlinear simulations.

12. The linear-elastic simulations report tensile stresses in the end zone reinforcement which are considerably lower (approximately 40%) than the similar models with elasto-plastic behavior. This is an indication of potential cracking and concrete tension softening upon the release of pretensioning.
13. Observations 11 and 12 above re-emphasize the need for proper nonlinear simulation of concrete behavior due to potential tensile cracking and subsequent material softening immediately after the release of the pretensioned strands. Otherwise, linear-elastic analysis may grossly under-estimate the magnitude tensile stresses in the end zone rebar.
14. The magnitude of tensile stresses are observed to be at the maximum level in the first end zone rebar near the end face of the girder. Thereafter, the magnitude of the axial stresses sharply decreases to neutral (zero stress) state near the theoretical transfer length. This observation is consistent with the recommendations of NCHRP Report No. 654 as previously discussed in Section 5.3.2.2.
15. The numerical results indicate that the axial stresses in the end zone and/or shear reinforcement increases to 1 ksi \pm (tension) beyond the theoretical transfer length.

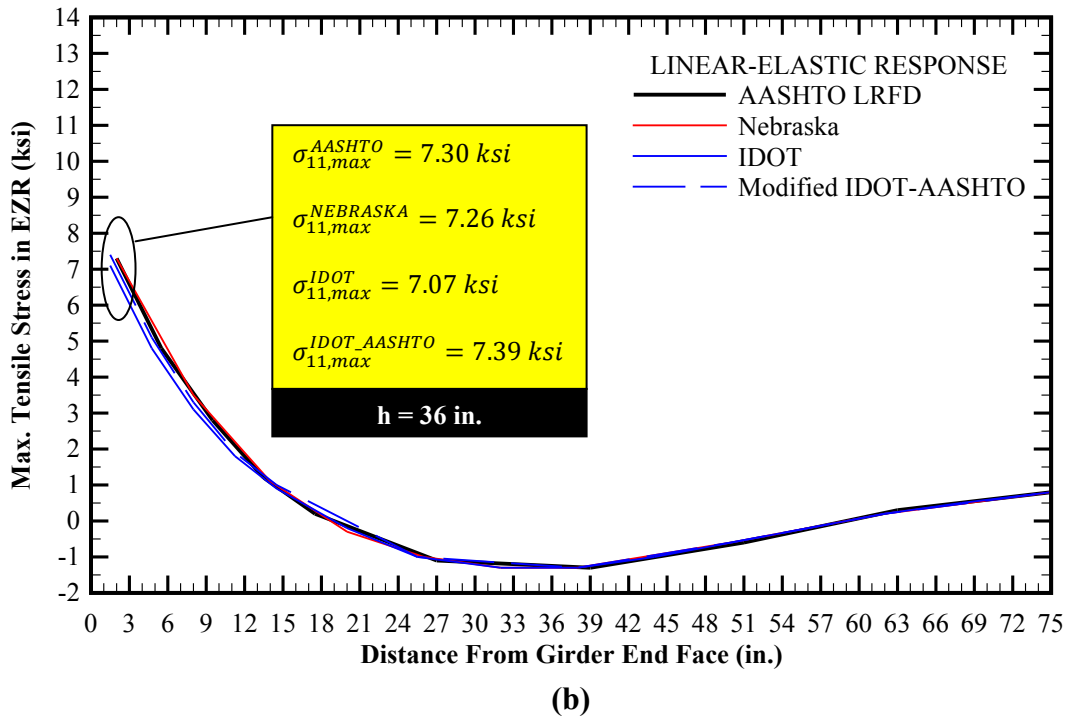
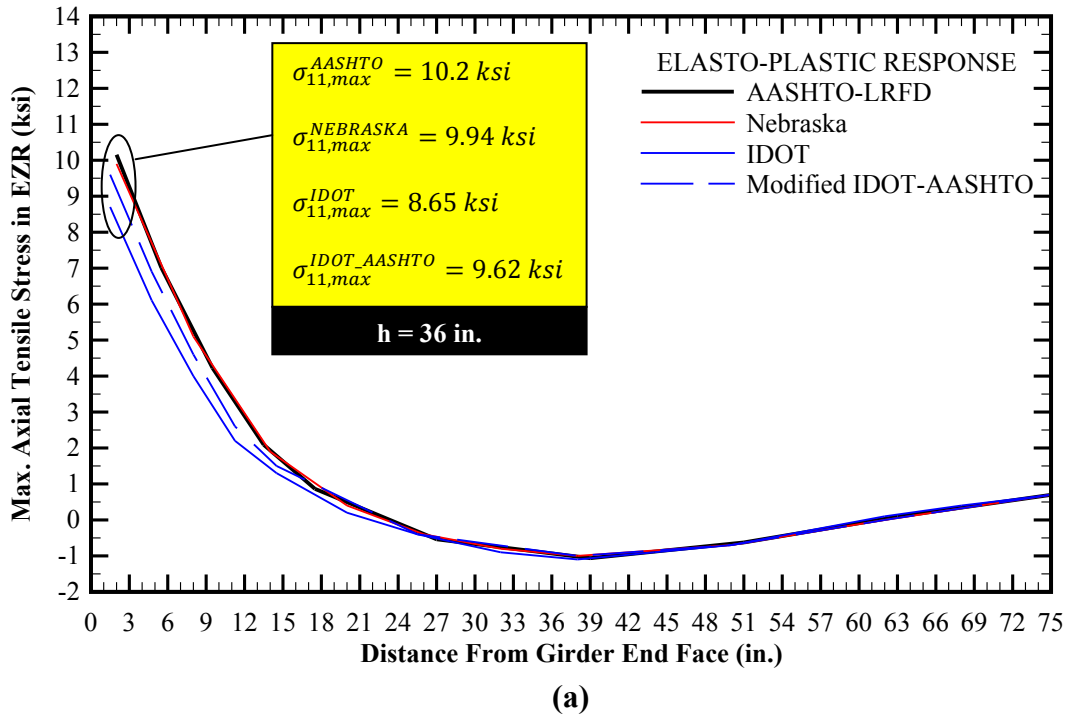


Figure 5-66: Comparison of axial stresses (S11) in the end zone rebar based on elasto-plastic finite element simulations of a typical BT-72 girder, reported at $h = 36$ in. along the height of the member (bottom of bottom flange is assumed as datum): (a) Elasto-plastic response, and (b) Linear-elastic response.

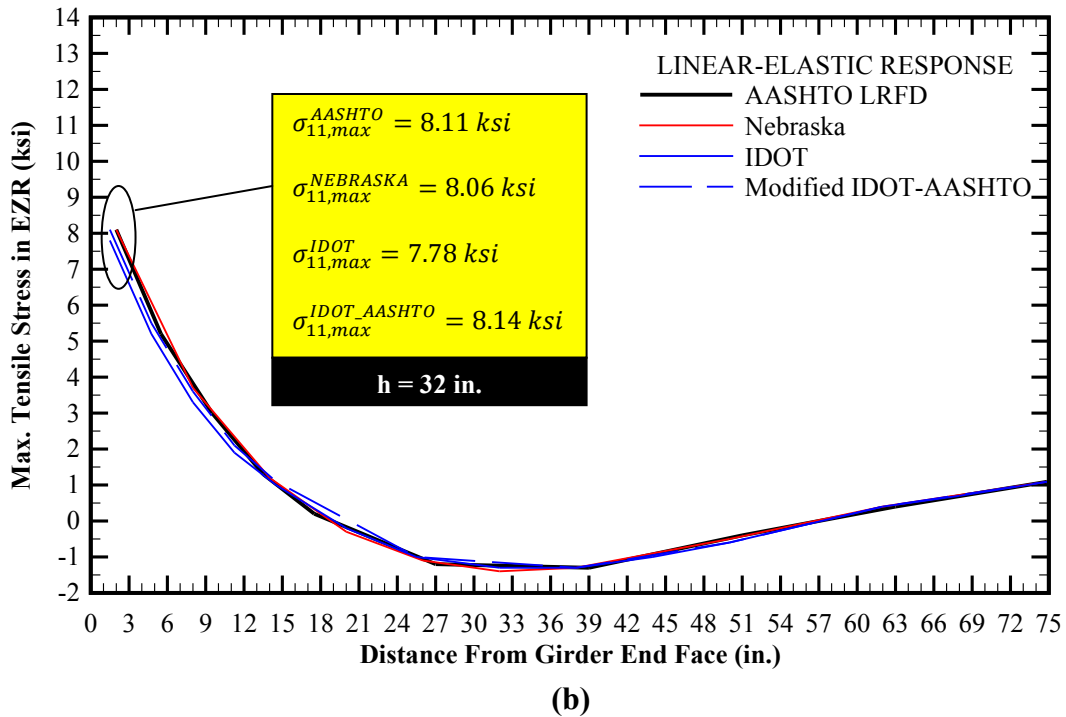
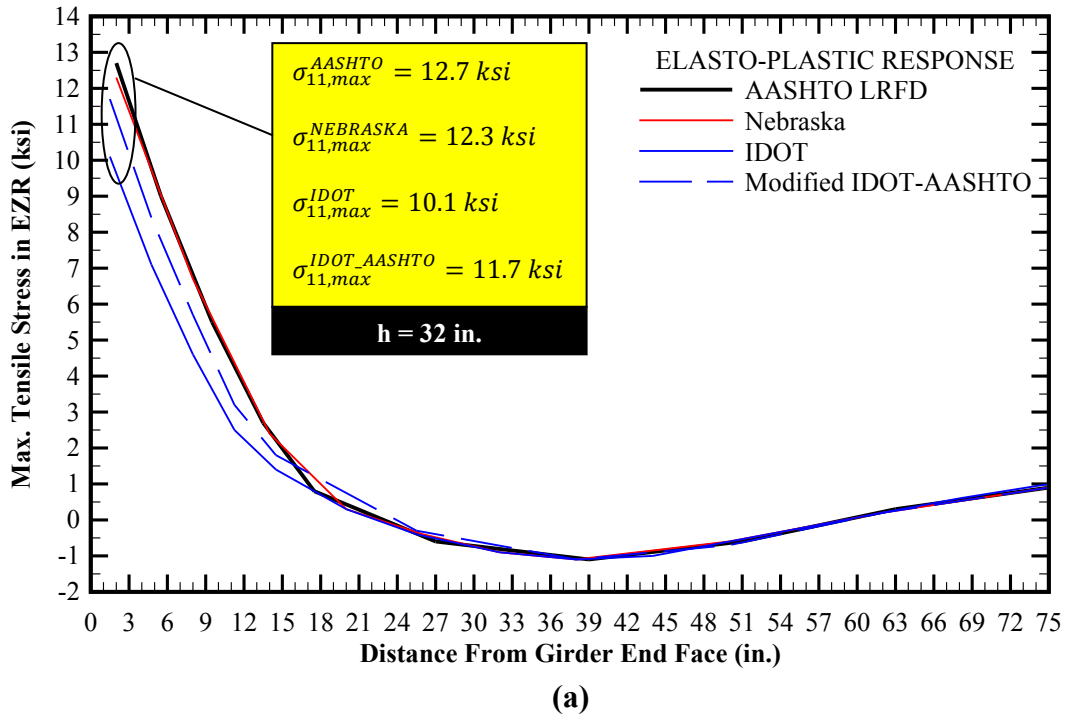
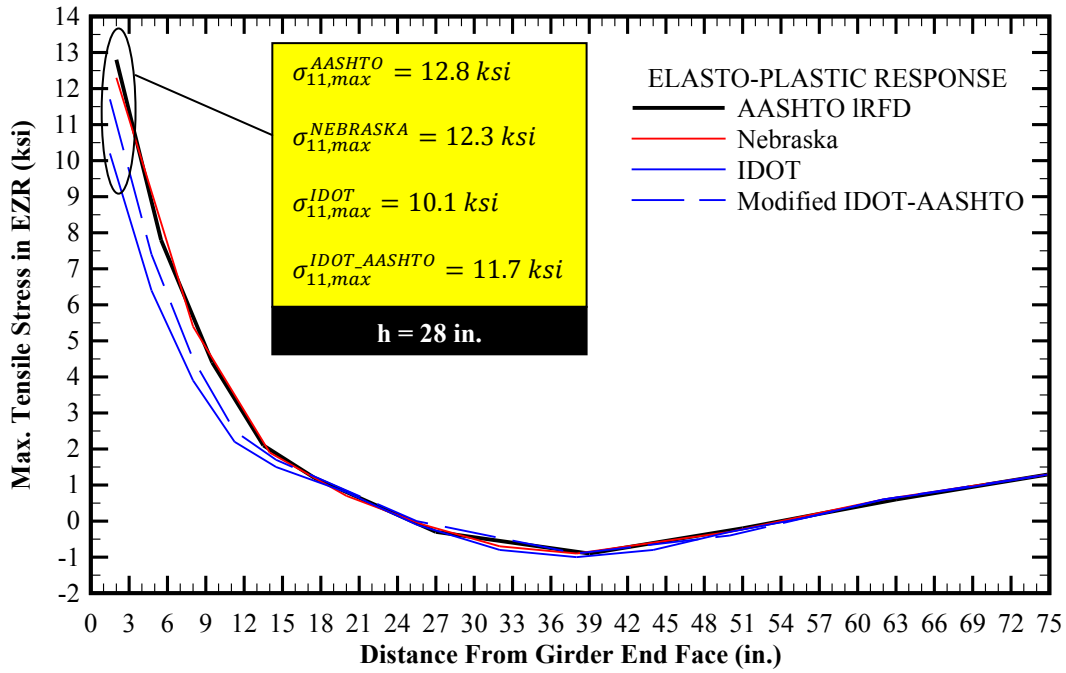
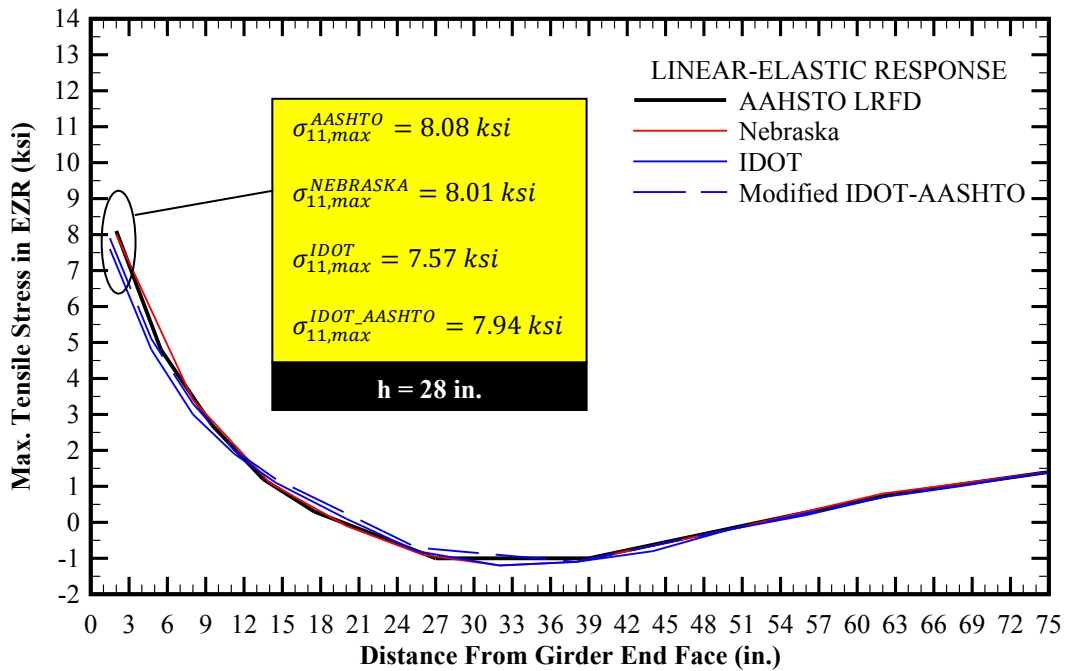


Figure 5-67: Comparison of axial stresses (S11) in the end zone rebar based on elasto-plastic finite element simulations of a typical BT-72 girder, reported at $h = 32$ in. along the height of the member (bottom of bottom flange is assumed as datum): (a) Elasto-plastic response, and (b) Linear-elastic response.



(a)



(b)

Figure 5-68: Comparison of axial stresses (S11) in the end zone rebar based on elasto-plastic finite element simulations of a typical BT-72 girder, reported at $h = 28 \text{ in.}$ along the height of the member (bottom of bottom flange is assumed as datum): (a) Elasto-plastic response, and (b) Linear-elastic response.

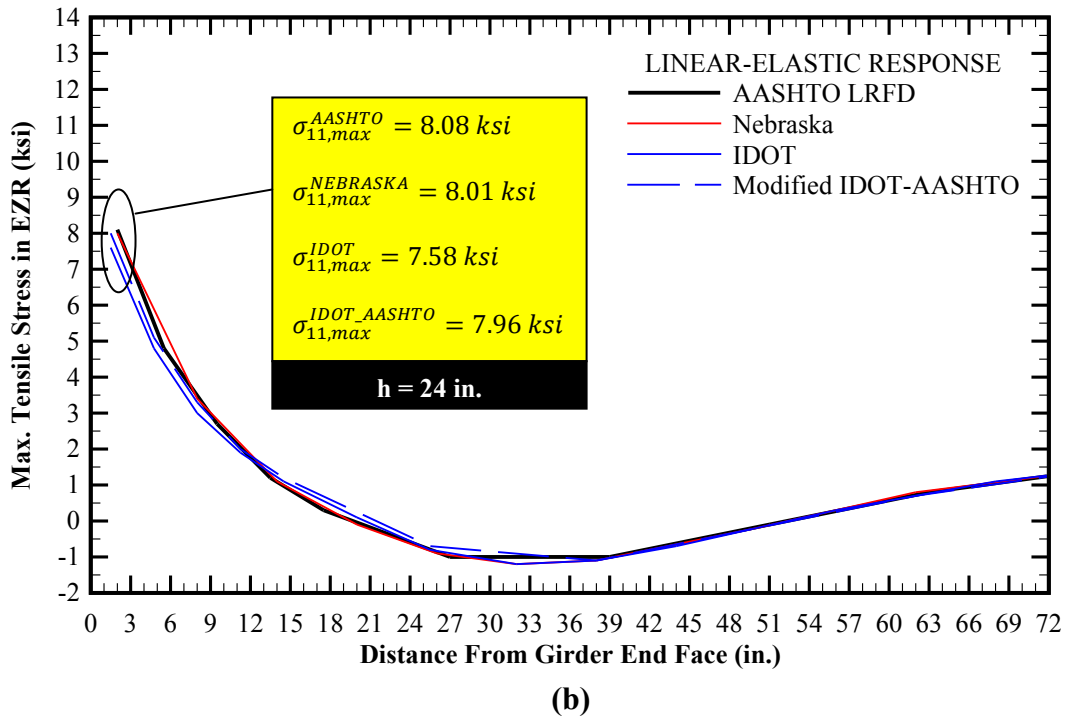
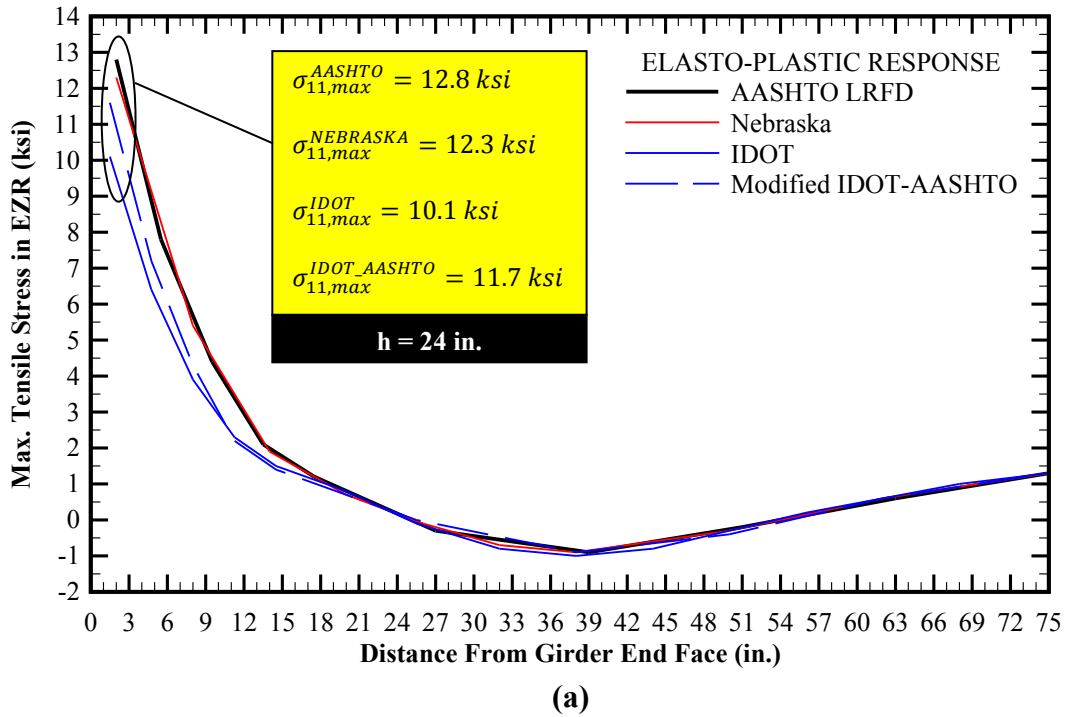


Figure 5-69: Comparison of axial stresses (S11) in the end zone rebar based on elasto-plastic finite element simulations of a typical BT-72 girder, reported at $h = 24$ in. along the height of the member (bottom of bottom flange is assumed as datum): (a) Elasto-plastic response, and (b) Linear-elastic response.

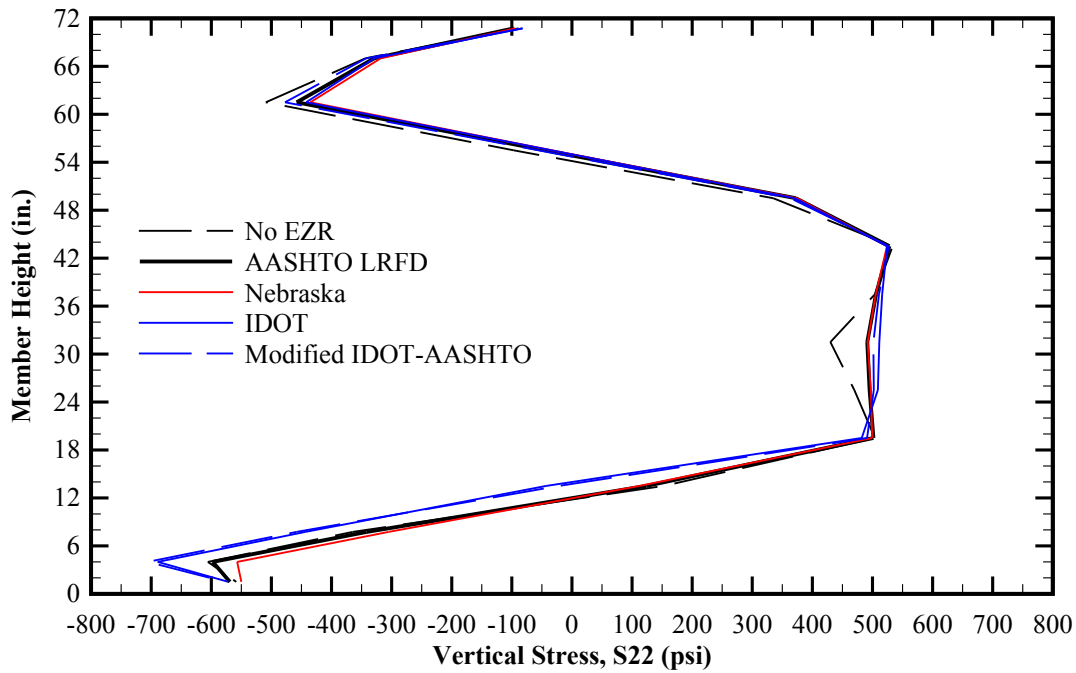


Figure 5-70: Comparison of vertical stress (S22) distribution along the height of finite element models of a typical BT-72 girder with end zone reinforcing details in accordance with AASHTO LRFD, Nebraska, IDOT and Modified IDOT-AASHTO schemes and based on elasto-plastic simulations. The results are reported at 3 in. from the member end face.

16. Figure 5-70 shows the vertical stress (S22) distribution along the height of typical BT-72 girders without end zone rebar and with AASHTO LRFD, Nebraska, IDOT or Modified IDOT-AASHTO end zone reinforcing bars. The results are reported at a cross-section 3 in. from the end face of the girder. The numerical simulations indicate potential tensile cracking and tension softening within a zone located 18 in. to 40 in. along the height of the member, measured from the bottom of the girder bottom flange. The level of tension softening is more severe in the finite element model without end zone rebar. The finite element models with AASHTO LRFD and Nebraska end zone details show

similar responses. Similarly, the simulations with IDOT and Modified IDOT-AASHTO end zone details show analogous trend.

17. Figure 5-71 shows the distribution of the planar shear stress (S_{23}) at the interface between the web and the bottom flange based on elasto-plastic numerical simulations with no end zone rebar and models including AASHTO LRFD, Nebraska, IDOT or Modified IDOT-AASHTO end zone details as well as shear and confinement reinforcement. It is observed that the end zone and shear reinforcement do not affect the magnitude and distribution of the shear-lag caused by the transfer of pretensioning from the bottom flange towards the web.

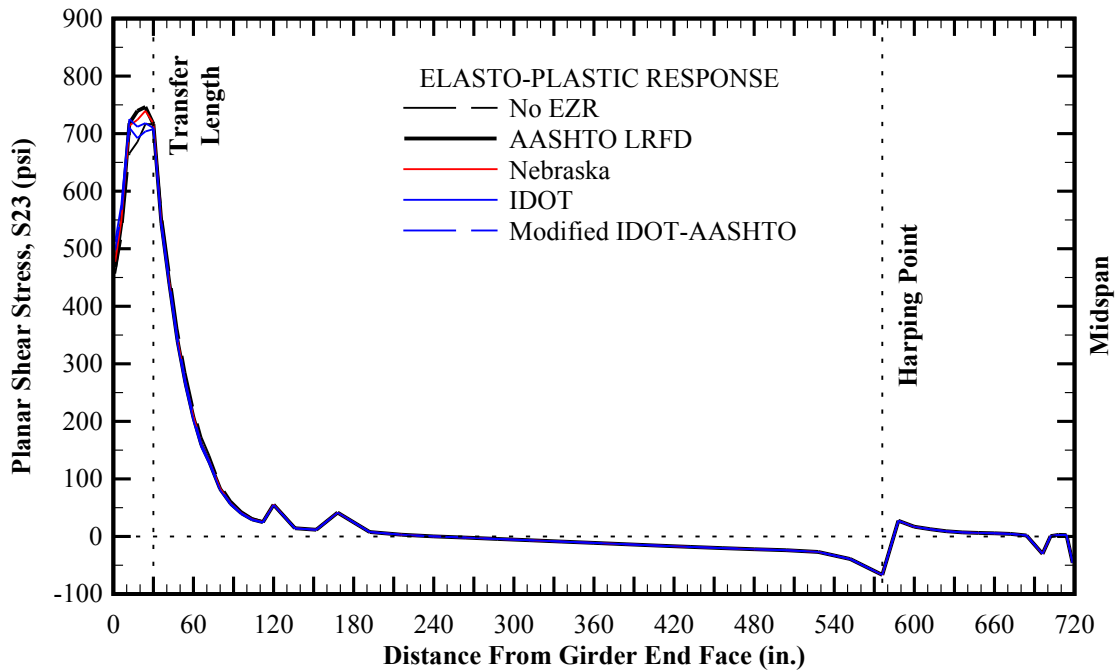


Figure 5-71: Comparison of planar shear stress (S_{23}) distribution along the span of finite element models of a typical BT-72 girder with end zone reinforcing details in accordance with AASHTO LRFD, Nebraska, IDOT and Modified IDOT-AASHTO schemes and based on elasto-plastic simulations. The results are reported at the interface between the web and bottom flange.

18. The numerical investigation of the typical BT-72 girders equipped with various schemes of end zone detailing indicate the Nebraska detail may offer an optimum remedy for end zone cracking of pretensioned girders based on the following:
- a. Placing larger magnitude of end zone rebar near the member end face extending towards $h/8$, where the maximum level of tensile stresses are anticipated in the rebar
 - b. No increase in the overall amount of end zone rebar required by the current AASHTO LRFD specifications
 - c. Larger spacing between the end zone rebar in comparison with the AASHTO LRFD scheme, reducing the congestion of reinforcement within the member end zone

Chapter 6 - Analytical Study of Eight WSDOT BWF100 Super-Girders with Experimental Verification

6.1. Introduction

The Alaskan Way Viaduct replacement project is a joint program by WSDOT in partnership with Federal Highway Administration (FHWA), City of Seattle-Washington, King County-Washington, and Port of Seattle-Washington. The project is comprised of several sub-tasks including the total replacement of State Route 99 double-deck via (led by WSDOT) and Elliot Bay seawall (WSDOT, 2011). As shown in Figure 6-1, the Alaskan Way Viaduct is a vital factor for economic sustainability while serving as a major transportation artery for the greater Seattle metropolitan. The risk of failure due to the past seismic events in combination with the irreversible damages from normal wear-and-tear has drawn special attention to this project. The main goals of this project are safety (structural reliability and durability) and traffic improvements (capacity increase in accordance with the standards of today while having in mind future mobility demands). Table 6-1 shows the outline of the budget proposal by Governor Gregoire for the Alaskan Way Viaduct Replacement Projects.



Figure 6-1: Map of the Alaskan Way Viaduct replacement project (WSDOT, 2011).

This chapter includes the analytical study of eight Washington State Department of Transportation (WSDOT) BWF100 girders which will be utilized in Span 2 of the four (4) span Alaskan Viaduct Northbound/Southbound Bridge No. 99/540. The corresponding bridge is included in Phase 2 of the project extending from S. Holgate to S. King streets, with the span lengths of

- 136'-11 1/8",

- 204'-11 1/2",
- 155'-0 1/4",
- Varies [163'-2 1/2" (max), 143'-10 5/8" (min)]

All eight (8) girders are 100 inches deep and over 204 feet in span each, the largest and longest precast pretensioned concrete girders used in practice in North America as of year 2011. Three (3) classes of the corresponding precast girders with different levels of pretensioning will be discussed later on this chapter.

Table 6-1: Proposed 2011 comprehensive budget outline for Alaskan Way Viaduct projects (WSDOT, 2011)

Alaskan Way Viaduct Replacement Projects	Budget (millions)*
Viaduct Replacement: S. Holgate Street to S. King Street	\$394.8
Viaduct Replacement: S. King Street to Battery Street (SR 99 bored tunnel)	\$1,960.7
Central Waterfront: Viaduct Removal and New Alaskan Way	\$290.0
Central Waterfront: Construction Mitigation	\$30.0
Program Management	\$75.0
Miscellaneous Tasks: Column safety repairs Utility relocations (Electrical lines) Battery street tunnel repairs South end viaduct: Construction Mitigation	\$187.2
Completed tasks: <ul style="list-style-type: none"> ▪ Environmental Impact Statement ▪ Right-of-Way study and acquisition ▪ Design costs 	\$163.7
Total	\$3,101.4

* All costs are expressed in terms of year 2011 expenditure dollars.

Concrete Technology Corporation (CTC) located in Olympia, Washington, was responsible for fabricating all eight girders based on in-house design by WSDOT. Since precast girders with such magnitude in length, size and/or pretensioning levels had not been cast before in North America, great concerns existed regarding the response at the time of release; more specifically, end zone cracking. Therefore, in a collaborative effort with WSDOT and CTC, the George Washington University (Washington, DC) instrumented and monitored all eight (8) girders to observe and investigate the potentials and patterns of end zone cracks in the precast girders immediately after the release of pretensioning.

In addition to End Zone Cracking, the following information was also collected as part of the experimentation:

- *Tie Bars* - The functionality of the staggered tie bars installed hooked between the vertical legs of the end zone and shear reinforcement along the web (Figure 6-2)
- *Transfer Length* - The transfer length of 0.6-in. diameter low-relaxation strands utilized for pretensioning the precast girders (Figure 6- 3)

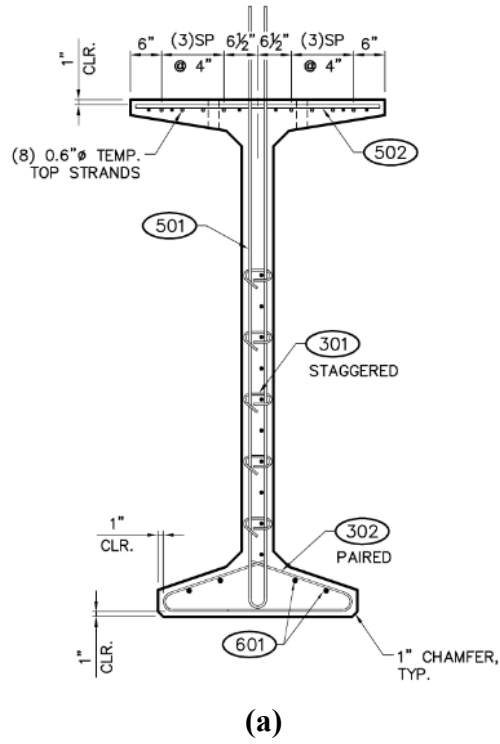


Figure 6-2: Staggered No.3 tie bars (301 series) hooked between the vertical legs of end zone and shear rebars: (a) Typical end section (CTC, 2010), and (b) typical strain gage mounted tie bar.



Figure 6- 3: 0.6-in. diameter strands with strain gages staggered over different rows

6.2. WSDOT BWF100 Super-Girders

As previously mentioned, eight WSDOT BWF100 production girders were instrumented for the analytical purposes of this research. The girders are divided into three classes: G93C (one specimen), G94C (six specimens) and G95C (one specimen). Figure 6-4 through Figure 6-6 show the fabrication shop drawings prepared by Concrete Technology Corporation, Inc. for G93C, G94C and G95C girders, respectively (CTC, 2010). It shall be noted that all three classes of the girders have the similar span length of 205'-2 1/2" with 3" added for shrinkage. Also both end faces of all specimens are skewed at 11° to conform to the bridge pier geometries.

The main difference among the three classes of the girders is the number of prestressing strands as follows:

- G93C girders include 46 straight strands and 26 draped strands (four bundles of 6 strands and one bundle of 2 strands);
- G94C girders include 46 straight strands and 25 draped strands (four bundles of 6 strands and one individual strand), and
- G95C girders include 46 straight strands and 26 draped strands (four bundles of 6 strands and one bundle of 2 strands).

Table 6-2 includes the basic material properties for the BWF100 specimens, including body concrete and prestressing strands. Similarly, Table 6-3 shows the sectional properties of the BWF100 specimens. The modulus of elasticity used for the analytical purposes of this research is based Equation (6.1):

$$E_c = 33 [w_c (pcf)]^{1.5} \sqrt{f'_c (psi)} \quad (6.1)$$

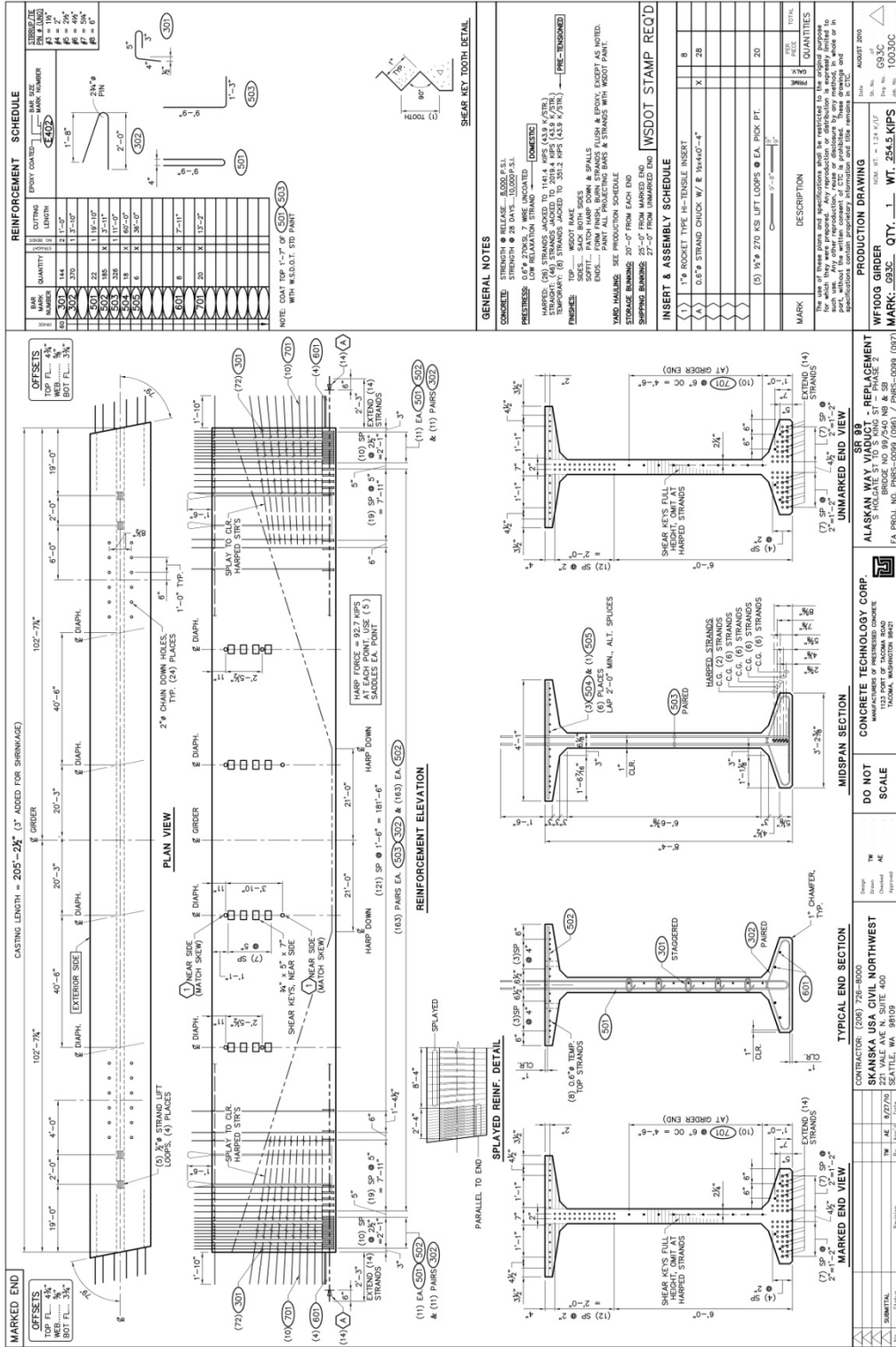


Figure 6-4: Fabrication shop drawings for BWF100 G93C girders (CTC, 2010).

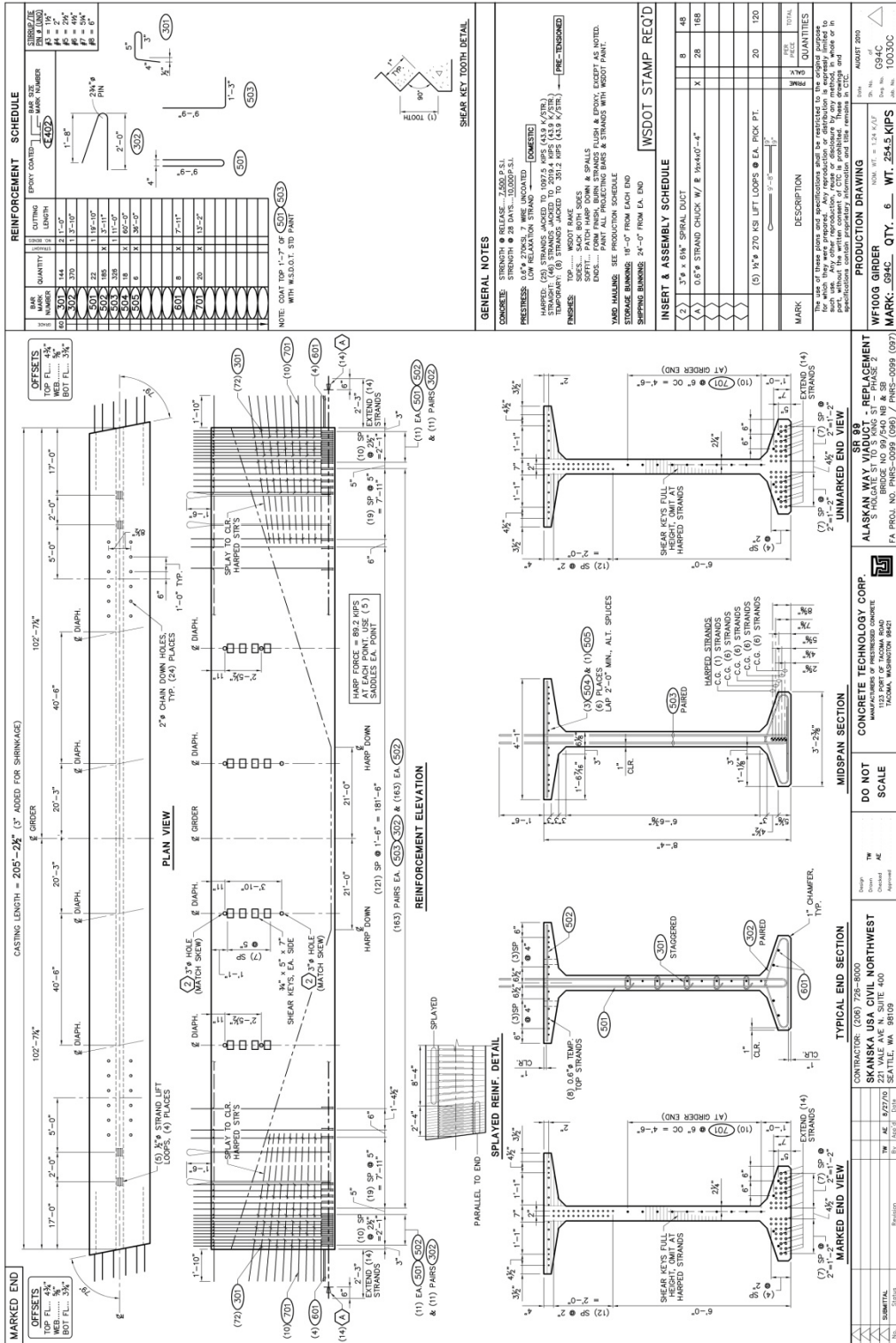


Figure 6-5: Fabrication shop drawings for BWF100 G94C girders (CTC, 2010).

Table 6-2: Basic material properties for BWF100 specimens.

Body Concrete	
Compressive strength at 28 days, f'_c	10,000 psi
Compressive strength at release, f'_{ci}	8,000 psi
Unit weight of concrete, w_c (including reinforcement)	165 pcf
Modulus of elasticity at 28 days, E_c	6,994 ksi
Modulus of elasticity at release, E_{ci}	6,255 ksi
Seven-Wire Low-Relaxation Prestressing Strands	
Strand diameter, d_p	0.6 in.
Ultimate tensile strength, f_{pu}	270 ksi
Modulus of elasticity, E_p	28,900 ksi

Table 6-3: Sectional properties of BWF100 specimens.

Non-Composite Properties	
Cross-sectional area, A_{nc}	1,083 in. ²
Moment of inertia, I_{nc}	1,524,912 in. ⁴
Section modulus at extreme top fiber, $S_{nc,t}$	29,481 in. ³
Section modulus at extreme bottom fiber, $S_{nc,b}$	31,589 in. ³
Distance from the top extreme top fiber to the member centroid, $y_{nc,t}$	51.73 in.
Distance from the bottom extreme top fiber to the member centroid, $y_{nc,b}$	48.27 in.

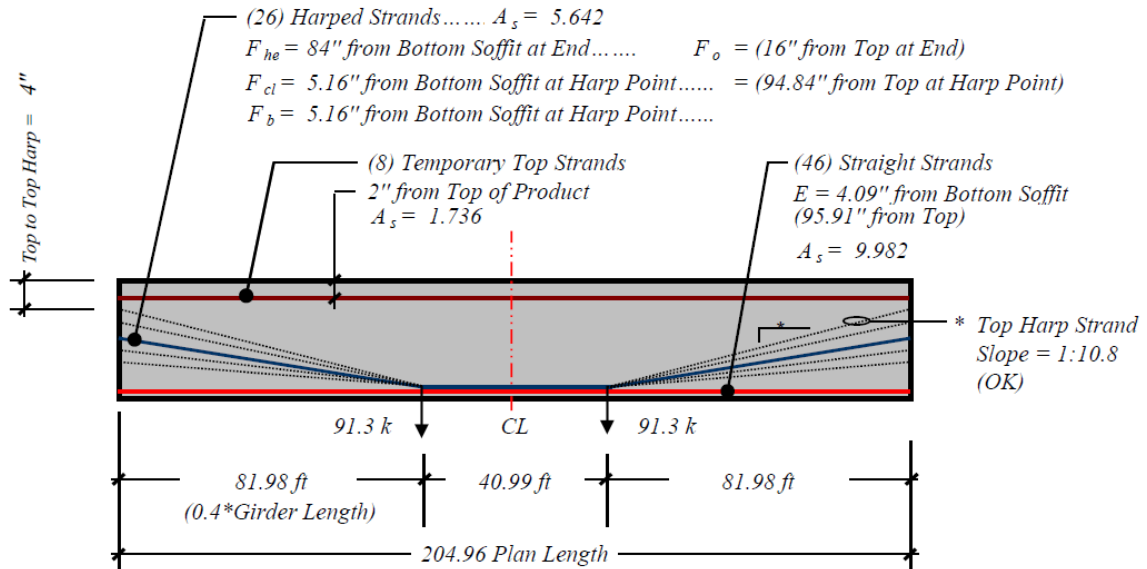


Figure 6-7: Prestressing layout (CTC, 2010).

Figure 6-7 shows the schematic prestressing layout corresponding to the G93C and G95C specimens. G04C girders have similar details except the number of the draped strands: 25 versus 26 bundled strands. This introduces negligible asymmetric lateral prestressing in the corresponding specimens. Therefore, the properties of G94C specimens will be used for the analytical purposes of this research.

Before releasing the straight strands, the girders were lifted or "bunked" from the casting bed in order to ensure no bonding between the bottom face of the bottom flange and the bed. Figure 6-8 shows the bunking the configuration and the anticipated weight distributions at the lifting points located approximately 8 ft from the member end faces. In reference to Section 5.2, this practice introduces new temporary boundary conditions and consequently, reversal of stresses during the fabrication process which will be discussed in more details later on this chapter.

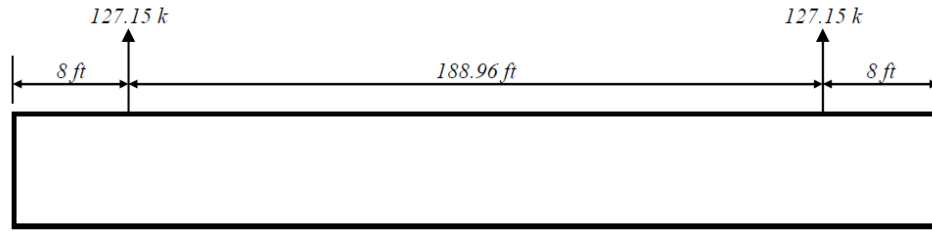


Figure 6-8: Balking configuration of the specimens at the release of straight strands (CTC, 2010).

6.3. Experimental Investigations

6.3.1. Test Specimens

As previously discussed, the test specimens are comprised of eight production girders as summarized in Table 6-4. Figure 6-9 shows typical reinforcement cage for Specimen No.1 in addition to the final girder while stored in the casting yard.

Table 6-4: Test specimens.

Specimen I.D.	Girder Type	Span Length (*)	# Straight Strands	# Draped Strands
No.1	G93C	205'-2 1/2"	46	26
No.2	G94C	205'-2 1/2"	46	25
No.3	G94C	205'-2 1/2"	46	25
No.4	G94C	205'-2 1/2"	46	25
No.5	G94C	205'-2 1/2"	46	25
No.6	G94C	205'-2 1/2"	46	25
No.7	G94C	205'-2 1/2"	46	25
No.8	G95C	205'-2 1/2"	46	26

(*) 3 in. is added to account for the anticipated shrinkage.



(a)



(b)

Figure 6-9: Test specimen No.1: (a) Reinforcement cage, and (b) Girder stored in the casting yard.

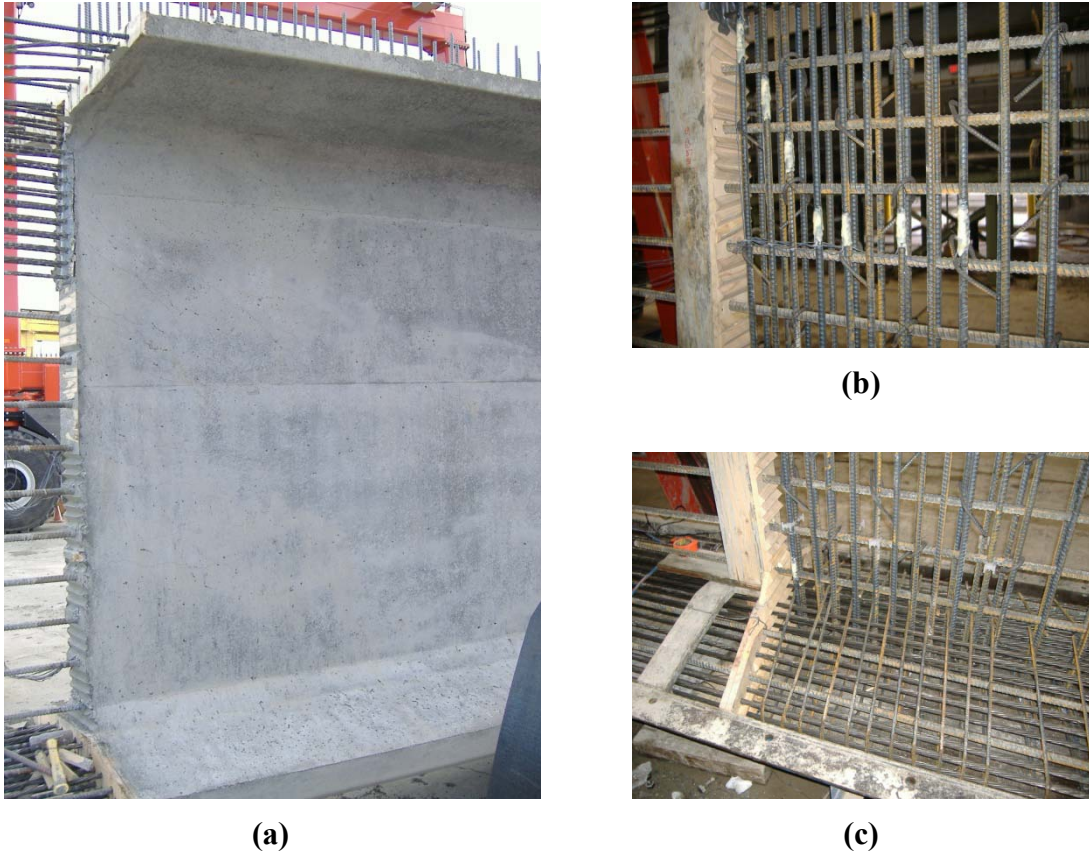
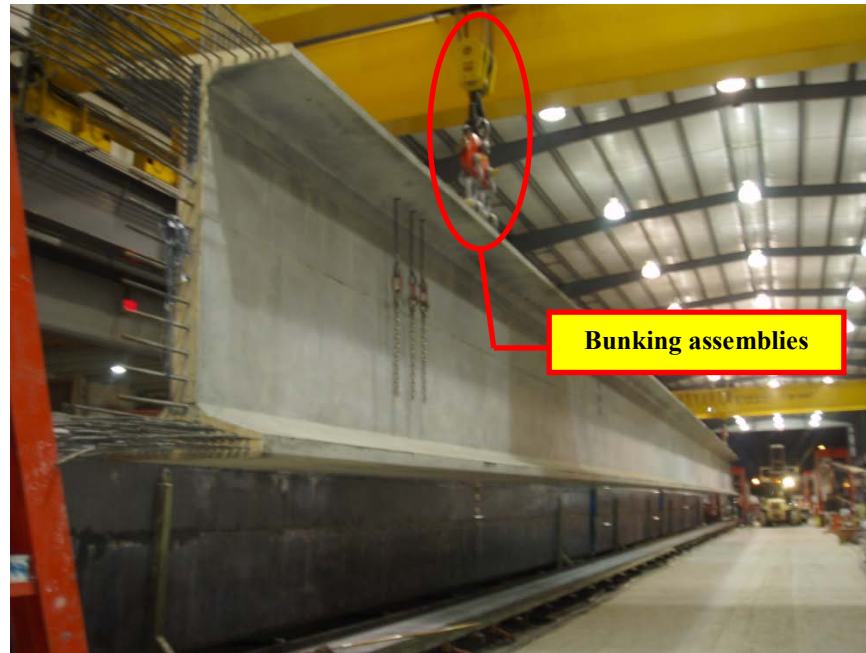


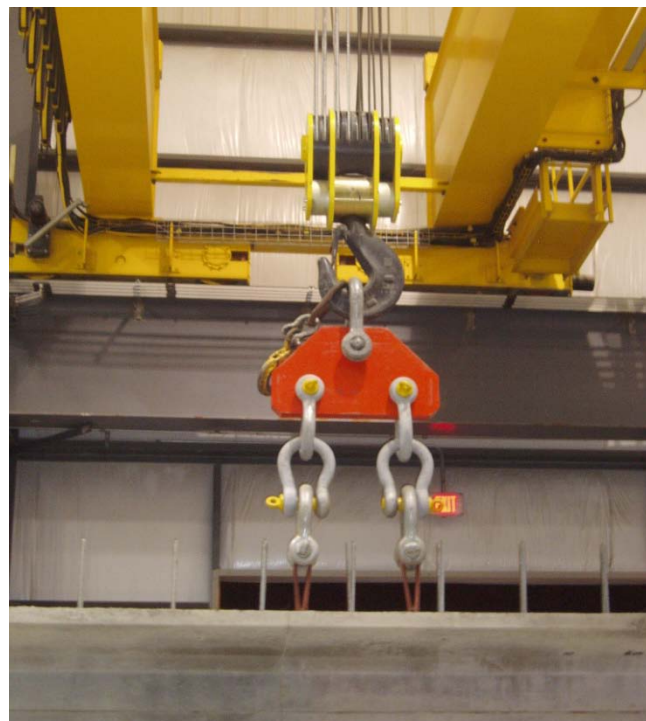
Figure 6-10: Test specimen No.5: (a) Typical end face, (b) Typical web reinforcement with strain gages, and (c) Typical bottom flange reinforcement.

Figure 6-10 shows typical details of Specimen No.5, including the concrete body after curing in addition to the typical reinforcing bars at the web and bottom flanges. Figure 6-9(b) and Figure 6-10 (a) show No.7 bars extending approximately 1'-10" beyond the web at both girder end faces. The corresponding No. 7 bars are intended to accommodate doweling into the pier diaphragms. In addition, Figure 6-10 (b) shows No3 tie bars which are incorporated in the web reinforcing cage to tie the vertical legs of the end zone or shear reinforcing bars along the 4 ft of the end zone at each end. In reference to Figure 6-4 through Figure 6-6, the above details are typical for all eight test specimens.

In addition, all eight test specimens are bunched in accordance with Figure 6-8. In other words, each specimen is lifted from the casting bed after the release of the draped strands but prior to the release of the straight strands. Figure 6-11 (a) shows a typical specimen lifted from the casting bed after the release of prestressed strands including the bunching assemblies. Figure 6-11 (b) shows typical lifting details including the overhead cranes in the precasting yard. The lifting points include two sets of loops comprised of five 1/2-in. diameter strands, located 17 ft and 19 ft from each end face of the girder, respectively. The lifting points are intended to facilitate transportation and erection of the girders.



(a)



(b)

Figure 6-11: Typical bunking configuration: (a) Specimen No.2 lifted from the casting bed after the release of pretensioning, and (b) Typical lifting details including the overhead cranes.

6.3.2. Guidelines for Installation of Strain Gages

The following section includes a step by step guideline for installation of strain gages on seven-wire 0.6-in. diameter strands. The instrumentation of pretensioning strands is a delicate task which requires extreme attention. Careless attempts may result in irreversible damage to individual wires, endangering the integrity of the entire strand.

The guidelines outlined herein is the result of past experiences as well as extensive discussion with the leading distributors of strain gages in the US.

Additionally, the procedure outlined in this section is also applicable for instrumentation of deformed rebars to be embedded in concrete with one exception that deformed reinforcement will generally require more involved surface grinding and preparation. The following includes the list of the basic equipments used for the purpose of data collection for this research.

6.3.2.1. Strain Gages

Various brands of commercial strain gages are currently available, which are applicable for installation on seven-wire strands. The recommended gages are generally very small in planar dimensions (typically 1 mm) to conform to the minimal surface area available by individual wires.

For the experimental purposes of this research, two types of strain gages by Texas Measurement, Inc. are utilized as follows (Texas Measurements, Inc., 2010):

- FLA-1-350-11-5LT strain gages for instrumentation of 0.6-in. diameter strands
- FLA-5-11-5LT strain gages for instrumentation of mild reinforcement

Figure 6-12 shows a typical FLA-1-350-11-5LT gage by Texas Measurements, Inc., which is approximately 3/16 in. long and 0.039370 in. (1 mm) wide.

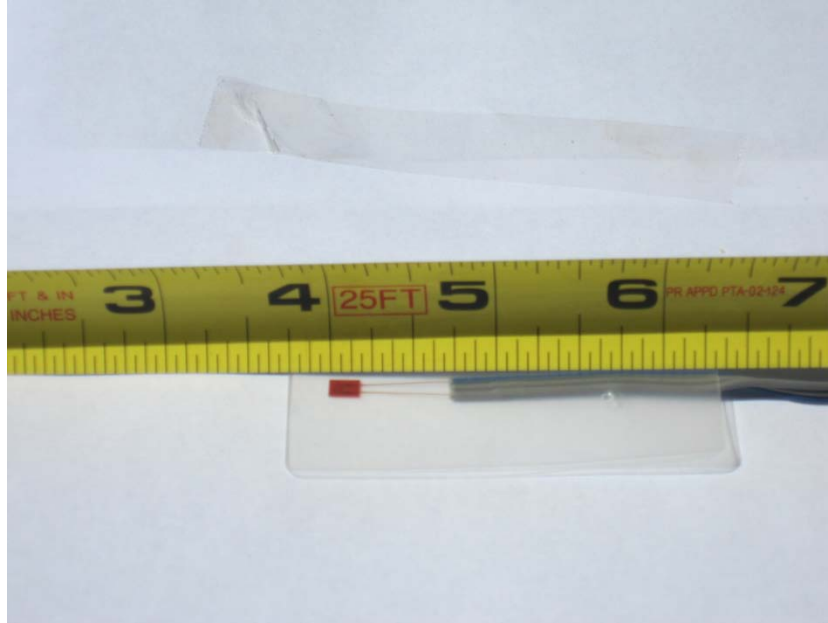


Figure 6-12: A typical FLA-1-5LT strain gage by Texas Measurements, Inc (Texas Measurements, Inc., 2010).

6.3.2.2. Grinder

Figure 6-13 shows atypical hand-held grinder required for surface preparation of the strands and mild reinforcing bars.



Figure 6-13: A typical hand-held grinder required for surface preparation.

6.3.2.3. Chemical Solutions for Surface Preparation

Before the strain gages are mounted onto the strands, the host surface shall be cleaned after being grinded. For the purposes of this research, a water-based two-part solution is by Vishay Precision Group as follows (Vishay Precision Group, 2010):

- *M-Prep Conditioner A*: A mild phosphoric-acid compound. Acts as a mild etchant and accelerates the cleaning process.
- *M-Prep Neutralizer 5A*: An ammonia-based material. Neutralizes any chemical reaction introduced by the Conditioner A, and produces optimum surface conditions for most strain gage adhesives.

6.3.2.4. Strain Gage Adhesive

Various commercial adhesive products are currently available for installation of strain gages onto steel hosts. For the purposes of this research, *M-Bond 200* is used, which is a two-part adhesive agent as shown in Figure 6-14.



Figure 6-14: M-Bond 200 adhesive kit by Vishay Precision Group (Vishay Precision Group, 2010).

6.3.2.5. Coating Agents

Since the strands as well as the mild reinforcing bars will be embedded in fresh concrete, adequate protective measure shall be considered in order to prevent potential damage to the strain gages. For the purposes of this research, a three-part coating mechanism is utilized as recommended by Texas Measurements, Inc., which is illustrated in Figure 6-15(Texas Measurements, Inc., 2010):

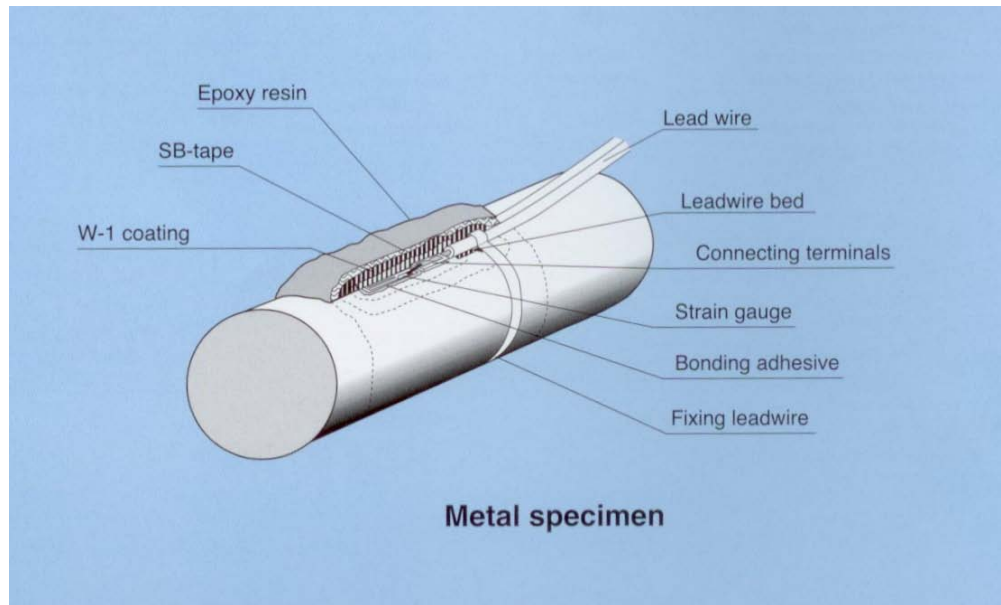


Figure 6-15: A three-part coating mechanism recommended by Texas Measurements, Inc. (Texas Measurements, Inc., 2010).

Per the instruction by Texas Measurements, Inc., the following coating agents are utilized to ensure the three part mechanism shown in Figure 6-15:

- *Epoxy Resin*: This product shall be melted and then applied onto the strain gage, over and under the lead wire base to ensure protective seal against water and other damaging agents.
- *SB Tape*: As shown in Figure 6-15, this product creates an additional adhesive layer over the epoxy resin (see Figure 6-16).

- *Araldite Standard*: This two-part agent provides W1-Coating over the SP tape, which generally cures in 12 hours under installation temperature of $60^{\circ}F \pm$ (Figure 6-17).



Figure 6-16: SB Tape by Texas Measurements, Inc. (Texas Measurements, Inc., 2010).



Figure 6-17: Araldite standard coating agent by Texas Measurements, Inc. (Texas Measurements, Inc., 2010).

6.3.3. Installation Steps

The following includes the general steps for the installation of the strain gages onto the prestressing strands as well as the non-prestressed [mild] reinforcing bars as utilized for the experimental purposes of this research:

- Step 1: Grinding for surface preparation (Figure 6-18);



Figure 6-18: A typical seven wire 0.6-in. diameter strand after being grinded to host a strain gage.

- Step 2: Mounting strain gages using the bond agent (Figure 6-19);
- Step 3: Managing the lead wire to allow for adequate (Figure 6-20), and
- Step 4: Application of the three-part coating agents: i) epoxy resin, ii) SB tap, and iii) two-part Araldite agent (Figure 6-21 thru Figure 6-23)



(a)



(b)

Figure 6-19: Installation of a typical FLA-1-350-11-5LT strain gage on a 0.6-in. diameter seven-wire prestressing strand: (a) Strain gage temporarily mounted on the strand using scotch tape and (b) Strain gage wrapped by electric tape during the curing of the surface bind agent.



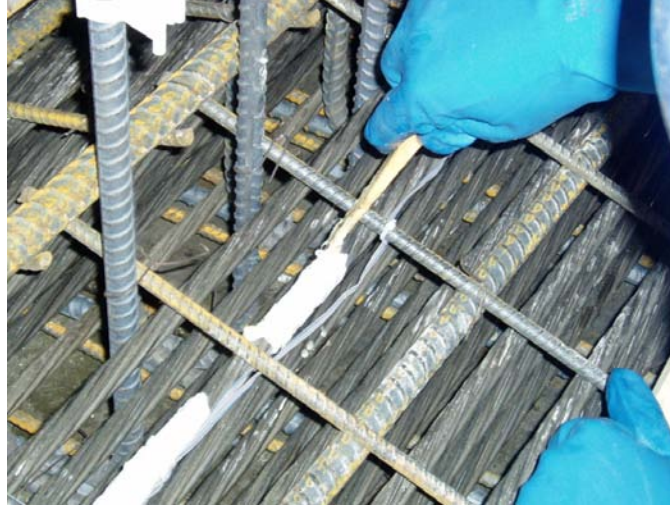
Figure 6-20: Lead wires attached to the strand using a typical plastic strap while allowing adequate slack in the wire adjacent to the gage.



Figure 6-21: Application of the epoxy resin (the first layer of coating) over a FLA-5-11-5LT strain gage mounted on a vertical leg of a typical No.5 end zone rebar.



Figure 6-22: Application of the second layer of coating protection, SB tape..



(a)



(b)

Figure 6-23: Araldite as the third layer of coating protection: (a) application of Araldite after the two agents are properly mixed, and (b) the final the assembly after Araldite coating has cured.

6.3.4. Data Acquisition

Figure 6-24 shows the data acquisition setup for the experimental purposes of this research. First, the lead wires were all labeled as R1 thru R8 and S1 thru S8 corresponding to FLA-5-11-5LT and FLA-1-350-11-5LT strain gages at the reinforcing bars and strands, respectively, for each girder. Then the lead wires were managed out of the precast forming, extending to the Data Acquisition equipment (DAQ) stationed on-site. Figure 6-24 (a) shows a typical wire management through the straight strands outside the girder bottom flange. The DAQ system was able to manage maximum of sixteen channels of data (R1 thru R8 and S1 thru S8) and was connected to a laptop thru USB connection. Figure 6-24 (b) shows a typical DAQ setup at the fabrication site. Then data collection is generally facilitated through a control software which can translate the input signals into readable (e.g., text format) strain versus time. Strain data was continuously collected, starting shortly before the start of release of pretensioning until few minutes after the entire strands were released in order to allow DAQ to capture stabilization of stresses/strains after the complete release of pretensioning.

Figure 6-25 thru Figure 6-32 show the field log corresponding to Girder No.1 thru Girder No.8, respectively. Each field log indicates the vertical or horizontal location of the strain gages R1 thru R8 and S1 thru S8 in relationship to the member geometry. In addition, the field logs indicate the casting and release date for each specimen. This is an important parameter which determines the age of the concrete at the time of release.

Also please note that Figure 6-29 thru Figure 6-32 indicate that the data collection for Girders No.5 thru No.8 was performed at the live end of the member.

Observation of straining sample strands indicated that due to the small size of FLA-1-350-11-5LT strain gages relative to the helical curvature of the seven-wire strands, the obtained strain data did not need to be calibrated.



(a)



(b)

Figure 6-24: Data acquisition: (a) typical wire management through the straight strands beyond the girder bottom flange, and (b) on-site DAQ setup.



Mark Number: G93C
Cast Date: Wed, 11/03/10
Release Date: Thu, 11/04/10

Girder #: 1

Rebar Gages (Mod4)...

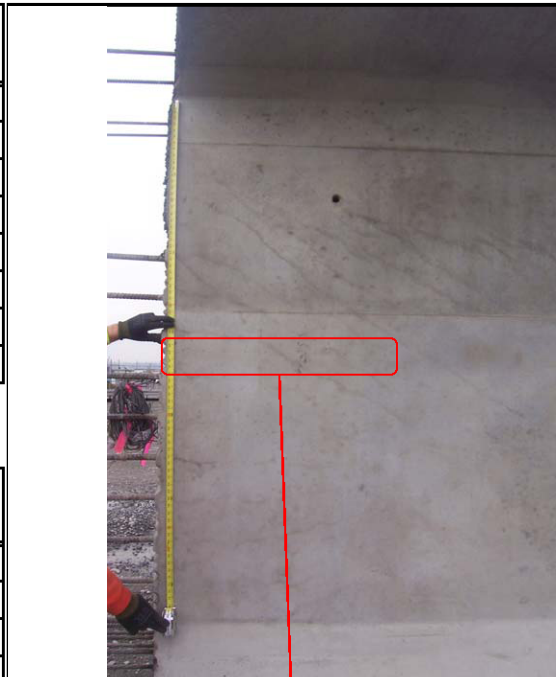
# Cr.	Gage #	Height (inches)	Dist From End (inches)
0	G1 -R1	52 (?)	3 (?)
1	G1 -R2	52.125	5.6250
2	G1 -R3	52.000	8.3750
3	G1 -R4	52.188	11.2500
4	G1 -R5	52.125	13.8750
5	G1 -R6	52.250	19.3750
6	G1 -R7	52.250	24.7500
7	G1 -R8	52.125	30.3125

3rd Level Strand Gages (Mod5)...

# Cr.	Gage #	Height (inches)	Dist From End (inches)
0	G1 -S1	6.25	19.5625
1	G1 -S2	6.125	205
2	G1 -S3	6.0625	28
3	G1 -S4	6.125	36.375

4th Level Strand Gages (Mod5)...

# Cr.	Gage #	Height (inches)	Dist From End (inches)
4	G1 -S5	8.1250	5.0625
5	G1 -S6	8.1250	15.5000
6	G1 -S7	8.0625	25.8750
7	G1 -S8	8.0625	31.0625



G1R1

G1R8

Figure 6-25: Girder No.1 (G93C) field log. Courtesy of Concrete Technology Corporation (CTC, 2010).



Mark Number: G94C Girder #: 2
Cast Date: Fri, 11/05/10
Release Date: Tue, 11/09/10

Rebar Gages (Mod4)...

Ch. #	Gage #	Height (inches)	Dist From End (inches)
0	G2 -R1	52.000	3.1250
1	G2 -R2	52.500	5.7500
2	G2 -R3	52.000	8.2500
3	G2 -R4	52.250	10.7500
4	G2 -R5	52.500	13.5000
5	G2 -R6	52.250	19.2500
6	G2 -R7	52.625	24.2500
7	G2 -R8	51.750	29.7500

3rd Level Strand Gages (Mod5)...

Ch. #	Gage #	Height (inches)	Dist From End (inches)
0	G2 -S1	6.3750	9.1250
1	G2 -S2	6.5000	19.1250
2	G2 -S3	6.3750	26.5000
3	G2 -S4	6.5000	35.5000

4th Level Strand Gages (Mod5)...

Ch. #	Gage #	Height (inches)	Dist From End (inches)
4	G2 -S5	8.1250	4.5000
5	G2 -S6	8.3750	14.1250
6	G2 -S7	8.2500	24.2500
7	G2 -S8	8.2500	30.7500

Figure 6-26: Girder No.2 (G94C) field log. Courtesy of Concrete Technology Corporation (CTC, 2010).



Mark Number: G94C Girder #: 3
 Cast Date: Wed, 11/10/10
 Release Date: Thu, 11/11/10

Rebar Gages (Mod4)...

Ch. #	Gage #	Height (inches)	Dist From End (inches)	Comments
0	G3 -R1	69.500	3.000	R1 through R4 were installed with the wires of the strain gage touching the rebar. This is how James and I instrumented Girder #1 & Girder #2
1	G3 -R2	63.000	5.5000	
2	G3 -R3	51.750	8.3750	
3	G3 -R4	51.750	10.3750	
4	G3 -R5	51.750	12.6250	R5 through R8 were installed with the wires of the strain gage facing up. This is how Amir remembers installing the gages.
5	G3 -R6	51.625	13.2500	
6	G3 -R7	52.375	22.3750	
7	G3 -R8	52.250	28.0000	

4th Level Strand Gages (Mod5)...

Ch. #	Gage #	Height (inches)	Dist From End (inches)	Comments
0	G3 -S1	8.125	5.000	Gages installed with wires "up". All strand gages were installed on the same strand. We lost the signal to G3-S2.
1	G3 -S2	8.000	9.750	
2	G3 -S3	8.250	14.500	
3	G3 -S4	8.250	19.500	
4	G3 -S5	8.1250	24.7500	
5	G3 -S6	8.1250	30.7500	
6	G3 -S7	8.0000	36.7500	
7	G3 -S8	8.1250	46.2500	

Figure 6-27: Girder No.3 (G94C) field log. Courtesy of Concrete Technology Corporation (CTC, 2010).



Mark Number: G94C Girder #: 4
 Cast Date: Fri, 11/12/10
 Release Date: Sat, 11/13/10

Rebar Gages (Mod4)...

# C	Gage #	Height (inches)	Dist From End (inches)	Comments
0	G4 -R1	69.875	2.000	
1	G4 -R2	63.000	5.0000	
2	G4 -R3	55.250	7.5000	
3	G4 -R4	52.000	9.7500	
4	G4 -R5	52.125	12.0000	
5	G4 -R6	52.250	17.8750	Residual gauze stuck to the surface of the rebar
6	G4 -R7	52.250	22.5000	
7	G4 -R8	52.000	28.2500	

Strand Gages (Mod5)...

# C	Gage #	Height (inches)	Dist From End (inches)	Comments
0	G4 -S1	8.125	5.250	We staggered two gages on four strands. The longitudinal distance between each gage on the same strand was approximately 20 inches. The intent of this arrangement was to reduce the amount of debonding on the gaged strand that results from the coating of the gages.
1	G4 -S2	6.250	10.000	
2	G4 -S3	6.250	15.250	
3	G4 -S4	4.250	19.750	
4	G4 -S5	8.1250	25.5000	
5	G4 -S6	6.2500	31.0000	
6	G4 -S7	6.2500	36.0000	
7	G4 -S8	4.2500	41.5000	

Strand	S1	S2	S3	S4	S5	S6	S7	S8	Height (in)
Strand A					S5				8.125
Strand B		S2				S6			6.25
Strand C			S3				S7		6.25
Strand D				S4				S8	4.25
	5.25	10.00	15.25	19.75	25.50	31.00	36.00	41.50	
	Distance from End (in)								

Figure 6-28: Girder No.4 (G94C) field log. Courtesy of Concrete Technology Corporation (CTC, 2010).



Mark Number: G94C Girder #: 5
 Cast Date: Mon, 11/15/10 End: LIVE
 Release Date: Tue, 11/16/10

Rebar Gages (Mod4)...

# G	Gage #	Height (inches)	Dist From End (inches)	Comments
0	G5 -R1	69.000	2.250	
1	G5 -R2	63.250	5.2500	
2	G5 -R3	57.250	7.7500	
3	G5 -R4	51.000	10.7500	
4	G5 -R5	50.750	13.5000	
5	G5 -R6	50.875	18.5000	
6	G5 -R7	51.000	23.7500	
7	G5 -R8	13.500	2.7500	This gage is at the bottom flange / web interface

Strand Gages (Mod5)...

# S	Gage #	Height (inches)	Dist From End (inches)	Comments
0	G5 -S1	8.000	7.250	
1	G5 -S2	6.250	10.000	
2	G5 -S3	6.000	15.000	
3	G5 -S4	4.000	20.000	
4	G5 -S5	8.0000	25.2500	
5	G5 -S6	6.0000	31.7500	
6	G5 -S7	6.0000	36.2500	
7	G5 -S8	4.2500	41.5000	

Strand A	S1			S5				8.000	Height (in)																
Strand B		S2			S6			6.250																	
Strand C			S3			S7		6.000																	
Strand D				S4			S8	4.000																	
<table border="1"> <tr> <td>7.25</td> <td>10.00</td> <td>15.00</td> <td>20.00</td> <td>25.25</td> <td>31.75</td> <td>36.25</td> <td>41.50</td> </tr> <tr> <td colspan="8">Distance from End (in)</td> </tr> </table>									7.25	10.00	15.00	20.00	25.25	31.75	36.25	41.50	Distance from End (in)								
7.25	10.00	15.00	20.00	25.25	31.75	36.25	41.50																		
Distance from End (in)																									


Figure 6-29: Girder No.5 (G94C) field log. Courtesy of Concrete Technology Corporation (CTC, 2010).



Mark Number: G94C
Cast Date: Wed, 11/17/10
Release Date: Thu, 11/18/10

Girder #: 6
End: LIVE

Rebar Gages (Mod4)...

# Cr.	Gage #	Height (inches)	Dist From End (inches)	Comments
0	G6 -R1	69.000	3.2500	All gages are installed on the opposite face of the web as the longitudinal #7 bars. 
1	G6 -R2	63.000	5.7500	
2	G6 -R3	56.750	9.5000	
3	G6 -R4	52.250	12.5000	
4	G6 -R5	51.750	15.5000	
5	G6 -R6	51.750	21.7500	
6	G6 -R7	52.000	27.7500	
7	G6 -R8	52.000	33.7500	

Strand Gages (Mod5)...

# Cr.	Gage #	Height (inches)	Dist From End (inches)	Comments
0	G6 -S1	12.250	3.500	Placed on EZR
1	G6 -S2	12.500	5.750	
2	G6 -S3	12.500	9.000	
3	G6 -S4	11.750	12.000	
4	G6 -S5	8.0000	11.5000	Placed on Strand
5	G6 -S6	6.0000	23.2500	
6	G6 -S7	6.0000	33.7500	
7	G6 -S8	4.0000	43.2500	

Strand A	S5							8.000	Height (in)
Strand B		S6						6.000	
Strand C			S7					6.000	
Strand D				S8				4.000	
		11.50	23.25	33.75	43.25				
Distance from End (in)									

Figure 6-30: Girder No.6 (G94C) field log. Courtesy of Concrete Technology Corporation (CTC, 2010).



Mark Number: G94C
Cast Date: Thu, 11/18/10
Release Date: Fri, 11/19/10

Girder #: 7
End: LIVE

Rebar Gages (Mod4)...

# Cr.	Gage #	Height (inches)	Dist From End (inches)
0	G7 -R1	69.250	3.2500
1	G7 -R2	63.000	5.5000
2	G7 -R3	57.000	7.2500
3	G7 -R4	51.000	10.5000
4	G7 -R5	51.000	13.2500
5	G7 -R6	51.000	18.5000
6	G7 -R7	51.000	23.5000
7	G7 -R8	51.000	29.2500

All gages are on the opp. face of the web as the longit. #7 bars.

Strand Gages (Mod5)...

# Cr.	Gage #	Height (inches)	Dist From End (inches)
0	G7 -S1	12.000	3.250
1	G7 -S2	12.500	5.500
2	G7 -S3	13.000	8.000
3	G7 -S4	12.500	10.500
4	G7 -S5	49.0000	11.5000
5	G7 -S6	48.5000	21.5000
6	G7 -S7	25.0000	11.5000
7	G7 -S8	24.5000	22.0000

Placed on EZR
Placed on #3 ties



Figure 6-31: Girder No.7 (G94C) field log. Courtesy of Concrete Technology Corporation (CTC, 2010).



Mark Number: G95C-A
Cast Date: Mon, 11/22/10
Release Date: Tue, 11/23/10

Girder #: 8
End: LIVE

Rebar Gages (Mod4)...

# Ch.	Gage #	Height (inches)	Dist From End (inches)		Comments
0	G8 -R1	69.000	4.0000	All gages are on the opp. face of the web as the longit. #7 bars.	
1	G8 -R2	63.000	6.5000		
2	G8 -R3	57.000	9.5000		
3	G8 -R4	51.000	12.5000		
4	G8 -R5	51.000	15.0000		
5	G8 -R6	51.000	21.0000		
6	G8 -R7	51.250	26.5000		
7	G8 -R8	51.000	32.0000		Lost (would not calibrate)

Strand Gages (Mod5)...

# Ch.	Gage #	Height (inches)	Dist From End (inches)		Comments
0	G8 -S1	12.250	6.500	Placed on EZR	All gages on Mod 5 were not recorded. The data was displayed on the screen but did not get saved to the log.
1	G8 -S2	12.500	12.000		
2	G8 -S3	12.250	20.500		
3	G8 -S4	12.000	31.000		
4	G8 -S5	47.7500	8.0000	Placed on Longit. #7	Lost (would not calibrate)
5	G8 -S6	47.2500	19.7500		Lost (would not calibrate)
6	G8 -S7	18.0000	13.5000		
7	G8 -S8	17.7500	24.5000		

Figure 6-32: Girder No.8 (G95C) field log. Courtesy of Concrete Technology Corporation (CTC, 2010).

Figure 6-33 and Figure 6-34 show the strain data reported by strain gages R1 thru R8 at the vertical legs of the end zone reinforcing bars and S1 thru S8 at the prestressing strands of Girder No.1 (G93C). As previously mentioned, the data was collected over a continuous time domain starting shortly before the process or release of pretensioning, extending few minutes after the completion of release to allow for internal stabilization of stresses. As the result, the strain data is plotted versus duration of the pretensioning release. Thus, the x-axis represents the number of discrete data points based on the duration of the each step of pretensioning release.

The pretensioned strands are released using a hydraulic abutment at the live end of the girder as shown in Figure 6-35. The process of detensioning of the prestressed strands is outlined below:

- Step 1: The draped strands are detensioned to 50% of the jacking stress.
- Step 2: The draped strands are completely released.
- Step 3: The girder is lifted or "bunked" from the casting bed.
- Step 4: The straight strands are completely released.

Therefore, three distinct steps are observed in the data reported by the strain gages corresponding to Steps 1, 2 and 4 above.

Figure 6-36 shows the mapping of the maximum tensile stresses corresponding to the strain data shown in Figure 6-33 and Figure 6-34. It appears that the data reported by strain gages R1, R7, and S1 should not be accounted for due to possible malfunctioning.

Similarly, Figure 6-37 thru Figure 6-39 show the straining of the end zone rebar and prestressing strands as well as the mapping of the corresponding maximum tensile stresses for Girder No.2 (G94C).

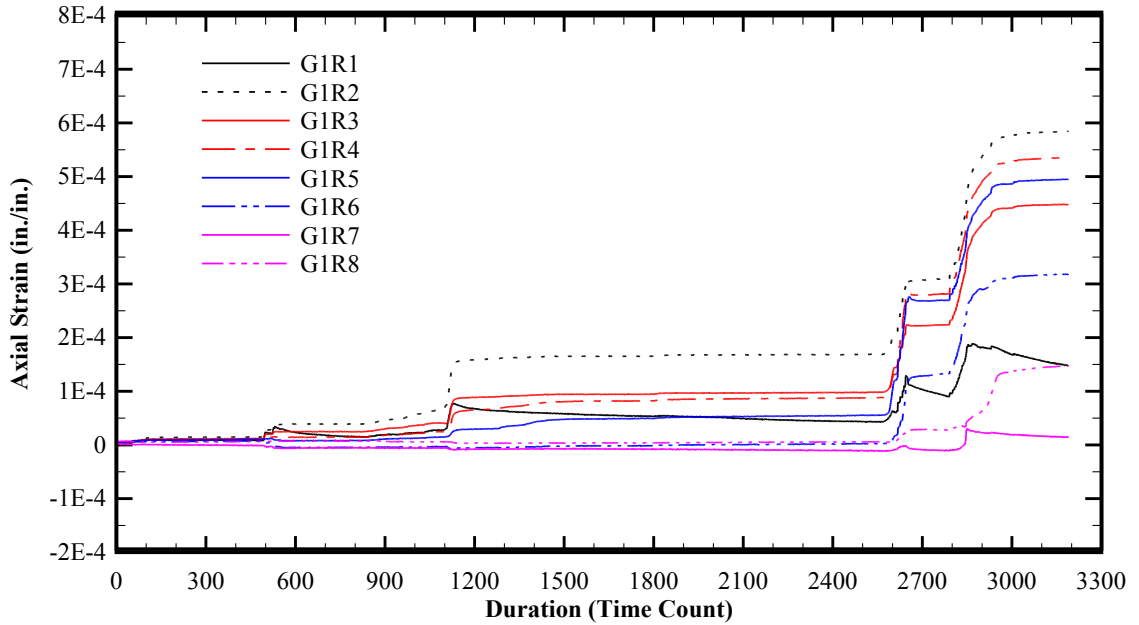


Figure 6-33: Girder No.1 (G93C) R1 thru R8 axial strain data at the end zone reinforcing bars.

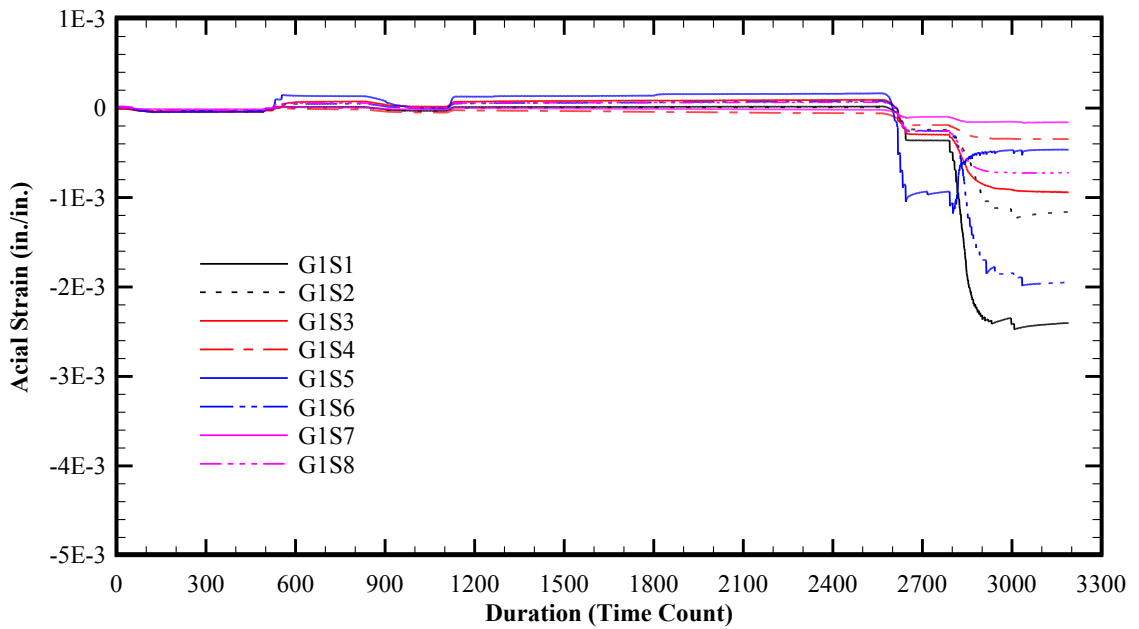


Figure 6-34: Girder No.1 (G93C) S1 thru S8 axial strain data at the prestressing strands.



(a)



(b)

Figure 6-35: Hydraulic abutment utilized for release of pretensioned strands: (a) typical anchorage of the draped strands at the abutments, and (b) pressure gage for control of detensioning. Courtesy of Concrete Technology Corporation (CTC, 2010).

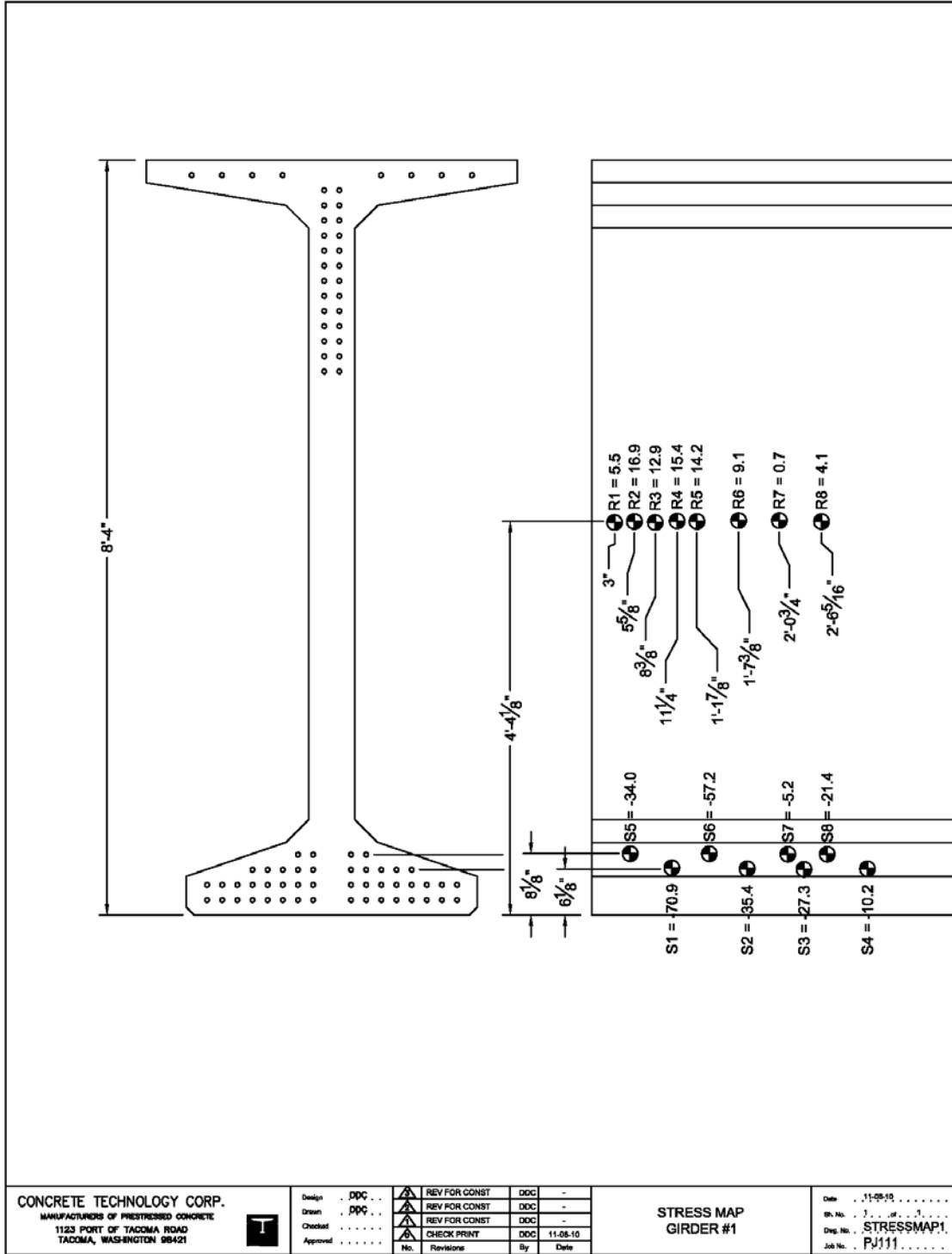


Figure 6-36: Girder No.1 (G93C) summary of stresses at the reinforcing bars and the prestressing strands. Note that the stresses at the prestressing strands indicate the pretensioning loss immediately after the release of pretensioning measured at the dead end. Courtesy of Concrete Technology Corporation (CTC, 2010).

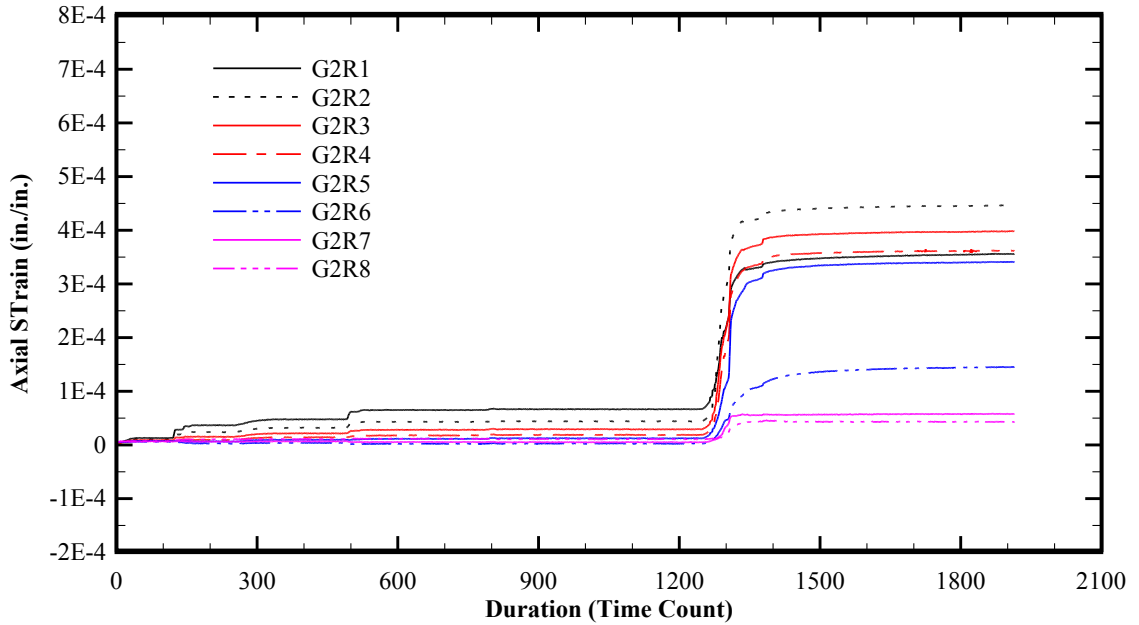


Figure 6-37: Girder No.2 (G94C) R1 thru R8 axial strain data at the end zone reinforcing bars.

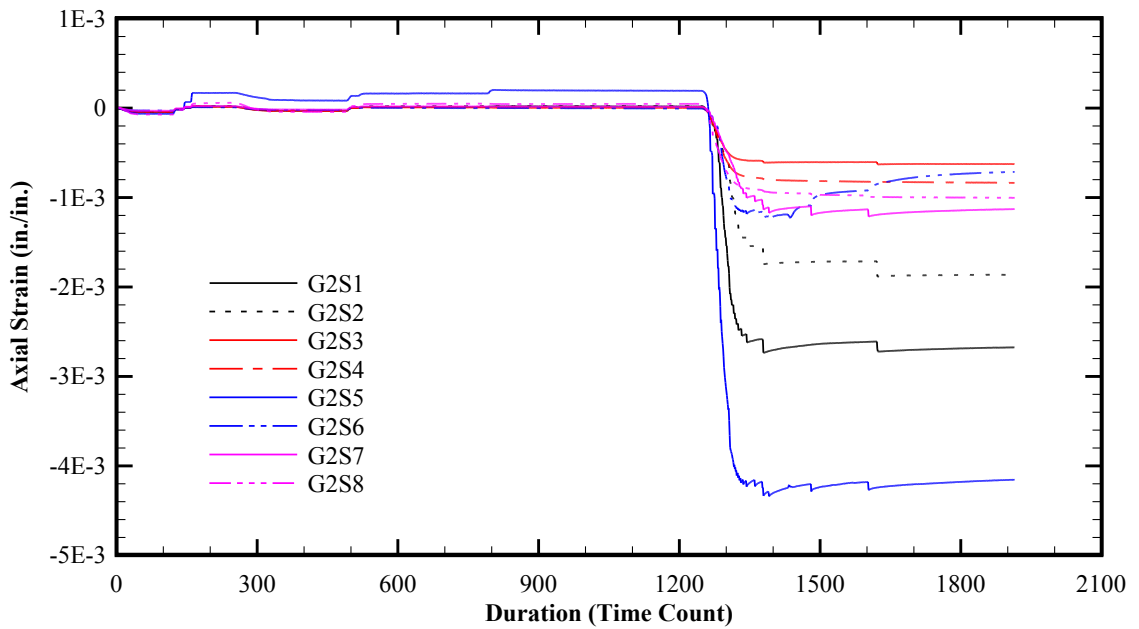


Figure 6-38: Girder No.2 (G94C) S1 thru S8 axial strain data at the prestressing strands.

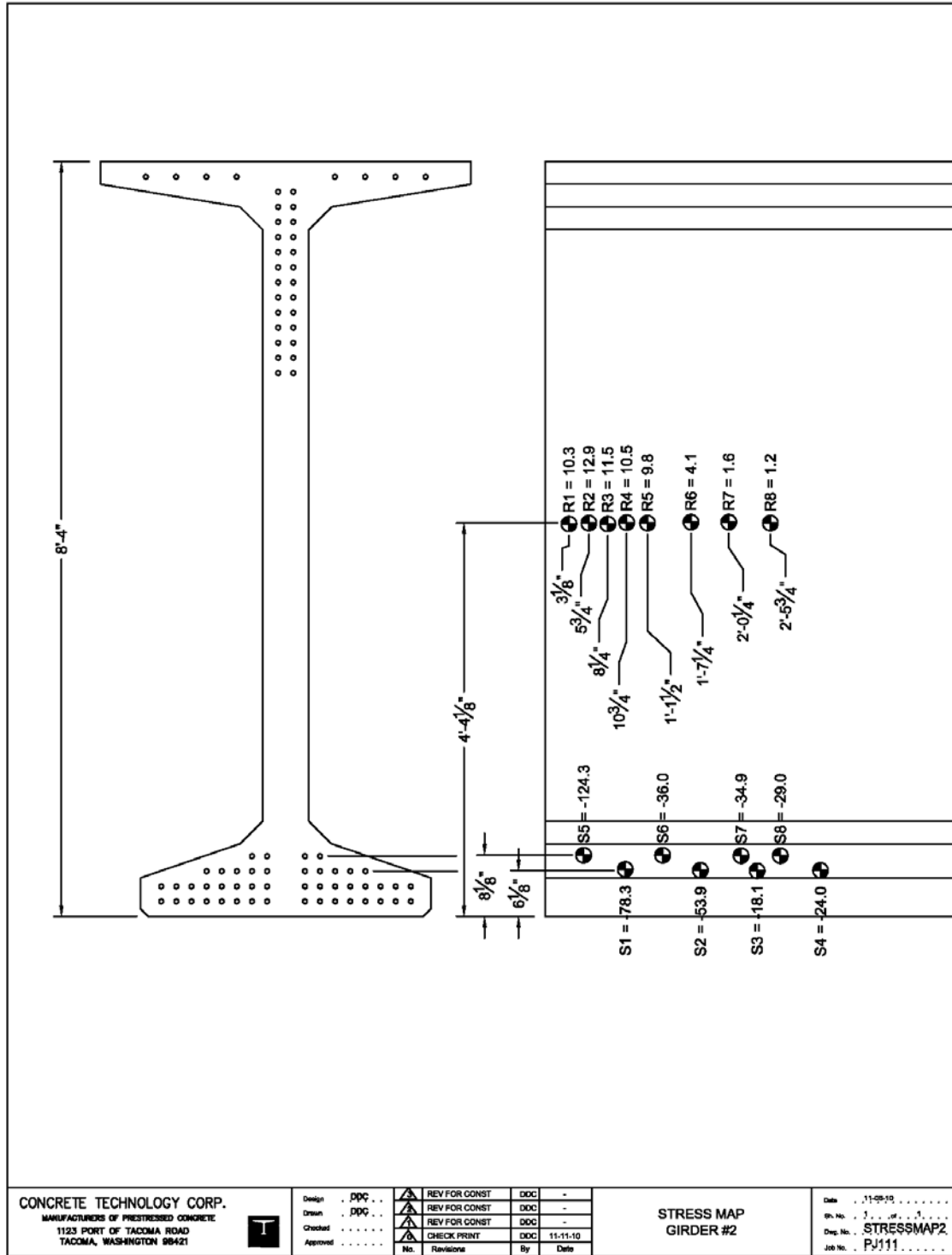


Figure 6-39: Girder No.2 (G94C) summary of stresses at the reinforcing bars and the prestressing strands. Note that the stresses at the prestressing strands indicate the pretensioning loss immediately after the release of prestensioning measured at the dead end. Courtesy of Concrete Technology Corporation (CTC, 2010).

Based on the experimental results obtained from Girders No.1 and No.2, it was decided to change the vertical orientation of the strain gages R1 thru R8 for the rest of the six specimens with the intention of capturing the maximum tensile straining (or stresses) during the process of release of the pretensioned strands. Figure 6-40 thru Figure 6-45 include the strain data and the mapping of the corresponding maximum tensile stresses for Girders No.3 and No.4. In the case of both specimens, the data was collected at the dead end of the member.

The data collection for remaining specimens Girder No. 5 thru No.8 was performed at the live end. Also, consistent with past experience, noticeable cracking along of the interface between the web and bottom flange was observed at Girders No.1 thru No.4. Therefore, it was decided to investigate the straining of the end zone rebar along the interface of web and bottom flange in addition to the zones along the height of the web.

Figure 6-46 thru Figure 6-48 show the strain data and the mapping of the corresponding maximum tensile stresses for Girders No.5. As shown in Figure 6-48, the vertical leg of the end zone rebar near the end face of the member hosted two strain gages R1 and R8 located above the mid height of the web and at the interface of the web and bottom flange, respectively. R8 reported a tensile stress of 19.5 ksi versus 13.7 ksi obtained by R1. This confirmed the discussion above that the maximum end zone cracking may potentially occur along the web and bottom flange rather than higher zones in the web.

In addition, Figure 6-47 indicates that strain gages S1 and S2 at the prestressing strands have potentially malfunctioned, and therefore, the obtained data will be ignored.

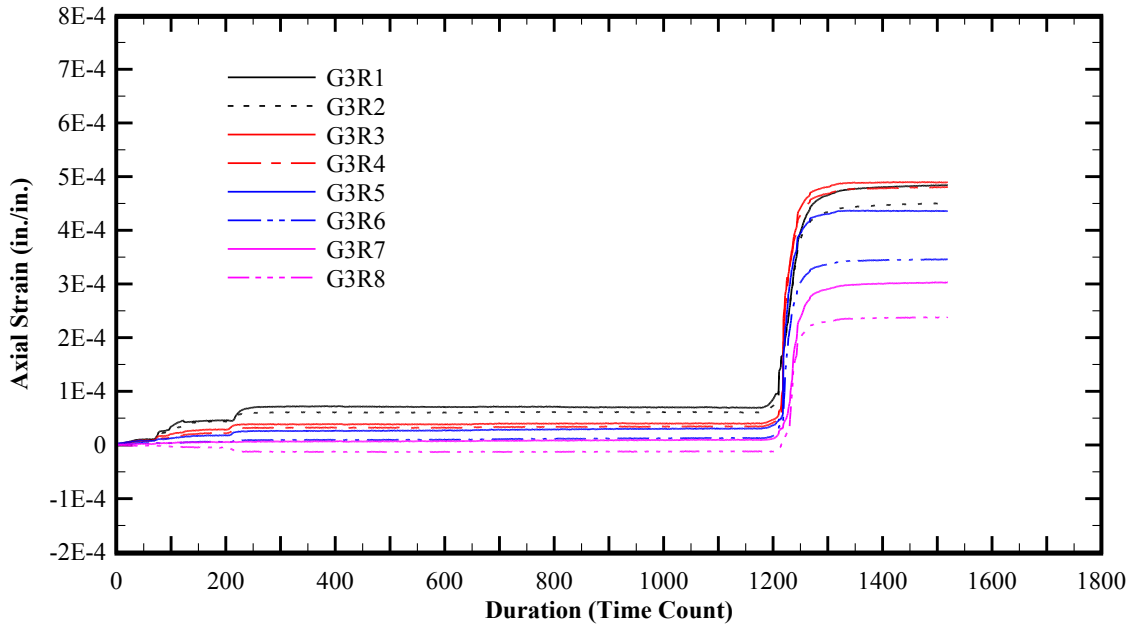


Figure 6-40: Girder No.3 (G94C) R1 thru R8 axial strain data at the end zone reinforcing bars.

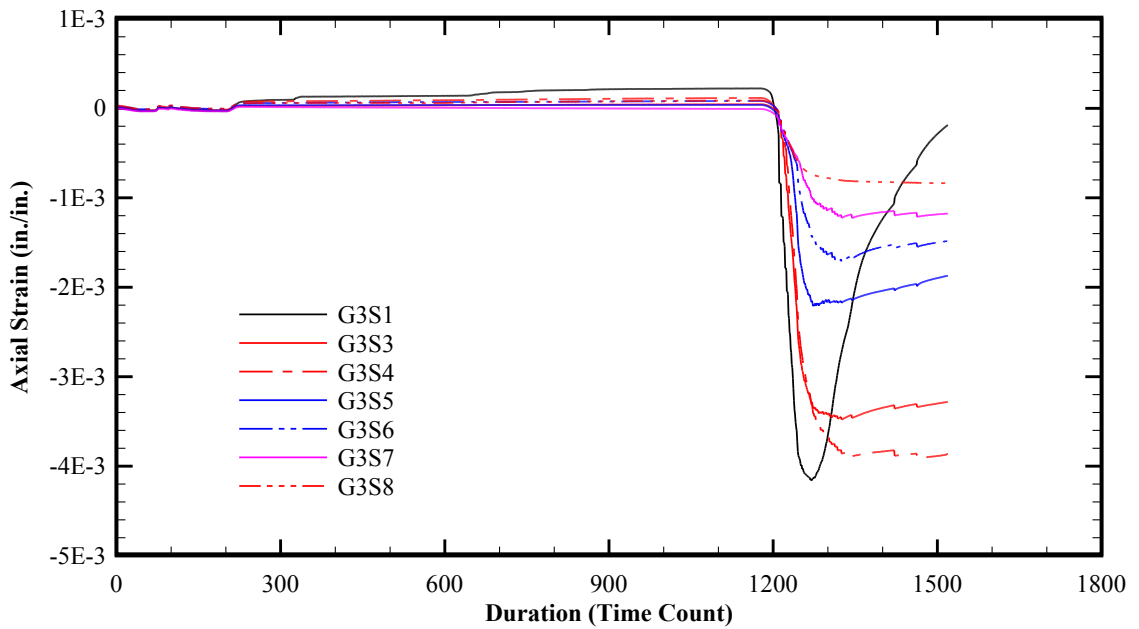


Figure 6-41: Girder No.3 (G94C) S1 thru S8 axial strain data at the prestressing strands.

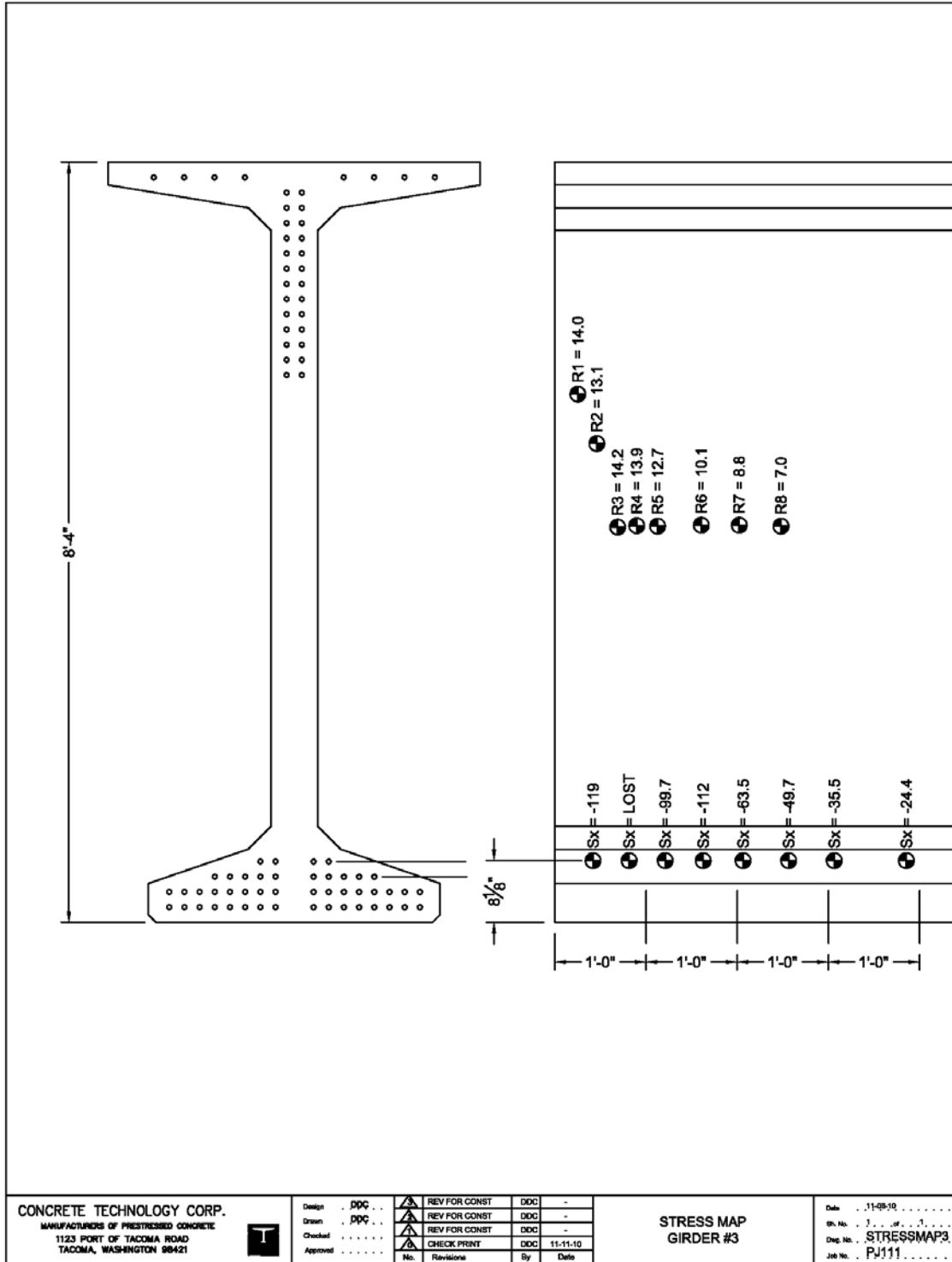


Figure 6-42: Girder No.3 (G94C) summary of stresses at the reinforcing bars and the prestressing strands. Note that the stresses at the prestressing strands indicate the pretensioning loss immediately after the release of pretensioning measured at the dead end. Courtesy of Concrete Technology Corporation (CTC, 2010).

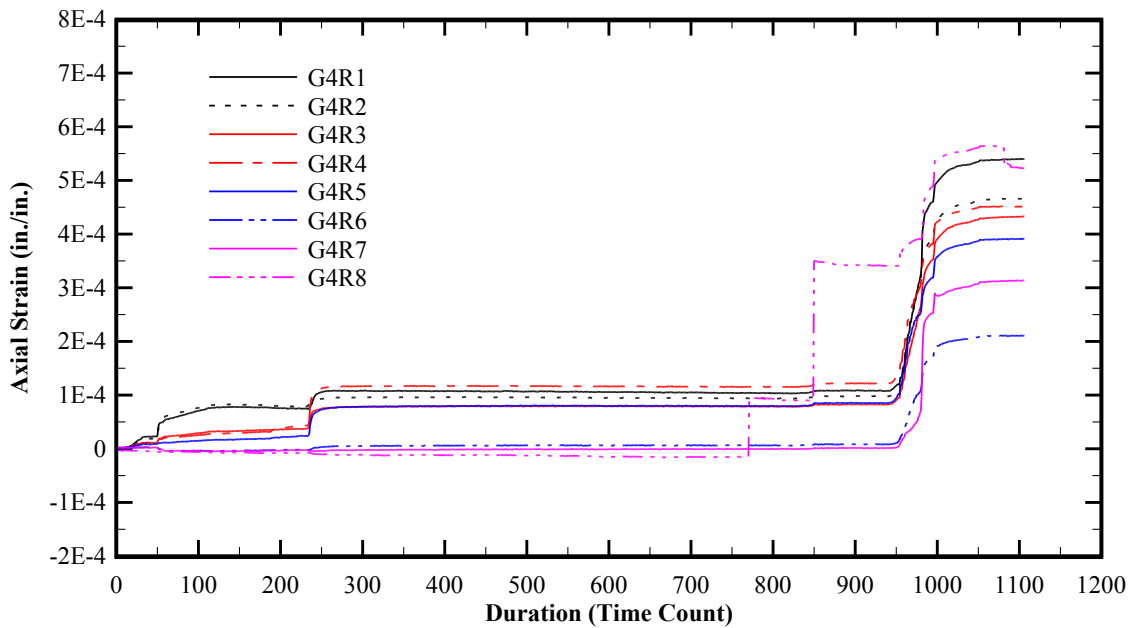


Figure 6-43: Girder No.4 (G94C) R1 thru R8 axial strain data at the end zone reinforcing bars.

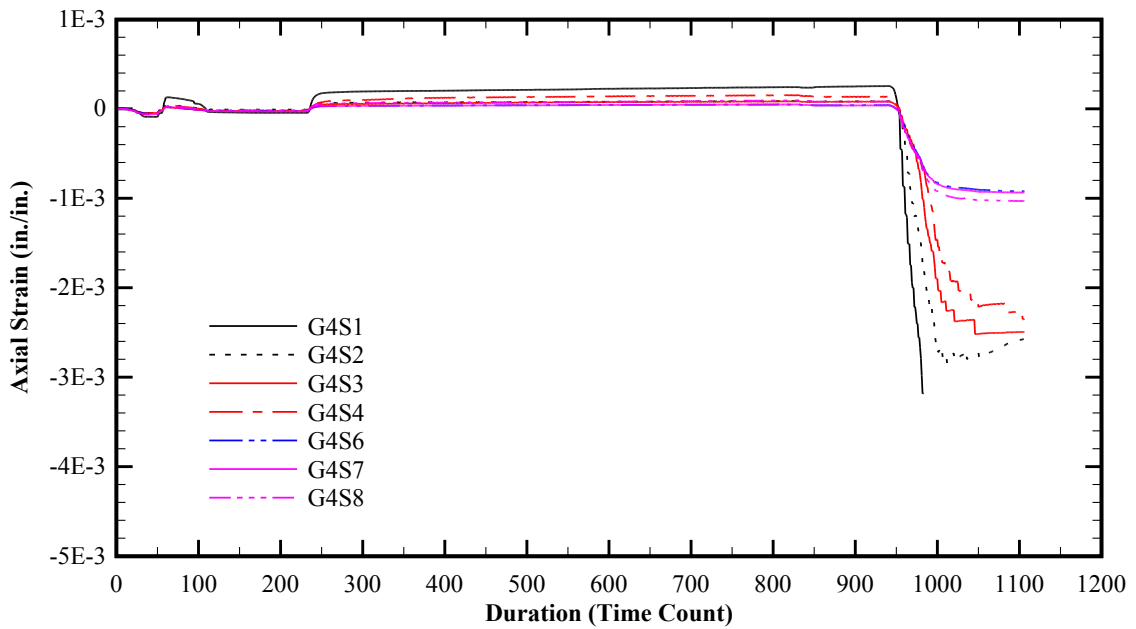


Figure 6-44: Girder No.4 (G94C) S1 thru S8 axial strain data at the prestressing strands.

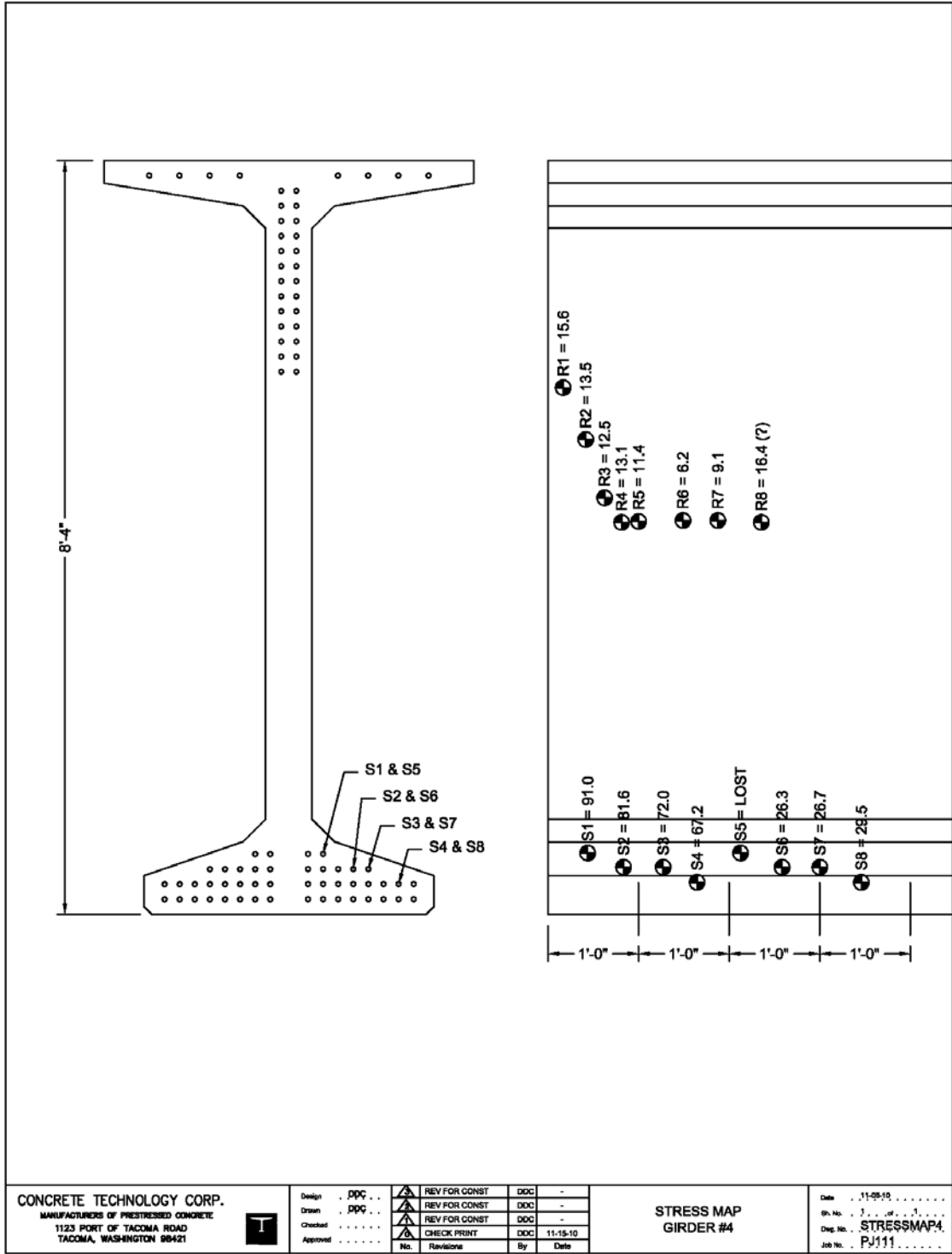


Figure 6-45: Girder No.4 (G94C) summary of stresses at the reinforcing bars and the prestressing strands. Note that the stresses at the prestressing strands indicate the pretensioning loss immediately after the release of pretensioning measured at the dead end. Courtesy of Concrete Technology Corporation (CTC, 2010).

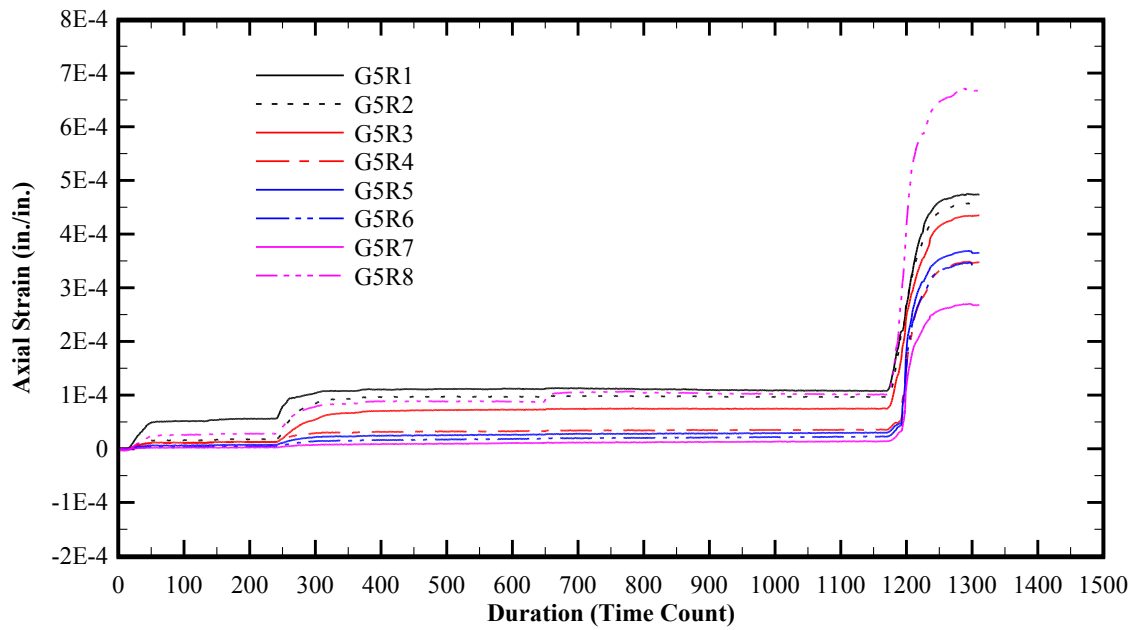


Figure 6-46: Girder No.5 (G94C) R1 thru R8 axial strain data at the end zone reinforcing bars.

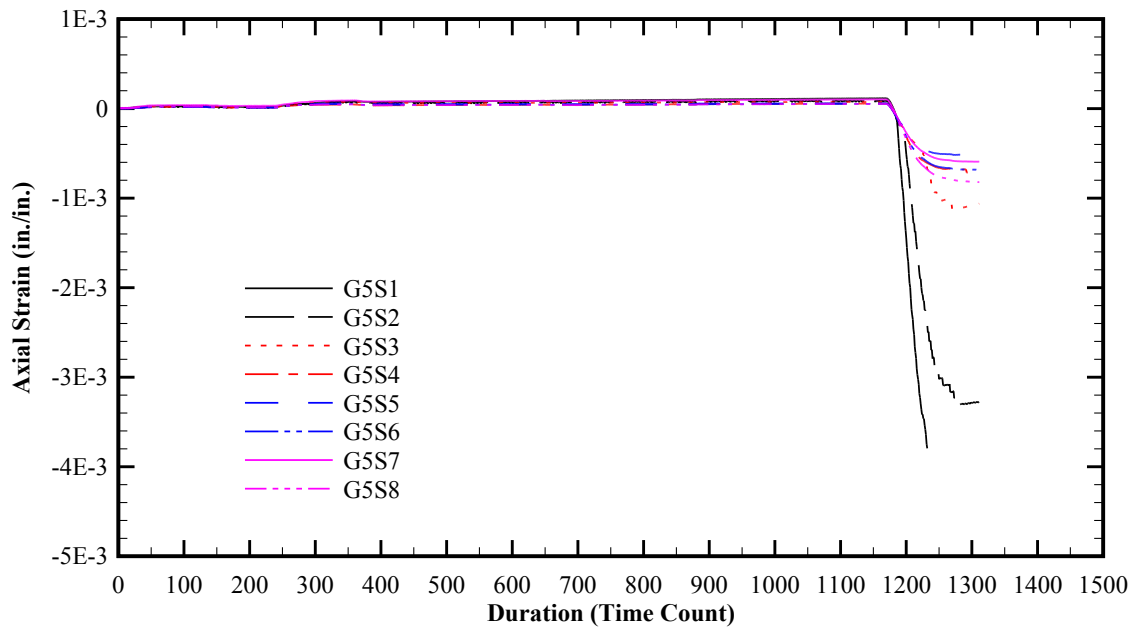


Figure 6-47: Girder No.5 (G94C) S1 thru S8 axial strain data at the prestressing strands.

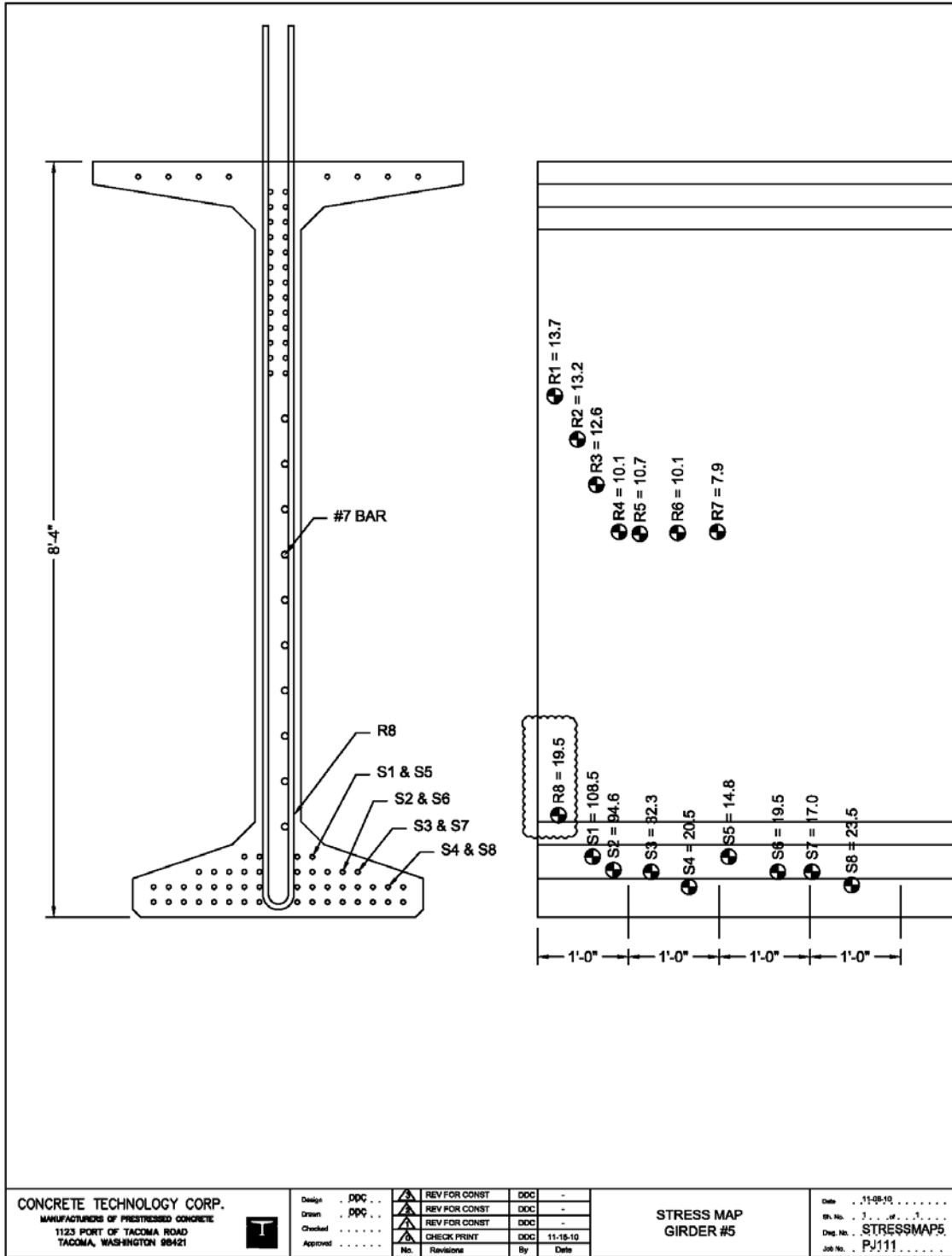


Figure 6-48: Girder No.5 (G94C) summary of stresses at the reinforcing bars and the prestressing strands. Note that the stresses at the prestressing strands indicate the pretensioning loss immediately after the release of pretensioning measured at the live end. Courtesy of Concrete Technology Corporation (CTC, 2010).

Based on the results of Girder No.5, the strain gages S1 thru S4 were installed on the first four end zone bars of Girders No.6 and No.7 along the interface of web and bottom flange. In the case of Girder No.6, the remaining strain gages S5 thru S8 were installed on the prestressing strands. Figure 6-49 thru Figure 6-51 show the strain data and the mapping of the corresponding maximum tensile stresses for Girder No.6. Strain gages S1 and S2 reported maximum tensile stresses of 37.7 ksi and 30.6 ksi, respectively, much larger than previous observations at Girders No.1 thru No.4. Also, it appears that strain gages S3 and S4 have malfunctioned based on the very minimal straining of the rebar hosting the corresponding gages. Similarly, Figure 6-50 indicates that strain gages S6 and S8 at the prestressing strands have possibly malfunctioned and therefore, the corresponding data will be ignored.

Girder No.7 was instrumented similar to Girder No.6 with the exception that strain gages S5 thru S8 were installed at four random No.3 ties instead of the prestressing strands, extending in between the vertical legs of the end zone rebar at various vertical orientations. Figure 6-52 thru Figure 6-54 show the strain data and the mapping of the corresponding maximum tensile stresses for Girder No.7. All sixteen strain gages survived during the release of the pretensioned strands. Similar to Girder No.6, strain gages S1 thru S4 indicate larger tensile stresses (maximum tensile stress of 25.7 ksi at strain gage S1) strain gage at the interface between web and bottom flange in comparison with the data reported by strain gages R1 thru R8 installed at the higher locations along the web height (maximum tensile stress of 12.7 ksi at strain gage R3). In addition, strain gages S5 thru S8 report negligible straining of the random No.3 tie bars with maximum tensile stress of 1.3 ksi.

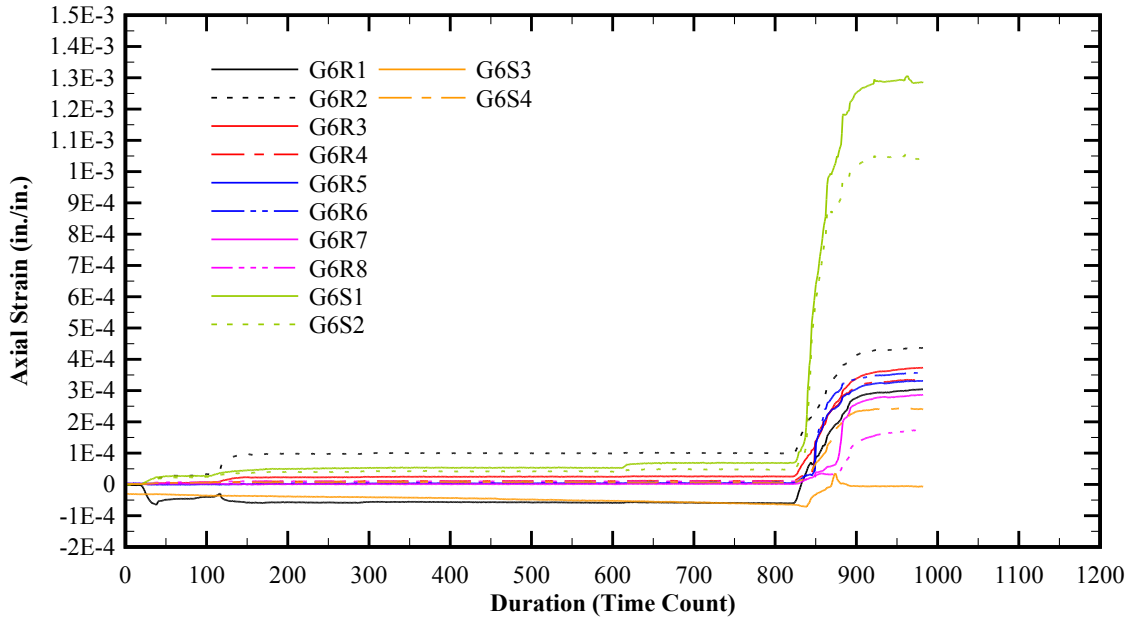


Figure 6-49: Girder No.6 (G94C) R1 thru R8 and S1 thru S4 axial strain data at the end zone reinforcing bars.

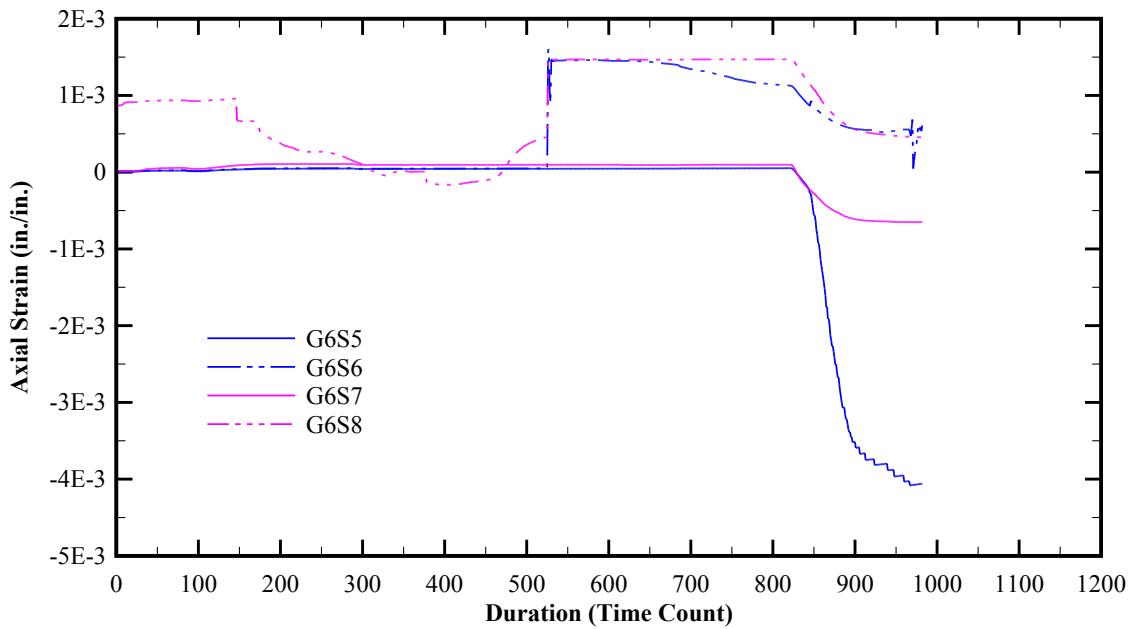


Figure 6-50: Girder No.6 (G94C) S5 thru S8 axial strain data at the prestressing strands.

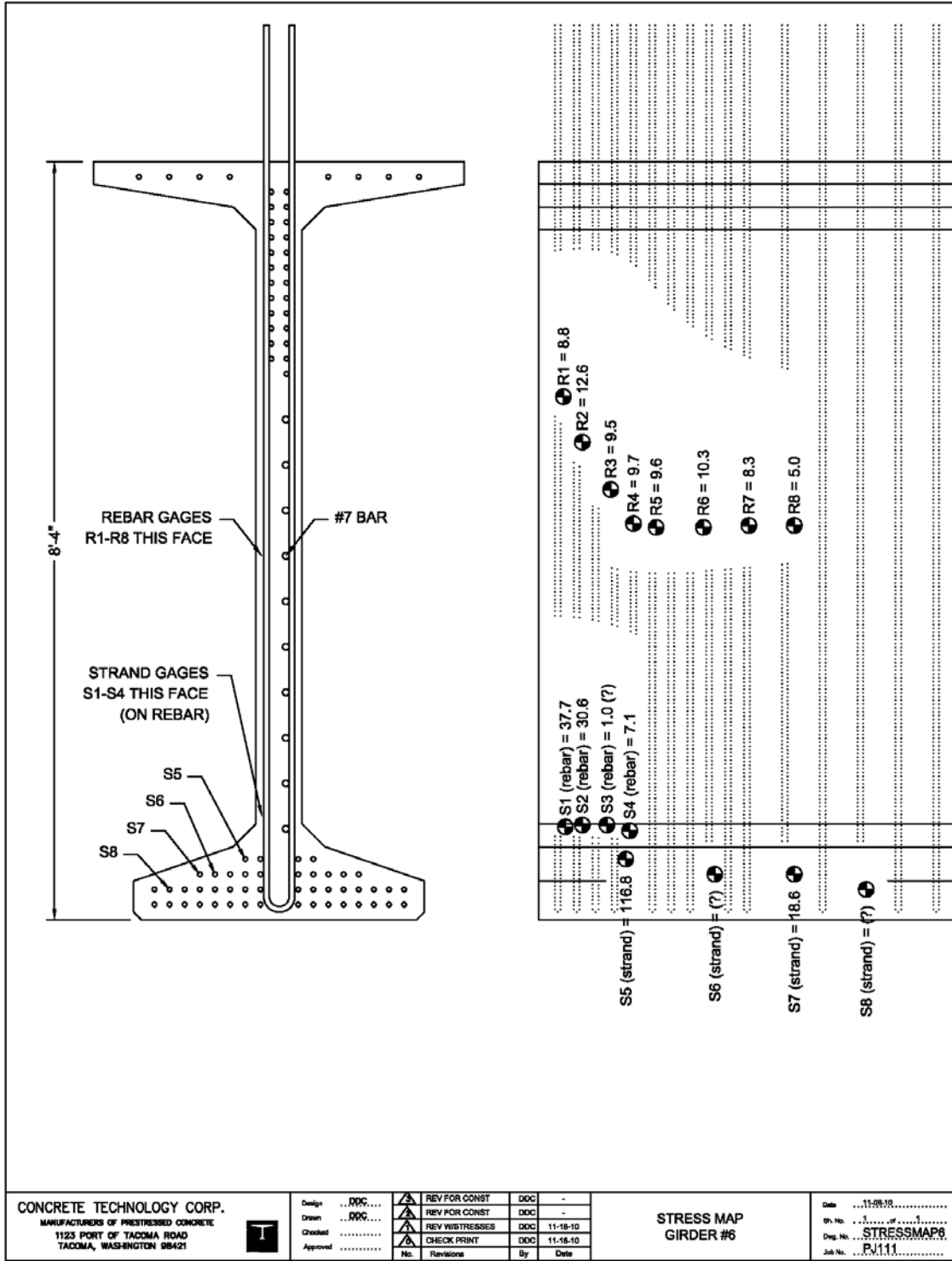


Figure 6-51: Girder No.6 (G94C) summary of stresses at the reinforcing bars and the prestressing strands. Note that the stresses at the prestressing strands indicate the pretensioning loss immediately after the release of pretensioning measured at the live end. Courtesy of Concrete Technology Corporation (CTC, 2010).

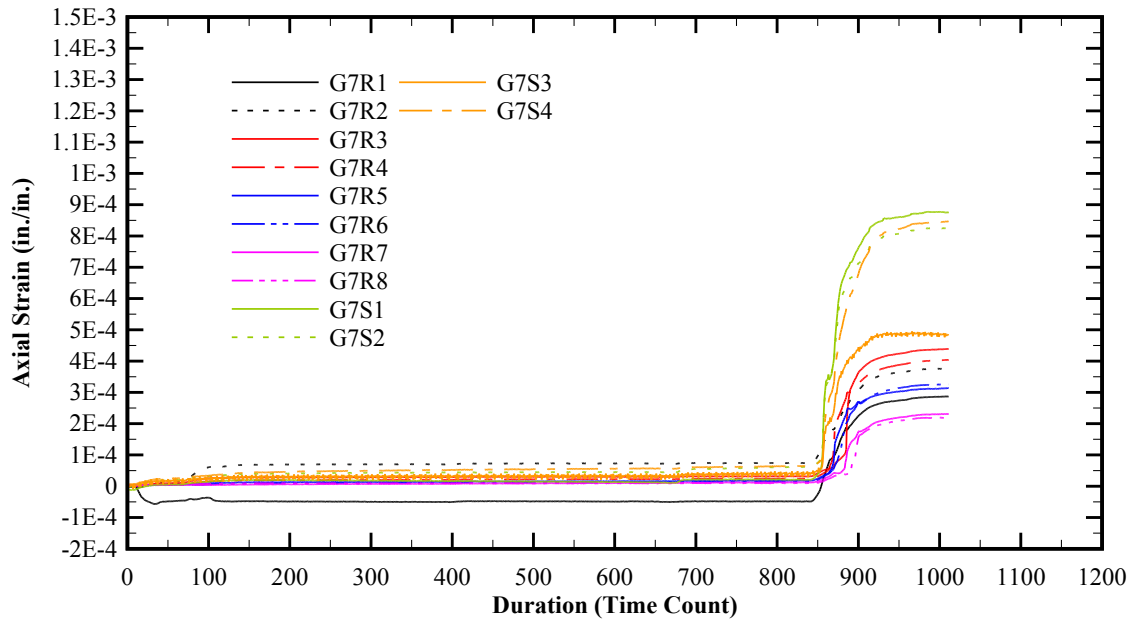


Figure 6-52: Girder No.7 (G94C) R1 thru R8 and S1 thru S4 axial strain data at the end zone reinforcing bars.

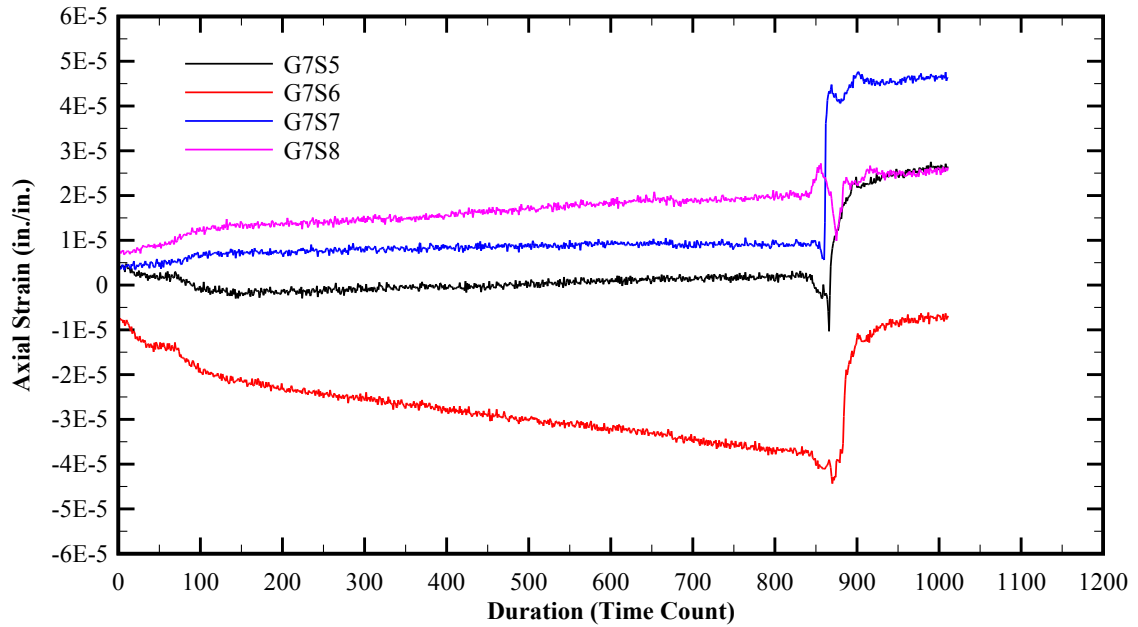


Figure 6-53: Girder No.7 (G94C) S5 thru S8 axial strain data at No.3 tie bars.

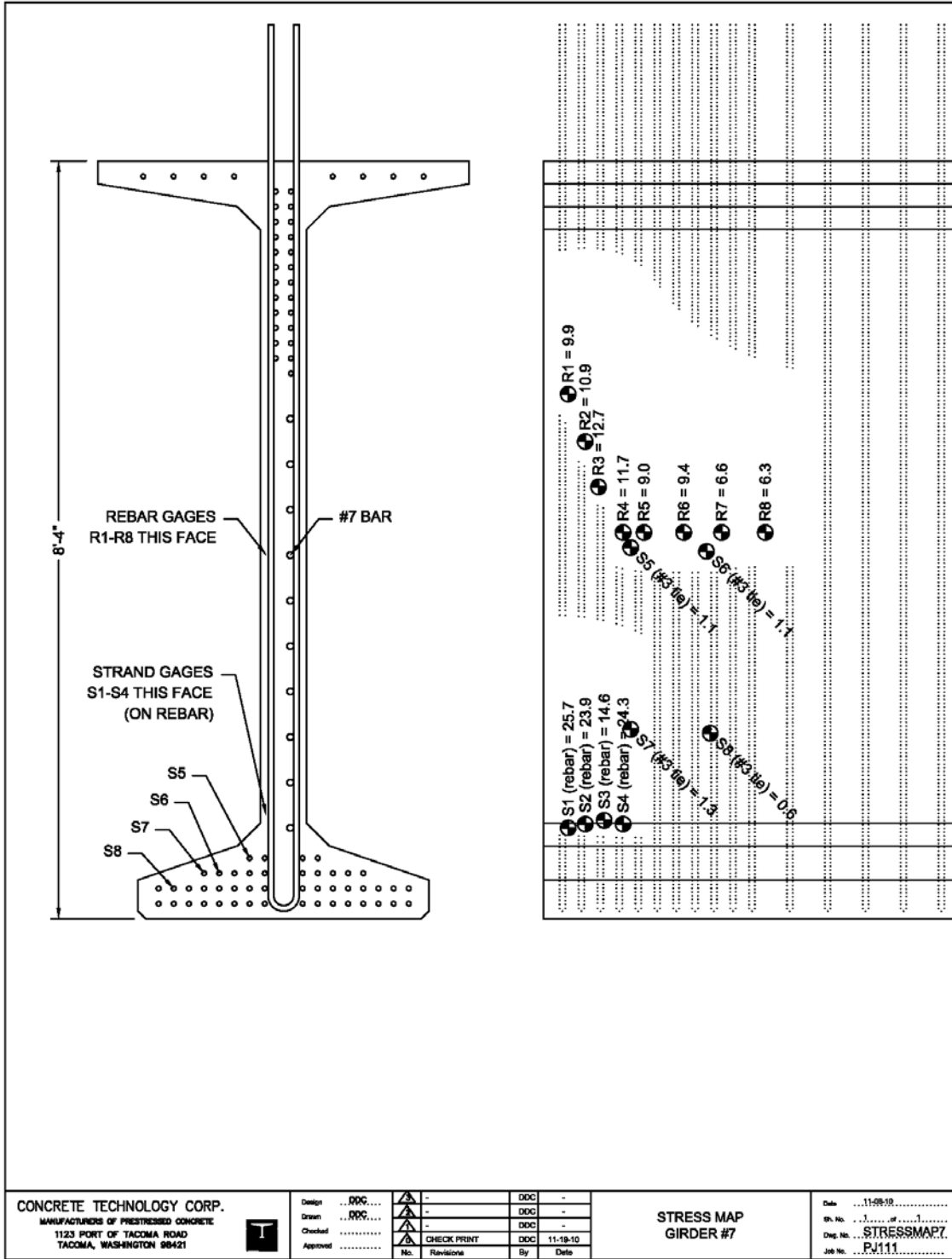


Figure 6-54: Girder No.7 (G94C) summary of stresses at the reinforcing bars and the prestressing strands. Note that the stresses at the prestressing strands indicate the pretensioning loss immediately after the release of pretensioning measured at the live end. Courtesy of Concrete Technology Corporation (CTC, 2010).

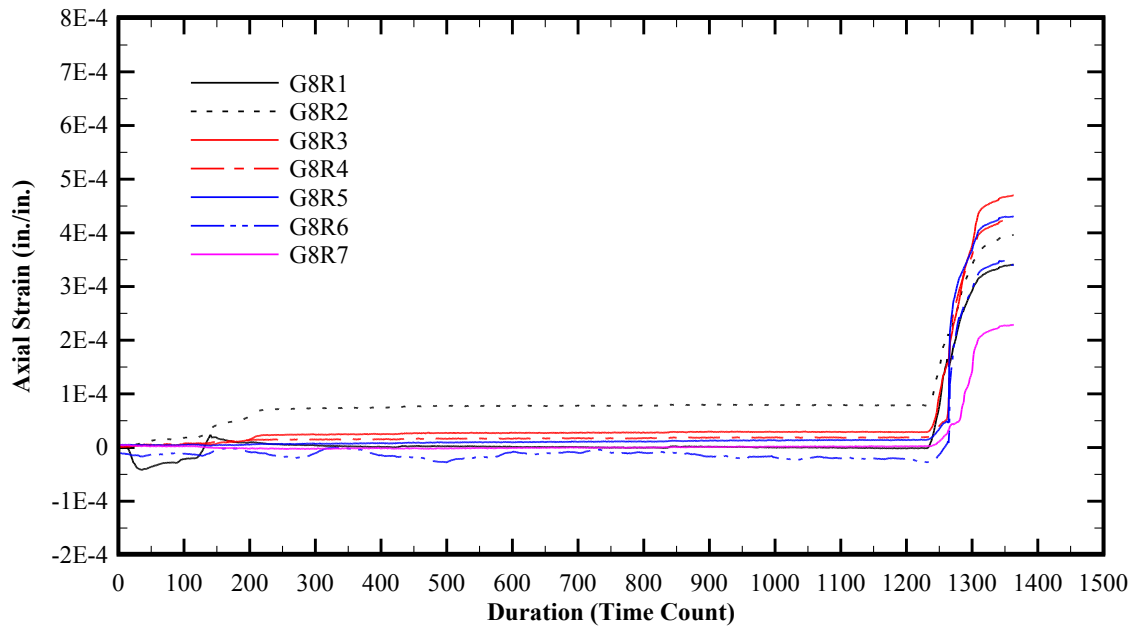


Figure 6-55: Girder No.8 (G95C) R1 thru R7 axial strain data at the end zone reinforcing bars.

As indicated by Figure 6-55 and Figure 6-56, strain gages R8 and S1 thru S8 did not survive during the process of detensioning of the prestressed strands and therefore, no dependable data could be obtained from the corresponding gages. The trend and magnitude of the tensile strains/stresses reported by the rest of the strain gages R1 thru R7 are similar to those observed at the previous specimens.

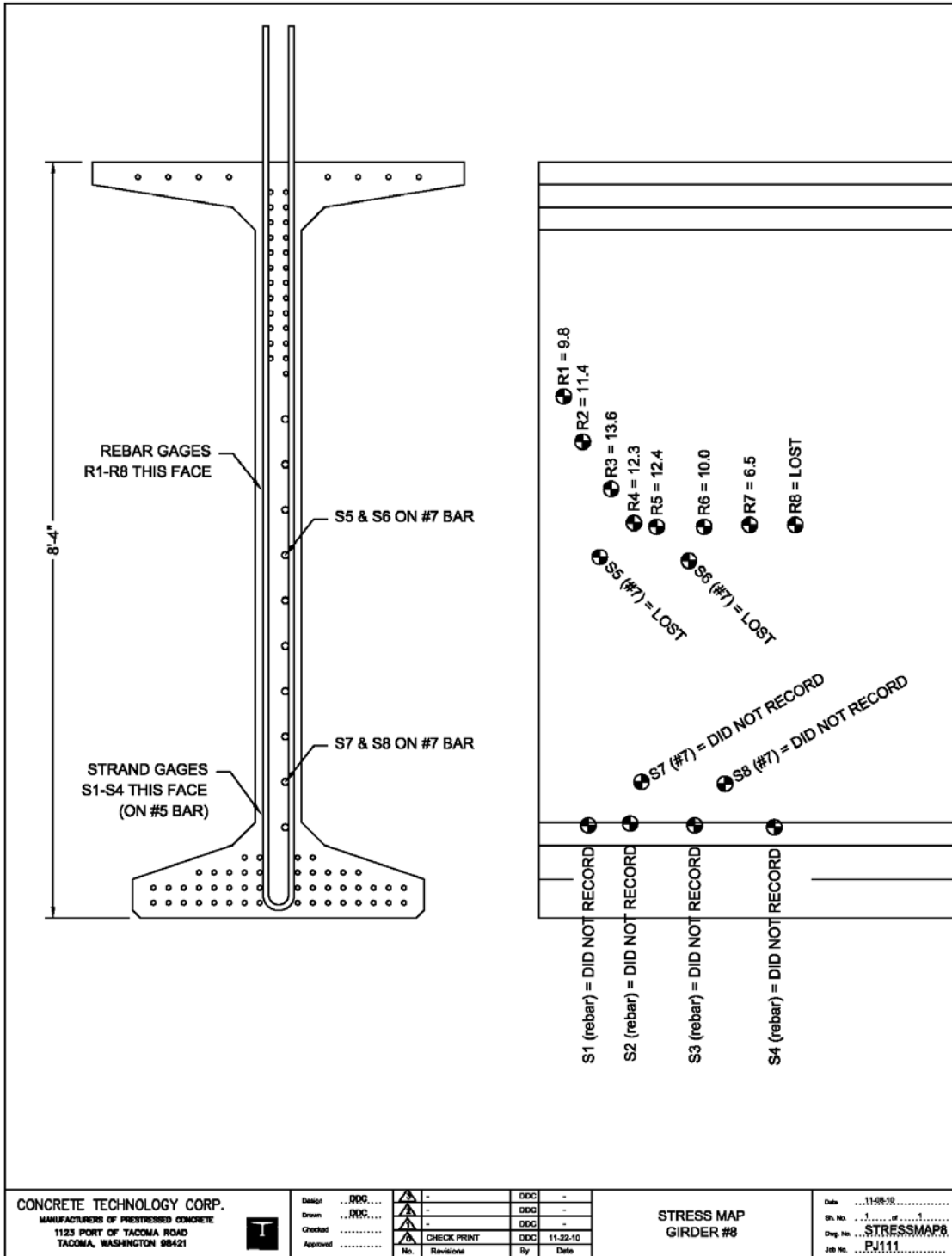


Figure 6-56: Girder No.8 (G95C) summary of stresses at the reinforcing bars. Note that the strain gages S1 thru S2 did report any data due to malfunctioning. Courtesy of Concrete Technology Corporation (CTC, 2010).

6.3.5. Experimental Observations

6.3.5.1. End Zone Cracking

As implied by the magnitude of the tensile stresses in the reinforcing bars, the end zone of all eight specimens experienced cracking during the process of pretensioning as outlined in the previous section.

Figure 6-57 (a) shows live end zone of Specimen No.1 hosting a typical network of spalling and bursting-splitting cracks in the web and at the web-bottom flange interface, respectively. Figure 6-57 (b) shows the close-up of a typical spalling crack in dead end of Specimen No.1 within the upper portion of the web. The spalling cracks have the tendency of starting at mid to upper portions of the web, extending downwards at approximately 45° . The cracks which are developed within the lower portion of the web have a tendency flattening as getting closer to the bottom flange.

Figure 6-57 (c) shows typical bursting-splitting cracks in the vicinity of the web-bottom flange interface of Specimen No.6. The observation is made at the dead end of the girder while the dead end shows similar trend of cracking. The corresponding cracks are generally observed to be initiated near the end face extending approximately 2 ft towards the mid-span of the member. Additionally, Figure 6-57 (c) the location of the cracks in relation to the strain gages installed at the vertical legs of the reinforcing bars within the cracked zone. In reference to Figure 6-51, maximum tensile stress of 37.7 ksi was recorded at the end zone bar placed 2 in. from the member end face.



(a)



(b)



(c)

Figure 6-57: Typical end zone cracks: (a) Specimen No.1 end zone (live end) showing spalling and bursting-splitting cracks at web and web-bottom flange interface, respectively, (b) close-up of a typical spalling crack at Specimen No.1 web (dead end), and (c) typical bursting and splitting cracks at Specimen No.6 web-bottom flange (live end) relative to the location of the strain gages shown in red dots.

6.3.5.2. Transfer Length

As previously discussed, Specimens No.1 thru 7 were instrumented with strain gages in order to measure the actual transfer length immediately after the release of prestressed strands. The corresponding strain gages were installed at four locations on selected straight strands in the bottom flange.

Appendix J includes the summary and post-processing of the data obtained during the process of pretensioning release as outlined in the previous section. Figure 6-58 shows the parabolic path of the transfer obtained from Specimens No.1 through No.7. The transfer length has been optimized over the magnitude of pretensioning stresses in order to represent a general trend. The linearized transfer length prescribed by AASHTO LRFD is also shown for the purpose of comparison.

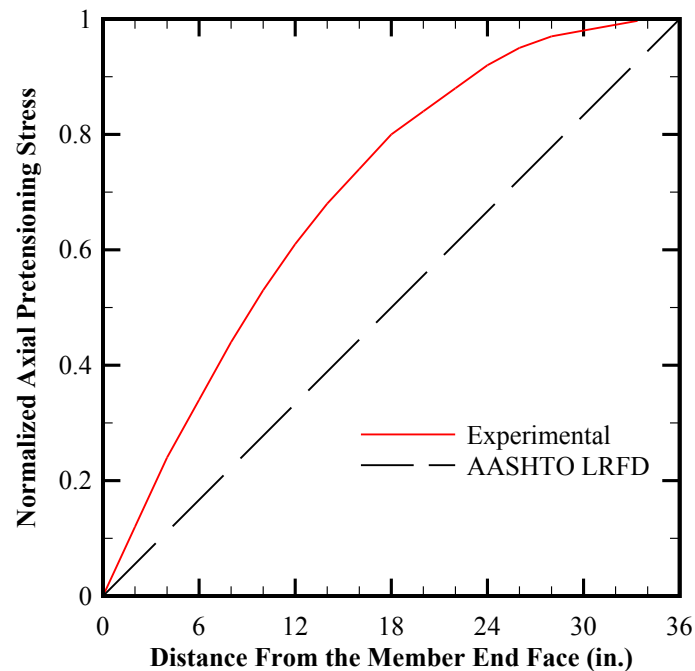


Figure 6-58: Transfer length normalized over the magnitude of pretensioning stresses.

Equation (6.2) represents a parabola that has been best-fit through the obtained data:

$$(f_{pi})_{normalized} = (6E-06)x^3 - (1.2E-03)x^2 + (6.21E-02)x \quad (6.2)$$

Table 6- 5 shows the normalized distribution of axial prestressing stress in the strands along the longitudinal axis of the member measured from the end face. The results are based on the best-fit parabolic path immediately after the release of pretensioning. It is observed that 34% of the pretensioning force is transferred to concrete body at the distance 6 in. from the member ends. Subsequently, 80% and finally 100% of the transfer occur at 18 in. and 36 in. from the member ends, respectively.

Table 6- 5: Normalized transfer length.

x (in.)	% $(f_{pi})_{normalized}$
0	0
6	34%
12	61%
18	80%
24	92%
30	98%
36	100%

The following observations are made based on the experimental results:

1. The transfer length reaches linearization at a distance approximately 30 to 36 in. from the member end face. This is equivalent to:

$$L_t = (50 \sim 60)d_p \quad (6.3)$$

Equation (6.3) indicates that the actual nominal transfer length obtained from the seven specimens is approximately equal to the theoretical transfer length recommended by AASHTO LRFD defined as $60 d_p$.

2. The linearization of transfer length as recommended by AASHTO LRFD and widely assumed in current practice may result in significant under-estimation of the tensile stresses developed in the member end zone immediately after the release of pretensioning.

6.3.5.3. Web Tie Bars

As previously discussed, one of the objectives of this section is to determine the efficiency of the No.3 tie bars located throughout the web. Specimen No.7 included strain gages installed at four No.3 tie bars as shown in Figure 6-59.

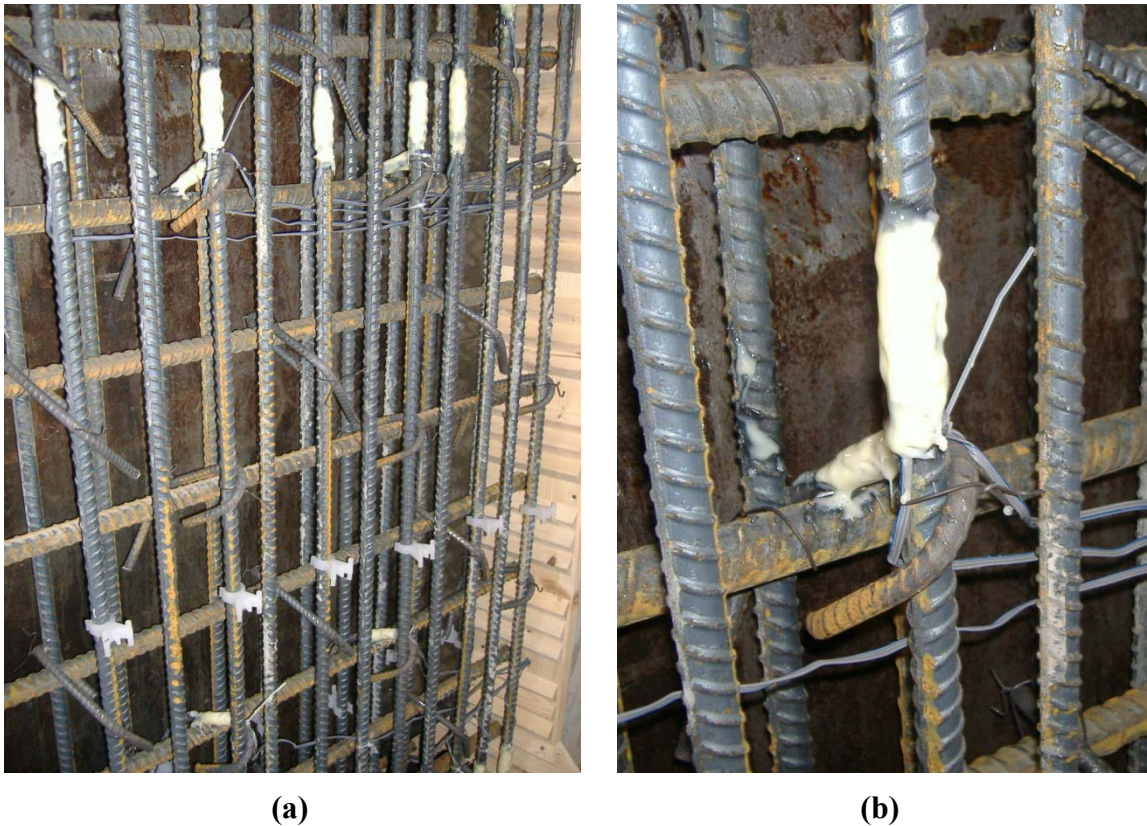


Figure 6-59: Girder No.7 (G94C): (a) web reinforcement cage showing the location of strain gages at the vertical rebar and No.3 web tie bars, and (b) close-up of a typical No.3 tie bar.

In reference to Figure 6-53 and Figure 6-54, the axial tensile stresses observed at the web tie bars vary from minimum of 0.6 ksi to maximum of 1.3 ksi. Therefore, the experimental data indicate that the web tie bars experience negligible axial straining immediately after the release of prestressed strands.

6.4. Analytical Solutions

6.4.1. Closed-Form Solutions

6.4.1.1. Gregly-Sozen Method

In reference to the discussion of Section 5.2.2.1, the following includes the analysis of the end zone of the BWF100 in accordance with Gregly-Sozen Method. As previously discussed, the corresponding procedure is based on a linear-elastic approach to analyze the end zone of the prestressed (pre- or post-tensioned) members assumed to be cracked at a certain elevation along the height of the member. Table 6-6 includes the summary of the internal moments due to the self weight of the each specimen and the pretensioning forces imposed by the straight, draped and temporary strands immediately after the release. The internal moments reflect the simply-supported conditions based on the assumption that the girders were bunched at 8-ft from both girder ends during the release in accordance to Figure 6-8. Please note that L_t represents the theoretical transfer length; M_{DL} indicates the internal moments due to the self-weight of the members; M_{pi} reflects the internal moments due to pretensioning, and e_p indicates the eccentricity of the strands in relation to the concrete body.

Accordingly, Table 6-7 includes the summary of the stresses at the extreme top and bottom fibers of the specimens immediately after the release of pretensioned strands. It is observed that the extreme top and bottom fiber stresses remain in state of longitudinal compression along the entire span of the specimens immediately after the release of the

strands. The results include the effects of losses due to strands relaxation and member elastic shortening.

Figure 6-60 shows the linear distribution of the longitudinal stresses along the height of the member at the theoretical transfer length $L_t = 36$ in. from the end face immediately after the release of pretensioning. The corresponding stress diagram is based on the following assumptions:

- i. Stresses reach linearization near the theoretical transfer length,
- ii. Specimens are bunched at 8-0ft from both end faces in accordance with Figure 6-8, and
- iii. Stresses are affected by the applicable losses at the release including relaxation of strands and elastic shortening of the concrete body.

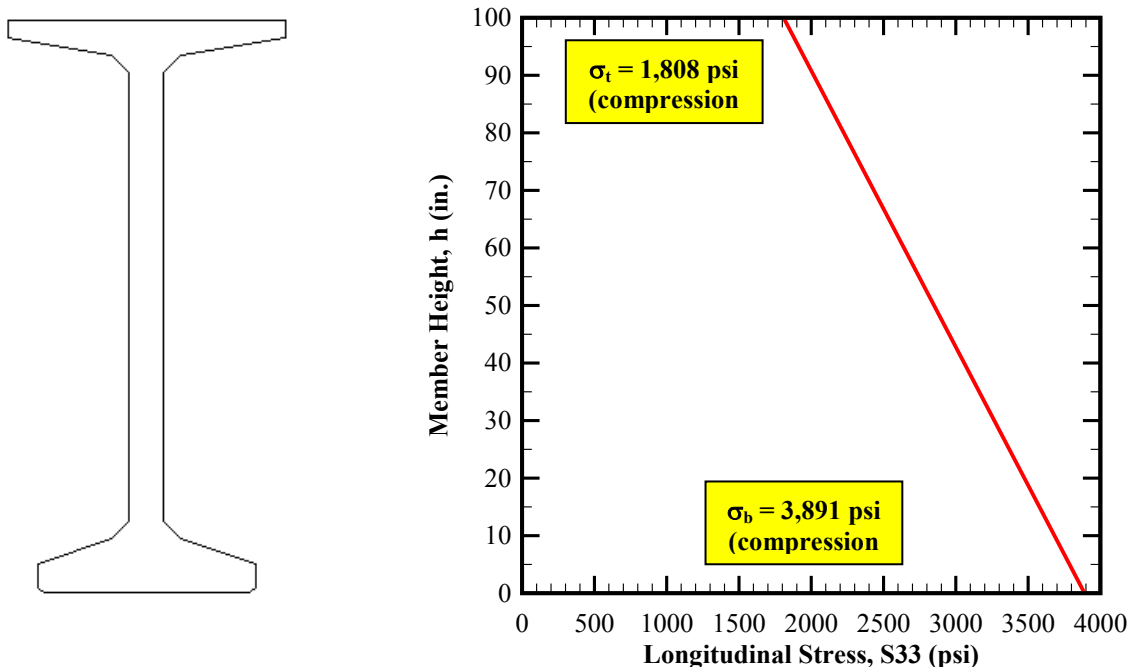


Figure 6-60: Distribution of longitudinal stresses (S_{33}) along the height of the BWF100 specimens at the theoretical transfer length. Note that positive stresses denote state of compression.

Table 6-6: Summary of the internal moments for BWF100 specimens immediately after the release of pretensioning based on the assumption that the specimens are bunched at 8-ft from both ends during the release. The results include the effects of strands relaxation and member elastic shortening.

x (ft)	M _{DL} (ft-kips)	e _{p, straight} (in.)	e _{p, draped} (in.)	M _{pi, straight} (ft-kips)	M _{pi, draped} (ft-kips)	M _{pi} (ft-kips)	Location
0.0000	0.0	44.1425	-36.2506	0.0	0.0	0.0	End face
1.0417	-5.2	44.1425	-35.2423	1870.6	-1009.6	861.0	h/8
2.0833	-10.3	44.1425	-34.2340	3741.1	-1961.4	1779.7	h/4
3.0000	-14.9	44.1425	-33.3466	5387.2	-2751.3	2636.0	L _t
4.1667	-20.7	44.1425	-32.2173	5387.2	-2658.1	2729.1	h/2
8.3333	-0.6	44.1425	-28.1841	5387.2	-2325.3	3061.9	h
82.08333	5256.0	44.1425	43.2044	5387.2	3564.6	8951.8	Draped Point
102.6042	5517.4	44.1425	43.2044	5387.2	3564.6	8951.8	Mid-Span

Table 6-7: Summary of the extreme top and bottom fiber stresses immediately after the release of pretensioning based on the assumption that the specimens are bunched at 8-ft from both ends during the release. The results include the effects of strands relaxation and member elastic shortening.

Location	Extreme Bottom Fiber				Extreme Top Fiber			
	P _i /A (psi)	M _{pi} /S _b (psi)	M _{DL} /S _b (psi)	σ _b (psi)	P _i /A (psi)	M _{pi} /S _t (psi)	M _{DL} /S _t (psi)	σ _t (psi)
End face	0	0	0	0	0	0	0	0
h/8	-1002	-326	-2	-1331	-1002	350	2	-650
h/4	-2005	-674	-4	-2683	-2005	724	4	-1277
L _t	-2887	-999	-6	-3891	-2887	1072	6	-1808
h/2	-2887	-1034	-8	-3929	-2887	1110	8	-1768
h	-2887	-1160	0	-4047	-2887	1246	0	-1641
Draped Point	-2887	-3392	1992	-4287	-2887	3641	-2138	-1383
Mid-Span	-2887	-3392	2091	-4188	-2887	3641	-2244	-1490

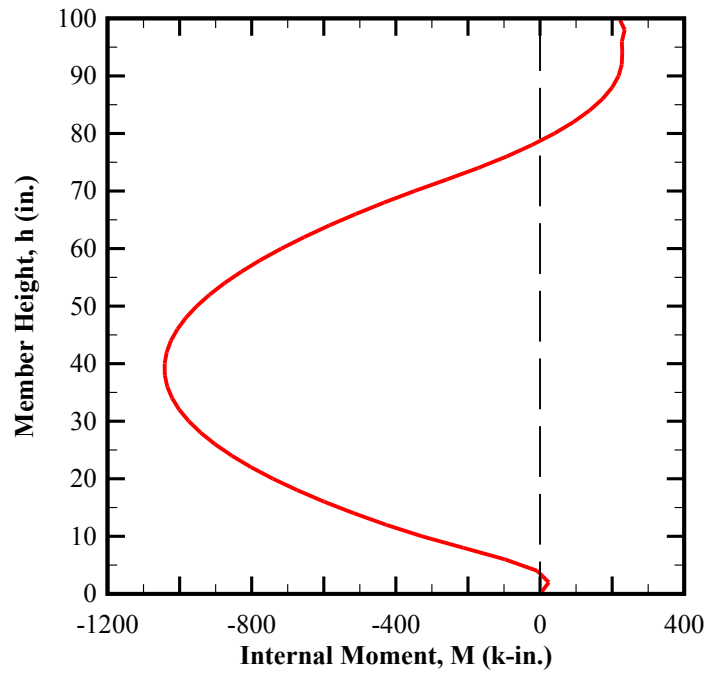


Figure 6-61: Distribution of internal moments along the height of the member at the theoretical transfer length based on Gregly-Sozen method.

Figure 6-61 shows the distribution of the internal moments along the height of the member at the theoretical transfer length in accordance with Gregly-Sozen method.

Appendix I includes the supporting details of the closed-form analysis.

Based on the Gregly-Sozen method, the maximum moment at the transfer length immediately after the release of pretensioning is as follows:

$$M_{\max} = 1,042 \text{ kip-ft} \quad @ \quad h_{\max} = 42.00 \text{ in.} \quad (6.4)$$

In reference to Figure 5-11 and based on Figure 6-62, the location of the vertical tension and compression components of the internal moment is assumed as such that the moment arm, L , is estimated as

$$L = h - \frac{h}{8} = 87.50 \text{ i} \quad (6.5)$$

Therefore,

$$T_{\max} = \frac{M_{\max}}{L} = 142.8 \text{ kips} = 4.6\% P_i \quad (6.6)$$

Note that in accordance with AASHTO LRFD, the members shall include end zone reinforcing bars to withstand at least 4% of the total applied pretensioning estimated to be . The comparison of the Gregly-Sozen method with the current AASHTO LRFD specifications indicates that

$$\frac{T_{\max}}{4\% P_i} = 115\% \quad (6.7)$$

In accordance with Figure 6-62, T_2 shall be evenly distributed between the end face of the member and $h/4$ (25 in.). Based on Figure 6-4 through Figure 6-6, the area steel provided within the corresponding zone is

$$A_{EZR} = 6.2 \text{ in.}^2 \quad (6.8)$$

Therefore, based on Gregly-Sozen analysis, the maximum tensile stress in the end zone reinforcing bars is estimated to be

$$f_{EZR,s} = \frac{T_{\max}}{A_{EZR}} = 23.0 \text{ ksi} = 1.15 f_{EZR,allowable} \quad (6.9)$$

6.4.1.2. Strut-and-Tie Approach

In reference to Section 5.2.2.2, the double-tie strut-and-tie model developed by Crispino et. al. will be utilized in order to estimate the vertical tensile force in the end zone of Girders No.1 thru No.8 immediately after the release of prestressed strands.

Similar to Figure 5-12, Figure 6-62 shows the basic properties of the corresponding model where

$$P1 = 1,821.7 \text{ kips} \quad \dots\dots\dots \text{Pretensioning force due to the straight strands (total of 46) after the initial losses due to relaxation of strands and elastic shortening immediately after the release of strands} \quad (6.10)$$

$$P2 = 1,306.9 \text{ kips} \quad \dots\dots\dots \text{Pretensioning force due to the draped (total of 25) and temporary (total of 8) strands after the initial losses due to relaxation of strands and elastic shortening immediately after the release of strands} \quad (6.11)$$

$$h = 100 \text{ in.} \quad \dots\dots\dots \text{Total non-composite height of the member} \quad (6.12)$$

$$y \quad \dots\dots\dots \text{the vertical distance between the resultant force and applied prestress force and } P1 \text{ and } P2 \quad (6.13)$$

It should be noted that $P1$ and $P2$ are based on the initial loss of 10% due to the combined effects of relaxation of the strands and elastic shortening immediately after the release of pretensioning.

Since all Girders No.1 thru No.8 have the same geometric properties and the identical pretensioning composure and magnitude in the bottom flange, one strut-and-tie analysis is deemed sufficient for the analytical purposes of this research.

In accordance with Crispino, The maximum tensile force is then estimated based on Equation (5.11) as follows (Crispino, 2007):

$$T1 = T2 = \frac{8 P1 y}{7 h} \quad (6.14)$$

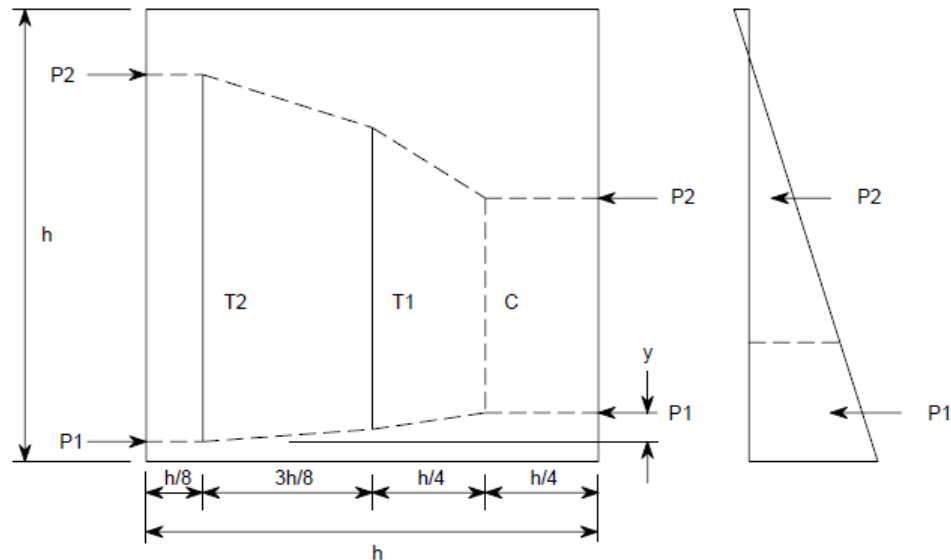


Figure 6-62: The double-tie, strut-and-tie model utilized for end anchorage analysis of Girders No.1 thru No.8. Adapted from (Crispino, Cousins, & Roberts-Wollmann, Anchorage Zone Design for Pretensioned Precast Bulb-T Bridge Girders in Virginia, 2009).

where Equation (6.14) needs to be evaluated in relevance to the parameter y as defined by Equation (6.13). Given the bottom flange of the girders have the following eccentricity relative to the bottom of the bottom flange assumed as vertical datum:

$$e_{p, \text{straight}} = 4.0870 \text{ in.} \quad (6.15)$$

As recommended by Crispino, the loser strut-and-tie model is solved by integration of concrete stresses starting from the bottom of the bottom flange upwards until a compression force equal to the applied pretensioning by the straight strands (PI) is observed. At a distance equal to h (100 in.) from the end face of the member, the top and bottom fiber are as follows:

$$\sigma_t = 1641 \text{ psi (compression)} \quad (6.16)$$

$$\sigma_b = 4047 \text{ psi (compression)} \quad (6.17)$$

At a height of 36 in. from the bottom of the bottom flange, an equivalent compression force of 1820 kips is obtained. Figure 6-63 shows the partial cross section of a typical BWF100 girder required to resist the axial pretensioning force imposed by the straight strands with equivalent compression force at the distance $h = 100$ in. from the member end face. Appendix J includes the details of the supporting calculations.

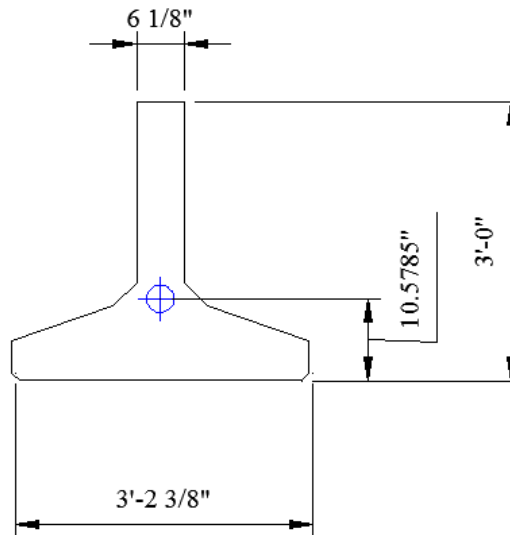


Figure 6-63: Partial cross section of the BWF100 girder required to resist the pretensioning force by the straight strands with equivalent compression force at the distance $h = 100$ in. from the member end face, immediately after the release of the prestressed strands.

Accordingly, the centroid of the corresponding section is estimated at

$$y_c = 10.5785 \text{ in.} \quad (6.18)$$

Therefore,

$$y = y_c - e_{p, \text{straight}} = 6.4914 \text{ in.} \quad (6.19)$$

In accordance with Equation (6.14), the vertical tie forces $T1$ and $T2$ are estimated to be

$$T1 = T2 = 220.2 \text{ kips} \approx 7.07\% P_i \quad (6.20)$$

In accordance with Figure 6-62, $T2$ shall be evenly distributed between the end face of the member and $h/4$ (25 in.). As discussed in the previous section, the area steel provided within the corresponding zone is

$$A_{EZR} = 6.2 \text{ in.}^2 \quad (6.21)$$

Thus, the maximum tensile stress in the end zone reinforcing bars is anticipated to be

$$f_{EZR,s} = \frac{T1}{A_{EZR}} = 35.5 \text{ ksi} = 1.78 f_{EZR, \text{allowable}} \quad (6.22)$$

6.4.1.3. Shear-Friction Analogy for Bursting Effects

As previously discussed, the differential axial pretensioning forces imposed on the member by the straight, draped and temporary strands at the top flange (if any) are expected to create a shear lag at the interface between the web and the bottom flange. Depending on the magnitude and scheme of pretensioning, the corresponding shear lag may force the web-bottom flange interface into shear friction resistance.

In accordance with Article 5.8.4 of AASHTO LRFD, the interface shear transfer is comprised of two important parameters: cohesion at the interface between the two mediums and the friction resistance by the combination of reinforcement and the permanent vertical force acting on the interface:

$$V_{ni} = c A_{cv} + \mu_f (A_{vf} f_y + P_c) \quad (6.23)$$

where,

$$V_{ni} \quad \dots\dots\dots \text{Nominal shear resistance at the interface} \quad (6.24)$$

$$c = 400 \text{ psi} \quad \dots\dots\dots \text{Cohesion in accordance with Table 3-3} \quad (6.25)$$

$$A_{cv} = 612.5 \text{ in.}^2 \quad \dots\dots\dots \text{Area of the concrete anticipated to be} \quad (6.26)$$

involved in shear friction transfer over the longitudinal distance of $h = 100$ in. from the girder end face

$$\mu_f = 1.4 \quad \dots\dots\dots \text{Friction factor in accordance with Table 3-3} \quad (6.27)$$

$$A_{vf} = 15.5 \text{ in.}^2 \quad \dots\dots\dots \text{Area of reinforcement crossing the shear} \quad (6.28)$$

interface over the longitudinal distance of $h = 100$ in. from the girder end face

$$f_y = 60 \text{ ksi} \quad \dots\dots\dots \text{Yield strength of steel reinforcing bars} \quad (6.29)$$

$$P_c = 16.1 \text{ kips} \quad \dots\dots\dots \text{Permanent compressive force acting normal} \quad (6.30)$$

to the shear plane due to self-weight and

vertical component of draped strands

Since the analysis of this research is the investigation of the cracked concrete body, it will be assumed that the contribution by cohesion has already overcome by the magnitude of the planar shear and therefore, it will be ignored. Also, since the zone near the end face of the member is anticipated to be under tension immediately after the release of pretensioning, the entire contribution by P_c will be conservatively eliminated from the interface shear capacity. Therefore, Equation (6.23) is rewritten to the following form in order to estimate the average stress in the end zone reinforcing bars due to the anticipated shear lag:

$$\left(f_{EZR,s}\right)_{average} = \frac{\Delta V_{shear}}{\mu_f A_{vf}} \quad (6.31)$$

where ΔV_{shear} corresponds to the difference between the pretensioning force imposed by the straight strands and the compression developed in the concrete at the web-bottom flange interface. As shown in Appendix I, the shear lag at a distance equal to $h = 100$ in. from the girder ends is estimated to be

$$\Delta V_{shear} = 513.6 \text{ kips} \quad (6.32)$$

Thus,

$$\left(f_{EZR,s}\right)_{average} = 22.6 \text{ kips} \approx 1.13 f_{EZR,allowable} \quad (6.33)$$

It should be noted that Equation (6.33) assumes uniform distribution of the anticipated shear lag over the entire effective length equal to h (100 in.) from the girder ends. Therefore, it is anticipated that the reinforcing bars near the end face experience larger differential shear lags as consequently undergo larger shear straining.

6.4.2. Numerical Modeling

For the analytical purposes of this research, the numerical modeling includes finite element simulation of a typical G94C specimen with asymmetric number of draped strands. Similar to the numerical simulation of the BT-72 girder as described in Chapter 5, the typical G94C specimen is modeled and analyzed as a three-dimensional continuum element while the prestressing strands are treated as truss (tension-compression only) members. Non-prestressed reinforcement such as end zone rebar, shear and confinement bars are simulated using beam elements which also provide shear stiffness.

Due to complexity of the pretensioning and the geometric characteristics of the G94C members, Embedment technique is used for the analytical and finite element simulation purposes of this chapter.

6.4.2.1. Constitutive Models

In reference to Section 3.4.1, Concrete Damage Plasticity constitutive model is utilized for the simulation of the linear elastic as well as elastoplastic response of concrete. The concrete properties at the time of pretensioning release were provided by the Fabricator and are summarized in Table 6-8. In addition, Table 6-8 includes the fundamental elastic properties of the prestressing strands and non-prestressed rebar.

Table 6-8: Summary of constitutive parameters used in finite element analyses.

Parameter	Value Used in Analysis
Concrete	
Compressive strength at time of release (f'_{ci})	8.000 (ksi)
Tensile [Rupture] strength at time of release(f_{ti})	0.671 (ksi)
Density (w_c)	165 (lb/ft ³)
Young's Elastic Modulus (E_{ci})	5784 (ksi)
Poisson's Ratio (ν_c)	0.2
Dilation Angle(ψ)	47.2°
Flow potential eccentricity (ε_c)	0.1
Ratio of the initial equibiaxial compressive yield stress to initial uniaxial compressive yield stress (σ_{bo}/σ_{o0})	1.16
Ratio of the second stress invariant to that of the compressive meridian at the initial yield (K_c)	0.778
Viscosity Parameter(μ_c)	0.0
Prestressing Strands	
Ultimate tensile strength (f_{pu})	270 (ksi)
Density (w_p)	490 (lb/ft ³)
Young's Elastic Modulus (E_p)	28,500 (ksi)
Poisson's Ratio (ν_p) (same for all other reinforcement)	0.2
Non-Prestressed Reinforcement	
Yield Strength (f_y)	60 (ksi)
Density (w_p)	490 (lb/ft ³)
Young's Elastic Modulus (E_p)	29,000 (ksi)

6.4.2.2. Simulation of the Composite Interaction Between Concrete and Prestressing Strands and Other Reinforcement

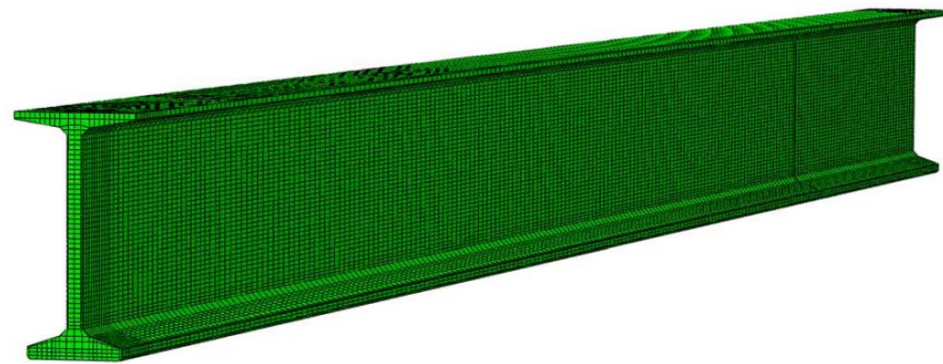
The numerical simulation of the G94C specimens is in accordance with the same methodology used for finite element modeling of the BT-72 samples as described in Chapter 5. Similarly, the prestressing strands are modeled as truss elements which are embedded inside the concrete continuum serving as host. In addition, multiple levels of embedded elements are included in the model for simulation of the end zone and shear stirrups, and confinement rebar in the bottom flange.

The non-prestressed reinforcing bars such as the end zone, shear and confinement reinforcement are simulated using three-dimensional beam elements. This ensures that the corresponding elements provide the shear stiffness based on individual material and geometric properties.

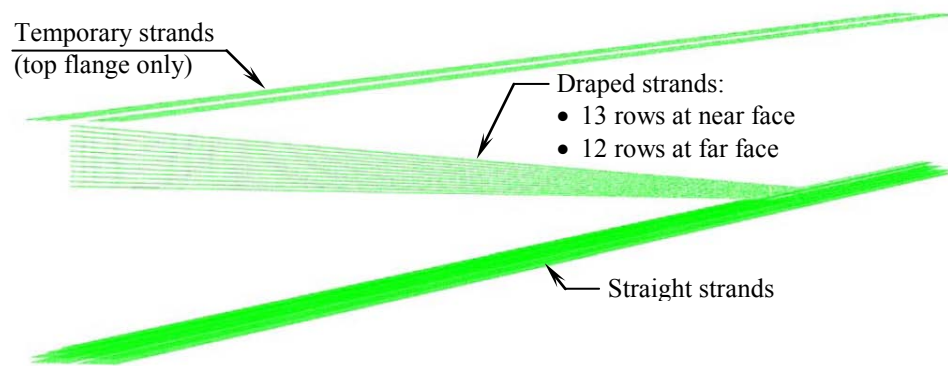
Figure 5-20 shows a typical finite element simulation of the G94C girders using the embedment technique. The basic components of such simulation are the solid elements representing the girder, truss elements simulating each individual straight or draped strand, and beam elements modeling the end zone, shear and confinement reinforcing bars.

6.4.2.3. Simulation of Pretensioning

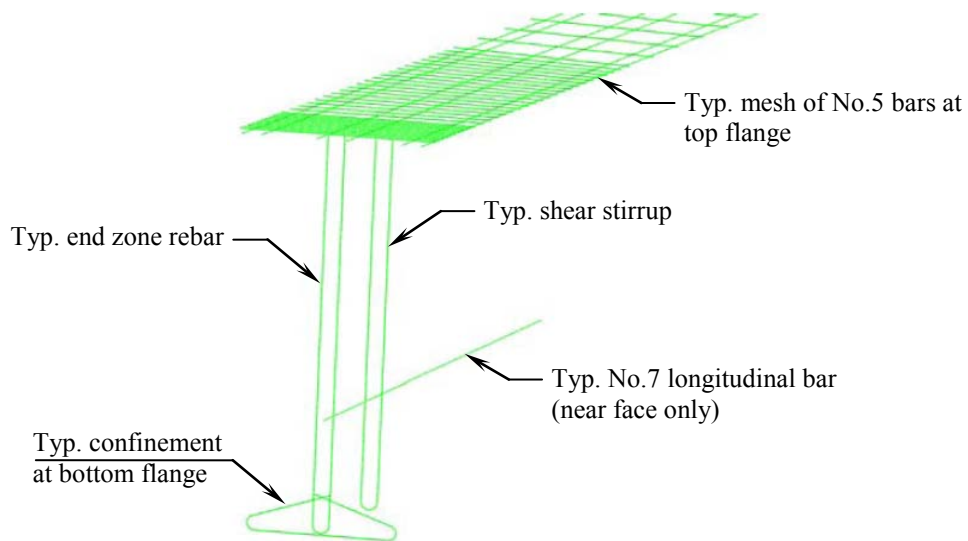
In reference to Section 0, the process of pretensioning release is simulated through initial conditions and based on strain compatibility between concrete as the host and the prestressing strands as the embedded elements. The corresponding steps required for the simulation of pretensioning are described in Section 5.4.3.



(a)



(b)



(c)

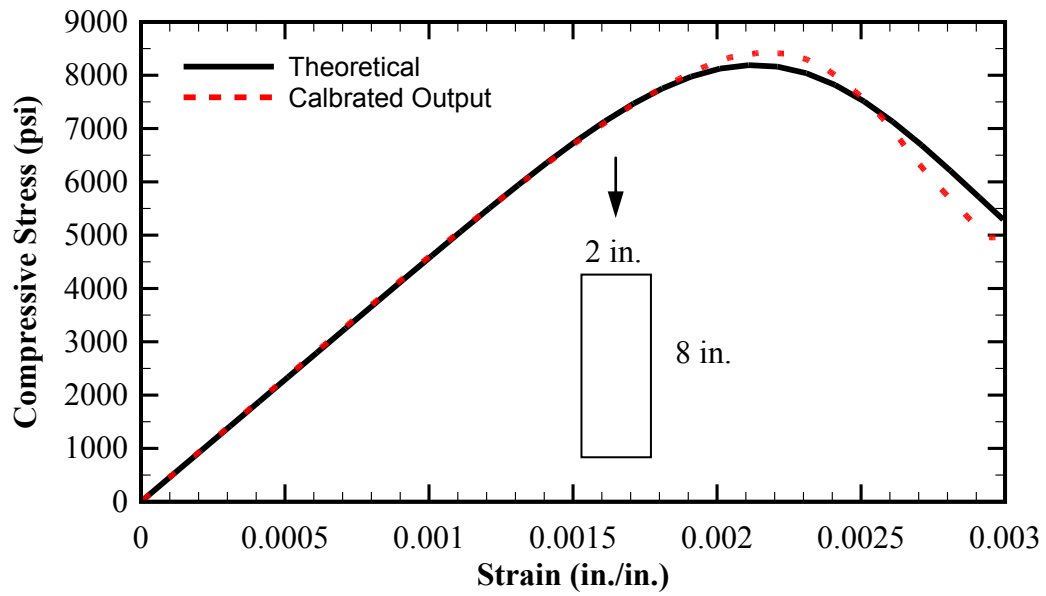
Figure 6-64: Typical components of a finite element model of a typical G94C girder using embedment technique: (a) Solid concrete continuum simulating the girder, (b) truss elements simulating the straight, draped, and temporary strands, and (c) beam elements simulating the end zone, shear reinforcement, and the confinement bars embedded inside the bottom flange.

6.4.2.4. Transfer Length

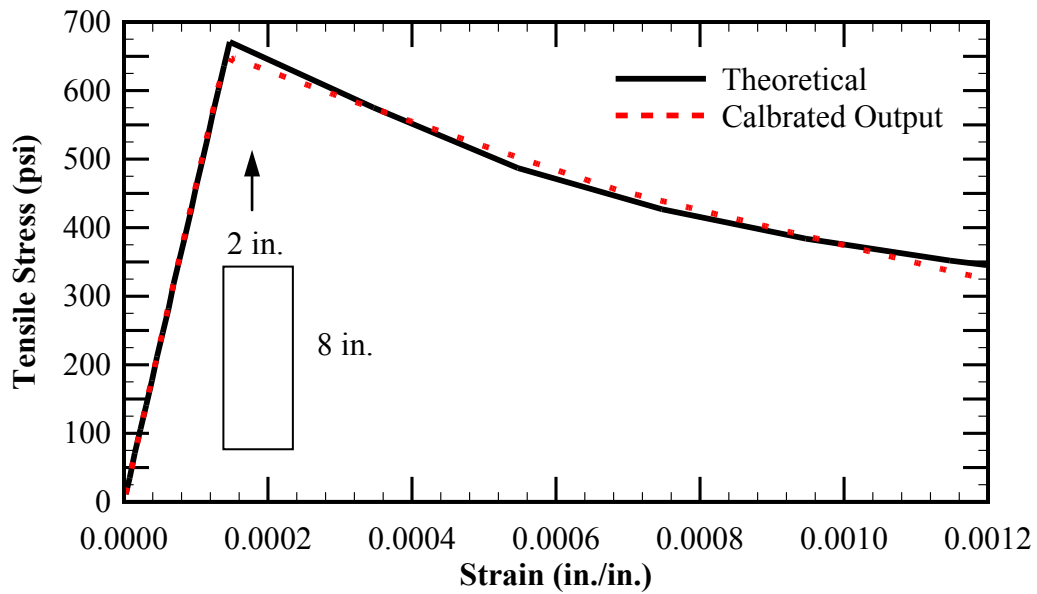
As discussed in the previous chapters, one of the characteristics of the embedment technique is that the transfer length is treated as a model input. In reference to Section 6.3.5.2, the finite elements simulating the straight, draped and temporary strands are subject to prestressing initial condition in accordance to Figure 6-58. It shall be noted that the transfer length used for the analytical purposes of this chapter is based on the measured parabolic stress path as opposed to the bilinear simulation utilized in Chapter 5 in accordance with Figure 3- 19.

6.4.3. Calibration of Material Constitutive Models

As previously stated in Section 6.4.2.1, Table 6-8 includes the summary of the material constitutive parameters used in the finite element analyses. The corresponding parameters are obtained based on an iterative process as described in details in Chapter 3. Figure 6-65 (a) and (b) show the compressive and tensile stress-strain models used for the analytical purposes of this research based on initial compressive strength of 8,000 (psi) at the time of release. Consistent with the calibration methodology described in Section 3.5.2.1, the calibration of the concrete constitutive model is performed by analyzing the response of a 2 in. x 8 in. finite element prism to uniaxial compressive and tensile straining. Figure 6-65 (a) and (b) show the convergence of the response of the calibrated models towards the theoretical uniaxial compressive and tensile stress-strain curves, respectively, after several iterations.



(a)



(b)

Figure 6-65: Comparison of the stress-strain relationships obtained by the constitutive model with the theoretical stress-strain curves assumed for a concrete with initial compressive strength of $f'_{ci} = 8,000$ psi: a) subject due to uniaxial compression, and (b) subject to uniaxial tension.

6.4.4. Numerical Simulations

Appendix J includes the theoretical stress profiles in the extreme top and bottom fibers of a typical G94C specimen immediately after the release of pretensioning. The anticipated results are obtained based the linear-elastic beam theory as previously discussed in Section 5.3.1. Subsequently, Table 6-9 includes the comparison of the theoretical top and bottom fiber stresses at the midspan of the member versus the corresponding values obtained by the nonlinear finite element analysis. The comparison of the results indicates both top and bottom fibers remain in compression immediately after the release of pretensioning. As previously discussed in Chapter 5, it is observed that the inclusion of the end zone, shear and confinement reinforcement does not significantly affect the longitudinal stresses at the top and bottom fibers in the mid-span of the member, which is consistent with the assumptions of the beam theory. The comparison of the results indicates a close convergence of the theoretical and numerical results.

Table 6-9: Comparison of the results obtained by the G94C finite element model with versus the closed form solutions summarized in Appendix J.

	Nonlinear Response	Closed Form Solution	$\frac{\text{Elasto - plastic}}{\text{Closed Form Solution}}$
Stress in the extreme top fiber at mid-span, $\sigma_t^{\text{Midspan}}$ (psi)	-1490	-1502	0.85%
Stress in the extreme bottom fiber at mid-span, $\sigma_c^{\text{Midspan}}$ (psi)	-4188	-4124	-1.53%
Notes: 1. Positive stresses correspond to the state of tension. 2. Negative stresses correspond to the state of compression.			

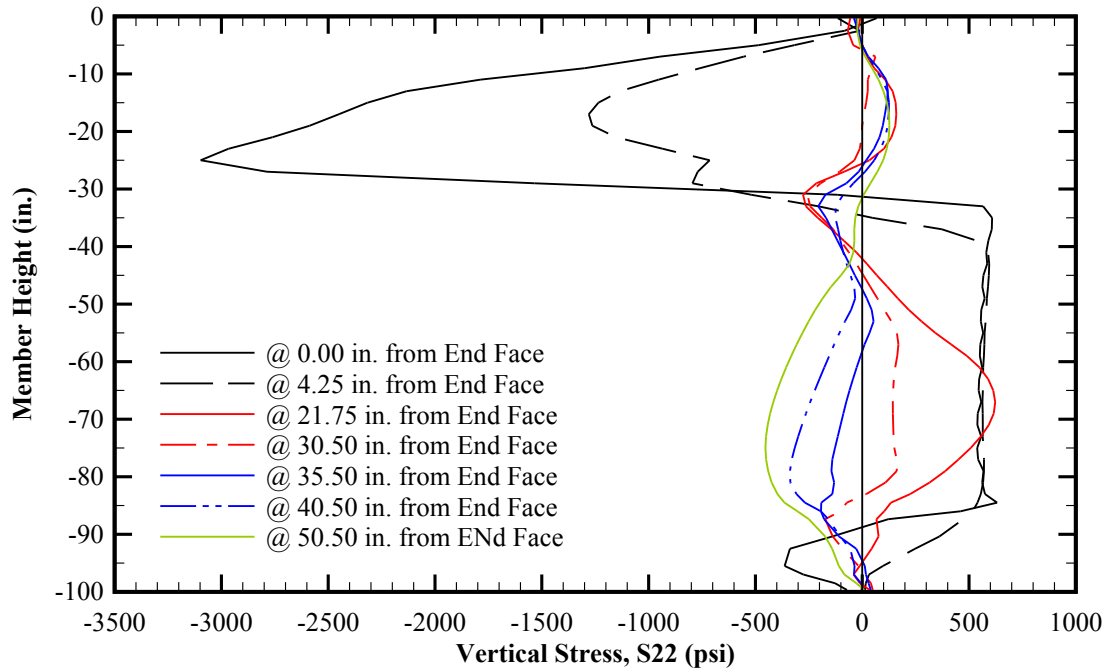


Figure 6-66: Vertical stress (S22) distribution along the height of a typical G94C girder with AASHTO LRFD end zone rebar in addition to shear and confinement reinforcement in accordance with Figure 6-5.

Note: Positive stresses indicate state of tension; negative stresses indicate state of compression.

Figure 6-66 shows the distribution of the vertical stresses (S22) along the height of a typical G94C girder, measured at various distances from the member end face. It is observed that significant softening of concrete occurs within a domain confined between the member end face and 22 in. away from the girder end. The magnitude of the vertical tensile stresses indicates that potential cracking is anticipated along the height of the girder web especially in the lower segment near the bottom flange.

Similarly, Figure 6-67 includes the pressure distribution along the height of the G94C girder at the same distances from the girder end face, respectively. The pressure distribution indicates that the member is susceptible to cracking immediately after the release of pretensioned strands starting from the member end face up to 22 in. away.

Additionally, the numerical results anticipate extensive softening of the concrete host up to 4.25 in. from the member end. The nonlinear response is skewed more towards the lower segment of the member starting from the interface between the web and the bottom flange. Beyond 22 in. from the end face, the entire height of the member is observed to remain in overall state of compression.

Besides, the numerical results show a close similarity between the trend of the vertical stress and pressure distribution. This is an indication the near the member end face, the overall state of the pressure is governed by the vertical component of the stress. (S22).

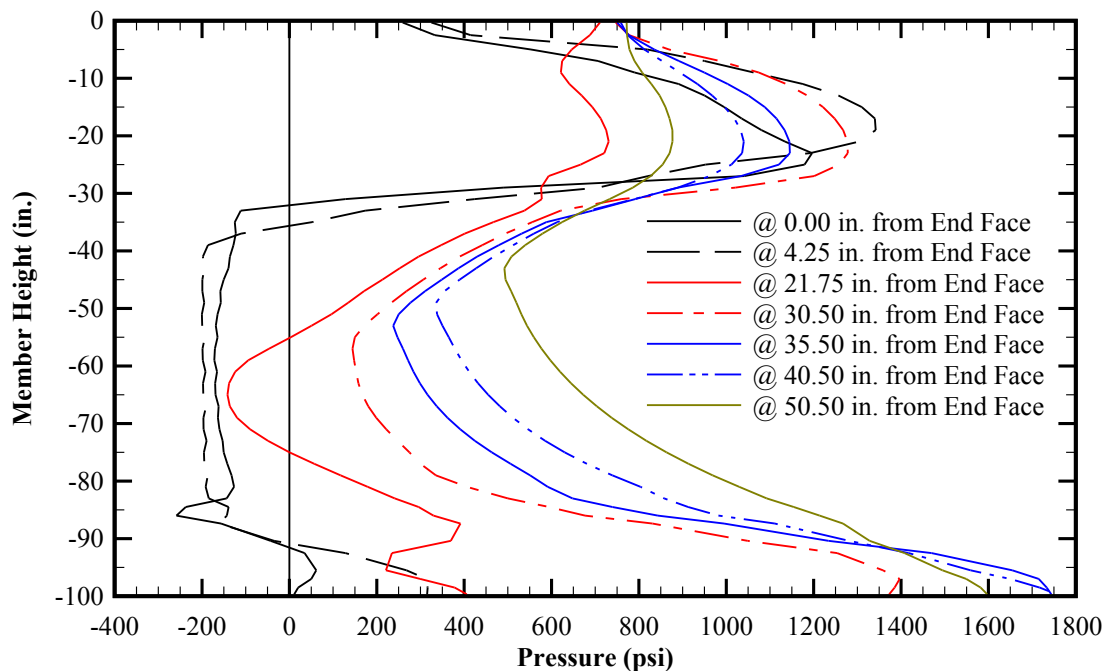


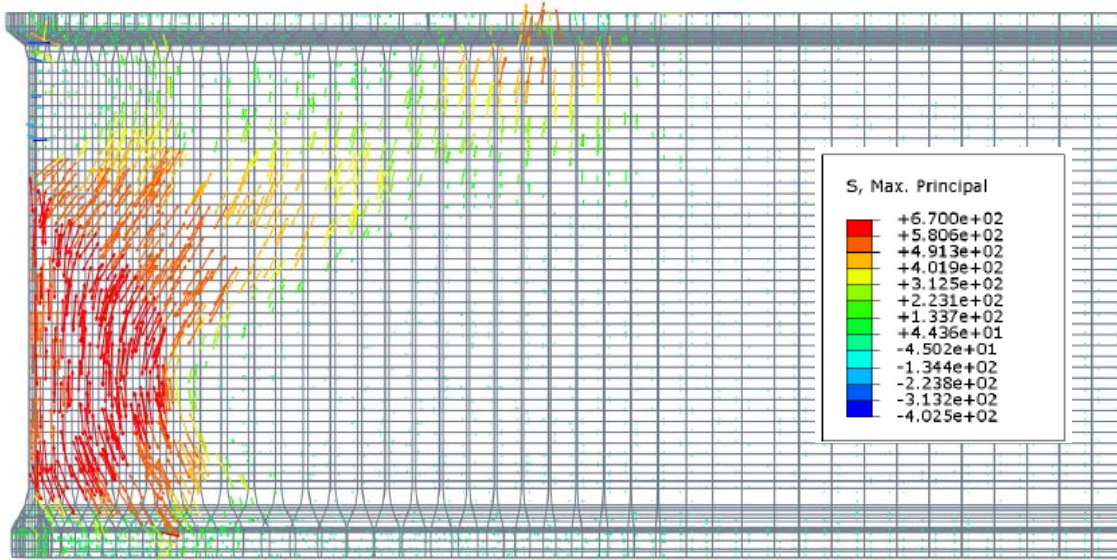
Figure 6-67: Pressure distribution along the height of a typical G94C girder with AASHTO LRFD end zone rebar in addition to shear and confinement reinforcement in accordance with Figure 6-5.

Note: Positive pressure indicates state of compression; negative pressure indicates state of tension.

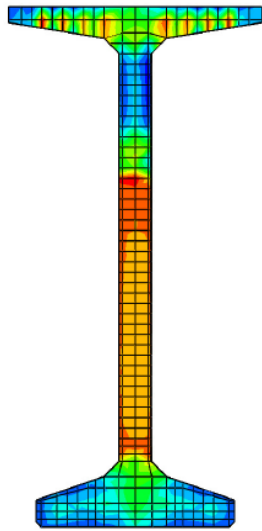
Figure 6-68 shows the state of maximum principal stress along the end zone of the G94C girder based on nonlinear (e.g., elasto-plastic concrete response) simulation. Figure 6-68 (a) shows the maximum principal vector contours near the girder end face, indicating tensile stresses near rupture strength (f_r) initiating in a zone immediately above the interface between the web and bottom flange. Therefore, the web is potentially vulnerable to cracking along the height of the web with more concentration of the tensile stresses along the interface with the bottom flange. This is consistent with the observations at the casting yard.

Similarly, Figure 6-68 (b) shows the maximum principal stress distribution at the member end face. The finite element results indicate that the of entire fascia of the lower segment the web down to the interface with the bottom flange may experience material softening and subsequent stress re-distribution due to the tensile stresses approaching near and beyond the anticipated rupture modulus. It is also observed that the potential for through-cracks exists at the web-bottom flange interface as well the upper segment of the web. Additionally, the numerical results indicate that the finite element simulation accounts for the skewed end face.

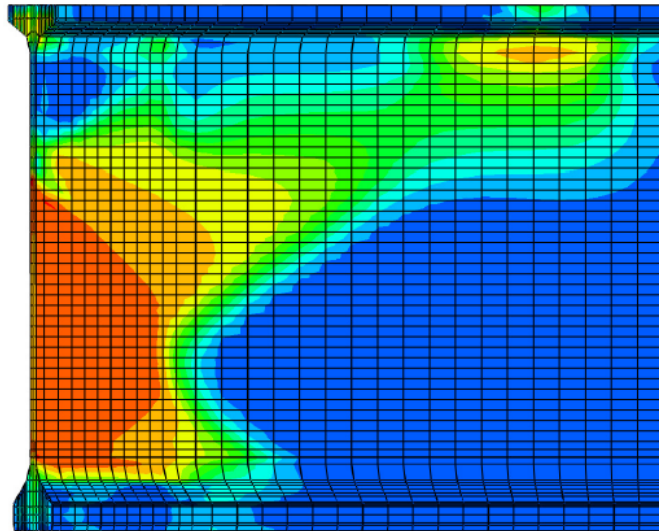
Figure 6-68 (c) shows the maximum principal stress distribution along the member end zone. The stress contours indicate that the potential tensile cracking of the girder web is confined to an area extending from the member end face up to approximately 24 in. away. This is consistent with the numerical distribution of the pressure and vertical stress component (S22).



(a)



(b)



(c)

Figure 6-68: Elasto-plastic response of a typical G94C girder with end zone rebar, shear and confinement reinforcement in accordance with Figure 6-5 immediately after the release of pretensioning: (a) Maximum principal vector contour along the end zone, (b) Maximum principal stress contour at member end face and (c) Maximum principal stress contour along the end zone.

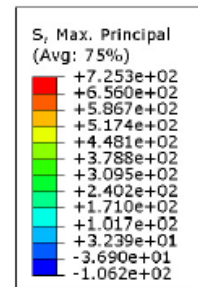


Figure 6-69 (a) shows the distribution of the planar shear stress (S23) averaged across the thickness of the web, along the span of the girder based on the elasto-plastic simulation. The numerical results indicate tensile softening along the first 24 in. of the girder immediately after the release of pretensioning: maximum shear stress of 746 (psi) at 24 in. versus 830 (psi) at 18 in. from the girder end face based on elasto-plastic and linear-elastic responses, respectively.

Figure 6-69 (b) shows the planar shear stress (S23) contour at the outside face of the web based on elasto-plastic response of concrete, measured at various heights of the member. It is observed that the transfer of the axial pretensioning from the bottom flange upwards into the web results in significant concentration of shear stress at the bottom flange interface with the web. This shear transfer mechanism is anticipated to be due to the shear-lag caused by the difference in the magnitude of pretensioning in the bottom flange and web as previously discussed in Chapter 5. The maximum planar shear stress (S23) is observed at a height of 14 in. from the bottom of the bottom flange, 1-3/8 in. higher than the web-bottom flange interface. Beyond the optimum height of 14 in., it is observed that as the height along the member web increases, the planar shear stress (S23) decreases. The shear concentration is eventually resolved into the web over a distance approximately equal to the transfer length.

In reference to the discussions of Section 6.4.1.3, the above shear lag phenomenon may contribute to equivalent shear-friction cracking in the vicinity of the web and bottom flange, increasing the tensile stresses in the end zone reinforcement along the corresponding zone.

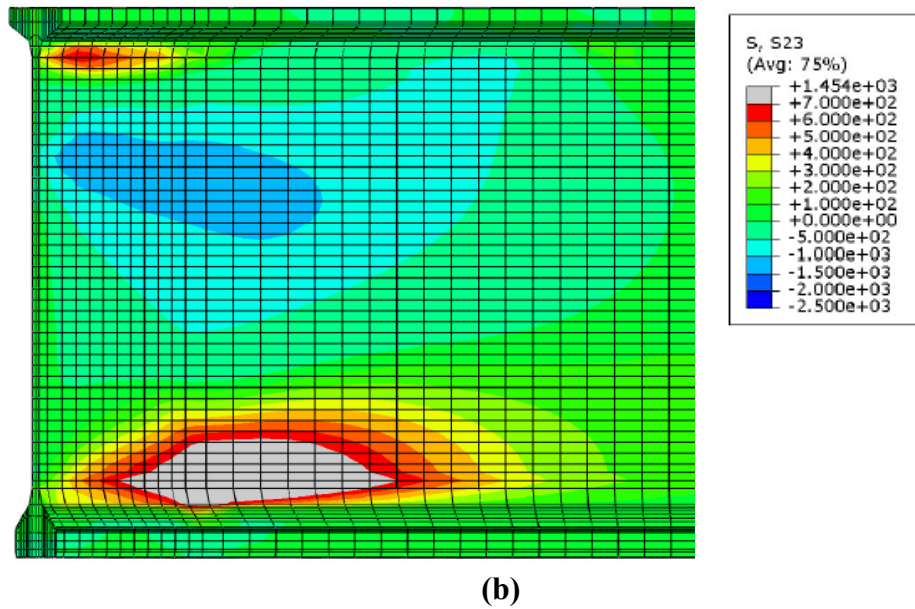
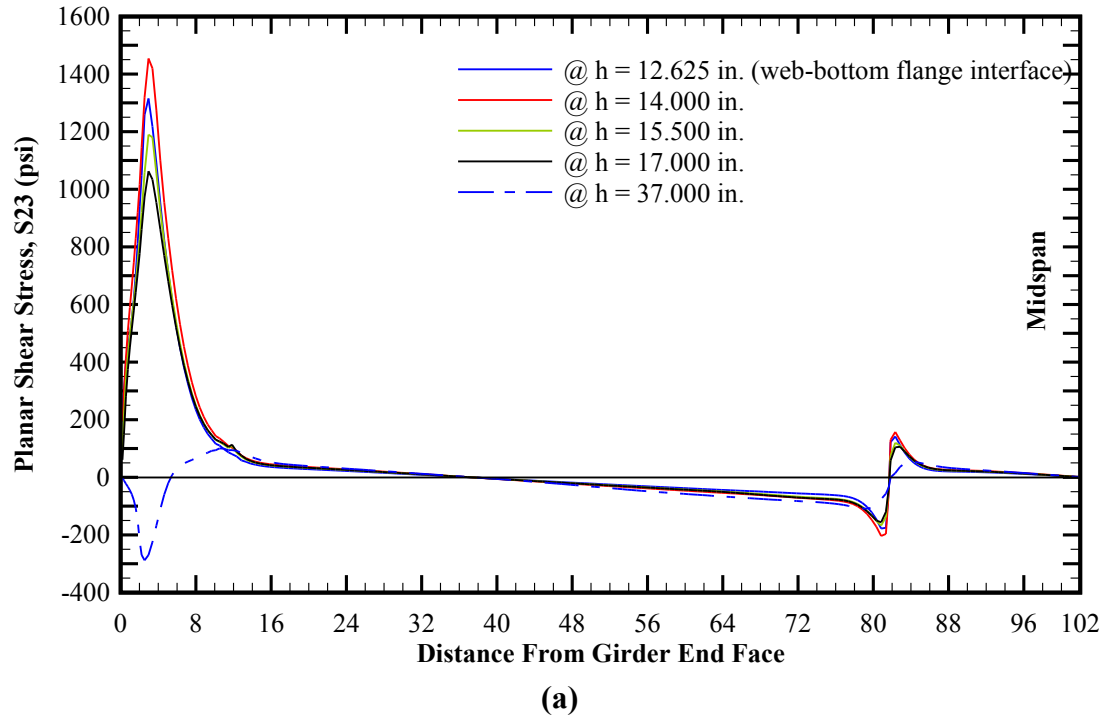


Figure 6-69: Planar shear stress (S_{23}) distribution along the span of a typical G94C girder with zone rebar, shear and confinement reinforcement in accordance with Figure 6-5 immediately after the release of pretensioning: (a) Average shear stress across the width of the web, and (b) Shear stress contour at the outside face of the web base don elasto-plastic response.

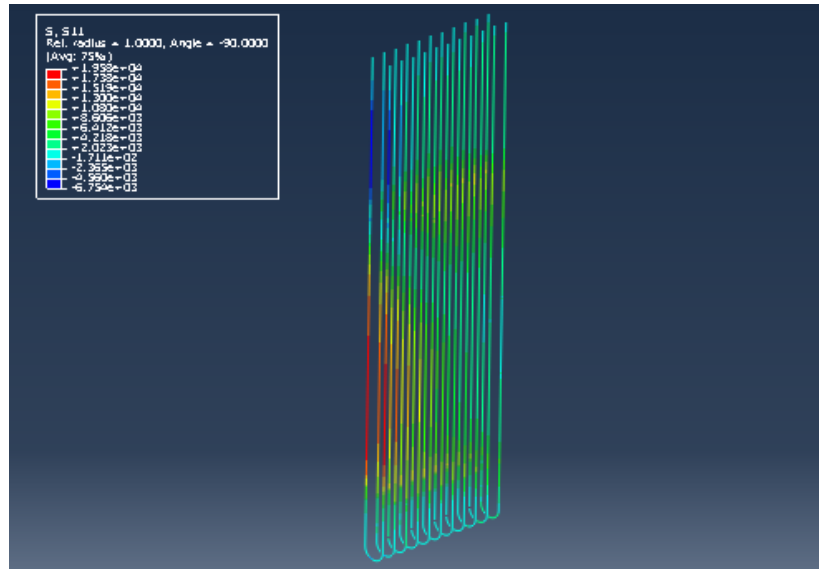
Figure 6-70 (a) shows the state of axial stresses (S11) in the end zone reinforcing bars immediately after the release of pretensioning and based on elasto-plastic (e.g., nonlinear) response of concrete. It is observed that the magnitude of axial stresses in the end zone rebar reaches the maximum near the end face of the girder. Figure 6-70 (b) comparatively shows the maximum axial stress (S11) at the first three end zone bars near the end face of the member. It shall be noted that positive axial stress indicates state of tension; negative axial stress indicates compression in the bars. The numerical results indicate that the maximum tensile stress is observed near the end face of the member consistent with the numerical observations in the previous chapters. Also consistent with the previous observations, the magnitude of the tensile stress significantly decreases as moving away from the end face. As opposed to the previous observations, the axial stress distributions shown in Figure 6-70 (a) indicate that the location of the maximum tensile stresses shifts upwards from approximately the lower quarter-point of EZR No.1 to approximately third-point of EZR Nos. 3. Table 6-10 shows the summary of the maximum tensile stresses in EZR No.1 thru 3 as discussed, including the stress magnitude as well as the location along the height of the bar measured in relation to the bottom of the girder bottom flange assumed as datum. This observation may be contributed to the fact that the G93C, G94C and G95C test specimens are all bunched at about 8-ft from either end. This causes reversal of bending moments at the end cantilevers during the process of pretensioning release.

The numerical results indicate that the maximum tensile stresses observed by the finite element simulations (20.153 ksi) is slightly over the allowable limit (20.0 ksi) specified by AASHTO LRFD in reference to Equation (5.20).

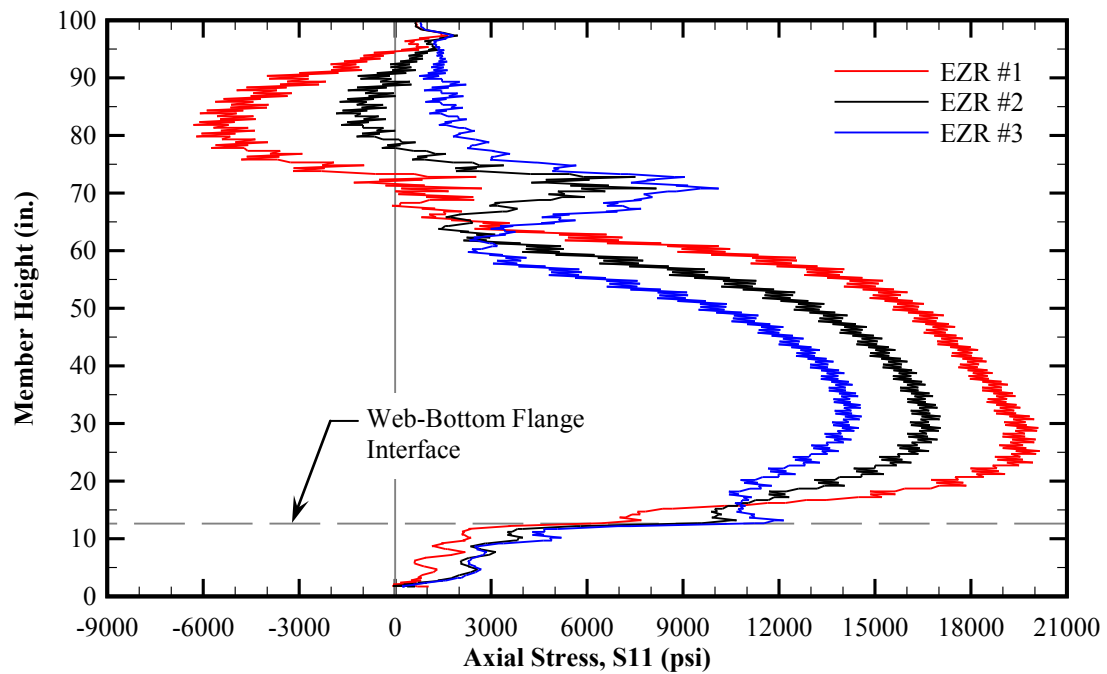
Table 6-10: Summary of the maximum tensile stresses in the first three end zone reinforcing bars closest to the member end face, obtained from the nonlinear numerical simulations of a typical G94C girder with end zone rebar, shear and confinement reinforcement in accordance with Figure 6-5 immediately after the release of pretensioning.

I.D.	Max. Axial Stress at EZR (ksi)	Height along the Rebar (in.)
EZR #1	20.153	25.229
EZR #2	17.057	29.237
EZR #3	14.584	31.241

Similarly, Figure 6-71 (a) and (b) shows the axial stress (S11) distribution in the confinement reinforcement and the maximum stress per each rebar, respectively. The maximum tensile stress of 6.4 ksi is observed at a distance equivalent to 0.26 d (26% of the member height). Beyond a distance equivalent to 0.85 d (85% of the member height), the axial stresses in the confinement reinforcing bars stabilize on a constant magnitude of approximately 4.0 ksi.



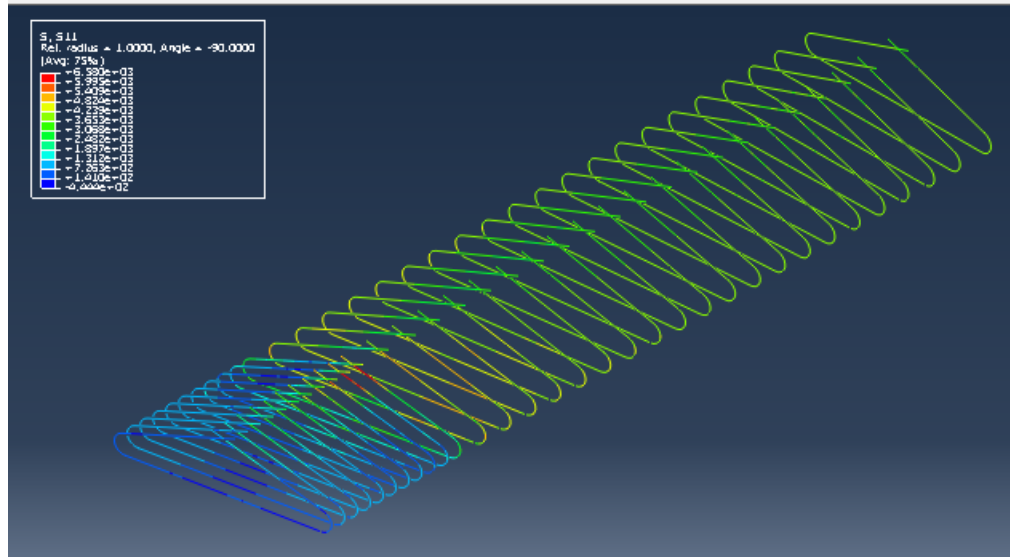
(a)



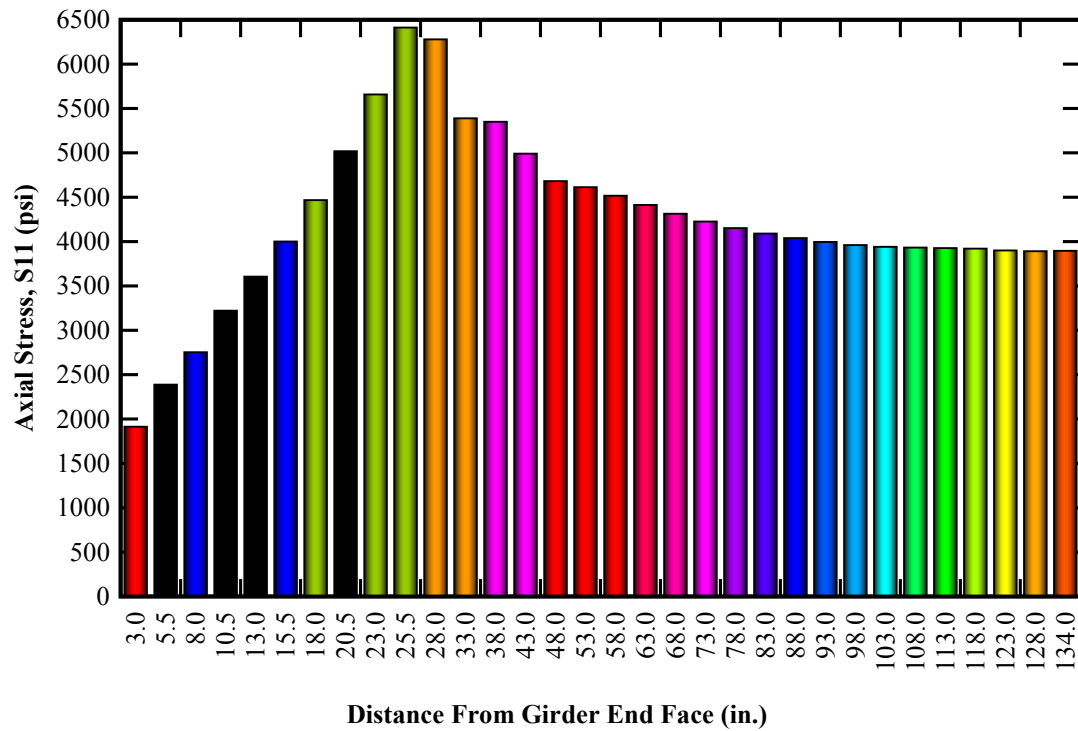
(b)

Figure 6-70: Axial stress (S11) in the end zone reinforcing bars of a typical G94C girder with end zone rebar, shear and confinement reinforcement in accordance with Figure 6-5 immediately after the release of pretensioning: (a) Numerical results obtained by the nonlinear finite element simulation and (b) maximum stress at both legs of the first end zone bars closest to the member end face.

Note: Positive axial stress indicates tension; negative axial stress indicate compression



(a)



(b)

Figure 6-71: Axial stress (S11) in the confinement reinforcement of a typical G94C girder with end zone rebar, shear and confinement reinforcement in accordance with Figure 6-5 immediately after the release of pretensioning: (a) Numerical results obtained by nonlinear finite element simulation and (b) maximum stress per each confinement rebar.

Note: Positive axial stress indicates tension; negative axial stress indicates compression.

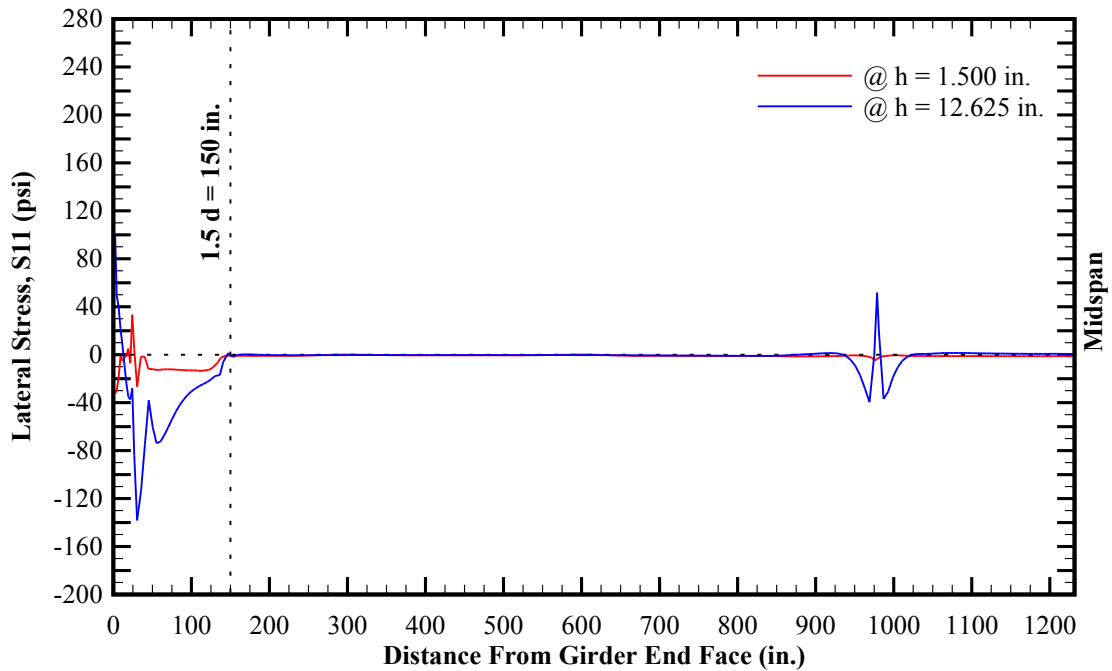


Figure 6-72: Lateral stress (S11) distribution within the bottom flange (elasto-plastic response) of a typical G94C girder with end zone rebar, shear and confinement reinforcement in accordance with Figure 6-5.

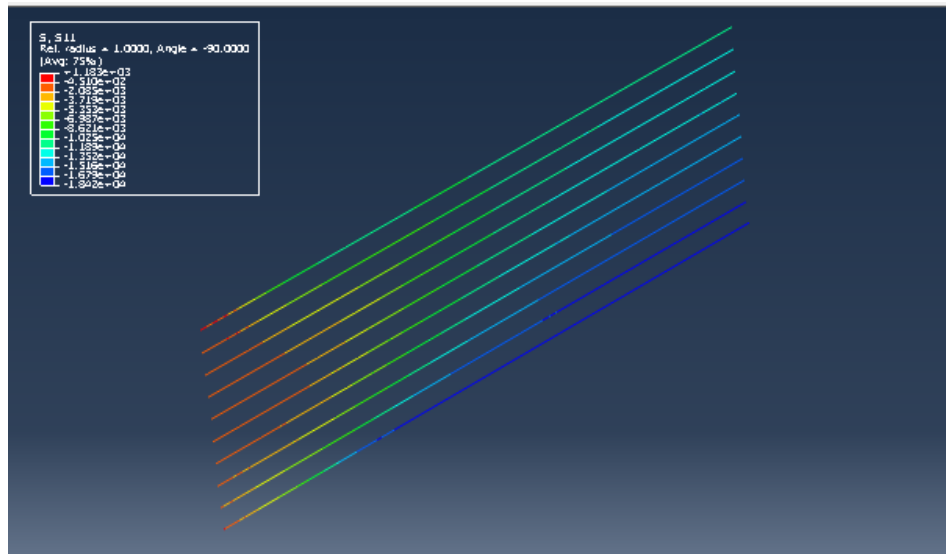
Note: Positive pressure indicates state of compression; negative pressure indicates state of tension.

Figure 6-72 shows the lateral stress (S11) distribution within the bottom flange of a typical G94C girder with elasto-plastic response. As previously discussed, the current AASHTO LRFD specifications require confinement reinforcement to extend over a distance equal to 1.5 times the height of the precast member. The numerical simulations show a maximum lateral tensile stress of 251 psi near the top of the bottom flange at the member end face. However, the lateral tensile stresses are resolved into state of compression at a distance approximately 150 in. from the girder end face, which is equal to 1.5 times the height of the member. This is consistent with the current AASHTO LRFD specifications.

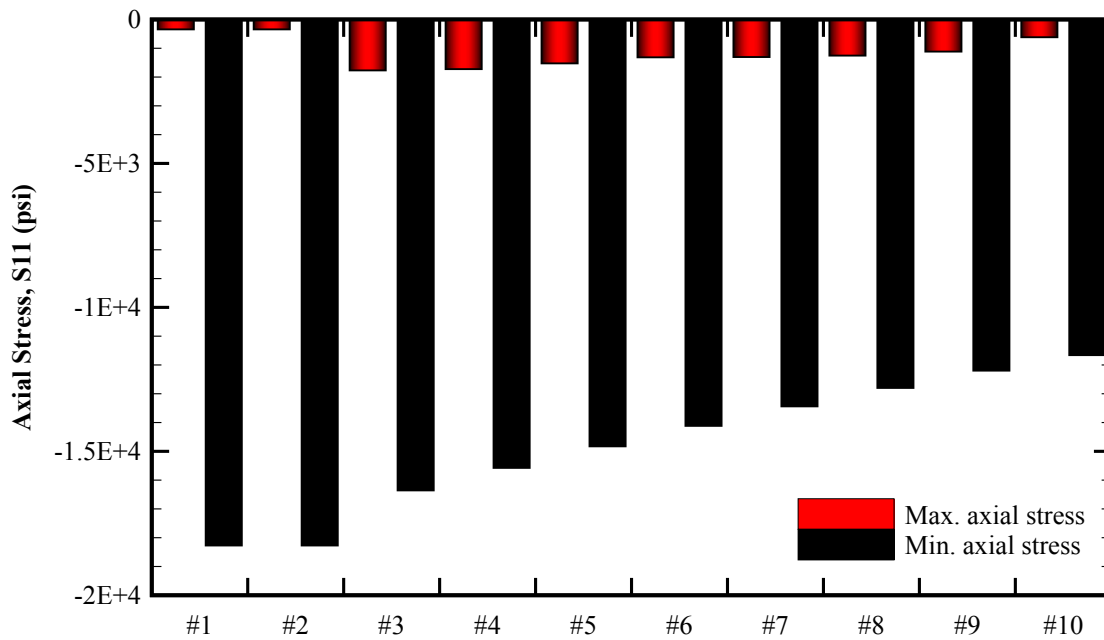
As shown in Figure 6-4 thru Figure 6-6, all the test specimens include ten No.7 longitudinal bars embedded in one side of the specimens web only. The corresponding bars are intended to facilitate the continuity of the girders through the closed pier diaphragms.

Figure 6-73 (a) shows the axial stress (S11) contours based on the elasto-plastic numerical simulation discussed in the section immediately after the release of pretensioning. Figure 6-73 (b) includes the summary of the maximum/minimum axial stresses per each rebar. The numerical results indicate that all ten No.7 bars remain in state compression with maximum value of -18.3 ksi at lowest No.7 bars.

As mentioned above, the reversal of bending moments due to lifting of the members during the pretensioning release is anticipated to also affect the response of the corresponding No.7 bars due to strain compatibility with the concrete host. Therefore, the observation of the maximum axial compression in lowest No.7 rebar is consistent with the behavior of the member end cantilevers (approximately 8 ft) during the release.



(a)



(b)

Figure 6-73: Axial stress (S11) in the longitudinal No.7 bars embedded in the web (one side only) of a typical G94C girder with end zone rebar, shear and confinement reinforcement in accordance with Figure 6-5 immediately after the release of pretensioning: (a) Numerical results obtained by nonlinear finite element simulation and (b) maximum/minimum stresses per each rebar.

Note: Positive axial stress indicates tension; negative axial stress indicates compression.

6.5. Comparison of Results

The following section includes the comparison of the experimental and analytical axial stresses (s_{11}) in the three end zone bars (EZR #1 thru EZR #3) closest to the end zone of G94C specimens, including Girders #2 thru #7 immediately after the release of pretensioning.

As previously mentioned, the finite element analysis was limited to the G94C girders with asymmetrical number of draped strands. Therefore, the experimental data obtained from Girder #1 (G93C) and Girder #8 (G95C) are excluded from the comparative analysis of the results.

Figure 6-74 shows the profile of the axial stresses (S_{11}) along the length of the EZR #1 thru EZR #3 based on the analytical solutions versus the experimental measurements. It is observed that the finite element solutions capture a lower boundary of tensile stresses in EZR #1 and EZR #3 along the upper mid-height of the web. The numerical solutions for EZR #3 offer a lower boundary with more pronounced deviation in comparison with the experimental observations. It is also observed that the experimental results do not indicate significant decrease in the magnitude of the axial tensile stresses from EZR #1 towards EZR #3 as expected based on the findings of Chapter 5. This is mainly anticipated to the bunched configuration of the girders during the release as discussed in Section 6.2.

As previously discussed, the largest magnitude of the axial tensile stresses was experimentally measured along the web-bottom flange interface due to shear lag between the bottom flange and the web. As observed in Figure 6-74, the finite element simulation is not able to capture this phenomenon in spite of the excessive planar shear (S_{23}) as shown in Figure 6-69.

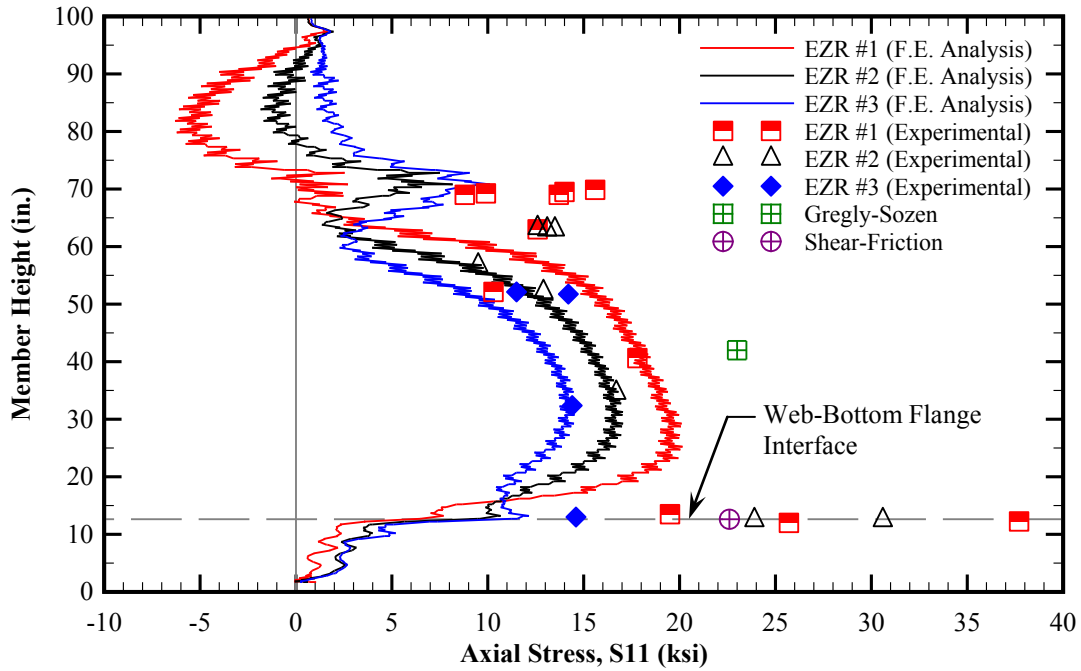


Figure 6-74: Comparison of the axial stresses (S11) at the three end zone rebar closest to the end face of a typical G94C girder with end zone rebar, shear and confinement reinforcement in accordance with Figure 6-5 based on the analytical solutions versus the experimental observations.

Note: Positive pressure indicates state of compression; negative pressure indicates state of tension.

Figure 6-75 shows a comparison between the experimental axial stresses at EZR #1 thru EZR #3 versus the analytical solutions obtained by nonlinear finite element simulation, Gregly-Sozen method, strut-&-tie procedure and shear-friction analogy as described in the previous section. It is observed that:

1. The maximum tensile stress (20.2 ksi) at EZR#1 obtained by the nonlinear finite element solution corresponds to the average of the experimental strains measured at EZR #1 thru EZR #3.
2. Strut-&-tie procedure results in a maximum tensile stress in the end zone bars near the end face of the member, which corresponds to the corresponding maximum experimental measurement.

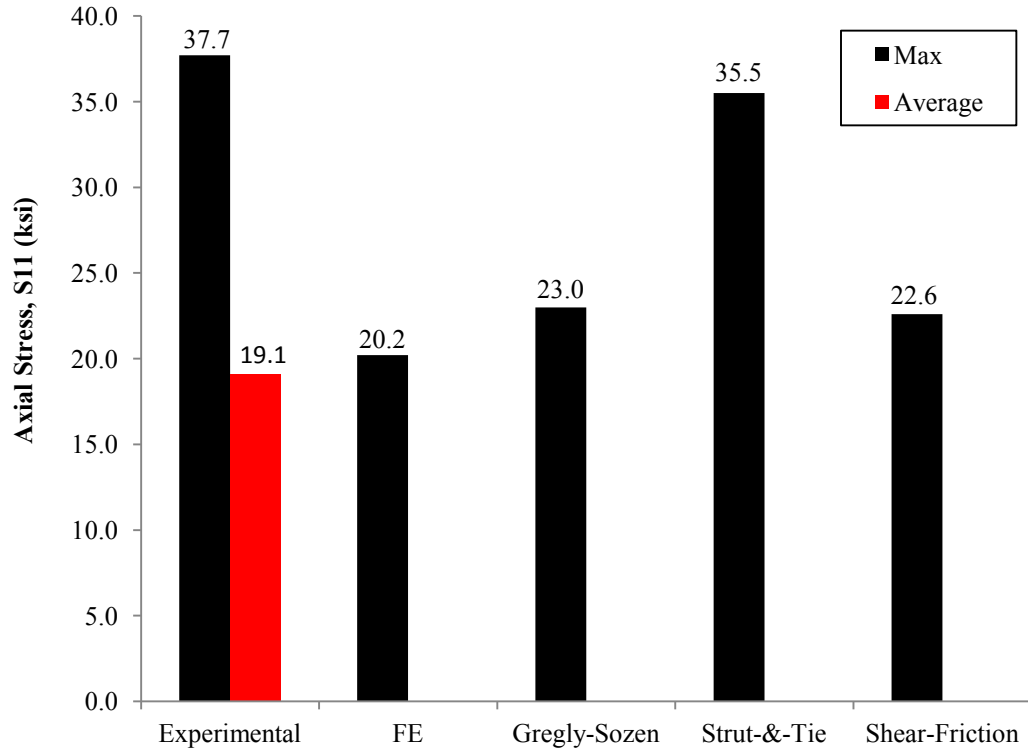


Figure 6-75: Comparison of the axial stress (S11) at the three end zone rebar closest to the end face of a typical G94C girder with end zone rebar, shear and confinement reinforcement in accordance with Figure 6-5 based on analytical solutions versus experimental observations.

Note: Positive pressure indicates state of compression; negative pressure indicates state of tension.

3. Gregly-Sozen method and shear-friction analogy result in similar maximum tensile stresses but at different heights along the member, 42 in. and 12-5/8" (web-bottom flange interface), respectively.
4. The Gregly-Sozen method is observed to be overestimate the magnitude and the vertical location of the maximum tensile stress in the end zone rebar, and
5. The maximum tensile stress estimated by shear-friction analogy is observed to fall within the lower bound of the experimental observations at the web-bottom flange interface.

Chapter 7 - Conclusions and Recommendations for Future Research

7.1. Concluding Remarks

The main objective of this research was to evaluate two finite element techniques for numerical simulation of behavior of pretensioned concrete girders immediately after the release of prestressing: extrusion and embedment techniques. The analytical results indicate that both techniques are viable methodologies for the finite element modeling of the pretensioned concrete members. Each technique has specific advantages and disadvantages depending on the objectives of analysis. Extruded models generally provide more details at the interface of the concrete and released strands (i.e., slippage, transfer length, etc.) while they are usually complex in nature and computationally expensive. On the other hand, the embedded models are generally less complicated and computationally much less expensive. While embedded models give results with acceptable convergence towards the corresponding extruded simulations, the interaction of the released strands with the concrete matrix is treated as input data and can only be simulated and controlled during the initial conditions through stepwise stressing of the strands.

Parametric studies also show that: i) direct slippage of strand-over-concrete using the friction simulation provides an acceptable approximation of the pretensioning mechanism, including the transfer length phenomenon, ii) friction coefficients of 0.70 and 1.4, in combination with Poisson's effect and other contact parameters, appear to adequately provide lower and upper bound interface interactions between the strands and concrete host immediately after the release of pretensioning, and iii) the variation of axial stresses in the strands along the transfer length zone is found to be of nonlinear

(parabolic) nature rather than the linear approximation recommended by the codes and guidelines used in current practice.

In addition to the modeling techniques used for the simulation of pretensioning mechanism, material nonlinearity with proper calibration of the required parameters can significantly affect the response of the prestressed beam. Depending on the objectives of the analysis, it is important to note that unless the material response remains within the elastic regime, accuracy of the finite element analysis is significantly affected and governed by material nonlinearity and hence the reliability of the selected constitutive models.

Once the proposed finite element techniques were verified and validated against the available closed form solutions and experimental observations, respectively, they were utilized for the investigation of 0.7-in. diameter strands and end zone cracking.

Based on the current guidelines for the design and detailing of prestressed concrete members, strands shall not be spaced closer than four times the diameter. This constitutes minimum strand spacing of 2.80 in. for 0.70-in. diameter strands. As the results, the precasters will be required to apply significant and costly modifications to the current means and methods. In this research, the effect of reduced spacing of 2.00 in. for 0.70-in. diameter strands was studied, which conforms to the widely accepted reduced spacing for 0.60-in. diameter strands as well as the common setups in most of the precasting yards across the U.S.

As the spacing of the strands decreases from 2.80 in. (four times the diameter) to 2.00 in., pronounced effects are observed in the stresses around the central strand. The analytical results show a notable increase (by as much as 165%) in the tensile stresses in

the vicinity of the interior strand symmetrically confined by other strands. Meanwhile, depending on the strength of the concrete at the time of pretensioning release, the corresponding increase in the tensile stresses is observed to be below the acceptable limits of the current guidelines. In other words, initial compressive strength of concrete at the time of pretensioning release is observed to be a critical parameter for using 0.7-in. diameter strands at 2.00 in. spacing which is less than the recommended four times the strand diameter. These analytical observations are consistent with the findings of the past research by Morcous and Tadros (2011).

The analytical results indicate that the spacing of confinement reinforcement does not have significant effect on the response of the specimens regardless of the strands spacing. However, non-confined members show notable differences in the magnitude of the tensile stresses imposed by the pretensioned strands. Therefore, confinement reinforcement is observed to be a critical component of the pretensioned members as required by the current state of practice.

In addition to the strands spacing, quality of the interface contact between concrete and strands is also observed to have notable effects on the level of the imposed stresses along the end segment of the specimens.

Finally, the numerical simulations of a family of rectangular beam-columns, confined with No.3 closed stirrups spaced at 3.00 in. on center and pretensioned using 0.70-in. diameter strands, indicate that the transfer length of 0.70-in. diameter strands is anticipated to be between 24 and 42 in. from the member ends. Based on the finite element simulation, the spacing of the strands does not significantly affect the compressive strains of the specimens. However, the number of the strands and

consequently the magnitude of pretensioning affect the pretensioning path (transfer length mechanism) within the end zone of the member. The obtained boundary values for transfer length are less than or equal to 60 times the strand diameter limit recommended. Additionally, the range of the analytical results hosts the transfer length of 31 in. for 0.70-in. diameter strands recommended by Morcous et. al. (Morcous, Hanna, & Tadros, 2010).

Thus, it is concluded that 0.7-in. diameter strands can be potentially spaced at reduced spacing of 2-in. on center under certain conditions including minimum compressive strength of 10,000 psi at the time of release. When the project economy allows for high strength concrete mixes, the use of 0.7-in. diameter strands may be considered as a measure for reducing the cost of pretensioning due to the efficiency and reduction of number of strands.

Another objectives of this research was the comparative analysis of various end zone details in minimizing the tensile cracking of concrete immediately after the release of pretensioned strands, including: AASHTO LRFD, Nebraska, IDOT and Modified IDOT-AASHTO end zone reinforcing details. For the analytical purposes of this research, a typical AASHTO-PCI bulb-tee girder was numerically analyzed for the comparative study of the response in the end zone with different end zone reinforcing details immediately after the release of the pretensioned strands. As the result, the following observations were made:

1. The response of the specimens with the AASHTO LRFD and Nebraska end zone reinforcing details were approximately the same immediately after the release of identical pretensioning.

2. The Nebraska detail required the reinforcing bars to be spaced at 6 in. on center versus 4 in. spacing required by AASHTO LRFD specifications, minimizing the congestion of rebars along the member end zone.
3. The analytical results indicated that the vertical tensile stresses are maximum near the member end face and significantly decrease farther away from the end face. This observation is consistent with the previous findings by Tadros et. al. (Tadros, Tuan, Yehia, & Jongpitaksseel, 2004).
4. The IDOT end zone detail significantly reduced the level of maximum tensile stresses in the rebar by over 20%.
5. Addition of the top and bottom end plates to the end zone rebars required by AASHTO LRFD was observed to result in notable reduction in the magnitude of the tensile stresses in the end zone rebar by approximately 10%.
6. The magnitude of tensile stresses were observed to be at the maximum level in the first end zone rebar near the end face of the girder. Thereafter, the magnitude of the axial stresses sharply decreases. This observation is consistent with the recommendations of NCHRP Report No. 654 (Tadros, Badie, & Tuan, 2010).
7. The numerical results pertaining to the typical AASHTO/PCI bulb-tee girder indicated that magnitude of the tensile stresses in the end zone reinforcing bars was observed to be well below the allowable limit of 20.0 ksi by AASHTO LRFD specifications.
8. The linear-elastic models reported approximately the same magnitude of axial tension (8 ksi \pm) in the AASHTO LRFD, Nebraska, IDOT and Modified IDOT-

AASHTO end zone reinforcing bars, notably different from those resulted by the nonlinear simulations. This indicates the importance of nonlinear simulation of concrete behavior due to potential tensile cracking and subsequent material softening immediately after the release of the pretensioned strands. Otherwise, linear-elastic analysis may grossly under-estimate the magnitude tensile stresses in the end zone rebar.

9. Significant planar shear were observed along the interface between the web and the bottom flange. This is anticipated to be caused due to the transfer of the pretensioning force congested in the bottom flange towards the relative narrow web walls.
10. The end zone stresses have a three-dimensional nature which cannot be fully captured by the conventional elastic beam theory.
11. The numerical investigation of a typical AASHTO-PCI bulb-tee girder indicates that the Nebraska detail may offer an optimum remedy for end zone cracking of pretensioned girders based on the following:
 - a. Placing larger magnitude of end zone rebar near the member end face extending towards $h/8$, where the maximum level of tensile stresses are anticipated in the rebar
 - b. No increase in the overall amount of end zone rebar required by the current AASHTO LRFD specifications
 - c. Larger spacing between the end zone rebar in comparison with the AASHTO LRFD scheme, reducing the congestion of reinforcement within the member end zone

- d. No significant change to the current specifications except the revision of the spacing requirements

The final section of this research included the monitoring of eight super-girders during the pretensioning process in the casting yard. All eight girders were production members as part of the Alaskan Way Viaduct project in the state of Washington. The field observations indicated that the all eight specimens responded to the release pretensioning similar to other I-girders commonly used in practice. Additionally, all eight specimens experienced end zone cracking immediately after the release of pretensioning, including a typical network of spalling and bursting-splitting cracks along the web height and the web-bottom flange interface, respectively.

The most severe tensile stresses were measured along the web-bottom flange interface. Similar observations were made at both dead and live ends of the girder. These cracks were generally observed to be originated near the end face extending approximately 2 ft towards the mid-span of the member. The maximum tensile stresses in the end zone bars were measured to be 20.2 ksi and 37.7 ksi in along the web height and the web-bottom flange interface, respectively. The spalling stresses (20.2 ksi max.) in the web height were observed to conform to the allowable stress recommended by AASHTO LRFD specifications. However, the maximum bursting-splitting stresses (37.7 ksi max.) were measured to be approximately 1.89 times the tensile stress allowable stress.

Additionally, the experimental data indicated that the pretensioning transfer occurs along a parabolic path instead of the linearized transfer length prescribed by AASHTO LRFD. It was observed that 34% of the pretensioning force is transferred to concrete

body at the distance 6 in. from the member ends. Subsequently, 80% and finally 100% of the transfer occur at 18 in. and 36 in. from the member ends, respectively. Therefore, linearization of transfer length as recommended by AASHTO LRFD and widely assumed in the current practice may result in significant under-estimation of the tensile stresses developed in the member end zone immediately after the release of pretensioning.

Finally, the experimental observations indicated that the axial tensile stresses in the web tie bars vary from minimum of 0.6 ksi to maximum of 1.3 ksi immediately after the release of prestressed strands. Therefore, it was concluded the web tie bars do not significantly contribute to resistance against lateral stresses.

Finally, in addition to nonlinear finite element simulation of the specimens, three closed-form solutions have been used to analyze the end zone stresses immediately after the release of pretensioning: Gregly-Sozen method, strut-&-tie procedure and shear-friction analogy. The later method is proposed based on the findings of this research, indicating that the significant planar shear transfer occurs from the bottom flange towards the web. The concentration of the straight strands in the bottom flange in combination with the relatively narrow web walls is anticipated to cause a shear lag at the web-bottom flange interface, which can potentially cause cracking along the member end zone.

It is observed that:

1. The maximum tensile stress (20.2 ksi) by the nonlinear finite element solution corresponds to the average of the experimental data.
2. Strut-&-tie procedure results in a maximum tensile stress in the end zone bars near the end face of the member, which corresponds to the corresponding maximum experimental measurement.

3. Gregly-Sozen method and shear-friction analogy result in similar maximum tensile stresses but at different heights along the member, 42 in. and 12-5/8" (web-bottom flange interface), respectively.
4. The Gregly-Sozen method is observed to be overestimate the magnitude and the vertical location of the maximum tensile stress in the end zone rebar, and
5. The maximum tensile stress estimated by shear-friction analogy is observed to conform to the range of experimental observations.

As shown in this research, the current AASHTO LRFD Specifications for the design of bursting reinforcement may not adequately address the shear-lag phenomenon along the web-bottom flange interface. Therefore, the proposed closed-form solution based on shear friction theory may offers another alternative for the approximation of the bursting-splitting cracks along the web-bottom flange interface.

7.2. Recommendations for Future Research

The following includes the recommendations for future research:

1. The friction contact formulation utilized in the extrusion technique is an approximation of the combined contributions by Hoyer's effect and mechanical interlocking. A more precise contact simulation may include parameters that not only control the Hoyer's effect and mechanical interlocking, but also accounts for the cohesion between the strand and concrete host. Such formulation should be able to function in two steps as follows:
 - a. First, only cohesion only is activated.
 - b. Once the cohesion is overcome, the combined effect of Hoyer's' effect and mechanical interlocking become activated.

2. It is observed that the finite element simulations of this research are not able to capture cracking due to shear-friction. Thus, the constitutive formulations for modeling concrete need be enhanced in order to be able to address the shear-friction cracking and subsequent stress redistribution to the neighboring zones as well as embedded elements (i.e., rebar).
3. The findings of this research indicate more sever bursting-splitting stresses along the web-bottom flange interface of I-girders versus the spalling stresses along the web height as conventionally addresses by the current specifications. Therefore, more experimental observation of pretensioned concrete members is recommended for validation of this observation.
4. This research is focused on the behavior of pretensioned concrete girders immediately after the release of prestressing. Additionally, the members can be analytically evaluated and experimentally monitored to investigate the effect of the following factors on the end zone comprised after the release and over the anticipated service life (75 years):
 - a. Temperature, creep and shrinkage
 - b. Structural configurations (e.g., continuous arrangement at multi-span bridges, application of deck slab and super-imposed composite dead loads)
 - c. Cyclic loading due to transient loads (i.e., construction loads, regular traffic, permit vehicles, wind, etc.)
 - d. Member behavior at failure

References

- AASHTO LRFD. (2010). *AASHTO LRFD Bridge Design Specifications* (5th ed.). Washington, D.C., USA: American Association of State Highway and Transportation Officials.
- ABAQUS. (2010). *ABAQUS Documentation*. Providence, RI, USA: Dassault Systèmes Simulia Corp.
- ACI. (2008). *Building Code Requirements for Structural Concrete (AC 318-09) and Commentary (ACI 318R-09)*. Farmington Hills, MI: American Concrete Institute.
- Akhnoukh, A. K. (2008). *Development of High Performance Precast/Prestressed Bridge Girders*. Lincoln: University of Nebraska (Doctoral Dissertation) .
- Ayoub, A., & Filippou, F. (2010, April). Finite-Element Model for Pretensioned Prestressed Concrete Girders. *Journal of Structural Engineering* , 401-409.
- Carrasquillo, R. L., Nilson, A. H., & Slate, F. O. (1981). Properties of High Strength Concrete Subject to Short Term Loads. *ACI Journal* , Vol. 78, No. 3 (May-June), 171-178.
- Chen, W. F. (2007). *Plasticity in Reinforced Concrete*. New York: J. Ross Publishing.
- Chen, W. F., & Han, D. J. (1988). *Plasticity for Structural Engineers*. New York: J. Ross Publishing.
- Chinn, J., & Zimmerman, R. M. (1965). *Behavior of Plain Concrete under Various High Triaxial Compression Loading Conditions*. Kirtland Air Force Base, Albuquerque, New Mexico: Air Force Weapons Lab.
- Collins, M. P., & Mitchell, D. (1997). *Prestressed Concrete Structures*. Toronto, Ontario, Canada: Response Publications.

- Crispino, E. D. (2007). *Anchorage Zone Design for Pretensioned Bulb-Tee Bridge Girders in Virginia*. Blacksburg: Virginia Tech.
- Crispino, E. D., Cousins, T. E., & Roberts-Wollmann, C. L. (2009). *Anchorage Zone Design for Pretensioned Precast Bulb-T Bridge Girders in Virginia*. Virginia Polytechnic Institute & State University, Department of Civil and Environmental Engineering. Richmond: Virginia Transportation Research Council.
- CTC. (2010). Concrete Technology Corporation. Olympia, Washington, U.S.A.
- Gergley, P., & Sozen, M. A. (1967). Design of Anchorage-Zone Reinforcement in Prestressed Concrete Beams. *PCI Journal* , Vol. 12, No.2, 63-75.
- Kaewunruen, S., & Remennikov, A. (2006). Nonlinear Finite Element Modeling of Railway Prestressed Concrete Sleeper. *10th East Asia-Pacific Conference on Structural Engineering and Construction; Real Structures: Bridges & Tall Buildings'*; pp. 323-328, 4.
- Kannel, J., French, K., & Stolarski, H. (1997). Release Methodology of Strands to Reduce End Zone Cracking in Pretensioned Concrete Girders. *PCI Journal* , 42 (1), 42-54.
- Koyuncu, Y., Birgul, R., Ahlborn, T. M., & Aktan, H. M. (2003). Identifying Causes for Distress in Prestressed Concrete (PC). *Proceedings of TRB 2003 Annual Meeting*. Washington, D.C.: Transportation Research Board.
- Kupfer, H., Hilsdorf, H. K., & Rusch, H. (1969). Behavior of Concrete Under Biaxial Stresses. *ACI Journal* 66(8) , 656-666.
- Lee, J., & Fenves, G. L. (1998). Plastic-Damage Model for Cyclic Loading of Concrete Structures. *Journal of Engineering Mechanics* (August), 892-900.

- Li, Q., & Ansari, F. (1999, January). Mechanics of Damage and Constitutive Relationships for High-Strength Concrete in Triaxial Compression. *Journal of Engineering Mechanics* , pp. 1-9.
- Lubliner, J., Oliver, J., & Onate, E. (1990). A Plastic Damage Model for Concrete. *International Journal of Solids and Structures* , 25 (3), 299-326.
- Marshall, W. T., & Mattock, A. H. (1962). Control of Horizontal Cracking in the End of Pretensioned Prestressed Concrete Girders. *PCI Journal* , 56-74.
- McHugh, P. (2007). *Non-Linear Finite Element Analysis: Finite Element Solution Schemes I & II*. Galway, Ireland: P. McHugh.
- Mirza, J. F., & Tawfik, M. E. (1978, March-April). End Cracking in Prestressed Members During Detensioning. *PCI Journal* , 66-79.
- Mitchell, D., Cook, W. D., Khan, A. A., & Tham, T. (1993). Influence of High Strength Concrete on Transfer and Development Length of Pretensioning Strand. *PCI Journal*, 14(4) , 62-74.
- Morcous, G., & Tadros, M. K. (2011). *Impact of 0.7 Inch Diameter Strands on NU I-Girders*. The University of Nebraska. Lincoln: Nebraska Department of Roads (NDOR).
- Morcous, G., Hanna, K., & Tadros, M. K. (2010). Transfer and Development Length of 0.7-in.(17.8 mm) Diameter Strands in Pretensioned Concrete Bridge Girders. *HPC Bridge Views* (64).
- Nilson, A. H. (1987). *Design of Prestressed Concrete*. New York: John Wiley and Sons.
- O'Callaghan, M. R., & Bayrak, O. (2008). *Tensile Stresses in the End Regions of Pretensioned I-Beams at Release*. Austin: University of Texas at Austin.

- Palaniswamy, R., & Shah, S. P. (1974). Fracture and Stress-Strain Relationship of Concrete Under Triaxial Compression. *Journal of Structural Division, ASCE* 100(ST5) , 901-916.
- PCI. (2003). *PCI Bridge Design Manual: Precast Prestressed Concrete* (5th ed.). Chicago, IL: Precast/Prestressed Concrete Institute.
- Piyasena, R. (2002). *Crack Spacing, Crack Width and Tension Stiffening Effect in Reinforced Concrete Beams and One-Way Slabs*. Doctor of Philosophy Dissertation, Griffith University - Gold Coast Campus, School of Engineering.
- Popovics, S. (1970). A Review of Stress-Strain Relationships for Concrete. *ACI Journal* , Vol. 67 (No. 3), pp.243-248.
- Prakhya, G. K., & Morley, C. T. (1990). Tension-Stiffening and Moment-Curvature Relations of Reinforced Concrete Elements. *ACI Structural Journal* , Vol. 87 (No. 5), pp. 597-605.
- Rabczuk, T., & Eibl, J. (2004). Numerical Analysis of Prestressed Concrete Beams Using A Coupled Element Free Galerkin/Finite Element Approach. *International Journal of Solids and Structures* , 1061-1080.
- Reinhardt, H. W. (1984). Fracture Mechanics of an Elastic Softening Material Like Concrete. *Heron* , 29 (2), 1-29.
- Russell, B. W., & Burns, N. H. (1996, Sept.-Oct.). Measured Transfer Lengths of 0.5 in and 0.6 in. *PCI Journal* , 44-63.
- Russell, H. G., Volz, J. S., & Bruce, R. N. (1997). *Optimized Sections for High-Strength Concrete Bridge*. U.S. Department of Transportation. Washington: FHWA.

- Schuler, G. (2009). Producer's Experience with 10,000 psi Concrete and 0.7-in. Diameter Strands. *HPC Bridge Views* (54).
- Shah, S. P., & Chandra, S. (1968). Critical Stress Volume Change and Microcracking of Concrete. *ACI Journal* 65(9) , 770-781.
- Stephen, E. (2006). *Simulation of the Long-Term Behavior of Precast/Prestressed Concrete Bridges*. Master of Science Thesis, University of Cincinnati, Department of Civil and Environmental Engineering.
- Tadors, M. K., Tuan, C. Y., Yehia, S. A., & Jongpitaksseel, N. (2004). End Zone Reinforcement for Pretensioned Concrete Girders. *PCI Journal* , 68-82.
- Tadros, M. K., Badie, S. S., & Tuan, C. (2010). *NCHRP Report 654: Evaluation and Repair Procedures for Precast/Prestressed Concrete Girders with Longitudinal Cracking in the Web*. National Cooperative Highway Research Program. Washington, D.C.: Transportation Research Board.
- Texas Measurements, Inc. (2010). College Station, Texas, USA.
- Thorenfeldt, E., Tomaszewicz, A., & Jensen, J. J. (June 1987). Mechanical Properties of High-Strength Concrete and Application in Design. In T. Tapir (Ed.), *Proceedings of the Symposium "Utilization of High Strength Concrete"*, (pp. 149-159). Stavanger, Norway.
- Ujil, A. J. (1983). *Tensile Stresses in the Transimssion Zones of Hollow-Core Slabs Prestressed with Pretensioned Strands*. Stevinlaboratory. Delft: Technische Hogeschool Delft.
- Vadivelu, J. (2009). *Impact of Larger Diameter Strands on AASHTO/PCI Bulb-Tees*. Knoxville: The University of Tennessee.

Vishay Precision Group. (2010). Malvern, PA, USA.

WSDOT. (2011). *SR 99 - Alaskan Way Viaduct and Seawall Replacement*. Retrieved 7 5,

2011, from Washington State Department of Transportation:

<http://www.wsdot.wa.gov/projects/Viaduct/>

Yang, T. Y. (1986). *Finite Element Strucural Analysis*. Englewood Cliffs, New Jersey:

Prentice-Hall.

Appendix A

Sample Finite Element Code (ABAQUS) for 6"x6" Rectangular Beams Pretensioned with One Concentric or Eccentric 0.6-in. Diameter Strand Based on Extrusion Technique

*Heading

RCBM 6x6x96 with one concentric strand, linear response, max slippage (u=0.7), and prestressing + remeshed longitudinally (scheme 1)!!!

** Job name: RCBM_6x6x96_1S_con_blkless_SlipMax_r2 Model name:

RCBM_6x6x96_1S_con_blkless_SlipMax_r2

*Preprint, echo=NO, model=NO, history=NO, contact=NO

**

** PARTS

**

*Part, name=Beam-1

*Node

1,	-0.5,	0.5,	48.
2,	-0.5,	-0.5,	48.
3,	-0.5,	-0.5,	0.
4,	-0.5,	0.5,	0.
5,	-3.,	-0.5,	48.
6,	-3.,	-0.5,	0.
7,	-3.,	0.5,	0.
8,	-3.,	0.5,	48.
9,	0.5,	-0.5,	48.
10,	0.5,	0.5,	48.

...

*Element, type=C3D8

1,	162,	701,	1337,	639,	1,	33,	577,	96
2,	701,	164,	670,	1337,	33,	2,	34,	577
3,	639,	1337,	1338,	640,	96,	577,	578,	95
4,	1337,	670,	671,	1338,	577,	34,	35,	578
5,	640,	1338,	1339,	641,	95,	578,	579,	94
6,	1338,	671,	672,	1339,	578,	35,	36,	579
7,	641,	1339,	1340,	642,	94,	579,	580,	93
8,	1339,	672,	673,	1340,	579,	36,	37,	580
9,	642,	1340,	1341,	643,	93,	580,	581,	92
10,	1340,	673,	674,	1341,	580,	37,	38,	581

...

*Nset, nset=_PickedSet10, internal, generate

1, 1584, 1

*Elset, elset=_PickedSet10, internal, generate

1, 1024, 1

*Nset, nset=Beam-1, generate

1, 1584, 1

*Elset, elset=Beam-1, generate

1, 1024, 1

*Elset, elset=_Beam-1-Host_S2, internal

1, 2, 3, 4, 5, 6, 7, 8, 9, 10, 11, 12, 13, 14, 15, 16
17, 18, 19, 20, 21, 22, 23, 24, 25, 26, 27, 28, 29, 30, 31, 32
33, 34, 35, 36, 37, 38, 39, 40, 41, 42, 43, 44, 45, 46, 47, 48

49, 50, 51, 52, 53, 54, 55, 56, 57, 58, 59, 60, 61, 62, 63, 64
 129, 130, 131, 132, 133, 134, 135, 136, 137, 138, 139, 140, 141, 142, 143, 144
 145, 146, 147, 148, 149, 150, 151, 152, 153, 154, 155, 156, 157, 158, 159, 160
 161, 162, 163, 164, 165, 166, 167, 168, 169, 170, 171, 172, 173, 174, 175, 176
 177, 178, 179, 180, 181, 182, 183, 184, 185, 186, 187, 188, 189, 190, 191, 192
 641, 642, 643, 644, 645, 646, 647, 648, 649, 650, 651, 652, 653, 654, 655, 656
 657, 658, 659, 660, 661, 662, 663, 664, 665, 666, 667, 668, 669, 670, 671, 672
 673, 674, 675, 676, 677, 678, 679, 680, 681, 682, 683, 684, 685, 686, 687, 688
 689, 690, 691, 692, 693, 694, 695, 696, 697, 698, 699, 700, 701, 702, 703, 704
 *Elset, elset=_Beam-1-Host_S1, internal, generate
 577, 640, 1
 *Surface, type=ELEMENT, name=Beam-1-Host
 _Beam-1-Host_S2, S2
 _Beam-1-Host_S1, S1
 *Elset, elset=_Beam-1-Slave_S5, internal
 289, 290, 291, 292, 293, 294, 295, 296, 297, 298, 299, 300, 301, 302, 303, 304
 305, 306, 307, 308, 309, 310, 311, 312, 313, 314, 315, 316, 317, 318, 319, 320
 353, 354, 355, 356, 357, 358, 359, 360, 361, 362, 363, 364, 365, 366, 367, 368
 369, 370, 371, 372, 373, 374, 375, 376, 377, 378, 379, 380, 381, 382, 383, 384
 *Elset, elset=_Beam-1-Slave_S2, internal
 513, 514, 515, 516, 517, 518, 519, 520, 521, 522, 523, 524, 525, 526, 527, 528
 529, 530, 531, 532, 533, 534, 535, 536, 537, 538, 539, 540, 541, 542, 543, 544
 545, 546, 547, 548, 549, 550, 551, 552, 553, 554, 555, 556, 557, 558, 559, 560
 561, 562, 563, 564, 565, 566, 567, 568, 569, 570, 571, 572, 573, 574, 575, 576
 769, 770, 771, 772, 773, 774, 775, 776, 777, 778, 779, 780, 781, 782, 783, 784
 785, 786, 787, 788, 789, 790, 791, 792, 793, 794, 795, 796, 797, 798, 799, 800
 801, 802, 803, 804, 805, 806, 807, 808, 809, 810, 811, 812, 813, 814, 815, 816
 817, 818, 819, 820, 821, 822, 823, 824, 825, 826, 827, 828, 829, 830, 831, 832
 *Surface, type=ELEMENT, name=Beam-1-Slave
 _Beam-1-Slave_S5, S5
 _Beam-1-Slave_S2, S2
 *Elset, elset=_Beam-1-BC_S6, internal
 257, 289, 321, 353, 513, 545, 577, 609, 769, 801, 833, 865, 897, 929, 961, 993
 *Elset, elset=_Beam-1-BC_S5, internal
 63, 64, 127, 128, 191, 192, 255, 256, 703, 704, 767, 768
 *Elset, elset=_Beam-1-BC_S2, internal, generate
 385, 388, 1
 *Surface, type=ELEMENT, name=Beam-1-BC
 _Beam-1-BC_S6, S6
 _Beam-1-BC_S5, S5
 _Beam-1-BC_S2, S2
 ** Section: Beam
 *Solid Section, elset=_PickedSet10, material=Conc_5800psi
 1.,
 *End Part
 **

*Part, name=Beam-2

*Node

1,	0.212132037,	0.212132037,	48.
2,	0.212132037,	0.212132037,	0.
3,	0.300000012,	0.,	0.
4,	0.300000012,	0.,	48.
5,	0.5,	0.5,	0.
6,	0.5,	0.,	0.
7,	0.5,	0.,	48.
8,	0.5,	0.5,	48.
9,	-0.5,	0.,	48.
10,	-0.5,	0.,	0.

...

*Element, type=C3D8

1,	8, 125, 126,	7, 1, 33, 94,	4
2,	125, 124, 127, 126,	33, 34, 93,	94
3,	124, 123, 128, 127,	34, 35, 92,	93
4,	123, 122, 129, 128,	35, 36, 91,	92
5,	122, 121, 130, 129,	36, 37, 90,	91
6,	121, 120, 131, 130,	37, 38, 89,	90
7,	120, 119, 132, 131,	38, 39, 88,	89
8,	119, 118, 133, 132,	39, 40, 87,	88
9,	118, 117, 134, 133,	40, 41, 86,	87
10,	117, 116, 135, 134,	41, 42, 85,	86

...

*Nset, nset=_PickedSet15, internal, generate

1, 528, 1

*Elset, elset=_PickedSet15, internal, generate

1, 256, 1

*Nset, nset=Beam-2, generate

1, 528, 1

*Elset, elset=Beam-2, generate

1, 256, 1

*Elset, elset=_Beam-2-Host_S1, internal, generate

33, 64, 1

*Elset, elset=_Beam-2-Host_S2, internal

1, 2, 3, 4, 5, 6, 7, 8, 9, 10, 11, 12, 13, 14, 15, 16
17, 18, 19, 20, 21, 22, 23, 24, 25, 26, 27, 28, 29, 30, 31, 32
65, 66, 67, 68, 69, 70, 71, 72, 73, 74, 75, 76, 77, 78, 79, 80
81, 82, 83, 84, 85, 86, 87, 88, 89, 90, 91, 92, 93, 94, 95, 96
97, 98, 99, 100, 101, 102, 103, 104, 105, 106, 107, 108, 109, 110, 111, 112
113, 114, 115, 116, 117, 118, 119, 120, 121, 122, 123, 124, 125, 126, 127, 128
129, 130, 131, 132, 133, 134, 135, 136, 137, 138, 139, 140, 141, 142, 143, 144
145, 146, 147, 148, 149, 150, 151, 152, 153, 154, 155, 156, 157, 158, 159, 160
193, 194, 195, 196, 197, 198, 199, 200, 201, 202, 203, 204, 205, 206, 207, 208
209, 210, 211, 212, 213, 214, 215, 216, 217, 218, 219, 220, 221, 222, 223, 224

*Elset, elset=_Beam-2-Host_S4, internal
 161, 162, 163, 164, 165, 166, 167, 168, 169, 170, 171, 172, 173, 174, 175, 176
 177, 178, 179, 180, 181, 182, 183, 184, 185, 186, 187, 188, 189, 190, 191, 192
 225, 226, 227, 228, 229, 230, 231, 232, 233, 234, 235, 236, 237, 238, 239, 240
 241, 242, 243, 244, 245, 246, 247, 248, 249, 250, 251, 252, 253, 254, 255, 256
 *Surface, type=ELEMENT, name=Beam-2-Host
 _Beam-2-Host_S1, S1
 _Beam-2-Host_S2, S2
 _Beam-2-Host_S4, S4
 *Elset, elset=_Beam-2-Slave_S1, internal
 1, 2, 3, 4, 5, 6, 7, 8, 9, 10, 11, 12, 13, 14, 15, 16
 17, 18, 19, 20, 21, 22, 23, 24, 25, 26, 27, 28, 29, 30, 31, 32
 65, 66, 67, 68, 69, 70, 71, 72, 73, 74, 75, 76, 77, 78, 79, 80
 81, 82, 83, 84, 85, 86, 87, 88, 89, 90, 91, 92, 93, 94, 95, 96
 97, 98, 99, 100, 101, 102, 103, 104, 105, 106, 107, 108, 109, 110, 111, 112
 113, 114, 115, 116, 117, 118, 119, 120, 121, 122, 123, 124, 125, 126, 127, 128
 129, 130, 131, 132, 133, 134, 135, 136, 137, 138, 139, 140, 141, 142, 143, 144
 145, 146, 147, 148, 149, 150, 151, 152, 153, 154, 155, 156, 157, 158, 159, 160
 193, 194, 195, 196, 197, 198, 199, 200, 201, 202, 203, 204, 205, 206, 207, 208
 209, 210, 211, 212, 213, 214, 215, 216, 217, 218, 219, 220, 221, 222, 223, 224
 *Elset, elset=_Beam-2-Slave_S2, internal, generate
 33, 64, 1
 *Elset, elset=_Beam-2-Slave_S6, internal
 161, 162, 163, 164, 165, 166, 167, 168, 169, 170, 171, 172, 173, 174, 175, 176
 177, 178, 179, 180, 181, 182, 183, 184, 185, 186, 187, 188, 189, 190, 191, 192
 225, 226, 227, 228, 229, 230, 231, 232, 233, 234, 235, 236, 237, 238, 239, 240
 241, 242, 243, 244, 245, 246, 247, 248, 249, 250, 251, 252, 253, 254, 255, 256
 *Surface, type=ELEMENT, name=Beam-2-Slave
 _Beam-2-Slave_S1, S1
 _Beam-2-Slave_S2, S2
 _Beam-2-Slave_S6, S6
 *Elset, elset=_Beam-2-BC_S4, internal
 32, 64, 128, 224
 *Elset, elset=_Beam-2-BC_S5, internal
 256,
 *Elset, elset=_Beam-2-BC_S3, internal
 161,
 *Elset, elset=_Beam-2-BC_S6, internal
 65, 129
 *Surface, type=ELEMENT, name=Beam-2-BC
 _Beam-2-BC_S4, S4
 _Beam-2-BC_S5, S5
 _Beam-2-BC_S6, S6
 _Beam-2-BC_S3, S3
 ** Section: Beam
 *Solid Section, elset=_PickedSet15, material=Conc_5800psi

```

1.,
*End Part
**
*Part, name=Bed
*Node
  1,    3.,    -1.,    50.
  2,    3.,    -1.,    48.
  3,    5.,    -1.,    48.
  4,    5.,    -1.,    50.
  5,    3.,    0.,    48.
  6,    5.,    0.,    48.
  7,    5.,    0.,    50.
  8,    3.,    0.,    50.
  9,    3.,    0.,    0.
 10,    5.,    0.,    0.
...
*Element, type=C3D8
1, 8, 5, 6, 7, 1, 2, 3, 4
2, 12, 129, 130, 11, 9, 37, 98, 10
3, 129, 128, 131, 130, 37, 38, 97, 98
4, 128, 127, 132, 131, 38, 39, 96, 97
5, 127, 126, 133, 132, 39, 40, 95, 96
6, 126, 125, 134, 133, 40, 41, 94, 95
7, 125, 124, 135, 134, 41, 42, 93, 94
8, 124, 123, 136, 135, 42, 43, 92, 93
9, 123, 122, 137, 136, 43, 44, 91, 92
10, 122, 121, 138, 137, 44, 45, 90, 91
...
*Nset, nset=_PickedSet2, internal, generate
  1, 408, 1
*Elset, elset=_PickedSet2, internal, generate
  1, 165, 1
*Nset, nset=Bed, generate
  1, 408, 1
*Elset, elset=Bed, generate
  1, 165, 1
*Elset, elset=_Bed-Host_S1, internal
  67, 68, 69, 70, 71, 72, 73, 74, 75, 76, 77, 78, 79, 80, 81, 82
  83, 84, 85, 86, 87, 88, 89, 90, 91, 92, 93, 94, 95, 96, 97, 98
 101, 102, 103, 104, 105, 106, 107, 108, 109, 110, 111, 112, 113, 114, 115, 116
 117, 118, 119, 120, 121, 122, 123, 124, 125, 126, 127, 128, 129, 130, 131, 132
*Elset, elset=_Bed-Host_S6, internal, generate
 133, 164, 1
*Surface, type=ELEMENT, name=Bed-Host
  _Bed-Host_S1, S1
  _Bed-Host_S6, S6

```

```

*Elset, elset=_Bed-BC-bot_S2, internal
  1, 34, 35, 36, 37, 38, 39, 40, 41, 42, 43, 44, 45, 46, 47, 48
  49, 50, 51, 52, 53, 54, 55, 56, 57, 58, 59, 60, 61, 62, 63, 64
  65, 67, 68, 69, 70, 71, 72, 73, 74, 75, 76, 77, 78, 79, 80, 81
  82, 83, 84, 85, 86, 87, 88, 89, 90, 91, 92, 93, 94, 95, 96, 97
  98, 101, 102, 103, 104, 105, 106, 107, 108, 109, 110, 111, 112, 113, 114, 115
  116, 117, 118, 119, 120, 121, 122, 123, 124, 125, 126, 127, 128, 129, 130, 131
  132,
*Elset, elset=_Bed-BC-bot_S4, internal, generate
  133, 164, 1
*Elset, elset=_Bed-BC-bot_S1, internal
  2, 3, 4, 5, 6, 7, 8, 9, 10, 11, 12, 13, 14, 15, 16, 17
  18, 19, 20, 21, 22, 23, 24, 25, 26, 27, 28, 29, 30, 31, 32, 33
  66, 99, 100
*Elset, elset=_Bed-BC-bot_S3, internal
  165,
*Surface, type=ELEMENT, name=Bed-BC-bot
  _Bed-BC-bot_S2, S2
  _Bed-BC-bot_S4, S4
  _Bed-BC-bot_S1, S1
  _Bed-BC-bot_S3, S3
*Elset, elset=_Bed-BC-side_S6, internal
  2, 34
*Elset, elset=_Bed-BC-side_S4, internal
  98, 132
*Elset, elset=_Bed-BC-side_S5, internal
  164,
*Surface, type=ELEMENT, name=Bed-BC-side
  _Bed-BC-side_S6, S6
  _Bed-BC-side_S4, S4
  _Bed-BC-side_S5, S5
** Section: Bed
*Solid Section, elset=_PickedSet2, material=Steel_36ksi
  1.,
*End Part
**
*Part, name=Strand
*Node
  1, -0.300000012, 0., 12.
  2, 0., 0.300000012, 12.
  3, 0., 0.300000012, 0.
  4, -0.300000012, 0., 0.
  5, 0., 0., 12.
  6, 0., 0., 0.
  7, 0., -0.300000012, 12.
  8, 0., -0.300000012, 0.

```

```

9,      0.,      0.,      18.
10,     0., -0.300000012,    18.
...
*Element, type=C3D8
1, 293, 294, 676, 672, 49, 50, 285, 284
2, 294, 295, 677, 676, 50, 51, 286, 285
3, 295, 296, 678, 677, 51, 52, 287, 286
4, 296, 55, 291, 678, 52, 1, 53, 287
5, 297, 298, 669, 668, 293, 294, 676, 672
6, 298, 299, 670, 669, 294, 295, 677, 676
7, 299, 300, 671, 670, 295, 296, 678, 677
8, 300, 54, 292, 671, 296, 55, 291, 678
9, 291, 63, 307, 678, 53, 2, 56, 287
10, 678, 307, 308, 677, 287, 56, 57, 286
...
*Nset, nset=_PickedSet9, internal, generate
1, 875, 1
*Elset, elset=_PickedSet9, internal, generate
1, 680, 1
*Nset, nset=Strand, generate
1, 875, 1
*Elset, elset=Strand, generate
1, 680, 1
*Nset, nset=PS-1
31, 32, 33, 34, 35, 36, 37, 38, 39, 40, 215, 216, 217, 218, 219, 227
228, 229, 230, 231, 232, 233, 234, 235, 236, 237, 238, 239, 240, 241, 242, 243
247, 248, 249, 250, 251, 252, 253, 254, 255, 256, 257, 258, 259, 260, 261, 262
266, 555, 556, 574, 575, 576, 577, 578, 579, 580, 581, 582, 583, 584, 585, 586
587, 588, 589, 590, 591, 592, 602, 603, 604, 605, 606, 607, 608, 609, 610, 611
612, 613, 614, 615, 616, 617, 618, 619, 620, 621, 622, 623, 624, 625, 626, 627
640, 641, 642, 643, 644, 820, 821, 822, 823, 824, 825, 832, 833, 834, 835, 836
837, 838, 839, 840, 841, 842, 843, 856, 857, 858, 859, 860, 861
*Elset, elset=PS-1
481, 482, 483, 484, 485, 486, 487, 488, 489, 490, 491, 492, 493, 494, 495, 496
497, 498, 499, 500, 521, 522, 523, 524, 525, 526, 527, 528, 529, 530, 531, 532
533, 534, 535, 536, 537, 538, 539, 540, 541, 542, 543, 544, 545, 546, 547, 548
549, 550, 551, 552, 553, 554, 555, 556, 557, 558, 559, 560, 601, 602, 603, 604
605, 606, 607, 608, 609, 610, 611, 612, 613, 614, 615, 616, 617, 618, 619, 620
*Nset, nset=PS-2
26, 27, 28, 29, 30, 31, 32, 33, 34, 38, 192, 193, 194, 195, 196, 200
201, 202, 206, 207, 208, 209, 210, 211, 212, 213, 214, 215, 216, 217, 218, 219
220, 221, 222, 223, 224, 225, 226, 227, 228, 229, 247, 248, 252, 261, 263, 264
265, 525, 526, 536, 537, 538, 539, 540, 541, 542, 543, 544, 545, 546, 547, 548
549, 550, 551, 552, 553, 554, 555, 556, 563, 564, 565, 566, 567, 568, 569, 570
571, 572, 573, 574, 575, 611, 612, 624, 625, 628, 629, 630, 631, 632, 633, 634
635, 636, 637, 638, 639, 796, 797, 798, 799, 800, 801, 814, 815, 816, 817, 818

```

819, 844, 845, 846, 847, 848, 849, 850, 851, 852, 853, 854, 855

*Elset, elset=PS-2

401, 402, 403, 404, 405, 406, 407, 408, 409, 410, 411, 412, 413, 414, 415, 416
417, 418, 419, 420, 461, 462, 463, 464, 465, 466, 467, 468, 469, 470, 471, 472
473, 474, 475, 476, 477, 478, 479, 480, 561, 562, 563, 564, 565, 566, 567, 568
569, 570, 571, 572, 573, 574, 575, 576, 577, 578, 579, 580, 581, 582, 583, 584
585, 586, 587, 588, 589, 590, 591, 592, 593, 594, 595, 596, 597, 598, 599, 600

*Nset, nset=PS-3

21, 22, 23, 24, 25, 26, 27, 28, 29, 30, 162, 163, 164, 165, 166, 170
171, 172, 182, 183, 184, 185, 186, 187, 188, 189, 190, 191, 192, 193, 194, 195
196, 197, 198, 199, 200, 201, 202, 203, 204, 205, 209, 210, 211, 226, 244, 245
246, 472, 473, 483, 484, 503, 504, 508, 509, 510, 511, 512, 513, 514, 515, 516
517, 518, 519, 520, 521, 522, 523, 524, 525, 526, 527, 528, 529, 530, 531, 532
533, 534, 535, 536, 537, 541, 542, 569, 570, 593, 594, 595, 596, 597, 598, 599
600, 601, 645, 646, 647, 784, 785, 786, 787, 788, 789, 790, 791, 792, 793, 794
795, 826, 827, 828, 829, 830, 831, 862, 863, 864, 865, 866, 867

*Elset, elset=PS-3

361, 362, 363, 364, 365, 366, 367, 368, 369, 370, 371, 372, 373, 374, 375, 376
377, 378, 379, 380, 381, 382, 383, 384, 385, 386, 387, 388, 389, 390, 391, 392
393, 394, 395, 396, 397, 398, 399, 400, 501, 502, 503, 504, 505, 506, 507, 508
509, 510, 511, 512, 513, 514, 515, 516, 517, 518, 519, 520, 621, 622, 623, 624
625, 626, 627, 628, 629, 630, 631, 632, 633, 634, 635, 636, 637, 638, 639, 640

*Nset, nset=PS-4

15, 16, 18, 19, 20, 21, 22, 23, 24, 25, 133, 134, 135, 136, 137, 145
146, 147, 152, 153, 154, 155, 156, 157, 158, 159, 160, 161, 162, 163, 164, 165
166, 167, 168, 169, 170, 171, 172, 173, 174, 175, 179, 180, 181, 182, 183, 184
188, 420, 421, 433, 434, 453, 454, 455, 456, 457, 458, 459, 460, 461, 462, 463
464, 465, 466, 467, 468, 469, 470, 471, 472, 473, 474, 475, 476, 477, 478, 479
480, 481, 482, 483, 484, 494, 495, 496, 497, 498, 499, 500, 501, 502, 503, 504
511, 512, 560, 561, 562, 754, 755, 756, 757, 758, 759, 760, 761, 762, 763, 764
765, 772, 773, 774, 775, 776, 777, 808, 809, 810, 811, 812, 813

*Elset, elset=PS-4

261, 262, 263, 264, 265, 266, 267, 268, 269, 270, 271, 272, 273, 274, 275, 276
277, 278, 279, 280, 281, 282, 283, 284, 285, 286, 287, 288, 289, 290, 291, 292
293, 294, 295, 296, 297, 298, 299, 300, 321, 322, 323, 324, 325, 326, 327, 328
329, 330, 331, 332, 333, 334, 335, 336, 337, 338, 339, 340, 441, 442, 443, 444
445, 446, 447, 448, 449, 450, 451, 452, 453, 454, 455, 456, 457, 458, 459, 460

*Nset, nset=PS-5

9, 10, 12, 13, 15, 16, 17, 18, 19, 20, 99, 100, 101, 102, 103, 111
112, 113, 124, 125, 126, 127, 128, 129, 130, 131, 132, 133, 134, 135, 136, 137
138, 139, 140, 141, 142, 143, 144, 145, 146, 147, 149, 150, 151, 152, 153, 154
158, 365, 366, 378, 379, 403, 404, 405, 406, 407, 408, 409, 410, 411, 412, 413
414, 415, 416, 417, 418, 419, 420, 421, 422, 423, 424, 425, 426, 427, 428, 429
430, 431, 432, 433, 434, 444, 445, 446, 447, 448, 449, 450, 451, 452, 453, 454
464, 465, 557, 558, 559, 722, 723, 724, 725, 726, 727, 728, 729, 730, 731, 732
733, 748, 749, 750, 751, 752, 753, 802, 803, 804, 805, 806, 807

*Elset, elset=PS-5

161, 162, 163, 164, 165, 166, 167, 168, 169, 170, 171, 172, 173, 174, 175, 176
177, 178, 179, 180, 181, 182, 183, 184, 185, 186, 187, 188, 189, 190, 191, 192
193, 194, 195, 196, 197, 198, 199, 200, 241, 242, 243, 244, 245, 246, 247, 248
249, 250, 251, 252, 253, 254, 255, 256, 257, 258, 259, 260, 421, 422, 423, 424
425, 426, 427, 428, 429, 430, 431, 432, 433, 434, 435, 436, 437, 438, 439, 440

*Nset, nset=PS-6

1, 2, 5, 7, 9, 10, 11, 12, 13, 17, 53, 54, 55, 63, 64, 77
78, 86, 90, 91, 92, 93, 94, 95, 96, 97, 98, 99, 100, 101, 102, 103
104, 105, 106, 107, 108, 109, 110, 111, 112, 113, 127, 128, 132, 141, 176, 177
178, 291, 292, 337, 338, 348, 349, 350, 351, 352, 353, 354, 355, 356, 357, 358
359, 360, 361, 362, 363, 364, 365, 366, 367, 368, 369, 370, 371, 372, 373, 374
375, 376, 377, 378, 379, 409, 410, 425, 426, 485, 486, 487, 488, 489, 490, 491
492, 493, 505, 506, 507, 696, 697, 698, 699, 700, 701, 702, 703, 704, 705, 706
707, 766, 767, 768, 769, 770, 771, 778, 779, 780, 781, 782, 783

*Elset, elset=PS-6

81, 82, 83, 84, 85, 86, 87, 88, 89, 90, 91, 92, 93, 94, 95, 96
97, 98, 99, 100, 101, 102, 103, 104, 105, 106, 107, 108, 109, 110, 111, 112
113, 114, 115, 116, 117, 118, 119, 120, 301, 302, 303, 304, 305, 306, 307, 308
309, 310, 311, 312, 313, 314, 315, 316, 317, 318, 319, 320, 341, 342, 343, 344
345, 346, 347, 348, 349, 350, 351, 352, 353, 354, 355, 356, 357, 358, 359, 360

*Nset, nset=PS-7

1, 2, 3, 4, 5, 6, 7, 8, 11, 14, 46, 47, 48, 49, 50, 51
52, 53, 54, 55, 56, 57, 58, 59, 60, 61, 62, 63, 64, 65, 66, 67
68, 69, 70, 71, 72, 73, 74, 75, 76, 77, 78, 79, 80, 81, 82, 83
84, 85, 86, 87, 88, 89, 93, 97, 98, 107, 114, 115, 116, 117, 118, 119
120, 121, 122, 123, 148, 284, 285, 286, 287, 288, 289, 290, 291, 292, 293, 294
295, 296, 297, 298, 299, 300, 301, 302, 303, 304, 305, 306, 307, 308, 309, 310
311, 312, 313, 314, 315, 316, 317, 318, 319, 320, 321, 322, 323, 324, 325, 326
327, 328, 329, 330, 331, 332, 333, 334, 335, 336, 337, 338, 339, 340, 341, 342
343, 344, 345, 346, 347, 357, 358, 370, 371, 380, 381, 382, 383, 384, 385, 386
387, 388, 389, 390, 391, 392, 393, 394, 395, 396, 397, 398, 399, 400, 401, 402
435, 436, 437, 438, 439, 440, 441, 442, 443, 668, 669, 670, 671, 672, 673, 674
675, 676, 677, 678, 679, 680, 681, 682, 683, 684, 685, 686, 687, 688, 689, 690
691, 692, 693, 694, 695, 708, 709, 710, 711, 712, 713, 714, 715, 716, 717, 718
719, 720, 721, 734, 735, 736, 737, 738, 739, 740, 741, 742, 743, 744, 745, 746
747,

*Elset, elset=PS-7

1, 2, 3, 4, 5, 6, 7, 8, 9, 10, 11, 12, 13, 14, 15, 16
17, 18, 19, 20, 21, 22, 23, 24, 25, 26, 27, 28, 29, 30, 31, 32
33, 34, 35, 36, 37, 38, 39, 40, 41, 42, 43, 44, 45, 46, 47, 48
49, 50, 51, 52, 53, 54, 55, 56, 57, 58, 59, 60, 61, 62, 63, 64
65, 66, 67, 68, 69, 70, 71, 72, 73, 74, 75, 76, 77, 78, 79, 80
121, 122, 123, 124, 125, 126, 127, 128, 129, 130, 131, 132, 133, 134, 135, 136
137, 138, 139, 140, 141, 142, 143, 144, 145, 146, 147, 148, 149, 150, 151, 152
153, 154, 155, 156, 157, 158, 159, 160, 201, 202, 203, 204, 205, 206, 207, 208

209, 210, 211, 212, 213, 214, 215, 216, 217, 218, 219, 220, 221, 222, 223, 224
225, 226, 227, 228, 229, 230, 231, 232, 233, 234, 235, 236, 237, 238, 239, 240
*Elset, elset=_Strand-Slave_S2, internal
1, 2, 3, 4, 9, 10, 11, 12, 17, 18, 19, 20, 25, 26, 27, 28
101, 102, 105, 106, 109, 110, 113, 114, 121, 122, 123, 124, 129, 130, 131, 132
137, 138, 139, 140, 145, 146, 147, 148, 181, 182, 185, 186, 189, 190, 193, 194
241, 242, 245, 246, 249, 250, 253, 254, 301, 302, 305, 306, 309, 310, 313, 314
357, 358, 361, 362, 365, 366, 369, 370, 373, 374, 401, 402, 405, 406, 409, 410
413, 414, 437, 438, 441, 442, 445, 446, 449, 450, 453, 454, 497, 498, 541, 542
545, 546, 549, 550, 553, 554, 561, 562, 565, 566, 569, 570, 573, 574, 597, 598
637, 638
*Elset, elset=_Strand-Slave_S4, internal
46, 48, 50, 52, 66, 68, 70, 72, 74, 76, 78, 80, 82, 84, 94, 96
98, 100, 164, 166, 174, 176, 178, 180, 214, 216, 218, 220, 262, 264, 274, 276
278, 280, 284, 286, 294, 296, 298, 300, 330, 332, 348, 350, 382, 384, 394, 396
398, 400, 422, 424, 434, 436, 464, 466, 474, 476, 478, 480, 490, 492, 504, 506
514, 516, 518, 520, 522, 524, 534, 536, 538, 540, 582, 584, 594, 596, 604, 606
614, 616, 618, 620, 624, 626, 634, 636
*Elset, elset=_Strand-Slave_S3, internal
53, 54, 55, 56, 89, 90, 167, 168, 205, 206, 207, 208, 225, 227, 229, 231
233, 234, 235, 236, 269, 270, 287, 288, 321, 322, 333, 335, 337, 338, 343, 344
353, 355, 389, 390, 429, 430, 467, 468, 481, 482, 493, 495, 507, 508, 529, 530
589, 590, 607, 608, 627, 628
*Surface, type=ELEMENT, name=Strand-Slave
_Strand-Slave_S2, S2
_Strand-Slave_S4, S4
_Strand-Slave_S3, S3
*Elset, elset=_Strand-BC_S3, internal
25, 29, 61, 73, 74, 145, 149, 213, 214
*Elset, elset=_Strand-BC_S4, internal
20, 24, 40, 56, 60, 140, 144, 160, 224, 236, 240
*Surface, type=ELEMENT, name=Strand-BC
_Strand-BC_S3, S3
_Strand-BC_S4, S4
** Section: Strand
*Solid Section, elset=_PickedSet9, material=Strand_270ksi
1.,
*End Part
**
**
** ASSEMBLY
**
*Assembly, name=Assembly
**
*Instance, name=Beam-1, part=Beam-1
*End Instance

```

**
*Instance, name=Beam-2, part=Beam-2
*End Instance
**
*Instance, name=Bed, part=Bed
    0.,    -3.,    0.
*End Instance
**
*Instance, name=Strand, part=Strand
*End Instance
**
*Nset, nset=_PickedSet10, internal, instance=Beam-1, generate
    1, 1584, 1
*Nset, nset=_PickedSet10, internal, instance=Beam-2, generate
    1, 528, 1
*Nset, nset=_PickedSet10, internal, instance=Strand, generate
    1, 875, 1
*Nset, nset=_PickedSet10, internal, instance=Bed, generate
    1, 408, 1
*Elset, elset=_PickedSet10, internal, instance=Beam-1, generate
    1, 1024, 1
*Elset, elset=_PickedSet10, internal, instance=Beam-2, generate
    1, 256, 1
*Elset, elset=_PickedSet10, internal, instance=Strand, generate
    1, 680, 1
*Elset, elset=_PickedSet10, internal, instance=Bed, generate
    1, 165, 1
*Nset, nset=_PickedSet11, internal, instance=Beam-1
    3, 4, 6, 7, 11, 12, 14, 15, 18, 20, 21, 22, 26, 27, 30, 32
    65, 129, 161, 163, 197, 261, 293, 295, 329, 362, 363, 365, 366, 367, 465, 467
    468, 471, 473, 505, 539, 540, 574, 575, 702, 828, 891, 924, 1081, 1208, 1240,
    1304
*Nset, nset=_PickedSet11, internal, instance=Beam-2
    2, 3, 5, 6, 10, 11, 13, 14, 17, 20, 22, 23, 25, 26, 29, 31
*Nset, nset=_PickedSet11, internal, instance=Strand
    3, 4, 6, 8, 14, 65, 66, 67, 68, 69, 87, 88, 89, 121, 122, 123
    148, 321, 322, 346, 347, 401, 402, 442, 443
*Nset, nset=_PickedSet11, internal, instance=Bed
    9, 10, 11, 12, 13, 16, 19, 20, 26, 27, 29, 30
*Elset, elset=_PickedSet11, internal, instance=Beam-1
    63, 64, 127, 128, 191, 192, 255, 256, 257, 289, 321, 353, 385, 386, 387, 388
    513, 545, 577, 609, 703, 704, 767, 768, 769, 801, 833, 865, 897, 929, 961, 993
*Elset, elset=_PickedSet11, internal, instance=Beam-2
    32, 64, 65, 128, 129, 161, 224, 256
*Elset, elset=_PickedSet11, internal, instance=Strand
    20, 24, 25, 29, 40, 56, 60, 61, 73, 74, 140, 144, 145, 149, 160, 213

```


214, 224, 236, 240
*Elset, elset=_PickedSet11, internal, instance=Bed
2, 34, 98, 132, 164
*Nset, nset=_PickedSet12, internal, instance=Bed
1, 2, 3, 4, 11, 12, 13, 14, 15, 16, 23, 24, 25, 26, 27, 28
34, 36, 99, 100, 101, 102, 103, 104, 105, 106, 107, 108, 109, 110, 111, 112
113, 114, 115, 116, 117, 118, 119, 120, 121, 122, 123, 124, 125, 126, 127, 128
129, 130, 131, 132, 133, 134, 135, 136, 137, 138, 139, 140, 141, 142, 143, 144
145, 146, 147, 148, 149, 150, 151, 152, 153, 154, 155, 156, 157, 158, 159, 160
161, 162, 163, 164, 165, 166, 167, 168, 169, 170, 171, 172, 173, 174, 175, 176
177, 178, 179, 180, 181, 182, 183, 184, 185, 186, 187, 188, 189, 190, 191, 192
193, 194, 195, 196, 197, 198, 199, 200, 201, 202, 203, 204, 205, 206, 207, 208
209, 210, 211, 212, 213, 214, 215, 216, 217, 218, 219, 220, 221, 222, 285, 286
287, 288, 289, 290, 291, 292, 293, 294, 295, 296, 297, 298, 299, 300, 301, 302
303, 304, 305, 306, 307, 308, 309, 310, 311, 312, 313, 314, 315, 316, 317, 318
319, 320, 321, 322, 323, 324, 325, 326, 327, 328, 329, 330, 331, 332, 333, 334
335, 336, 337, 338, 339, 340, 341, 342, 343, 344, 345, 346
*Elset, elset=_PickedSet12, internal, instance=Bed, generate
1, 165, 1
*Nset, nset=_PickedSet13, internal, instance=Strand
41, 42, 43, 44, 45, 270, 271, 272, 273, 274, 276, 277, 278, 280, 281, 282
283, 653, 654, 658, 659, 663, 664, 666, 667
*Elset, elset=_PickedSet13, internal, instance=Strand
646, 647, 648, 649, 650, 656, 657, 658, 659, 660, 666, 667, 668, 669, 670, 676
677, 678, 679, 680
*Nset, nset=_PickedSet15, internal, instance=Beam-1
22, 24, 27, 28, 371, 372, 373, 374, 375, 376, 377, 378, 379, 380, 381, 382
383, 384, 385, 386, 387, 388, 389, 390, 391, 392, 393, 394, 395, 396, 397, 398
399, 400, 401, 472, 473, 474, 475, 476, 477, 478, 479, 480, 481, 482, 483, 484
485, 486, 487, 488, 489, 490, 491, 492, 493, 494, 495, 496, 497, 498, 499, 500
501, 502, 503, 504, 1145, 1146, 1147, 1148, 1149, 1150, 1151, 1152, 1153, 1154,
1155, 1156
1157, 1158, 1159, 1160, 1161, 1162, 1163, 1164, 1165, 1166, 1167, 1168, 1169, 1170,
1171, 1172
1173, 1174, 1175
*Elset, elset=_PickedSet15, internal, instance=Beam-1, generate
705, 768, 1
** Constraint: Beam1-Beam2
*Tie, name=Beam1-Beam2, adjust=yes
Beam-2.Beam-2-Slave, Beam-1.Beam-1-Host
*End Assembly
**
** -----
** **IMPLEMENTATION OF MATERIAL CONSTITUTIVE LAWS**
**
** MATERIALS

**
 *Material, name=Conc_5000psi
 ** Concrete with initial compressive strength of 5000 psi
 *Density
 0.00022465,
 *Elastic
 4.28683e+06, 0.15
 *Concrete Damaged Plasticity
 52.9, 0.1, 1.16, 0.778, 0.
 *Concrete Compression Hardening
 2802.4, 0.
 3681., 1e-05
 4095.9, 2e-05
 4485.9, 4e-05
 4843., 6e-05
 5158.8, 9e-05
 5425.3, 0.00013
 5635., 0.00019
 5782.5, 0.00026
 5864.5, 0.00034
 5880.8, 0.00044
 5834., 0.00055
 5729.6, 0.00067
 5574.9, 0.0008
 5379.1, 0.00094
 5151.5, 0.00109
 4901.7, 0.00125
 4638.1, 0.00141
 4368.3, 0.00156
 4098.6, 0.00172
 3833.9, 0.00188
 3577.8, 0.00204
 3332.9, 0.00219
 3100.9, 0.00234
 *CONCRETE TENSION STIFFENING, TYPE=DISPLACEMENT
 554.00 ,0
 370.60 ,0.002605709
 248.92 ,0.004873008
 166.85 ,0.006827835
 111.85 ,0.008668898
 74.975 ,0.010421969
 50.24 ,0.012129449
 33.688 ,0.013785433
 22.580 ,0.015517244
 15.130 ,0.017234016
 10.125 ,0.018982874

*CONCRETE TENSION DAMAGE, TYPE=DISPLACEMENT

0 ,0
0.381217 ,0.002605709
0.617107 ,0.004837008
0.763072 ,0.006826772
0.853393 ,0.00869685
0.909282 ,0.010421969
0.943865 ,0.012129449
0.965265 ,0.013785433
0.978506 ,0.015517244
0.9867 ,0.017234016
0.99177 ,0.018982874

*Material, name=Steel_36ksi

** Steel with yield strength of 36 ksi

*Density

0.00073386,

*Elastic

2.9e+07, 0.2

*Material, name=Strand_270ksi

** Low-relaxation strand with tensile strength of 270 ksi

*Density

0.00073386,

*Elastic

2.85e+07, 0.2

**

** -----

** **SIMULATION OF SLIPPAGE AT STRAND/CONCRETE INTERFACE**

**

** INTERACTION PROPERTIES

**

*Surface Interaction, name=Beam2-Strand

1.,

*Friction, slip tolerance=0.005

0.7,

*Surface Behavior, pressure-overclosure=HARD

**

** -----

** **SIMULATION OF INTERFACE BETWEEN BEAM & CASTING BED**

*Surface Interaction, name=Bed

1.,

*Friction

0.,

*Surface Behavior, pressure-overclosure=HARD

**

** -----

** **APPLICATION OF PRETENSIONING TO STRAND ELEMENTS**

```

**
*Initial Conditions, Type=Stress
Strand.PS-1, 0,0,155415,0,0,0
Strand.PS-2, 0,0,155415,0,0,0
Strand.PS-3, 0,0,155415,0,0,0
Strand.PS-4, 0,0,155415,0,0,0
Strand.PS-5, 0,0,155415,0,0,0
Strand.PS-6, 0,0,155415,0,0,0
Strand.PS-7, 0,0,155415,0,0,0
** -----
** BOUNDARY CONDITIONS
**
** Name: Beam-Transverse Type: Displacement/Rotation
*Boundary
_PickedSet15, 1, 1
** Name: Bed-Support Type: Symmetry/Antisymmetry/Encastre
*Boundary
_PickedSet12, ENCASTRE
** Name: DEACTIVE-BEAM2 Type: Symmetry/Antisymmetry/Encastre
*Boundary
Beam-2.Beam-2, ENCASTRE
** Name: DEACTIVE-Beam1 Type: Symmetry/Antisymmetry/Encastre
*Boundary
Beam-1.Beam-1, ENCASTRE
** Name: Strand-End Type: Displacement/Rotation
*Boundary
_PickedSet13, 1, 1
_PickedSet13, 2, 2
_PickedSet13, 6, 6
** Name: Z-SYMM Type: Symmetry/Antisymmetry/Encastre
*Boundary
_PickedSet11, ZSYMM
**
** INTERACTIONS
**
** Interaction: Beam2-Strand
*Contact Pair, interaction=Beam2-Strand, type=SURFACE TO SURFACE
Strand.Strand-Slave, Beam-2.Beam-2-Host
** Interaction: Bed-Beam1
*Contact Pair, interaction=Bed
Beam-1.Beam-1-Slave, Bed.Bed-Host
** -----
** DEACTIVATION OF STRAIN-COMPATIBILITY BETWEEN STRAND &
** CONCRETE
**
** STEP: Prestress

```

```

**
*Step, name=Prestress, inc=10000
Deactivate Beam-1 & Beam-2 and apply the initial conditions (prestressing) !!!
*Static
0.01, 1., 1e-10, 1.
**
** -----
*Model Change, Remove
Beam-1.Beam-1
Beam-2.Beam-2
** -----
** OUTPUT REQUESTS
**
*Restart, write, frequency=0
**
** FIELD OUTPUT: F-Output-1
**
*Output, field, variable=PRESELECT
**
** HISTORY OUTPUT: H-Output-1
**
*Output, history, variable=PRESELECT
*End Step
** -----
** ACTIVATION OF STRAIN-COMPATIBILITY BETWEEN STRAND &
** CONCRETE
**
** STEP: Release
**
*Step, name=Release, inc=10000
Activate Beam-1 and Beam-2 with strain compatibility (release) !!!!
*Static
0.01, 1., 1e-10, 1.
**
** -----
*Model Change, Add=With Strain
Beam-1.Beam-1
Beam-2.Beam-2
** -----
** BOUNDARY CONDITIONS
**
** Name: Beam-Transverse Type: Displacement/Rotation
*Boundary, op=NEW
_PickedSet15, 1, 1
** Name: Bed-Support Type: Symmetry/Antisymmetry/Encastre
*Boundary, op=NEW

```

```

_PickedSet12, ENCASTRE
** Name: DEACTIVE-BEAM2 Type: Symmetry/Antisymmetry/Encastre
*Boundary, op=NEW
** Name: DEACTIVE-Beam1 Type: Symmetry/Antisymmetry/Encastre
*Boundary, op=NEW
** Name: Strand-End Type: Displacement/Rotation
*Boundary, op=NEW
_PickedSet13, 1, 1
_PickedSet13, 2, 2
_PickedSet13, 6, 6
** Name: Z-SYMM Type: Symmetry/Antisymmetry/Encastre
*Boundary, op=NEW
_PickedSet11, ZSYMM
**
** LOADS
**
** Name: Self-Weight Type: Gravity
*Dload
_PickedSet10, GRAV, 386.4, 0., -1., 0.
**
** OUTPUT REQUESTS
**
*Restart, write, frequency=0
**
** FIELD OUTPUT: F-Output-1
**
*Output, field, variable=PRESELECT
**
** HISTORY OUTPUT: H-Output-1
**
*Output, history, variable=PRESELECT
*End Step

```

Appendix B

**Sample Finite Element Code (ABAQUS) for 6"x6" Rectangular Beams
Pretensioned with One Concentric or Eccentric 0.6-in. Diameter Strand
Based on Embedment Technique**

```

*Heading
RCBM 6x6x96 with one concentric strand, nonlinear response, embedded strands (no
slippage), and prestressing with "Nonlinear Slip-Max" transfer length simulation !!!
** Job name: RCBM_6x6x96_1S_con_weight_Embed Model name:
RCBM_6x6x96_1S_con_Embed
*Preprint, echo=NO, model=NO, history=NO, contact=NO
**
** PARTS
**
*Part, name=Beam
*Node
  1,    0.5,   -0.5,   12.
  2,   -0.5,   -0.5,   12.
  3,   -0.5,   -0.5,   18.
  4,    0.5,   -0.5,   18.
  5,   -0.5,    0.5,   12.
  6,   -0.5,    0.5,   18.
  7,    0.5,    0.5,   18.
  8,    0.5,    0.5,   12.
  9,   -3.,    0.5,   12.
 10,   -3.,    0.5,    0.
...
*Element, type=C3D8
1, 1, 2, 129, 130, 8, 5, 131, 132
2, 130, 129, 3, 4, 132, 131, 6, 7
3, 5, 133, 401, 140, 2, 141, 404, 146
4, 133, 9, 134, 401, 141, 12, 144, 404
5, 140, 401, 402, 139, 146, 404, 405, 147
6, 401, 134, 135, 402, 404, 144, 143, 405
7, 139, 402, 403, 138, 147, 405, 406, 148
8, 402, 135, 136, 403, 405, 143, 142, 406
9, 138, 403, 137, 11, 148, 406, 145, 14
10, 403, 136, 10, 137, 406, 142, 13, 145
...
*Nset, nset=Beam, generate
  1, 612, 1
*Elset, elset=Beam, generate
  1, 400, 1
*Nset, nset=_PickedSet4, internal, generate
  1, 612, 1
*Elset, elset=_PickedSet4, internal, generate
  1, 400, 1
*Nset, nset=Beam-PS-1
  95, 96, 97, 98, 109, 113, 118, 122, 352, 362, 371, 380
*Elset, elset=Beam-PS-1
  343, 344

```


*Nset, nset=Beam-PS-2
 73, 74, 75, 76, 95, 96, 97, 98, 332, 333, 334, 335
 *Elset, elset=Beam-PS-2
 277, 278
 *Nset, nset=Beam-PS-3
 60, 61, 62, 63, 73, 74, 75, 76, 283, 284, 285, 286
 *Elset, elset=Beam-PS-3
 191, 192
 *Nset, nset=Beam-PS-4
 41, 42, 43, 44, 60, 61, 62, 63, 256, 257, 258, 259
 *Elset, elset=Beam-PS-4
 141, 142
 *Nset, nset=Beam-PS-5
 3, 4, 6, 7, 41, 42, 43, 44, 213, 214, 215, 216
 *Elset, elset=Beam-PS-5
 75, 76
 *Nset, nset=Beam-PS-6
 1, 2, 3, 4, 5, 6, 7, 8, 129, 130, 131, 132
 *Elset, elset=Beam-PS-6
 1, 2
 *Nset, nset=Beam-PS-7
 1, 2, 5, 8, 11, 14, 25, 26, 138, 139, 140, 146, 147, 148, 172, 173
 174, 175, 176, 177
 *Elset, elset=Beam-PS-7, generate
 353, 356, 1
 *Elset, elset=_Beam-Slave_S6, internal
 43, 45, 47, 49, 51, 53, 55, 57, 349, 351
 *Elset, elset=_Beam-Slave_S1, internal
 63, 64, 65, 66, 69, 70, 101, 102, 103, 104, 113, 114, 115, 116, 117, 118
 119, 120, 171, 172, 173, 174, 177, 178, 219, 220, 225, 226, 227, 228, 273, 274
 275, 276, 281, 282, 331, 332, 333, 334, 347, 348
 *Elset, elset=_Beam-Slave_S4, internal
 122, 124, 126, 128, 160, 162, 164, 166, 242, 244, 246, 248, 250, 252, 254, 256
 308, 310, 312, 314, 394, 396, 398, 400
 *Elset, elset=_Beam-Slave_S5, internal
 367, 368, 371, 372
 *Surface, type=ELEMENT, name=Beam-Slave
 _Beam-Slave_S6, S6
 _Beam-Slave_S1, S1
 _Beam-Slave_S4, S4
 _Beam-Slave_S5, S5
 *Elset, elset=_Beam-BC_S5, internal
 9, 10, 25, 26, 33, 34, 38, 42, 49, 50, 57, 58, 92, 96, 100, 104
 111, 112, 119, 120, 199, 200, 207, 208
 *Elset, elset=_Beam-BC_S2, internal
 353,

```

*Surface, type=ELEMENT, name=Beam-BC
  _Beam-BC_S5, S5
  _Beam-BC_S2, S2
** Section: Beam
*Solid Section, elset=_PickedSet4, material=Conc_5000psi
  1.,
*End Part
**
*Part, name=Bed
*Node
  1,      3.,    -1.,    50.
  2,      3.,    -1.,    48.
  3,      5.,    -1.,    48.
  4,      5.,    -1.,    50.
  5,      3.,     0.,    48.
  6,      5.,     0.,    48.
  7,      5.,     0.,    50.
  8,      3.,     0.,    50.
  9,      3.,     0.,     0.
 10,     5.,     0.,     0.
...
*Element, type=C3D8
  1, 8, 5, 6, 7, 1, 2, 3, 4
  2, 12, 57, 58, 11, 9, 37, 50, 10
  3, 57, 56, 59, 58, 37, 38, 49, 50
  4, 56, 55, 60, 59, 38, 39, 48, 49
  5, 55, 54, 61, 60, 39, 40, 47, 48
  6, 54, 53, 62, 61, 40, 41, 46, 47
  7, 53, 52, 63, 62, 41, 42, 45, 46
  8, 52, 51, 64, 63, 42, 43, 44, 45
  9, 51, 2, 3, 64, 43, 5, 6, 44
 10, 20, 85, 86, 19, 13, 65, 78, 16
...
*Nset, nset=_PickedSet2, internal, generate
  1, 120, 1
*Elset, elset=_PickedSet2, internal, generate
  1, 45, 1
*Nset, nset=Bed, generate
  1, 120, 1
*Elset, elset=Bed, generate
  1, 45, 1
*Elset, elset=_Bed-Host_S1, internal
 19, 20, 21, 22, 23, 24, 25, 26, 29, 30, 31, 32, 33, 34, 35, 36
*Elset, elset=_Bed-Host_S6, internal, generate
 37, 44, 1
*Surface, type=ELEMENT, name=Bed-Host

```

```

_Bed-Host_S1, S1
_Bed-Host_S6, S6
*Elset, elset=_Bed-BC-bot_S2, internal
  1, 10, 11, 12, 13, 14, 15, 16, 17, 19, 20, 21, 22, 23, 24, 25
  26, 29, 30, 31, 32, 33, 34, 35, 36
*Elset, elset=_Bed-BC-bot_S4, internal, generate
  37, 44, 1
*Elset, elset=_Bed-BC-bot_S1, internal
  2, 3, 4, 5, 6, 7, 8, 9, 18, 27, 28
*Elset, elset=_Bed-BC-bot_S3, internal
  45,
*Surface, type=ELEMENT, name=Bed-BC-bot
  _Bed-BC-bot_S2, S2
  _Bed-BC-bot_S4, S4
  _Bed-BC-bot_S1, S1
  _Bed-BC-bot_S3, S3
*Elset, elset=_Bed-BC-side_S6, internal
  2,10
*Elset, elset=_Bed-BC-side_S4, internal
  26, 36
*Elset, elset=_Bed-BC-side_S5, internal
  44,
*Surface, type=ELEMENT, name=Bed-BC-side
  _Bed-BC-side_S6, S6
  _Bed-BC-side_S4, S4
  _Bed-BC-side_S5, S5
** Section: Bed
*Solid Section, elset=_PickedSet2, material=Steel_36ksi
  1.,
*End Part
**
*Part, name=Strand
*Node
  1,      0.,      0.,      0.
  2,     12.,      0.,      0.
  3,     18.,      0.,      0.
  4,     24.,      0.,      0.
  5,     30.,      0.,      0.
  6,     36.,      0.,      0.
  7,     42.,      0.,      0.
  8, 47.9500008,    0.,      0.
  9,      1.5,      0.,      0.
  10,     3.,      0.,      0.
...
*Element, type=T3D2
  1, 1, 9

```

2, 9, 10
 3, 10, 11
 4, 11, 12
 5, 12, 13
 6, 13, 14
 7, 14, 15
 8, 15, 2
 9, 2, 16
 10, 16, 17
 ...
 *Nset, nset=Strand, generate
 1, 33, 1
 *Elset, elset=Strand, generate
 1, 32, 1
 *Nset, nset=PS-1
 7, 8, 31, 32, 33
 *Elset, elset=PS-1, generate
 29, 32, 1
 *Nset, nset=PS-2
 6, 7, 28, 29, 30
 *Elset, elset=PS-2, generate
 25, 28, 1
 *Nset, nset=PS-3
 5, 6, 25, 26, 27
 *Elset, elset=PS-3, generate
 21, 24, 1
 *Nset, nset=PS-4
 4, 5, 22, 23, 24
 *Elset, elset=PS-4, generate
 17, 20, 1
 *Nset, nset=PS-5
 3, 4, 19, 20, 21
 *Elset, elset=PS-5, generate
 13, 16, 1
 *Nset, nset=PS-6
 2, 3, 16, 17, 18
 *Elset, elset=PS-6, generate
 9, 12, 1
 *Nset, nset=PS-7
 1, 2, 9, 10, 11, 12, 13, 14, 15
 *Elset, elset=PS-7, generate
 1, 8, 1
 *Nset, nset=_PickedSet25, internal, generate
 1, 33, 1
 *Elset, elset=_PickedSet25, internal, generate
 1, 32, 1

```

** Section: Strand
*Solid Section, elset=_PickedSet25, material=Strand_270ksi
0.217,
*End Part
**
**
** ASSEMBLY
**
*Assembly, name=Assembly
**
*Instance, name=Bed, part=Bed
    0.,    -3.,    0.
*End Instance
**
*Instance, name=Beam, part=Beam
*End Instance
**
*Instance, name=Strand, part=Strand
    0.,    0.,    0.
    0.,    0.,    0.,    0.,    -1.,    0., 89.9999990194245
*End Instance
**
*Nset, nset=_PickedSet10, internal, instance=Bed, generate
    1, 120, 1
*Elset, elset=_PickedSet10, internal, instance=Bed, generate
    1, 45, 1
*Nset, nset=_PickedSet12, internal, instance=Bed
    1, 2, 3, 4, 11, 12, 13, 14, 15, 16, 23, 24, 25, 26, 27, 28
    34, 36, 51, 52, 53, 54, 55, 56, 57, 58, 59, 60, 61, 62, 63, 64
    65, 66, 67, 68, 69, 70, 71, 72, 73, 74, 75, 76, 77, 78, 93, 94
    95, 96, 97, 98, 99, 100, 101, 102, 103, 104, 105, 106
*Elset, elset=_PickedSet12, internal, instance=Bed, generate
    1, 45, 1
*Nset, nset=_PickedSet19, internal, instance=Beam
    16, 17, 23, 24, 40, 48, 51, 58, 70, 78, 89, 100, 101, 104, 110, 127
    150, 166, 167, 168, 211, 222, 229, 230, 231, 251, 276, 292, 314, 337, 346, 354
    377, 396
*Elset, elset=_PickedSet19, internal, instance=Beam
    71, 72, 89, 90, 91, 92, 179, 180, 209, 210, 291, 292, 323, 324, 374, 376
*Nset, nset=_PickedSet20, internal, instance=Bed
    9, 10, 11, 12, 13, 16, 19, 20, 26, 27, 29, 30
*Nset, nset=_PickedSet20, internal, instance=Beam
    10, 11, 13, 14, 22, 24, 25, 26, 27, 28, 31, 32, 51, 52, 53, 77
    137, 145, 164, 169, 170, 184, 186, 188, 193, 197, 232, 236, 237, 241, 290, 291
    423, 440, 468, 503
*Nset, nset=_PickedSet20, internal, instance=Strand

```

1,
*Elset, elset=_PickedSet20, internal, instance=Bed
2, 10, 26, 36, 44
*Elset, elset=_PickedSet20, internal, instance=Beam
9, 10, 25, 26, 33, 34, 38, 42, 49, 50, 57, 58, 92, 96, 100, 104
111, 112, 119, 120, 199, 200, 207, 208, 353
** Constraint: Beam-Strand-1
*Embedded Element, host elset=Beam.Beam-PS-1
Strand.PS-1
** Constraint: Beam-Strand-2
*Embedded Element, host elset=Beam.Beam-PS-2
Strand.PS-2
** Constraint: Beam-Strand-3
*Embedded Element, host elset=Beam.Beam-PS-3
Beam.Beam-PS-3
** Constraint: Beam-Strand-4
*Embedded Element, host elset=Beam.Beam-PS-4
Strand.PS-4
** Constraint: Beam-Strand-5
*Embedded Element, host elset=Beam.Beam-PS-5
Strand.PS-5
** Constraint: Beam-Strand-6
*Embedded Element, host elset=Beam.Beam-PS-6
Strand.PS-6
** Constraint: Beam-Strand-7
*Embedded Element, host elset=Beam.Beam-PS-7
Strand.PS-7
*End Assembly
**
** -----
** **IMPLEMENTATION OF MATERIAL CONSTITUTIVE LAWS**
**
** MATERIALS
**
*Material, name=Conc_5000psi
** Concrete with initial compressive strength of 5000 psi
*Density
0.00022465,
*Elastic
4.28683e+06, 0.15
*Concrete Damaged Plasticity
52.9, 0.1, 1.16, 0.778, 0.
*Concrete Compression Hardening
2802.4, 0.
3681., 1e-05
4095.9, 2e-05

4485.9, 4e-05
4843., 6e-05
5158.8, 9e-05
5425.3, 0.00013
5635., 0.00019
5782.5, 0.00026
5864.5, 0.00034
5880.8, 0.00044
5834., 0.00055
5729.6, 0.00067
5574.9, 0.0008
5379.1, 0.00094
5151.5, 0.00109
4901.7, 0.00125
4638.1, 0.00141
4368.3, 0.00156
4098.6, 0.00172
3833.9, 0.00188
3577.8, 0.00204
3332.9, 0.00219
3100.9, 0.00234

*CONCRETE TENSION STIFFENING, TYPE=DISPLACEMENT

554.00 ,0
370.60 ,0.002605709
248.92 ,0.004873008
166.85 ,0.006827835
111.85 ,0.008668898
74.975 ,0.010421969
50.24 ,0.012129449
33.688 ,0.013785433
22.580 ,0.015517244
15.130 ,0.017234016
10.125 ,0.018982874

*CONCRETE TENSION DAMAGE, TYPE=DISPLACEMENT

0 ,0
0.381217 ,0.002605709
0.617107 ,0.004837008
0.763072 ,0.006826772
0.853393 ,0.00869685
0.909282 ,0.010421969
0.943865 ,0.012129449
0.965265 ,0.013785433
0.978506 ,0.015517244
0.9867 ,0.017234016
0.99177 ,0.018982874

*Material, name=Steel_36ksi

```

** Steel with yield strength of 36 ksi
*Density
0.00073386,
*Elastic
2.9e+07, 0.2
*Material, name=Strand_270ksi
** Low-relaxation strand with tensile strength of 270 ksi
*Density
0.00073386,
*Elastic
2.85e+07, 0.2
**
** -----
** SIMULATION OF INTERFACE BETWEEN BEAM & CASTING BED
**
** INTERACTION PROPERTIES
**
*Surface Interaction, name=Bed
1.,
*Friction
0.,
*Surface Behavior, pressure-overclosure=HARD
**
** -----
** APPLICATION OF PRETENSIONING TO STRAND ELEMENTS
**
*Initial Conditions, Type=Stress
Strand.PS-1, 8229
Strand.PS-2, 94248
Strand.PS-3, 144980
Strand.PS-4, 172260
Strand.PS-5, 184470
Strand.PS-6, 188890
Strand.PS-7, 202500
** -----
** BOUNDARY CONDITIONS
**
** Name: Beams-Transverse Type: Displacement/Rotation
*Boundary
_PickedSet19, 1, 1
** Name: Bed-Support Type: Symmetry/Antisymmetry/Encastre
*Boundary
_PickedSet12, ENCASTRE
** Name: DEACTIVE-BEAM Type: Symmetry/Antisymmetry/Encastre
*Boundary
Beam.Beam, ENCASTRE

```



```

** Name: DEACTIVE-STRAND Type: Symmetry/Antisymmetry/Encastre
*Boundary
Strand.Strand, ENCASTRE
** Name: Z-SYMM Type: Symmetry/Antisymmetry/Encastre
*Boundary
_PickedSet20, ZSYMM
**
** INTERACTIONS
**
** Interaction: Bed-Beam
*Contact Pair, interaction=Bed, type=SURFACE TO SURFACE
Beam.Beam-Slave, Bed.Bed-Host
** -----
** DEACTIVATION OF STRAIN-COMPATIBILITY BETWEEN STRAND &
** CONCRETE
**
** STEP: Prestress
**
*Step, name=Prestress, inc=10000
Deactivate Beam-1 & Beam-2 and apply the initial conditions (prestressing) !!!
*Static
0.01, 1., 1e-10, 1.
**
** OUTPUT REQUESTS
**
*Restart, write, frequency=0
**
** FIELD OUTPUT: F-Output-1
**
*Output, field, variable=PRESELECT
**
** HISTORY OUTPUT: H-Output-1
**
*Output, history, variable=PRESELECT
*End Step
** -----
** ACTIVATION OF STRAIN-COMPATIBILITY BETWEEN STRAND &
** CONCRETE
**
** STEP: Release
**
*Step, name=Release, inc=10000
Activate Beam-1 and Beam-2 with strain compatibility (release) !!!!
*Static
0.01, 1., 1e-10, 1.
**

```

```

** BOUNDARY CONDITIONS
**
** Name: Beams-Transverse Type: Displacement/Rotation
*Boundary, op=NEW
_PickedSet19, 1, 1
** Name: Bed-Support Type: Symmetry/Antisymmetry/Encastre
*Boundary, op=NEW
_PickedSet12, ENCASTRE
** Name: DEACTIVE-BEAM Type: Symmetry/Antisymmetry/Encastre
*Boundary, op=NEW
** Name: DEACTIVE-STRAND Type: Symmetry/Antisymmetry/Encastre
*Boundary, op=NEW
** Name: Z-SYMM Type: Symmetry/Antisymmetry/Encastre
*Boundary, op=NEW
_PickedSet20, ZSYMM
**
** LOADS
**
** Name: Self-Weight Type: Gravity
*Dload
_PickedSet10, GRAV, 386.4, 0., -1., 0.
**
** OUTPUT REQUESTS
**
*Restart, write, frequency=0
**
** FIELD OUTPUT: F-Output-1
**
*Output, field, variable=PRESELECT
**
** HISTORY OUTPUT: H-Output-1
**
*Output, history, variable=PRESELECT
*End Step

```

Appendix C

Closed-Form Solution for 6"x6" Rectangular Beams Pretensioned with One Concentric or Eccentric 0.6-in. Diameter Strand

Step 1: Optimizing Strand Eccentricity

INSTRUCTIONS

- 1) **Model Dimensions Module:** Input the values in cells marked as x.xxx
- 2) **Elastic Shortening:** Assume an initial value for strand eccentricity (e).
- 3) **Design Module:** Assume a percentage of rupture modulus as allowable tensile stress.
- 4) **Design Module:** Iterate for strand eccentricity (GOAL SEAK).

1.a Model Dimensions (Tensile St. = +ve sign, Comp. St. = -ve sign)				Password 123	
Concrete Material		Strand material		Section geometrical properties	
f'ci	5.800 ksi	fpu	270.000 ksi	b	6.000 in
Unit wt	0.150 kcf	Unit wt	0.490 kcf	h	6.000 in
Unit wt	0.038 klf	% of fpu just before release	75% ---	A	36.000 in2
0.6f'ci	-3.480 ksi	fpo (just before Release)	202.500 ksi	S top (= S bottom)	36.000 in3
fr = 7.5 sqrt f'ci	0.571 ksi	Strand diameter (0.5 or 0.6)	0.600 in.	I (inertia)	108.000 in4
Eci	4617.053 ksi	Ap, Strand area	0.217 in2	Member length	96.000 in
		Po (just before release)	43.943 kips	Member length	8.000 ft
		Transfer length (60 dp)	36.000 in	Mg at transfer length	0.281 k-ft
		Transfer length (60 dp)	3.000 ft	Mg at midspan	0.300 k-ft
		Ep	28500.000 ksi		

1.b Elastic shortening losses		
Assume e	0.000 in.	
f cir	-1.221 ksi	stress at midspan at cg of strands just before release = $-(Po/A) - (Po * e^2)/I + (Mg \text{ at midspan} * e)/I$
ES loss	-7.535 ksi	= $(Ep / Eci) * f \text{ cir}$ Ref.: AASHTO LRFD 4th Edition with 2008 Interims Article 5.9.5.2.3
fpi	194.965 ksi	Strand stress immediately after release
Ppi	42.307 kips	Strand force immediately after release

1.c Design based on allowable tensile st. at top fiber at the transfer length and using PI					
% of fr	100%	Top stress	0.571 ksi		
Ppi/A	-1.175 ksi	Mg / S top	-0.094 ksi	Ppi / S top	1.175 k/in3

e = 0.000 in e (assumed)/e (calculated) = #DIV/0!
 Check against assumed value for eccentricity : #DIV/0!

1.d Check solution at transfer length					
(P / S top)*e	0.000 ksi	Total top st.	-1.269 ksi	= (% of fr)*fr (OK) Fiber in Compression
		Total bottom st	-1.081 ksi	< 0.6f'ci (OK) Fiber in Compression

Step 2: Section Properties

Use: $h_p = 0.000$ in. Strand location relative to the bottom face of P/S beam

2.1 Gross Section Properties

$A_g = 36.000 \text{ in}^2$ Gross area
 $I_g = 108.000 \text{ in}^4$ Gross moment of inertia
 $Y_{g,b} = 3.000 \text{ in.}$ Distance between C.G. and the bottom fiber
 $Y_{g,t} = 3.000 \text{ in.}$ Distance between C.G. and the top fiber
 $S_{g,b} = 36.000 \text{ in}^3$ Gross moment of inertia
 $S_{g,t} = 36.000 \text{ in}^3$ Gross moment of inertia
 $w_{b,g} = 0.03750 \text{ kif}$ Gross weight of the P/S beam per linear foot
 $M_{b,g,x} = \frac{w_{b,g} \times (L_{span} - x)^2}{2}$

x in.	Δx in.	L_{span} ft	$M_{b,g,x}$	
			kip-ft	kip-in.
0.000	6.000	8.000	0.000	0.000
6.000			0.070	0.844
12.000			0.131	1.575
18.000			0.183	2.194
24.000			0.225	2.700
30.000			0.258	3.094
36.000			0.281	3.375
42.000			0.295	3.544
48.000			0.300	3.600

2.2 Net Section Properties

	A in. ²	Y_b in.	I_o in. ³	I_o in. ⁴	D in.	$A D^2$ in. ⁴	I in. ⁴
Beam	36.000	3.000	108.000	108.000	0.018	0.0119155	108.012
Strand	0.217	0.000	0.000	0.263	0.0037472	3.018	1.9767591
	35.783	3.018	108.000				106.031

$A_n = 35.783 \text{ in}^2$ Net area
 $I_n = 106.031 \text{ in}^4$ Net moment of inertia
 $Y_{n,b} = 3.018 \text{ in.}$ Distance between C.G. and the bottom fiber
 $Y_{n,t} = 2.982 \text{ in.}$ Distance between C.G. and the top fiber
 $S_{n,b} = 35.131 \text{ in}^3$ Net section modulus (bottom)
 $S_{n,t} = 35.559 \text{ in}^3$ Net section modulus (top)
 $w_{b,n} = 0.03801 \text{ kif}$ Net weight of the P/S beam per linear foot including the weight of strand
 $M_{b,n,x} = \frac{w_{b,n} \times (L_{span} - x)^2}{2}$

x in.	Δx in.	L_{span} ft	$M_{b,n,x}$	
			kip-ft	kip-in.
0.000	6.000	8.000	0.000	0.000
6.000			0.071	0.855
12.000			0.133	1.597
18.000			0.185	2.224
24.000			0.228	2.737
30.000			0.261	3.136
36.000			0.285	3.421
42.000			0.299	3.592
48.000			0.304	3.649

2.3 Transformed Section Properties

$$E_{ci} = 4617 \text{ ksi}$$

$$E_p = 28500 \text{ ksi}$$

$$n = E_p/E_{ci} = 6.173$$

	A in. ²	y _b in.	A y _b in. ³	R _{p,eq} in.	I ₀ in. ⁴	D in.	A D ² in. ⁴	I in. ⁴
Beam	35.783	3.018	108.000		106.031	-0.109	0.4244007	106.456
Strand	1.339	0.000	0.000	0.653	0.1427808	2.909	11.337389	11.480
	37.122	2.909	108.000					117.936

$$A_t = 37.122 \text{ in}^2 \quad \dots\dots\dots \text{Transformed area}$$

$$I_t = 117.936 \text{ in}^4 \quad \dots\dots\dots \text{Transformed moment of inertia}$$

$$y_{t,b} = 2.909 \text{ in.} \quad \dots\dots\dots \text{Distance between C.G. and the bottom fiber}$$

$$y_{t,t} = 3.091 \text{ in.} \quad \dots\dots\dots \text{Distance between C.G. and the top fiber}$$

$$S_{t,b} = 40.538 \text{ in}^3 \quad \dots\dots\dots \text{Transformed section modulus (bottom)}$$

$$S_{t,t} = 38.158 \text{ in}^3 \quad \dots\dots\dots \text{Transformed section modulus (top)}$$

$$w_{o,t} = 0.03801 \text{ klf} \quad \dots\dots\dots \text{Transformed weight of the P/S beam per linear foot including the weight of strand}$$

$$M_{bt,x} = \frac{w_{b,t} x}{2} (L_{span} - x)$$

x in.	Δx in.	L _{span} ft	M _{bt,x}	
			kip-ft	kip-in.
0.000	6.000	8.000	0.000	0.000
6.000			0.071	0.855
12.000			0.133	1.597
18.000			0.185	2.224
24.000			0.228	2.737
30.000			0.261	3.136
36.000			0.285	3.421
42.000			0.299	3.592
48.000			0.304	3.649

Step 3: Prestressing

3.1 Prestressing Force

$$f_{pi} = 202.500 \text{ ksi} \quad \text{Initial prestressing before Elastic Shortening}$$

$$L_t = 60 \text{ dp} = 36.000 \text{ in.} \quad \text{Transfer length}$$

x in.	f_{pi} ksi	P_i kips
0.000	0.000	0.000
6.000	33.750	7.324
12.000	67.500	14.648
18.000	101.250	21.971
24.000	135.000	29.295
30.000	168.750	36.619
36.000	202.500	43.943
42.000	202.500	43.943
48.000	202.500	43.943

3.2 Elastic Shortening (Method 1 - Gross Section Properties)

Ref.: AASHTO LRFD 4th Edition with 2008 Interims, Eq. (5.9.5.2.3a-1)

Assume: $\Delta f_{pES} = 4.56\% f_{pi}$ Loss due to Elastic Shortening
 $= 9.225 \text{ ksi}$

Thus,

$$f_{pi} = 193.275 \quad \text{Prestressing after Elastic Shortening}$$

$$e_{p,g} = 3.000$$

$$P_i = 41.941 \text{ kips} \quad \text{Prestressing force after Elastic Shortening}$$

$$E_p/E_{ci} = 6.173$$

$$f_{cgp} = \frac{P_i}{A_g} + \frac{P_i e_{p,g}^2}{I_g} - \frac{M_{bg} e_{p,g}}{I_g}$$

$$\Delta f_{pES} = \frac{E_p}{E_{ci}} f_{cgp}$$

Elastic Shortening based on Gross Section Properties							
x in.	M_{bg} kip-in.	P_i kips	P_i/A_g ksi	$P_i e_{p,g}^2 / I_g$ ksi	$M_{bg} e_{p,g} / I_g$ ksi	f_{cgp} ksi	Δf_{pES} ksi
0.000	0.000	0.000	0.000	0.000	0.000	0.000	0.000
6.000	0.844	6.990	0.194	0.583	0.070	0.706	4.360
12.000	1.575	13.980	0.388	1.165	0.131	1.422	8.778
18.000	2.194	20.970	0.583	1.748	0.183	2.147	13.254
24.000	2.700	27.960	0.777	2.330	0.225	2.882	17.788
30.000	3.094	34.951	0.971	2.913	0.258	3.626	22.380
36.000	3.375	41.941	1.165	3.495	0.281	4.379	27.030
42.000	3.544	41.941	1.165	3.495	0.295	4.365	26.943
48.000	3.600	41.941	1.165	3.495	0.300	4.360	26.914

$$\frac{(\Delta f_{pES})_{\text{assumed}}}{(\Delta f_{pES})_{\text{calculated}}} = 0.3427523 \quad \text{Iterate to optimize the initial value !!!}$$

3.3 Elastic Shortening (Method 2 - Net Section Properties)

Ref.: AASHTO LRFD 4th Edition with 2008 Interims, Eq. (5.9.5.2.3a-1)

Assume: $\Delta f_{pES} = 6.06\% f_{pi}$ Loss due to Elastic Shortening
 $= 12.269 \text{ ksi}$

Thus,

$$f_{pi} = 190.231 \quad \text{Prestressing after Elastic Shortening}$$

$$e_{p,n} = 3.018$$

$$P_i = 41.280 \text{ kips} \quad \text{Prestressing force after Elastic Shortening}$$

$$E_p/E_{ci} = 6.173$$

$$f_{cnp} = \frac{P_i}{A_n} + \frac{P_i e_{p,n}^2}{I_n} - \frac{M_{bn} e_{p,n}}{I_n}$$

$$\frac{P_i}{A_n} + \frac{P_i e_{p,n}^2}{I_n} - \frac{M_{bn} e_{p,n}}{I_n}$$

$$\Delta f_{pES} = \frac{E_p}{E_{ci}} f_{cnp}$$

Elastic Shortening based on Net Section Properties							
x in.	M _{bn} kip-in.	P _i kips	P _i /A _n ksi	P _i e _{p,n} ² /I _n ksi	M _{bn} e _{p,n} /I _n ksi	f _{cnp} ksi	Δf _{pES} ksi
0.000	0.000	0.000	0.000	0.000	0.000	0.000	0.000
6.000	0.855	6.880	0.192	0.591	0.073	0.710	4.382
12.000	1.597	13.760	0.385	1.182	0.137	1.430	8.824
18.000	2.224	20.640	0.577	1.773	0.191	2.159	13.327
24.000	2.737	27.520	0.769	2.364	0.235	2.898	17.890
30.000	3.136	34.400	0.961	2.955	0.269	3.647	22.514
36.000	3.421	41.280	1.154	3.547	0.294	4.406	27.199
42.000	3.592	41.280	1.154	3.547	0.309	4.392	27.108
48.000	3.649	41.280	1.154	3.547	0.314	4.387	27.078

$$\frac{(\Delta f_{pES})_{\text{assumed}}}{(\Delta f_{pES})_{\text{calculated}}} = 0.4530913 \dots \dots \dots \text{Iterate to optimize the initial value !!!}$$

3.4 Elastic Shortening (Method 3 - Transformed Section Properties)

Ref.: AASHTO LRFD 4th Edition with 2008 Interims, Eq. (C5.9.5.2.3a-1)

$$\Delta f_{pES} = \frac{P_i}{A_t} + \frac{P_i e_{p,t}^2}{I_t} - \frac{M_{bt} e_{p,t}}{I_t}$$

e_{p,t} = 2.909 in.

Elastic Shortening based on Transformed Section Properties									
x in.	M _{bt} kip-in.	P _i kips	P _i /A _t ksi	P _i e _{p,t} ² /I _t ksi	M _{bt} e _{p,t} /I _t ksi	f _{ctp} ksi	Δf _c ksi	Δf _{pES} ksi	P _t kips
0.000	0.000	0.000	0.000	0.000	0.000	0.000	0.000	0.000	0.000
6.000	0.855	7.324	0.197	0.526	0.021	0.702	-0.702	4.332	6.384
12.000	1.597	14.648	0.395	1.051	0.039	1.406	-1.406	8.681	12.764
18.000	2.224	21.971	0.592	1.577	0.055	2.114	-2.114	13.048	19.140
24.000	2.737	29.295	0.789	2.102	0.068	2.824	-2.824	17.432	25.512
30.000	3.136	36.619	0.986	2.628	0.077	3.537	-3.537	21.834	31.881
36.000	3.421	43.943	1.184	3.154	0.084	4.253	-4.253	26.253	38.246
42.000	3.592	43.943	1.184	3.154	0.089	4.249	-4.249	26.226	38.251
48.000	3.649	43.943	1.184	3.154	0.090	4.247	-4.247	26.218	38.253

3.5 Prestressing the Gross Section

A_g = 36.000 in²
 I_g = 108.000 in⁴
 y_{g,t} = 3.000 in.
 y_{g,b} = 3.000 in.
 e_{p,g} = 3.000 in. Strand eccentricity relative to C.G. of gross section

$$f_{g,t} = -\frac{P_i}{A_g} + \frac{(P_i e_{p,g}) y_{g,t}}{I_g} - \frac{M_{bg} y_{g,t}}{I_g}$$

$$f_{g,b} = -\frac{P_i}{A_g} - \frac{(P_i e_{p,g}) y_{g,b}}{I_g} + \frac{M_{bg} y_{g,b}}{I_g}$$

x in.	P/A _R ksi	P _i e _{p,n} y _n /I _n ksi		M _{bn} y _n /I _n ksi		f _n ksi	
		Top	Bottom	Top	Bottom	Top	Bottom
0.000	0.000	0.000	0.000	0.000	0.000	0.000	0.000
6.000	0.194	0.583	0.583	0.023	0.023	0.365	-0.753
12.000	0.388	1.165	1.165	0.044	0.044	0.733	-1.510
18.000	0.583	1.748	1.748	0.061	0.061	1.104	-2.269
24.000	0.777	2.330	2.330	0.075	0.075	1.478	-3.032
30.000	0.971	2.913	2.913	0.086	0.086	1.856	-3.797
36.000	1.165	3.495	3.495	0.094	0.094	2.236	-4.566
42.000	1.165	3.495	3.495	0.098	0.098	2.232	-4.562
48.000	1.165	3.495	3.495	0.100	0.100	2.230	-4.560

3.6 Prestressing the Net Section

$A_n = 35.783 \text{ in}^2$
 $I_n = 106.031 \text{ in}^4$
 $y_{n,b} = 3.018 \text{ in.}$
 $y_{n,t} = 2.982 \text{ in.}$
 $e_{p,n} = 3.018 \text{ in.}$ Strand eccentricity relative to C.G. of net section

$$f_{n,t} = -\frac{P_i}{A_n} + \frac{(P_i e_{p,n}) y_{n,t}}{I_n} - \frac{M_{bn} y_{n,t}}{I_n}$$

$$f_{n,b} = -\frac{P_i}{A_n} - \frac{(P_i e_{p,n}) y_{n,b}}{I_n} + \frac{M_{bn} y_{n,b}}{I_n}$$

x in.	P/A _n ksi	P _i e _{p,n} y _n /I _n ksi		M _{bn} y _n /I _n ksi		f _n ksi	
		Top	Bottom	Top	Bottom	Top	Bottom
0.000	0.000	0.000	0.000	0.000	0.000	0.000	0.000
6.000	0.192	0.584	0.591	0.024	0.024	0.368	-0.759
12.000	0.385	1.168	1.182	0.045	0.045	0.738	-1.521
18.000	0.577	1.752	1.773	0.063	0.063	1.113	-2.287
24.000	0.769	2.336	2.364	0.077	0.078	1.490	-3.056
30.000	0.961	2.920	2.955	0.088	0.089	1.870	-3.828
36.000	1.154	3.504	3.547	0.096	0.097	2.254	-4.603
42.000	1.154	3.504	3.547	0.101	0.102	2.249	-4.598
48.000	1.154	3.504	3.547	0.103	0.104	2.248	-4.596

3.7 Prestressing the Transformed Section

$A_t = 37.122 \text{ in}^2$
 $I_t = 117.936 \text{ in}^4$
 $y_{t,b} = 2.909 \text{ in.}$
 $y_{t,t} = 3.091 \text{ in.}$
 $e_{p,t} = 2.909 \text{ in.}$ Strand eccentricity relative to C.G. of transformed section

$$f_{t,t} = -\frac{P_i}{A_t} + \frac{(P_i e_{p,t}) y_{t,t}}{I_t} - \frac{M_{bt} y_{t,t}}{I_t}$$

$$f_{t,b} = -\frac{P_i}{A_t} - \frac{(P_i e_{p,t}) y_{t,b}}{I_t} + \frac{M_{bt} y_{t,b}}{I_t}$$

x in.	Δf _{pES} ksi	P _i ksi	P _i /A _t ksi	P _i e _{p,t} y _t /I _t ksi		M _{bt} y _t /I _t ksi		f _t ksi	
				Top	Bottom	Top	Bottom	Top	Bottom
0.000	0.000	0.000	0.000	0.000	0.000	0.000	0.000	0.000	0.000
6.000	4.332	7.324	0.197	0.558	0.526	0.022	0.021	0.339	-0.702
12.000	8.681	14.648	0.395	1.117	1.051	0.042	0.039	0.680	-1.406
18.000	13.048	21.971	0.592	1.675	1.577	0.058	0.055	1.025	-2.114
24.000	17.432	29.295	0.789	2.234	2.102	0.072	0.068	1.373	-2.824
30.000	21.834	36.619	0.986	2.792	2.628	0.082	0.077	1.723	-3.537
36.000	26.253	43.943	1.184	3.350	3.154	0.090	0.084	2.077	-4.253
42.000	26.226	43.943	1.184	3.350	3.154	0.094	0.089	2.072	-4.249
48.000	26.218	43.943	1.184	3.350	3.154	0.096	0.090	2.071	-4.247

Step 5: Optimizing Strand Eccentricity

INSTRUCTIONS

- 1) **Model Dimensions Module:** Input the values in cells marked as x.xxx
- 2) **Elastic Shortening:** Assume an initial value for strand eccentricity (e).
- 3) **Design Module:** Assume a percentage of rupture modulus as allowable tensile stress.
- 4) **Design Module:** Iterate for strand eccentricity (GOAL SEAK).

5.a Model Dimensions (Tensile St. = +ve sign, Comp. St. = -ve sign)				Password 123	
Concrete Material		Strand material		Section geometrical properties	
f'ci	5.800 ksi	fpu	270.000 ksi	b	6.000 in
Unit wt	0.150 kcf	Unit wt	0.490 kcf	h	6.000 in
Unit wt	0.038 klf	% of fpu just before release	75% ---	A	36.000 in2
0.6f'ci	-3.480 ksi	fpo (just before Release)	202.500 ksi	S top (= S bottom)	36.000 in3
fr =7.5 sqrt f'ci	0.571 ksi	Strand diameter (0.5 or 0.6)	0.600 in.	I (inertia)	108.000 in4
Eci	4617.053 ksi	Ap, Strand area	0.217 in2	Member length	96.000 in
		Po (just before release)	43.943 kips	Member length	8.000 ft
		Transfer length (60 dp)	36.000 in	Mg at transfer length	0.281 k-ft
		Transfer length (60 dp)	3.000 ft	Mg at midspan	0.300 k-ft
		Ep	28500.000 ksi		

5.b Elastic shortening losses		
Assume e	1.584 in.	
f cir	-2.188 ksi	stress at midspan at cg of strands just before release = -(Po/A) - (Po * e^2)/I + (Mg at midspan * e)/I
ES loss	-13.508 ksi	= (Ep / Eci) * f cir Ref.: AASHTO LRFD 4th Edition with 2008 Interims Article 5.9.5.2.3
fpi	188.992 ksi	Strand stress immediately after release
Ppi	41.011 kips	Strand force immediately after release

5.c Design based on allowable tensile st. at top fiber at the transfer length and using PI			
% of fr	100%	Top stress	0.571 ksi
Ppi/A	-1.139 ksi	Mg / S top	-0.094 ksi
		Ppi / S top	1.139 k/in3

e = 1.584 in e (assumed)/e (calculated) = 0.999991
 Check against assumed value for eccentricity : OK, Difference is <=1%

5.d Check solution at transfer length			
(P / S top)*e	1.804 ksi	Total top st.	0.571 ksi
		Total bottom st	-2.850 ksi
		= (% of fr)*fr (OK) Fiber in Tension
		< 0.6f'ci (OK) Fiber in Compression

Step 6: Section Properties

Use: $h_p = 1.450$ in. Strand location relative to the bottom face of P/S beam

6.1 Gross Section Properties

$A_g = 36.000 \text{ in}^2$ Gross area
 $I_g = 108.000 \text{ in}^4$ Gross moment of inertia
 $Y_{g,b} = 3.000 \text{ in.}$ Distance between C.G. and the bottom fiber
 $Y_{g,t} = 3.000 \text{ in.}$ Distance between C.G. and the top fiber
 $S_{g,b} = 36.000 \text{ in}^4$ Gross moment of inertia
 $S_{g,t} = 36.000 \text{ in}^4$ Gross moment of inertia

$w_{b,g} = 0.03750 \text{ klf}$ Gross weight of the P/S beam per linear foot

$$M_{b,g,x} = \frac{w_{b,g} \times (L_{\text{span}} - x)}{2}$$

x in.	Δx in.	L_{span} ft	$M_{b,g,x}$	
			kip-ft	kip-in.
0.000	6.000	8.000	0.000	0.000
6.000			0.070	0.844
12.000			0.131	1.575
18.000			0.183	2.194
24.000			0.225	2.700
30.000			0.258	3.094
36.000			0.281	3.375
42.000			0.295	3.544
48.000			0.300	3.600

6.2 Net Section Properties

	A in. ²	Y_b in.	I_o in. ⁴	D in.	$A D^2$ in. ⁴	I in. ⁴		
Beam	36.000	3.000	108.000		108.000	0.009	0.0031808	108.003
Strand	0.217	1.450	0.315	0.263	0.0037472	1.559	0.5276849	0.531
	35.783	3.009	107.685					107.472

$A_n = 35.783 \text{ in}^2$ Net area
 $I_n = 107.472 \text{ in}^4$ Net moment of inertia
 $Y_{n,b} = 3.009 \text{ in.}$ Distance between C.G. and the bottom fiber
 $Y_{n,t} = 2.991 \text{ in.}$ Distance between C.G. and the top fiber
 $S_{n,b} = 35.712 \text{ in}^4$ Net section modulus (bottom)
 $S_{n,t} = 35.937 \text{ in}^4$ Net section modulus (top)
 $w_{b,n} = 0.03801 \text{ klf}$ Net weight of the P/S beam per linear foot including the weight of strand

$$M_{b,n,x} = \frac{w_{b,n} \times (L_{\text{span}} - x)}{2}$$

x in.	Δx in.	L_{span} ft	$M_{b,n,x}$	
			kip-ft	kip-in.
0.000	6.000	8.000	0.000	0.000
6.000			0.071	0.855
12.000			0.133	1.597
18.000			0.185	2.224
24.000			0.228	2.737
30.000			0.261	3.136
36.000			0.285	3.421
42.000			0.299	3.592
48.000			0.304	3.649

6.3 Transformed Section Properties

$E_{ci} = 4617 \text{ ksi}$
 $E_p = 28500 \text{ ksi}$
 $n = E_p/E_{ci} = 6.173$

	A	y _b	A y _b	R _{p,eq}	I _o	D	A D ²	I
	in. ²	in.	in. ³	in.	in. ⁴	in.	in. ⁴	in. ⁴
Beam	35.783	3.009	107.685		107.472	-0.056	0.1132914	107.585
Strand	1.339	1.450	1.942	0.653	0.1427808	1.503	3.0264531	3.169
	37.122	2.953	109.628					110.754

$A_t = 37.122 \text{ in}^2$ Transformed area
 $I_t = 110.754 \text{ in}^4$ Transformed moment of inertia
 $y_{t,b} = 2.953 \text{ in.}$ Distance between C.G. and the bottom fiber
 $y_{t,t} = 3.047 \text{ in.}$ Distance between C.G. and the top fiber
 $S_{t,b} = 37.504 \text{ in}^4$ Transformed section modulus (bottom)
 $S_{t,t} = 36.350 \text{ in}^4$ Transformed section modulus (top)

$w_{b,t} = 0.03801 \text{ kif}$ Transformed weight of the P/S beam per linear foot including the weight of strand

$$M_{bt,x} = \frac{w_{b,t} x}{2} (L_{span} - x)$$

x	Δx	L _{span}	M _{bt,x}	
			kip-ft	kip-in.
in.	in.	ft		
0.000	6.000	8.000	0.000	0.000
6.000			0.071	0.855
12.000			0.133	1.597
18.000			0.185	2.224
24.000			0.228	2.737
30.000			0.261	3.136
36.000			0.285	3.421
42.000			0.299	3.592
48.000			0.304	3.649

Step 7: Prestressing

7.1 Prestressing Force

$f_{pi} = 202.500$ ksi Initial prestressing before Elastic Shortening
 $L_t = 60$ dp = 36.000 in. Transfer length

x in.	f_{pi} ksi	P_i kips
0.000	0.000	0.000
6.000	33.750	7.324
12.000	67.500	14.648
18.000	101.250	21.971
24.000	135.000	29.295
30.000	168.750	36.619
36.000	202.500	43.943
42.000	202.500	43.943
48.000	202.500	43.943

7.2 Elastic Shortening (Method 1 - Gross Section Properties)

Ref.: AASHTO LRFD 4th Edition with 2008 Interims, Eq. (5.9.5.2.3a-1)

Assume: $\Delta f_{pES} = 4.56\%$ f_{pi} Loss due to Elastic Shortening
 = 9.225 ksi

Thus,

$f_{pi} = 193.275$ Prestressing after Elastic Shortening
 $e_{p,g} = 1.550$
 $P_i = 41.941$ kips Prestressing force after Elastic Shortening
 $E_p/E_{ci} = 6.173$

$$f_{cgp} = \frac{P_i}{A_g} + \frac{P_i e_{p,g}^2}{I_g} - \frac{M_{bg} e_{p,g}}{I_g}$$

$$\Delta f_{pES} = \frac{E_p}{E_{ci}} f_{cgp}$$

Elastic Shortening based on Gross Section Properties							
x in.	M_{bg} kip-in.	P_i kips	P_i/A_g ksi	$P_i e_{p,g}^2 / I_g$ ksi	$M_{bg} e_{p,g} / I_g$ ksi	f_{cgp} ksi	Δf_{pES} ksi
0.000	0.000	0.000	0.000	0.000	0.000	0.000	0.000
6.000	0.844	6.990	0.194	0.155	0.019	0.331	2.043
12.000	1.575	13.980	0.388	0.311	0.035	0.664	4.101
18.000	2.194	20.970	0.583	0.466	0.049	1.000	6.174
24.000	2.700	27.960	0.777	0.622	0.060	1.339	8.263
30.000	3.094	34.951	0.971	0.777	0.069	1.680	10.367
36.000	3.375	41.941	1.165	0.933	0.075	2.023	12.487
42.000	3.544	41.941	1.165	0.933	0.079	2.019	12.464
48.000	3.600	41.941	1.165	0.933	0.080	2.018	12.456

$\frac{(\Delta f_{pES})_{assumed}}{(\Delta f_{pES})_{calculated}} = 0.7405769$ Iterate to optimize the initial value !!!

7.3 Elastic Shortening (Method 2 - Net Section Properties)

Ref.: AASHTO LRFD 4th Edition with 2008 Interims, Eq. (5.9.5.2.3a-1)

Assume: $\Delta f_{pES} = 6.06\%$ f_{pi} Loss due to Elastic Shortening
 = 12.269 ksi

Thus,

$f_{pi} = 190.231$ Prestressing after Elastic Shortening
 $e_{p,n} = 1.559$
 $P_i = 41.280$ kips Prestressing force after Elastic Shortening
 $E_p/E_{ci} = 6.173$

$$f_{cnp} = \frac{P_i}{A_n} + \frac{P_i e_{p,n}^2}{I_n} - \frac{M_{bn} e_{p,n}}{I_n}$$

$$\Delta f_{pES} = \frac{E_p}{E_{ci}} f_{cnp}$$

Elastic Shortening based on Net Section Properties							
x in.	M _{bn} kip-in.	P _i kips	P _i /A _n ksi	P _i e _{p,n} ² /I _n ksi	M _{bn} e _{p,n} /I _n ksi	f _{cnp} ksi	Δf _{pES} ksi
0.000	0.000	0.000	0.000	0.000	0.000	0.000	0.000
6.000	0.855	6.880	0.192	0.156	0.019	0.329	2.028
12.000	1.597	13.760	0.385	0.311	0.036	0.660	4.073
18.000	2.224	20.640	0.577	0.467	0.050	0.994	6.133
24.000	2.737	27.520	0.769	0.623	0.062	1.330	8.209
30.000	3.136	34.400	0.961	0.778	0.071	1.669	10.301
36.000	3.421	41.280	1.154	0.934	0.077	2.010	12.409
42.000	3.592	41.280	1.154	0.934	0.081	2.006	12.385
48.000	3.649	41.280	1.154	0.934	0.083	2.005	12.377

$$\frac{(\Delta f_{pES})_{\text{assumed}}}{(\Delta f_{pES})_{\text{calculated}}} = 0.9912475 \dots \dots \dots \text{Iterate to optimize the initial value !!!}$$

7.4 Elastic Shortening (Method 3 - Transformed Section Properties)

Ref.: AASHTO LRFD 4th Edition with 2008 Interims, Eq. (C5.9.5.2.3a-1)

$$\Delta f_{pES} = \frac{P_i}{A_t} + \frac{P_i e_{p,t}^2}{I_t} - \frac{M_{bt} e_{p,t}}{I_t}$$

e_{p,t} = 1.503 in.

Elastic Shortening based on Transformed Section Properties									
x in.	M _{bt} kip-in.	P _i kips	P _i /A _t ksi	P _i e _{p,t} ² /I _t ksi	M _{bt} e _{p,t} /I _t ksi	f _{cnp} ksi	Δf _c ksi	Δf _{pES} ksi	P _i kips
0.000	0.000	0.000	0.000	0.000	0.000	0.000	0.000	0.000	0.000
6.000	0.855	7.324	0.197	0.149	0.012	0.335	-0.335	2.068	6.875
12.000	1.597	14.648	0.395	0.299	0.022	0.672	-0.672	4.146	13.748
18.000	2.224	21.971	0.592	0.448	0.030	1.010	-1.010	6.234	20.619
24.000	2.737	29.295	0.789	0.598	0.037	1.350	-1.350	8.331	27.487
30.000	3.136	36.619	0.986	0.747	0.043	1.691	-1.691	10.438	34.354
36.000	3.421	43.943	1.184	0.896	0.046	2.034	-2.034	12.554	41.218
42.000	3.592	43.943	1.184	0.896	0.049	2.031	-2.031	12.539	41.221
48.000	3.649	43.943	1.184	0.896	0.050	2.031	-2.031	12.535	41.222

7.5 Prestressing the Gross Section

A_g = 36.000 in²
 I_g = 108.000 in⁴
 y_{g,b} = 3.000 in.
 y_{g,t} = 3.000 in.
 e_{p,g} = 1.550 in. Strand eccentricity relative to C.G. of gross section

$$f_{g,t} = -\frac{P_i}{A_g} + \frac{(P_i e_{p,g}) y_{g,t}}{I_g} - \frac{M_{bg} y_{g,t}}{I_g}$$

$$f_{g,b} = -\frac{P_i}{A_g} - \frac{(P_i e_{p,g}) y_{g,b}}{I_g} + \frac{M_{bg} y_{g,b}}{I_g}$$

x in.	P/A _R ksi	P _i e _{p,R} y _R /I _R ksi		M _{bn} y _R /I _R ksi		f _R ksi	
		Top	Bottom	Top	Bottom	Top	Bottom
0.000	0.000	0.000	0.000	0.000	0.000	0.000	0.000
6.000	0.194	0.301	0.301	0.023	0.023	0.083	-0.472
12.000	0.388	0.602	0.602	0.044	0.044	0.170	-0.947
18.000	0.583	0.903	0.903	0.061	0.061	0.259	-1.424
24.000	0.777	1.204	1.204	0.075	0.075	0.352	-1.906
30.000	0.971	1.505	1.505	0.086	0.086	0.448	-2.390
36.000	1.165	1.806	1.806	0.094	0.094	0.547	-2.877
42.000	1.165	1.806	1.806	0.098	0.098	0.542	-2.872
48.000	1.165	1.806	1.806	0.100	0.100	0.541	-2.871

7.6 Prestressing the Net Section

$A_n = 35.783 \text{ in}^2$
 $I_n = 107.472 \text{ in}^4$
 $y_{n,b} = 3.009 \text{ in.}$
 $y_{n,t} = 2.991 \text{ in.}$
 $e_{p,n} = 1.559 \text{ in.}$ Strand eccentricity relative to C.G. of net section

$$f_{n,t} = -\frac{P_i}{A_n} + \frac{(P_i e_{p,n}) y_{n,t}}{I_n} - \frac{M_{bn} y_{n,t}}{I_n}$$

$$f_{n,b} = -\frac{P_i}{A_n} - \frac{(P_i e_{p,n}) y_{n,b}}{I_n} + \frac{M_{bn} y_{n,b}}{I_n}$$

x in.	P/A _n ksi	P _i e _{p,n} y _n /I _n ksi		M _{bn} y _n /I _n ksi		f _n ksi	
		Top	Bottom	Top	Bottom	Top	Bottom
0.000	0.000	0.000	0.000	0.000	0.000	0.000	0.000
6.000	0.192	0.299	0.300	0.024	0.024	0.082	-0.469
12.000	0.385	0.597	0.601	0.044	0.045	0.168	-0.941
18.000	0.577	0.896	0.901	0.062	0.062	0.257	-1.416
24.000	0.769	1.194	1.202	0.076	0.077	0.349	-1.894
30.000	0.961	1.493	1.502	0.087	0.088	0.444	-2.376
36.000	1.154	1.791	1.803	0.095	0.096	0.542	-2.860
42.000	1.154	1.791	1.803	0.100	0.101	0.538	-2.856
48.000	1.154	1.791	1.803	0.102	0.102	0.536	-2.854

7.8 Prestressing the Transformed Section

$A_t = 37.122 \text{ in}^2$
 $I_t = 110.754 \text{ in}^4$
 $y_{t,b} = 2.953 \text{ in.}$
 $y_{t,t} = 3.047 \text{ in.}$
 $e_{p,t} = 1.503 \text{ in.}$ Strand eccentricity relative to C.G. of transformed section


$$f_{t,t} = -\frac{P_i}{A_t} + \frac{(P_i e_{p,t}) y_{t,t}}{I_t} - \frac{M_{bt} y_{t,t}}{I_t}$$

$$f_{t,b} = -\frac{P_i}{A_t} - \frac{(P_i e_{p,t}) y_{t,b}}{I_t} + \frac{M_{bt} y_{t,b}}{I_t}$$

x in.	Δf _{pES} ksi	P _i ksi	P _i /A _t ksi	P _i e _{p,t} y _t /I _t ksi		M _{bt} y _t /I _t ksi		f _t ksi	
				Top	Bottom	Top	Bottom	Top	Bottom
0.000	0.000	0.000	0.000	0.000	0.000	0.000	0.000	0.000	0.000
6.000	2.068	7.324	0.197	0.303	0.294	0.024	0.023	0.082	-0.468
12.000	4.146	14.648	0.395	0.606	0.587	0.044	0.043	0.167	-0.939
18.000	6.234	21.971	0.592	0.909	0.881	0.061	0.059	0.256	-1.413
24.000	8.331	29.295	0.789	1.211	1.174	0.075	0.073	0.347	-1.890
30.000	10.438	36.619	0.986	1.514	1.468	0.086	0.084	0.442	-2.370
36.000	12.554	43.943	1.184	1.817	1.761	0.094	0.091	0.539	-2.854
42.000	12.539	43.943	1.184	1.817	1.761	0.099	0.096	0.535	-2.849
48.000	12.535	43.943	1.184	1.817	1.761	0.100	0.097	0.533	-2.848

Appendix D

Closed-Form Solution for a 7"x7" Rectangular Beam Concentrically Pretensioned with One 0.7-in. Diameter Strand

Department of Civil & Environmental Engineering	By	Amir A. Arab, P.E.	
	Date	7/15/2009	
Subject FE MODELING OF P/S CONCRETE MEMBERS A Theoretical Approach	CRN		
	Course No.	DISSERTATION	
	Professor	Dr. S. Badie/Dr. M. Manzari	

1 INTRODUCTION

The following includes a theoretical analysis of a rectangular prestressed (P/S) concrete member with one prestressing strand and no mild reinforcement. The effect of the prestressing will be investigated at an instance after the release as affected by all the applicable losses.

2 ASSUMPTIONS

1. The P/S member is pretensioned using only one prestressed strand.
2. The P/S member rests on a frictionless steel casting bed.
3. The P/S member can only camber up due to eccentricity of the prestressing strand, if any.
4. Based on Item No.3 above, the theoretical span for the analytical purposes of this study is assumed to be the end to end of the member given that the upward concaving occurs while pivoting around the bottom edges of the end faces of the member.

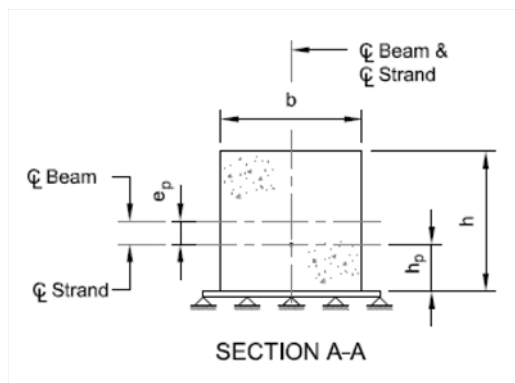
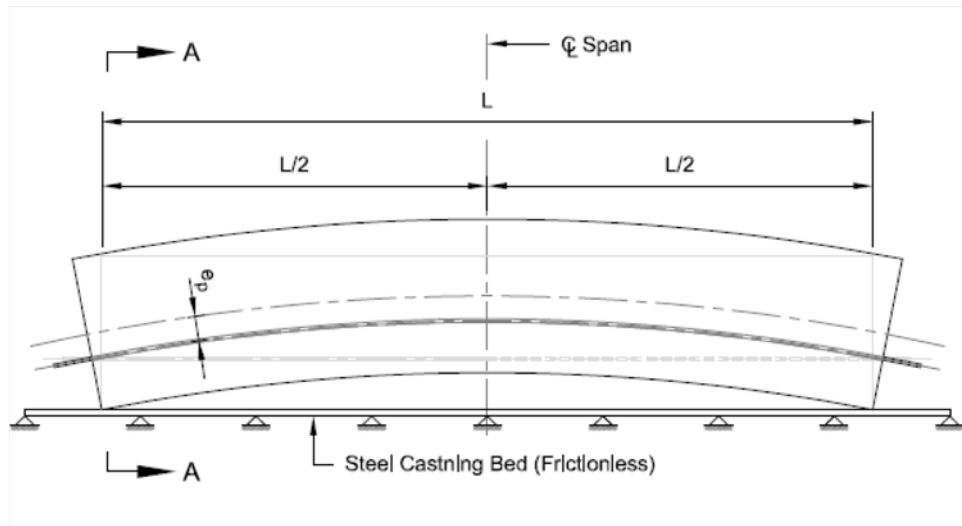


Figure 1, Schematic presentation of the proposed analysis

3 DESIGN PARAMETERS

The following includes the design parameters for the analytical purposes of this document:

3.1 CONCRETE BEAM

Input:

- $b := 7 \cdot \text{in}$ Width of the rectangular P/S beam
- $h := 7 \cdot \text{in}$ Height of the rectangular P/S beam
- $h_p := 0 \cdot \text{in}$ Location of the P/S strand from the bottom face of the P/S beam
- $L_b := 96 \cdot \text{in}$ Total span of P/S rectangular beam
- $f_{ci} := 3000 \cdot \text{psi}$ Compressive strength of concrete at release
- $w_c := 150 \cdot \text{pcf}$ Weight of concrete
- $\Xi := \text{"Other Cases"}$ Enter "Minimum Reinforcement" or "Other Cases"

Output:

- $A_b := b \cdot h$
- $A_b = 49 \cdot \text{in}^2$ Gross cross-sectional area of the rectangular beam
- $I_b := \frac{1}{12} \cdot b \cdot h^3$
- $I_b = 200.083 \cdot \text{in}^4$ Moment of inertia of rectangular beam
- $c_b := \frac{h}{2}$
- $c_b = 3.5 \cdot \text{in}$ Centroid of rectangular beam
- $E_{ci} := 33 \cdot \left(w_c \cdot \frac{1}{\text{pcf}} \right)^{1.5} \cdot \sqrt{f_{ci} \cdot 1000 \cdot \text{ksi}} \cdot \frac{1}{1000}$
- $E_{ci} = 3.321 \times 10^3 \cdot \text{ksi}$ Modulus of elasticity at release
- $f_{ri} := \begin{cases} 0.24 \cdot \sqrt{f_{ci} \cdot \text{ksi}} & \text{if } \Xi = \text{"Other Cases"} \\ 0.24 \cdot \sqrt{f_{ci} \cdot \text{ksi}} & \text{if } \Xi = \text{"Minimum Reinforcement"} \\ \text{"ERROR"} & \text{otherwise} \end{cases}$
- $f_{ri} = 0.416 \cdot \text{ksi}$ Modulus of rupture at release

3.2 P/S STRANDS

Input:

$N_p := 1$ Number of P/S strands

$d_p := 0.7 \cdot \text{in}$ Diameter of P/S strand

$$A_p := \begin{cases} 0.153 \cdot \text{in}^2 & \text{if } d_p = 0.5 \cdot \text{in} \\ 0.217 \cdot \text{in}^2 & \text{if } d_p = 0.6 \cdot \text{in} \\ 0.294 \cdot \text{in}^2 & \text{if } d_p = 0.7 \cdot \text{in} \\ \text{"USE 0.5, 0.6 or 0.7 in. Diameter Strands only"} & \text{otherwise} \end{cases}$$

$A_p = 0.294 \cdot \text{in}^2$ Area of P/S strand

$E_p := 28500 \cdot \text{ksi}$ Modulus of elasticity

$f_{pu} := 270 \cdot \text{ksi}$ Ultimate tensile strength of P/S strand

$\Theta := \text{"Low-relaxation"}$ Enter "Low-relaxation" or "Stress-relieved"

Output:

$$f_{py} := \begin{cases} (0.9 \cdot f_{pu}) & \text{if } \Theta = \text{"Low-relaxation"} \\ (0.85 \cdot f_{pu}) & \text{if } \Theta = \text{"Stress-relieved"} \end{cases}$$

$f_{py} = 243 \cdot \text{ksi}$ Yield strength of P/S strand

$$f_{po} := 0.75 \cdot f_{pu}$$

$f_{po} = 202.5 \cdot \text{ksi}$ Initial prestressing

4 RELEASING STAGE WITH CONCENTRIC STRAND ONLY

The following includes an estimation of the effect of the prestressing on the rectangular beam before and immediately after the release of the P/S strand:

4.1 Step No.1: Tensioning the P/S Strand

$t_1 := 0 \cdot \text{hr}$ Time at beginning of Step No.1

$f_{p1} := f_{po}$

$f_{p1} = 202.5 \cdot \text{ksi}$ Prestensioning stress in strand (Step No.1)

$\epsilon_{p1} := \frac{f_{p1}}{E_p}$

$\epsilon_{p1} = 7.105 \times 10^{-3}$ Initial strain in strand (Step No.1)

At this stage the concrete has not been cast yet; therefore,

$f_{c1} := 0 \cdot \text{ksi}$ Stress in concrete at Step No.1

$\epsilon_{c1} := \frac{f_{c1}}{E_{ci}}$

$\epsilon_{c1} = 0$ Strain in concrete at Step No.1

4.2 Step No.2: From Strand Tensioning to Strand Release

$t_2 := 1 \cdot \text{hr}$ Time at the beginning of Step No.2

$$f_{p2} := f_{p1} \cdot \left[1 - \frac{\log\left(\frac{t_2}{\text{hr}}\right)}{45} \cdot \left(\frac{f_{p1}}{f_{py}} - 0.55 \right) \right]$$

$f_{p2} = 202.5 \cdot \text{ksi}$ Tensioning in the strand after relaxation (Step No.2)

$\% \text{Loss}_{\text{relaxation}} := \left(1 - \frac{f_{p2}}{f_{p1}} \right)$

$\% \text{Loss}_{\text{relaxation}} = 0 \cdot \%$ Loss due to relaxation of steel

$\epsilon_{p2} := \epsilon_{p1}$

$\epsilon_{p2} = 7.105 \times 10^{-3}$ Strain after loss due to relaxation of steel (Step No.2)

At this stage the concrete has not been cast yet; therefore,

$$f_{c2} := 0 \cdot \text{ksi} \dots\dots\dots \text{Stress in concrete at Step No.2}$$

$$\epsilon_{c2} := \frac{f_{c1}}{E_{ci}}$$

$$\epsilon_{c2} = 0 \dots\dots\dots \text{Strain in concrete at Step No.2}$$

4.3 Step No.3: At the Instance after the Release the Strand

The applied prestress force will be distributed between concrete and strand immediately after the prestress release as follows:

$$f_{c3} := f_{ci}$$

$$f_{c3} = 3 \cdot \text{ksi} \dots\dots\dots \text{Compressive strength of concrete at the time of release}$$

$$E_{c3} := E_{ci}$$

$$E_{c3} = 3.321 \times 10^3 \cdot \text{ksi} \dots\dots\dots \text{Modulus of elasticity of concrete at the time of release}$$

$$n_3 := \frac{E_p}{E_{c3}}$$

$$n_3 = 8.583 \dots\dots\dots \text{Modular ratio at the time of release}$$

$$P_2 := N_p \cdot f_{p2} \cdot A_p$$

$$P_2 = 59.535 \cdot \text{kip} \dots\dots\dots \text{Total prestress force at the time of release}$$

$$\Delta f_{c3} := \frac{-P_2}{A_b + (n_3 - 1) \cdot A_p}$$

$$\Delta f_{c3} = -1.162 \cdot \text{ksi} \dots\dots \text{Change of stress in concrete immediately after the prestressing release}$$

$$\Delta f_{p3} := n_3 \cdot \Delta f_{c3}$$

$$\Delta f_{p3} = -9.974 \cdot \text{ksi} \dots\dots \text{Change of stress in strand immediately after the prestressing release}$$

And consequently,

$$\Delta \epsilon_{c3} := \frac{\Delta f_{c3}}{E_{c3}}$$

$$\Delta \epsilon_{c3} = -3.5 \times 10^{-4} \dots\dots\dots \text{Change of strain in concrete immediately after the prestressing release}$$

$$\Delta \epsilon_{p3} := \frac{\Delta f_{p3}}{E_p}$$

$\Delta\varepsilon_{p3} = -3.5 \times 10^{-4}$ Change of strain in strand immediately after the prestressing release

Therefore, at the end of Step 3, the stress and strain in concrete and strand(s) are as follows:

<u>Concrete</u>	<u>Strand</u>	<u>Loss Due to Elastic Shortening</u>
$f_{c3} := f_{c2} + \Delta f_{c3}$	$f_{p3} := f_{p2} + \Delta f_{p3}$	$\%Loss_{ES} := \frac{f_{p2} - f_{p3}}{f_{p2}}$
$f_{c3} = -1.162 \cdot \text{ksi}$	$f_{p3} = 192.526 \cdot \text{ksi}$	
$\varepsilon_{c3} := \varepsilon_{c2} + \Delta\varepsilon_{c3}$	$\varepsilon_{p3} := \varepsilon_{p2} + \Delta\varepsilon_{p3}$	$\%Loss_{ES} = 4.926 \cdot \%$
$\varepsilon_{c3} = -3.5 \times 10^{-4}$	$\varepsilon_{p3} = 6.755 \times 10^{-3}$	
$\left \frac{f_{c3}}{f_{ci}} \right = 0.387$	$P_3 := f_{p3} \cdot N_p \cdot A_p$	
	$P_3 = 56.603 \cdot \text{kip}$	

Appendix E

Closed-Form Solution for a 7"x7" Rectangular Beam Concentrically Pretensioned with Nine 0.7-in. Diameter Strand

Department of Civil & Environmental Engineering	By	Amir A. Arab, P.E.	
	Date	7/15/2009	
Subject FE MODELING OF P/S CONCRETE MEMBERS A Theoretical Approach	CRN		
	Course No.	DISSERTATION	
	Professor	Dr. S. Badie/Dr. M. Manzari	

1 INTRODUCTION

The following includes a theoretical analysis of a rectangular prestressed (P/S) concrete member with nine prestressing strand and no mild reinforcement. The effect of the prestressing will be investigated at an instance after the release as affected by all the applicable losses.

2 ASSUMPTIONS

1. The P/S member is pretensioned using only one prestressed strand.
2. The P/S member rests on a frictionless steel casting bed.
3. The P/S member can only camber up due to eccentricity of the prestressing strand, if any.
4. Based on Item No.3 above, the theoretical span for the analytical purposes of this study is assumed to be the end to end of the member given that the upward concaving occurs while pivoting around the bottom edges of the end faces of the member.

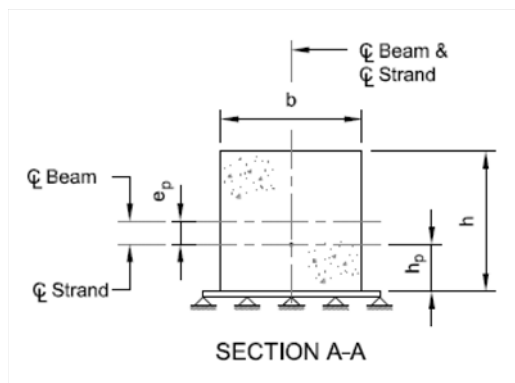
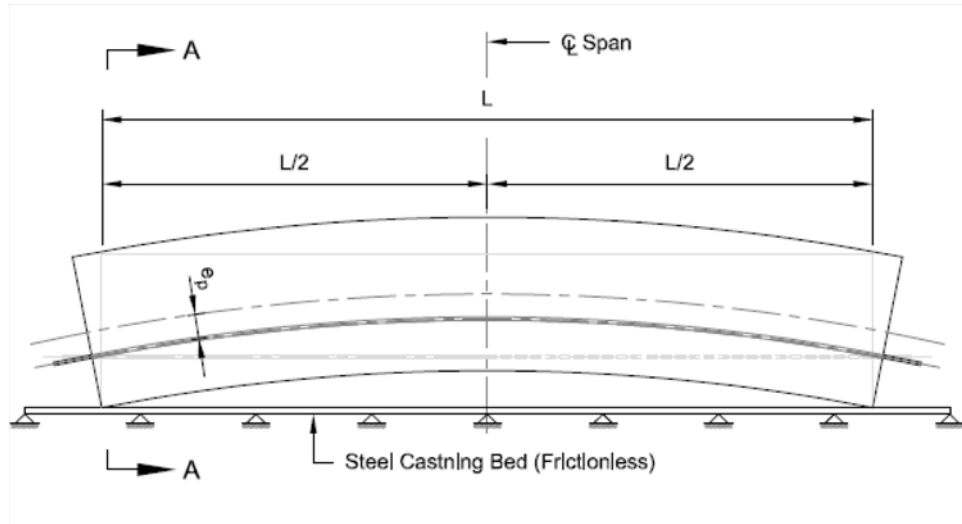


Figure 1, Schematic presentation of the proposed analysis

3 DESIGN PARAMETERS

The following includes the design parameters for the analytical purposes of this document:

3.1 CONCRETE BEAM

Input:

- $b := 11 \cdot \text{in}$ Width of the rectangular P/S beam
- $h := 11 \cdot \text{in}$ Height of the rectangular P/S beam
- $h_p := 0 \cdot \text{in}$ Location of the P/S strand from the bottom face of the P/S beam
- $L_b := 240 \cdot \text{in}$ Total span of P/S rectangular beam
- $f_{ci} := 8000 \cdot \text{psi}$ Compressive strength of concrete at release
- $w_c := 150 \cdot \text{pcf}$ Weight of concrete
- $\Xi := \text{"Other Cases"}$ Enter "Minimum Reinforcement" or "Other Cases"

Output:

- $A_b := b \cdot h$
- $A_b = 121 \cdot \text{in}^2$ Gross cross-sectional area of the rectangular beam
- $I_b := \frac{1}{12} \cdot b \cdot h^3$
- $I_b = 1.22 \times 10^3 \cdot \text{in}^4$ Moment of inertia of rectangular beam
- $c_b := \frac{h}{2}$
- $c_b = 5.5 \cdot \text{in}$ Centroid of rectangular beam
- $E_{ci} := 33 \cdot \left(w_c \cdot \frac{1}{\text{pcf}} \right)^{1.5} \cdot \sqrt{f_{ci} \cdot 1000 \cdot \text{ksi}} \cdot \frac{1}{1000}$
- $E_{ci} = 5.422 \times 10^3 \cdot \text{ksi}$ Modulus of elasticity at release
- $f_{ri} := \begin{cases} 0.24 \cdot \sqrt{f_{ci} \cdot \text{ksi}} & \text{if } \Xi = \text{"Other Cases"} \\ 0.24 \cdot \sqrt{f_{ci} \cdot \text{ksi}} & \text{if } \Xi = \text{"Minimum Reinforcement"} \\ \text{"ERROR"} & \text{otherwise} \end{cases}$
- $f_{ri} = 0.679 \cdot \text{ksi}$ Modulus of rupture at release

3.2 P/S STRANDS

Input:

$N_p := 9$ Number of P/S strands

$d_p := 0.7 \cdot \text{in}$ Diameter of P/S strand

$$A_p := \begin{cases} 0.153 \cdot \text{in}^2 & \text{if } d_p = 0.5 \cdot \text{in} \\ 0.217 \cdot \text{in}^2 & \text{if } d_p = 0.6 \cdot \text{in} \\ 0.294 \cdot \text{in}^2 & \text{if } d_p = 0.7 \cdot \text{in} \\ \text{"USE 0.5, 0.6 or 0.7 in. Diameter Strands only"} & \text{otherwise} \end{cases}$$

$A_p = 0.294 \cdot \text{in}^2$ Area of P/S strand

$E_p := 28500 \cdot \text{ksi}$ Modulus of elasticity

$f_{pu} := 270 \cdot \text{ksi}$ Ultimate tensile strength of P/S strand

$\Theta := \text{"Low-relaxation"}$ Enter "Low-relaxation" or "Stress-relieved"

Output:

$$f_{py} := \begin{cases} (0.9 \cdot f_{pu}) & \text{if } \Theta = \text{"Low-relaxation"} \\ (0.85 \cdot f_{pu}) & \text{if } \Theta = \text{"Stress-relieved"} \end{cases}$$

$f_{py} = 243 \cdot \text{ksi}$ Yield strength of P/S strand

$$f_{po} := 0.75 \cdot f_{pu}$$

$f_{po} = 202.5 \cdot \text{ksi}$ Initial prestressing

4 RELEASING STAGE WITH CONCENTRIC STRAND ONLY

The following includes an estimation of the effect of the prestressing on the rectangular beam before and immediately after the release of the P/S strand:

4.1 Step No.1: Tensioning the P/S Strand

$t_1 := 0 \cdot \text{hr}$ Time at beginning of Step No.1

$f_{p1} := f_{po}$

$f_{p1} = 202.5 \cdot \text{ksi}$ Prestensioning stress in strand (Step No.1)

$\epsilon_{p1} := \frac{f_{p1}}{E_p}$

$\epsilon_{p1} = 7.105 \times 10^{-3}$ Initial strain in strand (Step No.1)

At this stage the concrete has not been cast yet; therefore,

$f_{c1} := 0 \cdot \text{ksi}$ Stress in concrete at Step No.1

$\epsilon_{c1} := \frac{f_{c1}}{E_{ci}}$

$\epsilon_{c1} = 0$ Strain in concrete at Step No.1

4.2 Step No.2: From Strand Tensioning to Strand Release

$t_2 := 1 \cdot \text{hr}$ Time at the beginning of Step No.2

$f_{p2} := f_{p1} \cdot \left[1 - \frac{\log\left(\frac{t_2}{\text{hr}}\right)}{45} \cdot \left(\frac{f_{p1}}{f_{py}} - 0.55 \right) \right]$

$f_{p2} = 202.5 \cdot \text{ksi}$ Tensioning in the strand after relaxation (Step No.2)

$\% \text{Loss}_{\text{relaxation}} := \left(1 - \frac{f_{p2}}{f_{p1}} \right)$

$\% \text{Loss}_{\text{relaxation}} = 0 \cdot \%$ Loss due to relaxation of steel

$\epsilon_{p2} := \epsilon_{p1}$

$\epsilon_{p2} = 7.105 \times 10^{-3}$ Strain after loss due to relaxation of steel (Step No.2)

At this stage the concrete has not been cast yet; therefore,

$$f_{c2} := 0 \cdot \text{ksi} \dots\dots\dots \text{Stress in concrete at Step No.2}$$

$$\epsilon_{c2} := \frac{f_{c1}}{E_{ci}}$$

$$\epsilon_{c2} = 0 \dots\dots\dots \text{Strain in concrete at Step No.2}$$

4.3 Step No.3: At the Instance after the Release the Strand

The applied prestress force will be distributed between concrete and strand immediately after the prestress release as follows:

$$f_{c3} := f_{ci}$$

$$f_{c3} = 8 \cdot \text{ksi} \dots\dots\dots \text{Compressive strength of concrete at the time of release}$$

$$E_{c3} := E_{ci}$$

$$E_{c3} = 5.422 \times 10^3 \cdot \text{ksi} \dots\dots\dots \text{Modulus of elasticity of concrete at the time of release}$$

$$n_3 := \frac{E_p}{E_{c3}}$$

$$n_3 = 5.256 \dots\dots\dots \text{Modular ratio at the time of release}$$

$$P_2 := N_p \cdot f_{p2} \cdot A_p$$

$$P_2 = 535.815 \cdot \text{kip} \dots\dots\dots \text{Total prestress force at the time of release}$$

$$\Delta f_{c3} := \frac{-P_2}{A_b + (n_3 - 1) \cdot A_p}$$

$$\Delta f_{c3} = -4.383 \cdot \text{ksi} \dots\dots \text{Change of stress in concrete immediately after the prestressing release}$$

$$\Delta f_{p3} := n_3 \cdot \Delta f_{c3}$$

$$\Delta f_{p3} = -23.036 \cdot \text{ksi} \dots\dots \text{Change of stress in strand immediately after the prestressing release}$$

And consequently,

$$\Delta \epsilon_{c3} := \frac{\Delta f_{c3}}{E_{c3}}$$

$$\Delta \epsilon_{c3} = -8.083 \times 10^{-4} \dots\dots\dots \text{Change of strain in concrete immediately after the prestressing release}$$

$$\Delta \epsilon_{p3} := \frac{\Delta f_{p3}}{E_p}$$


$\Delta\varepsilon_{p3} = -8.083 \times 10^{-4}$ Change of strain in strand immediately after the prestressing release

Therefore, at the end of Step 3, the stress and strain in concrete and strand(s) are as follows:

<u>Concrete</u>	<u>Strand</u>	<u>Loss Due to Elastic Shortening</u>
$f_{c3} := f_{c2} + \Delta f_{c3}$	$f_{p3} := f_{p2} + \Delta f_{p3}$	$\%Loss_{ES} := \frac{f_{p2} - f_{p3}}{f_{p2}}$
$f_{c3} = -4.383 \cdot \text{ksi}$	$f_{p3} = 179.464 \cdot \text{ksi}$	
$\varepsilon_{c3} := \varepsilon_{c2} + \Delta\varepsilon_{c3}$	$\varepsilon_{p3} := \varepsilon_{p2} + \Delta\varepsilon_{p3}$	$\%Loss_{ES} = 11.376 \cdot \%$
$\varepsilon_{c3} = -8.083 \times 10^{-4}$	$\varepsilon_{p3} = 6.297 \times 10^{-3}$	
$\left \frac{f_{c3}}{f_{ci}} \right = 0.548$	$P_3 := f_{p3} \cdot N_p \cdot A_p$	
	$P_3 = 474.861 \cdot \text{kip}$	

Appendix F

Experimental Data Related to Transfer Length

Department of Civil & Environmental Engineering Subject Appendix F Transfer Length	By	Amir A. Arab, P.E.	 THE GEORGE WASHINGTON UNIVERSITY
	Date	3/10/2012	
	CRN		
	Course No.	CEE 399	
	Advisors	Dr. Badie/Dr. Manzari	

FROM TEST DATA (GIRDERS #1)


	1	2	3	4	5	6	7	8
GAGE I.D.	G1S1	G1S2	G1S3	G1S4	G1S5	G1S6	G1S7	G1S8
L_{end face} (in.)	10.5625	20.5000	28.0000	36.3750	5.0625	15.5000	25.8750	31.0625
STRAIN (UC)	-0.00248	-0.00124	-0.00095	-0.00036	-0.00119	-0.002	-0.00018	-0.00075
E_p (ksi)	28600	28600	28600	28600	28600	28600	28600	28600
γ_{calibration}	0.9511	0.9511	0.9511	0.9511	0.9511	0.9511	0.9511	0.9511
E_{p,eff} (ksi)	30072	30072	30072	30072	30072	30072	30072	30072
STRAIN (C)	-0.00236	-0.00118	-0.00091	-0.00034	-0.00113	-0.0019	-0.00017	-0.00071
Δσ_{Loss} (ksi)	-67.423	-33.709	-25.933	-9.686	-32.311	-54.386	-4.967	-20.326
f_i (ksi)	182.500	182.500	182.500	182.500	182.500	182.500	182.500	182.500
f_t (ksi)	115.077	148.791	156.567	172.814	150.189	128.114	177.533	162.174

FROM TEST DATA (GIRDERS #2)

	9	10	11	12	13	14	15	16
GAGE I.D.	G2S1	G2S2	G2S3	G2S4	G2S5	G2S6	G2S7	G2S8
L_{end face} (in.)	9.1250	19.1250	26.5000	35.5000	4.5000	14.1250	24.2500	30.7500
STRAIN (UC)	-0.00274	-0.00189	-0.00063	-0.00084	-0.00435	-0.00126	-0.00122	-0.00101
E_p (ksi)	28600	28600	28600	28600	28600	28600	28600	28600
γ_{calibration}	0.9511	0.9511	0.9511	0.9511	0.9511	0.9511	0.9511	0.9511
E_{p,eff} (ksi)	30072	30072	30072	30072	30072	30072	30072	30072
STRAIN (C)	-0.0026	-0.00179	-0.0006	-0.0008	-0.00413	-0.0012	-0.00116	-0.00096
Δσ_{Loss} (ksi)	-74.453	-51.298	-17.234	-22.850	-118.212	-34.213	-33.208	-27.541
f_i (ksi)	182.500	182.500	182.500	182.500	182.500	182.500	182.500	182.500
f_t (ksi)	108.047	131.202	165.266	159.650	64.288	148.287	149.292	154.959

FROM TEST DATA (GIRDERS #3)

	17	18	19	20	21	22	23	24
GAGE I.D.	G3S1	G3S2	G3S3	G3S4	G3S5	G3S6	G3S7	G3S8
L_{end face} (in.)	5.0000	9.7500	14.5000	19.5000	24.7500	30.7500	36.7500	46.2500
STRAIN (UC)	-0.00417	0	-0.00348	-0.00392	-0.00222	-0.00174	-0.00124	-0.00085
E_p (ksi)	28600	28600	28600	28600	28600	28600	28600	28600
γ_{calibration}	0.9511	0.9511	0.9511	0.9511	0.9511	0.9511	0.9511	0.9511
E_{p,eff} (ksi)	30072	30072	30072	30072	30072	30072	30072	30072
STRAIN (C)	-0.00396	0	-0.00331	-0.00373	-0.00211	-0.00165	-0.00118	-0.00081
Δσ_{Loss} (ksi)	-113.297	0.000	-94.780	-106.550	-60.389	-47.300	-33.762	-23.249
f_i (ksi)	182.500	182.500	182.500	182.500	182.500	182.500	182.500	182.500
f_t (ksi)	69.203	182.500	87.720	75.950	122.111	135.200	148.738	159.251

Department of Civil & Environmental Engineering	By	Amir A. Arab, P.E.	 THE GEORGE WASHINGTON UNIVERSITY	
	Date	3/10/2012		
	Subject	Appendix F Transfer Length		
	CRN			
	Course No.			CEE 399
Advisors	Dr. Badie/Dr. Manzari			

FROM TEST DATA (GIRDERS #4)


	25	26	27	28	29	30	31	32
GAGE I.D.	G4S1	G4S2	G4S3	G4S4	G4S5	G4S6	G4S7	G4S8
L_{end face} (in.)	5.2500	10.0000	15.2500	19.7500	25.5000	31.0000	36.0000	41.5000
STRAIN (UC)	-0.00318	-0.00285	-0.00252	-0.00235	0	-0.00092	-0.00093	-0.00103
E_p (ksi)	28600	28600	28600	28600	28600	28600	28600	28600
γ_{calibration}	0.9511	0.9511	0.9511	0.9511	0.9511	0.9511	0.9511	0.9511
E_{p,eff} (ksi)	30072	30072	30072	30072	30072	30072	30072	30072
STRAIN (C)	-0.00303	-0.00271	-0.00239	-0.00224	0	-0.00087	-0.00089	-0.00098
Δσ_{Loss} (ksi)	-86.583	-77.606	-68.483	-63.954	0.000	-24.984	-25.365	-28.030
f_i (ksi)	182.500	182.500	182.500	182.500	182.500	182.500	182.500	182.500
f_t (ksi)	95.917	104.894	114.017	118.546	182.500	157.516	157.135	154.470

FROM TEST DATA (GIRDERS #5)

	33	34	35	36	37	38	39	40
GAGE I.D.	G5S1	G5S2	G5S3	G5S4	G5S5	G5S6	G5S7	G5S8
L_{end face} (in.)	7.2500	10.0000	15.0000	20.0000	25.2500	31.7500	36.2500	41.5000
STRAIN (UC)	-0.00379	-0.00331	-0.00113	-0.00072	-0.00052	-0.00068	-0.00059	-0.00082
E_p (ksi)	28600	28600	28600	28600	28600	28600	28600	28600
γ_{calibration}	0.9511	0.9511	0.9511	0.9511	0.9511	0.9511	0.9511	0.9511
E_{p,eff} (ksi)	30072	30072	30072	30072	30072	30072	30072	30072
STRAIN (C)	-0.00361	-0.00315	-0.00107	-0.00068	-0.00049	-0.00065	-0.00056	-0.00078
Δσ_{Loss} (ksi)	-103.208	-89.952	-30.705	-19.469	-14.072	-18.558	-16.132	-22.339
f_i (ksi)	182.500	182.500	182.500	182.500	182.500	182.500	182.500	182.500
f_t (ksi)	79.292	92.548	151.795	163.031	168.428	163.942	166.368	160.161

FROM TEST DATA (GIRDERS #6)


	41	42	43	44	45	46	47	48
GAGE I.D.	G6S1	G6S2	G6S3	G6S4	G6S5	G6S6	G6S7	G6S8
L_{end face} (in.)	0.0000	0.0000	0.0000	0.0000	11.5000	23.2500	33.75	43.2500
STRAIN (UC)	0	0	0	0	-0.00408	8.52E-06	-0.00065	-0.00017
E_p (ksi)	0	0	0	0	28600	28600	28600	28600
γ_{calibration}	0.9511	0.9511	0.9511	0.9511	0.9511	0.9511	0.951057	0.9511
E_{p,eff} (ksi)	0	0	0	0	30072	30072	30071.82	30072
STRAIN (C)	0	0	0	0	-0.00388	8.1E-06	-0.00062	-0.00016
Δσ_{Loss} (ksi)	0.000	0.000	0.000	0.000	-111.045	0.232	-17.7277	-4.489
f_i (ksi)	0.000	0.000	0.000	0.000	182.500	182.500	182.5	182.500
f_t (ksi)	0.000	0.000	0.000	0.000	71.455	182.732	164.7723	178.011

Department of Civil & Environmental Engineering Subject Appendix F Transfer Length	By	Amir A. Arab, P.E.	 THE GEORGE WASHINGTON UNIVERSITY
	Date	3/10/2012	
	CRN		
	Course No.	CEE 399	
	Advisors	Dr. Badie/Dr. Manzari	

FROM TEST DATA (GIRDERS #7)

	49	50	51	52	53	54	55	56
GAGE I.D.	G6S1	G6S2	G6S3	G6S4	G6S5	G6S6	G6S7	G6S8
L_{end face} (in.)	0.0000	0.0000	0.0000	0.0000	11.5000	23.2500	33.7500	43.2500
STRAIN (UC)	0	0	0	0	7.45E-06	9.29E-06	1.01E-05	0.000909
E_p (ksi)	0	0	0	0	28600	28600	28600	28600
γ_{calibration}	0.9511	0.9511	0.9511	0.9511	0.9511	0.9511	0.9511	0.9511
E_{p,eff} (ksi)	0	0	0	0	30072	30072	30072	30072
STRAIN (C)	0	0	0	0	7.08E-06	8.84E-06	9.57E-06	0.000865
Δσ_{Loss} (ksi)	0.000	0.000	0.000	0.000	0.203	0.253	0.274	24.732
f_i (ksi)	0.000	0.000	0.000	0.000	182.500	182.500	182.500	182.500
f_i (ksi)	0.000	0.000	0.000	0.000	182.703	182.753	182.774	207.232

L_{end face} (in.)	STRAIN (C)	Δσ_{Loss} (ksi)	f_i (ksi)	f_i (ksi)	f_{i norm} (ksi)
0.0000	0.0000	0.0000	0.0000	0.0000	0.0000
4.9531	-0.0031	-87.6006	182.5000	94.8994	0.5612
7.2500	-0.0036	-103.2084	182.5000	79.2916	0.4689
10.2375	-0.0029	-84.0958	182.5000	98.4042	0.5820
14.8750	-0.0020	-56.5132	182.5000	125.9868	0.7451
19.7750	-0.0019	-54.9961	182.5000	127.5039	0.7541
25.3250	-0.0009	-25.9742	182.5000	156.5258	0.9257
28.0000	-0.0009	-25.9335	182.5000	156.5665	0.9260
31.0625	-0.0010	-27.7416	182.5000	154.7584	0.9153
33.7500	-0.0006	-17.7277	182.5000	164.7723	0.9745
36.1750	-0.0008	-21.5590	182.5000	160.9410	0.9518
41.5000	-0.0009	-25.1847	182.5000	157.3153	0.9304
42.3750	-0.0005	-13.4141	182.5000	169.0859	1.0000

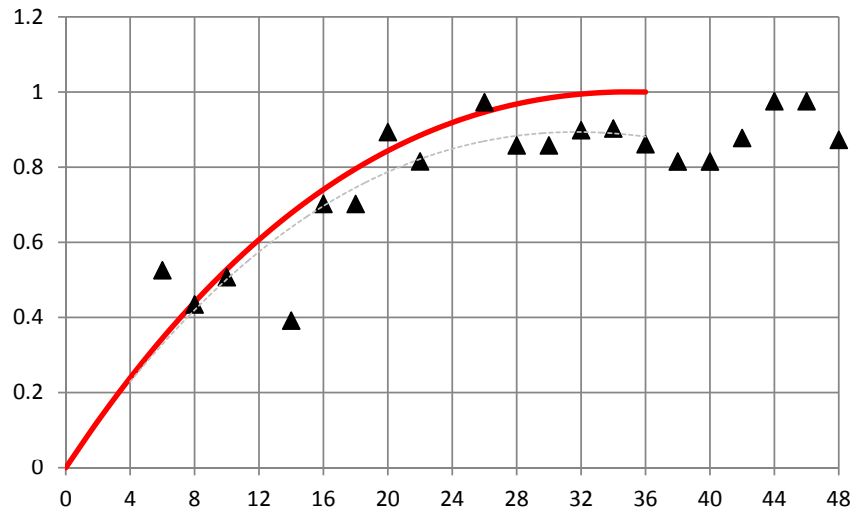
Department of Civil & Environmental Engineering		By Amir A. Arab, P.E.	
Subject Appendix F Transfer Length		Date 3/10/2012	
		CRN	
		Course No. CEE 399	
		Advisors Dr. Badie/Dr. Manzari	

BEST-FIT APPROXIMATION

L_{end_face} (in.)	f_j (ksi)	f_i (ksi)	f_{i_norm} (ksi)
0	182.5	0	0.00
2	182.5	21.79926	0.12
4	182.5	41.89908	0.24
6	182.5	60.35202	0.34
8	182.5	77.21064	0.44
10	182.5	92.5275	0.53
12	182.5	106.3552	0.61
14	182.5	118.7462	0.68
16	182.5	129.7531	0.74
18	182.5	139.4285	0.80
20	182.5	147.825	0.84
22	182.5	154.9951	0.88
24	182.5	160.9913	0.92
26	182.5	165.8662	0.95
28	182.5	169.6724	0.97
30	182.5	172.4625	0.98
32	182.5	174.289	0.99
34	182.5	175.2044	1.00
36	182.5	175.2613	1.00
38	182.5	174.5123	1.00
40	182.5	173.01	0.99


$$y = 6E-06x^3 - 0.0012x^2 + 0.0621x$$

$$R^2 = 0.7437$$



Appendix G


Gregly-Sozen Model @ $L_t = 36$ in.

Department of Civil & Environmental Engineering	By Amir A. Arab, P.E.	
Subject Appendix G SOZEN-GREGLY MODEL @ $L_t = 36$ in.	Date 12/10/2011	
	CRN	
	Course No. CEE 399	
	Professor Dr. Badio/Dr. Manzari	

**Longitudinal Stress Profile Due to Self-Weight
@ Theoretical Transfer Length $L_t = 36$ in.**

x (ft)	V_{DL} (Ins.)	M_{DL} (lbs-in.)	σ_b^{DL} (psi)	σ_t^{DL} (psi)
0.0000	0	0	0	0
1.0417	1294	-62092	-2	2
2.0833	2587	-124183	-4	4
3.0000	3725	-178824	-6	6
4.1667	5174	-248366	-8	8
8.3333	-117069	-7761	0	0
9.0000	-116241	925476	29	-31
10.0000	-114999	2312913	73	-78
11.0000	-113757	3685448	116	-125
12.0000	-112515	5043081	159	-171
13.0000	-111273	6385813	202	-216
14.0000	-110032	7713642	244	-261
15.0000	-108790	9026569	285	-306
16.0000	-107548	10324595	326	-350
17.0000	-106306	11607718	367	-393
18.0000	-105064	12875939	407	-436
19.0000	-103822	14129259	446	-479
20.0000	-102581	15367676	485	-521
21.0000	-101339	16591191	524	-562
22.0000	-100097	17799805	562	-603
23.0000	-98855	18993516	600	-644
24.0000	-97613	20172325	637	-684
25.0000	-96371	21336233	674	-723
26.0000	-95130	22485238	710	-762
27.0000	-93888	23619342	746	-801
28.0000	-92646	24738543	781	-839
29.0000	-91404	25842843	816	-876
30.0000	-90162	26932240	851	-913
31.0000	-88920	28006736	884	-949
32.0000	-87679	29066329	918	-985
33.0000	-86437	30111021	951	-1021
34.0000	-85195	31140810	983	-1056
35.0000	-83953	32155698	1015	-1090
36.0000	-82711	33155683	1047	-1124
37.0000	-81469	34140767	1078	-1157
38.0000	-80228	35110948	1109	-1190
39.0000	-78986	36066228	1139	-1223
40.0000	-77744	37006605	1169	-1254
41.0000	-76502	37932081	1198	-1286
42.0000	-75260	38842655	1227	-1317
43.0000	-74018	39738326	1255	-1347
44.0000	-72777	40619096	1283	-1377
45.0000	-71535	41484963	1310	-1406
46.0000	-70293	42335929	1337	-1435
47.0000	-69051	43171993	1363	-1463
48.0000	-67809	43993154	1389	-1491
49.0000	-66567	44799414	1415	-1519
50.0000	-65326	45590772	1440	-1545
51.0000	-64084	46367228	1464	-1572
52.0000	-62842	47128781	1488	-1598
53.0000	-61600	47875433	1512	-1623
54.0000	-60358	48607183	1535	-1648
55.0000	-59116	49324030	1558	-1672
56.0000	-57875	50025976	1580	-1696


BUNKED @ 8 ft from each end face
Bunk_Left @ 8 ft
Bunk_Right @ 197.2083 ft

Department of Civil & Environmental Engineering	By Amir A. Arab, P.E.	 THE GEORGE WASHINGTON UNIVERSITY
Subject Appendix G SOZEN-GREGLY MODEL @ $L_t = 36$ in.	Date 12/10/2011	
	CRN	
	Course No. CEE 399	
	Professor Dr. Badie/Dr. Manzari	

**Longitudinal Stress Profile Due to Self-Weight
@ Theoretical Transfer Length $L_t = 36$ in.**

x (ft)	V_{DL} (Ins.)	M_{DL} (lbs-in.)	σ_b^{DL} (psi)	σ_t^{DL} (psi)
57.0000	-56633	50713020	1602	-1719
58.0000	-55391	51385162	1623	-1742
59.0000	-54149	52042402	1644	-1764
60.0000	-52907	52684739	1664	-1786
61.0000	-51665	53312175	1684	-1807
62.0000	-50424	53924709	1703	-1828
63.0000	-49182	54522341	1722	-1848
64.0000	-47940	55105071	1740	-1868
65.0000	-46698	55672899	1758	-1887
66.0000	-45456	56225824	1776	-1906
67.0000	-44214	56763848	1793	-1924
68.0000	-42973	57286970	1809	-1942
69.0000	-41731	57795190	1825	-1959
70.0000	-40489	58288508	1841	-1976
71.0000	-39247	58766924	1856	-1992
72.0000	-38005	59230438	1871	-2008
73.0000	-36763	59679050	1885	-2023
74.0000	-35522	60112760	1898	-2038
75.0000	-34280	60531568	1912	-2052
76.0000	-33038	60935474	1924	-2066
77.0000	-31796	61324478	1937	-2079
78.0000	-30554	61698580	1948	-2092
79.0000	-29312	62057780	1960	-2104
80.0000	-28071	62402078	1971	-2115
82.0000	-25587	63045968	1991	-2137
82.0833	-25483	63071503	1992	-2138
83.0000	-24345	63345560	2000	-2147
84.0000	-23103	63630250	2009	-2157
85.0000	-21861	63900038	2018	-2166
86.0000	-20620	64154924	2026	-2175
87.0000	-19378	64394908	2034	-2183
88.0000	-18136	64619991	2041	-2191
89.0000	-16894	64830171	2047	-2198
90.0000	-15652	65025449	2054	-2204
91.0000	-14410	65205825	2059	-2210
92.0000	-13169	65371299	2064	-2216
93.0000	-11927	65521871	2069	-2221
94.0000	-10685	65657542	2073	-2226
95.0000	-9443	65778310	2077	-2230
96.0000	-8201	65884176	2081	-2233
97.0000	-6959	65975140	2084	-2236
98.0000	-5718	66051202	2086	-2239
99.0000	-4476	66112363	2088	-2241
100.0000	-3234	66158621	2089	-2243
101.0000	-1992	66189977	2090	-2244
102.0000	-750	66206431	2091	-2244
102.6042	0	66209151	2091	-2244


BUNKED @ 8 ft from each end face
Bunk_Left @ 8 ft
Bunk_Right @ 197.2083 ft

Department of Civil & Environmental Engineering		By Amir A. Arab, P.E.	
Subject		Date 12/10/2011	
Appendix G SOZEN-GREGLY MODEL @ $L_t = 36$ in.		CRN	
		Course No. CEE 399 Professor Dr. Badie/Dr. Manzari	

Longitudinal Stress Profile Due to Pretensioning (Straight & Temporary Strands Only)

@ Theoretical Transfer Length $L_t = 36$ in.


x (in.)	$f_{pl_straight}$ (psi)	$P_{l_straight}$ (lbs)	$e_{p_straight}$ (in.)	P_{l_temp} (lbs)	e_{p_temp} (in.)	P/A (psi)	P e (lb-in.)	σ_b^P (psi)	σ_t^P (psi)
0	0	0	44.14246	0	-49.7706	0	0	0	0
12.5	63368.06	632539.9	44.14246	110006.9	-49.7706	685.1448	22446761	-1394	76
25	126736.1	1265080	44.14246	220013.9	-49.7706	1370.29	44893523	-2788	152
36	182500	1	44.14246	316820	-49.7706	1973.217	64646673	-4015	218
50	182500	1821715	44.14246	316820	-49.7706	1973.217	64646673	-4015	218
100	182500	1821715	44.14246	316820	-49.7706	1973.217	64646673	-4015	218
108	182500	1821715	44.14246	316820	-49.7706	1973.217	64646673	-4015	218
120	182500	1821715	44.14246	316820	-49.7706	1973.217	64646673	-4015	218
132	182500	1821715	44.14246	316820	-49.7706	1973.217	64646673	-4015	218
144	182500	1821715	44.14246	316820	-49.7706	1973.217	64646673	-4015	218
156	182500	1821715	44.14246	316820	-49.7706	1973.217	64646673	-4015	218
168	182500	1821715	44.14246	316820	-49.7706	1973.217	64646673	-4015	218
180	182500	1821715	44.14246	316820	-49.7706	1973.217	64646673	-4015	218
192	182500	1821715	44.14246	316820	-49.7706	1973.217	64646673	-4015	218
204	182500	1821715	44.14246	316820	-49.7706	1973.217	64646673	-4015	218
216	182500	1821715	44.14246	316820	-49.7706	1973.217	64646673	-4015	218
228	182500	1821715	44.14246	316820	-49.7706	1973.217	64646673	-4015	218
240	182500	1821715	44.14246	316820	-49.7706	1973.217	64646673	-4015	218
252	182500	1821715	44.14246	316820	-49.7706	1973.217	64646673	-4015	218
264	182500	1821715	44.14246	316820	-49.7706	1973.217	64646673	-4015	218
276	182500	1821715	44.14246	316820	-49.7706	1973.217	64646673	-4015	218
288	182500	1821715	44.14246	316820	-49.7706	1973.217	64646673	-4015	218
300	182500	1821715	44.14246	316820	-49.7706	1973.217	64646673	-4015	218
312	182500	1821715	44.14246	316820	-49.7706	1973.217	64646673	-4015	218
324	182500	1821715	44.14246	316820	-49.7706	1973.217	64646673	-4015	218
336	182500	1821715	44.14246	316820	-49.7706	1973.217	64646673	-4015	218
348	182500	1821715	44.14246	316820	-49.7706	1973.217	64646673	-4015	218
360	182500	1821715	44.14246	316820	-49.7706	1973.217	64646673	-4015	218
372	182500	1821715	44.14246	316820	-49.7706	1973.217	64646673	-4015	218
384	182500	1821715	44.14246	316820	-49.7706	1973.217	64646673	-4015	218
396	182500	1821715	44.14246	316820	-49.7706	1973.217	64646673	-4015	218
408	182500	1821715	44.14246	316820	-49.7706	1973.217	64646673	-4015	218
420	182500	1821715	44.14246	316820	-49.7706	1973.217	64646673	-4015	218
432	182500	1821715	44.14246	316820	-49.7706	1973.217	64646673	-4015	218
444	182500	1821715	44.14246	316820	-49.7706	1973.217	64646673	-4015	218
456	182500	1821715	44.14246	316820	-49.7706	1973.217	64646673	-4015	218
468	182500	1821715	44.14246	316820	-49.7706	1973.217	64646673	-4015	218
480	182500	1821715	44.14246	316820	-49.7706	1973.217	64646673	-4015	218
492	182500	1821715	44.14246	316820	-49.7706	1973.217	64646673	-4015	218
504	182500	1821715	44.14246	316820	-49.7706	1973.217	64646673	-4015	218
516	182500	1821715	44.14246	316820	-49.7706	1973.217	64646673	-4015	218
528	182500	1821715	44.14246	316820	-49.7706	1973.217	64646673	-4015	218
540	182500	1821715	44.14246	316820	-49.7706	1973.217	64646673	-4015	218
552	182500	1821715	44.14246	316820	-49.7706	1973.217	64646673	-4015	218
564	182500	1821715	44.14246	316820	-49.7706	1973.217	64646673	-4015	218
576	182500	1821715	44.14246	316820	-49.7706	1973.217	64646673	-4015	218
588	182500	1821715	44.14246	316820	-49.7706	1973.217	64646673	-4015	218
600	182500	1821715	44.14246	316820	-49.7706	1973.217	64646673	-4015	218
612	182500	1821715	44.14246	316820	-49.7706	1973.217	64646673	-4015	218
624	182500	1821715	44.14246	316820	-49.7706	1973.217	64646673	-4015	218
636	182500	1821715	44.14246	316820	-49.7706	1973.217	64646673	-4015	218
648	182500	1821715	44.14246	316820	-49.7706	1973.217	64646673	-4015	218
660	182500	1821715	44.14246	316820	-49.7706	1973.217	64646673	-4015	218
672	182500	1821715	44.14246	316820	-49.7706	1973.217	64646673	-4015	218

Department of Civil & Environmental Engineering		By Amir A. Arab, P.E.	 THE GEORGE WASHINGTON UNIVERSITY
Subject		Date 12/10/2011	
Appendix G SOZEN-GREGLY MODEL @ $L_t = 36$ in.		CRN	
		Course No. CEE 399 Professor Dr. Badie/Dr. Manzari	

Longitudinal Stress Profile Due to Pretensioning (Straight & Temporary Strands Only)

@ Theoretical Transfer Length $L_t = 36$ in.


x (in.)	$f_{pI_straight}$ (psi)	$P_{I_straight}$ (lbs)	$e_{p, straight}$ (in.)	P_{I_temp} (lbs)	$e_{p, temp}$ (in.)	P/A (psi)	P e (lb-in.)	σ_b^P (psi)	σ_t^P (psi)
684	182500	1821715	44.14246	316820	-49.7706	1973.217	64646673	-4015	218
696	182500	1821715	44.14246	316820	-49.7706	1973.217	64646673	-4015	218
708	182500	1821715	44.14246	316820	-49.7706	1973.217	64646673	-4015	218
720	182500	1821715	44.14246	316820	-49.7706	1973.217	64646673	-4015	218
732	182500	1821715	44.14246	316820	-49.7706	1973.217	64646673	-4015	218
744	182500	1821715	44.14246	316820	-49.7706	1973.217	64646673	-4015	218
756	182500	1821715	44.14246	316820	-49.7706	1973.217	64646673	-4015	218
768	182500	1821715	44.14246	316820	-49.7706	1973.217	64646673	-4015	218
780	182500	1821715	44.14246	316820	-49.7706	1973.217	64646673	-4015	218
792	182500	1821715	44.14246	316820	-49.7706	1973.217	64646673	-4015	218
804	182500	1821715	44.14246	316820	-49.7706	1973.217	64646673	-4015	218
816	182500	1821715	44.14246	316820	-49.7706	1973.217	64646673	-4015	218
828	182500	1821715	44.14246	316820	-49.7706	1973.217	64646673	-4015	218
840	182500	1821715	44.14246	316820	-49.7706	1973.217	64646673	-4015	218
852	182500	1821715	44.14246	316820	-49.7706	1973.217	64646673	-4015	218
864	182500	1821715	44.14246	316820	-49.7706	1973.217	64646673	-4015	218
876	182500	1821715	44.14246	316820	-49.7706	1973.217	64646673	-4015	218
888	182500	1821715	44.14246	316820	-49.7706	1973.217	64646673	-4015	218
900	182500	1821715	44.14246	316820	-49.7706	1973.217	64646673	-4015	218
912	182500	1821715	44.14246	316820	-49.7706	1973.217	64646673	-4015	218
924	182500	1821715	44.14246	316820	-49.7706	1973.217	64646673	-4015	218
936	182500	1821715	44.14246	316820	-49.7706	1973.217	64646673	-4015	218
948	182500	1821715	44.14246	316820	-49.7706	1973.217	64646673	-4015	218
960	182500	1821715	44.14246	316820	-49.7706	1973.217	64646673	-4015	218
984	182500	1821715	44.14246	316820	-49.7706	1973.217	64646673	-4015	218
985	182500	1821715	44.14246	316820	-49.7706	1973.217	64646673	-4015	218
996	182500	1821715	44.14246	316820	-49.7706	1973.217	64646673	-4015	218
1008	182500	1821715	44.14246	316820	-49.7706	1973.217	64646673	-4015	218
1020	182500	1821715	44.14246	316820	-49.7706	1973.217	64646673	-4015	218
1032	182500	1821715	44.14246	316820	-49.7706	1973.217	64646673	-4015	218
1044	182500	1821715	44.14246	316820	-49.7706	1973.217	64646673	-4015	218
1056	182500	1821715	44.14246	316820	-49.7706	1973.217	64646673	-4015	218
1068	182500	1821715	44.14246	316820	-49.7706	1973.217	64646673	-4015	218
1080	182500	1821715	44.14246	316820	-49.7706	1973.217	64646673	-4015	218
1092	182500	1821715	44.14246	316820	-49.7706	1973.217	64646673	-4015	218
1104	182500	1821715	44.14246	316820	-49.7706	1973.217	64646673	-4015	218
1116	182500	1821715	44.14246	316820	-49.7706	1973.217	64646673	-4015	218
1128	182500	1821715	44.14246	316820	-49.7706	1973.217	64646673	-4015	218
1140	182500	1821715	44.14246	316820	-49.7706	1973.217	64646673	-4015	218
1152	182500	1821715	44.14246	316820	-49.7706	1973.217	64646673	-4015	218
1164	182500	1821715	44.14246	316820	-49.7706	1973.217	64646673	-4015	218
1176	182500	1821715	44.14246	316820	-49.7706	1973.217	64646673	-4015	218
1188	182500	1821715	44.14246	316820	-49.7706	1973.217	64646673	-4015	218
1200	182500	1821715	44.14246	316820	-49.7706	1973.217	64646673	-4015	218
1212	182500	1821715	44.14246	316820	-49.7706	1973.217	64646673	-4015	218
1224	182500	1821715	44.14246	316820	-49.7706	1973.217	64646673	-4015	218
1231.25	182500	1821715	44.14246	316820	-49.7706	1973.217	64646673	-4015	218

Department of Civil & Environmental Engineering		By Amir A. Arab, P.E.	 THE GEORGE WASHINGTON UNIVERSITY
Subject		Date 12/10/2011	
Appendix G SOZEN-GREGLY MODEL @ $L_t = 36$ in.		CRN	
		Course No. CEE 399 Professor Dr. Badie/Dr. Manzari	

Longitudinal Stress Profile Due to Pretensioning (Draped Strands Only)

@ Theoretical Transfer Length $L_t = 36$ in.


Index	x (in.)	f_{pI_draped} (psi)	P_{I_draped} (lbs)	$e_{p,draped}$ (in.)	P/A (psi)	P e (lb-in.)	$\sigma_b^{P_draped}$ (psi)	$\sigma_t^{P_draped}$ (psi)
1	0	0	0	-36.2506	0	0	0	0
2	12.5	63368.06	343771.7	-35.2423	317.1966	-1.2E+07	65	-728
3	25	126736.1	687543.4	-34.234	634.3933	-2.4E+07	109	-1432
4	36	182500	990062.5	-33.3466	913.5263	-3.3E+07	129	-2033
5	50	182500	990062.5	-32.2173	913.5263	-3.2E+07	94	-1995
6	100	182500	990062.5	-28.1841	913.5263	-2.8E+07	-32	-1859
7	108	182500	990062.5	-27.5388	913.5263	-2.7E+07	-52	-1838
8	120	182500	990062.5	-26.5708	913.5263	-2.6E+07	-83	-1805
9	132	182500	990062.5	-25.6028	913.5263	-2.5E+07	-113	-1773
10	144	182500	990062.5	-24.6348	913.5263	-2.4E+07	-143	-1740
11	156	182500	990062.5	-23.6668	913.5263	-2.3E+07	-174	-1708
12	168	182500	990062.5	-22.6989	913.5263	-2.2E+07	-204	-1675
13	180	182500	990062.5	-21.7309	913.5263	-2.2E+07	-234	-1643
14	192	182500	990062.5	-20.7629	913.5263	-2.1E+07	-264	-1610
15	204	182500	990062.5	-19.7949	913.5263	-2E+07	-295	-1578
16	216	182500	990062.5	-18.8269	913.5263	-1.9E+07	-325	-1545
17	228	182500	990062.5	-17.859	913.5263	-1.8E+07	-355	-1513
18	240	182500	990062.5	-16.891	913.5263	-1.7E+07	-385	-1480
19	252	182500	990062.5	-15.923	913.5263	-1.6E+07	-416	-1448
20	264	182500	990062.5	-14.955	913.5263	-1.5E+07	-446	-1415
21	276	182500	990062.5	-13.987	913.5263	-1.4E+07	-476	-1383
22	288	182500	990062.5	-13.0191	913.5263	-1.3E+07	-506	-1350
23	300	182500	990062.5	-12.0511	913.5263	-1.2E+07	-537	-1318
24	312	182500	990062.5	-11.0831	913.5263	-1.1E+07	-567	-1285
25	324	182500	990062.5	-10.1151	913.5263	-1E+07	-597	-1253
26	336	182500	990062.5	-9.14715	913.5263	-9056249	-628	-1221
27	348	182500	990062.5	-8.17917	913.5263	-8097888	-658	-1188
28	360	182500	990062.5	-7.21119	913.5263	-7139528	-688	-1156
29	372	182500	990062.5	-6.24321	913.5263	-6181168	-718	-1123
30	384	182500	990062.5	-5.27523	913.5263	-5222807	-749	-1091
31	396	182500	990062.5	-4.30725	913.5263	-4264447	-779	-1058
32	408	182500	990062.5	-3.33927	913.5263	-3306086	-809	-1026
33	420	182500	990062.5	-2.37129	913.5263	-2347726	-839	-993
34	432	182500	990062.5	-1.40331	913.5263	-1389366	-870	-961
35	444	182500	990062.5	-0.43533	913.5263	-431005	-900	-928
36	456	182500	990062.5	0.532648	913.5263	527355.3	-930	-896
37	468	182500	990062.5	1.500628	913.5263	1485716	-960	-863
38	480	182500	990062.5	2.468608	913.5263	2444076	-991	-831
39	492	182500	990062.5	3.436588	913.5263	3402436	-1021	-798
40	504	182500	990062.5	4.404567	913.5263	4360797	-1051	-766
41	516	182500	990062.5	5.372547	913.5263	5319157	-1082	-733
42	528	182500	990062.5	6.340527	913.5263	6277518	-1112	-701
43	540	182500	990062.5	7.308506	913.5263	7235878	-1142	-668
44	552	182500	990062.5	8.276486	913.5263	8194238	-1172	-636
45	564	182500	990062.5	9.244466	913.5263	9152599	-1203	-603
46	576	182500	990062.5	10.21245	913.5263	10110959	-1233	-571
47	588	182500	990062.5	11.18043	913.5263	11069320	-1263	-538
48	600	182500	990062.5	12.1484	913.5263	12027680	-1293	-506
49	612	182500	990062.5	13.11638	913.5263	12986040	-1324	-473
50	624	182500	990062.5	14.08436	913.5263	13944401	-1354	-441
51	636	182500	990062.5	15.05234	913.5263	14902761	-1384	-408
52	648	182500	990062.5	16.02032	913.5263	15861122	-1414	-376
53	660	182500	990062.5	16.9883	913.5263	16819482	-1445	-343
54	672	182500	990062.5	17.95628	913.5263	17777842	-1475	-311

Department of Civil & Environmental Engineering		By Amir A. Arab, P.E.	 THE GEORGE WASHINGTON UNIVERSITY
Subject		Date 12/10/2011	
Appendix G SOZEN-GREGLY MODEL @ $L_t = 36$ in.		CRN	
		Course No. CEE 399 Professor Dr. Badie/Dr. Manzari	

Longitudinal Stress Profile Due to Pretensioning (Draped Strands Only)

@ Theoretical Transfer Length $L_t = 36$ in.

Index	x (in.)	$f_{p,draped}$ (psi)	$P_{l,draped}$ (lbs)	$e_{p,draped}$ (in.)	P/A (psi)	P e (lb-in.)	$\sigma_b^{P_{draped}}$ (psi)	$\sigma_t^{P_{draped}}$ (psi)
55	684	182500	990062.5	18.92426	913.5263	18736203	-1505	-278
56	696	182500	990062.5	19.89224	913.5263	19694563	-1535	-246
57	708	182500	990062.5	20.86022	913.5263	20652924	-1566	-213
58	720	182500	990062.5	21.8282	913.5263	21611284	-1596	-181
59	732	182500	990062.5	22.79618	913.5263	22569644	-1626	-148
60	744	182500	990062.5	23.76416	913.5263	23528005	-1657	-116
61	756	182500	990062.5	24.73214	913.5263	24486365	-1687	-83
62	768	182500	990062.5	25.70012	913.5263	25444726	-1717	-51
63	780	182500	990062.5	26.6681	913.5263	26403086	-1747	-18
64	792	182500	990062.5	27.63608	913.5263	27361446	-1778	14
65	804	182500	990062.5	28.60406	913.5263	28319807	-1808	46
66	816	182500	990062.5	29.57204	913.5263	29278167	-1838	79
67	828	182500	990062.5	30.54002	913.5263	30236528	-1868	111
68	840	182500	990062.5	31.508	913.5263	31194888	-1899	144
69	852	182500	990062.5	32.47598	913.5263	32153248	-1929	176
70	864	182500	990062.5	33.44396	913.5263	33111609	-1959	209
71	876	182500	990062.5	34.41194	913.5263	34069969	-1989	241
72	888	182500	990062.5	35.37992	913.5263	35028330	-2020	274
73	900	182500	990062.5	36.3479	913.5263	35986690	-2050	306
74	912	182500	990062.5	37.31588	913.5263	36945050	-2080	339
75	924	182500	990062.5	38.28386	913.5263	37903411	-2111	371
76	936	182500	990062.5	39.25184	913.5263	38861771	-2141	404
77	948	182500	990062.5	40.21982	913.5263	39820132	-2171	436
78	960	182500	990062.5	41.1878	913.5263	40778492	-2201	469
79	984	182500	990062.5	43.12376	913.5263	42695213	-2262	534
80	985	182500	990062.5	43.20442	913.5263	42775076	-2264	537
81	996	182500	990062.5	43.20442	913.5263	42775076	-2264	537
82	1008	182500	990062.5	43.20442	913.5263	42775076	-2264	537
83	1020	182500	990062.5	43.20442	913.5263	42775076	-2264	537
84	1032	182500	990062.5	43.20442	913.5263	42775076	-2264	537
85	1044	182500	990062.5	43.20442	913.5263	42775076	-2264	537
86	1056	182500	990062.5	43.20442	913.5263	42775076	-2264	537
87	1068	182500	990062.5	43.20442	913.5263	42775076	-2264	537
88	1080	182500	990062.5	43.20442	913.5263	42775076	-2264	537
89	1092	182500	990062.5	43.20442	913.5263	42775076	-2264	537
90	1104	182500	990062.5	43.20442	913.5263	42775076	-2264	537
91	1116	182500	990062.5	43.20442	913.5263	42775076	-2264	537
92	1128	182500	990062.5	43.20442	913.5263	42775076	-2264	537
93	1140	182500	990062.5	43.20442	913.5263	42775076	-2264	537
94	1152	182500	990062.5	43.20442	913.5263	42775076	-2264	537
95	1164	182500	990062.5	43.20442	913.5263	42775076	-2264	537
96	1176	182500	990062.5	43.20442	913.5263	42775076	-2264	537
97	1188	182500	990062.5	43.20442	913.5263	42775076	-2264	537
98	1200	182500	990062.5	43.20442	913.5263	42775076	-2264	537
99	1212	182500	990062.5	43.20442	913.5263	42775076	-2264	537
100	1224	182500	990062.5	43.20442	913.5263	42775076	-2264	537
101	1231.25	182500	990062.5	43.20442	913.5263	42775076	-2264	537

Department of Civil & Environmental Engineering		By Amir A. Arab, P.E.	 THE GEORGE WASHINGTON UNIVERSITY
Subject		Date 12/10/2011	
Appendix G SOZEN-GREGLY MODEL @ $L_t = 36$ in.		CRN	
		Course No. CEE 399 Professor Dr. Badie/Dr. Manzari	


Detail Analysis Based on Location of All Strands

@ Theoretical Transfer Length $L_t = 36$ in.

h (in.)	σ_c (psi)	$h_{c,i}$ (in.)	A_c (in. ²)	F_c (kips)	M_c (in.-kips)	M_{pl} (in.-kips)	M_{max} (in.-kips)
100	1808.412	2	98	179.2656	193359.1	-190725.6	2633.5
98	1850.07	2	91.85	171.8421	187288.7	-184468.4	2820.3
96	1891.728	2	48.83	93.39016	181569.5	-178844.9	2724.6
94	1933.386	2	20.25	39.57285	176115.5	-173379.7	2735.7
92	1975.044	2	13.25	26.44532	170794.4	-168073.0	2721.4
90	2016.702	2	12.25	24.95976	165539.4	-162924.7	2614.7
88	2058.36	2	12.25	25.47007	160335.8	-157934.8	2401.0
86	2100.018	2	12.25	25.98038	155182.6	-153103.3	2079.3
84	2141.676	2	12.25	26.49069	150080.8	-148430.2	1650.6
82	2183.334	2	12.25	27.001	145031.5	-143915.5	1116.1
80	2224.992	2	12.25	27.51131	140035.8	-139559.2	476.5
78	2266.65	2	12.25	28.02162	135094.5	-135361.3	-266.9
76	2308.308	2	12.25	28.53193	130208.7	-131321.9	-1113.1
74	2349.966	2	12.25	29.04224	125379.6	-127440.8	-2061.3
72	2391.624	2	12.25	29.55256	120607.9	-123718.2	-3110.3
70	2433.283	2	12.25	30.06287	115894.9	-120074.8	-4179.9
68	2474.941	2	12.25	30.57318	111241.5	-116431.4	-5189.8
66	2516.599	2	12.25	31.08349	106648.8	-112787.9	-6139.2
64	2558.257	2	12.25	31.5938	102117.7	-109144.5	-7026.8
62	2599.915	2	12.25	32.10411	97649.2	-105501.1	-7851.8
60	2641.573	2	12.25	32.61442	93244.5	-101857.6	-8613.1
58	2683.231	2	12.25	33.12473	88904.5	-98214.2	-9309.7
56	2724.889	2	12.25	33.63504	84630.2	-94570.8	-9940.6
54	2766.547	2	12.25	34.14535	80422.7	-90927.3	-10504.7
52	2808.205	2	12.25	34.65567	76282.9	-87283.9	-11001.0
50	2849.863	2	12.25	35.16598	72212.0	-83640.5	-11428.5
48	2891.521	2	12.25	35.67629	68210.9	-79997.1	-11786.2
46	2933.179	2	12.25	36.1866	64280.6	-76353.6	-12073.0
44	2974.837	2	12.25	36.69691	60422.2	-72710.2	-12288.0
42	3016.495	2	12.25	37.20722	56636.7	-69066.8	-12430.1
40	3058.153	2	12.25	37.71753	52925.1	-65423.3	-12498.3
38	3099.811	2	12.25	38.22784	49288.4	-61779.9	-12491.5
36	3141.469	2	12.25	38.73815	45727.6	-58136.5	-12408.8
34	3183.127	2	12.25	39.24847	42243.8	-54493.0	-12249.2
32	3224.785	2	12.25	39.75878	38838.0	-50849.6	-12011.6
30	3266.443	2	12.25	40.26909	35511.3	-47206.2	-11694.9
28	3308.101	2	12.25	40.7794	32264.5	-43562.8	-11298.3
26	3349.76	2	12.25	41.28971	29098.8	-39919.3	-10820.5
24	3391.418	2	12.25	41.80002	26015.1	-36275.9	-10260.8
22	3433.076	2	12.25	42.31033	23014.6	-32632.5	-9617.9
20	3474.734	2	12.25	42.82064	20098.1	-28989.0	-8890.9
18	3516.392	2	12.25	43.33095	17266.8	-25345.6	-8078.8
16	3558.05	2	12.25	43.84126	14521.7	-21702.2	-7180.5
14	3599.708	2	12.64	45.76359	11863.7	-18058.7	-6195.1
12	3641.366	2	18.75	68.66615	9295.3	-14415.3	-5120.0
10	3683.024	2	31.81	117.8196	6841.3	-10771.9	-3930.6
8	3724.682	2	54.88	205.5536	4573.9	-7128.5	-2554.6
6	3766.34	2	74.52	282.2198	2629.8	-3801.8	-1172.1
4	3807.998	2	76.75	293.8625	1173.4	-1267.3	-93.8
2	3849.656	2	75.75	293.1892	293.2	0.0	293.2
0	3891.314	0	0	0	0.0	0.0	0.0

Appendix H

Strut-&-Tie Model @ h = 100 in.


Department of Civil & Environmental Engineering		By Amir A. Arab, P.E.	 THE GEORGE WASHINGTON UNIVERSITY
Subject		Date 12/11/2011	
Appendix H STRUT-&TIE MODEL @ h = 100 in.		CRN	
		Course No. CEE 399	
		Professor Dr. Badie/Dr. Manzari	

**Detail Analysis Based on Location of All Strands
@ h = 100 in.**


h (in.)	σ_c (psi)	$h_{c,i}$ (in.)	A_c (in. ²)	F_c (kips)	M_c (in.-kips)	M_{pi} (in.-kips)	M_{max} (in.-kips)	ΣF_c (kips)
100	-1640.94	2	98	-163.171	-198276.5	-190725.6	-389002.2	-3124.7
98	-1689.07	2	91.85	-157.352	-192190.4	-184468.4	-376658.8	-2961.5
96	-1737.2	2	48.83	-86.0025	-186424.7	-178844.9	-365269.6	-2804.1
94	-1785.33	2	20.25	-36.6402	-180902.4	-173379.7	-354282.2	-2718.1
92	-1833.46	2	13.25	-24.6121	-175502.8	-168073.0	-343575.8	-2681.5
90	-1881.58	2	12.25	-23.3442	-170164.4	-162924.7	-333089.1	-2656.9
88	-1929.71	2	12.25		-164873.9	-157934.8	-322808.7	-2633.5
86	-1977.84	2	12.25	-24.5233	-159630.8	-153103.3	-312734.0	-2609.6
84	-2025.97	2	12.25	-25.1129	-154436.1	-148430.2	-302866.2	-2585.1
82	-2074.09	2	12.25	-25.7024	-149291.0	-143915.5	-293206.5	-2560.0
80	-2122.22	2	12.25	-26.292	-144196.7	-139559.2	-283755.9	-2534.3
78	-2170.35	2	12.25	-26.8816	-139154.5	-135361.3	-274515.8	-2508.0
76	-2218.48	2	12.25	-27.4711	-134165.4	-131321.9	-265487.3	-2481.1
74	-2266.6	2	12.25	-28.0607	-129230.6	-127440.8	-256671.5	-2453.6
72	-2314.73	2	12.25	-28.6502	-124351.4	-123718.2	-248069.6	-2425.6
70	-2362.86	2	12.25	-29.2398	-119528.9	-120074.8	-239603.7	-2396.9
68	-2410.99	2	12.25	-29.8294	-114764.3	-116431.4	-231195.7	-2367.7
66	-2459.11	2	12.25	-30.4189	-110058.8	-112787.9	-222846.7	-2337.9
64	-2507.24	2	12.25	-31.0085	-105413.5	-109144.5	-214558.0	-2307.4
62	-2555.37	2	12.25	-31.5981	-100829.7	-105501.1	-206330.7	-2276.4
60	-2603.5	2	12.25	-32.1876	-96308.4	-101857.6	-198166.0	-2244.8
58	-2651.62	2	12.25	-32.7772	-91851.0	-98214.2	-190065.2	-2212.6
56	-2699.75	2	12.25	-33.3668	-87458.5	-94570.8	-182029.2	-2179.9
54	-2747.88	2	12.25	-33.9563	-83132.1	-90927.3	-174059.4	-2146.5
52	-2796.01	2	12.25	-34.5459	-78873.1	-87283.9	-166157.0	-2112.5
50	-2844.14	2	12.25	-35.1354	-74682.5	-83640.5	-158323.0	-2078.0
48	-2892.26	2	12.25	-35.725	-70561.7	-79997.1	-150558.7	-2042.9
46	-2940.39	2	12.25	-36.3146	-66511.7	-76353.6	-142865.3	-2007.1
44	-2988.52	2	12.25	-36.9041	-62533.7	-72710.2	-135243.9	-1970.8
42	-3036.65	2	12.25	-37.4937	-58629.0	-69066.8	-127695.8	-1933.9
40	-3084.77	2	12.25	-38.0833	-54798.7	-65423.3	-120222.0	-1896.4
38	-3132.9	2	12.25	-38.6728	-51043.9	-61779.9	-112823.8	-1858.3
36	-3181.03	2	12.25	-39.2624	-47365.9	-58136.5	-105502.4	-1819.7
34	-3229.16	2	12.25	-39.8519	-43765.9	-54493.0	-98258.9	-1780.4
32	-3277.28	2	12.25	-40.4415	-40244.9	-50849.6	-91094.5	-1740.5
30	-3325.41	2	12.25	-41.0311	-36804.2	-47206.2	-84010.4	-1700.1
28	-3373.54	2	12.25	-41.6206	-33445.1	-43562.8	-77007.8	-1659.1
26	-3421.67	2	12.25	-42.2102	-30168.5	-39919.3	-70087.8	-1617.5
24	-3469.79	2	12.25	-42.7998	-26975.8	-36275.9	-63251.7	-1575.2
22	-3517.92	2	12.25	-43.3893	-23868.1	-32632.5	-56500.6	-1532.4
20	-3566.05	2	12.25	-43.9789	-20846.6	-28989.0	-49835.7	-1489.1
18	-3614.18	2	12.25	-44.5685	-17912.5	-25345.6	-43258.1	-1445.1
16	-3662.3	2	12.25	-45.158	-15066.9	-21702.2	-36769.1	-1400.5
14	-3710.43	2	12.64	-47.204	-12311.0	-18058.7	-30369.8	-1355.4
12	-3758.56	2	18.75	-70.9242	-9647.5	-14415.3	-24062.9	-1308.1
10	-3806.69	2	31.81	-121.856	-7102.2	-10771.9	-17874.1	-1237.2
8	-3854.82	2	54.88	-212.873	-4749.6	-7128.5	-11878.0	-1115.4
6	-3902.94	2	74.52	-292.641	-2731.7	-3801.8	-6533.6	-902.5
4	-3951.07	2	76.75	-305.092	-1219.4	-1267.3	-2486.7	-609.9
2	-3999.2	2	75.75	-304.762	-304.8	0.0	-304.8	-304.8
0	-4047.33	0	0	0	0.0	0.0	0.0	0.0

Appendix I


Shear-Friction Model @ $h = 100$ in.

Department of Civil & Environmental Engineering		By Amir A. Arab, P.E.	 THE GEORGE WASHINGTON UNIVERSITY
Subject		Date 12/11/2011	
Appendix I SHEAR-FRICTION @ h = 100 in.		CRN	
		Course No. CEE 399 Professor Dr. Badie/Dr. Manzari	


CALCULATION OF A_{vf}						
Rebar Index	$\Delta_{End\ Face}$ in.	Spacing		N	A_{vf} (in. ²)	
		Index	in.		Area (Each)	Area (Total)
1	3	0	3	2	0.62	0.62
2	5.5	0	2.5	2	0.62	1.24
3	8	0	2.5	2	0.62	1.86
4	10.5	0	2.5	2	0.62	2.48
5	13	0	2.5	2	0.62	3.1
6	15.5	0	2.5	2	0.62	3.72
7	18	0	2.5	2	0.62	4.34
8	20.5	0	2.5	2	0.62	4.96
9	23	0	2.5	2	0.62	5.58
10	25.5	0	2.5	2	0.62	6.2
11	28	0	2.5	2	0.62	6.82
12	33	0	5	2	0.62	7.44
13	38	1	5	2	0.62	8.06
14	43	2	5	2	0.62	8.68
15	48	3	5	2	0.62	9.3
16	53	4	5	2	0.62	9.92
17	58	5	5	2	0.62	10.54
18	63	6	5	2	0.62	11.16
19	68	7	5	2	0.62	11.78
20	73	8	5	2	0.62	12.4
21	78	9	5	2	0.62	13.02
22	83	10	5	2	0.62	13.64
23	88	11	5	2	0.62	14.26
24	93	12	5	2	0.62	14.88
25	98	13	5	2	0.62	15.5
26	103	14	5	2	0.62	16.12
27	108	15	5	2	0.62	16.74
28	113	16	5	2	0.62	17.36
29	118	17	5	2	0.62	17.98
30	123	18	5	2	0.62	18.6
31	128	19	5	2	0.62	19.22
32	134	0	6	2	0.62	19.84
33	150.5	0	16.5	2	0.62	20.46
34	168.5	1	18	2	0.62	21.08
35	186.5	2	18	2	0.62	21.7
36	204.5	3	18	2	0.62	22.32
37	222.5	4	18	2	0.62	22.94
38	240.5	5	18	2	0.62	23.56
39	258.5	6	18	2	0.62	24.18
40	276.5	7	18	2	0.62	24.8
41	294.5	8	18	2	0.62	25.42
42	312.5	9	18	2	0.62	26.04
43	330.5	10	18	2	0.62	26.66
44	348.5	11	18	2	0.62	27.28
45	366.5	12	18	2	0.62	27.9
46	384.5	13	18	2	0.62	28.52
47	402.5	14	18	2	0.62	29.14
48	420.5	15	18	2	0.62	29.76
49	438.5	16	18	2	0.62	30.38
50	456.5	17	18	2	0.62	31
51	474.5	18	18	2	0.62	31.62
52	492.5	19	18	2	0.62	32.24

Department of Civil & Environmental Engineering		By Amir A. Arab, P.E.	
Subject		Date 12/11/2011	
Appendix I SHEAR-FRICTION @ h = 100 in.		CRN	
		Course No. CEE 399 Professor Dr. Badie/Dr. Manzari	


CALCULATION OF A_{vf}						
Rebar Index	$\Delta_{End\ Face}$ in.	Spacing		N	A_{vf} (in. ²)	
		Index	in.		Area (Each)	Area (Total)
1	3	0	3	2	0.62	0.62
53	510.5	20	18	2	0.62	32.86
54	528.5	21	18	2	0.62	33.48
55	546.5	22	18	2	0.62	34.1
56	564.5	23	18	2	0.62	34.72
57	582.5	24	18	2	0.62	35.34
58	600.5	25	18	2	0.62	35.96
59	618.5	26	18	2	0.62	36.58
60	636.5	27	18	2	0.62	37.2
61	654.5	28	18	2	0.62	37.82
62	672.5	29	18	2	0.62	38.44
63	690.5	30	18	2	0.62	39.06
64	708.5	31	18	2	0.62	39.68
65	726.5	32	18	2	0.62	40.3
66	744.5	33	18	2	0.62	40.92
67	762.5	34	18	2	0.62	41.54
68	780.5	35	18	2	0.62	42.16
69	798.5	36	18	2	0.62	42.78
70	816.5	37	18	2	0.62	43.4
71	834.5	38	18	2	0.62	44.02
72	852.5	39	18	2	0.62	44.64
73	870.5	40	18	2	0.62	45.26
74	888.5	41	18	2	0.62	45.88
75	906.5	42	18	2	0.62	46.5
76	924.5	43	18	2	0.62	47.12
77	942.5	44	18	2	0.62	47.74
78	960.5	45	18	2	0.62	48.36
79	978.5	46	18	2	0.62	48.98
80	996.5	47	18	2	0.62	49.6
81	1014.5	48	18	2	0.62	50.22
82	1032.5	49	18	2	0.62	50.84
83	1050.5	50	18	2	0.62	51.46
84	1068.5	51	18	2	0.62	52.08
85	1086.5	52	18	2	0.62	52.7
86	1104.5	53	18	2	0.62	53.32
87	1122.5	54	18	2	0.62	53.94
88	1140.5	55	18	2	0.62	54.56
89	1158.5	56	18	2	0.62	55.18
90	1176.5	57	18	2	0.62	55.8
91	1194.5	58	18	2	0.62	56.42
92	1212.5	59	18	2	0.62	57.04
93	1230.5	60	18	2	0.62	57.66
94	1248.5	61	18	2	0.62	58.28
95	1266.5	62	18	2	0.62	58.9
96	1284.5	63	18	2	0.62	59.52
97	1302.5	64	18	2	0.62	60.14
98	1320.5	65	18	2	0.62	60.76
99	1338.5	66	18	2	0.62	61.38
100	1356.5	67	18	2	0.62	62
101	1374.5	68	18	2	0.62	62.62
102	1392.5	69	18	2	0.62	63.24
103	1410.5	70	18	2	0.62	63.86
104	1428.5	71	18	2	0.62	64.48
105	1446.5	72	18	2	0.62	65.1
106	1464.5	73	18	2	0.62	65.72

Department of Civil & Environmental Engineering		By Amir A. Arab, P.E.	 THE GEORGE WASHINGTON UNIVERSITY
Subject		Date 12/11/2011	
Appendix I SHEAR-FRICTION @ h = 100 in.		CRN	
		Course No. CEE 399 Professor Dr. Badie/Dr. Manzari	

CALCULATION OF A_{vf}						
Rebar Index	$\Delta_{End\ Face}$ in.	Spacing		N	A_{vf} (in. ²)	
		Index	in.		Area (Each)	Area (Total)
1	3	0	3	2	0.62	0.62
107	1482.5	74	18	2	0.62	66.34
108	1500.5	75	18	2	0.62	66.96
109	1518.5	76	18	2	0.62	67.58
110	1536.5	77	18	2	0.62	68.2
111	1554.5	78	18	2	0.62	68.82
112	1572.5	79	18	2	0.62	69.44
113	1590.5	80	18	2	0.62	70.06
114	1608.5	81	18	2	0.62	70.68
115	1626.5	82	18	2	0.62	71.3
116	1644.5	83	18	2	0.62	71.92
117	1662.5	84	18	2	0.62	72.54
118	1680.5	85	18	2	0.62	73.16
119	1698.5	86	18	2	0.62	73.78
120	1716.5	87	18	2	0.62	74.4
121	1734.5	88	18	2	0.62	75.02
122	1752.5	89	18	2	0.62	75.64
123	1770.5	90	18	2	0.62	76.26
124	1788.5	91	18	2	0.62	76.88
125	1806.5	92	18	2	0.62	77.5
126	1824.5	93	18	2	0.62	78.12
127	1842.5	94	18	2	0.62	78.74
128	1860.5	95	18	2	0.62	79.36
129	1878.5	96	18	2	0.62	79.98
130	1896.5	97	18	2	0.62	80.6
131	1914.5	98	18	2	0.62	81.22
132	1932.5	99	18	2	0.62	81.84
133	1950.5	100	18	2	0.62	82.46
134	1968.5	101	18	2	0.62	83.08
135	1986.5	102	18	2	0.62	83.7
136	2004.5	103	18	2	0.62	84.32
137	2022.5	104	18	2	0.62	84.94
138	2040.5	105	18	2	0.62	85.56
139	2058.5	106	18	2	0.62	86.18
140	2076.5	107	18	2	0.62	86.8
141	2094.5	108	18	2	0.62	87.42
142	2112.5	109	18	2	0.62	88.04
143	2130.5	110	18	2	0.62	88.66
144	2148.5	111	18	2	0.62	89.28
145	2166.5	112	18	2	0.62	89.9
146	2184.5	113	18	2	0.62	90.52
147	2202.5	114	18	2	0.62	91.14
148	2220.5	115	18	2	0.62	91.76
149	2238.5	116	18	2	0.62	92.38
150	2256.5	117	18	2	0.62	93
151	2274.5	118	18	2	0.62	93.62
152	2292.5	119	18	2	0.62	94.24
153	2310.5	120	18	2	0.62	94.86
154	2328.5	121	18	2	0.62	95.48
155	2334.5	0	6	2	0.62	96.1
156	2339.5	1	5	2	0.62	96.72
157	2344.5	2	5	2	0.62	97.34
158	2349.5	3	5	2	0.62	97.96
159	2354.5	4	5	2	0.62	98.58
160	2359.5	5	5	2	0.62	99.2

Department of Civil & Environmental Engineering		By Amir A. Arab, P.E.	
Subject		Date 12/11/2011	
Appendix I SHEAR-FRICTION @ h = 100 in.		CRN	
		Course No. CEE 399	
		Professor Dr. Badie/Dr. Manzari	

CALCULATION OF A_{vf}						
Rebar Index	$\Delta_{End\ Face}$ in.	Spacing		N	A_{vf} (in. ²)	
		Index	in.		Area (Each)	Area (Total)
1	3	0	3	2	0.62	0.62
161	2364.5	6	5	2	0.62	99.82
162	2369.5	7	5	2	0.62	100.44
163	2374.5	8	5	2	0.62	101.06
164	2379.5	9	5	2	0.62	101.68
165	2384.5	10	5	2	0.62	102.3
166	2389.5	11	5	2	0.62	102.92
167	2394.5	12	5	2	0.62	103.54
168	2399.5	13	5	2	0.62	104.16
169	2404.5	14	5	2	0.62	104.78
170	2409.5	15	5	2	0.62	105.4
171	2414.5	16	5	2	0.62	106.02
172	2419.5	17	5	2	0.62	106.64
173	2424.5	18	5	2	0.62	107.26
174	2429.5	19	5	2	0.62	107.88
175	2434.5	0	5	2	0.62	108.5
176	2437	1	2.5	2	0.62	109.12
177	2439.5	2	2.5	2	0.62	109.74
178	2442	3	2.5	2	0.62	110.36
179	2444.5	4	2.5	2	0.62	110.98
180	2447	5	2.5	2	0.62	111.6
181	2449.5	6	2.5	2	0.62	112.22
182	2452	7	2.5	2	0.62	112.84
183	2454.5	8	2.5	2	0.62	113.46
184	2457	9	2.5	2	0.62	114.08
185	2459.5	10	2.5	2	0.62	114.7

Department of Civil & Environmental Engineering	By	Amir A. Arab, P.E.	 THE GEORGE WASHINGTON UNIVERSITY
	Date	12/11/2011	
Subject	CRN		
	Course No.	CEE 399	
Appendix I SHEAR-FRICTION @ h = 100 in.		Professor	Dr. Badie/Dr. Manzari

Shear Friction Theory

Ref.: AASHTO LRFD Article 5.8.4.1

The nominal shear resistance at the interface between the web and top of bottom flange is as follows:

$$V_{ni} = cA_{cv} + \mu (A_{vf} f_y + P_c) \leq K_1 f_c A_{cv} \leq K_2 A_{cv}$$

Where for concrete placed monolithically,

$$\begin{aligned} c &= 0.000 \text{ ksi} \\ \mu &= 1.400 \\ K_1 &= 0.250 \\ K_2 &= 1.500 \text{ ksi} \\ P_c &= 16.111 \text{ kips} \end{aligned}$$


	L_{cv}		A_{cv}	A_{vf}	P_c	$V_{n,1}$	$V_{n,2}$	$V_{n,3}$	V_n
	%h	in.	in. ²	in. ²	kips	kips	kips	kips	kips
@ Release	100%	100	612.500	15.500	0.0	1302.0	1225.0	918.8	918.8

SHEAR DUE TO STRESS DIAGRAM	
ΔV_{shear}	513.6 kips
f_{vsj}	23.7 ksi
$f_{allowable}$	20.0 ksi
C/D	1.18 ksi

$$\begin{aligned} \Leftrightarrow \Sigma F_c &= -1308.15 \text{ kips @ } h = 12 \text{ in.} \\ &\text{(From Appendix E)} \\ P_{i, \text{straight}} &= 1821.72 \\ \Delta V_{\text{compression}} &= P_i - \Sigma F_c \\ &= 513.6 \end{aligned}$$

Appendix J


Theoretical Stress Profile Based on Linear-Elastic Beam Theory

Department of Civil & Environmental Engineering		By Amir A. Arab, P.E.	 THE GEORGE WASHINGTON UNIVERSITY
		Date 1/15/2012	
Subject Appendix J Stress Profile (Linear-Elastic Beam Theory)		CRN	
		Course No. CEE 399	
		Professor Dr. Badie/Dr. Manzari	

Longitudinal Stress Profile Due to Self-Weight


x (ft)	V _{DL} (Ins.)	M _{DL} (lbs-in.)	σ_b^{DL} (psi)	σ_t^{DL} (psi)
0.00	0	0	0.00	0.00
1.04	1294	-62092	-1.96	2.10
2.08	2587	-124183	-3.92	4.21
3.00	3725	-178824	-5.65	6.06
4.17	5174	-248366	-7.84	8.42
8.33	-117069	-7761	-0.25	0.26
9.00	-116241	925476	29.23	-31.37
10.00	-114999	2312913	73.04	-78.41
11.00	-113757	3685448	116.39	-124.93
12.00	-112515	5043081	159.26	-170.95
13.00	-111273	6385813	201.66	-216.47
14.00	-110032	7713642	243.60	-261.48
15.00	-108790	9026569	285.06	-305.99
16.00	-107548	10324595	326.05	-349.99
17.00	-106306	11607718	366.57	-393.49
18.00	-105064	12875939	406.62	-436.48
19.00	-103822	14129259	446.20	-478.97
20.00	-102581	15367676	485.31	-520.95
21.00	-101339	16591191	523.95	-562.42
22.00	-100097	17799805	562.12	-603.39
23.00	-98855	18993516	599.82	-643.86
24.00	-97613	20172325	637.04	-683.82
25.00	-96371	21336233	673.80	-723.27
26.00	-95130	22485238	710.09	-762.22
27.00	-93888	23619342	745.90	-800.67
28.00	-92646	24738543	781.25	-838.61
29.00	-91404	25842843	816.12	-876.04
30.00	-90162	26932240	850.52	-912.97
31.00	-88920	28006736	884.46	-949.40
32.00	-87679	29066329	917.92	-985.32
33.00	-86437	30111021	950.91	-1020.73
34.00	-85195	31140810	983.43	-1055.64
35.00	-83953	32155698	1015.48	-1090.04
36.00	-82711	33155683	1047.06	-1123.94
37.00	-81469	34140767	1078.17	-1157.33
38.00	-80228	35110948	1108.81	-1190.22
39.00	-78986	36066228	1138.98	-1222.60
40.00	-77744	37006605	1168.67	-1254.48
41.00	-76502	37932081	1197.90	-1285.86
42.00	-75260	38842655	1226.66	-1316.72
43.00	-74018	39738326	1254.94	-1347.08
44.00	-72777	40619096	1282.76	-1376.94
45.00	-71535	41484963	1310.10	-1406.29
46.00	-70293	42335929	1336.97	-1435.14
47.00	-69051	43171993	1363.38	-1463.48
48.00	-67809	43993154	1389.31	-1491.32
49.00	-66567	44799414	1414.77	-1518.65
50.00	-65326	45590772	1439.76	-1545.48
51.00	-64084	46367228	1464.28	-1571.80
52.00	-62842	47128781	1488.33	-1597.61
53.00	-61600	47875433	1511.91	-1622.92
54.00	-60358	48607183	1535.02	-1647.73
55.00	-59116	49324030	1557.66	-1672.03
56.00	-57875	50025976	1579.83	-1695.82
57.00	-56633	50713020	1601.52	-1719.11
58.00	-55391	51385162	1622.75	-1741.90

BUNKED @ 8.0000 ft from each end face
 Bunk_Left @ 8.00000 ft
 Bunk_Right @ 197.2083 ft

Department of Civil & Environmental Engineering		By Amir A. Arab, P.E.	 THE GEORGE WASHINGTON UNIVERSITY
		Date 1/15/2012	
Subject Appendix J Stress Profile (Linear-Elastic Beam Theory)		CRN	
		Course No. CEE 399	
		Professor Dr. Badie/Dr. Manzari	


Longitudinal Stress Profile Due to Self-Weight

x (ft)	V _{DL} (Ins.)	M _{DL} (lbs-in.)	σ_b^{DL} (psi)	σ_t^{DL} (psi)
59.00	-54149	52042402	1643.50	-1764.18
60.00	-52907	52684739	1663.79	-1785.95
61.00	-51665	53312175	1683.60	-1807.22
62.00	-50424	53924709	1702.95	-1827.99
63.00	-49182	54522341	1721.82	-1848.25
64.00	-47940	55105071	1740.22	-1868.00
65.00	-46698	55672899	1758.16	-1887.25
66.00	-45456	56225824	1775.62	-1905.99
67.00	-44214	56763848	1792.61	-1924.23
68.00	-42973	57286970	1809.13	-1941.96
69.00	-41731	57795190	1825.18	-1959.19
70.00	-40489	58288508	1840.76	-1975.92
71.00	-39247	58766924	1855.87	-1992.13
72.00	-38005	59230438	1870.50	-2007.85
73.00	-36763	59679050	1884.67	-2023.05
74.00	-35522	60112760	1898.37	-2037.76
75.00	-34280	60531568	1911.59	-2051.95
76.00	-33038	60935474	1924.35	-2065.64
77.00	-31796	61324478	1936.63	-2078.83
78.00	-30554	61698580	1948.45	-2091.51
79.00	-29312	62057780	1959.79	-2103.69
80.00	-28071	62402078	1970.66	-2115.36
82.00	-25587	63045968	1991.00	-2137.19
82.08	-25483	63071503	1991.81	-2138.05
83.00	-24345	63345560	2000.46	-2147.34
84.00	-23103	63630250	2009.45	-2156.99
85.00	-21861	63900038	2017.97	-2166.14
86.00	-20620	64154924	2026.02	-2174.78
87.00	-19378	64394908	2033.60	-2182.92
88.00	-18136	64619991	2040.71	-2190.55
89.00	-16894	64830171	2047.34	-2197.67
90.00	-15652	65025449	2053.51	-2204.29
91.00	-14410	65205825	2059.21	-2210.40
92.00	-13169	65371299	2064.43	-2216.01
93.00	-11927	65521871	2069.19	-2221.12
94.00	-10685	65657542	2073.47	-2225.72
95.00	-9443	65778310	2077.29	-2229.81
96.00	-8201	65884176	2080.63	-2233.40
97.00	-6959	65975140	2083.50	-2236.48
98.00	-5718	66051202	2085.90	-2239.06
99.00	-4476	66112363	2087.84	-2241.14
100.00	-3234	66158621	2089.30	-2242.70
101.00	-1992	66189977	2090.29	-2243.77
102.00	-750	66206431	2090.81	-2244.32
102.60	0	66209151	2090.89	-2244.42

Department of Civil & Environmental Engineering		By Amir A. Arab, P.E.	 THE GEORGE WASHINGTON UNIVERSITY
Subject		Date 1/15/2012	
Appendix J Stress Profile (Linear-Elastic Beam Theory)		CRN	
		Course No. CEE 399 Professor Dr. Badie/Dr. Manzari	


Longitudinal Stress Profile Due to Pretensioning (Straight & Temporary Strands Only)

x (in.)	f _{pi, straight} (psi)	P _{i, straight} (lbs)	e _{p, straight} (in.)	P _{L, temp} (lbs)	e _{p, temp} (in.)	P/A (psi)	P e (lb-in.)	σ _b ^P (psi)	σ _t ^P (psi)
0.0	0.0	0	44.1	0.0	-49.8	0.0	0	0.0	0.0
12.5	63368.1	632540	44.1	110006.9	-49.8	685.1	22446761	-1394.0	75.8
25.0	126736.1	1265080	44.1	220013.9	-49.8	1370.3	44893523	-2788.0	151.6
36.0	182500.0	1821715	44.1	316820.0	-49.8	1973.2	64646673	-4014.8	218.2
50.0	182500.0	1821715	44.1	316820.0	-49.8	1973.2	64646673	-4014.8	218.2
100.0	182500.0	1821715	44.1	316820.0	-49.8	1973.2	64646673	-4014.8	218.2
108.0	182500.0	1821715	44.1	316820.0	-49.8	1973.2	64646673	-4014.8	218.2
120.0	182500.0	1821715	44.1	316820.0	-49.8	1973.2	64646673	-4014.8	218.2
132.0	182500.0	1821715	44.1	316820.0	-49.8	1973.2	64646673	-4014.8	218.2
144.0	182500.0	1821715	44.1	316820.0	-49.8	1973.2	64646673	-4014.8	218.2
156.0	182500.0	1821715	44.1	316820.0	-49.8	1973.2	64646673	-4014.8	218.2
168.0	182500.0	1821715	44.1	316820.0	-49.8	1973.2	64646673	-4014.8	218.2
180.0	182500.0	1821715	44.1	316820.0	-49.8	1973.2	64646673	-4014.8	218.2
192.0	182500.0	1821715	44.1	316820.0	-49.8	1973.2	64646673	-4014.8	218.2
204.0	182500.0	1821715	44.1	316820.0	-49.8	1973.2	64646673	-4014.8	218.2
216.0	182500.0	1821715	44.1	316820.0	-49.8	1973.2	64646673	-4014.8	218.2
228.0	182500.0	1821715	44.1	316820.0	-49.8	1973.2	64646673	-4014.8	218.2
240.0	182500.0	1821715	44.1	316820.0	-49.8	1973.2	64646673	-4014.8	218.2
252.0	182500.0	1821715	44.1	316820.0	-49.8	1973.2	64646673	-4014.8	218.2
264.0	182500.0	1821715	44.1	316820.0	-49.8	1973.2	64646673	-4014.8	218.2
276.0	182500.0	1821715	44.1	316820.0	-49.8	1973.2	64646673	-4014.8	218.2
288.0	182500.0	1821715	44.1	316820.0	-49.8	1973.2	64646673	-4014.8	218.2
300.0	182500.0	1821715	44.1	316820.0	-49.8	1973.2	64646673	-4014.8	218.2
312.0	182500.0	1821715	44.1	316820.0	-49.8	1973.2	64646673	-4014.8	218.2
324.0	182500.0	1821715	44.1	316820.0	-49.8	1973.2	64646673	-4014.8	218.2
336.0	182500.0	1821715	44.1	316820.0	-49.8	1973.2	64646673	-4014.8	218.2
348.0	182500.0	1821715	44.1	316820.0	-49.8	1973.2	64646673	-4014.8	218.2
360.0	182500.0	1821715	44.1	316820.0	-49.8	1973.2	64646673	-4014.8	218.2
372.0	182500.0	1821715	44.1	316820.0	-49.8	1973.2	64646673	-4014.8	218.2
384.0	182500.0	1821715	44.1	316820.0	-49.8	1973.2	64646673	-4014.8	218.2
396.0	182500.0	1821715	44.1	316820.0	-49.8	1973.2	64646673	-4014.8	218.2
408.0	182500.0	1821715	44.1	316820.0	-49.8	1973.2	64646673	-4014.8	218.2
420.0	182500.0	1821715	44.1	316820.0	-49.8	1973.2	64646673	-4014.8	218.2
432.0	182500.0	1821715	44.1	316820.0	-49.8	1973.2	64646673	-4014.8	218.2
444.0	182500.0	1821715	44.1	316820.0	-49.8	1973.2	64646673	-4014.8	218.2
456.0	182500.0	1821715	44.1	316820.0	-49.8	1973.2	64646673	-4014.8	218.2
468.0	182500.0	1821715	44.1	316820.0	-49.8	1973.2	64646673	-4014.8	218.2
480.0	182500.0	1821715	44.1	316820.0	-49.8	1973.2	64646673	-4014.8	218.2
492.0	182500.0	1821715	44.1	316820.0	-49.8	1973.2	64646673	-4014.8	218.2
504.0	182500.0	1821715	44.1	316820.0	-49.8	1973.2	64646673	-4014.8	218.2
516.0	182500.0	1821715	44.1	316820.0	-49.8	1973.2	64646673	-4014.8	218.2
528.0	182500.0	1821715	44.1	316820.0	-49.8	1973.2	64646673	-4014.8	218.2
540.0	182500.0	1821715	44.1	316820.0	-49.8	1973.2	64646673	-4014.8	218.2
552.0	182500.0	1821715	44.1	316820.0	-49.8	1973.2	64646673	-4014.8	218.2
564.0	182500.0	1821715	44.1	316820.0	-49.8	1973.2	64646673	-4014.8	218.2
576.0	182500.0	1821715	44.1	316820.0	-49.8	1973.2	64646673	-4014.8	218.2
588.0	182500.0	1821715	44.1	316820.0	-49.8	1973.2	64646673	-4014.8	218.2
600.0	182500.0	1821715	44.1	316820.0	-49.8	1973.2	64646673	-4014.8	218.2
612.0	182500.0	1821715	44.1	316820.0	-49.8	1973.2	64646673	-4014.8	218.2
624.0	182500.0	1821715	44.1	316820.0	-49.8	1973.2	64646673	-4014.8	218.2
636.0	182500.0	1821715	44.1	316820.0	-49.8	1973.2	64646673	-4014.8	218.2
648.0	182500.0	1821715	44.1	316820.0	-49.8	1973.2	64646673	-4014.8	218.2
660.0	182500.0	1821715	44.1	316820.0	-49.8	1973.2	64646673	-4014.8	218.2
672.0	182500.0	1821715	44.1	316820.0	-49.8	1973.2	64646673	-4014.8	218.2
684.0	182500.0	1821715	44.1	316820.0	-49.8	1973.2	64646673	-4014.8	218.2
696.0	182500.0	1821715	44.1	316820.0	-49.8	1973.2	64646673	-4014.8	218.2

Department of Civil & Environmental Engineering		By Amir A. Arab, P.E.	 THE GEORGE WASHINGTON UNIVERSITY
Subject		Date 1/15/2012	
Appendix J Stress Profile (Linear-Elastic Beam Theory)		CRN	
		Course No. CEE 399 Professor Dr. Badie/Dr. Manzari	


Longitudinal Stress Profile Due to Pretensioning (Straight & Temporary Strands Only)

x (in.)	f _{pi, straight} (psi)	P _{i, straight} (lbs)	e _{p, straight} (in.)	P _{L, temp} (lbs)	e _{p, temp} (in.)	P/A (psi)	P e (lb-in.)	σ _b ^P (psi)	σ _t ^P (psi)
708.0	182500.0	1821715	44.1	316820.0	-49.8	1973.2	64646673	-4014.8	218.2
720.0	182500.0	1821715	44.1	316820.0	-49.8	1973.2	64646673	-4014.8	218.2
732.0	182500.0	1821715	44.1	316820.0	-49.8	1973.2	64646673	-4014.8	218.2
744.0	182500.0	1821715	44.1	316820.0	-49.8	1973.2	64646673	-4014.8	218.2
756.0	182500.0	1821715	44.1	316820.0	-49.8	1973.2	64646673	-4014.8	218.2
768.0	182500.0	1821715	44.1	316820.0	-49.8	1973.2	64646673	-4014.8	218.2
780.0	182500.0	1821715	44.1	316820.0	-49.8	1973.2	64646673	-4014.8	218.2
792.0	182500.0	1821715	44.1	316820.0	-49.8	1973.2	64646673	-4014.8	218.2
804.0	182500.0	1821715	44.1	316820.0	-49.8	1973.2	64646673	-4014.8	218.2
816.0	182500.0	1821715	44.1	316820.0	-49.8	1973.2	64646673	-4014.8	218.2
828.0	182500.0	1821715	44.1	316820.0	-49.8	1973.2	64646673	-4014.8	218.2
840.0	182500.0	1821715	44.1	316820.0	-49.8	1973.2	64646673	-4014.8	218.2
852.0	182500.0	1821715	44.1	316820.0	-49.8	1973.2	64646673	-4014.8	218.2
864.0	182500.0	1821715	44.1	316820.0	-49.8	1973.2	64646673	-4014.8	218.2
876.0	182500.0	1821715	44.1	316820.0	-49.8	1973.2	64646673	-4014.8	218.2
888.0	182500.0	1821715	44.1	316820.0	-49.8	1973.2	64646673	-4014.8	218.2
900.0	182500.0	1821715	44.1	316820.0	-49.8	1973.2	64646673	-4014.8	218.2
912.0	182500.0	1821715	44.1	316820.0	-49.8	1973.2	64646673	-4014.8	218.2
924.0	182500.0	1821715	44.1	316820.0	-49.8	1973.2	64646673	-4014.8	218.2
936.0	182500.0	1821715	44.1	316820.0	-49.8	1973.2	64646673	-4014.8	218.2
948.0	182500.0	1821715	44.1	316820.0	-49.8	1973.2	64646673	-4014.8	218.2
960.0	182500.0	1821715	44.1	316820.0	-49.8	1973.2	64646673	-4014.8	218.2
984.0	182500.0	1821715	44.1	316820.0	-49.8	1973.2	64646673	-4014.8	218.2
985.0	182500.0	1821715	44.1	316820.0	-49.8	1973.2	64646673	-4014.8	218.2
996.0	182500.0	1821715	44.1	316820.0	-49.8	1973.2	64646673	-4014.8	218.2
1008.0	182500.0	1821715	44.1	316820.0	-49.8	1973.2	64646673	-4014.8	218.2
1020.0	182500.0	1821715	44.1	316820.0	-49.8	1973.2	64646673	-4014.8	218.2
1032.0	182500.0	1821715	44.1	316820.0	-49.8	1973.2	64646673	-4014.8	218.2
1044.0	182500.0	1821715	44.1	316820.0	-49.8	1973.2	64646673	-4014.8	218.2
1056.0	182500.0	1821715	44.1	316820.0	-49.8	1973.2	64646673	-4014.8	218.2
1068.0	182500.0	1821715	44.1	316820.0	-49.8	1973.2	64646673	-4014.8	218.2
1080.0	182500.0	1821715	44.1	316820.0	-49.8	1973.2	64646673	-4014.8	218.2
1092.0	182500.0	1821715	44.1	316820.0	-49.8	1973.2	64646673	-4014.8	218.2
1104.0	182500.0	1821715	44.1	316820.0	-49.8	1973.2	64646673	-4014.8	218.2
1116.0	182500.0	1821715	44.1	316820.0	-49.8	1973.2	64646673	-4014.8	218.2
1128.0	182500.0	1821715	44.1	316820.0	-49.8	1973.2	64646673	-4014.8	218.2
1140.0	182500.0	1821715	44.1	316820.0	-49.8	1973.2	64646673	-4014.8	218.2
1152.0	182500.0	1821715	44.1	316820.0	-49.8	1973.2	64646673	-4014.8	218.2
1164.0	182500.0	1821715	44.1	316820.0	-49.8	1973.2	64646673	-4014.8	218.2
1176.0	182500.0	1821715	44.1	316820.0	-49.8	1973.2	64646673	-4014.8	218.2
1188.0	182500.0	1821715	44.1	316820.0	-49.8	1973.2	64646673	-4014.8	218.2
1200.0	182500.0	1821715	44.1	316820.0	-49.8	1973.2	64646673	-4014.8	218.2
1212.0	182500.0	1821715	44.1	316820.0	-49.8	1973.2	64646673	-4014.8	218.2
1224.0	182500.0	1821715	44.1	316820.0	-49.8	1973.2	64646673	-4014.8	218.2
1231.3	182500.0	1821715	44.1	316820.0	-49.8	1973.2	64646673	-4014.8	218.2

Department of Civil & Environmental Engineering		By Amir A. Arab, P.E.	 THE GEORGE WASHINGTON UNIVERSITY
Subject		Date 1/15/2012	
Appendix J Stress Profile (Linear-Elastic Beam Theory)		CRN	
		Course No. CEE 399 Professor Dr. Badie/Dr. Manzari	


Combined Longitudinal Stress Profile (Straight & Temporary Strands Only)

x (in.)	σ_b^{DL+P} (psi)	σ_t^{DL+P} (psi)
0	0	0
12.5	-1396	77.88014
25	-2792	155.7603
36	-4020	224.2948
50	-4023	226.6522
100	-4015	218.496
108	-3986	186.8603
120	-3942	139.8277
132	-3898	93.3003
144	-3856	47.27806
156	-3813	1.760972
168	-3771	-43.251
180	-3730	-87.7577
192	-3689	-131.759
204	-3648	-175.256
216	-3608	-218.247
228	-3569	-260.733
240	-3529	-302.714
252	-3491	-344.19
264	-3453	-385.161
276	-3415	-425.626
288	-3378	-465.586
300	-3341	-505.042
312	-3305	-543.992
324	-3269	-582.436
336	-3234	-620.376
348	-3199	-657.811
360	-3164	-694.74
372	-3130	-731.164
384	-3097	-767.083
396	-3064	-802.497
408	-3031	-837.406
420	-2999	-871.809
432	-2968	-905.708
444	-2937	-939.101
456	-2906	-971.989
468	-2876	-1004.37
480	-2846	-1036.25
492	-2817	-1067.62
504	-2788	-1098.49
516	-2760	-1128.85
528	-2732	-1158.71
540	-2705	-1188.06
552	-2678	-1216.91
564	-2651	-1245.25
576	-2625	-1273.09
588	-2600	-1300.42
600	-2575	-1327.24
612	-2550	-1353.56
624	-2526	-1379.38
636	-2503	-1404.69
648	-2480	-1429.5
660	-2457	-1453.8
672	-2435	-1477.59
684	-2413	-1500.88
696	-2392	-1523.67

Department of Civil & Environmental Engineering		By Amir A. Arab, P.E.	 <small>THE GEORGE WASHINGTON UNIVERSITY</small>
Subject		Date 1/15/2012	
Appendix J Stress Profile (Linear-Elastic Beam Theory)		CRN	
		Course No. CEE 399 Professor Dr. Badie/Dr. Manzari	


Combined Longitudinal Stress Profile (Straight & Temporary Strands Only)

x (in.)	σ_b^{DL+P} (psi)	σ_t^{DL+P} (psi)
708	-2371	-1545.95
720	-2351	-1567.72
732	-2331	-1588.99
744	-2312	-1609.75
756	-2293	-1630.01
768	-2275	-1649.77
780	-2257	-1669.02
792	-2239	-1687.76
804	-2222	-1706
816	-2206	-1723.73
828	-2190	-1740.96
840	-2174	-1757.68
852	-2159	-1773.9
864	-2144	-1789.61
876	-2130	-1804.82
888	-2116	-1819.52
900	-2103	-1833.72
912	-2090	-1847.41
924	-2078	-1860.6
936	-2066	-1873.28
948	-2055	-1885.46
960	-2044	-1897.13
984	-2023	-1919.82
985	-2024	-1918.95
996	-2014	-1929.11
1008	-2005	-1938.76
1020	-1997	-1947.91
1032	-1989	-1956.55
1044	-1981	-1964.68
1056	-1974	-1972.31
1068	-1967	-1979.44
1080	-1961	-1986.06
1092	-1956	-1992.17
1104	-1950	-1997.78
1116	-1946	-2002.89
1128	-1941	-2007.48
1140	-1937	-2011.58
1152	-1934	-2015.17
1164	-1931	-2018.25
1176	-1929	-2020.83
1188	-1927	-2022.9
1200	-1925	-2024.47
1212	-1924	-2025.53
1224	-1924	-2026.09
1231.25	-1924	-2026.18

Department of Civil & Environmental Engineering		By Amir A. Arab, P.E.	 THE GEORGE WASHINGTON UNIVERSITY
Subject Appendix J Stress Profile (Linear-Elastic Beam Theory)		Date 1/15/2012	
		CRN	
		Course No. CEE 399 Professor Dr. Badie/Dr. Manzari	


Longitudinal Stress Profile Due to Pretensioning (Draped Strands Only)

x (in.)	f _{pi,draped} (psi)	P _{i,draped} (lbs)	e _{p,draped} (in.)	P/A (psi)	P e (lb-in.)	σ _{b,draped} (psi)	σ _{t,draped} (psi)
0	0	0	-36.2506	0	0	0	0
12.5	63368.06	343771.7	-35.2423	317.1966	-1.2E+07	65.40569	-727.892
25	126736.1	687543.4	-34.234	634.3933	-2.4E+07	108.9182	-1432.28
36	182500	990062.5	-33.3466	913.5263	-3.3E+07	129.0992	-2032.71
50	182500	990062.5	-32.2173	913.5263	-3.2E+07	93.78986	-1994.8
100	182500	990062.5	-28.1841	913.5263	-2.8E+07	-32.3148	-1859.44
108	182500	990062.5	-27.5388	913.5263	-2.7E+07	-52.4916	-1837.78
120	182500	990062.5	-26.5708	913.5263	-2.6E+07	-82.7567	-1805.3
132	182500	990062.5	-25.6028	913.5263	-2.5E+07	-113.022	-1772.81
144	182500	990062.5	-24.6348	913.5263	-2.4E+07	-143.287	-1740.32
156	182500	990062.5	-23.6668	913.5263	-2.3E+07	-173.552	-1707.83
168	182500	990062.5	-22.6989	913.5263	-2.2E+07	-203.817	-1675.35
180	182500	990062.5	-21.7309	913.5263	-2.2E+07	-234.082	-1642.86
192	182500	990062.5	-20.7629	913.5263	-2.1E+07	-264.347	-1610.37
204	182500	990062.5	-19.7949	913.5263	-2E+07	-294.613	-1577.88
216	182500	990062.5	-18.8269	913.5263	-1.9E+07	-324.878	-1545.4
228	182500	990062.5	-17.859	913.5263	-1.8E+07	-355.143	-1512.91
240	182500	990062.5	-16.891	913.5263	-1.7E+07	-385.408	-1480.42
252	182500	990062.5	-15.923	913.5263	-1.6E+07	-415.673	-1447.93
264	182500	990062.5	-14.955	913.5263	-1.5E+07	-445.938	-1415.45
276	182500	990062.5	-13.987	913.5263	-1.4E+07	-476.203	-1382.96
288	182500	990062.5	-13.0191	913.5263	-1.3E+07	-506.469	-1350.47
300	182500	990062.5	-12.0511	913.5263	-1.2E+07	-536.734	-1317.99
312	182500	990062.5	-11.0831	913.5263	-1.1E+07	-566.999	-1285.5
324	182500	990062.5	-10.1151	913.5263	-1E+07	-597.264	-1253.01
336	182500	990062.5	-9.14715	913.5263	-9056249	-627.529	-1220.52
348	182500	990062.5	-8.17917	913.5263	-8097888	-657.794	-1188.04
360	182500	990062.5	-7.21119	913.5263	-7139528	-688.059	-1155.55
372	182500	990062.5	-6.24321	913.5263	-6181168	-718.324	-1123.06
384	182500	990062.5	-5.27523	913.5263	-5222807	-748.59	-1090.57
396	182500	990062.5	-4.30725	913.5263	-4264447	-778.855	-1058.09
408	182500	990062.5	-3.33927	913.5263	-3306086	-809.12	-1025.6
420	182500	990062.5	-2.37129	913.5263	-2347726	-839.385	-993.112
432	182500	990062.5	-1.40331	913.5263	-1389366	-869.65	-960.624
444	182500	990062.5	-0.43533	913.5263	-431005	-899.915	-928.137
456	182500	990062.5	0.532648	913.5263	527355.3	-930.18	-895.65
468	182500	990062.5	1.500628	913.5263	1485716	-960.445	-863.162
480	182500	990062.5	2.468608	913.5263	2444076	-990.711	-830.675
492	182500	990062.5	3.436588	913.5263	3402436	-1020.98	-798.188
504	182500	990062.5	4.404567	913.5263	4360797	-1051.24	-765.7
516	182500	990062.5	5.372547	913.5263	5319157	-1081.51	-733.213
528	182500	990062.5	6.340527	913.5263	6277518	-1111.77	-700.726
540	182500	990062.5	7.308506	913.5263	7235878	-1142.04	-668.238
552	182500	990062.5	8.276486	913.5263	8194238	-1172.3	-635.751
564	182500	990062.5	9.244466	913.5263	9152599	-1202.57	-603.264
576	182500	990062.5	10.21245	913.5263	10110959	-1232.83	-570.776
588	182500	990062.5	11.18043	913.5263	11069320	-1263.1	-538.289
600	182500	990062.5	12.1484	913.5263	12027680	-1293.36	-505.801
612	182500	990062.5	13.11638	913.5263	12986040	-1323.63	-473.314
624	182500	990062.5	14.08436	913.5263	13944401	-1353.89	-440.827
636	182500	990062.5	15.05234	913.5263	14902761	-1384.16	-408.339
648	182500	990062.5	16.02032	913.5263	15861122	-1414.42	-375.852
660	182500	990062.5	16.9883	913.5263	16819482	-1444.69	-343.365
672	182500	990062.5	17.95628	913.5263	17777842	-1474.95	-310.877
684	182500	990062.5	18.92426	913.5263	18736203	-1505.22	-278.39
696	182500	990062.5	19.89224	913.5263	19694563	-1535.48	-245.903

Department of Civil & Environmental Engineering		By Amir A. Arab, P.E.	 THE GEORGE WASHINGTON UNIVERSITY
Subject Appendix J Stress Profile (Linear-Elastic Beam Theory)		Date 1/15/2012	
		CRN	
		Course No. CEE 399 Professor Dr. Badie/Dr. Manzari	


Longitudinal Stress Profile Due to Pretensioning (Draped Strands Only)

x (in.)	f _{pi,draped} (psi)	P _{i,draped} (lbs)	e _{p,draped} (in.)	P/A (psi)	P e (lb-in.)	σ _b ^{P_draped} (psi)	σ _t ^{P_draped} (psi)
708	182500	990062.5	20.86022	913.5263	20652924	-1565.75	-213.415
720	182500	990062.5	21.8282	913.5263	21611284	-1596.01	-180.928
732	182500	990062.5	22.79618	913.5263	22569644	-1626.28	-148.441
744	182500	990062.5	23.76416	913.5263	23528005	-1656.54	-115.953
756	182500	990062.5	24.73214	913.5263	24486365	-1686.81	-83.466
768	182500	990062.5	25.70012	913.5263	25444726	-1717.07	-50.9787
780	182500	990062.5	26.6681	913.5263	26403086	-1747.34	-18.4913
792	182500	990062.5	27.63608	913.5263	27361446	-1777.6	13.99603
804	182500	990062.5	28.60406	913.5263	28319807	-1807.87	46.48337
816	182500	990062.5	29.57204	913.5263	29278167	-1838.13	78.97072
828	182500	990062.5	30.54002	913.5263	30236528	-1868.4	111.4581
840	182500	990062.5	31.508	913.5263	31194888	-1898.66	143.9454
852	182500	990062.5	32.47598	913.5263	32153248	-1928.93	176.4327
864	182500	990062.5	33.44396	913.5263	33111609	-1959.19	208.9201
876	182500	990062.5	34.41194	913.5263	34069969	-1989.46	241.4074
888	182500	990062.5	35.37992	913.5263	35028330	-2019.72	273.8948
900	182500	990062.5	36.3479	913.5263	35986690	-2049.99	306.3821
912	182500	990062.5	37.31588	913.5263	36945050	-2080.26	338.8695
924	182500	990062.5	38.28386	913.5263	37903411	-2110.52	371.3568
936	182500	990062.5	39.25184	913.5263	38861771	-2140.79	403.8442
948	182500	990062.5	40.21982	913.5263	39820132	-2171.05	436.3315
960	182500	990062.5	41.1878	913.5263	40778492	-2201.32	468.8188
984	182500	990062.5	43.12376	913.5263	42695213	-2261.85	533.7935
985	182500	990062.5	43.20442	913.5263	42775076	-2264.37	536.5008
996	182500	990062.5	43.20442	913.5263	42775076	-2264.37	536.5008
1008	182500	990062.5	43.20442	913.5263	42775076	-2264.37	536.5008
1020	182500	990062.5	43.20442	913.5263	42775076	-2264.37	536.5008
1032	182500	990062.5	43.20442	913.5263	42775076	-2264.37	536.5008
1044	182500	990062.5	43.20442	913.5263	42775076	-2264.37	536.5008
1056	182500	990062.5	43.20442	913.5263	42775076	-2264.37	536.5008
1068	182500	990062.5	43.20442	913.5263	42775076	-2264.37	536.5008
1080	182500	990062.5	43.20442	913.5263	42775076	-2264.37	536.5008
1092	182500	990062.5	43.20442	913.5263	42775076	-2264.37	536.5008
1104	182500	990062.5	43.20442	913.5263	42775076	-2264.37	536.5008
1116	182500	990062.5	43.20442	913.5263	42775076	-2264.37	536.5008
1128	182500	990062.5	43.20442	913.5263	42775076	-2264.37	536.5008
1140	182500	990062.5	43.20442	913.5263	42775076	-2264.37	536.5008
1152	182500	990062.5	43.20442	913.5263	42775076	-2264.37	536.5008
1164	182500	990062.5	43.20442	913.5263	42775076	-2264.37	536.5008
1176	182500	990062.5	43.20442	913.5263	42775076	-2264.37	536.5008
1188	182500	990062.5	43.20442	913.5263	42775076	-2264.37	536.5008
1200	182500	990062.5	43.20442	913.5263	42775076	-2264.37	536.5008
1212	182500	990062.5	43.20442	913.5263	42775076	-2264.37	536.5008
1224	182500	990062.5	43.20442	913.5263	42775076	-2264.37	536.5008
1231.25	182500	990062.5	43.20442	913.5263	42775076	-2264.37	536.5008

Department of Civil & Environmental Engineering		By Amir A. Arab, P.E.	 THE GEORGE WASHINGTON UNIVERSITY
Subject		Date 1/15/2012	
Appendix J Stress Profile (Linear-Elastic Beam Theory)		CRN	
		Course No. CEE 399 Professor Dr. Badie/Dr. Manzari	

Longitudinal Stress Profile Due to Combined Effects of Self-Weight & Pretensioning

x (in.)	σ_b^{DL+P} (psi)	σ_t^{DL+P} (psi)
0	0	0
12.5	-1330.57	-650.011
25	-2683.04	-1276.52
36	-3891.31	-1808.41
50	-3928.82	-1768.15
100	-4047.33	-1640.94
108	-4038.03	-1650.92
120	-4024.48	-1665.47
132	-4011.4	-1679.51
144	-3998.79	-1693.04
156	-3986.65	-1706.07
168	-3974.99	-1718.6
180	-3963.79	-1730.62
192	-3953.06	-1742.13
204	-3942.81	-1753.14
216	-3933.02	-1763.64
228	-3923.71	-1773.64
240	-3914.86	-1783.14
252	-3906.49	-1792.12
264	-3898.58	-1800.61
276	-3891.15	-1808.59
288	-3884.19	-1816.06
300	-3877.7	-1823.03
312	-3871.68	-1829.49
324	-3866.13	-1835.45
336	-3861.05	-1840.9
348	-3856.44	-1845.85
360	-3852.3	-1850.29
372	-3848.63	-1854.23
384	-3845.44	-1857.66
396	-3842.71	-1860.58
408	-3840.46	-1863
420	-3838.67	-1864.92
432	-3837.36	-1866.33
444	-3836.51	-1867.24
456	-3836.14	-1867.64
468	-3836.24	-1867.53
480	-3836.8	-1866.92
492	-3837.84	-1865.81
504	-3839.35	-1864.19
516	-3841.33	-1862.06
528	-3843.78	-1859.43
540	-3846.7	-1856.3
552	-3850.09	-1852.66
564	-3853.96	-1848.51
576	-3858.29	-1843.86
588	-3863.09	-1838.71
600	-3868.37	-1833.04
612	-3874.11	-1826.88
624	-3880.33	-1820.21
636	-3887.01	-1813.03
648	-3894.17	-1805.35
660	-3901.8	-1797.16
672	-3909.89	-1788.47
684	-3918.46	-1779.27
696	-3927.5	-1769.57

Department of Civil & Environmental Engineering		By Amir A. Arab, P.E.	 <small>THE GEORGE WASHINGTON UNIVERSITY</small>
Subject		Date 1/15/2012	
Appendix J Stress Profile (Linear-Elastic Beam Theory)		CRN	
		Course No. CEE 399	
		Professor Dr. Badie/Dr. Manzari	

Longitudinal Stress Profile Due to Combined Effects of Self-Weight & Pretensioning

x (in.)	σ_b^{DL+P} (psi)	σ_t^{DL+P} (psi)
708	-3937.01	-1759.36
720	-3946.99	-1748.65
732	-3957.44	-1737.43
744	-3968.36	-1725.71
756	-3979.75	-1713.48
768	-3991.62	-1700.75
780	-4003.95	-1687.51
792	-4016.75	-1673.76
804	-4030.03	-1659.51
816	-4043.77	-1644.76
828	-4057.99	-1629.5
840	-4072.67	-1613.74
852	-4087.83	-1597.47
864	-4103.46	-1580.69
876	-4119.55	-1563.41
888	-4136.12	-1545.63
900	-4153.16	-1527.34
912	-4170.67	-1508.54
924	-4188.65	-1489.24
936	-4207.1	-1469.44
948	-4226.02	-1449.12
960	-4245.42	-1428.31
984	-4285.61	-1385.16
985	-4287.33	-1383.32
996	-4278.67	-1392.61
1008	-4269.68	-1402.26
1020	-4261.16	-1411.41
1032	-4253.11	-1420.05
1044	-4245.54	-1428.18
1056	-4238.43	-1435.81
1068	-4231.79	-1442.94
1080	-4225.62	-1449.56
1092	-4219.93	-1455.67
1104	-4214.7	-1461.28
1116	-4209.95	-1466.38
1128	-4205.66	-1470.98
1140	-4201.85	-1475.08
1152	-4198.5	-1478.67
1164	-4195.63	-1481.75
1176	-4193.23	-1484.33
1188	-4191.3	-1486.4
1200	-4189.84	-1487.97
1212	-4188.85	-1489.03
1224	-4188.33	-1489.59
1231.25	-4188.24	-1489.68